Development of the Zinc-Chloride Battery for Utility Applications

EM-1417
Research Project 226-3

Interim Report, May 1980

Work Period
April 1, 1978–March 31, 1980

Prepared by

ENERGY DEVELOPMENT ASSOCIATES
A Gulf + Western Company
1100 W. Whitcomb Avenue
Madison Heights, Michigan 48071

Prepared for

Electric Power Research Institute
3412 Hillview Avenue
Palo Alto, California 94304

EPRI Project Manager
D. L. Douglas

Energy Storage Program
Energy Management and Utilization Division

DISTRIBUTION OF THIS DOCUMENT IS UNLIMITED

DISCLAIMER

This report was prepared as an account of work sponsored by an agency of the United States Government. Neither the United States Government nor any agency thereof, nor any of their employees, makes any warranty, express or implied, or assumes any legal liability or responsibility for the accuracy, completeness, or usefulness of any information, apparatus, product, or process disclosed, or represents that its use would not infringe privately owned rights. Reference herein to any specific commercial product, process, or service by trade name, trademark, manufacturer, or otherwise does not necessarily constitute or imply its endorsement, recommendation, or favoring by the United States Government or any agency thereof. The views and opinions of authors expressed herein do not necessarily state or reflect those of the United States Government or any agency thereof.

DISCLAIMER

Portions of this document may be illegible in electronic image products. Images are produced from the best available original document.

ORDERING INFORMATION

Requests for copies of this report should be directed to Research Reports Center (RRC), Box 50490, Palo Alto, CA 94303, (415) 965-4081. There is no charge for reports requested by EPRI member utilities and affiliates, contributing nonmembers, U.S. utility associations, U.S. government agencies (federal, state, and local), media, and foreign organizations with which EPRI has an information exchange agreement. On request, RRC will send a catalog of EPRI reports.

Copyright © 1980 Electric Power Research Institute, Inc.

EPRI authorizes the reproduction and distribution of all or any portion of this report and the preparation of any derivative work based on this report, in each case on the condition that any such reproduction, distribution, and preparation shall acknowledge this report and EPRI as the source.

NOTICE

This report was prepared by the organization(s) named below as an account of work sponsored by the Electric Power Research Institute, Inc. (EPRI). Neither EPRI, members of EPRI, the organization(s) named below, nor any person acting on their behalf: (a) makes any warranty or representation, express or implied, with respect to the accuracy, completeness, or usefulness of the information contained in this report, or that the use of any information, apparatus, method, or process disclosed in this report may not infringe privately owned rights; or (b) assumes any liabilities with respect to the use of, or for damages resulting from the use of, any information, apparatus, method, or process disclosed in this report.

Prepared by
Energy Development Associates
Madison Heights, Michigan

ABSTRACT

Energy storage in zinc-chloride load-leveling plants offers the prospect of more efficient use of baseload and intermediate generating capacity for electric utilities and the corresponding conservation of substantial quantities of oil otherwise consumed in turbine-peaking units. The technical feasibility of this battery for load-leveling was confirmed (RP226-1), successful scale-up to the 20-kWh level was demonstrated (RP226-2), and a 45- kWh integrated battery module -- the basic unit in the Mark 4 100-MWh plant design -- was built and tested (Phase I of RP226-3). The three principal thrusts of this two-year program, Phase II of RP226-3, were: (a) understanding the causes of the unexpectedly low electrochemical energy efficiencies of the 45-kWh module; (b) refurbishment of the module to yield a delivered energy and electrochemical energy efficiency of 50 kWh and 63%, respectively; and (c) development of prototypes for all major components for advanced-technology battery modules to be built as part of a separate DOE-EDA Program. Research and development programs on efficiency maximization, electrolyte characterization, battery-performance verification, and low-cost materials were conducted in support of these objectives.

Intercell zinc-growth formation during charge was shown to be the principal cause of the efficiency shortfall. Module refurbishment increased the delivered energy from an average of 43 kWh to 53.6 kWh. Simultaneously, the electrochemical energy efficiency was raised from 48% to 60.3%. This successful refurbishment established the feasibility of the battery-module concept. In parallel, a new battery stack was designed, based on the use of flat-plate porous-graphite chlorine electrodes. Prototype stacks demonstrated electrochemical energy efficiencies of 62-64% at the targeted value for delivered energy. Prototypes for the electrolyte pump, gas pump, and hydrate-formation heat exchanger were also developed. In order to eliminate inert gases, e.g., carbon dioxide or air, from the battery module, an inerts-rejection device was built and successfully tested.

Significant accomplishments in the research and development programs during Phase II were as follows: (a) development of a data base on the density, conductivity, viscosity, chlorine solubility, and the zinc transference number for $ZnCl_2$-KCl-NaCl electrolytes; (b) development of a model describing the hydrodynamic phenomena occurring between individual zinc and chlorine electrodes during charge; (c) demonstration of cell electrochemical energy efficiencies of 74% for delivered capacity densities of 500 Wh/cm^2; (d) completion of reliability studies for 100-MWh battery plants which discuss quantitatively plant availability and electricity cost in terms of module-failure rate; (e) invention of a module-bypass switch concept which isolates a failed module in a series-connected string thereby avoiding string outage; (f) development of a computer model for module operation which allows prediction of the effects of component changes on module performance; and (g) accumulation of 1250 cycles -- 50% of the target for battery-stack life -- on a 1.7-kWh system with negligible performance degradation.

EPRI PERSPECTIVE

PROJECT DESCRIPTION

EPRI, the Department of Energy (DOE), and Gulf+Western Industries, Inc., through its subsidiary, Energy Development Associates, are engaged in a closely integrated program to develop and commercialize a zinc-chloride battery for utility energy storage. The objective of the EPRI portion, Research Project (RP) 226, of this program is to provide the technology base; RP226-3 is a 39-month effort initiated in January 1977. The $7.6 million cost has been shared equally between EPRI and EDA. The DOE-funded program (a $11.5-million DOE contract initiated in January 1979) has the goal of design and fabrication of a 4-megawatthour (MWh) battery for the Battery Energy Storage Test (BEST) Facility evaluation.

This is the final report for RP226-3 and covers Phase II, the period April 1978 to contract completion, March 31, 1980. An interim report, EPRI EM-1051, dated April 1979, described the earlier results on which the present work is based.

PROJECT OBJECTIVES

Phase II of RP226-3 had two principal objectives. The first was to refurbish the 45-kilowatthour (kWh) zinc-chloride module to attain capacity and efficiency goals. The second objective was to design the 50-kWh module intended as the building block for the 4-MWh BEST Facility battery. Subobjectives included: (1) development of key components, e.g., battery stacks with flat plate chlorine electrodes, pumps, heat exchangers, and the inert-gas rejection device; and (2) continued life testing of the 1.7-kWh battery.

PROJECT RESULTS

The 45-kWh module had performed well as a system but delivered only 43 kWh and manifested an efficiency of only 48 percent, well below the target of 63 percent. Refurbishment, completed under Phase II, increased the delivered energy to 53.6 kWh and the electrochemical energy efficiency to 60.3 percent. A new battery stack was designed. Prototype stacks displayed efficiencies of 62 to 64 percent. A breadboard, inert-gas rejection device has been successfully demonstrated. The design for the BEST module is a great improvement in manufacturability but has not yet achieved the efficiency goal of 65 percent. Over 1250 cycles, equivalent to one-half of the desired 10-year life, were completed on the 1.7-kWh battery without appreciable degradation.

Present difficulties with the first module prototype suggest that the BEST Facility battery may not represent commercial hardware. Further iteration in design and fabrication will be required for the cost, reliability, and performance goals to be achieved. This need is being addressed in a three-year, $7.2-million, follow-on project, of which EPRI will fund two-thirds.

The zinc-chloride battery is the most highly developed of the advanced batteries that are expected to meet utility application goals. Encouraging progress has been made; but many problems remain to be solved, and commercial hardware is at least five years away.

David L. Douglas, Project Manager
Energy Storage Program
Energy Management and Utilization Division

Preceding page blank

ACKNOWLEDGMENTS

The dedication and diligence of the EDA personnel who contributed to the success of Phase II of RP226-3 is gratefully acknowledged. The staff of the Engineering Department, under the direction of Mr. Peter Carr, contributed heavily to the module and component engineering programs. Special appreciation must be accorded Mr. D. Aller, Mr. H. Bjorkman, and Dr. Henry Catherino who made major contributions during the first half of Phase II.

The guidance and advice of Mr. J. Rowan were gratefully appreciated. The willing assistance of the staff of the Reports and Presentations Section, headed by Ms. K. Mitchell, is also gratefully acknowledged. This list would not be complete without an appreciation of the encouragement and direction of Dr. J. Birk, Dr. D. Douglas, and Mr. W. Spindler of the Electric Power Research Institute.

REPORT AUTHORS

Energy Development Associates

C. Warde
B. Brummet
R. Clubb
G. Henriksen

S. Argade
J. Bennett
L. Bieman
C. Blevins
S. Countess
N. Gibbons
M. Hammond
I. Handsy
S. Kilic
W. Klems
S. Kodali
A. Laethem
S. Liu
M. Mihm
P. Racenis
B. Singh
G. Sussman
L. Thorell
S. Wharton
C. Whittlesey

Mashikian & Associates

M. Mashikian

University of Michigan

C. Vest
W. Yang

Wayne State University

J. Jorne
W. T. Ho
A. Kermani
D. Smolenski

Preceding page blank

CONTENTS

Section		Page
	PART I -- INTRODUCTION	
1	INTRODUCTION TO REPORT CONTENT	1-1
2	BACKGROUND TO PHASE II OF RP226-3	2-1
	RP226-1	2-1
	RP226-2	2-2
	RP226-3: Phase I	2-3
	Related Programs at EDA	2-6
	References	2-6
3	HOW ZINC-CHLORIDE BATTERIES STORE AND DELIVER ELECTRIC ENERGY	3-1
4	GLOSSARY FOR ZINC-CHLORIDE BATTERY SYSTEMS	4-1
	PART II -- ZINC-CHLORIDE LOAD-LEVELING BATTERY PLANTS	
5	PROGRAM STATUS: COMMERCIAL BATTERY PLANTS	5-1
	Introduction and Background	5-1
	Battery Plant Issues	5-2
	References	5-7
6	DESIGN OF COMMERCIAL BATTERY PLANTS	6-1
	Abstract	6-1
	Introduction	6-2
	Battery Module	6-3
	Rack Assembly	6-4
	Battery Unit	6-5
	Refrigeration and Cooling Systems	6-6
	Battery Auxiliaries Circuit	6-8
	Power-Conditioning System	6-8
	Controls for Battery Operation	6-9
	Discussion	6-10
	Reference	6-11

Preceding page blank

Section		Page
7	ELECTRICITY-COST TARGETS FOR COMMERCIAL BATTERY PLANTS	7-1
	Abstract	7-1
	Introduction	7-1
	Busbar Cost of Electricity Generated from Combustion Turbines	7-1
	Busbar Cost of Electricity Delivered from a Pumped Hydro Storage System	7-2
	Busbar Cost of Electricity Delivered from Compressed Air Storage System	7-3
	Parametric Analysis of Busbar Cost of Electricity for Battery System	7-5
	Discussion	7-8
	References	7-9
8	CAPITAL COST OF BATTERY PLANTS	8-1
	Abstract	8-1
	Introduction	8-1
	Design of a Commercial Battery Plant	8-2
	Capital Cost of Battery Modules - Semimature Market	8-3
	Capital Cost of Plant Auxiliaries - Semimature Market	8-3
	Discussion	8-4
	Reference	8-5
9	EFFICIENCY OF BATTERY PLANTS	9-1
	Abstract	9-1
	Introduction	9-1
	Electrochemical Energy Losses	9-2
	Auxiliary Equipment Energy Consumption	9-7
	Discussion	9-12
	References	9-14
10	RELIABILITY ASPECTS OF BATTERY-PLANT O&M COSTS	10-1
	Abstract	10-1
	Introduction	10-2
	Equations for Module-Related O&M Costs	10-2
	System Design and Reliability	10-4
	Module Reliability - Mark 4B Design	10-5
	Discussion	10-7
	References	10-10
11	SAFETY ISSUES FOR ZINC-CHLORIDE BATTERY PLANTS	11-1
	Abstract	11-1
	Introduction	11-1
	Safety Issues	11-1
	Discussion	11-3
	Acknowledgments	11-5
	References	11-5

Section		Page
12	COMMERCIALIZATION OF ZINC-CHLORIDE BATTERY PLANTS	12-1
	Abstract	12-1
	Introduction	12-1
	BEST Facility	12-2
	Demonstration Plant	12-3
	Discussion	12-4
	References	12-5
	PART III -- REFURBISHMENT OF 45-kWh MODULE	
13	PROGRAM STATUS: 45-kWh MODULE	13-1
	Introduction	13-1
	Refurbishment Program	13-1
	Other Programs	13-3
	References	13-4
14	45-kWh MODULE: CELL STUDIES	14-1
	Abstract	14-1
	Introduction	14-1
	Cell Design	14-1
	Procedures and Results	14-2
	Discussion	14-5
15	45-kWh MODULE: SUBMODULE STUDIES	15-1
	Abstract	15-1
	Introduction	15-1
	Submodule Design	15-1
	Test System	15-1
	Submodule Testing	15-2
	Qualification of Submodules	15-6
	References	15-8
16	REFURBISHING AND TESTING OF THE 45-kWh MODULE	16-1
	Abstract	16-1
	Introduction	16-1
	Submodule Improvement	16-1
	Module Reconfiguration	16-2
	Testing of the Refurbished Module	16-3
	Discussion	16-4
	Reference	16-6
17	COMPUTER MODELING OF MODULE OPERATION	17-1
	Abstract	17-1
	Introduction	17-1
	Model Construction	17-2
	Model Verification	17-5
	Discussion	17-9

Section		Page
18	45-kWh MODULE FAILURE MODES AND EFFECTS ANALYSIS	18-1
	Abstract	18-1
	Introduction	18-1
	Design of FMEA Study	18-2
	Results	18-2
	Discussion	18-6
	Conclusions	18-7
	Recommendations	18-7
19	45-kWh MODULE: SUPPLEMENTAL STUDIES	19-1
	Abstract	19-1
	Introduction	19-1
	Charge Stand Experiment	19-1
	Short-Circuit Tests	19-4
	Module Reconfiguration	19-6
	Discussion	19-7

PART IV -- CYCLE TESTING OF 1.7-kWh BATTERY

20	PROGRAM STATUS: 1.7-kWh SYSTEM	20-1
	References	20-3
21	1.7-kWh BATTERY SYSTEM: THE FIRST 1000 CYCLES	21-1
	Abstract	21-1
	Introduction	21-1
	System Description	21-1
	System Operation	21-4
	Data Acquisition and Control System	21-5
	Results and Discussion	21-6
	References	21-8
22	DATA-BASE MANAGEMENT SYSTEM FOR THE 1.7-kWh SYSTEM	22-1
	Abstract	22-1
	Introduction	22-1
	Data-Base Organization	22-2
	Data-Base Maintenance	22-4
	Report Generation	22-5
	Nomad Interfaces	22-7
	Discussion	22-8
23	THE 1.7-kWh SYSTEM: CYCLES 1000-1250	23-1
	Abstract	23-1
	Introduction	23-1
	Modified System	23-1
	Results and Discussion	23-3

Section | Page

PART V -- DEVELOPMENT OF BEST-BATTERY TECHNOLOGY

24 PROGRAM STATUS: BEST-BATTERY TECHNOLOGY 24-1

Introduction 24-1
Module Design 24-1
EPRI-EDA Program Support 24-2
BEST-Battery System 24-3

25 SPECIFICATION AND DESIGN OF THE BEST-BATTERY MODULE 25-1

Abstract 25-1
Introduction 25-1
Electrochemical Specifications 25-1
Design and Operation 25-2
Program Integration 25-3

26 MATERIALS QUALIFICATION: I. PLASTICS 26-1

Abstract 26-1
Introduction 26-1
Chemical Screening Tests 26-2
Electrochemical Tests 26-2
Results and Discussion 26-3
Status 26-8
References 26-9

27 MATERIALS QUALIFICATION: II. GRAPHITES 27-1

Abstract 27-1
Introduction 27-1
Experimental Detail 27-2
Experimental Results and Discussion 27-6
References 27-14

28 BATTERY STACK: CELL DEVELOPMENT 28-1

Abstract 28-1
Introduction 28-1
Frame Designs 28-2
Experimental Details 28-3
Results and Discussion 28-4
References 28-7

29 BATTERY STACK: SUBMODULE DEVELOPMENT 29-1

Abstract 29-1
Introduction 29-1
Submodule Design 29-1
Experimental Details 29-3
Results and Discussion 29-4
Program Status 29-7

Section		Page
30	PASSIVE HYDROGEN-RECOMBINATION REACTOR DEVELOPMENT	30-1
	Abstract	30-1
	Introduction	30-1
	Reaction of Hydrogen and Chlorine	30-2
	Subcontractor Investigation	30-2
	EDA Studies	30-3
	Discussion	30-9
	References	30-10
31	PUMP DEVELOPMENT	31-1
	Abstract	31-1
	Introduction	31-1
	Electrolyte Pump	31-2
	Gas/Hydrate Former Pump	31-3
	Program Status	31-5
	Reference	31-6
32	HYDRATE-FORMER HEAT EXCHANGER DEVELOPMENT	32-1
	Abstract	32-1
	Introduction	32-1
	Requirements for Hydrate-Former Heat Exchanger	32-2
	Design of Water/Glycol Cooled Heat Exchanger	32-3
	Design of Direct Refrigerant-Cooled Heat Exchanger	32-4
	Experimental	32-6
	Results and Discussion	32-8
	Program Status	32-9
	References	32-10
33	INERTS-REJECTION DEVICE: I. PROOF OF CONCEPT	33-1
	Abstract	33-1
	Introduction	33-1
	Experimental Detail	33-2
	Results and Discussion	33-3
	References	33-4
34	INERTS-REJECTION DEVICE: II. HOW AND WHEN WILL IT OPERATE?	34-1
	Abstract	34-1
	Introduction	34-1
	Initial Model	34-2
	Refined Model	34-5
	Comparison of Module Data and Model	34-7
	Status	34-10
	References	34-10

Section		Page
35	INERTS-REJECTION DEVICE: III. PROTOTYPE FABRICATION AND TESTING	35-1
	Abstract	35-1
	Introduction	35-1
	Cell Studies	35-1
	Prototype Inerts-Rejection Subsystem	35-6
	Program Status	35-9
	PART VI -- ADVANCED-TECHNOLOGY STUDIES	
36	PROGRAM STATUS: ADVANCED TECHNOLOGY DEVELOPMENT	36-1
	Introduction	36-1
	Efficiency	36-1
	Capacity Density	36-3
	Introduction to Part VI Content	36-4
37	ELECTROLYTE PROPERTIES: I. DENSITY	37-1
	Abstract	37-1
	Introduction	37-1
	Experimental	37-2
	Experimental Results	37-3
	Empirical Density Relationships for Molal Scale	37-6
	Empirical Density Relationships for Molar Scale	37-9
	Discussion	37-10
	References	37-11
38	ELECTROLYTE PROPERTIES: II. CONDUCTIVITY	38-1
	Abstract	38-1
	Introduction	38-1
	Experimental	38-2
	Experimental Results	38-2
	Empirical Conductivity Relationships for Molar Scale	38-5
	Empirical Conductivity Relationships for Molar Scale	38-5
	General Conductivity Relationship on Molar Scale	38-7
	Discussion	38-7
	Conclusions	38-8
39	ELECTROLYTE PROPERTIES: III. VISCOSITY	39-1
	Abstract	39-1
	Introduction	39-1
	Experimental	39-1
	Experimental Results	39-2
	Discussion	39-5
	Conclusions	39-7

Section		Page
40	ELECTROLYTE PROPERTIES: IV. CHLORINE SOLUBILITY	40-1
	Abstract	40-1
	Introduction	40-1
	Experimental	40-2
	Results	40-4
	Discussion	40-9
	Conclusions	40-11
	References	40-11
41	ELECTROLYTE PROPERTIES: V. TRANSFERENCE NUMBERS OF ZINC	41-1
	Abstract	41-1
	Introduction	41-1
	Experimental	41-2
	Results and Discussion	41-4
	Conclusions	41-6
	References	41-7
42	COULOMBIC EFFICIENCY: I. THEORETICAL BACKGROUND	42-1
	Abstract	42-1
	Introduction	42-1
	Sources of Coulombic Inefficiency	42-3
	Analysis of Major Inefficiency Sources	42-5
	Results and Discussion	42-8
	References	42-9
43	COULOMBIC EFFICIENCY: II. EFFECT OF FORCED CONVECTION ON CHLORINE TRANSPORT	43-1
	Abstract	43-1
	Introduction	43-1
	Model Development	43-2
	Experimental	43-4
	Results and Discussion	43-4
	Status	43-7
	References	43-8
44	COULOMBIC EFFICIENCY: III. EFFECT OF NATURAL CONVECTION ON MASS TRANSPORT OF CHLORINE	44-1
	Abstract	44-1
	Introduction	44-1
	Theoretical Background	44-2
	Experimental	44-3
	Results and Discussion	44-5
	Conclusions	44-7
	References	44-7

Section		Page
45	COULOMBIC EFFICIENCY: IV. DETERMINATION OF $ZnCl_2$ CONCENTRATION PROFILES UNDER NATURAL CONVECTION	45-1
	Abstract	45-1
	Introduction	45-1
	Experimental	45-2
	Results	45-5
	Discussion	45-7
	Conclusions	45-9
46	COULOMBIC EFFICIENCY: V. COMBINED CONVECTION AT AMBIENT PRESSURE	46-1
	Abstract	46-1
	Introduction	46-1
	Experimental	46-1
	Results and Discussion	46-3
	Conclusions	46-6
	References	46-7
47	COULOMBIC EFFICIENCY: VI. COMBINED CONVECTION AT REDUCED PRESSURE	47-1
	Abstract	47-1
	Introduction	47-1
	Experimental	47-2
	Results and Discussion	47-4
	Conclusions	47-8
	References	47-8
48	OPTIMAL CELL GAP FOR ENERGY EFFICIENCY	48-1
	Abstract	48-1
	Introduction	48-1
	Electrochemical Energy Efficiency During Charge	48-1
	Coulombic Efficiency During Charge	48-2
	Voltaic Efficiency During Charge	48-3
	Optimal Cell Gap	48-4
	Conclusions	48-5
	References	48-6
49	CELL GAPS AND ELECTROLYTE COMPOSITIONS	
	Abstract	49-1
	Introduction	49-1
	Experimental	49-2
	Results	49-3
	Discussion	49-5
	Conclusions	49-6

Section		Page
50	SHORT-CIRCUIT CHARACTERISTICS OF ZINC-CHLORIDE CELL	50-1
	Abstract	50-1
	Introduction	50-1
	Experimental	50-1
	Results and Discussion	50-2
	Conclusions	50-6
51	ELECTRODE SIZE STUDY	51-1
	Abstract	51-1
	Introduction	51-1
	Background	51-1
	Experimental	51-3
	Results and Discussion	51-5
	Status	51-7
	References	51-7

SUMMARY

Storage of off-peak electric energy in batteries, and the availability of this energy during periods of peak-power demand, would permit more efficient utilization of baseload and intermediate generating capacity. These load-leveling battery systems would allow conservation of oil or natural gas which would otherwise be consumed in turbine-peaking units. The Electric Power Research Institute (EPRI), the United States Department of Energy (DOE), and Energy Development Associates (EDA) are presently engaged in a program to develop the zinc-chloride battery for this application.

The first major objective of this program is to place a 4-MWh zinc-chloride battery system in the Battery Energy Storage Test (BEST) Facility by mid-1981. The technology base was provided in a 39-month EPRI-EDA Program, designated RP226-3, which was initiated in January 1977. Total expenditures during RP226-3 were $7.6 million, with EDA and EPRI each providing one-half. A separate 33-month program, termed the DOE-EDA BEST-Battery Program, began in January 1979. This program funds the design, engineering, and manufacturing activities for the 4-MWh battery system. Total expenditures are anticipated to be $11.5 million, with EDA providing $1.7 million. From January 1979 through the end of Phase II, the EPRI-EDA and DOE-EDA Programs were conducted as an integrated effort at the request of DOE and EPRI. This report, which reviews progress in the EPRI-EDA Program, covers a period from April 1978 through March 1980 -- designated as Phase II of RP226-3 -- and program expenditures of $5.2 million.

BATTERY ENERGY-STORAGE PLANTS

Conceptual designs of 100-MWh zinc-chloride battery plants have been prepared and analyzed in previous EPRI-EDA programs, in order to ensure the relevance of the concurrent development and battery scale-up activities. An artist's rendition of the updated design of a 100-MWh battery plant -- prepared as part of the DOE-EDA BEST-Battery Program -- is shown in Figure 1. It consists of four independent 25-MWh (5-MW) units, each complete with battery, refrigeration, power-conditioning, and control subsystems. A battery subsystem comprises four strings, each containing 120 series-connected modules on two 3-tiered racks. The refrigeration subsystem, required for chlorine-hydrate formation on charge and electrolyte-temperature control, consists of a compressor, two condensors, and a Freon receiver with pumps and controls. Each string is controlled by one of four independent bridges in the 24-pulse power-conditioning subsystem -- each bridge being capable of separately controlling

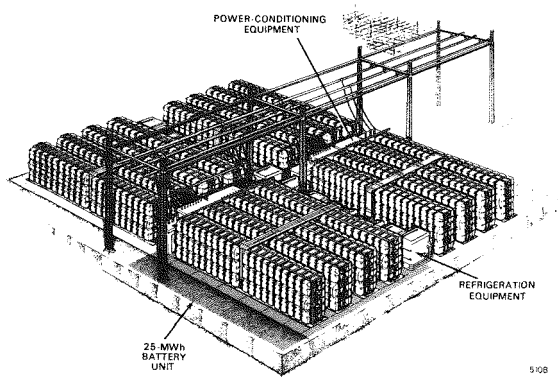

Figure 1. Artist's rendition of 100-MWh zinc-chloride battery plant.

the current and voltage in each string. The 25-MWh unit is supervised by a microprocessor-based control subsystem. Adequate space is provided in and between the subsystems to permit easy access for maintenance.

A significant advance was made during Phase II which will minimize the effect of single module failure in a 120-module string. In the event of module failure, a module-bypass switch will be closed. This will effectively short-circuit the module and simultaneously isolate it from the rest of the modules in the string. This concept is rendered practical because of the storage of chlorine external to the battery stack. The power-conditioning subsystem is designed so that the string can continue to accept or deliver energy despite multiple module failures. As the module-bypass switch has only to close under load, it will be a relatively inexpensive component. Prototype switches have already been built and successfully tested as part of the DOE-EDA Program.

A comparison of electricity costs from combustion turbines and zinc-chloride battery plants for utility load leveling indicated that battery energy storage can be economically competitive, particularly in view of the rapidly escalating cost of fuel. Using reasonable estimates for charging energy, plant auxiliaries, and O&M costs, the battery subsystem cost can be as high as $100/kWh, and still be competitive with combustion turbines. In 1980 dollars, battery module costs in full production, i.e., 100 modules per day, have been estimated to be $50/kWh, underlining the potential economic attractiveness of energy storage in zinc-chloride battery plants. A parallel parametric assessment indicated the importance of meeting the capital-cost target.

REFURBISHMENT OF 45-kWh MODULE

The battery-module prototype was designed, fabricated, assembled, and tested during Phase I of RP226-3. The design goals for delivered energy and electrochemical energy efficiency were 45 kWh and 63%, respectively. The prototype delivered an average of 43 kWh at an average electrochemical energy efficiency of 48% over 10 cycles. The major contributor to the efficiency shortfall was the coulombic efficiency which averaged 59% -- significantly below the design level of 73%.

Early in Phase II, inter-cell zinc-growth formation during charge was diagnosed as the principal contributor to the coulombic-efficiency shortfall. This problem was resolved by minor modifications to the battery stacks. An additional coulombic-efficiency penalty was incurred because of excessive heat transfer from the electrolyte sump to the chlorine-hydrate store, both of which were located side by side in the lower part of the module. As shown in Figure 2 -- the refurbished module -- a case segment was added to allow reloca-

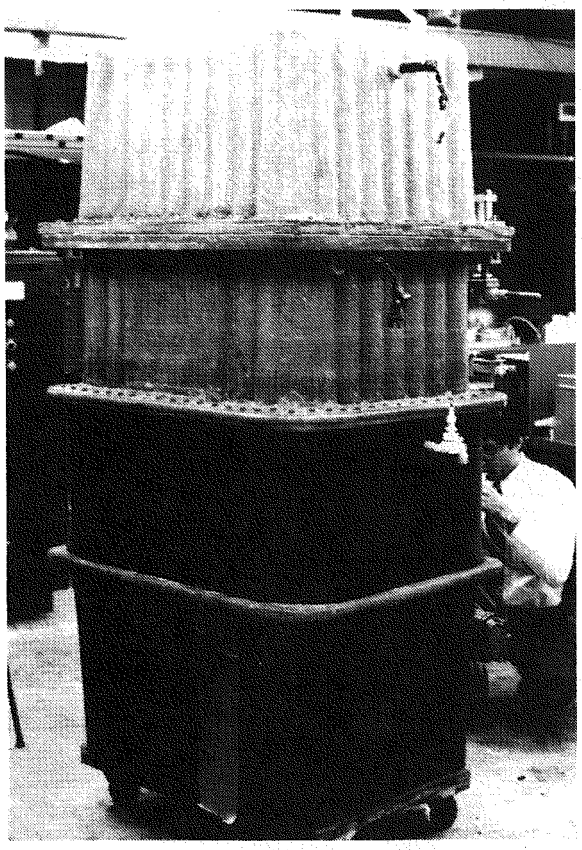

Figure 2. Refurbished 45-kWh module.

tion of the electrolyte sump to the upper half of the module. The chlorine-hydrate store thus occupied the lower half of the module.

Figure 3 presents averaged data for the module before and after refurbishment. A significant increase -- 59% to 71% -- was observed for coulombic efficiency. Simultaneously, the delivered energy and electrochemical efficiency were increased to 50 kWh and 59%, respectively. Subsequent component refurbishment further increased the delivered energy to a maximum of 53.6 kWh. In the same series of experiments, the maximum electrochemical energy efficiency observed was 60.3%. This successful refurbishment established the technical feasibility of the battery-module concept.

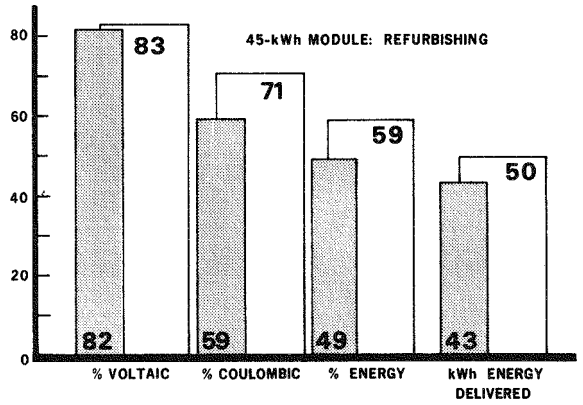

Figure 3. Module performance before and after refurbishment.

BEST-BATTERY TECHNOLOGY DEVELOPMENT

By mid-1981, EDA will place a 4.2-MWh zinc-chloride battery system in the BEST Facility, as part of the DOE-EDA BEST-Battery Program. As shown in Figure 4, the battery subsystem will consist of two strings, with each string comprising 40 series-connected modules. Each module is targeted to deliver 52.3 kWh at an electrochemical energy efficiency of 65%. One of the principal objectives of the EPRI-EDA Program during Phase II was the development of prototypes for all major components in the battery module.

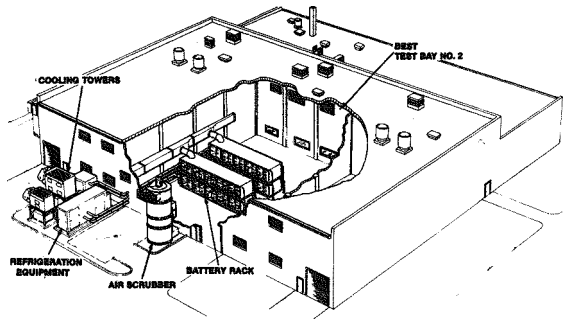

Figure 4. Artist's rendition of 4.2-MWh zinc-chloride battery system in BEST Facility.

A new battery-stack design based on the use of flat-plate porous-graphite chlorine electrodes was prepared. Prototype 10-cell units, termed submodules, were built and tested. Injection-molded parts fabricated from a special PVC formulation were successfully employed in these submodules. In addition, graphites which offer the prospect of meeting the cost targets for commercialization were used in the fabrication of electrodes and busbars for the submodule. At the targeted value for delivered energy, the submodule prototypes demonstrated electrochemical energy efficiencies of 62-64%. An exploded view of the submodule is shown in Figure 5.

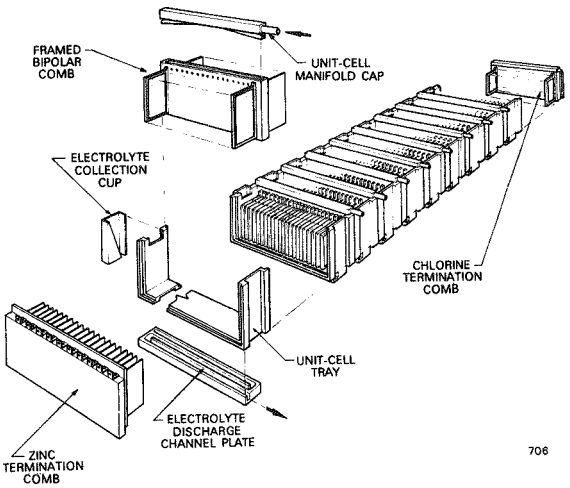

Figure 5. Exploded view of BEST-battery submodule. Rating: 8.7 kWh dc.

Prototype electrolyte and gas pumps, designed for higher efficiency and lower cost, were built and tested. A commercially-available plate-coil titanium heat exchanger, which operates with Freon refrigerant, was tested for heat removal from the store during charge. Particular emphasis was placed on the development of a device to remove foreign or inert gases, e.g., carbon dioxide and air, which will accumulate during battery-module operation. A prototype inerts-rejection device, shown in Figure 6, was built and successfully tested. In this three-stage chlorine-electrowinning cell, chlorine is separated from the electrochemically inert gases. Purified chlorine is returned to the gas spaces in the module, while the inert gases are vented to ambient.

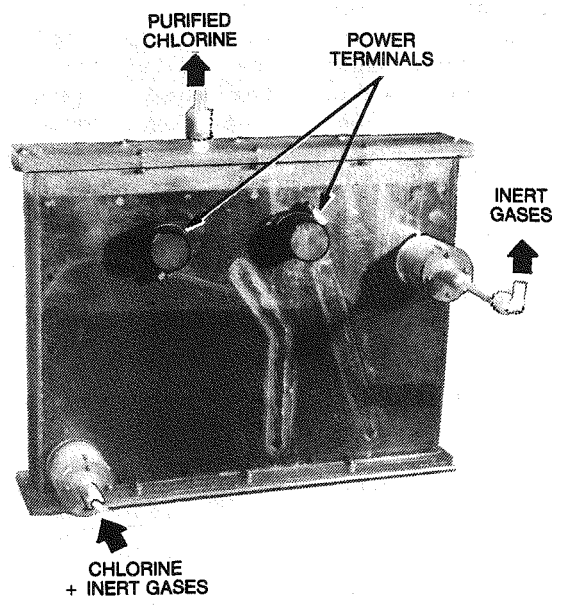

Figure 6. Prototype inerts-rejection device, which prevents build-up of air and carbon dioxide in module.

RESEARCH AND DEVELOPMENT PROGRAMS

During Phase II, experimental and theoretical studies were performed in order to minimize battery costs, maximize efficiency, and to determine the useful life of the zinc-chloride battery. Particular emphasis was placed on the battery stack, which determines module efficiency, dominates the materials and assembly costs, and is considered to be the life-limiting component. The new submodule, described above, was designed with manufacturability and cost as major criteria. Successful programs were conducted to identify plastics and graphites which would meet the cost targets for the commercialization of this technology. The identification of a polypropylene formulation, which is not only more injection moldable than PVC but also one-half its cost, is one example of these significant advances.

Efficiency continued as a major theme in the research and development programs. In order to achieve an ac-to-ac efficiency of 65%, electrochemical energy efficiencies of 75% or greater must be realized at the module level. The key to maximizing efficiency lies in the development of an understanding of the hydrodynamic phenomena in the cell gap, i.e., between individual zinc and chlorine electrodes. It was established that transport of dissolved chlorine to the zinc electrode during charge -- the principal cell inefficiency -- is determined by three major convection phenomena: (a) forced convection due to electrolyte circulation, (b) natural convection at the zinc electrode, and (c) bubble-induced convection at the chlorine electrode.

These theoretical studies, and concurrent experimental investigations, strongly suggested that there was an optimum value for inter-electrode separation in the range of 0.3-0.4 cm. Figure 7 presents cell data for three technology stages during Phase II. The 1978 data was taken with cells in which the inter-electrode separation was 0.2 cm. Higher cell efficiencies were observed during 1979 with cell gaps of 0.25-0.35 cm. Most recently, efficiencies as high as 74% have been noted at current densities of 50 mA/cm^2 for a cell gap of 0.3 cm. Future experimental studies are expected to raise the electrochemical energy efficiency at the cell, submodule, and module levels to values in excess of 75%.

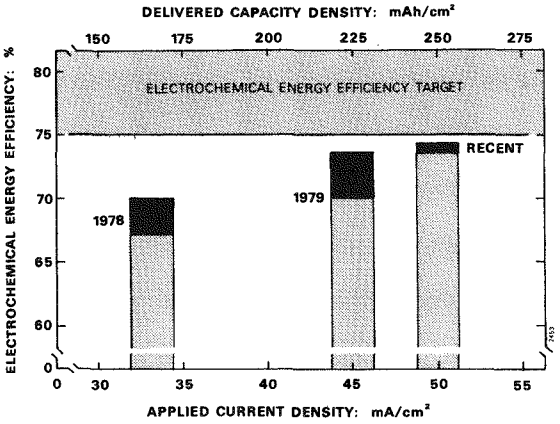

Figure 7. Cell efficiencies for three technology stages during Phase II.

The average life of a battery module must exceed 10 years in commercial service. This life criterion corresponds to a requirement that a module undergo 2500 charge-discharge cycles, i.e., 5 cycles per week for 50 weeks per year for 10 years. A 1.7-kWh battery, which incorporates many features of present-day EDA stack technology, has been under test since February 1976. Through the end of Phase II, a total of 1250 cycles has been accumulated. As shown in Figure 8, there has been negligible deterioration in the coulombic, voltaic, or electrochemical energy efficiencies over the past four years. These results suggest that zinc-chloride battery stacks, based on the use of graphite electrodes and buses, will meet the life target for commercialization.

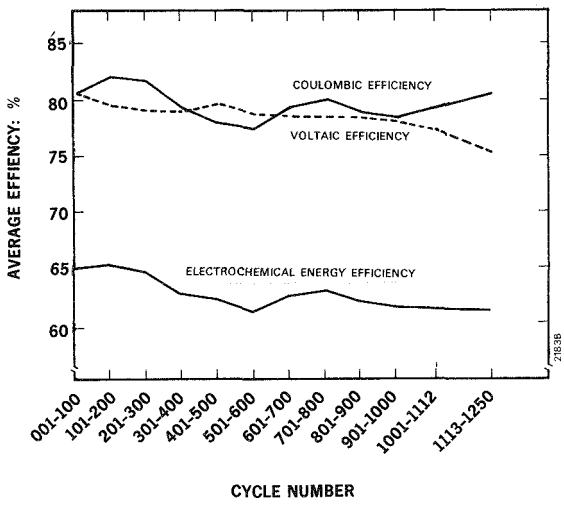

Figure 8. Cycle-test data for 1.7-kWh battery stack showing performance stability through 1250 cycles.

PART I

INTRODUCTION

Section 1

INTRODUCTION TO REPORT CONTENT

The Electric Power Research Institute (EPRI), the United States Department of Energy (DOE), and Energy Development Associates (EDA) are presently engaged in a major program to develop the zinc-chloride battery for utility load-leveling applications. The first major objective of this closely-coordinated program is to place a 4-MWh zinc-chloride battery system in the Battery Energy Storage Test (BEST) Facility by mid-1981. The technology base was provided in a 39-month EPRI-EDA Program, designated RP226-3, which was initiated in January 1977. A separate 33-month program -- termed the DOE-EDA BEST-Battery Program and begun in January 1979 -- supports the design, engineering, and manufacturing activities for the 4-MWh battery system. This report, which reviews progress in the EPRI-EDA Program, covers a period from April 1978 through March 1980, designated as Phase II of RP226-3.

As shown in the work-statement outline in Table 1-1, there were six technical tasks and a reporting task in Phase II. From a funding standpoint, EPRI sponsored Tasks 1, 4, 5, and 7. EDA was responsible for Tasks 2, 3, and 6. Task 1 activities included studies on electrodes, electrolyte formulations, and maximizing electrochemical energy efficiency. Tasks 2 and 3 focused on ensuring the availability of high-performance components for the modules to be built in the DOE-EDA BEST-Battery Program. In Task 2, the primary emphasis was on the design, assembly, and qualification of 8.3-kWh 10-cell submodules, fabricated with flat-plate porous-graphite chlorine electrodes. Task 3 was devoted to the development of the other components in the battery module. The safety, reliability, and efficiency aspects of 100-MWh zinc-chloride battery plants were analyzed as part of Task 4. The two major thrusts of Task 5 were the refurbishment of the 45-kWh module, built and tested during Phase I, and continuation of cycle-testing of a 1.7-kWh battery, built as part of RP226-2. Task 6 activities related to the manufacturing and marketing aspects of 100-MWh zinc-chloride battery plants.

Table 1-1

MAJOR TASKS IN PHASE II OF RP226-3

Task No.	Title
1	Cell Research and Development
2	Electrochemical Component Development
3	Component Development
4	System Design and Analysis
5	Testing and Qualification
6	Commercialization
7	Reporting

In April of 1978 -- the first month of Phase II -- the EPRI-EDA Program was dominated by three major concerns: (a) understanding the causes of the unexpectedly low electrochemical efficiency

of the 45-kWh module; (b) refurbishment of the module to yield a delivered energy and electrochemical energy efficiency of 50 kWh and 63%, respectively; and (c) development of module components for the first prototype to be built in the DOE-EDA BEST-Battery Program. Accordingly, Tasks 1, 2, 3, and 5 were emphasized at the expense of Tasks 4 and 6. Because of the anticipated impact of reliability considerations on the design of the 4-MWh BEST-Battery system, work was initiated on Task 4 in October 1978. Simultaneously, a limited amount of manpower was made available to Task 6 for the preparation of preliminary quality-assurance studies -- once again in preparation for the DOE-EDA BEST-Battery Program.

From January 1979 through the end of Phase II, March 1980, the EPRI-EDA and DOE-EDA Programs were conducted as an integrated effort. This was done at the request of DOE and EPRI. Accordingly, Tasks 2 and 3 were emphasized to ensure the availability of components for module prototypes, to be built and tested as part of the DOE-EDA Program. Similarly, further refurbishment and testing of the 45-kWh module -- Task 5 -- was conducted to allow optimization of prototype design. In parallel with the preparation of a site-specific conceptual design of a 100-MWh zinc-chloride battery plant for the DOE-EDA Program, reliability, safety, efficiency, and module-design studies were performed in Task 4 of the EPRI-EDA Program. Accordingly, Tasks 1 and 6 were de-emphasized in the last half of Phase II.

The format of this report does not directly follow the work-statement outline of Table 1-1. Instead, similar activities are clustered in six separate parts, as shown in Table 1-2. Part I serves to introduce the remainder of the report. Section 2 summarizes not only the accomplishments in previous EPRI-EDA programs but also the related battery programs at EDA. A brief description of how the zinc-chloride battery works is provided in Section 3, while Section 4 lists and explains terms specific to the zinc-chloride program at EDA.

Table 1-2

BREAKDOWN OF REPORT FOR PHASE II OF RP226-3

Part No.		Section Nos.
I	Introduction	1 - 4
II	Zinc-Chloride Load-Leveling Battery Plants	5 - 12
III	Refurbishment of 45-kWh Module	13 - 19
IV	Cycle Testing of 1.7-kWh Battery	20 - 23
V	Development of BEST-Battery Technology	24 - 35
VI	Advanced-Technology Studies	36 - 51

Part II, which deals with 100-MWh zinc-chloride battery plants, is based on work performed in Tasks 4 and 6. As shown in Section 6, EDA has refined the design for Mark 4 battery plants. Each 25-MWh segment is a self-contained system with its own refrigeration and power-conditioning subsystems. In Section 7, EPRI methodology for economic assessment of competing technologies is employed in order to establish that electricity cost at which battery energy storage is competitive with other technologies, principally combustion turbines. In addition, a parametric assessment of the cost of electricity from zinc-chloride battery plants is presented which indicates the major importance of capital costs. Sections 8, 9, and 10 review battery-plant capital costs, overall efficiencies, and O&M costs, respectively. Section 11,

which reviews battery-plant safety issues mainly from a chlorine-release standpoint, suggests that zinc-chloride battery plants can be sited without major objection at residential, commercial, industrial, and rural substations on the utility subtransmission and distribution network. This update, which includes a brief description of recent chlorine-hydrate spill tests conducted by Factory Mutual Research Corporation, echoes earlier studies in this regard. Commercialization of this technology is discussed in Section 12. An executive summary of Part II is provided in Section 5.

Part III reviews one of the major successes in Phase II, i.e., the successful refurbishment of the 45-kWh module to a maximum delivered energy of 53.6 kWh and a maximum electrochemical energy efficiency of 60.3%. Section 14 recounts the results of cell studies, conducted at the beginning of Phase II. These experiments were performed to ensure that phenomena at the single cell level were not responsible for the coulombic-efficiency shortfall observed in module testing during Phase I. The discovery that zinc growths around and below the submodule busbar were causing the observed inefficiencies, and the steps taken to ameliorate this problem, are described in Section 15. The refurbishment and testing of the 45-kWh module are outlined in Section 16. Sections 17, 18, and 19 describe additional analytical and experimental studies performed on this module. A summary of all work performed is provided in Section 13.

Part IV focuses solely on the life testing of the 1.7-kWh 2-V battery built and tested as part of RP226-2. The battery stack in this system is of particular interest in that it employs many of the design concepts utilized in present EDA technology, e.g., porous-graphite chlorine electrodes, dense-graphite zinc electrodes, and interference fits between electrodes and buses. As described in Section 20 -- the overall summary for Part IV -- 750 additional cycles were accumulated for a total of 1250 full charge-discharge cycles. This represents 50% of the commercial target for load-leveling batteries, i.e., 2500 cycles, or 5 cycles per week for 50 weeks per year for 10 years. Section 21 reviews the data for the first 1000 cycles. Section 23 describes the subsequent testing through 1250 cycles, during which simplification of the 1.7-kWh system was accomplished in order to permit more rapid cycle accumulation. The development of a data-base management system, specifically for the 1.7-kWh battery, is described in Section 22.

Part V recounts the efforts in the EPRI-EDA Program during Phase II which led to the development of prototypes for all major components in the battery module. For background purposes, the specification and design of the BEST-battery module is described in Section 25. The successful qualification of plastics and graphites for use in the battery environment is detailed in Sections 26 and 27, respectively. Sections 28 and 29 describe the development of cells and submodules to meet the electrochemical-performance criteria required for BEST-battery modules. Following reports from an EDA subcontractor that a tritium-activated self-powered light (of a type used in emergency signs) was active in promoting the recombination of hydrogen with chlorine, an intensive effort was launched to qualify this concept for use in battery modules. As related in Section 30, this program was unsuccessful in that the self-powered light demonstrated no activity for hydrogen recombination in testing at EDA. The development of higher-efficiency lower-cost gas- and electrolyte-pumps is described in Section 31, while Section 32 outlines the results of on-going testing to replace glycol with Freon as the coolant in load-leveling battery systems. During normal module operation, gases other than chlorine -- so-called inerts, e.g., air and carbon dioxide -- will accumulate in the module gas spaces. Sections 33, 34, and 35 describe the research, development, and engineering which led to the successful fabrication and testing of a prototype inerts-rejection device to periodically

eliminate these gases from the module. An overall summary of the development of components for BEST-battery modules is provided in Section 24.

Part VI describes theoretical and experimental studies which were performed to maximize electrochemical energy efficiency in zinc-chloride cells. Sections 42 through 47 concentrate solely on the topic of cell coulombic efficiency. Theoretical and experimental investigations of the hydrodynamic phenomena in the inter-electrode gap were conducted in order to elucidate the effects of cell geometry and operational conditions on the corrosion of electrodepositing zinc by chlorine dissolved in the electrolyte. Inter-electrode separation was shown to be a critical cell characteristic. Further studies -- Sections 48 and 49 -- confirm that the optimum separation lay in the range of 0.25-0.35 cm. In parallel, five electrolyte properties were measured for a range of electrolyte formulations in order to provide an adequate data base for these theoretical and experimental studies. Sections 37 through 41 present data on density, conductivity, viscosity, chlorine solubility, and transference numbers for these electrolytes. Additional studies on cell transients and the effects of increasing electrode size are presented in Sections 50 and 51, respectively. A summary for Part VI is provided in Section 36.

Section 2

BACKGROUND TO PHASE II OF RP226-3

Since mid-1974, Energy Development Associates (EDA) and the Electric Power Research Institute (EPRI) have jointly funded research, development, and engineering at EDA to develop the zinc-chloride battery for utility load-leveling. This is the fourth in a series of reports describing the progress and problems in these programs. Earlier reports have described work performed on RP226-1, RP226-2, and Phase I of RP226-3 (1,2,3). This report presents the work performed in the last 24 months -- Phase II -- of RP226-3. The programs, periods of performance, funding levels, and the corresponding EPRI reports are listed in Table 2-1. In this section, the major accomplishments of RP226-1, RP226-2, and Phase I of RP226-3 are briefly reviewed. The section concludes with a brief description of related programs at EDA.

RP226-1

In mid-1974, EPRI and EDA co-funded a program designated RP226-1 to explore the potential of the zinc-chloride battery for utility load-leveling. EDA designed and built a 1-kWh battery system, while EPRI provided the funding for battery testing. The twin objectives of this program were the attainment of an electrochemical efficiency of 70% and the demonstration of stable performance over one hundred consecutive charge-discharge cycles. Among the more important design features of this system were the use of ruthenia-catalyzed porous-titanium chlorine electrodes and chlorine desorption from the electrolyte during charge. This latter feature was of considerable importance in minimizing the corrosion of electrodepositing zinc by chlorine dis-

Table 2-1

PERIODS OF PERFORMANCE AND FUNDING IN EPRI-EDA PROGRAMS

Program No.	Phase No.	Period of Performance Start	End	Funding (millions of $) EPRI	EDA	EPRI Report No.
RP226-1	--	Jun '74	Dec '75	0.2	0.4	EM-249
RP226-2	--	Jan '75	Dec '76	0.5	0.6	EM-711
RP226-3	I	Jan '77	Mar '78	1.2	1.2	EM-1051
RP226-3	II	Apr '78	Mar '80	2.6	2.6	This report

solved in the electrolyte. Under test, the 1-kWh system displayed an electrochemical efficiency of 74.6% ±1.0%. The performance of the system shown in Figure 2-1, was stable over the one hundred cycles required by contract. This work, concluded in December 1975, has been described in detail in an earlier report (1).

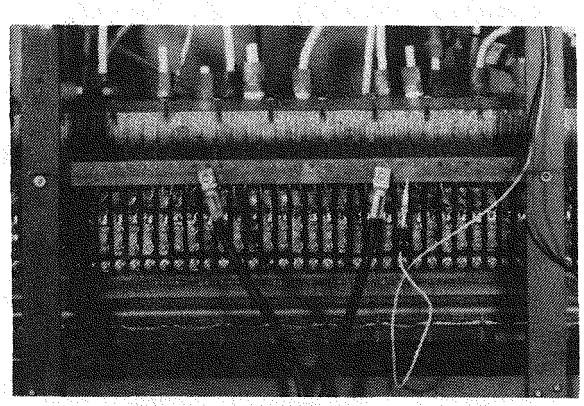

Figure 2-1. The battery stack in the 1-kWh system, built and tested as part of RP226-1.

In October 1975, EPRI funded a seven-month study, designated RP226-1-2, directed toward the preparation of a design and a detailed cost analysis of 100-MWh zinc-chloride load-leveling battery plants. This load-leveling plant design, designated Mark 2, was based on a preliminary Mark 1 design, used for discussion with EPRI and electric-utility representatives. A description of the Mark 2 design is provided in an earlier report (2). This study concluded that the Mark 2 design could meet the cost, performance, and siting criteria developed by EPRI for load-leveling battery plants. However, chlorine desorption from the electrolyte, as accomplished during operation of the 1-kWh system, was revealed by analysis to be impractical in a Mark 2 100-MWh battery plant because of cost considerations. Further, serious questions were raised as to the operability of the battery system and the significant energy penalty for desorber operation if this chlorine-desorption technique were employed.

RP226-2

In calendar 1976, EDA conducted a follow-on program designated RP226-2. This program was jointly funded by EPRI and EDA for a total cost of $1,100,000. There were four major objectives: firstly, the automation of the 1-kWh system to demonstrate that it could operate in the unattended mode; secondly, the construction and test of two battery systems, sized at approximately 2 kWh, in order to permit the making of an informed choice between porous graphite and ruthenia-catalyzed porous-titanium as a chlorine electrode material; thirdly, the design, assembly, and testing of a 20-kWh, 20-V battery system, based on the results of the testing of the two 2-kWh systems; and finally, preparation of an update, in late 1976, of the Mark 2 design and cost analysis, based on the technology improvements in the previous 12 months.

The automation of the 1-kWh system ran into immediate difficulties. Because of the abandonment of the chlorine-desorption technique, based on the results of the design and cost study, the electrochemical energy efficiency of the system decreased to 60%. A cell-development program was initiated to find a new set of operating conditions in order to recover battery capacity and electrochemical energy efficiency. The system was redesigned and then automated. With the redesign and a new cycling routine, the delivered energy was increased to 1.4 kWh. Simultaneously, the electrochemical energy efficiency was raised to approximately 67%.

Two additional systems -- a 1.7-kWh, 2-V system with porous-graphite chlorine electrodes and a 2-kWh, 4-V system with ruthenia-catalyzed porous-titanium chlorine electrodes -- were also designed, built, and tested to facilitate selection of the chlorine-electrode substrate material for the 20-kWh system. A photograph of the 1.7-kWh battery stack is shown in Figure 2-2. In

August 1976, porous graphite was chosen for the following four reasons: (a) the probability of meeting the desired cost target of $5-10/kWh for the chlorine electrodes in a 100-MWh battery system was much higher for porous graphite, (b) the voltaic-efficiency advantage offered by ruthenia-catalyzed porous-titanium electrodes was significantly reduced during 1976 by the development of improved activation techniques for porous-graphite electrodes, (c) operational experience with the 1.4-kWh and 1.7-kWh systems indicated that a system with ruthenia-catalyzed porous-titanium chlorine electrodes would be more difficult to control because of the sensitivity of cell performance to changes in electrolyte pH, and (d) a battery with porous-graphite chlorine electrodes would be intrinsically safer in malfunction, -- e.g., chlorine starvation during discharge or external short-circuiting -- because of the higher hydrogen overpotential of graphite.

A 20-kWh, 20-V battery system was designed, assembled, and tested in the last third of 1976. The battery stack

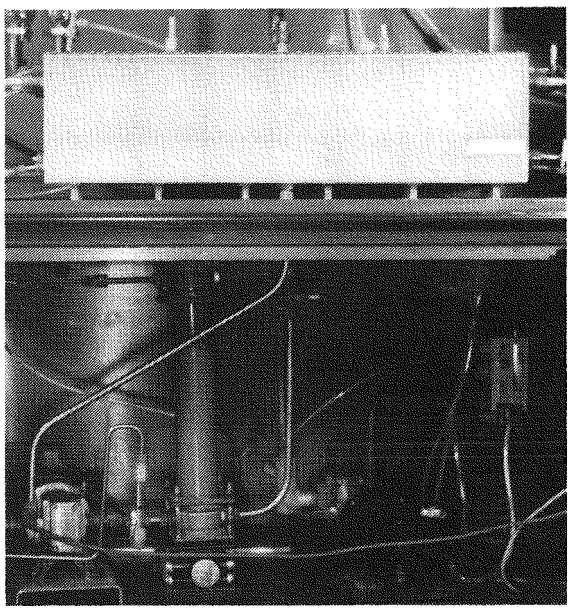

Figure 2-2. The 1.7-kWh 2-V battery system. Porous graphite is the chlorine-electrode material.

and the chlorine-hydrate former/store performed to specification in December 1976. However, excessive hydrogen evolution in the stack during discharge, attributable to electrolyte contamination, delayed coupling of stack and store to form a complete battery system. Following elimination of the contamination problem, the battery ran smoothly as a system in February 1977. At this point, further delays were caused by a dendrite problem which reduced battery capacity. Finally, 10 sequential cycles were taken during May 1977. The average delivered energy was 15 kWh while the average electrochemical efficiency was 60%. An eleventh cycle yielded a delivered energy of 18 kWh with the same electrochemical energy efficiency.

A new design of a 100-MWh utility load-leveling plant, designated Mark 3, was prepared in late 1976. The battery-stack modules, each 6 MWh, were larger than the 1 MWh modules in the Mark 2 design. However, the single underground chlorine-hydrate store of the Mark 2 design was replaced by 24 above-grade stores in the Mark 3 design (2). A cost analysis for this design indicated that it would meet the cost criteria for acceptance by the electric-utility industry.

RP226-3: PHASE I

In January 1977, EDA and EPRI agreed to jointly fund a 39-month program, designated RP226-3. This program, involving total expenditures of $7.6 million, was in two phases: Phase I extending from January 1977 through March 1978; and Phase II from April 1978 through March 1980. The major objective of this program was to provide a background of research, development, and engineering activities for an additional program, to be negotiated in 1978, which would lead to the design, fabrication, installation, and testing of a zinc-chloride battery system in the Battery Energy Storage Test (BEST) Facility by mid-1981. Expenditures during Phase I were $2.4 million with EPRI and EDA each supplying one-half of this total.

In response to concerns expressed about the efficiency, safety, and manufacturability of the Mark 2 and 3 designs, a new conceptual design of a 100-MWh battery plant located at a utility substation was prepared early in Phase I. This design, designated Mark 4, is based on the concept of fully-integrated zinc-chloride battery modules, i.e., each module contains not only the battery stack but also chlorine-hydrate formation, storage, and decomposition equipment. As shown in Figure 2-3, the battery plant comprises thirty-six independent strings -- each string consisting of 44 series-connected 66-kWh battery modules. A conceptual manufacturing plan for a production rate of 100 battery modules per day was prepared. The installed cost of the 100-MWh battery plant was estimated to be $26/kWh + $91/kW (1977 $). The safety, environmental, and legal aspects of siting 100-MWh zinc-chloride battery plants at substations in residential areas were also analyzed. The Mark 4 design was judged to be the best for performance, safety, and manufacturability, while comparing favorably in cost and reliability to the earlier designs.

The Mark 4 module prototype was designed, fabricated, assembled, and tested during Phase I. The principal design goals were to deliver 45 kWh at an electrochemical energy efficiency of 63%. As shown in an exploded view of this module in Figure 2-4, there are three compartments in the module. The uppermost compartment, i.e., above the separator plate, is termed the stack compartment. Located in this compartment are six 10-cell batteries, termed submodules. The electrolyte pump sits in the sump compartment, shown on the lower right. This pump is magnetically coupled to a motor attached to the outside of the module case. The store compartment is located on the lower left. The hardware necessary for chlorine-hydrate formation in charge, and decomposition in discharge, comprises two heat exchangers, a filter, and a gas pump, which is also magnetically coupled to a motor outside the case. A photograph of the fully-assembled module is shown also in Figure 2-4.

In March 1978, the module was tested through 10 consecutive charge-discharge cycles. The design target of 45 kWh

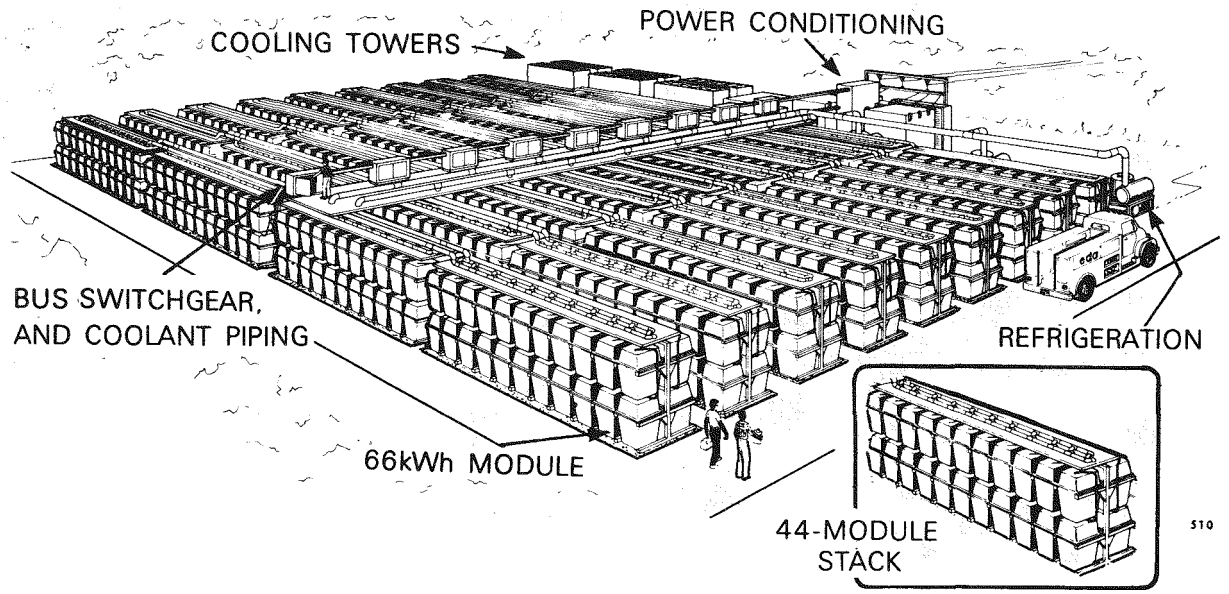

Figure 2-3. 100-MWh zinc-chloride load-leveling battery plant. The battery subsystem consists of 1584 modules on 36 44-module racks, one of which is shown inset.

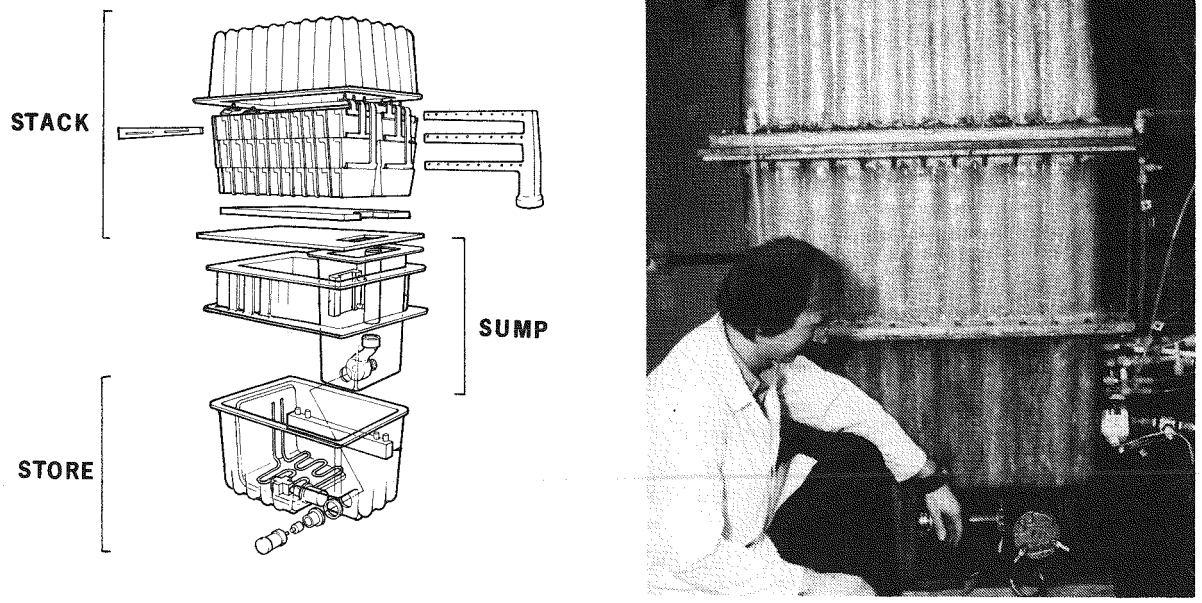

Figure 2-4. Photograph and exploded view of 45-kWh module. Note side-by-side arrangement of store and sump.

was exceeded in two cycles, while the average delivered energy was 43 kWh. However, the electrochemical energy efficiency averaging 49% was below the design target of 63%. The major contributor to this shortfall was the coulombic efficiency which averaged 59%, a full 14% below the design level of 73%. The principal causes of the unexpectedly low coulombic efficiency were shown later to be: (a) zinc growths around and below the intercell busbar in the submodule, which shorted the unit cells in the latter stages of charge; and (b) excessive heat transfer between sump and store during charge resulting in an excessively high chlorine pressure in the stack compartment.

Major advances were made during Phase I in the following development areas: (a) qualification of porous graphites -- the chlorine-electrode material -- and plastics which approach the cost targets for commercialization; (b) development of an in-situ technique for chlorine-electrode activation which shortened the time required from 10 or more days to a matter of hours; (c) invention of a dendrite-inhibiting additive which results in higher-efficiency lower-cost battery stacks; (d) understanding the major cause of significant levels of hydrogen evolution in battery systems, e.g., the 18-kWh battery of RP226-2; and (e) modeling and experimental studies which indicated that a doubling of the active cell dimensions -- 10 cm in height and 6 cm in width -- may be achievable in future stack designs.

The 1.7-kWh 2-volt battery system, built and automated as part of RP226-3, was cycle-tested through Phase I. A total of 500 cycles was accumulated with no measurable changes in delivered energy or electrochemical energy efficiency during this period. This represented 20% of the life target -- 2500 cycles, or 5 cycles per week for 50 weeks per year for 10 years. All of the work performed in Phase I of RP226-3 is described in detail elsewhere (3).

RELATED PROGRAMS AT EDA

The previous subsections, which relate progress in the EPRI-EDA Program from May 1974 through March 1978, serve to introduce Phase II of RP226-3. However, there are two other programs -- the electric-vehicle battery development and the BEST-Battery activities -- which had, and continue to have, a profound influence on the EPRI-EDA Program.

EDA has been developing the zinc-chloride battery for electric-vehicle applications since 1969. In late 1971, EDA installed a battery in a Chevrolet Vega with a mechanically rechargeable battery. This vehicle was capable of speeds up to 70 mph and traveled in excess of 150 miles on a single charge. These development activities continued with EDA funding through June 1976, when ERDA -- the forerunner of the research arm of DOE -- joined with EDA to fund an accelerated program.

RP226-1 grew out of related activities in the electric-vehicle battery program. Since then, the electric-vehicle and load-leveling battery programs have interacted to the advantage of both. Examples of this include the Mark 4 battery-plant concept -- conceived on the basis of series-connecting electric-vehicle battery modules -- and the development of low-cost plastics and more active electrodes in the EPRI-EDA Program, which aided the resolution of major problems in the electric-vehicle battery program. This high level of integration of both programs continues to prove advantageous for EDA in the development of battery technology for both applications.

In September 1978, the U.S. Department of Energy (DOE) and EDA signed a contract which will lead to the design, fabrication, and assembly of a 4.2-MWh zinc-chloride battery system. This program, entitled the DOE-EDA BEST-Battery Program, was formally started in January 1979. EDA was instructed by EPRI and DOE to integrate this new program with the EPRI-EDA Program. In general, the EPRI-EDA Program funded research and development on components through the prototype stage. The DOE-EDA Program funded the subsequent engineering phases. This program will lead to installation of the 4.2-MWh zinc-chloride battery system in the Battery Energy Storage Test (BEST) Facility in Hillsborough, New Jersey, by mid-1981.

REFERENCES

1. Evaluation of a 1-kWh Zinc-Chloride Battery System. Palo Alto, Calif.: Electric Power Research Institute, September 1976. EM-249.

2. Development of High-Efficiency, Cost-Effective Zinc-Chlorine Batteries for Utility Peak-Sharing, 1976. Palo Alto, Calif.: Electric Power Research Institute, March 1978. EM-711.

3. Development of the Zinc-Chlorine Battery for Utility Applications. Palo Alto, Calif.: Electric Power Research Institute, April 1979. EM-1051.

Section 3

HOW ZINC-CHLORIDE BATTERIES STORE AND DELIVER ELECTRIC ENERGY

A schematic of the zinc-chloride system in the fully-discharged state is presented in Figure 3-1. It consists of a cell and a separate container termed a store, which is filled with water. As shown, the cell consists of a zinc electrode, a chlorine electrode, and an electrolyte, which is 2M aqueous zinc chloride. The zinc-electrode substrate is fabricated of graphite, while the chlorine-electrode substrate may be fabricated from porous graphite or ruthenia-catalyzed porous titanium. In this mode, the cell voltage is 0.0 V, as both electrodes are inert, i.e., they do not contain active materials.

In charge, the zinc-chloride electrolyte is electrolyzed. Zinc is plated on one of the graphite substrates while gaseous chlorine is evolved on the other, as shown schematically in Figure 3-2. The chlorine passes from the gas space above the electrolyte into the store where it reacts with water cooled to less than 10°C. Chlorine hydrate, a pale yellow solid, is formed according to the reaction:

$$Cl_2\ (aq) + xH_2O = Cl_2 \cdot xH_2O(s)$$

where the value of x, which is dependent on the experimental conditions, can be as low as 5.7. This reaction is exothermic. The heat of formation of chlorine hydrate is approximately -18kCal/mole. Accordingly, the store must be chilled continuously during charge. In marked contrast to other battery systems, the charging voltage remains constant during charge.

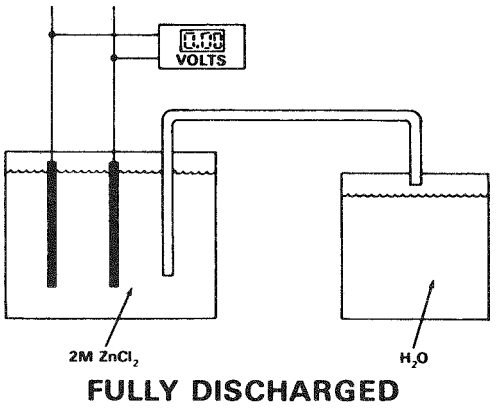

Figure 3-1. Schematic of a zinc-chloride system in a fully-discharged state.

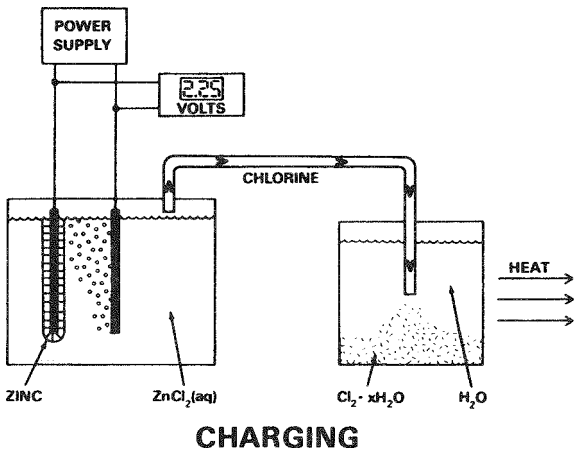

Figure 3-2. Schematic of zinc-chloride system in the charge mode.

At full charge, the zinc chloride concentration in the cell has decreased to 0.5M and the store is full of chlorine hydrate, as shown in Figure 3-3. Under standard conditions, the open-circuit voltage is 2.12 V, calculable from the standard free energy of the reaction:

$$ZnCl_2\ (aq) = Zn(s) + Cl_2\ (aq)$$

This reaction is highly reversible. At the zinc electrode, the exchange current density is high (at $1A/cm^2$) and therefore electrode polarizations at practical current densities, i.e., 25-50 mA/cm^2, are low. In contrast, the polarization of the chlorine electrode is highly dependent on the level of electrode activation.

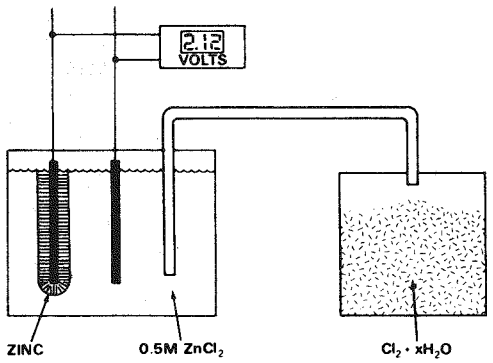

Figure 3-3. Schematic of a fully-charged zinc-chloride system on open circuit.

To initiate discharge, the chlorine hydrate-water mixture in the store is heated by heat exchange with the warmer (20°C-50°C) cell electrolyte. Chlorine passes from the store into the electrolyte adjacent to the porous-graphite chlorine electrode, as shown in Figure 3-4. Electrochemical reaction of zinc and chlorine occurs, releasing electrical energy. Heat is generated in the cell because of thermodynamic, electrochemical, and chemical inefficiencies in the cell reaction. Enough of this heat is transferred to the store to cause the desired amount of chlorine evolution by decomposition of chlorine hydrate. Zinc chloride is formed by the electrodissolution of zinc at the anode and chlorine reduction at the cathode. The battery is considered to be fully discharged when all of the zinc is dissolved. The battery thus returns to the fully discharged state, in which the zinc chloride concentration is 2M, as shown in Figure 3-1.

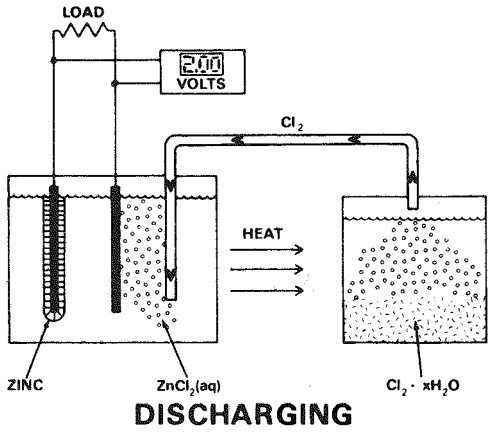

Figure 3-4. Schematic of a zinc-chloride system in discharge.

The simplified sequence in Figures 3-1 through 3-4 illustrates how the zinc-chloride battery system stores and delivers electric energy. In a practical system, however, means must be provided to achieve the desired flows of chlorine, electrolyte, water, and heat, as shown in Figure 3-5. Pump P1 delivers electrolyte to pockets between pairs of porous-graphite chlorine electrodes. The electrolyte passes through the porous-chlorine electrodes into the chamber between the zinc and chlorine electrodes, flows up between the electrodes, and eventually spills through high-resistance cascades back into the sump. Chlorine gas is pumped by P2 through line C. Before entering the pump, the chlorine is mixed with chilled water, which passes through line W and comes from the bottom of the store. The chlorine and chilled water are mixed in the gas pump, chlorine hydrate forms, and the chlorine hydrate-

water mixture is deposited in the store through line H. The water in line W is chilled by passage through a heat exchanger. Glycol cooled by means of a refrigeration system is passed through line R into this heat exchanger. It should be noted that the gas pump, P2, may be operated to significantly reduce the pressure above the battery stack and electrolyte sump. This mode of operation serves to lower the concentration of chlorine dissolved in the electrolyte, which in turn reduces the corrosion of zinc, particularly during charge, thereby increasing the electrochemical energy efficiency.

Figure 3-6 shows this system in discharge. The valve in line D is opened, permitting a stream of warm electrolyte to pass through a heat exchanger in the store. Chlorine is formed by decomposition of chlorine hydrate. On development of the required pressure in the store, the valve in line G is opened and chlorine passes into line E on the high pressure side of the electrolyte pump, P1. The chlorine dissolves in the electrolyte, which is then fed to the porous-graphite chlorine electrodes. The battery stack can now be discharged. Electrodissolution of zinc occurs at the zinc electrode, reduction

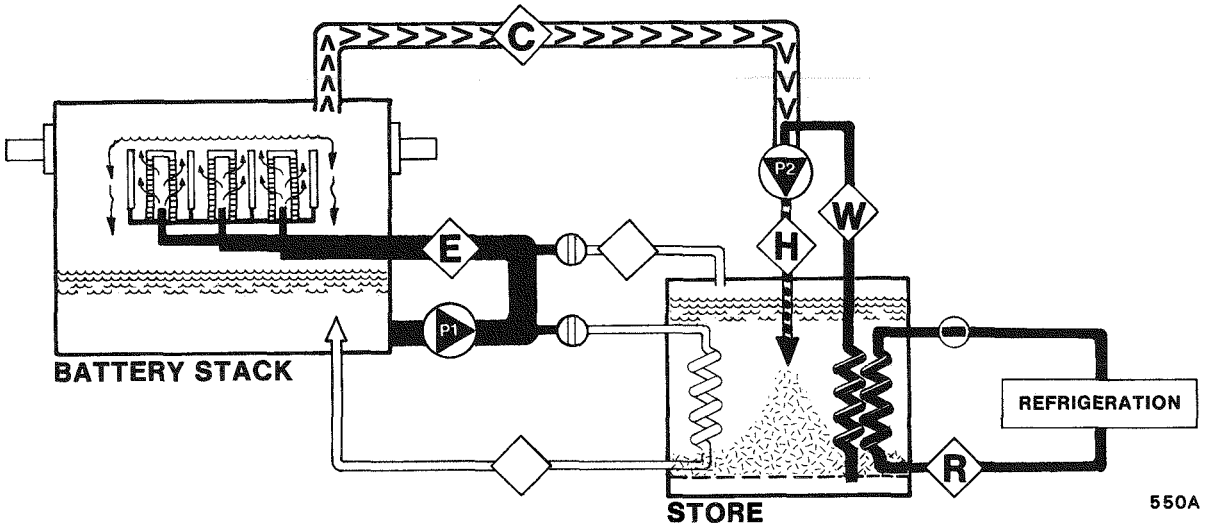

Figure 3-5. Schematic of a zinc-chloride system in charge.

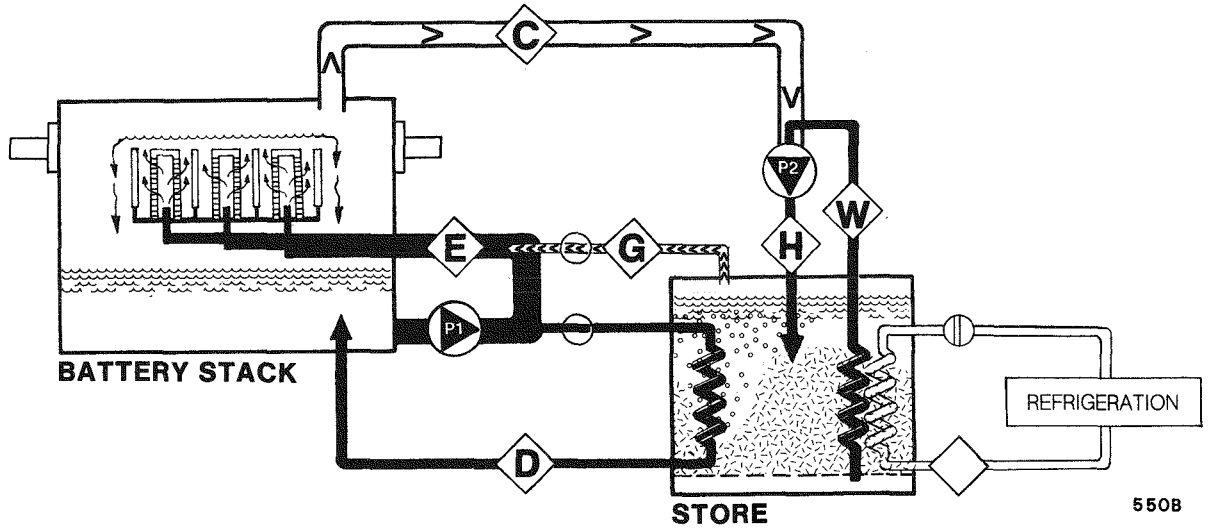

Figure 3-6. Schematic of a zinc-chloride battery in discharge.

of the dissolved chlorine occurs at the chlorine electrode, power is available at the battery terminals, and zinc chloride is formed in the electrolyte.

The above description of how the zinc-chloride battery operates in charge and discharge forms a base for understanding the operation of a battery module -- the basic unit in this technology. Figure 3-7 shows an operational schematic of the 45-kWh module, built and tested as part of Phase I of RP226-3. There are three compartments -- stack, sump, and store. The store is thermally isolated from the stack and sump. During charge and discharge, the store gas-space operates at a higher absolute pressure than the common stack and sump gas-space.

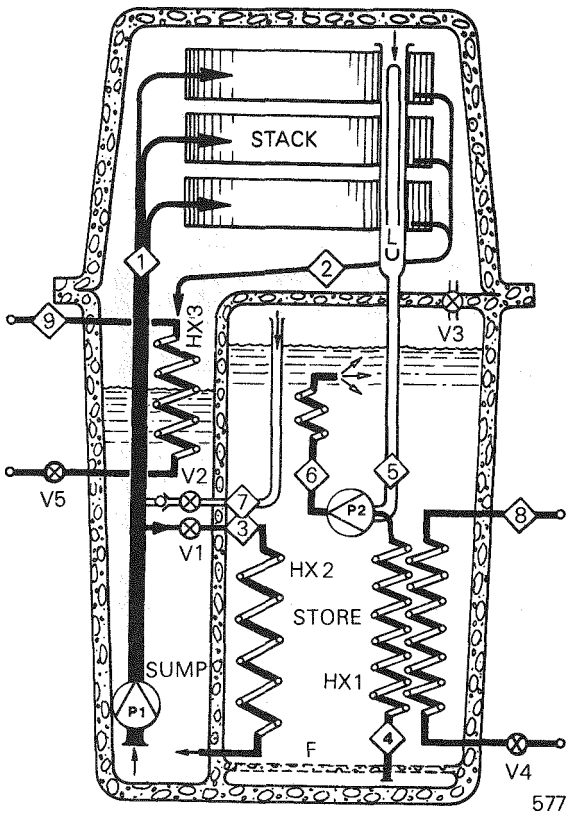

Figure 3-7. Operational schematic of the 45-kWh battery module.

In charge, the electrolyte pump, P1, serves to deliver electrolyte through Line 1 to six 10-cell submodules in the stack compartment. Electrolyte returns to the sump through Line 2. Chlorine from the stack compartment (Line 5) and chilled water (Line 4) are mixed in the gas pump, P2. The mixture of chlorine hydrate and excess chilled water are pumped into the store compartment through Line 6. Hydrogen, formed at the zinc electrodes, is recombined in a photochemical reactor, L, in Line 5. The water required for chlorine-hydrate formation is drawn from beneath the filter, F, located at the bottom of the store. This water is chilled on passing through the hydrate-formation heat exchanger, HX1. The coolant, glycol, is fed through Line 8 (with V4 open). Chlorine which accumulates in the store gas space is vented into the stack compartment through V3, a pressure-relief valve, when the pressure differential exceeds the preset value. At the end of charge, P2 is turned off, and W4, controlling the glycol flow, is closed.

In discharge, P1 continues to deliver electrolyte to the submodules. Valve V1 is opened, and warm electrolyte travels through Line 3 to the decomposition heat exchanger, HX2. Chlorine hydrate is thereby decomposed. The evolved chlorine travels through Line 7 (valve V2 open), and enters Line 1. The electrolyte is thereby saturated with chlorine, which is required for battery discharge. Valve V2 opens when the absolute pressure in the stack compartment -- a measure of whether or not enough chlorine is being supplied for discharge -- falls below a preset level. If the electrolyte temperature, which rises during discharge, exceeds 40°C, valve V5 is opened, allowing coolant to flow through the sump heat exchanger HX3 (Line 9). Further explanation of module operation is given in Part III of this report in which the refurbishment and testing of the 45 kWh module are described in detail.

Section 4

GLOSSARY FOR ZINC-CHLORIDE BATTERY SYSTEMS

Every new technology inevitably develops its own terminology. Zinc-chloride battery development at EDA is no exception. To assist the reader, a glossary of terms commonly used at EDA is presented below. It should be noted that the glossary is neither comprehensive nor does it provide an absolute definition of every term.

activation: method of lowering the polarization for chlorine evolution and/or reduction at the chlorine electrode. For porous graphite, two techniques -- treatment in concentrated HNO_3 for 7-13 days or an electrolytic process -- are commonly employed.

baseline current: the dc current flowing in a unit cell at an applied voltage below the decomposition potential of zinc chloride.

battery plant: zinc-chloride battery plant includes the entire collection of battery strings at a site, buswork and switchgear, power-conditioning equipment, refrigeration equipment including cooling towers, and control facilities.

battery stack: a combination of cells electrically connected in series and/or parallel.

bubble-induced convection: an upwards fluid motion in the electrolyte layer adjacent to the chlorine electrode. This effect occurs only in charge due to electrolyte entrainment by anodically-generated chlorine.

bypass design: a battery-plant design consisting of strings of series-connected modules in which a malfunctioning module can be electrically isolated from the system by closing the module-bypass switch.

bypass switch: a switch that when closed applies a direct short across a battery module. This device is used to isolate a malfunctioning module in a string of series-connected modules.

capacity density: the calculated number of milliampere-hours per square centimeter of zinc electrodeposited during charge, i.e., the product of the average current density and the charge time.

cell gap: separation of adjacent zinc and chlorine electrodes.

cell imbalance: the performance differences between single cells, unit cells, or submodules. This imbalance is observable in the variations of (a) the cell voltages, as the area of the zinc deposit remaining on the electrode determines the cell voltage; and (b) the usable coulombic efficiencies of cells in a submodule.

charge: that phase of battery operation during which zinc is electrodeposited on one electrode and chlorine gas is generated at the other electrode.

charge coulombic efficiency: actual weight of zinc deposited during charge divided by the theoretical weight calculable from Faraday's law.

chlorine electrode: a solid electric conductor providing a surface for the electron-transfer reactions in charge and discharge between chlorine gas and chloride ions. Both porous graphite and ruthenia-catalyzed porous-titanium have been employed as the chlorine electrode material used in the zinc-chloride battery. The chlorine electrode is the positive electrode.

cleanout: that phase of battery operation during which any residual zinc remaining after the completion of the discharge is stripped from the electrodes.

coefficient of performance (COP): dimensionless ratio of the cooling effect of a refrigeration subsystem and the energy input to the compressor.

comb-type bipolar battery stack: a busing arrangement in which the chlorine electrodes of one unit cell and the zinc electrodes of another unit cell are fitted into opposite faces of a common graphite bus to form a comblike structure.

combined convection: combination of three sources of fluid motion -- forced, natural, and bubble-induced convections -- during charge.

cooldown: that phase of battery operation preceding charge during which the store temperature is brought into the range required for hydrate formation.

corrosion current: self-discharge current resulting from the mass-transport-limited reaction of dissolved chlorine with electrodeposited zinc. This current is the major contributor to coulombic inefficiency.

coulombic efficiency: the number of ampere-hours delivered by a cell or battery during discharge divided by the number of ampere-hours supplied during charge.

cycle: one complete sequence of battery operation from standby to cleanout during which the battery is charged and subsequently discharged. Generally, a full cycle involves a five- to seven-hour charge and an approximately five-hour discharge.

delivered energy: the energy delivered during battery discharge in kWh, to the cutoff levels of current density and voltage.

dendrites: tree- or fern-like growths of electrodeposited zinc which may appear on the zinc plate during charge. Capacity density and charge coulombic efficiency may be decreased if they grow sufficiently to contact the chlorine electrode. In addition, nodular or columnar growths (often incorrectly identified as dendrites) may form with similar effects. See also **edge dendrites.**

discharge: that phase of battery operation during which the electrodeposited zinc and dissolved chlorine gas are electrochemically converted back to their respective ionic states, thereby generating electrical energy at the battery terminals.

discharge coulombic efficiency: the energy-average discharge voltage divided by the open-circuit voltage.

discharge profile: the voltage time characteristics of a zinc-chloride cell, submodule, or module from the initiation to termination of discharge.

edge dendrites: needle-like growths which appear at the edge of the zinc plate during charge. These growths, caused by inadequate electrode masking or misalignment of the zinc and chlorine electrodes, may lead to limitation of the capacity density and reduction of the charge coulombic efficiency.

electrochemical efficiencies: coulombic, voltaic, and energy efficiencies in which energy losses due to auxiliary equipment are not considered.

electrochemical energy efficiency: product of the usable coulombic efficiency and the energy-average voltaic efficiency, i.e., the quotient of the watt-hours delivered during discharge to the cut-off levels of current density and voltage and the charge watt-hours.

electrolyte: a chemical compound which upon dissolution in an appropriate solvent forms ions and thereby renders the solution electrically conducting. In the zinc-chloride battery, the solvent is water, and the electrolyte consists of zinc chloride. Supporting electrolytes, such as potassium chloride and sodium chloride, may also be present to improve electrolyte conductivity.

electrolytic activation: method of activating porous-graphite chlorine electrodes by anodizing the electrode in dilute aqueous chloride.

failure modes: the mechanisms by which a battery component or auxiliary unit fails to perform its required function.

flat-plate chlorine electrode: a chlorine electrode which is produced by cutting a plate of the desired thickness from a block of porous graphite. In contrast to the machined chlorine electrode, an internal cavity is created by the physical separation of the two flat electrodes in a plastic frame.

forced convection: the fluid motion between the zinc and chlorine electrodes, which is caused by the passage of electrolyte through the porous-graphite chlorine-electrode and up between the zinc and chlorine electrodes.

frame: an assembly, fabricated of plastic, which is used to hold two flat-plate chlorine electrodes. Electrolyte delivered to the chamber, thus formed by electrodes and frame, will flow through the porous chlorine electrode into the interelectrode gap.

full-power coulombic efficiency: the number of ampere-hours delivered by a cell or battery during discharge, at full-rated current to the point where the cut-off voltage is reached, divided by the total number of ampere-hours supplied to the cell during charge.

hydrate store: a cold-water reservoir in which chlorine gas and water are mixed to form solid chlorine hydrate during charge.

hydrogen/chlorine reactor: a chamber containing ultraviolet lights which acts to recombine hydrogen, formed at the zinc electrodes, with chlorine.

impurities: any organic and/or inorganic substances present in the electrolyte which are not part of the electrolyte formulation.

inerts: any gas present in the battery system other than chlorine, e.g., air, CO_2, H_2. The presence of inerts in the system decreases (a) the partial pressure of chlorine resulting in the requirement of lower temperatures for chlorine-hydrate formation, and (b) the solubility of chlorine in the electrolyte, leading to reduced cell voltage during discharge.

inerts-rejection device: a device which separates chlorine gas from other gases, e.g., carbon dioxide, carbon monoxide, oxygen, nitrogen, hydrogen, etc., -- and retains the purified chlorine in the battery while it rejects the other gases to the ambient.

inter-cell busbar: the common graphite bus in the comb-type bipolar cell design. The inter-cell busbar provides a means of electrically connecting unit cells in series.

inter-cell leakage: the presence of electrolyte paths between unit cells in a submodule due to an incomplete seal between the submodule container and the inter-cell busbar. Intercell leakage may be undesirable as it can (a) result in the establishment of

inter-cell leakage current, thereby reducing battery coulombic efficiency, or (b) lead to the formation of intercell shorting due to zinc growths.

interconnected design: a battery plant design consisting of strings of series-connected modules with buswork connecting equal potential points in the system. If a module fails, only that module is disconnected from the system.

leakage current: dc current flowing between adjacent cells due to intercell leakage. This leads to the self-discharge of zinc and chlorine electrodes attached to opposite sides of the intercell busbar.

leveling agent: an inorganic additive in the electrolyte, which effects a measurable increase in the battery capacity density by promoting the formation of flat, uniform zinc electrodeposits and a consequent reduction in the number of dendrites or other zinc growths.

levelization: the process of converting a variable stream of revenue requirements into an equivalent constant amount. The levelized annual revenue requirement is calculated by summing up the present worth of each year's revenue requirement and converting the sum into an equal-payment annuity. This provides a convenient technique for comparison of competing technologies with different capital costs, efficiencies, O&M charges, and useful lifetimes.

levelized annual busbar cost: the levelized revenue requirement of a generating option divided by its annual kilowatt-hour output, levelized over the life of the unit, and expressed in cents per kilowatt-hour.

levelizing factor: a factor which when multiplied by the first-year cost of a unit yields the levelized annual cost of the unit.

machined chlorine electrode: see profiled chlorine electrode.

masking: the practice of covering certain edges of the electrodes with a chemically inert material for the purpose of defining the active area of a cell. Masking is utilized to minimize the probability of the formation of dendrites or other growths at the edge of the zinc plate.

module (Mark 2): a similar assembly to the Mark 4 module but without an integrated hydrate store and hence, incapable of independent battery performance. The rated capacity of the Mark 2 module is one megawatt-hour.

module (Mark 3): a larger version of the Mark 2 module with a rated capacity of six megawatt-hours.

module (Mark 4): an assembly consisting of a battery stack (sized to deliver 50 kWh); an electrolyte sump; and a store for the formation, storage, and decomposition of chlorine hydrate.

module-bypass switch: see bypass switch.

monopolar comb: a busing arrangement in which electrodes of only one polarity are press-fitted into one face of a graphite bus. The joining of two monopolar combs of opposite polarities provides a convenient way of electrically connecting single cells in parallel to form a unit cell.

natural convection: the fluid motion generated by the density difference between the bulk electrolyte and the electrolyte adjacent to the zinc electrode. The density difference is caused by the concentration changes resulting from depletion or addition of zinc species in this layer during charge and discharge, respectively.

overall energy efficiency: the net ac energy output from the battery system divided by the total ac energy input to the system for a complete cycle. The total ac energy input includes energy supplied to auxiliaries and ac-dc conversion equipment.

overcharge: the charging of a battery beyond its rated capacity.

overdischarge: a mode in which the battery is operated in discharge with no zinc metal on the zinc electrodes. This process results in chlorine evolution on the zinc electrode. The zinc-chloride battery does not suffer performance-wise in subsequent charge-discharge cycles because of overdischarge.

parasitic current: an electric current flowing in the common electrolyte surrounding a collection of electrochemical cells electrically connected in series. This current is due to either the electrolyte paths in the inlet manifolds or the electrolyte return loops from the cells back to the sump.

Phase I submodule: first of two Mark 4 design submodules employing machined, and subsequently glued chlorine-electrode pairs. Nominal rating, 8.3 kWh, comprising 10 series-connected unit-cells using the comb-type bipolar design.

Phase II submodule: second of two Mark 4 submodule designs highlighting more effective unit-cell isolation for improved balance, framed flat-plate chlorine electrodes, and the use of PVC.

polarization: the voltage difference between the actual cell voltage and the theoretical reversible cell voltage when current flows through the cell.

power conditioning: that battery plant subsystem which accomplishes the conversion of ac electric power to dc electric power during the charging of the battery, and the conversion of the dc power output of the battery during discharge to ac power.

profiled chlorine electrode: a porous-graphite electrode into which is cut an internal cavity by machining. Two of these electrodes are cemented together with an adhesive to form a chlorine-electrode pair. Electrolyte delivered to the intra-electrode chamber thus formed flows out through the porous electrode.

pumping efficiency: the product of the pump and electric motor efficiencies. The motor efficiency consists of the power supplied to the pump shaft divided by the electric power supplied to the motor. The pump efficiency consists of the power delivered by the pump divided by the power supplied to the pump shaft.

rack: A steel structure on which are mounted a string of modules, and the piping and wiring networks supplying those modules.

refurbished 45-kWh module: the 45-kWh prototype load-leveling battery module, built and tested during Phase I of RP226-3, which was modified during Phase II to increase the delivered energy and electrochemical energy efficiency to greater than 50 kWh and 60%, respectively. The principal modifications were: (a) relocation of the sump to reduce heat transfer to the store during charge, and (b) elimination of intercell zinc growths in the submodules.

revenue requirement: the minimum dollar amount that must be recovered in order to compensate the utility for all the expenditures made as a result of investing in a generation option. The expenditures include operation and maintenance expense, fuel cost, debt and equity return, depreciation, taxes, and insurance.

reverse plating: zinc plating on the chlorine electrode. In general, it would only occur on a discharge cycle if the chlorine electrode receives an inadequate supply of chlorine to sustain the applied current density.

single cell: an electrochemical combination of a single positive electrode (referred to as the chlorine electrode) and a single negative electrode (referred to as the zinc electrode).

standby: that phase of automated battery operation during which the battery is in an idle state. The standby phase is always entered after the detection of a system failure.

string: a series-connected set of modules, sufficient in number to obtain the desired battery-plant voltage.

string-out design: a battery-plant design consisting of strings of series-connected modules. If a module in a given string fails, the entire string is disconnected from the system.

submodule: a combination of unit cells electrically connected in series, housed in a common container, and fed by a common electrolyte manifold. In the Mark 4 design, 10 unit cells form a submodule. Six submodules comprise the battery stack in a module.

sump: an electrolyte reservoir, located below the battery stack.

super-string: a combination of two or more battery strings electrically connected in parallel. In the Mark 3 design, six battery strings are paralleled to form a 36-MWh super-string.

total coulombic efficiency: the total number of ampere-hours delivered by a cell or battery during discharge to zero volts and zero current, divided by the total number of ampere-hours supplied to the cell during charge.

turnaround: that phase of battery operation following charge and during which the electrolyte is chlorinated in preparation for discharge.

unit cell: a combination of a number of single cells electrically connected in parallel. There are 10 unit cells in a Mark 4 submodule.

usable coulombic efficiency: the number of ampere-hours delivered by a cell or battery during discharge, at minimum-rated current until the cut-off voltage is reached, divided by the total number of ampere-hours supplied to the cell during charge.

vent hole: a small ($\sim$0.060") hole in the upper surface of a chlorine-electrode pair. This hole permits the release of chlorine from the pocket between the chlorine electrodes.

voltaic efficiency: the energy-average discharge voltage divided by the energy-average charge voltage. Product of charge and discharge voltaic efficiencies. Quotient of electrochemical energy efficiency and usable coulombic efficiency.

zinc electrode: a solid electric conductor providing a surface for the electron-transfer reactions in charge and discharge between metallic zinc and zinc ions. The zinc electrode substrate is fabricated of relatively dense graphite. The zinc electrode is the negative electrode.

PART II

ZINC-CHLORIDE LOAD-LEVELING BATTERY PLANTS

Section 5

PROGRAM STATUS: COMMERCIAL BATTERY PLANTS

INTRODUCTION AND BACKGROUND

The increasing demand for electricity and the high cost and short supply of petroleum oil and gas have created an urgent need for more efficient baseload generation (nuclear and coal-fired), and less dependence on petroleum-fired peaking units. The electric utilities use several different types of generating facilities to meet a load that is continuously varying with time. Baseload generation accounts for 50-60% of utility installed capacity. The balance is divided between coal and oil fired intermediate cycling equipment, and oil or gas fired turbines. If the electric utilities are to achieve a significant decrease in the use of petroleum fuels, alternatives such as solar, hydro, synthetic fuels, energy storage, and load management must receive increasing use in generating electricity.

Batteries which store off-peak electric energy to be used during peak demand, offer the potential for conserving substantial quantities of oil and gas that would otherwise be burned by combustion turbine peaking units. This concept provides the motivation for the continuing interest in advanced battery systems that are suitable for load-leveling service. Progress made in one of the most promising systems, the zinc-chloride battery, is reviewed in this report.

As development efforts in the zinc-chloride battery and other batteries have accelerated, attempts have been made to forecast the potential market (1,2), by assuming expected trends in GNP (gross national product), productivity, and employment; and acceptable battery performance and economics. Invariably, these studies have forecast a large market and significant conservation of petroleum-based fuels. Such market assessments have resulted in Electric Power Research Institute and Department of Energy funding of advanced-battery energy-storage systems suitable for utility load-leveling.

The commercially exciting market assessments should be tempered by the realization that they are based on assumptions that have a certain level of uncertainty. Even the assumed increasing use of coal and nuclear baseload generation can be questioned in view of environmental constraints. Never the less, there is a high probability that a substantial market will develop for load-leveling batteries during the next few years. To capture this market, accelerated development programs, pilot plant production, demonstration in a utility environment, and commercial production are required. In concert with this will be the development of marketing strategies and their implementation.

Assuming that electric utilities have broadly accepted the concept of petroleum conservation by the use of energy storage, the economic attractiveness of the various alternatives available must be carefully analyzed. Obviously, batteries must compete economically with combustion turbines. How favorably they compete will determine the rate of market penetration, and will be directly affected by the cost escalation rate for petroleum fuels. Other factors such as availability of suitable sites, environmental constraints, large investment, and long construction time must be considered when pumped

hydro and compressed-air storage are evaluated relative to batteries.

Commercialization considerations are an important part of the EPRI-EDA program and continue to be emphasized in the DOE-EDA BEST-Battery Program. Studies involving cost analyses, safety and environmental concerns, legal aspects of siting battery plants, module design and production, and finally the conceptual design of commercial battery plants have been addressed in earlier programs. These considerations led to the Mark 4 commercial plant design reported in an earlier EPRI Report (3). The continuing study of the issues that affect the market acceptability of the zinc-chloride battery are addressed in Part II of this report.

BATTERY PLANT ISSUES

Issues that must be satisfactorily resolved prior to commercial production and marketing of the zinc-chloride battery include the following: (a) commercial plant design, (b) cost of electricity, (c) capital costs, (d) efficiency, (e) reliability, (f) safety, and (g) commercialization. The progress made in each of these areas, and the project status relative to commercial production and marketing are reviewed in Part II of this report.

Design of a Commercial Zinc-Chloride Battery Plant

Section 6 presents a modified Mark 4 commercial battery plant design based on the most recent subsystem developments. It reflects a response to the requirements of electric utilities for plant unit capacity, reliability, and maintainability. Module operating characteristics derived from actual prototype performance and improved applications of the various plant subsystems are considered.

A layout of a 100-MWh plant as presently conceived is shown in Figure 5-1. It consists of four independent 25-MWh units. Like a conventional power plant generating unit, the battery unit is complete with modules, converter, refrigeration, and control subsystems. Each 25-MWh system contains four strings, each containing 120 series-connected modules controlled by one of four independent bridges of the converter.

The refrigeration/cooling subsystem consists of one compressor, two condensers, and a Freon receiver with pumps and controls. The battery unit is controlled and supervised by a microprocessor-based control subsystem. Adequate space is provided between the three-tier battery racks and the various subsystems to permit easy access for maintenance and replacement.

Based on discussions with representatives of both large and small electric utilities, it is apparent that the plant design must be flexible enough to accommodate the requirements of a specific station or substation. The present design provides electric utilities with planning and operating flexibility, and addresses important aspects of insulation coordination and circuit protection.

Electricity-Cost Targets for Commercial Battery Plants

Section 7 establishes targets for the cost of electricity generated by zinc-chloride battery plants. These targets are based on the levelized busbar cost of electricity generated by other energy storage systems available to the electric utilities. Concepts for energy storage that are at various levels of technical development include: thermal storage, flywheel energy storage, super-conducting magnetic storage, and other battery systems. However, combustion turbines, pumped hydro, and possibly compressed air storage are developed sufficiently to be commercially considered. Combustion turbines and pumped hydro storage are commonly used. The first commercial compressed air storage installation started operation in 1979 in Huntorf, Germany. The facility can generate 290 MW for two hours

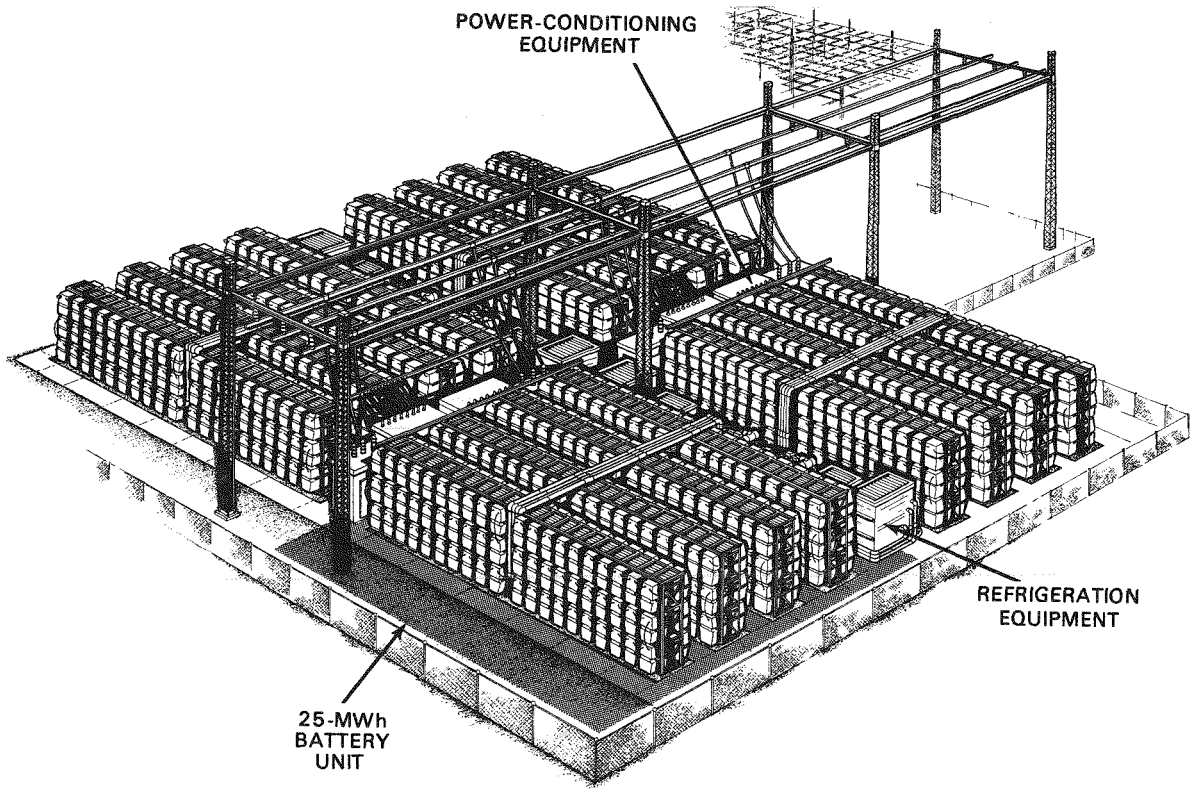

Figure 5-1. Artist's rendition of a 100-MWh zinc-chloride load-leveling battery plant located at a utility substation.

(4). The economic attractiveness will be established based on actual service over a period of time.

The levelized busbar cost of electricity for each storage system has been calculated in 1980 dollars to be 0.208 $/kWh for combustion turbines, 0.099 $/kWh for pumped hydro, and 0.149 $/kWh for compressed air storage. Although the economics favor both pumped hydro and compressed air over combustion turbines, there are other factors that must be evaluated, i.e., availability of suitable sites, environmental constraints, optimum size of storage system, large investment required, and the long construction period. It is apparent that the combustion turbine is the most significant competition to battery energy storage. Indeed, its operating cost establishes a target for the cost of electricity from zinc-chloride battery plants.

When reasonable values for the costs of plant auxiliaries, charging energy, operation and maintenance, and battery cycle life are assumed, it is shown that battery module cost can be as high as $100/kWh and the cost of electricity still be competitive with combustion turbines -- 0.208 $/kWh.

A parametric analysis of the cost elements that make up the total cost of electricity shows conclusively that variations in module costs more significantly affect the cost of electricity than variation in efficiency and cycle life, or cost of plant auxiliaries, charging energy, or operation and maintenance. The high sensitivity of levelized busbar cost to battery capital cost is shown in Figure 5-2. The relative significance of each cost element is analyzed in this section.

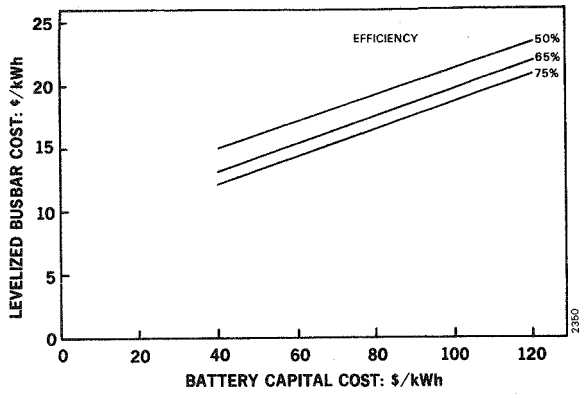

Figure 5-2. Levelized busbar cost of electricity vs. battery capital cost at various values of efficiency, showing relatively high sensitivity to capital cost variations.

Capital Costs of Battery Plants

Section 8 addresses capital costs in 1980 dollars of modules expressed in $/kWh and of plant auxiliaries expressed in $/kW. Having specified the plant design, reasonably accurate costs can be established for plant auxiliaries as shown in Table 5-1.

Table 5-1

ESTIMATED COST OF AUXILIARIES IN A COMMERCIAL ZINC-CHLORIDE BATTERY PLANT

Auxiliary	Estimated Cost $/kW
Power Converter	60
Refrigeration and Cooling	70
Battery Rack	5
Control Equipment	10
Site Preparation and Enclosure	30
Total	$175

However, the cost of modules has a much higher degree of uncertainty. A detailed cost analysis has not been made since that reported in EPRI Report EM-1051 (3). This projected cost of $27/kWh is updated to $47/kWh by correcting for inflation and a change in module capacity.

Assuming $175/kW for plant auxiliaries as shown in Table 5-1, a cost of electricity competitive to that for combustion turbines, and reasonable values for charging energy, operation and maintenance, and battery cycle life; it is shown that battery modules can cost as much as $100/kWh. A comparison of this upper cost limit with the updated cost of $47/kWh indicates a favorable probability of battery plants being economically competitive with combustion turbines.

Efficiency of Battery Plants

Section 9 addresses the efficiency of zinc-chloride battery plants in terms of the sources and types of energy losses in the system. The parametric assessment of electricity cost reported in Section 8 suggests that for certain values of capital and operation and maintenance (O&M) costs, a battery plant operating at an efficiency of 0.50 can compete economically with combustion turbines. However, pumped hydro plants display efficiencies in the range of 0.65 to 0.75. Accordingly, an overall efficiency target of 0.65 has been established for a zinc-chloride load-leveling system. This represents the ratio of ac energy delivered to and from the utility grid by the battery plant. Previous studies have shown that the electrochemical energy efficiency should lie at 0.73-0.75 in order to achieve an overall efficiency target of 0.65 (3). Thus, a target of 0.75 is established for module efficiency.

This section identifies and discusses energy losses in the cell and multicell battery stacks. Recent cell data suggest that the electrochemical efficiency target of 0.75 is achievable with improved technology.

The energy requirements for module components and auxiliary subsystems are identified and discussed. An analysis of the effect of individual component efficiencies on the net efficiency of a zinc-chloride load-leveling plant demonstrates that the electrochemical energy efficiency of the battery is the component efficiency that has the major impact.

An energy flow diagram shown in Figure 5-3 illustrates the influence of auxiliary component efficiencies on the net plant efficiency. Assuming an electrochemical energy efficiency of 0.75 and targeted values for component and subsystem efficiencies, the net result is an energy storage plant that operates at 0.65 energy efficiency.

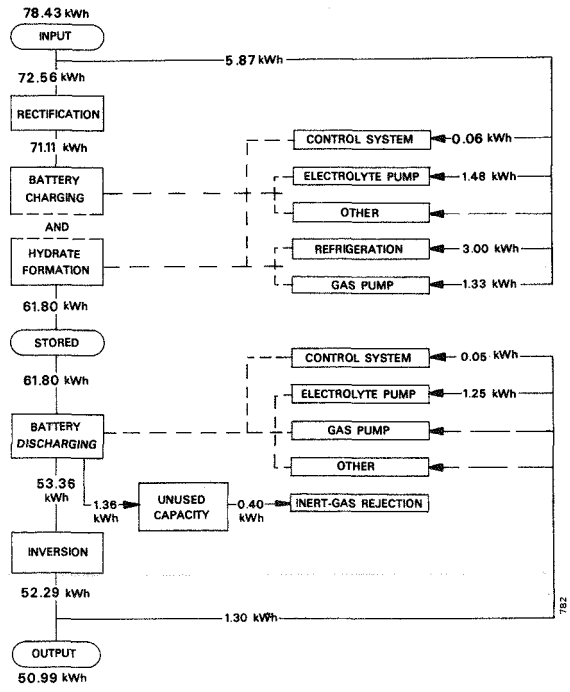

Figure 5-3. Energy flow diagram for a battery which operates at an ε_e of 0.75 and incorporates auxiliary components which operate at target efficiency levels. The net plant efficiency is 0.65.

Reliability Aspects of Battery-Plant O&M Costs

Section 10 quantifies reliability of zinc-chloride battery modules and systems in terms of O&M costs of a battery plant. Cost targets for O&M believed to be acceptable to the electric utilities are established.

The reliability of the series-parallel array of battery modules is identified as the major contributor to O&M costs. Analysis of this subsystem shows that acceptable reliability is achieved when a module-bypass switch is incorporated into the design. This concept -- rendered possible by the storage of chlorine external to the battery stack -- allows the isolation of a single module in the event of a module component failure.

The failure rate of a battery module cannot be accurately predicted because of the limited test data available. The module-failure rate is needed to obtain reliability related operating costs. It is shown that it will take approximately two years of testing to establish this rate directly from module cycling data. In view of this, failure rates published for components similar to those in the module are used to estimate module failure rate.

O&M costs based on the estimated failure rate show: (a) the cost of lost capacity caused by forced outage of modules meets the targeted value, and (b) the cost of repair and replacement of failed modules is significantly greater than the targeted value.

Module design modifications are necessary to reduce the cost of module repair and replacement. These include: (a) design simplification to reduce the number of components, (b) module reconfiguration to minimize repair costs, and (c) increasing the capacity of the module.

Safety Issues for Zinc-Chloride Battery Plants

Section 11 discusses safety and environmental acceptability of zinc-chloride battery plants. Safety features designed into both the battery module and plant are discussed. Chlorine can be released from the module only in the event of an accident or a module malfunction. Release in either event does not result in a hazardous condition. It is concluded that battery operation poses no hazard to either the public or the environment.

The theoretical analysis of the spread of accidentally-released chlorine was presented in an earlier EPRI Report (3). It was shown that in the worst case accident dangerous levels of chlorine concentration spread only 50 feet from the battery plant perimeter. Experimental data recently developed by Factory Mutual Research Corporation from actual spill tests show no significant deviation from the theoretical analysis. In these studies it was assumed that the plant would not be enclosed. Obviously, a building enclosure would provide additional possibilities for safe handling any release of chlorine. Properly designed zinc-chloride battery plants are safe and have unlimited siting possibilities.

Commercialization of Zinc-Chloride Battery Plants

Even though there have been no specific marketing activities addressed in this program, marketing studies supported by the Electric Power Research Institute, the Department of Energy, and private industry provide a basis for the development and implementation of a marketing strategy. Greater emphasis will be placed on this area as the total program moves toward production and sales.

An important step toward commercialization of the zinc-chloride battery is the evaluation and demonstration of a prototype, 4.2-MWh battery at the BEST Facility. Figure 5-4 shows the location of the battery and auxiliaries in the BEST Facility. A pilot plant located in Greensboro, North Carolina is nearing completion. Initially, this facility will have a capacity of one 50-kWh module per day. The development of this pilot production facility is identified as an important step toward commercialization. It provides an opportunity for closer evaluation of projected production costs, evaluation of design and process improvements, and a basis for design of a production facility that will serve a semimature market.

Following a successful demonstration at BEST, a full-size (50-100 MWh) demonstration plant will be necessary before the zinc-chloride battery will be broadly accepted by the utilities. The design and location of a demonstration plant is being considered in the DOE-EDA BEST-Battery Program. Future plans call for installation of a demonstration plant on a utility in the 1983 time frame.

Commercialization will require significant participation by the electric utility companies and the continued integration of EPRI-, DOE-, and EDA-supported programs in concert with the development and implementation of appropriate marketing strategies.

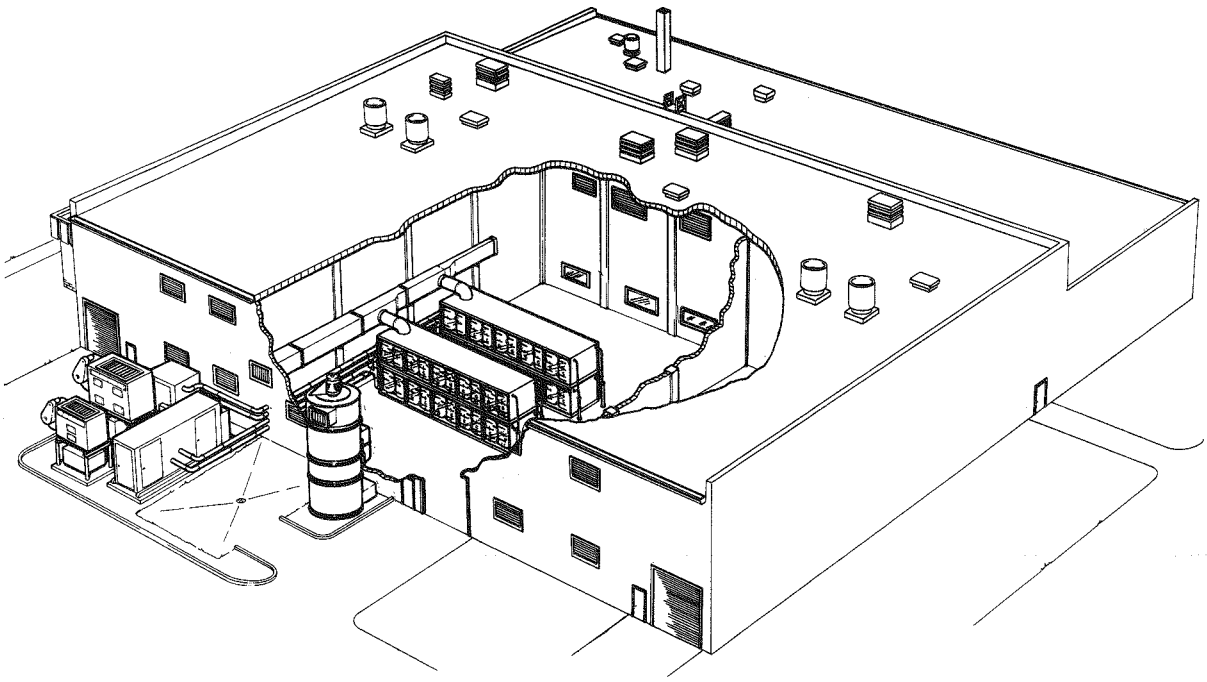

Figure 5-4. The 4.2-MWh zinc-chloride battery system in Test Bay No. 2 at the BEST Facility.

REFERENCES

1. J. R. Birk and J. W. Pepper. "Reducing Oil Requirements in the Electric Utility Industry; The Need For Energy Storage." In Proceedings of the Symposium on Load Leveling, Vol. 77-4, p. 61.

2. D. L. Douglas. "Commercialization of Advanced Batteries - Will It Happen?" In Proceedings of the Symposium on Load Leveling, Vol. 77-4, p. 179.

3. Development of the Zinc-Chlorine Battery for Utility Applications. Palo Alto, Calif.: Electric Power Research Institute, April 1979. EM-1051.

4. F. R. Kalhammer. "Energy Storage Systems." Scientific American, Vol. 241, p. 57.

Section 6

DESIGN OF COMMERCIAL BATTERY PLANTS

ABSTRACT

The design of a commercial zinc-chloride load-leveling battery plant based on the most recent battery-subsystem developments is presented. The new design is characterized by the implementation of a new concept -- the module-bypass switch -- the introduction of a 24-pulse converter with four independently-controlled thyristor bridges, the reduction of a battery-unit size to 25 MWh, 5 MW, and the improved land utilization resulting from a 3-tier rack configuration. A 100-MWh plant is comprised of four separate battery units. Each unit consists of four strings made of 120 series-connected modules. Each string is connected to one of four independent converter bridges. A new control scheme utilizing a microprocessor-based controller is also described. The new design substantially improves unit reliability. It provides electric utilities with greater planning and operating flexibility, and addresses important aspects of insulation coordination and circuit protection.

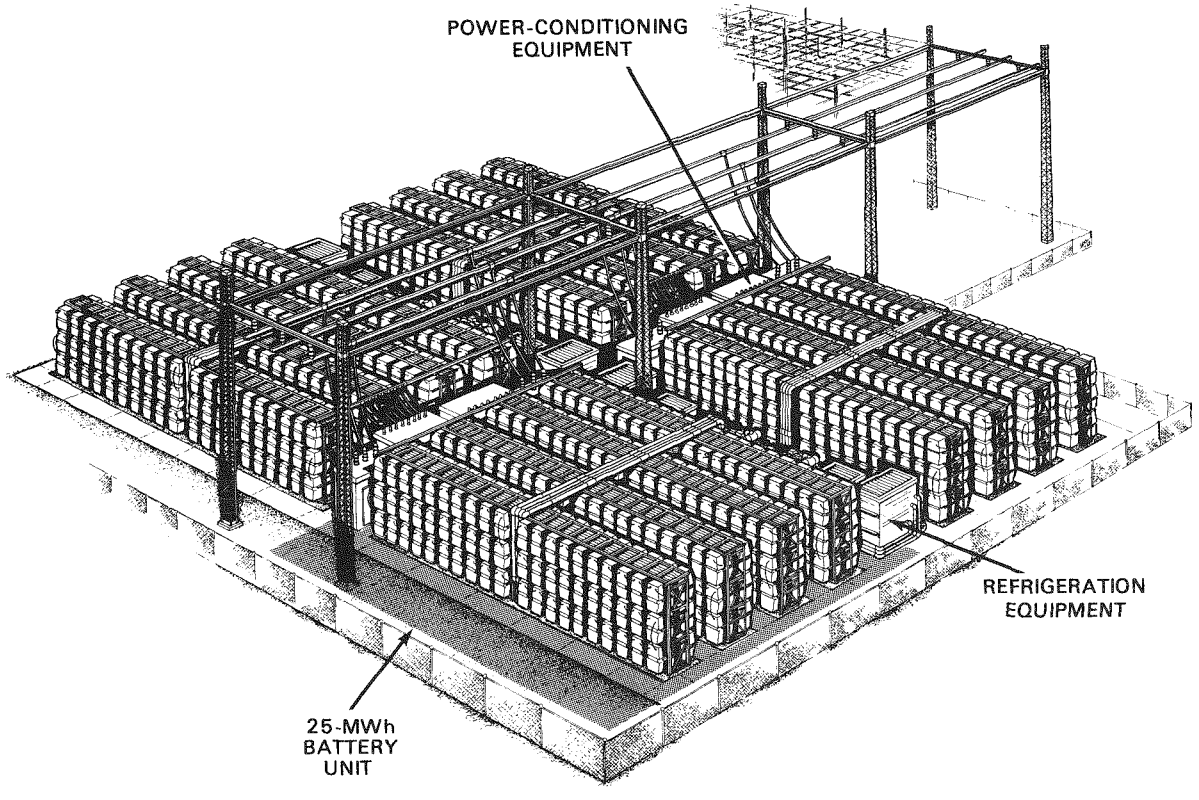

Figure 6-1. Artist's rendition of commercial 100-MWh load-leveling battery plant.

INTRODUCTION

The Mark 4 design for 100-MWh zinc-chloride load-leveling battery plants was conceived in early 1977 and described in an earlier EPRI report (1). Since that time, several iterations of this design have been performed, as a part of the EPRI-EDA and the DOE-EDA BEST-Battery Programs. In all these iterations, the battery module, as conceived in the Mark 4 design, has remained the major building block. The method of interconnecting modules, however, has experienced significant improvements made possible by the development of the module-bypass switch. The latest concept of a commercial zinc-chloride load-leveling plant reflects EDAs response to the requirements of electric utilities for plant-unit capacity, reliability, and maintainability. It utilizes module operating characteristics derived from actual prototype performance, and incorporates improved applications of the different battery-plant subsystems.

A commercial plant with a capacity to deliver 100 MWh of energy is illustrated in Figure 6-1. The layout of this plant, as presently conceived, is shown in Figure 6-2. It consists of four independent 25-MWh units. A battery unit, like the conventional generating unit in a power plant, is a separate entity, complete with its battery modules, converter, refrigeration and control subsystems. It comprises four battery strings. Each string contains 120 modules, electrically connected in

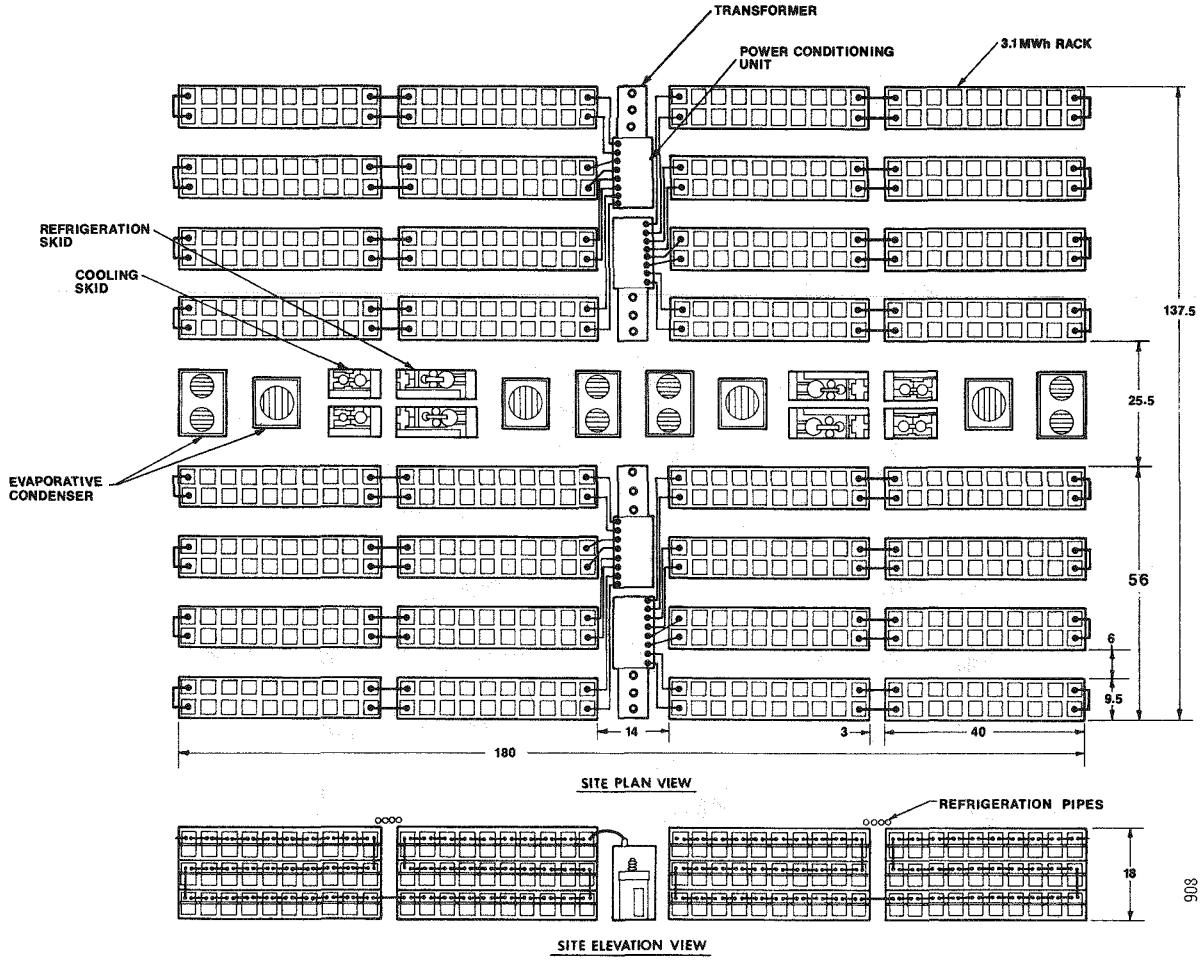

Figure 6-2. Plan and elevation layout of commercial 100-MWh load-leveling battery plant.

series, and controlled by one of four independent bridges of the converter. The battery unit, therefore, is equipped with one single power conditioning subsystem capable of separately controlling the current and voltage of each string, which is divided into two racks, as depicted by the blocks on Figure 6-2. The refrigeration/cooling subsystem consists of one compressor, two condensers, and a Freon receiver with pumps and controls. The operation of the entire unit is controlled and supervised by a microprocessor-based control subsystem. Figure 6-2 shows four such units laid in a symmetrical configuration to form a 100-MWh plant. Adequate spacing is maintained between strings, racks, and units to allow for easy access to the different plant components for maintenance or replacement. The relative position of the units can be modified to fit specific sites.

This section provides a detailed description of the different subsystems which constitute a unit battery. It gives the reasons underlying the selection of this design and discusses its salient features.

BATTERY MODULE

The building block of a battery unit is a module. The details of construction and performance of the module will be presented in subsequent sections of this report. Since this section, however, covers the design of the entire plant, those features of the module which may have a bearing on the overall design are briefly reviewed.

Physically, the module is 44 by 44 by 60 inches high and is a self-contained electrochemical storage unit, complete with stack (the cells), sump (electrolyte container), store (chlorine-hydrate container), heat exchangers, pumps, valves, inerts-rejection device, hydrogen-chlorine recombination reactor, and a stack-pressure measuring transducer. Pump motors, battery terminals, and coolant hose connections are all located on the front of the module facing the aisle space in the plant to facilitate easy installation, maintenance, and repair. Anticipated changes in the design are expected to reduce the size of the commercial module in each direction by a few inches.

A rolled-steel channel section is fastened around the module to the plastic case at approximately one-half the height with the two flanges protruding. One of these flanges will be used to support the module in the rack and the other will be used for handling the module with a fork lift or similar device. The design and construction of the module permit its handling either in a dry state or when it is filled with electrolyte and store fluids.

Electrically, the module is a dc source (or sink, on charge) having the following characteristics: open-circuit voltage, 21.2 volts; full-load current (charge/discharge), 544 amperes; charging voltage at full-load current, 22.2 volts; discharge voltage at full-load current, 19.6 volts; module capacity, 53.4 kWh; and charge/discharge durations, 7 and 5 hours, respectively.

Figure 6-3 is a black-box representation of the module showing the mechanical and electrical "ports" through which it is interconnected to the system. It is the intent of this section to specify the manner in which these interconnections are designed in order to fulfill the requirements of electric utilities for a battery load-leveling plant.

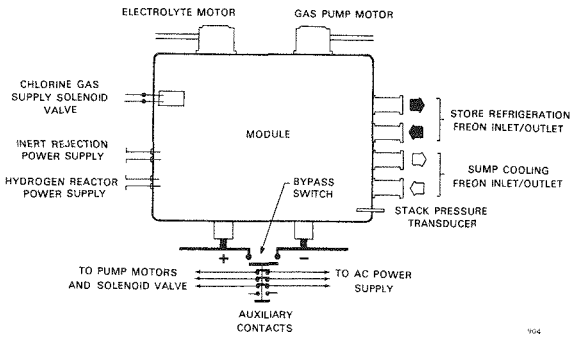

Figure 6-3. Black-box representation of the battery module and its major auxiliary devices.

The development of the bypass switch shown in Figure 6-3 has had a significant impact on the battery plant design. Its purpose is to short and bypass any module that shows signs of malfunction without affecting the operation of any other module in the system. A quantitative analysis of the impact this method will have on system reliability is presented in Section 10. However, a functional description of the switch, as well as the technical reasons supporting its use are given here.

The bypass switch, installed across the module terminals, is conceived to be a simple, robust, inexpensive, normally-open, single-pole switch with three normally-closed and one normally-open auxiliary contacts. The main contact is capable of continuously carrying the full-load current. It is designed to also carry the momentary short-circuit current without exceeding a temperature of 90°C in a 40°C ambient. As the switch is not intended to break dc current, its construction is unsophisticated. One of the auxiliary contacts (normally open) is for switch status indication. The remaining three auxiliary contacts are inserted in series with the feeds to the two pump motors and to the gas-supply control solenoid valve. When the switch is electromagnetically triggered, the main contact closes, shorting the module, while three auxiliary contacts open to turn off the pumps and the gas supply control valve. The fourth contact signals the status of the switch to the battery controller. Operator intervention is required to restore the switch to its open position.

The use of such a bypass switch is possible only because the zinc-chloride battery tolerates short-circuits without sustaining damage, and supplies a rapidly decaying short-circuit current, as illustrated in Figure 6-4. Upon shorting the module, its current instantly jumps from the full-load value of 540 A to 15,000 A, and proceeds to decay to its full-load value within approximately 15 seconds. This plot of current versus time was obtained with the pump and gas control valve turned off at the instant the short-circuit was initiated.

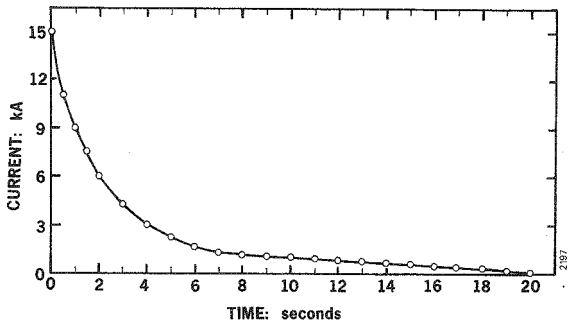

Figure 6-4. Short-circuit current vs. time for a zinc-chloride battery module. Pumps turned off and gas supply valve closed at initiation of short-circuit.

RACK ASSEMBLY

The details of the Mark 4 battery rack and the design philosophy were presented in EPRI EM-1051 (1). Since that time, improvements and changes in the design of the module have been made. The size and shape of the present module are significantly different from those of its predecessor. These changes in module design forced some changes in the design of the racks.

The rack will be the final factory assembled unit for ready shipment to any plant site. It will be completely self-contained with all the intermodular connections and other electrical and fluid connections in place. The only hookups needed in the field are one connection each between the main plant distribution (ac, dc, control, and coolant) lines, and the rack-assembled distribution lines. This design concept is followed to keep the on-site labor to a minimum. The work done in the factory will be assembly-line work with people trained for specific jobs and with properly designed tooling.

The plant layout (Figure 6-2) gives the plan and elevation views of the three-tier racks, with 32 racks making up a plant of 100-MWh capacity. Each rack consists of 60 modules, with 20 modules (2 wide and 10 long) in each tier. Each level of the three-tier rack is assembled and transported independently. These three subracks forming a rack are identical in design and con-

struction except for the bottom member where some modifications are needed to provide proper support depending on the site conditions.

The details of a subrack are shown in Figure 6-5. Structural steel with weatherproof coating is used to build the rack. The modules are assembled in the rack as shown in the figure and fastened to it. Refrigeration and coolant piping, and electrical wiring conduit for all the modules on the subrack, are also assembled and fastened to the rack. Coolant and electrical connections between the modules are made in the plant and the assembly, as a unit, is factory tested and trucked to the plant site. The length of each subrack is 40 feet and its width and height are 9-1/2 feet and 6 feet, respectively. The size and weight of the subrack assembly are within limits for road or rail transportation anywhere in the country.

At the plant site, the subracks will be stacked three high and the coolant and electrical connections made between them and the main distribution lines.

BATTERY UNIT

A battery unit, nominally rated at 25 MWh, 5 MW, comprises 480 modules grouped into four identical strings (Figure 6-6). Each string consists of 2 racks, or 120 modules electrically connected in series by means of 750 kcm, PVC (polyvinyl-chloride) or Hypalon (chlorosulfonated cross-linked polyethylene) insulated copper conductor cables. The nominal string dc voltage is 2.5 kV. This system is ungrounded to enhance battery safety, since contact between any single battery terminal and ground does not produce a power discharge. A provision is made, however, to detect string ground faults by means of the resistive voltage divider and dc relay shown in Figure 6-6. This scheme, similar to that used on large dc generator field circuits, is intended to signal an alarm rather than automatically disconnect the battery.

Each string is connected to a 6-pulse bridge of the converter through a remotely-operated disconnect switch. Unlike a circuit breaker, this switch is not intended to break dc current,

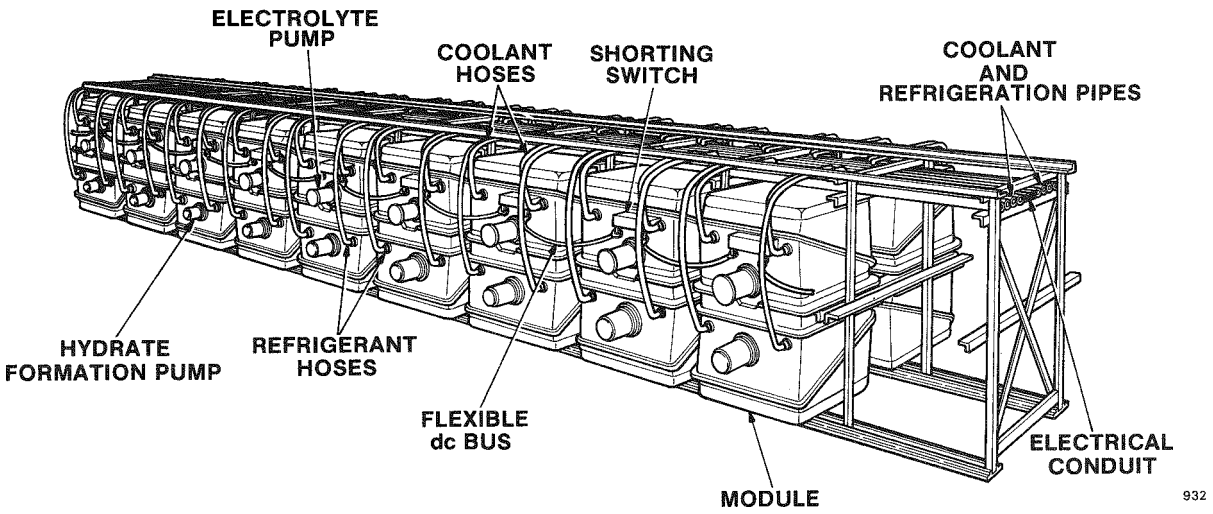

Figure 6-5. Single tier of a 3-tier Mark 4 battery assembly. Each tier is separately assembled as a complete unit with all the necessary plumbing and electrical connections. They will be shipped and stacked three high on the site.

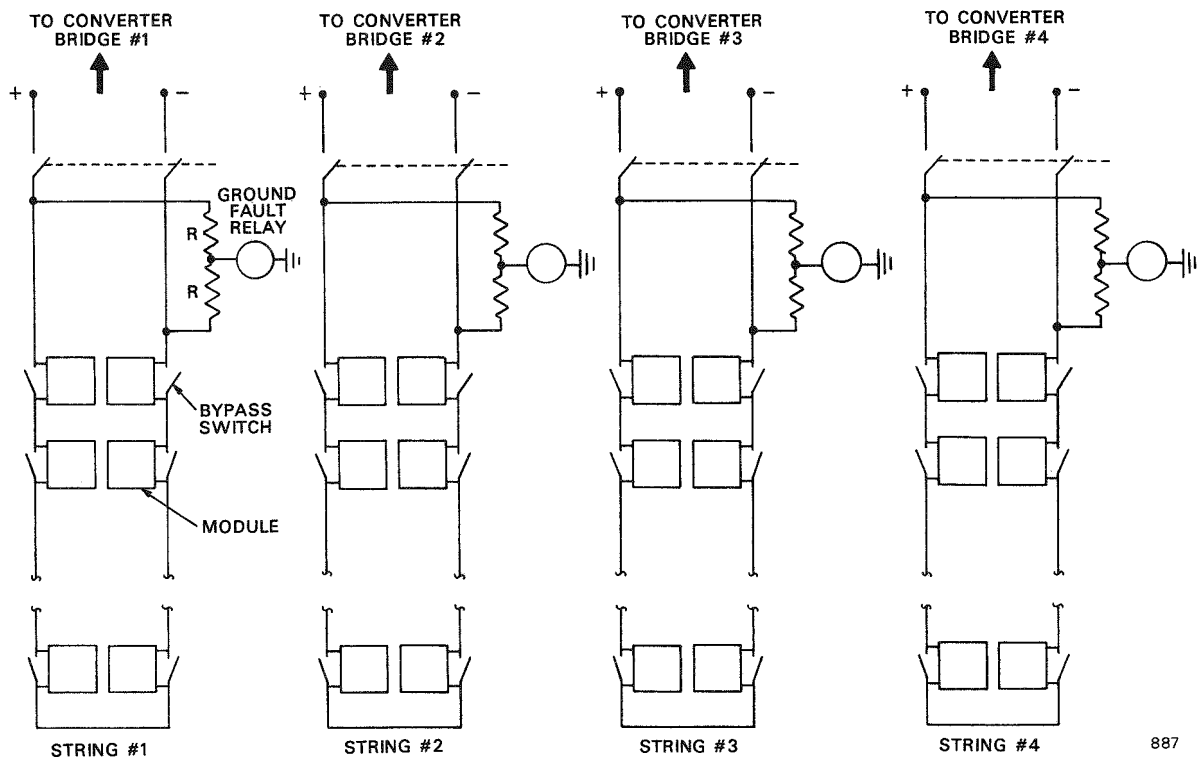

Figure 6-6. Battery dc circuit diagram, showing one 25-MWh unit with four independent strings.

but to disconnect the circuit on no-load. It is also intended to act as a safeguard during maintenance operations by visibly isolating the battery string from the electrical system. The absence of a dc circuit breaker or fuses to protect against short-circuits is another advantage which the zinc-chloride battery allows because of its inherent short-circuit characteristics. Should a fault develop across the battery terminals, the pumps, gas-supply control valve, and converter are turned off until the fault current has decayed to a very low value. The string in which the fault occurred is then disconnected.

If the battery is installed outdoors, protection against lightning overvoltages needs to be provided. It is expected that lightning arresters installed on the utility system side of the converter transformer, combined with overhead shielding wires above the battery racks will provide adequate protection against overvoltages produced by lightning and ac switching surges. As no dc current is expected to be interrupted, high dc overvoltages are not anticipated. Surge diverters are not contemplated on the dc system, unless future work on the characterization and transient analysis of the battery circuit warrants their use. Protection against converter commutation failures will be provided as an integral part of the converter.

REFRIGERATION AND COOLING SYSTEMS

Chilling of the store is required during charge for hydrate formation, and cooling of the sump is required during both charge and discharge. The heat generated in the stack is continuously transported to the sump by the circulation of electrolyte. This heat must be removed continuously to maintain a pre-

determined sump temperature. Wide deviations in sump temperature will result in the loss of electrochemical efficiency.

During the charge cycle, the chlorine generated in the stack is transferred to the store and mixed with chilled water to form hydrate. This is an exothermic reaction and unless the store cooling rate is matched with the rate of chlorine generation, the system will develop internal pressure imbalance.

Hydrate formation occurs in the store at 9.6°C. As this is usually below the normal ambient temperature, heat removal at this temperature requires refrigeration. On the other hand, the sump is to be maintained at 30°C and 45°C during charge and discharge, respectively. Both these temperatures are above the ambient wet-bulb temperature in almost all parts of the country so the sump can be cooled directly without refrigeration. This cooling may occasionally raise the sump temperature during charge a few degrees above the desired level (30°C). However, the savings realized by eliminating refrigeration for sump cooling outweighs the occasional minor energy losses caused by increased sump temperature. Hence, it is desired to use refrigeration for store chilling only and direct cooling (thermocycling) for sump cooling.

Centralized cooling and refrigeration systems are provided for each 25-MWh battery unit. All the modules in the unit are interconnected through the cooling equipment. As there is a large potential difference between modules interconnected by the coolant piping, it is essential to electrically isolate each of the modules from the cooling system. To achieve this, both the coolant and piping must be isolated electrically from the modules. Module heat exchangers are connected to the distribution pipes on the rack through hoses made of dielectric material. Two coolant alternatives -- deionized water and refrigerant R12 -- were analyzed. Both are excellent dielectrics. The latter offered several advantages over the former and, hence, was selected for use. A brief description of the refrigeration and sump cooling systems follows.

Refrigeration System

For each 25-MWh battery unit, a refrigeration skid with compressor, high-pressure and low-pressure refrigerant receivers, oil separators, coolant circulation pumps, and a control panel will be provided. An evaporative condenser sized for the skid-mounted refrigeration plant will be installed near the skid. Power supply and controls to this condenser will be integrated with the refrigeration skid.

The skid-mounted equipment will be completely pretested and delivered to the site. The control valves for the system will also be pretested and mounted on the skid. It was explained in the rack design that the distribution piping for each rack will be an integral part of the rack with complete plumbing to the modules. The control valves at the rack level will also form a part of the rack. The only piping needed in the field is the distribution piping between the refrigeration skid and the racks which the skid is serving. This design reduces the on-site mechanical contracting work to the minimum. The location of the skid will be such as to minimize the field piping.

Sump Cooling System

As in the refrigeration system, separate sump cooling is provided for each 25-MWh battery unit. Each sump cooling unit consists of a skid with a coolant receiver, circulating pumps, control valves, and power and control panel. An evaporative condenser for sump cooling will be mounted near the skid. Coolant-distribution piping between the coolant skids and the racks will be similar to that of the refrigeration piping.

From the layout (Figure 6-2) it can be seen that two refrigeration and two sump cooling skids are located adjacent to each other. Additional plumbing

between the adjacent skids will provide the flexibility of serving any one of two battery units from either of these two pieces of equipment.

BATTERY AUXILIARIES CIRCUIT

The battery auxiliaries include the refrigeration/cooling subsystems and the module-associated electrolyte and gas pumps, gas supply control valves, the hydrogen/chlorine reactors, and the inerts-rejection subsystem.

The refrigeration/cooling subsystem is generally delivered complete with its electrical control panel. The auxiliaries attached to the battery module are fed with ac power in accordance with Figure 6-7. Each of the four strings comprises five circuits, as shown, to feed the pump motors, the gas supply control valve, the hydrogen/chlorine reactor, and the inerts-rejection subsystem. Although the ac bus is three-phase, the individual auxiliary loads are intended to be single-phase. Each phase will, therefore, feed one-third (or 40) of the string modules. The control and coordination of these circuits are discussed under the section on Battery Operation and Control.

POWER-CONDITIONING SYSTEM

The 25-MWh battery unit is connected to a 24-pulse power-conditioning system as shown in Figure 6-8. Each of two transformer primary windings is associated with two secondary windings, independently feeding a six-pulse thyristor bridge. The transformer windings are designed to provide the phase shifts needed for a proper 24-pulse operation. The bridges are separately controlled so that variations in string dc voltage, due to shorted modules and other circuit imbalances, can be compensated for by changing thyristor firing angles. The intent of the control scheme is to keep the string dc currents well balanced.

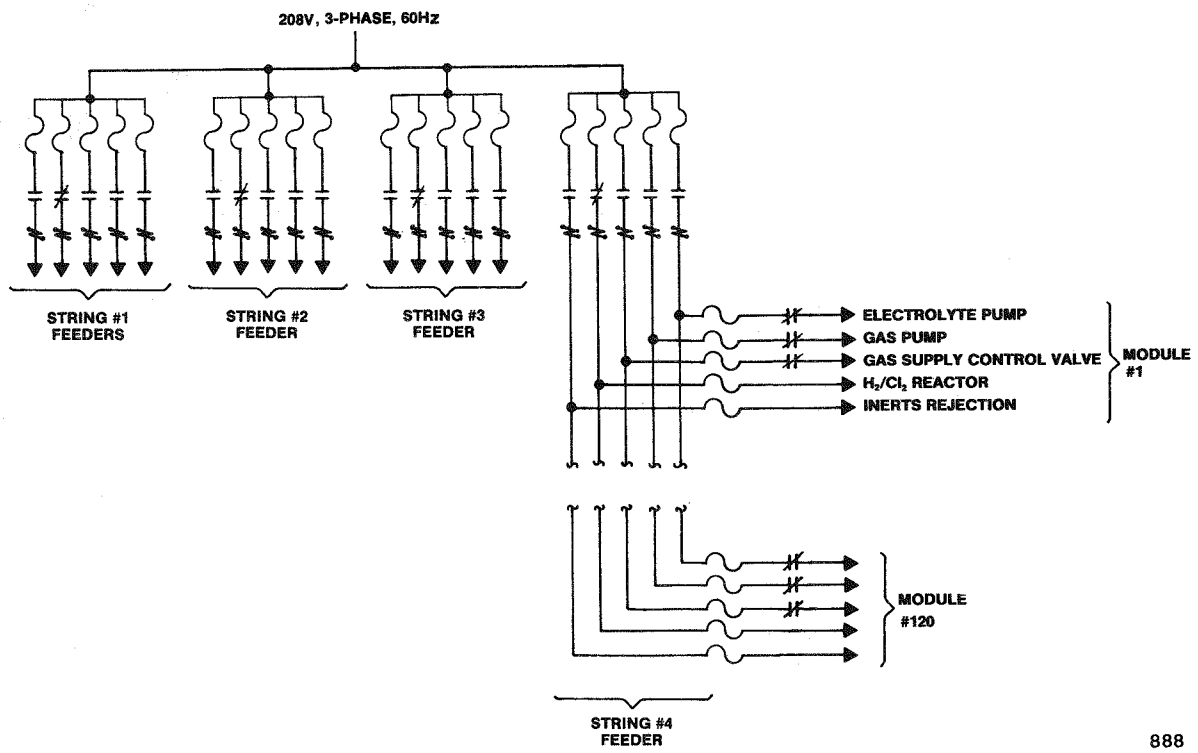

Figure 6-7. One-line circuit diagram of the ac power feeders to the battery auxiliary devices.

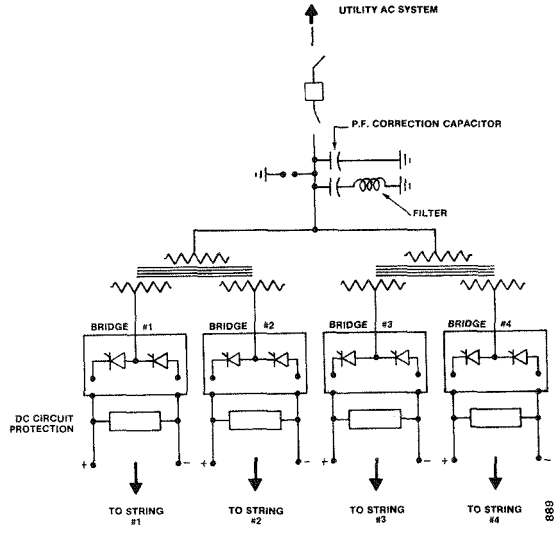

Figure 6-8. One-line diagram of 24-pulse power-conditioning unit, with four independently controlled bridges.

The percent string voltage variation allowed will be limited by the magnitude of harmonics tolerated on the system. A crowbar system equivalent to a shorting switch across the string terminals is envisioned to accommodate thyristor commutation failures. The selection of this protective method will take advantage of the ability of the zinc-chloride battery to withstand short-circuits and shut itself off within less than 20 seconds, provided the pumps and gas supply control valves are turned off. It may be possible to operate the converter with one or more strings out of service. A complete study of this possibility has yet to be made in conjunction with converter manufacturers. Power-factor correction capacitors, if required, and a harmonic filter are installed on the ac side. Either line-commutated or self-commutated converters should be acceptable.

CONTROLS FOR BATTERY OPERATION

The control system for a 100-MWh commercial plant features a hierarchical arrangement of microprocessor-based controllers. Each 25-MWh unit is provided with a microprocessor-based battery controller. The four battery controllers are, in turn, connected to another microprocessor-based controller which acts as a master unit. This master unit serves as the communications link between the battery plant and the utility dispatch center. Figure 6-9 depicts this master/slave arrangement.

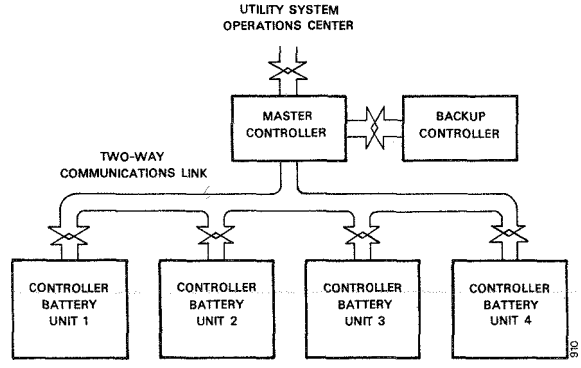

Figure 6-9. Master-slave controller arrangement for commercial 100-MWh load-leveling battery plant.

A block diagram of the control system for a 25-MWh unit is shown in Figure 6-10. The system components are monitored and regulated by the battery controller. The battery controller receives instructions from the master controller and operates the system accordingly. Normally, the battery controller checks the readiness and number of battery modules available for cycling

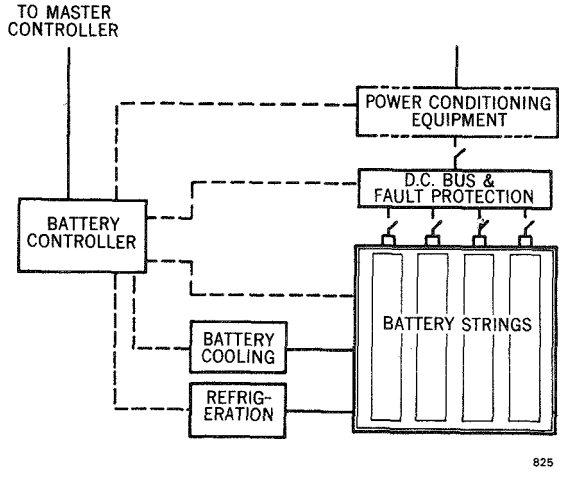

Figure 6-10. Block diagram of the control system for a commercial 25-MWh battery unit.

and instructs the power converter to deliver charge or discharge power at the appropriate level, checking to see that this is accomplished. Similarly, the battery controller sets and checks the dc switchgear, activates the refrigeration and cooling systems, and dispatches power to the pumps and valves of each operating module.

Under normal battery operation, the controller provides the necessary signals to operate the contactors of the ac circuits shown in Figure 6-7. For each string, these consist of the feeders to the following: electrolyte pumps, gas pumps, gas-supply valves, and inerts rejection devices. In addition, the controller initiates the operation of the converter, the sump cooling system, and the refrigeration system.

The battery controller is also programmed to respond to unusual or emergency operating conditions. If a system fault is detected, the battery controller takes the necessary actions to place the system in a safe condition. If module malfunction is detected, the battery controller activates the module's bypass switch, thus shorting that module. Any such unusual conditions are reported immediately to the master controller to ensure proper coordination with the remainder of the system.

As noted previously, the master controller serves as the communications link between the utility dispatch center and the battery plant. Based on instructions received from the utility dispatch center, the master controller issues the appropriate commands to the battery controllers. The master controller also transmits any system data or other information as required to the utility dispatch center. It is envisioned that a redundant master controller will be provided to take over system operation in the event of a malfunction of the master controller. In addition, the system will be such that in the event of a malfunction of a slave battery controller, the master controller could assume the function of the slave controller until the necessary repairs are made.

DISCUSSION

The design of a commercial load-leveling zinc-chloride battery plant is presented. This design is based on a 5-MW, 25-MWh battery unit consisting of four, 2.5-kV dc battery strings connected to separately controlled thyristor bridges of a 24-pulse converter system. The selection of this arrangement is based on several considerations which will be briefly discussed.

The subrack size was dictated by the requirement to accommodate the largest possible number of battery modules on a single transportable structure. This requirement fixed the size of a 3-tier rack to 60 modules. The string size, therefore, can be increased by multiples of 60 modules. Consequently, the nominal string voltage is increased by multiples of 1.25 kV. The selection of two series-connected racks per string (2.5 kV) is a compromise between the tendency to achieve some reduction in converter cost by operating at higher voltage and higher unit capacity, and the need to initially minimize the insulation coordination problems both at the battery string level and at the converter level.

A study of several American utilities, conducted during 1979 as part of the DOE-EDA BEST-Battery Program, has indicated that a 5-MW battery unit can often be more readily accommodated at existing distribution substations than a larger size, such as a 10- MW unit. For the unit size selected, a 24-pulse converter with four independently controlled bridges was preferred to a 12-pulse system, even at the expense of a slightly higher initial cost. This latter required either two independent strings at 5 kV, or four strings at 2.5 kV operated in two parallel pairs. The first option was ruled out, to reduce insulation problems. The second was discarded because it required sacrificing a good module in a string operating in parallel with another string where a malfunctioning module has been shorted out. This precaution is necessary to keep a balanced current in all strings. The 24-pulse system presents advantages with respect to lower harmonic genera-

tion and higher operating flexibility, and therefore, improved battery availability.

A three-tier module arrangement is necessary to obtain reasonably good land usage. However, should more land be available at a substation site, a two-tier construction can be adopted, and provide greater ease of maintenance.

The metallic rack structure is intended to be solidly connected to the substation grounding mat. Under normal operating conditions, the potential difference between various insulated parts of a module is not expected to exceed 1.25 kV. The dielectric design of the battery adequately meets the electric stress resulting from this potential difference. All auxiliary circuits are properly isolated to withstand the highest expected dc electric stresses.

Although the present design has stipulated the tendencies towards single-string converter controls and module bypass devices, the detailed implementation of these tendencies could be modified with the advent of new developments in the battery or as a result of converter manufacturer reaction to the proposed 24-pulse system.

REFERENCE

1. Development of the Zinc-Chlorine Battery for Utility Applications, RP226-3: Interim Report. Palo Alto, Calif.: Electric Power Research Institute, April 1979. EM-1051, Parts 1-3.

Section 7

ELECTRICITY-COST TARGETS FOR COMMERCIAL BATTERY PLANTS

ABSTRACT

The levelized busbar cost of electricity from a zinc-chloride battery plant is compared with that from pumped hydro, compressed-air storage, and combustion turbines. A parametric analysis indicates that the cost of electricity from the battery is more sensitive to variations in module cost than to efficiency, cycle life, or costs of plant auxiliaries, charging energy, and operation and maintenance. With reasonable estimates for charging energy, plant auxiliaries, and operation and maintenance, and a battery efficiency of 65%, the module cost can be as high as $100/kWh and still be competitive with combustion turbines. Comparisons of battery storage with pumped hydro and compressed air must consider other factors, i.e., environmental constraints, availability of suitable sites, modularity of battery systems, and time required for installation.

INTRODUCTION

The goal of the EPRI-EDA program is the commercialization of the zinc-chloride battery as an energy-storage system for the utility industry. A load-leveling battery that cycles daily is a form of peaking generation. It allows a utility to store low-cost energy generated from baseload units during off-peak periods and to discharge this energy during peak demand periods.

The commercial success of a zinc-chloride load-leveling battery system depends on the potential market for peak generation, the successful demonstration of a load-leveling battery, and the economic competitiveness of a battery system compared to alternate forms of peaking generation.

Peaking technologies that are either in commercial use or under development include combustion turbines, pumped hydro, compressed air, thermal storage, flywheels, hydrogen storage, superconducting magnetic storage, and other battery systems. Only pumped hydro, compressed air, and combustion turbines will be available when the zinc-chloride battery is first commercialized.

This section of the report will compute the cost of operating a combustion turbine, pumped hydro storage, and compressed air storage for peaking duty. The cost of operating a zinc-chloride battery will then be analyzed. The battery cost study will separate the battery system into the cost elements of battery capital, auxiliary plant, energy, and operation and maintenance. The relative effect of these costs on total cost of operating a battery system will be evaluated. Finally, the cost of competing peaking and storage systems will be compared. Battery cost targets will be chosen which will enable the zinc-chloride battery to be competitive with combustion turbines.

BUSBAR COST OF ELECTRICITY GENERATED FROM COMBUSTION TURBINES

The cost comparison of the zinc-chloride battery and the combustion turbine is based on the computed levelized annual busbar cost of electricity, as defined in the EPRI Technical Assessment Guide (1). This method computes the minimum revenue

requirement for each year of generation plant operation. The minimum revenue requirement is based on the sum of the operating cost (operation, maintenance, and fuel) and the fixed cost (return on investment, taxes, insurance, and depreciation) associated with the particular form of generation. The present worth of these future revenue requirements are levelized into a single equal annual revenue requirement. Busbar cost is defined as this levelized annual revenue requirement divided by the annual kilowatt-hour output, and is expressed in cents per kilowatt-hour (¢/kWh). This single figure is appropriate for comparing generation alternatives that provide the same function, in this case peaking energy.

Table 7-1 lists the investment and operating costs in 1980 dollars associated with a combustion turbine. Capital cost and fuel cost were taken from a survey of Michigan utilities. O&M costs were escalated from the 1977 cost in the EPRI Technical Assessment Guide. The most significant unknown in projecting the cost of electricity from a combustion turbine is the fuel escalation rate. The cost of distillate fuel oil has increased during the past five years at an annual rate of 18.7%, while the general inflation rate has been 8.2%. Therefore, fuel has escalated at a rate approximately 10% higher than inflation. A reasonable assumption is that fuel will continue to escalate at a higher rate than inflation. A 4.0% increase over inflation as used in the calculation is considered a conservative estimate.

Based on the cost elements presented in Table 7-1, the levelized annual busbar cost for a combustion turbine in 1980 dollars is 20.8 ¢/kWh.

Table 7-1

COST AND PERFORMANCE ELEMENTS USED TO COMPUTE LEVELIZED BUSBAR COST OF ELECTRICITY FROM COMBUSTION TURBINES

Capital cost of the turbine	$250/kW
Unit Life	30 years
Capacity factor	0.15
O&M cost	
Fixed	$0.60/kW/year
Variable	2.3 mills/kWh
Fuel cost	$5.00/$10^6$ Btu
Heat rate	14,000 Btu/kWh
Inflation rate	6%
Discount rate	10%
Fuel escalation rate	4%

BUSBAR COST OF ELECTRICITY DELIVERED FROM A PUMPED HYDRO STORAGE SYSTEM

A pumped hydro energy storage system stores energy by pumping water from one elevation to a higher elevation. The energy is recovered by passing the water from the higher to the lower elevation through a water turbine driving an electric generator. Conventional pumped hydro plants utilize two surface water reservoirs and the natural topography for the difference in elevation. Underground pumped hydro plants have one reservoir located in an excavated cavern to provide the difference in elevations.

Table 7-2 lists the investment and operating cost in 1980 dollars, and the operating characteristics associated with conventional and underground pumped hydro systems. The capital cost associated with conventional pumped hydro is dependent on the site topography. EPRI in "An Assessment of Energy Storage Systems Suitable for use by Electric Utilities" EM-264 (2) has a range of $5-$10/kWh for storage related cost, $100-$150/kW for balance of plant, and $5-$10/kW for plant substation in 1974 dollars. For this

report, the upper range of these values was chosen and escalated at 10% per year to 1980 dollars. Also, a transmission line cost was included to bring the power from the plant to the load. Underground pumped hydro was estimated in EM-264 at $3-$12/kWh for storage, $120-$160/kW for balance of plant, and $5-$10 for plant substation. The upper range was chosen for each of these costs and was escalated from 1974 dollars to 1980 dollars at 10%/year. Operation and maintenance cost was estimated in EM-264 at $1.60/kW-year. This was escalated at an annual rate of 10% to $2.83/kW-year to 1980 dollars. Efficiency, expected life, and discharge time were taken from EM-264. Charging energy cost, discharge cycles, inflation rate, and discount rate were chosen to be consistent with the cost analysis of battery systems.

Based on the cost estimates presented in Table 7-2, the levelized annual busbar cost for a conventional pumped hydro plant in 1980 dollars is 9.9 ¢/kWh. For underground pumped hydro plant, the busbar cost is 10.2 ¢/kWh. These costs are significantly lower than that of combusion turbines.

BUSBAR COST OF ELECTRICITY DELIVERED FROM COMPRESSED AIR STORAGE SYSTEM

Compressed air storage consists of compressing air in an underground storage cavern for use in combustion turbines. The savings result from this system because a conventional combustion turbine allocates two-thirds of its shaft power to compressor operation. Compressed air storage utilizes off-peak base loaded coal generated electricity

Table 7-2

COST AND PERFORMANCE ELEMENTS USED TO COMPUTE LEVELIZED BUSBAR COST OF ELECTRICITY FROM PUMPED HYDRO PLANTS

	Conventional	Underground
Capital Cost		
Plant & Substation	$266/kW	$283/kW
Storage	$177/kW	$213/kW
Transmission Line	$ 60/kW	$ 60/kw
TOTAL	$503/kW	$556/kW
Efficiency	72%	72%
O&M	$2.83/kW-year	$2.83/kW-year
Expected Life	60 years	60 years
Discharge Period	10 hours	10 hours
Charging Energy Cost	$0.02/kWh	$0.02/kWh
Discharge Cycles per year	250	250
Inflation Rate	6%	6%
Discount Rate	10%	10%

to drive a compressor and store the compressed air. During peak demand periods, the compressed air is routed to the combustion turbine and fuel is burned only for the generation of electricity.

Table 7-3 lists the cost and operating characteristics used to develop the busbar cost of electricity for a compressed air storage plant. EPRI EM-264 estimates the cost associated with a compressed air storage plant as $100-$210/kW for power related cost, and $4-$30/kWh for storage related cost in 1974 dollars. An upper range of these costs was escalated at 10% per year to 1980 dollars for this analysis. The wide variation in the capital cost is due to the effect of site conditions and type of underground structure. Efficiency consists of the efficiency of air compression and the efficiency of fuel combustion. EM-264 estimates a heat rate of 4200-5800 Btu/kWh for generation and 0.6-0.8 kWh in/kWh out for air compression. An average of these is shown in Table 7-3. Operation and maintenance costs are unknown because of the lack of operating experience. Because of the increased complexity of compressed air storage, the O&M expense of a conventional combustion turbine was doubled in this analysis. Discharge time is dependent on storage capacity; a 10-hour discharge period was chosen. Expected life was taken from EM-264, and the remaining factors were chosen to be consistent with the previous analysis.

Table 7-3

COST AND PERFORMANCE ELEMENTS USED TO COMPUTE LEVELIZED BUSBAR COST OF ELECTRICITY FROM COMPRESSED AIR PLANTS

Capital Cost	
Power Related	$372/kW
Storage Related	$531/kW
Transmission Line	$ 60/kW
	$963/kW
Efficiency	0.7 kWh/kWh compression 5000 Btu/kWh generation
Operation and Maintenance Cost	$1.20/kW-year $0.0046/kWh
Expected Life	20 years
Discharge Time	10 years
Final Cost	$5.00/$10^6$ Btu
Compression Energy Cost	$0.02/kWh
Inflation Rate	6%
Discount Rate	10%
Fuel Escalation Rate	4%

Table 7-4 presents the levelized busbar cost for combustion turbines, pumped hydro, and compressed air. Compressed air and pumped hydro costs are significantly less than combustion turbines. Battery systems will be compared to combustion turbines in order to develop cost targets.

Table 7-4

COMPARISON OF LEVELIZED BUSBAR COST OF PUMPED HYDRO, COMPRESSED AIR, AND COMBUSTION TURBINES

	Levelized Busbar Cost, ¢/kWh			
	Capital	Fuel	O&M	Total
Pumped Hydro				
Conventional	3.0	6.6	0.3	9.9
Underground	3.3	6.6	0.3	10.2
Compressed Air	5.8	8.3	0.8	14.9
Combustion Turbine	2.9	17.5	0.4	20.8

PARAMETRIC ANALYSIS OF BUSBAR COST OF ELECTRICITY FOR BATTERY SYSTEM

A parametric analysis of the cost of electricity derived from a zinc-chloride battery system has been made to determine which elements of cost most significantly impact the levelized annual busbar cost. Such an analysis provides guidance in determining where the major development emphasis should be placed. The variables included in the analysis were: (a) battery plant capital cost, (b) auxiliary plant capital cost, (c) off-peak energy cost, (d) maintenance cost or O&M cost, (e) battery life, and (f) system efficiency. The effect on levelized busbar cost of changing two variables through reasonable limits while holding the others constant was calculated.

Table 7-5 presents base battery cost data that will result in a levelized busbar cost of electricity equivalent to that generated by a combustion turbine.

Table 7-5

BASE BATTERY COST DATA FOR COMPUTING THE LEVELIZED COST OF ELECTRICITY

Battery Capital Cost	$100/kWh
Auxiliary Plant Capital Cost	$175/kW
Off-Peak Energy Cost	$0.02/kWh
O&M Cost	$0.01/kWh
Discharge Period	5 hours
Battery Plant Life	10 years
Auxiliary Plant Life	30 years
System Efficiency	65%
Battery Cycles	250/year
Base Inflation Rate	6%
Discount Rate	10%

The levelized busbar cost is composed of the following cost elements:

Auxiliary Plant Cost	2.1¢/kWh
Battery Plant Cost	10.8¢/kWh
Charging Energy Cost	5.8¢/kWh
Operation and Maintenance Cost	1.9¢/kWh
Total	20.6¢/kWh

Working from these base cost data the following cost elements were varied through reasonable ranges to determine the effect on the busbar cost of electricity.

- Off-Peak energy cost was varied from 1-3 ¢/kWh
- Efficiency was varied from 50 to 75%
- Battery cost was varied from $40 to $125/kWh
- Battery plant life was varied from 5 to 15 years

Auxiliary plant cost was not varied because it is a mature technology and the estimate of $175/kW is considered accurate.

Charging Energy Cost

Charging energy cost is the incremental cost for power delivered from a coal or nuclear unit. It does not include a charge for capacity since these units are assumed to be operating with excess capacity during periods of battery charge. Figure 7-1 shows the relative effect of charging energy cost and battery system efficiency on the levelized busbar cost.

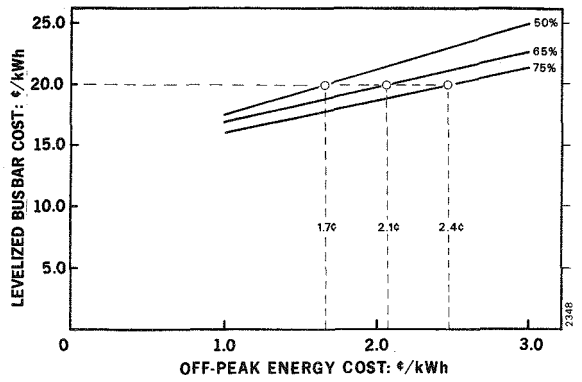

Figure 7-1. Levelized busbar cost of electricity from a battery vs. charging energy cost, for different values of battery efficiency, showing relative insensitivity of busbar costs to these two parameters.

The busbar cost of electricity is relatively insensitive to both efficiency and the off-peak energy cost. A 50% increase in the cost of off-peak electricity results in only a 14% increase in busbar cost when the battery system efficiency is 65%.

The combustion turbine calculation assumed a fuel escalation rate of 4% above the general inflation rate. This escalation rate significantly affects combustion turbine total cost and it is the factor which has the maximum uncertainty. Figure 7-2 is Figure 7-1 overlayed with the cost of electricity from combustion turbine at various fuel escalation rates. The battery system's position relative to combustion turbines improves as the escalation rate increases.

Battery Plant Capital Cost

In this analysis the battery capital cost includes only the cost of modules. The cost of all other components and the construction and installation costs are included in the auxiliary plant cost. Figure 7-3 depicts the effect of battery capital cost and system efficiency on total busbar cost.

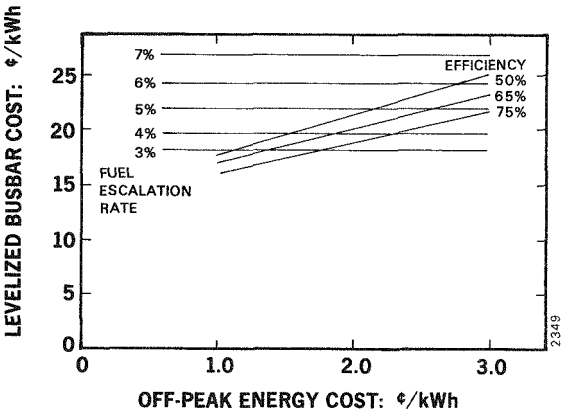

Figure 7-2. Effect of various fuel escalation rates on levelized busbar cost of electricity from turbines, and corresponding breakeven battery charging energy cost, for different values of battery efficiency.

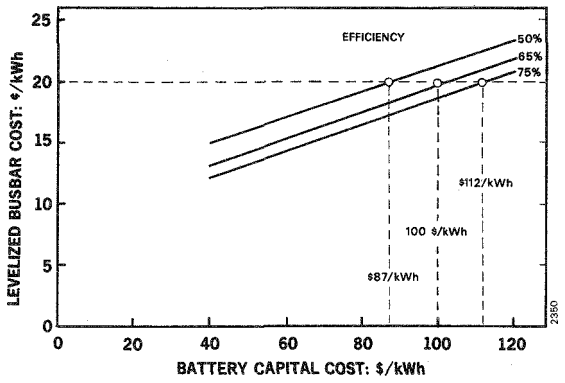

Figure 7-3. Levelized busbar cost of electricity vs. battery capital cost at various values of efficiency, showing relatively high sensitivity to capital cost variations.

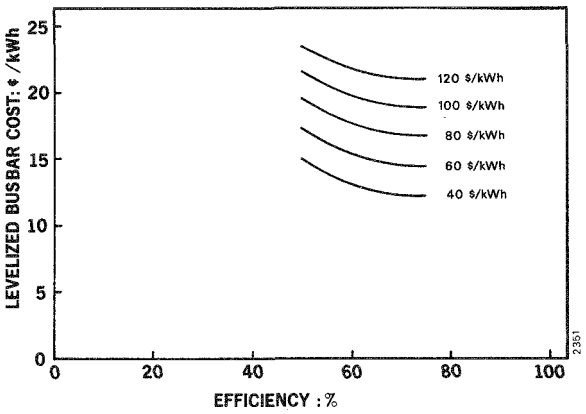

Figure 7-4. Levelized busbar cost of electricity vs. ac-to-ac efficiency for various battery capital costs, showing that efficiencies greater than 60% have minimal effect on busbar cost of electricity.

The busbar cost of electricity is very sensitive to changes in battery capital cost and relatively insensitive to changes in efficiency. A reduction of $20/kWh in battery capital cost is equivalent to an 11% decline in busbar cost. In contrast, an increase in efficiency from 65% to 75% is equivalent to only a 4% decline in busbar cost. The battery system is capital intensive; over 50% of the busbar cost of 20.6 ¢/kWh is in the battery capital cost. Efforts toward the reduction of module cost will have the major impact on the commercialication of the zinc-chloride battery system.

Efficiency

Efficiency is used in this analysis as the system efficiency (ac power output/ ac power input). It includes any power consumed by the auxiliaries. Figure 7-4 shows how the cost of electricity, corresponding to different battery capital costs, is affected by changes in battery efficiency.

The effect of increased efficiency on busbar cost diminishes at higher values of system efficiency. The graph shows that it may be cost effective to increase the module cost by $20/kWh to effect an efficiency increase from 50% to 60% but it is not cost effective if the efficiency increase is from 60% to 70%. This is very significant as it clearly shows that development effort to increase efficiency above 60% has little effect on busbar cost.

Battery Life

Battery life is the average useful life of battery modules in a system. This will be determined by deterioration in battery performance, maintenance cost, and system availability. Figure 7-5 illustrates the effect of battery life on busbar cost, for different values of battery capital cost.

The graph shows that the effect of increased battery life diminishes at higher life expectancies. Also, there is a tradeoff between module cost and module life. For example, a $60/kWh module which has a life expectancy of 5 years is equivalent to a $100/kWh module with a life of 10 years or a $120/kWh with a life of 15 years. Therefore, it is cost effective to increase the capital cost of the module by $40/kWh if life is increased from 5 to 10 years but it is not cost effective to increase the module cost by $40/kWh to increase its life from 10 to 15 years.

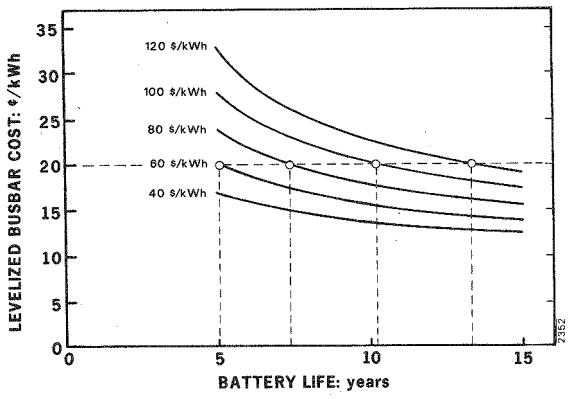

Figure 7-5. Levelized busbar cost of electricity vs. battery life, for different values of battery capital cost.

DISCUSSION

The study established a target of 20.6 ¢/kWh for the annual levelized busbar cost of electricity derived from a battery system. For the zinc-chloride battery system to meet this target, it must satisfy the specifications of Table 7-5. The target of 20.6 ¢/kWh is based on the cost of electricity generated from a combustion turbine. Combustion turbines are the chief competitor to load-leveling batteries because they are used extensively by utilities for meeting peak load demand. The cost of electricity from pumped hydro and compressed air is significantly less than this target. However, it is envisioned that the zinc-chloride battery will be able to compete successfully with pumped hydro and compressed air because of advantages that are not quantifiable in economic terms. These advantages are:

- Site Availability: Pumped hydro and compressed air are site limited. Conventional pumped hydro requires a site suitable for the storage of large quantities of water separated by several hundred feet of head but not too far apart in distance. This topography is not available everywhere. Underground pumped hydro requires a site that is suitable for a surface reservoir plus a geological formation feasible for an underground reservoir. Underground compressed air sites of interest include aquifer, salt mines, exploited oil and gas wells, and exploited mineral mines. Zinc-chloride batteries have no site restrictions.

- Environmental Acceptability: Environmental objections have delayed proposed pumped storage projects for extended periods and some may never be built. These concerns include: acceptable land use, irreversibility of the effects of the project, aesthetics of the structure such as dams, transmission lines, and penstocks, displacement of wildlife and damage to fish, temporary problems during construction, and increase in water temperature. These same objections are operative in underground pumped hydro plants. Compressed air plants with underground storage will concern the public with possible surface cave-ins, blowouts, and contaminating the underground water supply.

- Modularity: The economic size of compressed air and pumped hydro is from 200-2000 MW. The initial investment in these units requires large capital formation which restricts them to large utilities or a consortium of utilities. The zinc-chloride battery can be installed in 5 MW packages. This makes it available to small utilities such as cooperatives, municipals, and large industrial consumers in addition to large utilities.

- Location in the Distribution System: The zinc-chloride battery plant, because of the small size of the individual plant, can be located in the distribution system. The battery system may delay or reduce the need for new transmission and distribution network facilities. Dispersed storage reduces the peak load on

the substation and transmission lines and, therefore, postpones the need to upgrade these facilities with increasing load.

- Short Construction Period: Pumped hydro and compressed air storage systems are large facilities and have a construction lead time of 8-12 years. The zinc-chloride battery, because of its small size and simplicity, can have a construction period of approximately one year.

Turbine operating costs are sensitive to the rate of increase in the price of oil relative to the general inflation rate. An annual escalation rate of 4% above the general inflation rate is used to calculate the cost target. This is considered to be conservative. Because of the general instability in cost and availability of oil, this escalation rate may increase significantly.

The parametric analysis shows that 50% of the busbar cost of electricity from a zinc-chloride battery plant is attributable to the capital cost of the module. Busbar cost of electricity is more sensitive to variations in this cost than to changes in efficiency, life, or the cost of off-peak energy. Development efforts must be concentrated in those areas which can most significantly reduce module cost such as simplification of design, fewer components, less expensive materials, and low-cost manufacturing processes.

It is shown that the cost target of 20.6 ¢/kWh is achievable when the battery capital cost is $100/kWh. This is particularly attractive in view of previous cost analyses that have shown the feasibility of significantly lower module cost (3). Efficiency gains above 60% show a diminishing return. Development efforts that increase efficiency above this value but add to module cost must be carefully evaluated with respect to total cost. Gains in module life also have a diminishing return. Any increase in module cost that results in a life greater than 10 years must be carefully considered.

This section of the proposal establishes the baseline for the various cost elements that make up the total busbar cost of electricity from a zinc-chloride battery. In the following sections of Part II, the battery plant capital cost, efficiency, and reliability will be discussed in detail.

REFERENCES

1. Technical Assessment Guide. Palo Alto, Calif.: Electric Power Research Institute, June 1978. PS-866-SR.

2. An Assessment of Energy Storage Systems Suitable for Use by Electric Utilities. Palo Alto, Calif.: Electric Power Research Institute, July 1976. EM-264.

3. Development of the Zinc-Chlorine Battery for Utility Applications. Palo Alto, Calif.: Electric Power Research Institute, April 1979. EM-1051, Part II, Section 8.

Section 8

CAPITAL COST OF BATTERY PLANTS

ABSTRACT

The zinc-chloride battery will be attractive to utilities for load leveling when the busbar cost of electricity from a battery plant is economically competitive with that from combustion turbines. Earlier studies have shown that batteries may be economically competitive when the capital costs of modules and plant auxiliaries are as high as $100/kWh and $175/kW, respectively. A conceptual design of a 100-MWh commercial battery plant is briefly described. Based on this design, the cost (1980 dollars) of plant auxiliaries is estimated to be $175/kW. The minimum cost for modules, estimated in 1977, is updated to $47/kWh. This cost is then compared with the maximum cost permissible for batteries to remain competitive with combustion turbines.

INTRODUCTION

The objective of the load-leveling, zinc-chloride battery program is to develop a battery system that can be manufactured and marketed at costs that are competitive with alternative peaking devices. Electric utilities have traditionally met daily peak-load demands by either pumped hydro-storage plants, or combustion turbines that burn petroleum fuels or natural gas. These represent the competition to load-leveling batteries.

Pumped-hydro storage is site-limited, and licensing is becoming more difficult because of environmental considerations. The rapidly escalating cost of petroleum fuel has impacted the operating cost of combustion turbines so severely that alternate sources for meeting peak load demands may now be economically attractive. Zinc-chloride batteries that can be charged at off-peak periods with low-cost coal or nuclear generated energy, and discharged during periods of peak demand represent a viable alternative to combustion turbines.

In Section 7 of this proposal, the levelized busbar cost of electricity generated by combustion turbines is calculated in 1980 dollars to be $0.208/kWh. This cost is extremely sensitive to escalation in the cost of fuel. A conservative estimate for the escalation rate for fuel of 4% above the general inflation rate has been assumed. Thus the busbar cost of electricity generated by a zinc-chloride battery must be less than $0.208/kWh (combustion turbine cost) if the battery is to represent an attractive alternative.

The total cost of electricity generated by a battery system is composed of the following elements: capital cost of battery modules, capital cost of auxiliaries, cost of charging energy, and operation and maintenance costs. Assuming reasonable values for each cost element, it is shown in Section 7 that the most significant cost is that of the battery modules.

Relatively accurate costs can be established for plant auxiliaries, charging energy, and operation and maintenance. Based on these costs, and a target for total cost of electricity that is less than that for combustion turbines, it is shown in Section 7 that the capital cost of battery modules should not exceed $100/kWh. This has therefore been established as an initial module

capital cost target for a commercial battery plant in a semimature market.

This section will briefly discuss the design of a commercial battery plant, project the probable cost of both battery modules and plant auxiliaries in a semimature market, and consider the probability of meeting a target cost of electricity that is less than that for combustion turbines.

DESIGN OF A COMMERCIAL BATTERY PLANT

A commercial battery plant is composed of modular, 25-MWh battery units. The number of units in a commercial plant is determined by the specific requirements of the substation. A 100-MWh plant consists of four modular units, each complete with battery modules, power converter, refrigeration/cooling and control subsystems.

A battery unit consists of 4 battery strings, each containing 120 modules mounted on 2 battery racks. The modules in each string are electrically connected in series and controlled by one of four independent bridges in the converter that are capable of separately controlling the current and voltage of each string. Each 25-MWh modular battery unit has a refrigeration/cooling subsystem consisting of one compressor, two condensers, and a Freon receiver with pumps and controls. The operation of each unit is controlled and supervised by a microprocessor-based control subsystem. The design of the plant is discussed in detail in Section 6.

Figure 8-1 shows an artist's rendering of a commercial 100-MWh battery plant as described. The unit design provides flexibility in sizing a load-leveling plant to the specific requirements of a substation.

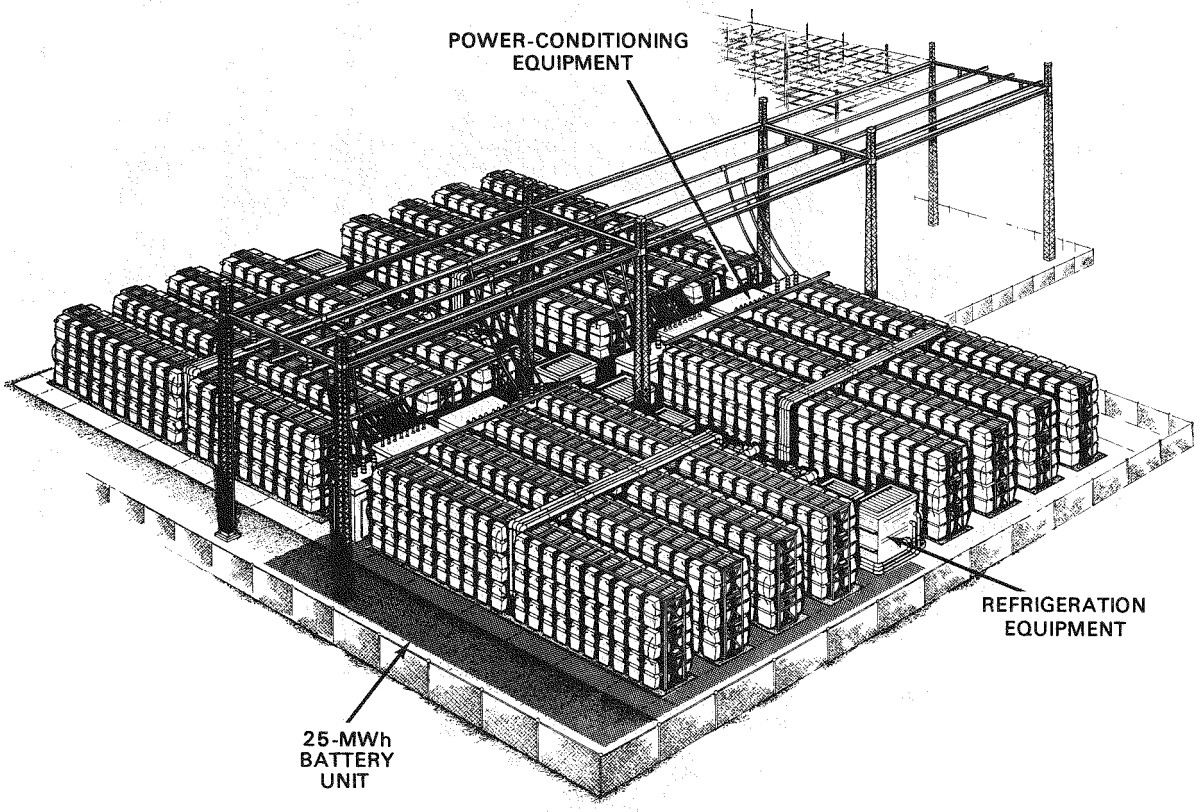

Figure 8-1. Artist's rendition of a 100-MWh zinc-chloride load-leveling battery plant, located at a utility substation.

CAPITAL COST OF BATTERY MODULES - SEMIMATURE MARKET

The cost of battery modules projected for a semimature market is understood to mean the cost when the market and the production operations supplying it (at a rate of 100, 50-kWh units/day) are well established, and the market is still capable of further expansion. For the zinc-chloride battery system, this is assumed to exist five years after initial commercialization.

An analysis of battery module cost for a battery plant in a semimature market was presented in considerable detail in Section 8 of EPRI EM-1051 (1). Engineering specifications, a proposed design, a production plan, and the projected costs were based on the state of the technology in 1977. Also, the cost projection for battery modules was based on a preconceived cost objective of $25/kWh. The costing moved toward this objective by adopting the lowest cost components conceivable at the time they were to be used. A highly automated, high volume system, with low labor content was assumed. Consequently, the projected cost represents the lower cost limit for the Mark 4B technology. This was established to be $27/kWh for battery modules. This number, when updated to 1980 dollars by applying an annual inflation rate of 12%, is $38/kWh. Another correction factor is required to take into account a change in module specification. Originally each module was designed to deliver 66 kWh. The specification was revised to 53.4 kWh on the basis of experimental experience with the present design. Applying this factor, the 1980 updated cost is $47/kWh.

A detailed cost analysis based on the technology as it exists in 1980 has not been made during the period of this report. Therefore, the most realistic analysis that can be made at this time is to compare the updated cost of $47/kWh with that required in order for the battery system to be cost competitive with combustion turbines. In Section 7, the levelized busbar cost of electricity from combustion turbines was calculated to be $0.208/kWh. Assuming reasonable costs for charging energy, operation and maintenance, and plant auxiliaries, the capital cost of battery modules can be as high as $100/kWh and still be competitive with combustion turbines. This analysis indicates that the estimated updated lower cost for modules could be in error by 100% and still be acceptable.

Obviously, the cost analysis made in 1977 needs to be updated in similar detail, and be based on improvements made in the technology since that time, and the experience gained in pilot plant production for the BEST Facility. This will be an important part of the continuing program.

CAPITAL COST OF PLANT AUXILIARIES - SEMIMATURE MARKET

The cost of plant auxiliaries consists of the following: (a) power converter, (b) refrigeration/cooling equipment, (c) battery control subsystem, (d) battery racks, and (e) site preparation and plant enclosure. These costs are not highly dependent on a developing technology, so can be estimated with greater accuracy. Costs for site preparation and plant enclosure, the refrigeration/cooling system, and power converter are dependent on the climatic conditions and the electrical requirements for the specific site. For the purposes of this report, average costs will be assumed.

An analysis of balance of plant costs was discussed in detail in EM-1051 (1), where it was estimated to be $89/kW. Updating this value to 1980 dollars by applying an annual inflation rate of 12% results in a balance of plant cost of $125/kW.

The design of a 100-MWh plant is discussed in considerable detail in Section 6. Based on this design, estimates have again been made for the cost of plant auxiliaries. Costs shown in Table 8-1 are subject to change as they are not yet based on actual quotations.

Table 8-1

ESTIMATED COST IN 1980 DOLLARS OF AUXILIARIES IN A COMMERCIAL ZINC-CHLORIDE BATTERY PLANT

Auxiliary	Estimated Cost $/kW
Power Converter	60
Refrigeration and Cooling	70
Battery Rack	5
Control Equipment	10
Site Preparation and Enclosure	30
TOTAL	$175

The cost of plant auxiliaries of $175/kW is believed to represent the actual cost in 1980 dollars. This cost is used in the calculation of levelized busbar cost of electricity for a zinc-chloride battery plant as discussed in detail in Section 7. Slight variations in these costs have an insignificant effect on the cost of electricity, i.e., a change of 15% in cost of auxiliaries is equivalent to a change of 1.5% in the levelized busbar cost of electricity. Thus, minor variations in this cost will not significantly impact the economic competitiveness of the zinc-chloride battery.

DISCUSSION

An analysis of capital cost of battery plants in comparable detail to that done in 1977 as reported in EM-1051 has not been done during Phase II of RP226-3. However, this will be done as part of the continuing DOE-EDA BEST-Battery Program. Included in this analysis will be the results from a separate EPRI contract with Airco Speer Carbon-Graphite Company to project zinc-chloride battery electrode costs when produced at the rate of 100, 50-kWh battery modules per day. The broad objective of this contract is to achieve a more complete understanding of graphite costs for both the zinc and chlorine electrodes. Electrode substrates are considered a major cost element for the zinc-chloride battery. Accurate graphite cost projections will contribute significantly to the total analysis of module capital costs when serving a semimature market.

The most realistic costs available are those previously reported but corrected for inflation. An additional correction factor is required to take into account the change in module specification. Originally, each module was designed to deliver 66 kWh. This specification was revised on the basis of experimental experience with the present design. More accurately, 53.4 kWh is now considered as the module capacity. Applying both inflation and capacity change corrections to the cost of modules, the updated cost is $47/kWh.

At this stage of the development there is substantial uncertainty in estimating the capital cost of the battery modules. However, the cost of plant auxiliaries based on the most recent design has been revised to $175/kW and is believed to be accurate. Thus, assuming an acceptable cost for operation and maintenance, and a realistic cost for charging energy, the limitation on battery module cost can be calculated on the assumption that the levelized busbar cost of electricity must be less than that of combustion turbines. This results in an upper limit of $100/kWh for the cost of modules.

The DOE-EDA BEST-Battery Program requires the installation of a 4-MWh zinc-chloride battery system at the BEST Facility in New Jersey during 1981. The pilot plant experience gained from the production of modules required by this contract will be useful in projecting module production costs when serving a semimature market. Subsequent development programs will identify areas where cost reductions can be made, consider specific technology

improvements for all components, and evaluate module design for simplification and cost reductions. The detailed cost analysis will be based on all these considerations and it is anticipated that the projected module cost will fall between the minimum updated value of $47/kWh and the maximum permissible value of $100/kWh.

REFERENCE

1. Development of the Zinc-Chlorine Battery for Utility Applications. Palo Alto, Calif.: Electric Power Research Institute, April 1979. EM-1051.

Section 9

EFFICIENCY OF BATTERY PLANTS

ABSTRACT

An ac-to-ac efficiency target of 0.65 has been established for a zinc-chloride battery. A discussion of the areas where energy losses occur includes: (a) electrochemical losses both coulombic and voltaic, and (b) energy consumption by auxiliary equipment; pumps, hydrogen reactor, inerts-rejection device, refrigeration, and power conditioner. The electrochemical energy efficiency of the battery delivered to the BEST Facility is targeted to be at or above 0.65. An increase in the electrochemical efficiency to 0.73 is required to meet the ac-to-ac target. Cells with an improved design have achieved an electrochemical efficiency in excess of 0.74.

INTRODUCTION

Energy-storage battery plants for the electric-utility load-leveling application must meet criteria in the areas of cost, performance, life, reliability, and environmental impact. This section discusses the efficiency issue in terms of the sources and types of energy losses in the system, as well as, approaches which can be pursued to achieve the commercial performance targets. Advanced technology studies relating to efficiency are discussed in Part VI.

Section 7, "Electricity-Cost Targets for Commercial Battery Plants," shows the relative insensitivity of the cost of electricity to the overall (ac to ac) efficiency. The parametric assessment of electricity cost suggests that, for certain values of capital and O&M costs, a battery plant operating at an efficiency of 0.5 can compete economically with combustion turbines. However, pumped hydroelectric plants -- the principal energy-storage technology now available to the utilities -- display efficiencies in the range of 0.65-0.75. Accordingly, an overall efficiency target of 0.65 has been established for a zinc-chloride load-leveling battery system. This efficiency represents the ratio of the ac energies delivered to, and from, the utility grid by the battery plant. Previous studies (1,2) have indicated that the electrochemical energy efficiency, defined as the ratio of the dc energies delivered by, and to, the battery module, should lie at 0.73-0.75 in order to achieve the overall efficiency target of 0.65. A target of 0.75 for electrochemical energy efficiency is therefore assumed for the battery module.

The next subsection provides a detailed discussion of the electrochemical energy losses in the cell and the multicell battery stacks. The constituent inefficiencies are identified. The limitations of the present stack technology, i.e., Mark 4B, are described. Recent cell data suggest that the electrochemical efficiency target of 0.75 is achievable with improved technology, based mainly on increased inter-electrode separation and higher applied current densities.

In the following subsection, the energy requirements for module components, and the auxiliary subsystems in the battery plant, are described. Table 9-1 lists the major auxiliary components and subsystems. In addition, this subsection

emphasizes the importance of meeting or exceeding the electrochemical energy efficiency target of 0.75. Although the electrochemical energy efficiency effectively determines the maximum overall efficiency, attention must also be paid to the minimization of component and subsystem inefficiencies. With an electrochemical energy efficiency of 0.75, it is shown that an overall efficiency of 0.65 is achievable.

Table 9-1

AUXILIARY COMPONENTS AND SUBSYSTEMS

Module-Level

Electrolyte and gas pumps
Hydrogen recombination subsystem
Inert-gas rejection subsystem

Plant-Level

Refrigeration subsystem
Power-conditioning subsystem
Computer control subsystem

ELECTROCHEMICAL ENERGY LOSSES

Two types of electrochemical inefficiencies occur simultaneously during operation of the zinc-chloride battery. These inefficiencies are commonly referred to as coulombic and voltaic inefficiencies. The fractional coulombic efficiency (ε_c) can be defined as the quantity of charge -- usually expressed in ampere-hours (Ah) -- which can be usefully delivered from the battery divided by the quantity charged to the battery:

$$\varepsilon_c = \frac{\text{Usable delivered Ah}}{\text{Ah charged}}$$

In a similar manner the voltaic efficiency (ε_v) can be defined as the energy-average discharge voltage divided by the energy-average charge voltage:

$$\varepsilon_v = \frac{\text{Energy-average discharge voltage}}{\text{Energy-average charge voltage}}$$

It is most conveniently and accurately determined by dividing the electrochemical energy efficiency (ε_e) by the usable coulombic efficiency:

$$\varepsilon_v = \frac{\varepsilon_e}{\varepsilon_c}$$

The coulombic and voltaic efficiencies can be broken down into charge and discharge efficiencies:

$$\varepsilon_c = \varepsilon_c^c \cdot \varepsilon_c^d$$

$$\varepsilon_v = \varepsilon_v^c \cdot \varepsilon_v^d$$

where the superscripts c and d refer to charge and discharge, respectively.

Table 9-2 summarizes the electrochemical performance demonstrated by the refurbished EPRI 45-kWh battery module and the performance targets for the BEST-battery (Mark 4B) modules. Under similar operating conditions the 4B modules are projected to demonstrate about a 5-point improvement in electrochemical energy efficiency. A projected 5-point improvement in usable coulombic efficiency and a 1.5-2 point improvement in voltaic efficiency are responsible for this projected change. Improved chlorine-electrode activation and internal busing will provide the ε_v gains. The improved battery-stack design and increased level of vacuum on the stack during charge will provide the ε_c gains. The projected delivered energy increase from the 4B modules is due to the improved efficiency.

Table 9-2

ELECTROCHEMICAL PERFORMANCE LEVELS

	Observed Refurbished 45kWh	Projected Mark 4B BEST
CHARGE MODE:		
Time (h)	6.8	6.6
Current Density (mA/cm^2)	33	33
Voltage (V/cell)	2.29	2.26
DISCHARGE MODE (5.0 h):		
Current Density (mA/cm^2)	33	33
Voltage (V/cell)	1.85	1.92
ROUND-TRIP EFFICIENCIES:		
Total Coulombic	0.772	0.80
Unusable Coulombic	0.060	0.04
Usable Coulombic	0.712	0.76
Voltaic	0.834	0.85
Energy	0.594	0.65
DELIVERED dc ENERGY (kWh):	50	52.3

Losses at the Cell Level

The major source of coulombic inefficiency at the cell level is the direct chemical reaction of chlorine dissolved in the electrolyte with electrodeposited zinc metal (3,4,5). The rate of this reaction has been shown to be controlled by the mass transfer of chlorine to the zinc-electrolyte interface (6). Recent coulombic efficiency modeling studies at EDA have identified the three major sources of fluid motion which control this mass transfer during the charge mode. Figure 9-1 illustrates the electrolyte flow patterns that would be established in the inter-electrode cell gap if each convective source existed by itself. Forced convection of electrolyte through the porous-graphite chlorine electrodes and vertically upwards between the zinc and chlorine electrodes is the preferred mode of operation in this flowing-electrolyte system. Natural convection of electrolyte is due to the formation of a low-density electrolyte layer adjacent to the zinc electrode created by the cathodic depletion of zinc-ion species. Bubble-induced convection of electrolyte is created by the anodic generation of chlorine gas at the chlorine electrode. The forced and natural convections also occur simultaneously during discharge. Natural convection, however, occurs in the opposite direction due to anodic dissolution of metallic zinc to form zinc-ion species in the electrolyte layer immediately adjacent to the zinc electrode.

Experimental data have indicated that the following parameters influence the coulombic efficiency of zinc-chloride cells by either affecting the concentration/activity of dissolved chlorine in the electrolyte or its mass transport to the zinc electrode:

- Partial pressure of chlorine in the gas phase above the cell electrolyte and cell stack.
- Applied current density.
- Flow rate of electrolyte.
- Inter-electrode cell gap.
- Temperature of electrolyte.
- Electrolyte composition and additives.

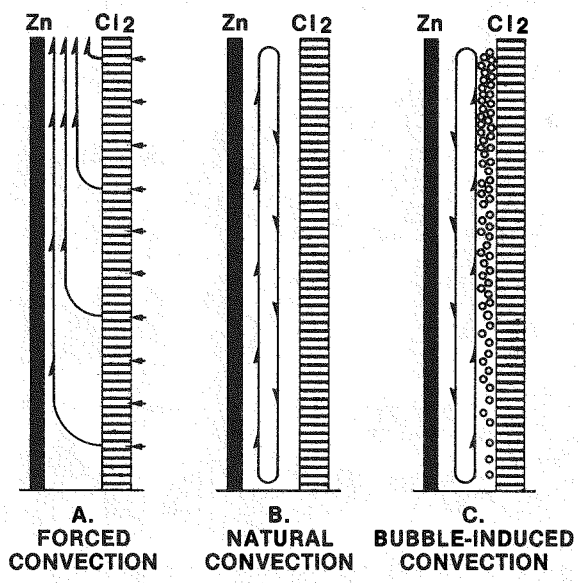

Figure 9-1. Schematic illustration of the individual electrolyte-flow patterns established in the cell gap by the three major sources of fluid convection during charge.

Because the dissolved chlorine concentration in the electrolyte follows Henry's Law and the chemical reaction of dissolved chlorine with metallic zinc is first order with respect to dissolved chlorine, the effect of chlorine partial pressure is obvious. Not so obvious is the influence of applied current density. Increasing the applied current density increases the coulombic efficiency. This can be most readily explained using a mathematical relationship for the coulombic efficiency, on either charge or discharge, which considers both the rate of the electrochemical and the chemical corrosion reactions. For charge this relationship is:

$$\varepsilon_c^c = 1 - \frac{i_{cor}}{i_a}$$

where i_a = applied current density and i_{cor} = corrosion current density. Although i_{cor} increases as i_a increases, due to increased natural and bubble-induced convections, the ratio i_{cor}/i_a decreases with a corresponding increase in coulombic efficiency. A similar phenomenon occurs on discharge.

Electrolyte flow rate and inter-electrode cell gap affect the magnitude of forced convection between the electrodes and therefore influence the corrosion current density. Preliminary experimental data suggest an optimal cell gap exists for a given set of operational conditions due to a balancing of opposing flows at the zinc electrode during charge (5).

The effects of temperature and electrolyte additives are less obvious. Temperature apparently has a dual influence by affecting the saturation solubility of chlorine, as well as, its activity and/or diffusion coefficient in the electrolyte. The net effect on coulombic efficiency is relatively insignificant.

More conventional approaches to increasing coulombic efficiency are also possible. One such approach is the use of separators. This approach introduces increased voltaic penalties, adds cost to the battery stack, and could limit the life of the battery.

The voltaic losses at the cell level are quite equally distributed between the electrolyte IR drop and electrode polarizations during charge. During discharge, however, the cathodic polarization of the chlorine electrode accounts for a greater portion of the voltaic inefficiency. Chemical and

electrochemical processes have been developed at EDA to increase the activity of porous-graphite chlorine-electrode substrates (1,7). The actual mechanism by which the activity is enhanced is not well understood however. Several possible mechanisms are:

- Increased hydrophilicity of the activated graphite.
- Formation of intercalation compounds in the activated region.
- Increase in the number of active pores by either modification of the pore size distribution or exposure of previously dead-ended pores in the activated region.

An increased understanding of this phenomenon could lead to improved processes and increased chlorine-electrode activity.

An alternative to porous-graphite substrates is ruthenia-catalyzed porous-titanium. Electrodes of this type were used in a previous EPRI-EDA 1 kWh system in 1974-75 (8). Voltaic efficiencies of 89% were routinely achieved with this breadboard system. As early as 1976, however, porous-graphite chlorine-electrode substrates were selected over ruthenia-catalyzed porous titanium for the following reasons: (a) large-scale demand for ruthenium could result in prohibitive costs, (b) performance of batteries with ruthenia-catalyzed titanium electrodes are sensitive to changes in electrolyte pH, and (c) ruthenia-catalyzed titanium electrodes have a lower overpotential for hydrogen formation.

Losses at the Stack and System Level

Additional sources of coulombic and voltaic inefficiencies are introduced as zinc-chloride cells are connected in parallel/series arrangements to form battery stacks. In terms of additional coulombic inefficiency the major sources are:

- Electrochemical corrosion couples.
- Self-discharge of bipolar combs.
- Inter-cell zinc growths.
- Shunt currents through the common electrolyte manifold and sump.
- Maldistribution of electrolyte flow.
- Conventional zinc dendrites bridging cells.

Electrochemical corrosion couples occur at both the cell and submodule levels when dissolved chlorine contacts exposed graphite extensions of the zinc electrode. These extensions include the zinc-electrode bus, as well as, exposed substrate. The rate of this corrosion is controlled by the mass transfer of dissolved chlorine to these areas.

The self-discharge of bipolar combs is another type of electrochemical corrosion couple. It occurs as a result of electrolyte continuity between adjacent series-connected cells. This continuity can occur through the bipolar graphite bus and/or through the bus-to-case seal region.

Inter-cell zinc growths also occur as a result of electrolyte continuity between adjacent series-connected cells. These growths can develop and accumulate in the bus-to-case seal region unless the seal is near-perfect or the electrolyte continuity is interrupted. Because the electrolyte trapped in the bus-to-case seal region is relatively stagnant, these zinc growths tend to accumulate with sequential charge cycles and the coulombic inefficiency caused by current bypass through these growths increases with time and the number of cycles. Coulombic inefficiencies as high as 30% during a single charge cycle have resulted from gross accumulations of this type (1).

Shunt currents in a series-arranged battery stack through the common electrolyte sump are well understood. An analytical model has been developed which allows the design specification of the inlet and outlet electrolyte manifolding to restrict these shunt currents to acceptably low levels, i.e, less than 1-2% coulombic inefficiency.

In a similar manner, electrolyte-flow distribution to the multiple chlorine-electrode packs has received extensive evaluation. Uniformity of flow is controlled to within ±10%.

Conventional zinc dendriting across the inter-electrode cell gap occurs in small cells, as well as battery stacks. The probability of occurrence in a battery stack containing 2640 single-cell units, however, is considerably greater. Use of the proper electrolyte formulation and operating conditions control dendriting to acceptable levels. Occasional dendriting of this type does not appear to have a major impact on coulombic efficiency because these dendrites "burn-off" at the chlorine electrode due to the plentiful supply of dissolved chlorine.

Assuming that deleterious interactions between cells can be controlled by the proper design of the battery stack, it can be demonstrated that the distribution function describing the coulombic efficiency of submodules and battery modules will have a smaller variance than the coulombic efficiency distribution for "single cells". Furthermore the average coulombic efficiency for submodules and modules will be within a couple percent of the average coulombic efficiency for "single cells". This occurs as a result of the leveling effect of parallel connected cells and the test regime employed.

Two additional sources of voltaic inefficiency are introduced as zinc-chloride cells are connected in parallel/series arrangements to form battery stacks. The first and least important source is maldistribution of electrolyte to the multiple chlorine-electrode packs. This is inconsequential during charge, but becomes more important during discharge when the supply rate of the dissolved chlorine reactant, at relatively low concentration varies significantly among the assembly of chlorine-electrode packs in the battery stack.

The most significant source of additional voltaic inefficiency is in the form of increased IR due to internal and external busing of the current between and among submodules and modules. EDA has developed improved titanium-to-graphite connection technology and continues to study improved internal busing techniques. A simple example of introducing a 1 milliohm resistance via the internal module busing will demonstrate the significance of this source. At an operating current of 550 amperes this resistance accounts for a 0.55 volt drop. This is an additional 2.75% voltaic inefficiency on both charge and discharge for a nominal 20-volt battery module. Inter-module busing presents a similar engineering problem.

Achieving the Electrochemical Efficiency Target

As stated in the introduction the electrochemical energy efficiency target for a commercial battery is 0.75. A realistic breakdown of the usable coulombic and voltaic efficiencies to achieve this target are 0.85 and 0.88, respectively. The refurbished 45-kWh module has delivered up to 53.6 kWh of dc energy at an ε_e of 0.61 on individual cycles. The near-term targets for the BEST-battery (Mark 4B) modules are 52.3 kWh of delivered dc energy at an ε_e of 0.65. The corresponing ε_c and ε_v targets for the Mark 4B modules are 0.76 and 0.85, respectively. Increasing the ε_v from 0.85 for the BEST-battery modules, to 0.88 for commercial Mark 4B modules, appears achievable without altering the stack design. Improvements in ε_c -- going from 0.80 to 0.87 -- were accomplished at the cell level by increasing the applied current density and the inter-electrode cell gap. This improve-

ment may not be realized with the present Mark 4B stack design but will be part of future designs enabling an advanced battery module to obtain 0.75 electrochemical efficiency.

AUXILIARY EQUIPMENT ENERGY CONSUMPTION

Unlike conventional lead-acid batteries, the zinc-chloride battery is a flowing-electrolyte battery which uses inert-graphite substrates and stores one of its electrochemically active components remote from the electrodes. The attractiveness of the battery in terms of minimal stand losses, no thermal runaway problem, and overcharge/overdischarge capabilities is counterbalanced by the need for mechanical support equipment. In the majority of instances this equipment consumes energy and is therefore a parasitic loss in terms of the net energy efficiency of a zinc-chloride energy-storage plant. As previously stated these devices can be categorized as module-level devices and plant-level devices.

To facilitate the analysis and discussion of some of these auxiliaries it is convenient to consider a hypothetical Mark 4B battery module which meets the electrochemical energy efficiency target of 0.75. It is assumed that this module operates under the conditions and limitations specified for the Mark 4B BEST-battery modules, but delivers an increased dc energy of 53.36 kWh due to the improved electrochemical energy efficiency. The corresponding charged and stored (at full charge) dc energies are assumed to be 71.11 kWh and 61.80 kWh, respectively. The 61.80 kWh of energy stored at the end of the 5.9-hour charge corresponds to 544 moles of chlorine hydrate stored per module. These values for the charged and delivered dc energies, as well as the quantity of chlorine hydrate formed and stored during charge, allows evaluation of the energy consumptions for the power conditioning and refrigeration subsystems at the module level. This simplifies comparison and discussion of the energy consumptions for the module-level and plant-level components and subsystems in a commercial load-leveling battery plant of the Mark 4B design.

Module-Level Devices

The category of module-level auxiliaries includes the electrolyte pump, the gas/hydrate former pump, the hydrogen recombination subsystem, and the inert-gas rejection subsystem. The efficiencies, power requirements, and resultant energy requirements for these auxiliaries are discussed below.

The electrolyte pump, which circulates electrolyte through the stack of the EPRI 45-kWh battery module, is a centrifugal pump with a 5-inch closed impeller suspended between two bearings. The pump is submerged in the sump electrolyte and coupled magnetically, through the battery case, to a 48-volt dc motor which is mounted outside the battery. A detailed description of this pump appears elsewhere (1).

For this application the hydraulic requirements are arrived at through a compromise between low hydraulic losses required for minimizing the energy and high hydraulic losses required for minimizing parasitic current losses. A summary of the hydraulic specifications for the electrolyte pump are given in Table 9-3. The hydraulic power requirement to meet these specifications is roughly 150 watts.

Table 9-3

ELECTROLYTE PUMP HYDRAULIC SPECIFICATIONS

Flow rate	330 ℓ/min
Inlet pressure	11 psia
Outlet pressure	15 psia

Figure 9-2 graphically illustrates the electrical power requirements for a pump to meet these specifications as a function of combined pump/motor efficiency. The present pump/motor combination operates at 380-400 watts or 0.4 fractional efficiency. At efficiencies below 0.4 the electrical power requirements increase rapidly. The present pump/motor combination is therefore marginally acceptable for this application. An efficiency of 0.6 is the commercial target for this component.

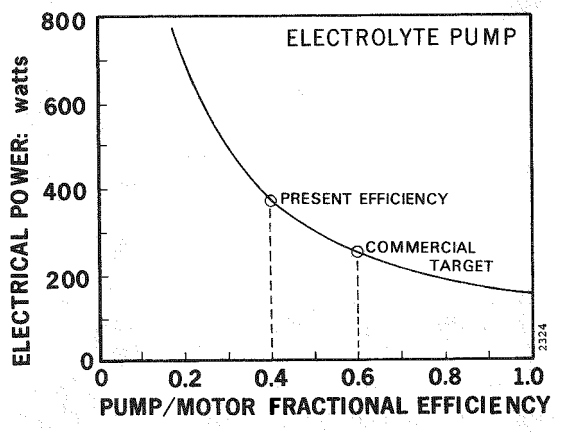

Figure 9-2. Electrical power requirement for the electrolyte pump as a function of combined pump/motor efficiency. Below an efficiency of 0.4 the electrical power requirement increases rapidly.

The hydraulic requirements for this pump are not likely to change significantly as long as the total electrode area in the battery stack is held constant. With this in mind, efforts were initiated during Phase II of the EPRI-EDA Program to design and develop more-efficient, cost-effective, and reliable pumps for this application. Two separate contracts were awarded: one to design an improved electrolyte pump, and another to design, fabricate, and supply a pump (centrifugal)/motor combination for this application. These pumps are being fabricated and tested under the DOE-EDA BEST-Battery Program.

The gas/hydrate-former pump, which transfers chlorine gas from the battery stack to the store and mixes it with prechilled store fluid to form chlorine hydrate in the 45-kWh battery module, is a positive displacement gear pump. Like the electrolyte pump, the gas pump is located inside the battery in the store fluid and coupled magnetically to a 48-volt dc motor mounted outside the battery. Details of the pump appear elsewhere (1).

Table 9-4 summarizes the hydraulic specifications for the gas pump during battery charge.

Table 9-4

GAS PUMP HYDRAULIC SPECIFICATIONS DURING BATTERY CHARGE

Chlorine gas flow rate	35 STD ℓ/min
Liquid flow rate	11 ℓ/min
Inlet pressure	10 psia
Outlet pressure	20 psia

As can be seen from the specification of the inlet pressure, this gas pump is also used to establish a -5 psig vacuum on the battery stack during charge. Using these specifications the hydraulic power requirement of the pump is ~56 watts.

Figure 9-3 illustrates the electrical power requirement for this pump as a function of combined pump/motor efficiency. The present pump/motor combination operates at 450 watts or 0.12 fractional efficiency. At efficiencies below 0.2 the electrical power requirement increases rapidly. The efficiency of 0.12 for the present pump/motor combination is therefore unacceptable for this application. An efficiency of 0.25 is the commercial target for this component during charge.

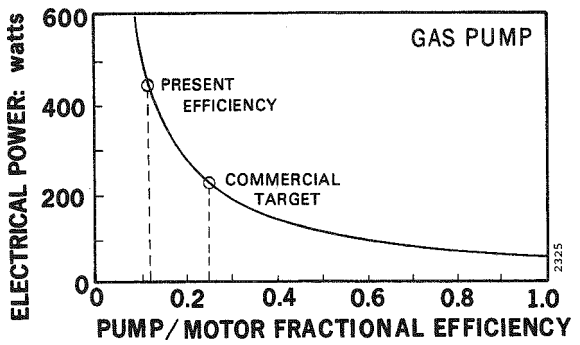

Figure 9-3. Electrical power requirement for the gas pump during charge as a function of combined pump/motor efficiency. Below an efficiency of 0.2 the electrical power requirement increases rapidly.

Unlike the electrolyte pump, the gas pump may not be operated during discharge. If it is, the hydraulic requirements will be quite different from those during charge. Table 9-5 summarizes typical hydraulic conditions for this pump, if it is operated during discharge. Using these conditions the hydraulic power requirement for the gas pump during discharge is ∿8 watts.

Table 9-5

TYPICAL GAS-PUMP HYDRAULIC CONDITIONS DURING DISCHARGE

Chlorine gas flow rate	5 ℓ/min
Liquid flow rate	5 ℓ/min
Inlet pressure	15 psia
Outlet pressure	22 psia

Figure 9-4 illustrates the electrical power requirement during discharge as a function of pump/motor efficiency. An electrical power requirement of 100 watts should be the upper limit. This corresponds to a fractional efficiency of ∿0.1 as the lower limit on combined efficiency during discharge. Data from the 45-kWh module indicates the present gas pump requires 105 watts of electrical power during discharge. This is marginally unacceptable. An efficiency of 0.25 is the commercial target for this component during discharge.

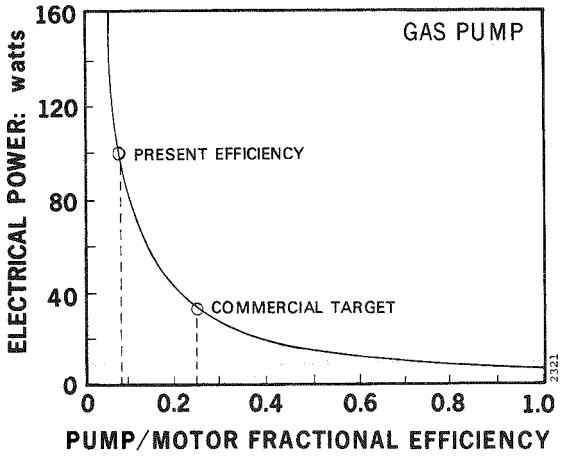

Figure 9-4. Electrical power requirement for the gas pump during discharge as a function of combined pump/motor efficiency. Below an efficiency of 0.10 the electrical power requirement increases rapidly.

Methods of achieving higher overall efficiencies for these pumps are discussed at length elsewhere (1). For some of these methods higher efficiency may be synonymous with shorter life or poorer reliability. Optimally designed pumps should provide the 10-year minimum life requirement, with minimum servicing and maintenance requirements, while meeting the commercial efficiency targets specified above.

The hydrogen-recombination subsystem requires an external power source. Because the zinc-chloride battery utilizes an aqueous electrolyte, gaseous hydrogen is formed chemically and/or electrochemically during normal battery operation. Although the rate of hydrogen formation can be controlled at very low levels via the proper selection of electrolyte and operating conditions, it is necessary to process the hydrogen to prevent its accumulation to the extent where it reacts spontan-

eously and explosively with the chlorine gas. This is presently accomplished by photochemically catalyzing the reaction between hydrogen and chlorine below its explosive level using fluorescent or ultraviolet lights.

The 45-kWh battery module reactor subsystem incorporates two 8-watt fluorescent lights. These lights are now located in the free gas space of the battery stack and are protected from the chlorine gas environment by quartz glass tubes. This reactor subsystem readily maintains the hydrogen concentration in the battery below 1% by volume. Including transformer losses the total electrical power consumption of this reactor subsystem is ∿20 watts. The electrical power can be supplied from either an ac or dc source. This 20-watt power requirement for the fluorescent-light reactor subsystem is relatively insignificant in terms of a parasitic energy loss.

The inert-gas rejection subsystem is presently under development at EDA. It is required in order to provide continuous closed-system operation of a battery module. Carbon dioxide, generated at a very low rate via the slow oxidation of the porous-graphite chlorine electrodes, and ambient gases, diffusing through the battery case, accumulate in the battery. These gases must be separated from the chlorine and rejected to the environment on a regular or intermittent basis to prevent deleterious effects on system performance. A detailed discussion of this subsystem is found in Sections 33-35.

The subsystem under development is based on multiple-stage electrowinning cells which will electrochemically process the chlorine and return it to the battery. The electrochemically-inert gases, left unprocessed, are rejected to the environment. Based on gas analysis data from the 45-kWh module and mathematical modeling of inert-gas accumulation in the module during operation, this inert-gas rejection subsystem will have to be capable of processing 95% chlorine and 5% inert-gas mixtures at the rate of 0.5 ℓ/min for a two-hour period during the end of discharge and/or the cleanout phase(s) of each battery cycle. Using performance data from laboratory electrowinning cells, this device will require 150 watts of electrical power. This amounts to 300 Wh of energy per module per cycle.

One approach to minimizing the external energy requirements for an electrowinning cell device is to utilize the electrical energy still available from the battery module at the end of its useful discharge to operate this device during cleanout. The amount of electrical energy still available from the module is at least a factor of three greater than that required for the operation of the inert-gas rejection device on a per cycle basis. This would, however, extend the duration of the cleanout phase to approximately two hours.

Evaluation of closed-system module operation may also demonstrate that this subsystem need only be operated every second or third cycle. Should this situation result, then the energy requirement per module-cycle would be reduced proportionately.

Plant-Level Devices

This category of auxiliaries includes the refrigeration, the power conditioning, and the control subsystems. A discussion of their efficiencies, power requirements, and resultant energy requirements follows.

The refrigeration subsystem is required to remove heat from the hydrate-store fluid of each battery module during charge. Each battery module has its own hydrate formation heat exchanger, but the coolant will be supplied from a central refrigeration subsystem in a 100-MWh load-leveling battery plant. The electrical energy required to operate the refrigeration equipment depends on the heat load and the coefficient of performance (COP) of the refrigeration unit. Despite the fact that the refrigeration subsystem operates at the

multiple-string or plant level, the following discussion of the influence of heat load and COP on the electrical energy requirement of the refrigeration unit will be handled at the battery-module level to be consistent with the preceding discussions.

At the module level the heat load is dictated primarily by the heat removal rate for forming chlorine hydrate. As stated earlier, 544 moles of chlorine gas will be formed and stored in the form of chlorine hydrate during the 5.9-hour charge cycle of this hypothetical Mark 4B module. Using this quantity of chlorine and the enthalpy of the hydrate formation reaction (-18.6 kCal/mole), 11.7 kWh of thermal energy needs to be removed per module-cycle during charge. Another 2-2.5 kWh of thermal energy from other sources also needs to be removed during charge. During discharge the heat required for decomposition of the chlorine hydrate nearly balances the heat of inefficiencies in the module and little if any cooling is required. Larger-than-expected inefficiencies during discharge can upset this thermal balance and some cooling during discharge may be required in some situations. The per module-cycle thermal energy to be removed will most probably fall in the range of 14-18 kWh for a commercial battery.

Figure 9-5 illustrates the effects of module heat load and the COP of the refrigeration unit on the electrical energy requirement of the unit per module-cycle. The COP of the refrigeration unit will depend on the ambient conditions of temperature and humidity, as well as, the size and type of refrigeration subsystem. Systems of the size and type previously considered for this application, which use deionized water or water-glycol coolants, are described in detail elsewhere (1). Under typical ambient conditions of 50-80°F these units operate with COPs of 5.0 to 3.0. Direct-cooling liquid-overflow Freon systems, discussed in Section 6, are presently being studied which should operate with COPs of 7.5 to 4.0 over the same range of ambient conditions. Depending on the system type, ambient conditions, and heat load, the electrical energy requirement of the refrigeration system will range from 2-6 kWh per module-cycle.

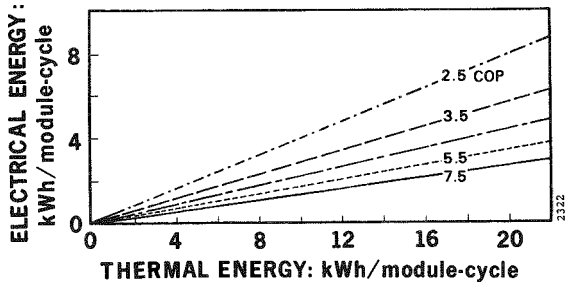

Figure 9-5. Electrical energy requirement of the refrigeration unit as a function of COP and module heat load.

The power-conditioning subsystem for a commercial load-leveling battery plant will interface the ac power from and to the utility high-voltage network with the dc power to and from the battery during charge and discharge, respectively. A power converter suitable for this application is described in Section 6. The unique voltaic performance characteristics of zinc-chloride batteries allow the use of cost-effective and high-efficiency power conversion equipment.

Presently line- and self-commutated converters are being studied and evaluated for their respective advantages and disadvantages in this application. Regardless of the final selection, the power conditioning subsystem will operate in the range of 0.96-0.98 efficiency in each direction. This means the round-trip efficiency (ac-dc-ac) will be in the range of 0.92-0.96.

Utilizing the charged and delivered dc energies for the hypothetical Mark 4B module, an estimate of the power conversion losses can be obtained at the module level. Table 9-6 summarizes the electrical energy losses per module-cycle for the above converter efficiencies.

Table 9-6

CONVERSION EQUIPMENT ENERGY REQUIREMENTS

	Energy Losses (kWh/module-cycle) 0.96 Efficiency	0.98 Efficiency
During Charge (71.11 kWh dc input)	2.96	1.45
During Discharge (53.36 kWh dc output)	2.13	1.07
TOTAL	5.09	2.52

The battery control subsystem will be a microprocessor-based computer system. It will utilize either solid state or electromechanical switching devices to control module, string, and plant operation. Depending upon the type and number (redundancy) of switching devices required, the total electrical energy to operate the switching devices is in the range of 5-25 watts/module. Added to this is another 5-15 watts/module required for powering the computer itself. The total power requirement for this subsystem is in the range of 10-40 watts/module. This electrical power requirement is similar to that for the present fluorescent-light reactor subsystem. They are both relatively insignificant parasitic energy drains on the total system.

DISCUSSION

An analysis of the effect of individual component efficiencies on the net efficiency of a zinc-chloride load-leveling plant demonstrates that the electrochemical energy efficiency of the battery is the only component efficiency which has a major effect. Figure 9-6 illustrates the effects of individual component and subsystem efficiencies on the battery-plant efficiency. The impact of individual component efficiency on plant efficiency is determined here by establishing a set of standard values for each component in a commercial energy-storage plant and then varying one of the component efficiencies while holding the others constant. The standard case efficiencies assumed are listed in Table 9-7.

From Figure 9-6, it can be seen that above certain minimum efficiencies, the

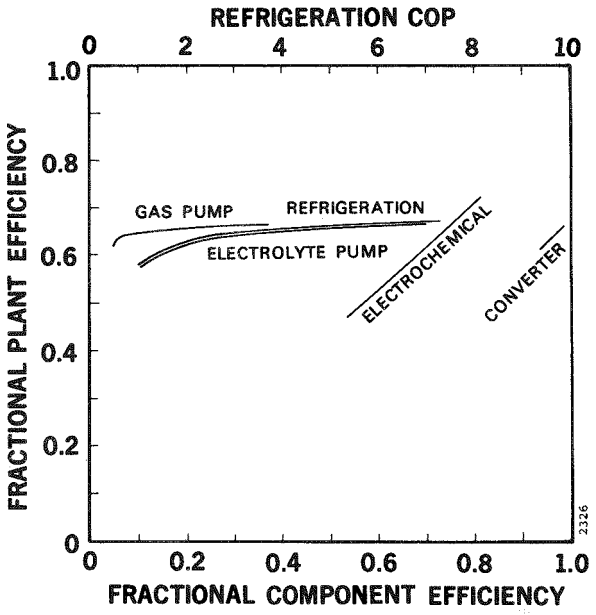

Figure 9-6. Efficiency of zinc-chloride battery energy-storage plant as a function of component efficiency. The single most important component efficiency is the electrochemical energy efficiency of the battery stack.

pumps and refrigeration subsystem have only a minor impact on plant efficiency. Similarly the power conditioning subsystem will also have a minor impact, because the technology for 0.96-0.98 conversion efficient equipment is mature. Therefore the only single component efficiency which has a major impact on plant efficiency is the electrochemical energy efficiency on the battery stack.

Table 9-7

STANDARD CASE EFFICIENCIES

Component	Efficiency
Electrochemical	0.75
Electrolyte Pump	0.60
Gas Pump	0.25
Converter	0.98
Refrigeration Subsystem	(5.0 COP)

Developing the battery-stack technology to deliver an electrochemical energy efficiency of 0.75 is still the single most important technical problem in the area of efficiency. During the last year, technology was developed which allows achievement of 0.74 electrochemical energy efficiency in zinc-chloride cells. This was achieved by enlarging the inter-electrode cell gap and operating at higher current densities.

In most cases, the energy requirements of individual components and subsystems are independent of one another. For example, the power conditioning subsystem is completely independent and will consume a given amount of energy per unit of converted energy. Similarly the control and hydrogen/chlorine reactor subsystems are completely independent. Because the total quantity of chlorine gas processed by the inert-gas rejection subsystem on a per module-cycle basis is relatively constant, this subsystem is almost entirely independent as well. The energy requirements for the two pumps will have a weak interdependency on the performance of the other subsystems, but will also be relatively independent. The electrochemical energy efficiency of the battery stack should also be relatively independent of the other subsystems as long as they are capable of maintaining the specified conditions in the battery stack.

The energy requirement for the refrigeration subsystem, however, will depend on the performance of other subsystems. At different efficiencies for the pumps and the battery stack, the heat load on the refrigeration subsystem will change. Changes in electrochemical energy efficiency will have the largest impact on the heat load. Figure 9-7 illustrates the significance of this effect for three different COPs. A drop of 10 points in the electrochemical efficiency results in 50% increase in the heat load and the energy requirement for the refrigeration subsystem. The energy requirement for the refrigeration subsystem would increase from 3.5-kWh/module-cycle at ε_e = 0.75 to 5.2-kWh/module-cycle at ε_e = 0.65 if

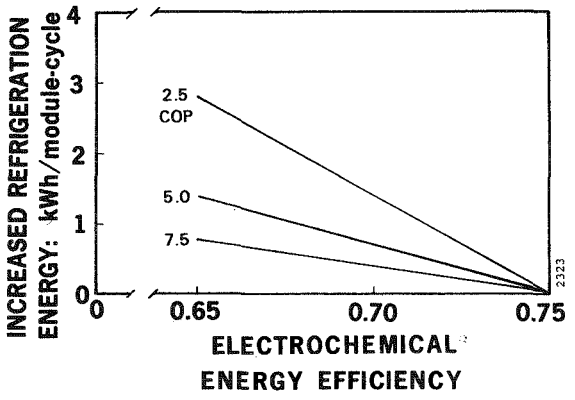

Figure 9-7. Increased electrical energy requirement of the refrigeration subsystem as a function of electrochemical energy efficiency (ε_e) and COP. A reduction in ε_e from 0.75 to 0.65 increases the heat load on the refrigeration subsystem by a factor of 1.5.

the COP of the refrigeration unit is 5.0. In reality, then, the plant efficiency is even more highly dependent on electrochemical energy efficiency than is illustrated in Figure 9-6.

An energy flow diagram shown in Figure 9-8 illustrates the influence of auxiliary component efficiencies on the net plant efficiency. An electrochemical energy efficiency of 0.75 is assumed and targeted values for component and subsystem efficiencies are used. The net result is an energy storage plant which operates at 0.65 energy efficiency. It should be noted that the efficiencies assumed for commercial components and subsystems in Figure 9-8 are conservative. It is not unreasonable to assume that efficiencies higher than those projected here can be achieved through the design and development of components and subsystems for the specific applications.

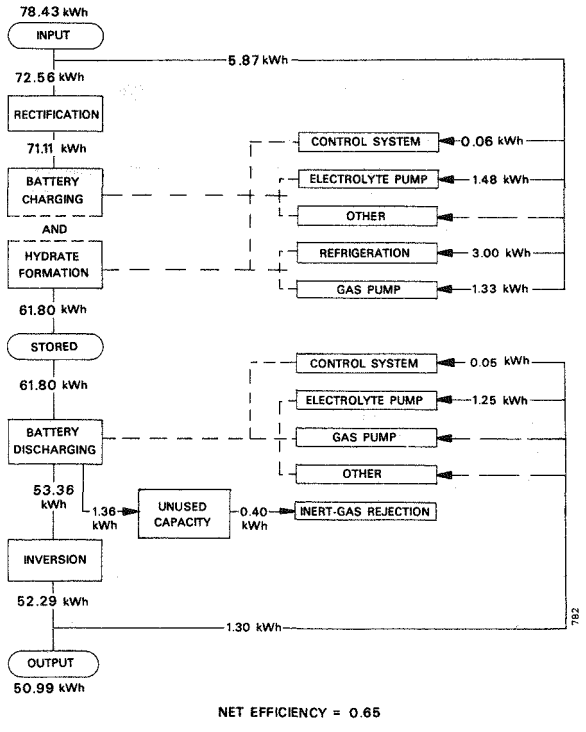

Figure 9-8. Energy flow diagram for the hypothetical Mark 4B battery which operates at an ε_e of 0.75 and incorporates auxiliary components which operate at improved efficiency levels. The net plant efficiency is 0.65.

REFERENCES

1. Development of the Zinc-Chlorine Battery for Utility Applications. Palo Alto, Calif.: Electric Power Research Institute. April 1979. EM-1051.

2. C. J. Warde, P. C. Symons, C. C. Whittlesey, and H. A. Catherino. "100-MWh Zinc-Chlorine Peak-Shaving Battery Plants." In Proceedings of the Thirteenth Intersociety Energy Conversion Engineering Conference, Vol. I, 1978, p. 755-763.

3. G. L. Henriksen, S. Kodali, J. Jorne, and C. J. Warde. "Zinc-Electrode Current Efficiency in Zinc-Chlorine Hydrate Batteries: I. Theoretical Aspects." Abs. 374, 155th Meeting of the Electrochemical Society, Boston, May 1979.

4. A. Kermani, J. Jorne, and S. Kodali. "Zinc-Electrode Current Efficiency in Zinc-Chlorine Hydrate Batteries: II. Experimental Studies." Abs. 378, 155th Meeting of the Electrochemical Society, Boston, May 1979.

5. S. Kodali, J. Jorne, and G. L. Henriksen. "Zinc-Electrode Current Efficiency in Zinc-Chlorine Hydrate Batteries: III. Natural Convection during Electrodeposition." Abs. 375, 155th Meeting of the Electrochemical Society, Boston, May 1979.

6. J. T. Kim and J. Jorne. "Mass Transfer of Dissolved Chlorine to a Rotating Zinc Hemisphere in $ZnCl_2$ Solutions." J. Electrochem. Soc. 125, 89-94 (1978).

7. A. F. Laethem and G. E. Sussman. "Activation of Porous-Graphite Chlorine Electrodes for Zinc-Chlorine Hydrate Batteries." Abs. 73, 154th Meeting of the Electrochemical Society, Pittsburgh, October 1978.

8. Evaluation of a 1-kWh Zinc-Chloride Battery System. Palo Alto, Calif.: Electric Power Research Institute. September 1976. EM-249.

Section 10

RELIABILITY ASPECTS OF BATTERY-PLANT O&M COSTS

ABSTRACT

Operation and maintenance (O&M) costs for electric-utility load-leveling battery plants will be determined by the reliability of the battery, refrigeration, and power-conditioning subsystems. This analysis focuses on the battery subsystem, which consists of a series-parallel array of 1920 53.4-kWh battery modules. From reliability considerations, the optimal design of this subsystem is shown to involve the use of a module-bypass switch. This concept -- rendered possible by the storage of chlorine external to the battery stack -- allows the isolation of a single module in the event of module-component failure. The reliability of the present module design -- estimated using failure rates published for components similar to those used in the module -- indicates that the cost of repair and replacement of failed modules will result in unacceptably high O&M costs. Module-design modifications are recommended to reduce reliability-related O&M costs. These include: (a) design simplification to reduce the number of components in a module, (b) module reconfiguration to minimize repair costs, and (c) expansion of module capacity.

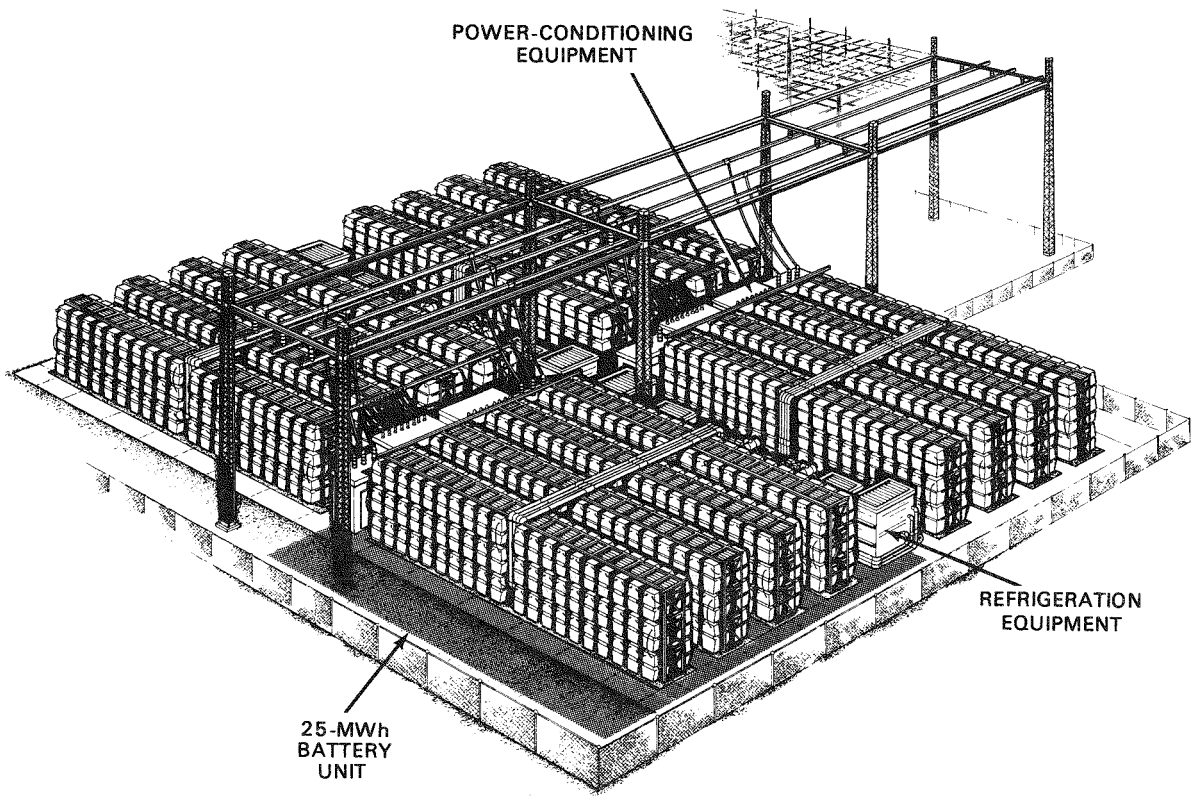

Figure 10-1. Artist's rendition of a 100-MWh zinc-chloride load-leveling battery plant, located at a utility substation.

INTRODUCTION

The present concept for a commercial zinc-chloride battery, shown in Figure 10-1, is a 100-MWh system composed of a series-parallel array of 1920 unitized battery modules. Each module is a self-contained, complete battery, except for an external source of cooling and chilling. The module will store 53.4 kWh of electrical energy. The total system, known as the Mark 4B Battery Plant, will contain the battery modules and auxiliaries. These auxiliaries include: (a) buswork to electrically connect the modules, (b) a cooling and refrigeration system with plumbing connections to each module, (c) a control system that permits unmanned operation, and (d) power-conditioning equipment that is the ac-to-dc interface between the utility power grid and the battery modules.

O&M cost targets have been developed for the Mark 4B battery. These are shown in Table 10-1. The costs were calculated on a levelized annual busbar basis (1). From the table, it can be seen that the major O&M concerns are the module-related costs, i.e., the cost of repair and replacement of failed modules, and the cost of lost capacity due to forced outages of modules.

Quantitative expressions for the two module-related O&M costs are developed in the next subsection. From the expressions, it will be seen that both costs depend on the module reliability, while system design only affects the cost of lost capacity. System design is then discussed. It is shown that the original design considered for the Mark 4B battery plant offered poor reliability but now a system has been designed which offers excellent reliability. Discussion of the failure rate of the 4B module follows. It is shown that it will take at least two years before the failure rate is established using module cycling data. In the absence of an experimental value, the failure rate of a Mark 4B module is approximated. Finally, the module-related O&M costs are calculated for the present 4B design. The O&M costs are excessive, indicating that improvements in module design are necessary. Design changes that will reduce module O&M costs are then discussed.

Table 10-1

OPERATION AND MAINTENANCE COST TARGETS

O&M Item	Targeted Cost (mills/kWh)
Repair/Replacement of Failed Modules	12
Lost Capacity due to Forced Outages of Modules	4
Repair/Replacement of Failed Auxiliary Units	2
Lost Capacity due to Forced Outages of Auxiliary Units	1
Preventive Maintenance	1

EQUATIONS FOR MODULE-RELATED O&M COSTS

The levelized annual busbar cost of module repair and replacement (CRR) can be calculated by taking the total cost of repairing and replacing modules for a year, dividing by the energy output of the battery system during that year, and then multiplying by a levelizing factor (LF). The total cost of repairing and replacing a module is the product of the number of module battery cycles during the year, c, the module failure rate, λ, and the average total module repair or replacement cost for a single failure, R. The energy output is the product of c and the module stor-

age capacity per cycle, Q. Thus, the levelized annual cost of module repair and replacement is

$$CRR = \frac{(c\ \lambda\ R)}{(c\ Q)}\ (LF) = \frac{\lambda\ R}{Q}\ (LF) \qquad (10\text{-}1)$$

It can be seen in Eq. 10-1 that CRR is very much dependent on the design of the module through the parameters λ, R, and Q. The other parameter (LF) is calculated from assumed inflation and discount rates.

The cost of lost capacity (CLC) is the difference between the true levelized annual busbar cost of stored electricity and the projected cost assuming no forced outages of modules.

To obtain an expression for CLC, the levelized annual busbar battery cost must be expressed as a function of $\bar{A}$, the average available capacity, divided by the maximum capacity. The total levelized annual busbar battery cost for $\bar{A} = 1$ is the sum of the capital cost CC, the operation and maintenance cost O&M, and the fuel cost FC. The total levelized annual busbar cost for a system with average available capacity $\bar{A}$ is,

$$LAC\ (\bar{A}) = \frac{CC}{\bar{A}} + O\&M + FC \qquad (10\text{-}2)$$

This is assuming that both O&M and FC are variable costs. Then the cost of lost capacity by definition is

$$CLC = LAC(\bar{A}) - LAC(1) \qquad (10\text{-}3)$$

Combining Eq. 10-2 and 10-3.

$$CLC = CC\ (\frac{1}{\bar{A}} - 1) \qquad (10\text{-}4)$$

The quantity $(\frac{1}{\bar{A}}-1)$ is defined by EPRI as the "Average Daily Unavailability" (1).

An expression for $\bar{A}$ can be obtained by averaging the instantaneous availability A(t) over the time period of interest. It is assumed that all repairs are made during a scheduled maintenance run. If the time between scheduled maintenance runs is τ and the capacity is brought up to its maximum value by this maintenance, then

$$\bar{A} = \frac{\int_0^\tau A(t)dt}{\tau} = \frac{1-A(\tau)}{n\lambda\tau} \qquad (10\text{-}5)$$

where,

$$A(t) = e^{-(n\lambda)t} \qquad (10\text{-}6)$$

with

$n\lambda$ = The failure rate of a unit of battery modules which is isolated from the system due to a single module failure, with n being the number of modules in the unit and λ the failure rate of a module (failures/cycle).

t = Time in cycles that has elapsed after the most recent maintenance

Thus, using Eq. 10-5, the Average Daily Unavailability becomes:

$$\frac{1}{\bar{A}} - 1 = \frac{n\lambda\tau}{1 - A(\tau)} - 1 \qquad (10\text{-}7)$$

If the number of modules, which are isolated during a maintenance interval, is significantly less than the total number of battery-system modules, i.e., $n\lambda\tau << 1$, then Eq. 10-7 reduces to:

$$\frac{1}{\bar{A}} - 1 \simeq n\lambda\tau/2 \qquad (10\text{-}8)$$

Combining Eq. 10-4 and 10-8, the cost of lost capacity becomes,

$$CLC \simeq CC\ (n\lambda\tau/2) \qquad (10\text{-}9)$$

From Eq. 10-9, it can be seen that the cost of lost capacity is affected by the system design through the variable n, and is also influenced by the module reliability which is measured in terms of λ.

SYSTEM DESIGN AND RELIABILITY

The quality of a system design from a reliability standpoint is a function of n, i.e., the number of modules removed from operation when a single module fails to perform properly and must be isolated. The fewer modules removed, the better the system reliability. The optimal system is one in which only the failed module is isolated.

The first design considered for the Mark 4B commercial battery plant was the string-out arrangement shown in Figure 10-2. It consisted of a number of parallel strings of series-connected battery modules. If one module in a given string failed to perform properly, the entire string was disconnected from the system.

Several advantages are offered by this system when there are many modules in a string. A major advantage of this series-connected arrangement is that the electrical variation between modules is averaged out. In addition, only one dc contactor is needed per string. However, reliability is maximized (i.e., minimum n) by placement of as few modules as possible in a string.

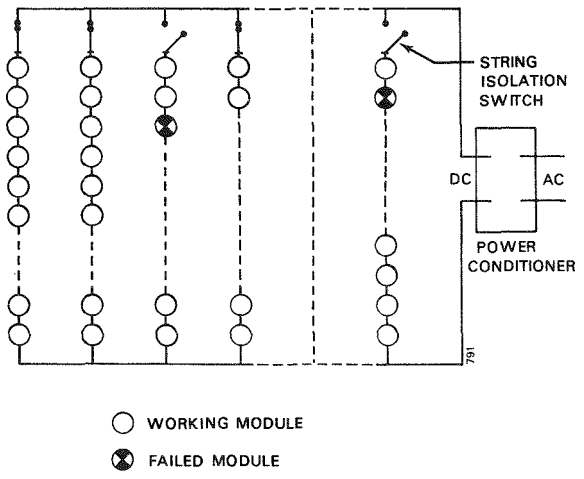

Figure 10-2. Schematic representation of the string-out design for the Mark 4B battery.

While a system of one module per string offers the maximum reliability, other design considerations make this system impractical. Efficiency and safety considerations suggest a low-voltage module (20 volts for the 4B design) while power-conditioning and utility considerations point to the use of high system voltage (thousands of volts). The accommodation of these considerations requires that a string contain many modules in series.

Alternate designs that offered better reliability were considered. The first of these was a fully-interconnected system, shown in Figure 10-3, which offers the optimal reliability. It is connected electrically in the same way as the string-out system, with the addition of disconnect switches on each module and buswork connecting equal potential points in the system. When a module fails, only that module is switched out, resulting in high system reliability. The drawbacks to this system include: (a) an electrical imbalance in the system that results when modules fail, (b) switches which must open under load are required to isolate each module, (c) extra buswork is needed, and (d) electrical variations between the modules are not averaged out by the parallel connection, resulting in a lower operating efficiency.

A system that offers high reliability without the disadvantages of the interconnected system is the bypass system shown in Figure 10-4. It consists of strings of modules connected in series. When a module fails, a bypass switch closes which shorts the battery module. This connection acts as a shunt because it allows current to flow through the string without passing through the failed module.

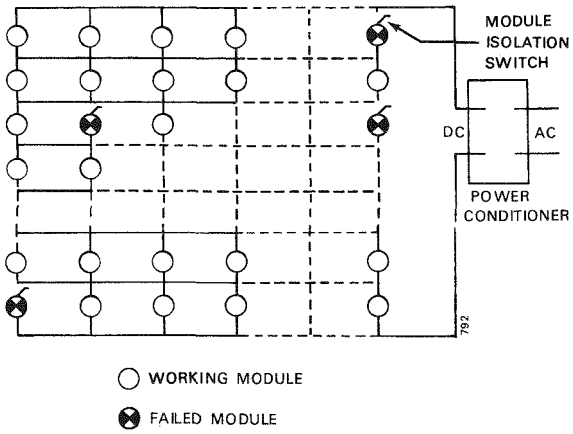

Figure 10-3. Schematic representation of the interconnected design for the Mark 4B battery.

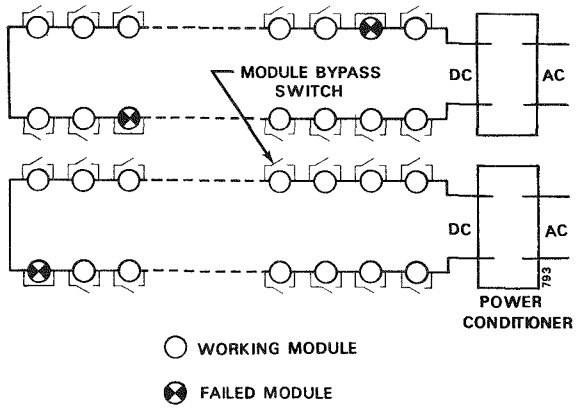

Figure 10-4. Schematic representation of the bypass design for the Mark 4B battery.

This system offers high reliability as only the failed module is removed from the network. The cost of the bypass switch is minimal because it is not required to interrupt the circuit. When the bypass switch is closed, the failed module shorts out and a very large current will pass through the electrical loop made up of the module and the shunt. If the pumps within the module are stopped before, or when, the module is shorted, this large current persists only for a few seconds. Experimentally, it has been established that the module and shunt can tolerate such current for this brief time. This is discussed in Section 19.

The bypass design, offering a reliability comparable to the interconnected design and the advantages of the string-out design, has been selected for the commercial load-leveling battery. The reliability of the bypass system is high enough to eliminate system design as a major reliability problem.

MODULE RELIABILITY - MARK 4B DESIGN

The reliability of the module must be known in order to determine the module-related O&M costs of the load-leveling battery. Unfortunately, at present it is difficult to determine the module failure rate because of the limited number of test cycles. A cycle being the time period during which a module is charged and then discharged. For load-leveling a cycle will be a duration of one day. Sufficient cycling data will not be available for at least two years to directly determine λ. This can be illustrated using Figure 10-5 which shows the cycling needed to determine the module failure to a given accuracy. The 10% line shows for a given λ, how many cycles it will take to determine experimentally this value of λ to an accuracy of ±10%. The 50% line gives the cycles needed to determine λ to an accuracy of ±50%. For example, following the arrows in Figure 10-5 indicates that it will take 2×10^4 cycles to determine a failure rate of 8×10^{-4} failures/cycle experimentally to an accuracy of ±50%. This failure rate is the value estimated in the next few paragraphs. If we want this failure rate measured to an accuracy of ±10%, then 5×10^5 module cycles are required.

A plot of the number of module cycles that will be accumulated over the next few years is shown in Figure 10-6. It can be seen that 2×10^4 cycles will have been run sometime in early 1982. Thus, for a module failure rate of 8×10^{-4} failure/ cycle it will be two years before we establish this value to an accuracy of ±50%. Of course, as can be

seen in Figure 10-5, if the failure rate is less, it will take longer to establish and vice versa. To insure that cycling data, once acquired, can be used to establish a module failure rate, a module event reporting scheme and database have been developed. An event is defined as anything not associated with the normal operation of a battery module, e.g., failures, nonscheduled shutdowns, repairs, design modifications, etc.

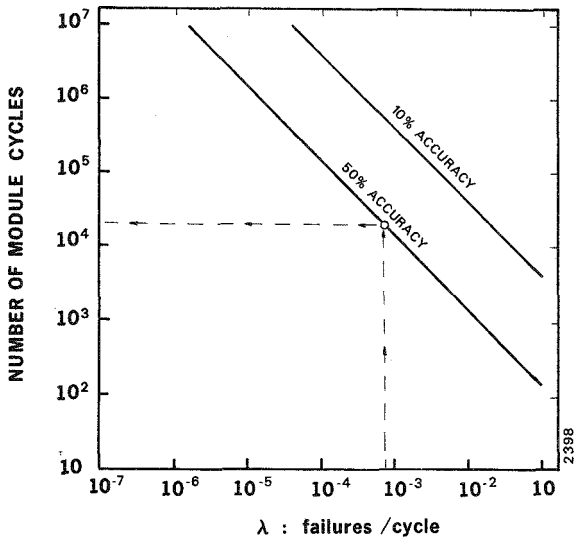

Figure 10-5. Module failure rate λ versus number of module test cycles needed to establish this failure rate to an accuracy of ±10% and ±50%.

An estimate of the Mark 4B module failure rate can be obtained if the failure rates of its component parts are known. The module, shown in Figure 10-7, is a small electrochemical factory that contains pumps, valves, heat exchangers, chemical cells, etc. For many of these components, their failure to operate properly will render the module inoperative. These critical components that will cause the module to fail were identified in a Failure Modes and Effects Analysis. If there is no dependence between the failure rates of these components, the failure rate for a module is given by the expression:

$$\lambda = \sum_{i=1}^{j} \lambda_i \qquad (10\text{-}10)$$

where λ_i is the failure rate of the ith critical component in the module and j is the number of critical components in the module (2).

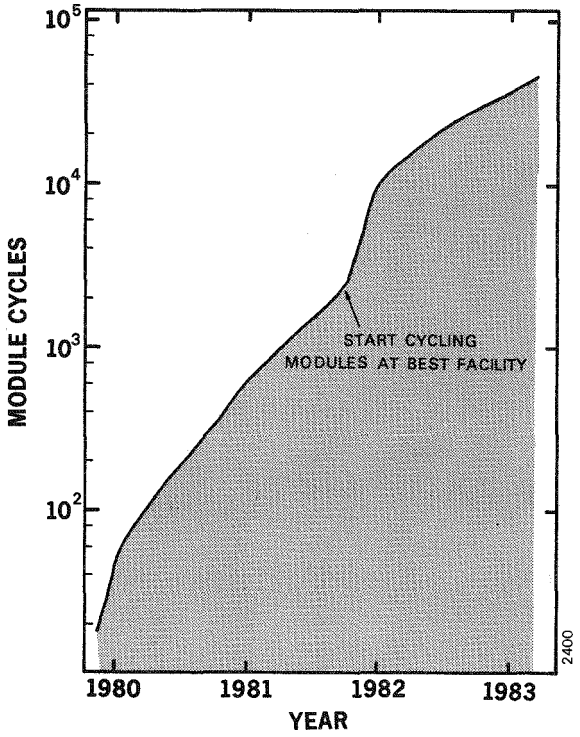

Figure 10-6. Estimated number of module cycles completed through 1982.

Hence, the failure rate of the module can be obtained from the failure rate of its critical components. The failure rates can be extracted from component cycling data. The module will be composed of nonstandard components with no previous cycling history, and these components are not yet available for cycling at EDA. Once cycling is initiated, the same event reporting procedure as described for the module will be used. However, failure rates are available for a number of similar standard production mechanical devices (3). Using these values, Table 10-2 lists estimated failure rates of critical components in the module.

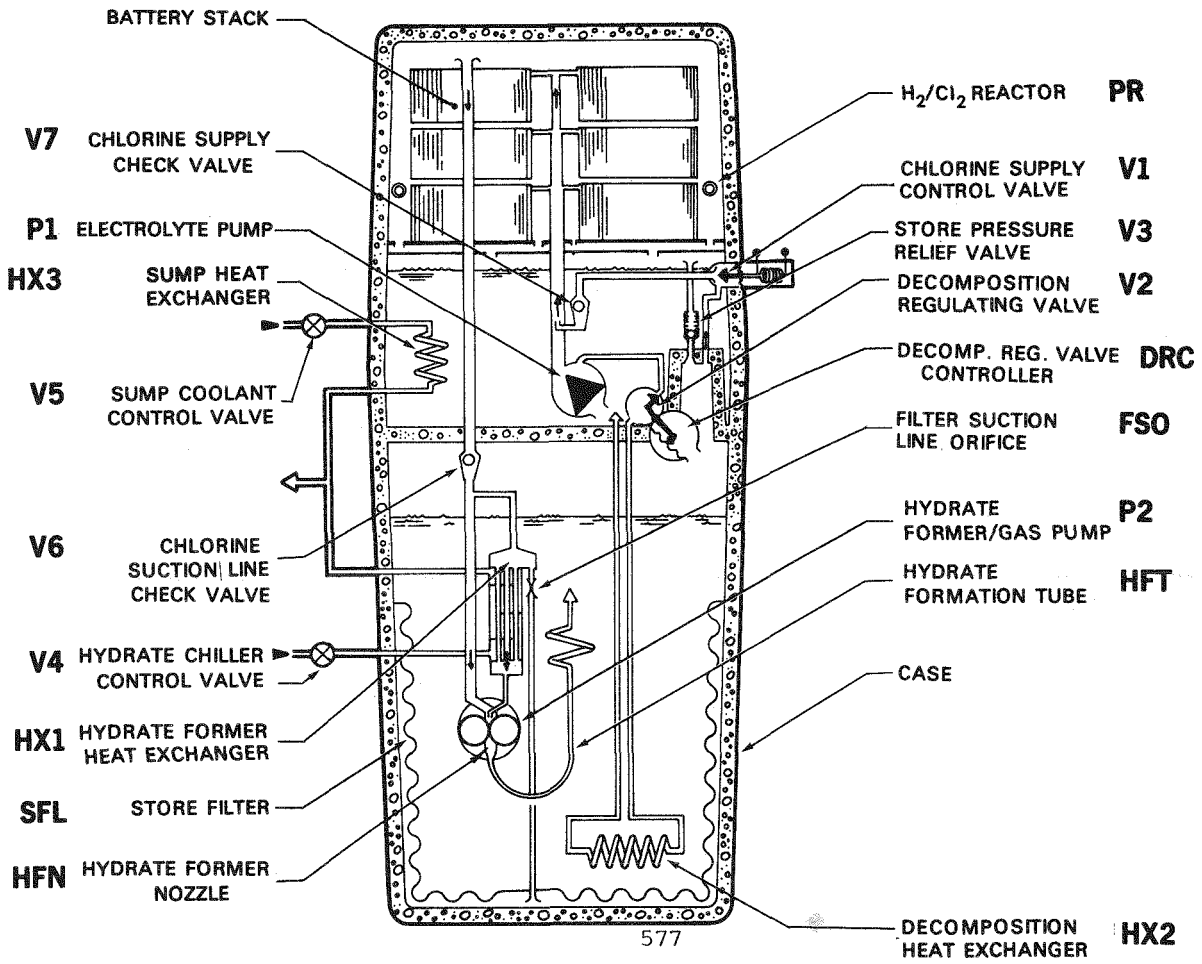

Figure 10-7. Schematic representation of Mark 4B module.

The sum of the failure rates of the components, shown at the bottom of Table 10-2, represents an approximate failure rate for a Mark 4B module. Components whose failure rate could not be estimated, were omitted from the table. Thus, the calculated module failure rate of 33.1×10^{-6} failures/hr represents a best-case or lower limit for the 4B design.

As the battery will operate in 24-hour cycles, it is useful to express the failure rate in cycles. Then,

$\lambda = 33.1 \times 10^{-6}$ failures/hr $\cdot$ 24 hr/cycle

$\lambda \simeq 8 \times 10^{-4}$ failure/cycle

This failure rate is equivalent to a mean time to failure for a module of 1250 cycles or 5 years assuming 250 cycles per year. As the targeted life of a module is 10 years, it is clear that a significant decrease in module failure rate is required.

DISCUSSION

Analyzing the module-related O&M costs of the bypass system highlights the reliability problem and suggests approaches to the solution. To implement this analysis, these costs will be calculated as a function of λ using Eq. 10-1 and 10-9.

Table 10-2

FAILURE RATES OF MARK 4B MODULE COMPONENTS

Component Label	Component Type	Failures per 10^6 hrs
DRC	pressure-sensitive switch	1.0
HX1	heat exchanger	0.9
HX2	heat exchanger	0.9
HX3	heat exchanger	0.9
P1	centrifugal pump	9.3
P2	geared pump	1.5
SFL	filter	3.0
V1	solenoid valve	1.6
V2	solenoid valve	1.6
V3	relief valve	1.6
V4	solenoid valve	1.6
V5	solenoid valve	1.6
V6	check valve	3.2
V7	ball valve	0.6
	case seal	3.8
	TOTAL	33.1

For the calculation, the values of CC,R,Q,n, τ , and LF must be assigned. The calculation will be used to determine whether or not the battery is cost-competitive with alternate means of meeting the energy demand. For the comparison to be meaningful, the battery system capital cost CC used to make the calculation must also be competitive. The cost-competitive value for CC, which has been determined to be 129 mills/kWh in Section 7, will be used.

At 129 mills/kWh, the module cost is approximately $5,000. The repair or replacement cost for a Mark 4B module which is not designed for on-site repair, includes: the cost of a good module ($\sim$\$5,000) less the credit received for the failed module ($\sim$\$1,500), cost of transporting the module ($\sim$\$250), and installation costs ($\sim$\$250). Thus, R is estimated to be $4,000.

For the bypass system, n=1. The capacity, Q, of a 4B module is 53.4 kWh. A reasonable value for τ is four months (80 cycles). In order for the calculations to be consistent with those in Section 7, LF must equal 1.88.

The module-related O&M costs calculated using the values just specified are shown in Figure 10-8. The most striking number on the curve is the total O&M cost of 118 mills/kWh for the estimated failure rate (shown by the dashed lines) of the Mark 4B design. This cost is significantly higher than the targeted cost shown in Table 10-1 -- 16 mills/kWh. Thus, it is clear that this cost of 118 mills/kWh must be reduced.

The curve also shows that with the bypass system design, the cost of lost capacity is significantly less than the cost of repair and replacement. For example, using the estimated 4B module failure rate, the cost of lost capacity is 4 mills/kWh and the cost of repair and replacement is 114 mills/kWh. Hence, the major emphasis should be on reducing the cost of repair and replacement. Of course, if λ is reduced, both costs will decrease. This can be seen

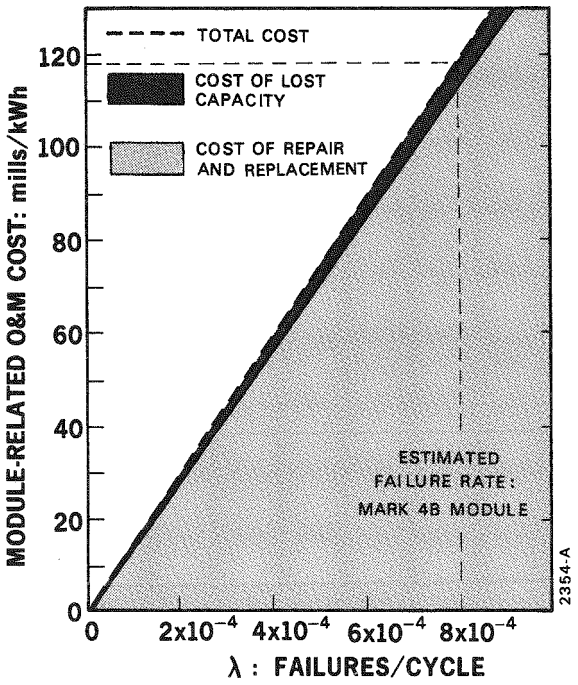

Figure 10-8. Module-related O&M cost as a function of module failure rate. This cost is calculated on a levelized annual busbar basis. The estimated Mark 4B module failure rate is shown by the dashed line.

in Figure 10-8. Reducing R and/or increasing Q will also reduce the cost of repair and replacement, as shown by inspection of Eq. 10-1.

An attractive way of increasing the module reliability is to simplify the module design (i.e., fewer module components, less chance for a component failure which renders the module inoperative). Simplification is also attractive because it most likely will reduce the cost of a module. This is not an easy solution though, since each component in the present 4B design has a specific purpose. Careful thought and consideration must be given to any simplification of the design to make sure that module performance does not degrade appreciably.

A second way to increase the reliability of the module is to increase the reliability of the components making up the module. However, cost-effectiveness must be determined before component changes are made. Also, module and component test runs should be carefully monitored to obtain experimental reliability values and to identify unreliable components for special attention.

Another method of increasing the module reliability is by having redundant components in the module. This approach should be investigated. However, it is probably of limited value because of: (a) additional complexity of module operation and control, and (b) increased component and manufacturing costs.

The O&M cost can be reduced by minimizing the average total cost of repairing or replacing a module, R. Presently, failed modules must be replaced because the 4B design does not allow on-rack repairs. Designing a module that can be repaired without removal from the battery rack may significantly reduce the cost of repair and replacement. To do this the module must be designed so that components that have relatively high failure rates can be serviced easily without removing the module from the rack. For example, if R is reduced from $4,000 to $400, the reduction in O&M cost is equivalent to that achieved by reducing the failure rate by an order of magnitude.

An increase in module storage capacity Q would reduce the O&M cost as long as the associated increase in R was not too large. A determination of the optimal module capacity will be important for future module designs.

Although the system-design problem has been eliminated for the Mark 4B battery plant, there is a major reliability problem at the module level. Module-design modifications are necessary. The module can be improved by:

- Simplifying the module design.
- Increasing the reliability of module components.
- Having redundancy of module components.
- Designing the module for inexpensive repair.
- Increasing the module storage capacity.

REFERENCES

1. Technical Assessment Guide. Palo Alto, Calif.: Electric Power Research Institute, June 1978. PS-866-SR.

2. K. C. Kapur and L. R. Lamberson. Reliability in Engineering Design. New York: Wiley, 1977.

3. D. W. Fulton. Nonelectronic Parts Reliability Data. Griffiss AFB, New York: IIT Research Institute, under auspices of the Reliability Center, Rome Air Development Center, 1978. Report NPRD-1.

Section 11

SAFETY ISSUES FOR ZINC-CHLORIDE BATTERY PLANTS

ABSTRACT

Successful commercialization of cost effective, load-leveling, zinc-chloride battery plants will be strongly influenced by their safety and environmental acceptability. Safety features incorporated in the design of the battery modules and plants are discussed in this report. Results of the theoretical studies by Energy Development Associates and experimental studies by Factory Mutual Research Corporation (FMRC) defining the extent of public hazard posed by these battery plants are also presented. These studies indicate that properly-designed zinc-chloride battery plants are safe and may be sited at residential, industrial, and commercial substations.

INTRODUCTION

Load-leveling zinc-chloride battery plants must not pose a hazard to either the public or the environment. The safety features of the battery modules and the site specific plant designs should permit unlimited siting of these plants in urban, suburban, and rural areas. The modules were scrutinized from the safety and environmental viewpoints and a detailed theoretical analysis was presented in an earlier EPRI report (1). Results of this analytical study clearly demonstrate that the battery plants do not pose any major safety or environmental problems.

Factory Mutual Research Corporation, under a contract from the Department of Energy (DOE) and the Electric Power Research Institute (EPRI), recently conducted theoretical and experimental studies on the safety of the zinc-chloride battery for use in electrical vehicles. The modules used for their studies were almost identical to the present load-leveling module. Hence, the experimental results of the FMRC studies can be applied to battery load-leveling plants. These results are compared here with the theoretical analysis presented by Energy Development Associates (EDA) in an earlier report (1).

The design of the zinc-chloride battery to be installed at the BEST Facility has been completed. Special safety features incorporated into this design are also discussed. The present work sets the tone and establishes design criteria for the safety of zinc-chloride load-leveling plants.

SAFETY ISSUES

Under normal operating conditions, zinc-chloride load-leveling battery plants are safe. Their interaction with the ambient is limited to the heat rejection through the refrigeration condensers both during the charge and discharge cycles, and to minute quantities of carbon dioxide that are purged periodically from each module. The modules are sealed with the stack operating slightly below ambient pressure and the store operating slightly above ambient pressure. Hence, the load-leveling battery plants do not normally pose any safety or environmental problems. However, abnormal operating conditions and accidents to the module must be considered when assessing safety issues. Proper module and plant designs can reduce the mishaps and minimize their effects.

An analysis of the module indicated that accidental release of gaseous chlorine and its spread in the atmosphere are the only hazards posed by these plants (1). Such releases can occur only when the battery case is ruptured. The following are some of the features in the module design that prevent such module ruptures:

- Near ambient operating temperatures and pressures.
- Numerous safety interlocks at module level to monitor possible failure modes and deactivate the module in the event of malfunction.
- Use of nonflammable coolant (R12).
- A hydrogen-chlorine reactor to insure low concentrations of hydrogen in the module.

In spite of these features, a module case rupture may occur if all the control devices fail, or if the case is damaged externally. In either case there is a possibility of chlorine escaping from the module. However, the rate of chlorine release is significantly suppressed by the following:

- Chlorine is stored in the form of nonflowing, solid hydrate.
- In the event of a minor module case fracture, the hydrate will remain inside the module and the chlorine release rate will be extremely small.
- The hydrate may spill onto the floor only in case of severe damage to the module.
- The modular concept uses 1920 independently packed stores, each containing about 90 pounds of chlorine as hydrate. This limits the maximum release of chlorine from a single module accident to 90 pounds.

The potential hazards associated with the zinc-chloride battery should not be compared with those associated with the storage and transport of liquid chlorine. Chlorine hydrate is a relatively stable material. The chlorine release rates from both liquid chlorine and chlorine hydrate depend on the rate of heat transfer to them. When spilled on the floor, the heat transfer to either depends on the exposed area and the temperature difference between the ambient and the medium. Hydrate, being solid, does not spread on the floor, thus, limiting the contact area. Its decomposition temperature at 9.6°C is much closer to the normal ambient temperature than liquid chlorine which boils at -34°C. In addition, the decomposition heat of hydrate is about four times as large as that of liquid chlorine. The combined effect is that chlorine stored as hydrate, when spilled on the floor in a severe module accident, will be released at a very slow rate relative to liquid chlorine.

Chlorine Dispersion

The above safety features in the module design and operation minimize the probability of battery accidents, and the mode of chlorine storage as hydrate limits the rates of chlorine release in the event of an accident. Under severe conditions, chlorine released from spilled hydrate may spread at objectional concentrations beyond the perimeter of the battery footprint. A complete analysis of the release rates for different accident scenarios is reported in (1). The worst-case scenario with chlorine concentrations of 50 ppm reaching the farthest from the site of accident is reproduced here as Figure 11-1. Even in this case the spread is within 50 feet from the site of accident. A 50 ppm concentration is chosen since it is reported (2) that exposure of humans to that level for periods of 30 minutes may be dangerous. The odor threshold level is reported (2) as 3.5 ppm. An isopleth of this level is also shown in Figure 11-1.

Hydrate Spill Tests

Prior to its proposed use in the zinc-chloride battery, chlorine hydrate was not considered to be a commercial product, and hence, no safety data are available. In the absence of any data, the above theoretical analysis (Figure 11-1), even if it is based on very rea-

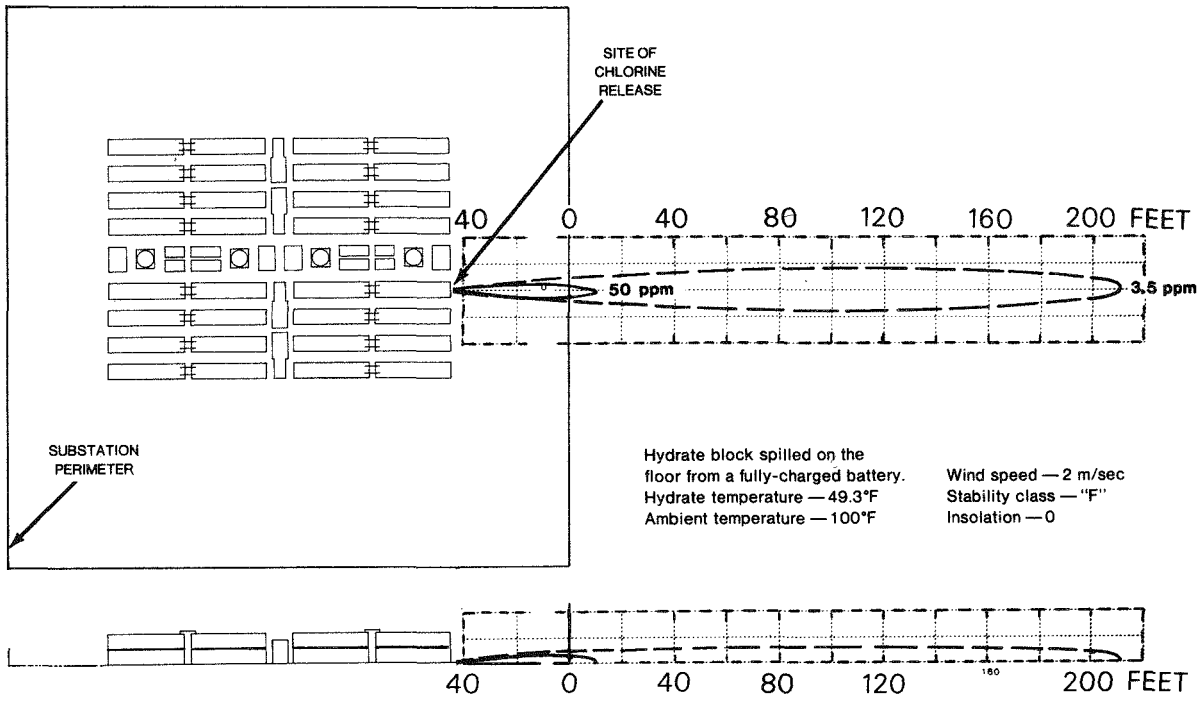

Figure 11-1. Chlorine dispersion for the worst-case accident scenario.

sonable assumptions, cannot be accepted without some experimental verification.

Factory Mutual Research Corporation, under DOE and EPRI contracts, conducted theoretical and experimental studies to determine the worst case accident scenarios involving a similar zinc-chloride vehicle module. They formed chlorine hydrate in a process similar to that used in the vehicle battery. An electric-vehicle crash was simulated by spilling the hydrate on a heated concrete surface. These tests were conducted in open air, and the spread of chlorine in the ambient was recorded.

Two of the plots of chlorine concentration, from two different spill tests, as reported by FMRC (3), are reproduced in Figures 11-2 and 11-3. The results in Figure 11-2 indicate unsteady concentrations mainly because of the meandering nature of the wind during the test. This plot gives average and peak concentrations at 75 feet in the downwind directions starting at 18 minutes after the spill. The average concentrations at this point are below 25 ppm. FMRC recorded concentrations in excess of 100 ppm for a short while immediately following the spill. The average concentration then decreased to below 5 ppm prior to increasing to about 20 ppm at 18 minutes after the spill. The results of another experiment presented in Figure 11-3 show average concentrations below 35 ppm at an even closer (50 feet) location from the spill in the downwind direction.

DISCUSSION

In the design of both modules and battery load-leveling plants, safety and environmental aspects are and will continue to be major considerations. Safety is one of the reasons for the modularized Mark 4 battery plant (1), as compared to the earlier designs that required centralized chlorine storage and the transport of gaseous chlorine between battery-stack modules and chlorine-hydrate stores.

In the modularized design, each module is self-contained and sealed; thus, no chlorine transport outside the module is required. The maximum quantity of chlorine in the form of hydrate in each module is 90 pounds and this occurs

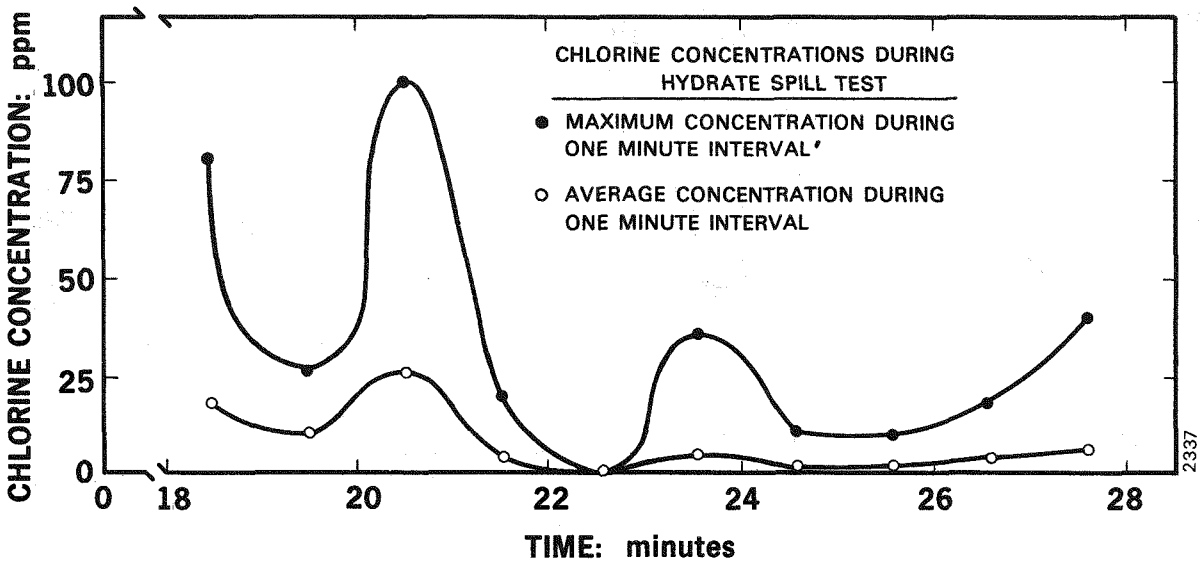

Figure 11-2. Factory Mutual Research Corporation's experimental data showing the measured chlorine concentrations in the air at 75 feet from the site of the chlorine-hydrate spillage in the downwind direction. Time begins from the instant of the spill simulating the accident [after Zalosh (3)].

only when the module is in the fully-charged state. Chlorine can be released only in the event of module fracture or rupture, and numerous module-level safety controls minimize the possibility of this occurrence.

Theoretical analysis (1) of the worst case accident, predicted dangerous levels of chlorine spread up to 50 feet away from the battery perimeter. Experimental work by Zalosh (3) for electric-vehicle battery accident scenarios demonstrated chlorine spreads of similar magnitude as predicted by the theoretical analysis. The maximum concentrations shown in Figures 11-2 and 11-3 are the periodic peaks recorded in the respective experiments and the physiological implications of such excursions are debatable. Similar studies on load-leveling battery scenarios may remove any residual doubts about the limited hazard posed by these plants.

Safety features limit the possibility of module rupture, but modules are still vulnerable to externally-caused accidents such as fires, severe impacts, etc. Plant-level safety devices are designed to reduce the possibility of external accidents and also to limit

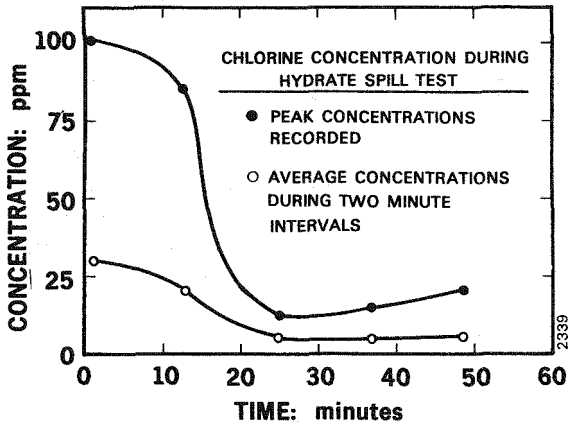

Figure 11-3. Factory Mutual Research Corporation's experimental data showing the measured chlorine concentrations in the air at 50 feet from the site of the chlorine-hydrate spillage in the downwind direction. Time begins from the instant of the spill simulating the accident [after Zalosh (3)].

the spread of chlorine to areas where people will not be exposed.

In the BEST design, rack enclosures are provided to protect visitors to the Facility from electrical leads and other auxiliary module-mounted motors,

probes, etc. The same hood also serves the secondary purpose of containing any chlorine released during module servicing. These hoods are connected to a chlorine scrubber. Similar devices can be used in commercial load-leveling plants to contain an accidental chlorine spill. For some installations it may be desirable to completely enclose the battery plant and, thus, provide additional possibilities for containing accidentally released chlorine. It was demonstrated that dangerous levels of chlorine from a single module rupture are unlikely to extend beyond 50 feet from the accident. Hence, in most cases, a fence around the plant at 50 feet from the outer racks may provide adequate public safety.

ACKNOWLEDGMENTS

We are very grateful to Dr. Zalosh and FMRC for sharing with us their prepublication data on hydrate spill tests.

Additional dispersion data on four other similar large-scale hydrate-spill tests by Zalosh (3) can be obtained directly from Factory Mutual Research Corporation, Norwood, Massachusetts.

REFERENCES

1. Development of the Zinc-Chloride Battery for Utility Applications. Palo Alto, Calif.: Electric Power Research Institute, April 1979. EM-1051, Section 9.

2. A. C. Fieldner, S. H. Katz, and S. P. Kinney. "Gas Masks for Gases Met in Fighting Fires." Bureau of Mines Technical Paper No. 248. Washington, D.C.: Government Printing Office, 1921.

3. R. G. Zalosh, et al. "Hazard Assessment of Zinc-Chloride Vehicle Batteries." Factory Mutual Research Corporation Final Report, DOE Contract EM-78-C-02-5088.

Section 12

COMMERCIALIZATION OF ZINC-CHLORIDE BATTERY PLANTS

ABSTRACT

Marketing studies supported by the Electric Power Research Institute (EPRI), the U.S. Department of Energy (DOE), the utilities, and private industry have identified a need for battery energy-storage systems suitable for utility load-leveling. The potential market is large. Impediments to achieving rapid market penetration are identified. The importance of the Battery Energy Storage Test (BEST) Facility and of a full-scale demonstration plant to the commercialization of zinc-chloride battery technology are discussed. Active participation by EPRI, DOE, and the electric-utility industry is required if the zinc-chloride battery is to be successfully commercialized.

INTRODUCTION

Commercialization considerations have been implicit in the EPRI-EDA Program since its inception. Although not specifically identified, design and specification of 100-MWh battery plants, cost analysis of commercial battery plants, safety and environmental considerations, legal aspects of siting battery plants in residential areas, and design and production of battery modules are all commercialization activities. Each activity is addressed in an earlier EPRI report (1). Neither market assessment of zinc-chloride load-leveling batteries nor the probable rate of market penetration were evaluated during Phase II of RP226-3.

The two basic marketing considerations are the need for load-leveling and the economic justification that supports the choice of zinc-chloride batteries over competing technologies. The need can be readily established by considering the projected future demand for peaking electricity, and the high cost and short supply of petroleum fuels required by combustion turbines commonly used for peak-load requirements.

A potential market for load-leveling batteries has been estimated based on the future demand for electricity. A minimum energy growth scenario devised by EPRI calls for the generation of 7500 billion kilowatt-hours (kWh) of energy in the year 2000 (2). If only 1% of this energy is provided on-peak by batteries that store off-peak energy, then 0.38-billion kWh of battery installation will be required for systems that discharge 5 hours per day or 1000 hours per year. Over the 15-year period of 1985 to 2000, an average of 25-million kWh of batteries must be installed annually. To meet this requirement, 250 battery plants with a capacity of 100 megawatt-hours (MWh) must be installed. An annual business volume of $1 billion will result if battery cost is $40 per kWh. Others have made similar estimates of the potential market for energy storage batteries (3). The fact that a large potential market exists for load-leveling battery systems cannot be disputed.

Penetration of this market by the zinc-chloride battery will be affected by alternate peaking technologies available to the utilities. These include: (a) combustion turbines, (b) pumped hydro, (c) compressed-air storage, (d) thermal energy storage, (e) fuel cells, (f) fly-wheels, and (g) other battery systems. Only a, b, and c will be available when the zinc-chloride battery is commercially introduced. Com-

pressed air and pumped hydro are site-limited, and the latter is fraught with environmental constraints. Thus, combustion turbines represent the major competition. The economic justification for zinc-chloride batteries has been discussed in Sections 7 and 8 of this report.

Even though the two criteria of need and economic justification appear to be readily satisfied, there are impediments to commercialization such as: (a) availability of low-cost generating capacity for charging batteries at off-peak periods, (b) siting constraints based on environmental considerations, (c) tendency of utilities to proceed cautiously before accepting a new technology, (d) effect of load-management techniques on peak loads, (e) effect of high cost of capital on acceptance of capital-intensive technologies, and (f) the large investment required to commercialize the zinc-chloride battery.

Commercialization of the zinc-chloride load-leveling battery involves both the development of a new technology and the development of a new application for that technology. The latter will require major participation by the electric utilities, EPRI, and DOE. It is likely that industries which are vulnerable to demand-charge impositions will also play a significant role. The next major step on the road to commercialization will be the installation, evaluation, and demonstration of a 4.2-MWh battery at the BEST Facility. Successful demonstration at BEST must then be followed by a full-scale demonstration plant to be operated in a commercial environment. This section will briefly review plans for these two activities and then discuss other factors that affect the probability of successful commercialization.

BEST FACILITY

Building on the technology base resulting from the joint EPRI-EDA Programs, RP226-1, -2, and -3, DOE and EDA signed a contract in September 1978 leading to the design, fabrication, and assembly of a 4.2-MWh zinc-chloride battery system. This program was completely integrated with Phase II of RP226-3 and will result in the installation of a battery system at BEST in mid-1981.

The zinc-chloride system will consist of eighty 50-kWh modules, two battery-rack enclosures, two cooling subsystems, a control subsystem, and the associated electrical wiring and plumbing. Two 904/768 volt (charge/discharge battery strings will interface with the BEST Facility power-conditioning system. Each string will consist of forty 22.6 V/19.2 V battery modules electrically connected in series and mounted on a battery rack. The rack structure containing the battery modules, coolant manifolding, control wiring, and microprocessor-based data-acquisition cards will be enclosed and connected to a ventilation/scrubbing subsystem. This subsystem will automatically ventilate the rack structure in the event of a chlorine leak. The ventilation-exhaust scrubber and the cooling/chilling subsystems will be located on a concrete pad outside the building. Two direct-cooling Freon subsystems will be employed. One will be used for forming chlorine hydrate, while the other will provide temperature control of battery electrolyte. A cutaway view of the system installed in the second bay at BEST is shown in Figure 12-1. Evaluation and demonstration of the zinc-chloride system at BEST will provide valuable test data to EDA and demonstrate concept feasibility to EPRI, DOE, and the utilities. A demonstration of this type is an essential step in the commercialization process.

To meet the requirements of this installation, a pilot production facility must be developed. A facility lease was signed in May 1979, with building occupancy scheduled for July 1, 1979, for a 41,000 sq. ft. pilot plant located in Greensboro, N.C. Lease-holding improvement drawings were submitted to the city building authorities in June, and the pilot plant was opened on July 9, 1979.

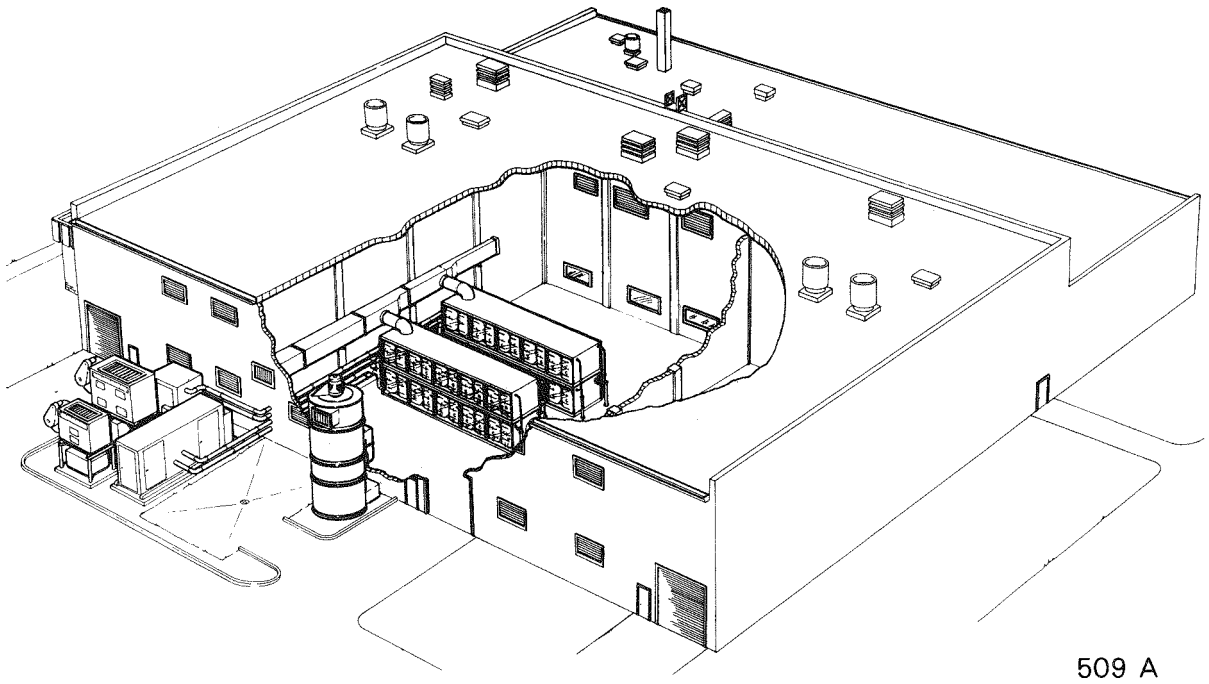

Figure 12-1. The 4.18-MWh zinc-chloride battery system in Test Bay No. 2 at the BEST Facility.

The development of the facility has proceeded on schedule. It is estimated that 80% of the lease-hold improvements are now complete. Equipment for graphite processing and submodule assembly is in place. Processing of graphite wafers started in November. The submodule assembly area was completed in early January and submodules are now being fabricated. A preliminary build plan for the manufacture of the load-leveling battery has been prepared and is now under review. The initial capacity of the pilot facility will be one 50-kWh module per day.

The completion and operation of the pilot plant are essential steps in the commercialization process. It provides an opportunity for a closer evaluation of projected production costs, evaluation of design and process improvements, and a basis for design of a production facility that will serve a semi-mature market.

DEMONSTRATION PLANT

Following successful testing at BEST, a full-size (50-100 MWh) demonstration plant will be necessary before the zinc-chloride battery will be broadly accepted by the utilities. The background for the design and location of the demonstration plant is currently being developed as part of the DOE-EDA BEST-Battery Program. Meetings with representatives from seven major electric utilities and two small electric cooperatives have been held to solicit utility guidance in designing a commercial plant and to develop criteria for appropriate site selection. An artist's rendering of a commercial battery plant is shown in Figure 12-2.

Future plans call for installation of a demonstration plant on a utility in the 1983 time frame. In concert with this development will be further identification of marketing considerations, complete cost analyses, and analysis of

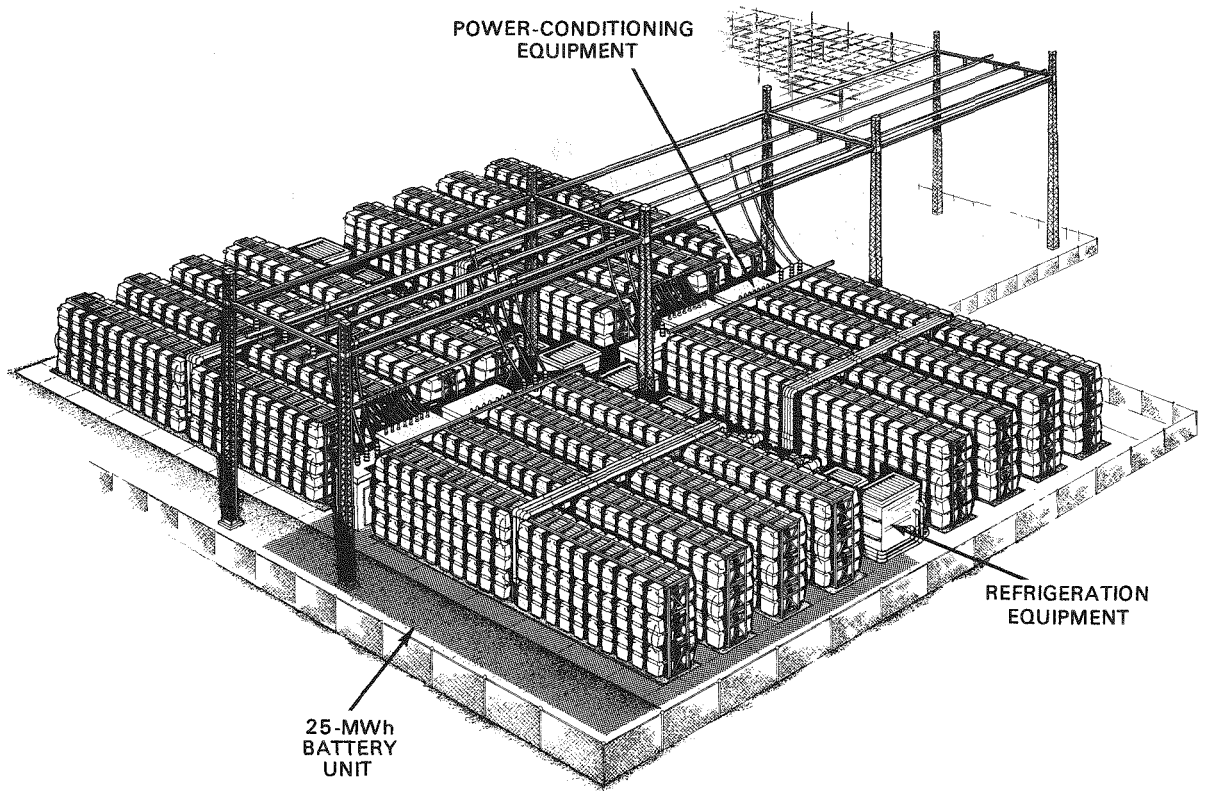

Figure 12-2. An artist's rendering of a commercial battery plant.

total battery credits that accrue to a utility from such an installation. A proposal for installation of a battery plant will be developed in 1980-1. With the participation of EPRI, DOE, and the utility, EDA will install the demonstration plant within two years after contract signing. Not only will this plant provide further information on the viability of a load-leveling battery system, but it will require additional production capability -- another step toward full-scale production.

DISCUSSION

The need for load-leveling batteries has been established by studies supported by DOE, EPRI, and private industry by projecting future demand for peaking electricity. Comparisons of alternate peaking technologies, and consideration of the short supply and high cost of oil reflect positively on the use of load-leveling batteries. Cost targets for zinc-chloride battery systems have been established, and projected manufacturing costs indicate a high probability of economic competitiveness. The plan for evaluation and demonstration at BEST has been described, and future plans for a demonstration plant have been reviewed.

All these accomplishments are positive steps toward commercialization. Unfortunately, they are not sufficient. There remain impediments to commercialization, as defined in the Introduction, that must be continuously evaluated. Only by the close cooperation of and effective communication between, EPRI, DOE, the electric utilities, and EDA can these impediments be overcome. EPRI has taken the lead in commissioning studies on commercialization of battery technology for utility applications. A recent example of this activity is a study performed by Decision Focus Inc. of Palo Alto and entitled

"Commercialization of Battery Energy Storage Systems." Further emphasis on commercialization by EPRI has resulted in the formation of Utility Battery Operations and Applications Team (UBOAT) composed of representatives from electric utilities who will address commercialization from their perspective. In addition to other responsibilities, this technical team will consider commercialization impediments and assist the developer in overcoming these impediments. The first meeting of UBOAT will be held on March 31, 1980.

As the zinc-chloride battery development moves closer to commercialization, the investment in facility and people increases rapidly. For example, it is projected that approximately 90 employees will be required at the Greensboro pilot plant to produce one 50-kWh module per day. The investment to supply modules for a full-size demonstration plant is obviously much greater. The large investment is further complicated by the significant time period between supplying modules for BEST and for a demonstration plant. Fortunately, a second market for zinc-chloride batteries -- battery-powered electric vehicles -- is developing rapidly. Because of the similarity of the two batteries, they can be produced at the same facility. This provides an opportunity for more rapid scale-up of production facilities and may fill the gap in the production cycle required to meet the needs of the load-leveling commercialization program. Even in view of these two commercially exciting programs, the large investment required, the high cost of money, and the risk associated with successful commercialization will be carefully evaluated by EDA and its parent company, Gulf +Western.

Continuing commercialization activities will require significant participation by the electric utility companies in addition to EPRI and DOE. The tendency of utilities to move cautiously before accepting a new technology is a significant impediment. Marketing strategies must be developed to convince electric utilities that zinc-chloride batteries represent an economically viable alternative for load leveling. Continued integration of EPRI-, DOE-, and EDA-supported programs are necessary to move this development to full-scale commercialization.

REFERENCES

1. Development of the Zinc-Chlorine Battery for Utility Applications. Palo Alto, Calif.: Electric Power Research Institute, April 1979. EM-1051. Part II, Section 8.

2. D. L. Douglas. "Commercialization of Advanced Batteries - Will It Happen?" In Proceedings of the Symposium on Load-Leveling, Vol. 77-4, 1977, p. 179.

3. J. R. Birk and J. W. Pepper. "Reducing Oil Requirements in the Electric Utility Industry; The Need for Energy Storage." In Proceedings of the Symposium on Load-Leveling, edited by N. P. Yao and J. R. Selman. Vol. 74-4.

4. Parametric Analysis of the Electric Utility Market for Advanced Load-Leveling Batteries. Arthur D. Little, Inc., under DOE Contract No. EC-77-C-01-5036.

PART III

REFURBISHMENT OF 45-kWh MODULE

Section 13

PROGRAM STATUS: 45-kWh MODULE

INTRODUCTION

The 45-kWh battery module, designed and built during Phase I of RP226-3, has been important to the zinc-chloride battery development program as the prototype that established the technical feasibility of an integrated module as the basic building block of a load-leveling battery plant. While earlier battery systems had been constructed in breadboard fashion, this module represented the first attempt to combine the stack, store, sump, and all auxiliary components into an integrated system. Except for external coolant supplies and line power for the pumps, the module is self-contained. As shown in the exploded view in Figure 13-1, there are three compartments in the module. The uppermost compartment, i.e., above the separator plate, is termed the stack compartment. Located in this compartment are six 10-cell batteries, termed submodules. The electrolyte pump sits in the sump compartment, shown on the lower right. This pump is magnetically coupled to a motor attached to the outside of the module case. The store compartment is located on the lower left. The hardware necessary for chlorine-hydrate formation and decomposition comprises two heat exchangers, a filter, and a gas pump, which is also magnetically coupled to a motor outside the case.

The prototype module, which performed well as a system, delivered an average of 43.2 kWh, close to the 45-kWh design level for dc energy output (1). However, the electrochemical energy efficiency of 48.4% was well below the design target of 63%. The major contributor to the efficiency shortfall was the coulombic efficiency which averaged 59%. This was significantly lower than the design level of 73%.

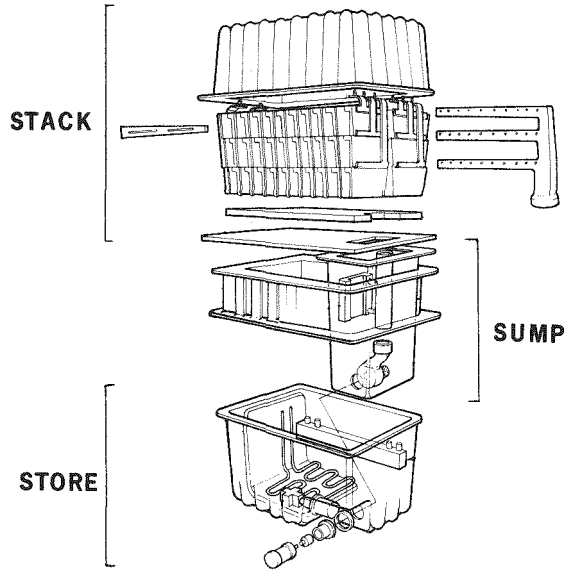

Figure 13-1. Exploded view of 45-kWh module prior to refurbishment.

REFURBISHMENT PROGRAM

A major effort was undertaken early in Phase II of RP226-3 to improve the efficiency and upgrade the energy delivery capability of the module. For this refurbishment program, delivery of 50 kWh at 60% electrochemical energy efficiency was set as the objective.

One cause of the low coulombic efficiency was readily identified. With the sump located alongside the store as shown in Figure 13-1, thermal insulation of the sump proved difficult. Consequently, excessive heat transfer from the sump to the store caused hydrate decomposition during charge. The addi-

tional chlorine thus generated taxed the capability of the gas pump to maintain the desired pressure level in the stack compartment. This resulted in a higher concentration of chlorine dissolved in the electrolyte, thereby significantly decreasing coulombic efficiency. To solve this problem, the sump was relocated as shown in Figure 13-2. Here, the electrolyte sump sits above the store and is thermally isolated from the chlorine hydrate by the chlorine gas space at the top of the store compartment. Simultaneously, the volume of the store was increased, thereby increasing its chlorine-hydrate storage capacity. These and other module changes are more fully described in Section 16.

Cell and submodule studies were conducted concurrently with module reconfiguration to find and correct performance deficiencies attributable to the stack. Studies at the cell level were undertaken to re-establish performance levels and repeatability of performance as well as to seek methods of improving performance. These studies, discussed in Section 14, confirmed the module performance targets and eliminated cell design deficiency as a cause of the low coulombic efficiency of the module.

Submodule studies focused upon finding the cause of the wide variation in performance among the submodules. This was traced to unit-cell imbalance, with intercell electrolyte continuity sus-

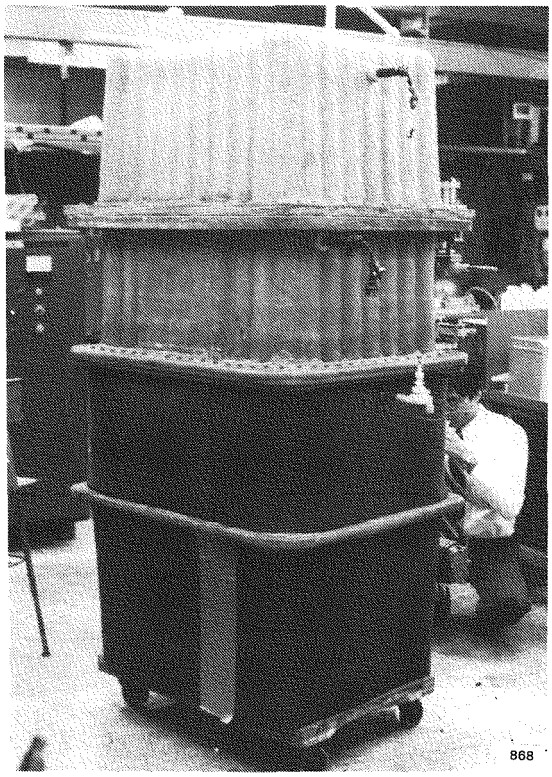

(a) photo view

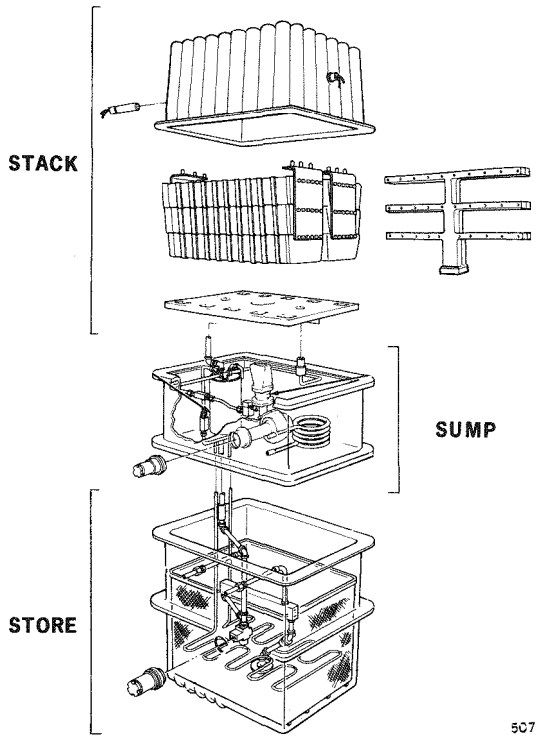

(b) exploded view

Figure 13-2. Refurbished 45-kWh module: (a) photo and (b) exploded view. Note relocation of electrolyte sump.

pected as the cause. The investigations described in Section 15 led to the discovery of zinc growths around and under the intercell busbars.

The zinc-growth problem was eliminated by modifications designed to minimize intercell electrolyte leakage. In addition, the contact resistances between the graphite end-buses and the titanium current collectors were significantly reduced by redesign. It should be noted that these modifications were made to the existing submodules, i.e., new submodules were not substituted.

The operational conditions employed during module testing after refurbishment are shown in Table 13-1. The experimental conditions prior to refurbishment are shown in parentheses. It should be noted that the relocation of the electrolyte sump allowed the achievement of significantly lower stack pressures during charge. It was possible, also, to raise the charge current density from 30 mA/cm^2 (495 A) to 32.8 mA/cm^2 (540 A).

Table 13-1

MODULE OPERATIONAL CONDITIONS
AFTER (AND BEFORE) REFURBISHMENT

Charge	
Current, A:	540 (495)
Stack Pressure, psig:	-2 (-0.5)
Temperature, °C:	30 (26)
Input Energy, kWh:	90 (90)
Discharge	
Current, A:	540 (540)
Stack Pressure, psig:	-4 (0)
Temperature, °C:	38 (32)

A comparison of results before and after refurbishment is depicted in Figure 13-3. Efficiency and delivered-energy data, averaged over 10 cycles before refurbishment, are compared to average values obtained from nine consecutive cycles after refurbishment. The refurbishment produced a dramatic increase in coulombic efficiency (from 59% to 71%), a slight increase in voltaic efficiency (from 82% to 83%), and, consequently, an increase in electrochemical energy efficiency from 48% to 59%.

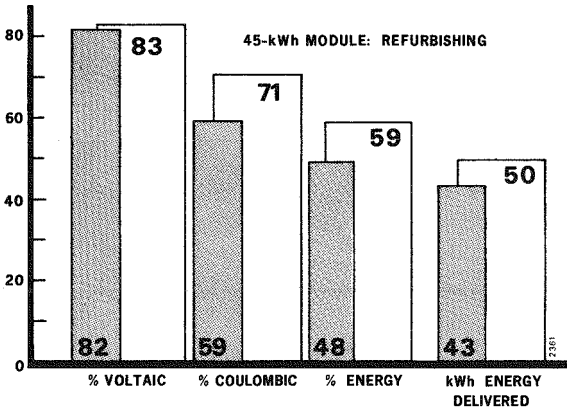

Figure 13-3. Module performance before and after refurbishment.

Subsequent refurbishment, involving increasing the thickness of the busing and rebuilding the gas/hydrate-former pump, increased the delivered energy to a maximum of 53.6 kWh. In the same series of experiments, the maximum electrochemical energy efficiency observed was 60.3%. Thus, the goals set for this refurbishment were met.

OTHER PROGRAMS

Development of a computer program to simulate the operation of the 45-kWh battery module is described in Section 17. This computer model, which has been shown to be quite accurate, can be a valuable tool for evaluating the feasibility and utility of proposed design changes and for helping to guide future developmental efforts.

A failure modes and effects analysis (FMEA) of the 45-kWh module is presented in Section 18. For this analysis the module was divided into discrete components which were then analyzed in

detail with respect to possible modes of failure, probability of occurrence, and severity of effect. This FMEA is the initial product of an ongoing program to characterize developing battery module designs in a similar fashion.

The 45-kWh module is now being used as a test bed for new concepts and components. To improve its utility for this purpose, the module has been reconfigured by relocating most of the internal components and piping outside the case so as to facilitate component substitution and maintenance. In its test-bed role, the module has been used for preliminary evaluation of an inerts-rejection device, for evaluation of the charge-stand state (battery charged and awaiting demand for delivery of energy), and for conducting a series of short-circuit tests to determine the feasibility of incorporating module bypass switches in a battery plant design. Reconfiguration of the module and supplementary uses of the module are discussed in Section 19.

REFERENCES

1. Development of the Zinc-Chlorine Battery for Utility Applications, RP226-3: Interim Report. Palo Alto, Calif.: Electric Power Research Institute, April 1979. EM-1051.

Section 14

45-kWh MODULE: CELL STUDIES

ABSTRACT

At the beginning of Phase II, the lower-than-expected electrochemical performance of the 45-kWh module was a major concern. Cell studies were conducted to establish the capabilities and limitations of the Phase I design (machined chlorine electrodes) at the cell level. Using similar conditions and electrolyte, these cells demonstrated repeatable and reproducible performances comparable to those of the 1.7-kWh battery. An improved electrolyte composition -- yielding 67-69% electrochemical energy efficiencies at delivered capacity densities of 185 mAh/cm^2 -- was developed for these cells. This cell technology was then successfully transferred to SRI International.

INTRODUCTION

As a result of the 48% electrochemical energy efficiency demonstrated by the 45-kWh battery module near the end of Phase I, a major effort was initiated early in Phase II to identify the cause(s) of this low efficiency and to upgrade its performance -- mainly in the area of coulombic efficiency. This section reviews a program to establish the capabilities and limitations of this Phase I design at the cell level. Phase I design refers to machined chlorine electrodes, two of which are glued together to form the chlorine-electrode pair. The following section (Section 15) discusses the program conducted to diagnose problems at the submodule level.

A dual approach was adopted. One study was charged with developing a data base on the coulombic efficiency achievable with the Phase I design when operating under conditions of the 1.7-kWh battery. A second parallel program was charged with evaluating operational parameters and arriving at a set of conditions which would improve Phase I submodule performance.

Six cells of the Phase I design were used in these studies. Five were used under the 1.7-kWh system operating conditions to generate a data base for comparison with the existing 1.7-kWh battery data base and to demonstrate repeatability and reproducibility of performance. Electrolyte screening studies were also conducted to establish an optimal electrolyte composition for the 45-kWh module.

One cell was delivered to SRI International for independent testing. The goal was to demonstrate successful transfer of the technology, and to verify EDA cell data with SRI personnel.

CELL DESIGN

The cutaway view, Figure 14-1, illustrates the construction of the cells, each incorporating two profiled porous-graphite chlorine-electrode pairs mated with three dense-graphite zinc-electrode substrates. The profiled chlorine electrodes -- formed by bonding together two plates from which material is machined away to form a cavity -- constitute the distinguishing characteristic of the Phase I design. Each cell contains 250 cm^2 of electrode area, with an inter-electrode cell gap of 0.2 cm. The press-fit bused electrodes are positioned in an inner cell case, which in turn is contained in an outer

chamber that also functions as the electrolyte sump. The outer case penetrations were sealed to allow operation under a vacuum produced by pumping water in a closed loop through an aspirator. As shown, provisions were made for power connections, electrolyte circulation, sump heating and chlorine supply.

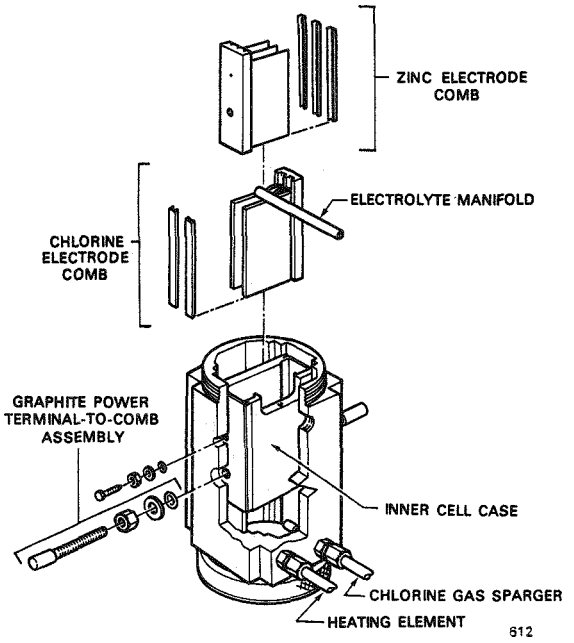

Figure 14-1. Test cell used for cycling studies and SRI investigation. The cell employs two chlorine-electrode pairs and three zinc electrodes.

PROCEDURES AND RESULTS

As mentioned earlier, the cell studies focused upon three objectives: comparison of performance with the 1.7-kWh battery data base; investigation of methods for improving performance; and verification of EDA cell data.

1.7-kWh Battery Conditions

The electrolyte and operating conditions of the 1.7-kWh battery were used initially in two cells to establish a preliminary coulombic-efficiency baseline. The electrolyte formulation was 2M $ZnCl_2$ + 3M KCl + 2M NaCl + a proprietary leveling agent. The electrolyte pH was adjusted to 0.2, and the temperature for cell operation was 40°C. The flow rate was 1.8 ml/min-cm^2 during an average charge of 4 hours at 35.5 mA/cm^2 followed by a discharge at 30.8 mA/cm^2. The average usable coulombic efficiency (ε_c) for both cells over a combined total of 9 cycles was 80.2%. The corresponding average voltaic (ε_v) and energy (ε_c) efficiencies were 87.4% and 70.1%, respectively.

A coulombic repeatability and reproducibility test was then initiated using a group of five cells with operating conditions altered slightly. A flow rate of 2 ml/min-cm^2 and an equal charge/discharge current density of 33 mA/cm^2 were utilized. The results are shown in Figure 14-2. The average usable coulombic efficiency was 75% over the first 13 cycles. At this point, a flow imbalance in cell 8 was found and corrected, improving its performance over the next 15 cycles as shown. Figure 14-2 clearly illustrates that coulombic efficiency repeatability and reproducibility from cell to cell stabilized with extended cycling.

In the charge mode of the 45-kWh module, a vacuum is produced in the stack area of the module. A vacuum (0.5 atm) applied to test cell 2A to approximate this condition produced an average coulombic efficiency of 82.5%, an increase of 5%, for cycles 30-32 in Figure 14-2.

Improved Conditions

Concurrent with the above investigation, another study was performed in similarly designed cells to specify the combination of electrolyte and operating conditions that would reproducibly achieve usable coulombic efficiencies of >80% and delivered capacity densities of >185 mAh/cm^2. Several sets of conditions were found to meet or exceed these criteria. These results are presented in Table 14-1.

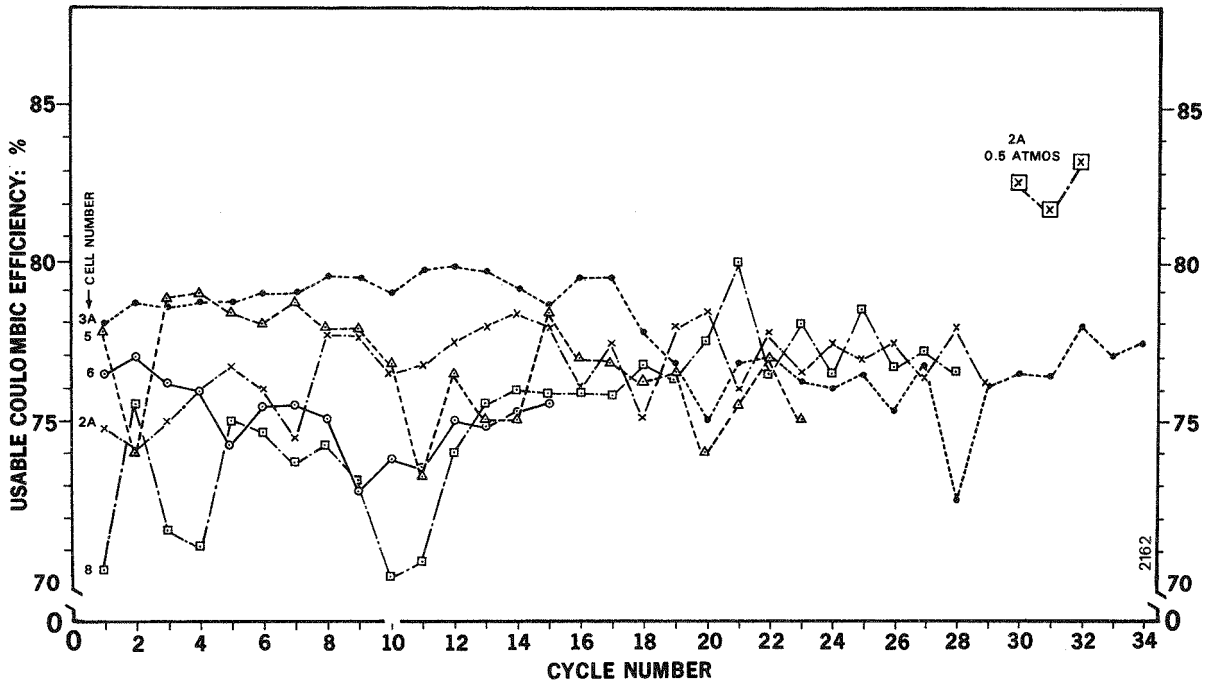

Figure 14-2. Cycling behavior of cells operating with modified 1.7-kWh battery conditions.

Table 14-1

ELECTROLYTE/OPERATING CONDITIONS GIVING ≥80% USABLE COULOMBIC EFFICIENCY

Molar Composition $ZnCl_2$, KCl, NaCl	mA/cm^2 Charge/ Disch.	T°C Charge/ Disch.	Charge Capacity mAh/cm^2	Dendrites	Pressure atm Ch.	Pressure atm Disch.	Efficiency, % Usable Coulombic	Efficiency, % Voltaic	Efficiency, % Energy
2.5, 3, 3	36/50	32/42	210	Yes	1	1	83.8	88	73.7
2.5, 3, 3	36/50	31/39	240	No	1	1	80.6	87	70.1
2.5, 3, 3	36/36	40/33	120	Yes	0.74	1	81.8	85	69.5
2.5, 1, 4	36/40	30/30	205	Yes	1	1	81.6	87	70.9
2.5, 2, 3	36/36	--	70	Yes	0.76	0.87	80.8	81	65.4
2.5, 3, 0	40/40	30/35	160	Yes	1	1	83.5	83	69.3
2.5, 2, 0	33/33	--	240	No	0.5	0.5	82.7	82	67.8
2.5, 2, 0	33/50	--	240	No	0.5	1	82.8	83	68.7
2.5, 2, 0	33/50	--	180	No	0.5	1	84.1	82	68.9
2.5, 0, 5	60/40	39/32	105	Yes	1	1	84.3	80	67.4
2.5, 0, 5	40/40	27.30	85	Yes	1(N_2)	1(N_2)	88	78	68.6
2.5, 0, 5	40/40	30/34	130	Yes	1	1	81.5	81	66.0

As shown in the table, satisfactory coulombic efficiency was indicated for these electrolyte formulations. Plating-capacity considerations were responsible for the selection of 2.5M $ZnCl_2$ + 2.0M KCl for additional testing. It is noteworthy that formulations such as 2.5M $ZnCl_2$ + 3M NaCl, although giving excellent coulombic and energy efficiencies, were excluded from consideration for the same reason as the 1.7-kWh electrolyte. High levels of supporting electrolyte had been found to result in precipitation of salts in the decomposition heat exchanger of the hydrate store during the discharge mode of the 45-kWh module.

The reproducibility of results from three cells using the new electrolyte at 0.5 atmosphere vacuum during 4-hour charges followed by ambient pressure discharge at 33 mA/cm^2 was good (Figure 14-3). A 79% average coulombic efficiency and 86.9% average voltaic efficiency yielded an average electrochemical energy efficiency of 68.6%. The reason for the less satisfactory performance of cell 8 is not known. This electrolyte was recommended and utilized in submodule and 45-kWh battery module qualification tests discussed in Sections 15 and 16 of this report.

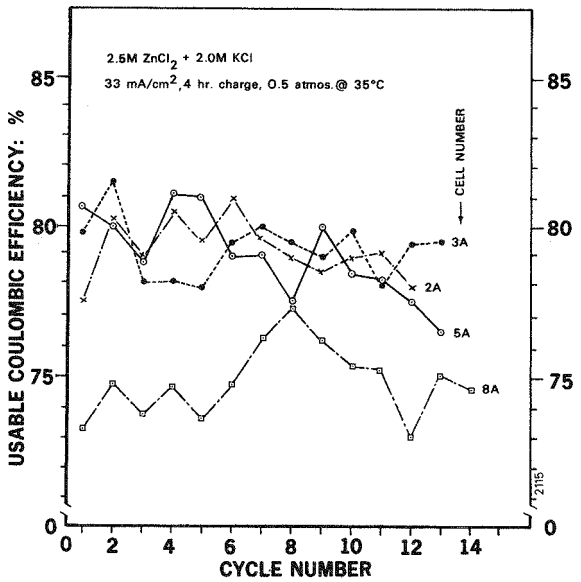

Figure 14-3. Cycling behavior of cells using qualified electrolyte composition from screening tests.

Verification of Cell Performance by SRI

Another objective of these cell studies was to build, test, and deliver to Stanford Research Institute (SRI) one Phase I design cell to be used for independent testing by SRI personnel.

The cell and system were assembled at EDA and the chlorine electrodes were activated electrolytically in dilute zinc chloride. Three cleanup runs were performed prior to accumulating eight normal cycles. On the first cycle using 2.5M $ZnCl_2$ + 2.0M KCl electrolyte, the cell demonstrated a 74.3% usable coulombic efficiency and a 65.2% energy efficiency while under a 0.5 atmosphere vacuum during charge. Other electrolyte compositions were utilized on subsequent cycles. The highest coulombic efficiency of 83.6% was achieved on the cell using 2.5M $ZnCl_2$ + 2.0M KCl + 2.0M NaCl electrolyte. The cell also achieved a charge capacity density of 233.6 mAh/cm^2 using 2.5M $ZnCl_2$ + 2M KCl + 1M NaCl electrolyte.

Following initial testing at EDA, the cell was transferred to SRI where initial testing was performed under the same conditions as those employed during the first cycle at EDA. The cell demonstrated a 75.4% usable coulombic efficiency and a 64.2% energy efficiency, verifying its electrochemical performance at EDA. Operation of the cell was then transferred to SRI personnel. In a subsequent test series of five cycles, it was shown to perform at the same level. EDA zinc-chloride cell technology had been successfully transferred to SRI, thereby satisfying a contractual obligation as part of RP226-3, Phase II.

As changes in electrolyte composition offer potential for the real-time monitoring of coulombic efficiency, SRI investigated techniques to monitor certain electrolyte characteristics as part of their efforts. After evaluating the use of refractive index,

specific volume resistivity, pH, zinc-ion concentration (by chemical assay) and total pressure, the most generally useful technique was found to be refractive index. Besides being unaffected by other changes, such as pH, it was found that the change in refractive index is proportional to the change in zinc-ion concentration, and thus is directly relatable to coulombic efficiency. SRI also measured zinc-ion diffusivities, developed a chlorine reference electrode, and developed sensors for flow-rate and pressure as part of their program with EPRI.

DISCUSSION

These cell-level tests verified the performance of the Phase I cell design, thereby eliminating cell design faults as a cause of depressed coulombic efficiency performance in Phase I submodules. Repeatability of performance and reproducibility from cell to cell was demonstrated using first the 1.7-kWh system electrolyte and then an electrolyte chosen through screening tests as a more optimal composition for the 45-kWh module. The average coulombic efficiency of 79% and electrochemical energy efficiency of 68.6% for these latter tests confirmed that the targeted goals of 75% and 63% for the module were reasonable. Subsequently, EDA zinc-chloride cell technology was successfully transferred to SRI International. Following this transfer, SRI performed independent cell studies which verified EDA performance levels.

Section 15

45-kWh MODULE: SUBMODULE STUDIES

ABSTRACT

An evaluation of Phase I submodules was performed to identify the cause of large coulombic-efficiency imbalances among the unit cells of these submodules. This phenomenon was believed to be largely responsible for the coulombic-efficiency shortfall observed for the 45-kWh battery module during Phase I. Diagnostic techniques were developed to permit the successful identification of the major cause -- intercell zinc growths accumulating in the bus-to-case seal regions of the submodules. Submodule refurbishment resulted in upgrading the electrochemical energy efficiency of the 45-kWh module to 60%.

INTRODUCTION

Early in Phase II a program was initiated to identify the cause of the low coulombic efficiency demonstrated by the 45-kWh battery module near the end of Phase I. The previous section -- Section 14 -- describes the program that was conducted to establish the capabilities and limitations of this Phase I design at the cell level. Here the Phase I design is evaluated at the submodule level.

During Phase I coulombic-efficiency imbalances of greater than 30% had been observed between unit cells in these submodules (1). These large unit-cell imbalances -- which were at least partially responsible for the suppressed coulombic efficiency in the 45-kWh module -- remained unexplained at the end of Phase I. The efforts during Phase II, therefore, concentrated on identifying the cause of this cell imbalance.

In this section, a brief review of the Phase I submodule design is followed by a description of the test system designed specifically for submodule testing. Then the testing program is discussed, which led to the identification of the problem and the demonstration of improved efficiency.

SUBMODULE DESIGN

The Phase I submodules, built with mid-1977 technology, employed profiled porous-graphite electrode pairs consisting of two plates bonded together after machining away material to form a cavity between the plates. As shown in Figure 15-1, 22 of these chlorine electrode pairs were inserted into a slotted graphite bus and 23 dense-graphite plates (zinc electrodes) were installed on the opposite side to form a bipolar comb. Assembly of these combs, with the chlorine and zinc electrodes interleaved, produced a submodule of ten unit cells connected in series. The major components of the submodule are illustrated in Figure 15-2, including a unit-cell manifold to distribute electrolyte into the cavity of each chlorine-electrode pair. Electrolyte flows through the porous electrode into the cell gap, overflows into a drain cup at one end of each unit cell, and drains back to the sump through a long flow channel designed to increase the electrical isolation between the cells and the sump.

TEST SYSTEM

The test system designed and built during Phase I of RP226-3 for submodule testing was used in this evaluation of the Phase I submodule performance (1). This system, shown schematically in Figure 15-3, was well suited for accurate control of operation, not only under conditions duplicating module

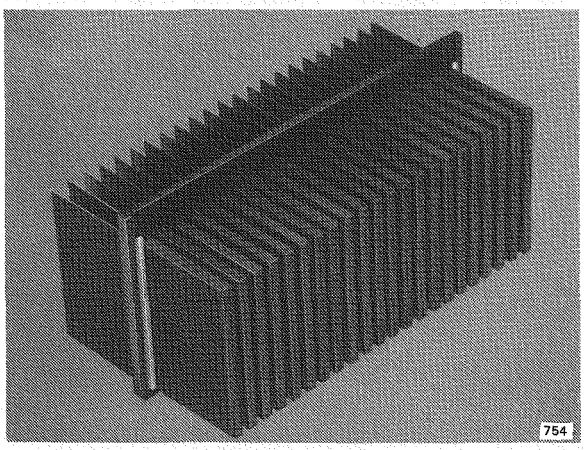

Figure 15-1. Phase I comb assembly showing porous-graphite chlorine-electrode pairs (foreground) and dense-graphite zinc electrodes (background) press-fitted into dense-graphite bipolar bus.

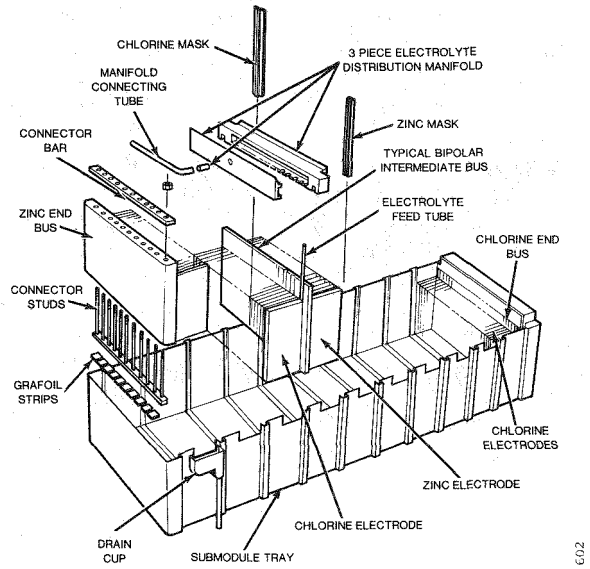

Figure 15-2. The Phase I submodule.

operation, but also under more varied conditions as well. Using a pump, the electrolyte was circulated over a heat exchanger and through a filter enroute to the unit-cell manifolding which distributed electrolyte to the cells of the submodule. The temperature of the electrolyte was maintained within $\pm$ 2°C in the range of 10 to 65°C by means of two constant-temperature glycol baths. The pressure of chlorine in the battery stack was controlled by the gas pump. With this pump, the absolute pressure could be reduced to 4 psia. Chlorine evolved during charge was vented through the exit port of the gas pump into the hood exhaust. Chlorine required for discharge was supplied by cylinder chlorine injected into the high-pressure side of the electrolyte pump. Voltage probes made of titanium were fitted into the bipolar buses in the submodule to allow monitoring of individual cell voltages with digital voltmeters and strip-chart recorders. Other instrumentation included a watt-hour meter for determining electro-chemical energy efficiency, and an ampere-minute counter for determining coulombic efficiency.

SUBMODULE TESTING

Initial Testing

Initial testing of the Phase I sub-modules early in Phase II of RP226-3 confirmed the existence of large coulombic imbalances between unit-cells as shown in Figure 15-4. Testing also showed that the degree of unit-cell imbalance was dependent upon the conductivity of the electrolyte. With the more conductive electrolytes, this imbalance could be as large as 30%. The effect is apparent in Table 15-1 which presents a comparison of unit-cell coulombic efficiencies for high- and low-conductivity electro-lytes. The use of more highly con-ductive electrolytes resulted in another unpredicted phenomenon, i.e., consecutive cycles produced progress-ively lower coulombic efficiencies as illustrated in Figure 15-5.

It is worthy to note, however, that the performance of some unit cells approxi-mated that demonstrated in the small zinc-chloride test cell i.e., approxi-mately 80% round-trip coulombic efficiency. This indicated that the perform-ance target set for the module was reasonable. Extending the coulombic performance of good cells to all the

Table 15-1

COULOMBIC EFFICIENCY FOR UNIT CELLS WITH TWO DIFFERENT ELECTROLYTES

UNIT CELL NO.	COULOMBIC EFFICIENCY, % High-Conductivity Electrolyte 30°C	40°C	Low-Conductivity Electrolyte 30°C	40°C
1	74.7	67.2	74.4	75.0
2	66.8	27.7	67.3	54.8
3	29.2	24.8	70.2	66.3
4	61.1	46.9	73.5	71.5
5	63.6	27.1	73.6	72.2
6	62.8	23.2	72.8	70.6
7	69.6	38.2	71.6	71.8
8	57.1	25.8	72.4	72.3
9	69.8	50.5	74.1	72.5
10	72.2	42.2	76.2	73.0
Average	62.6	37.4	72.6	70.0

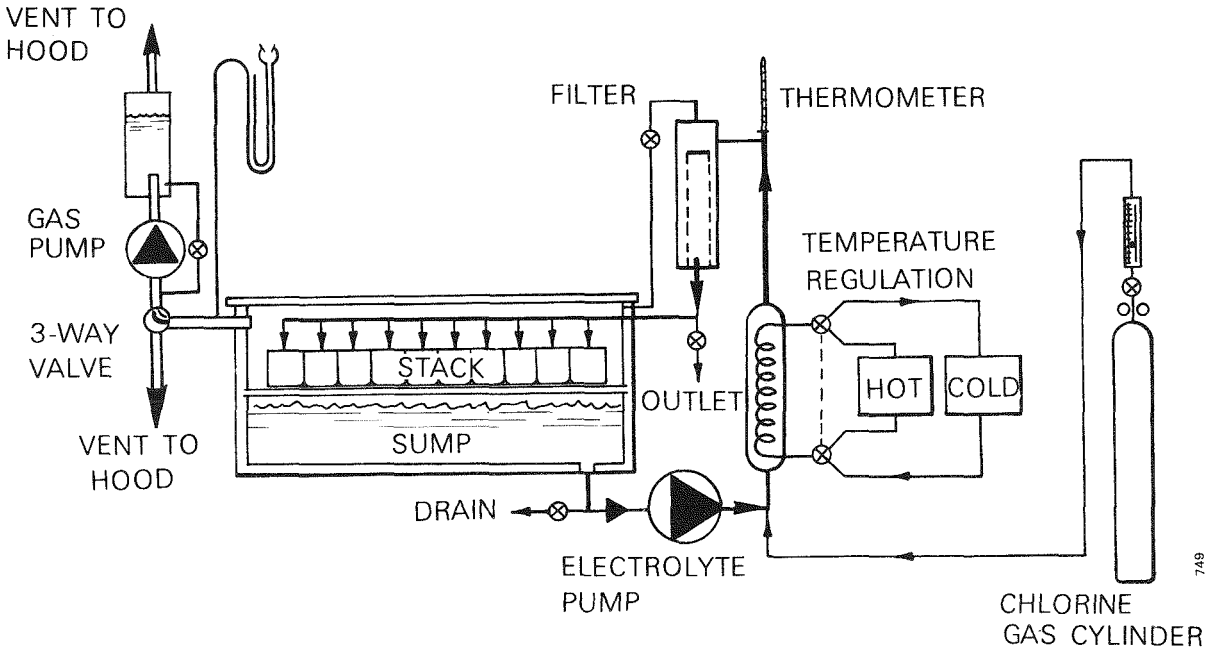

Figure 15-3. Schematic of test stand for Phase I submodule.

cells of the submodule would result in an electrochemical energy efficiency greater than the targeted 63%, when combined with the typical voltaic performance.

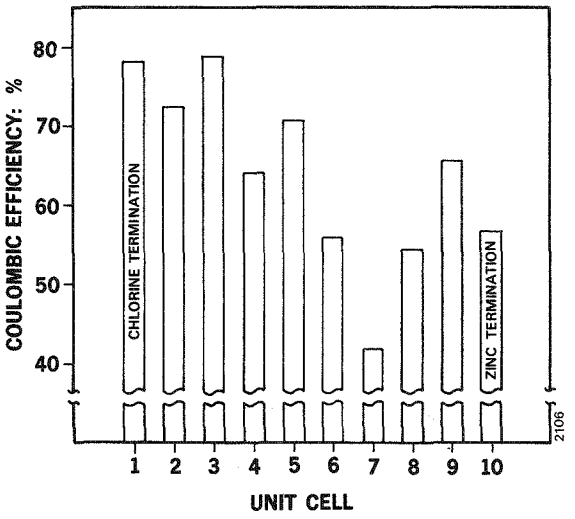

Figure 15-4. Unit-cell coulombic-efficiency imbalance in a typical Phase I submodule.

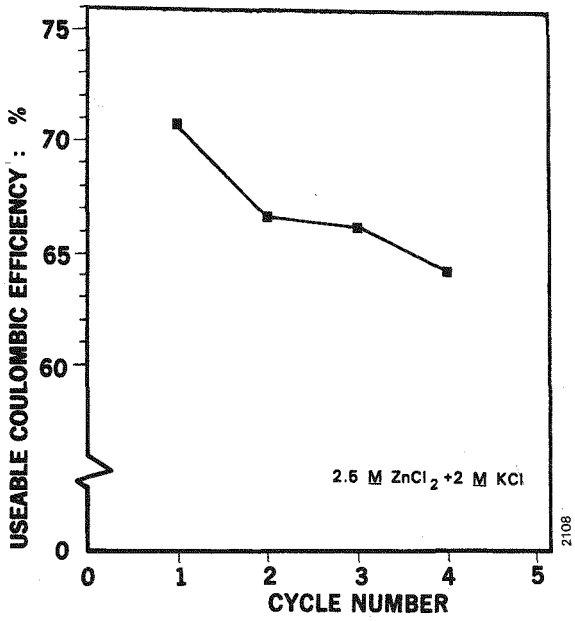

Figure 15-5. Effect of cycling on submodule coulombic efficiency.

Submodule testing during Phase I had demonstrated the fact that these large coulombic efficiency imbalances between adjacent unit cells occurred during charge. The submodule test system was instrumented with a mass flowmeter to continuously monitor the rate of chlorine evolution throughout the charge cycle. Not only did this technique prove to be an accurate device for measuring charge efficiencies, it also proved to be a very sensitive device for detecting dendrites and zinc growths.

Of particular interest was the magnitude of the chlorine-evolution excursions which occurred during these experiments. As illustrated in Figure 15-6, reduction in the chlorine evolution rate was greater than 30% in some instances. Excursions of this magnitude suggest self-discharge of unit-cells, in addition to complete current bypass via dendritic shorts. Alternative explanations are possible, however, based on multiple zinc growth accumulations throughout the submodule.

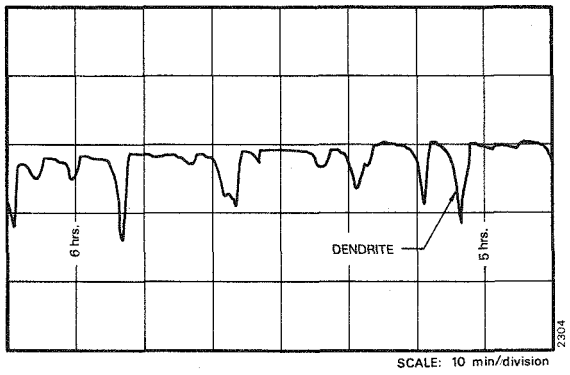

Figure 15-6. Chlorine evolution during charge showing excursions suggesting self-discharge of unit-cells as well as complete current bypass via dendrite shorts.

Bipolar Comb Testing

As potential problems associated with individual combs were indicated, a two-cell test unit, illustrated in Figure 15-7, was designed and built for evaluation of individual combs. The per-

formance demonstrated by cycle testing this two-cell unit was much the same as that observed during submodule testing. Coulombic efficiency of the series-connected cells was initially uniform but became unbalanced with additional cycling just as with the submodule. Disassembly and inspection led to the discovery of zinc growth accumulations between the bus-to-case seal and on the outer faces of the end zinc electrodes at the edge adjacent to the opposing chlorine bus. A photograph of these zinc growths is included as Figure 15-8. Subsequent examination of submodules confirmed similar formation and accumulation of zinc growths at the same locations.

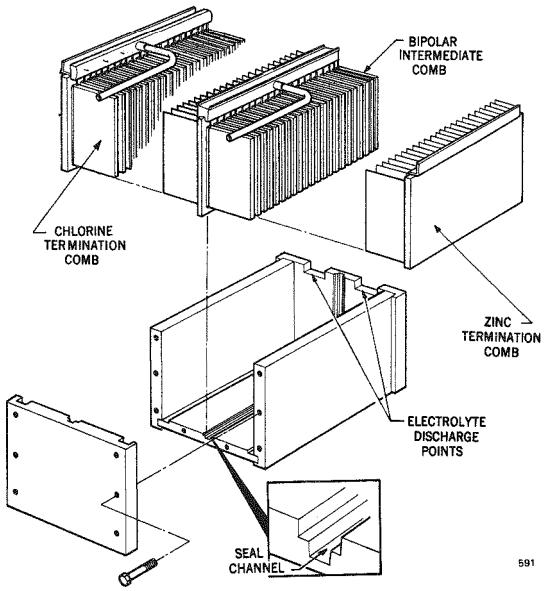

Figure 15-7. Test assembly for evaluation of individual bipolar combs. Note that provision is made for sealing the bipolar comb into the battery case.

Although discovery of the zinc growths offered at least a partial explanation for cell imbalance and loss of coulombic efficiency, there was no practical way to quantify the effect of these growths. Self-discharge of the intermediate bipolar-comb assembly due to electrolyte continuity either through or around the bipolar bus remained as a possible cause of cell imbalance. Therefore, the four-volt test unit was modified as shown in Figure 15-9 to determine the effects of intercell electrolyte continuity. Intercell resistance measurements were made with a Kynar plate serving as the intermediate bus, first with a "near perfect" Teflon seal and then with a 0.08-inch gap at the bottom. Then a used, wetted graphite bipolar bus with electrodes removed, was substituted for the Kynar plate and sealed in place. These resistance measurements were followed by leakage current measurements made by short-circuiting a plated zinc termination bus to a chlorine bus through a shunt as shown in Figure 15-9. The intermediate bus arrangement duplicated the conditions desribed above for the resistance measurements. A summary of the values obtained from these resistance and current measurements with a typical electrolyte is presented in Table 15-2. As the applied current during charge or discharge is 90A, these results showed that the magnitude of self-discharge losses attributable to the intercell electrolyte continuity in the Phase I submodule could not account for the large coulombic-efficiency imbalances observed.

Table 15-2

MAGNITUDE OF SELF-DISCHARGE ATTRIBUTABLE TO INTERCELL CONTINUITY

Inter-Cell Seal	Resistance (Ω)	Current (A)
Kynar plate	135	0.015
Graphite bus	5	0.4
Kynar Plate + 0.080 in. gap	2	1.0

Finally, poorly performing cells from a submodule were tested in this two-cell test unit to assess the hypothesis that cell imbalance could be due simply to defective comb assemblies. When evaluated in this manner, "bad combs" demonstrated performances equivalent to the good combs. Therefore, the "bad comb" hypothesis was ruled out as a major contributor to unit-cell imbalance.

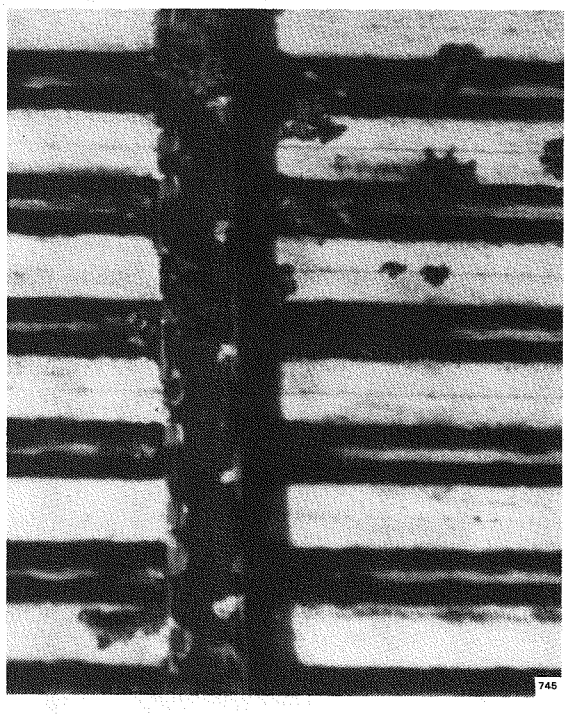

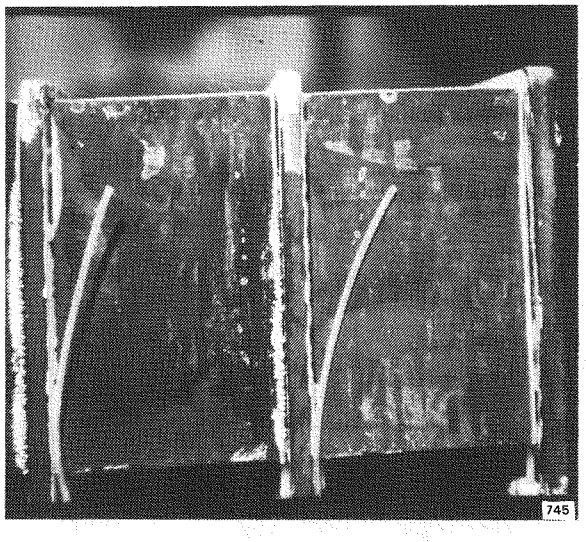

Figure 15-8. Zinc-growths from shorting paths. Growths form in two regions: a) the bus/case groove, and b) the outer faces of the termination zinc substrates.

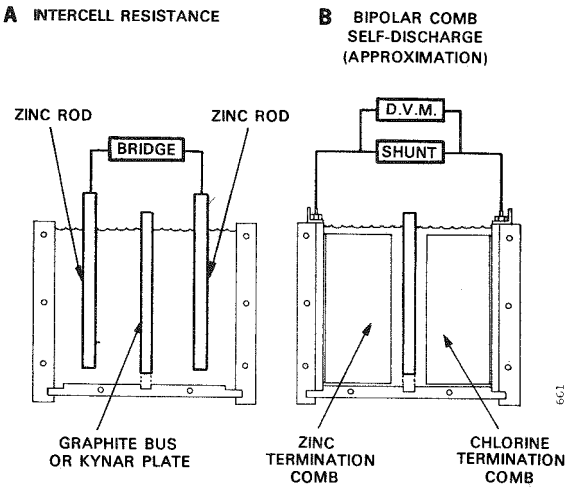

Figure 15-9. Test assemblies employed in evaluating the effect of inter-cell continuity in the Phase I design: a) ac/dc resistance measurements and b) method of approximating bipolar-comb self-discharge.

QUALIFICATION OF SUBMODULES

The last task of this test program was to qualify six submodules of the Phase I design for use in the refurbished module. The submodules were modified to arrange for a flow of chlorinated electrolyte to prevent or minimize accumulation of zinc growths. Testing of the modified submodules produced the efficiency data presented in Figure 15-10, and the delivered-energy data shown in Figure 15-11. Five of the submodules exhibited quite consistent results with coulombic efficiencies ranging from 69.2 to 72.8%, electro-chemical energy efficiencies from 59.4 to 62.4%, and delivered energy from 7.75 to 8.16 kWh. The exceptional performance of submodule no. 1 can be attributed to better sealing between the case and the inter-cell buses. In general, the performance of all six submodules represented a marked improvement. For comparison purposes, typical submodule performance characteristics before and after refurbish-

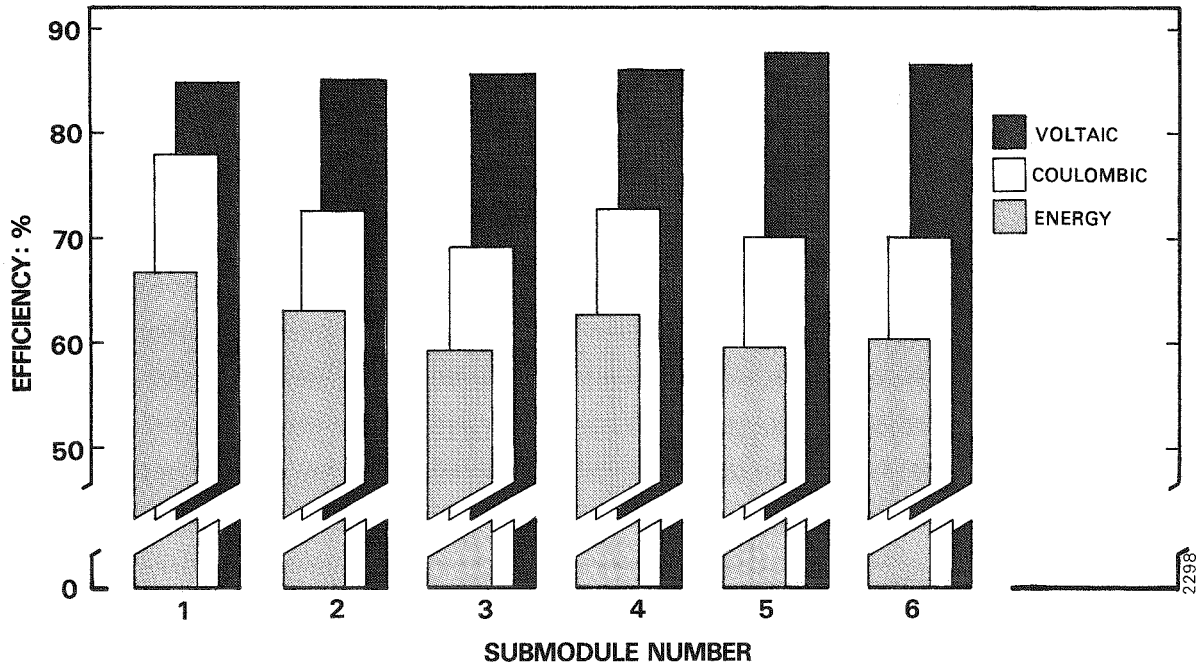

Figure 15-10. Efficiency data for Phase I submodules after modification to prevent zinc growths.

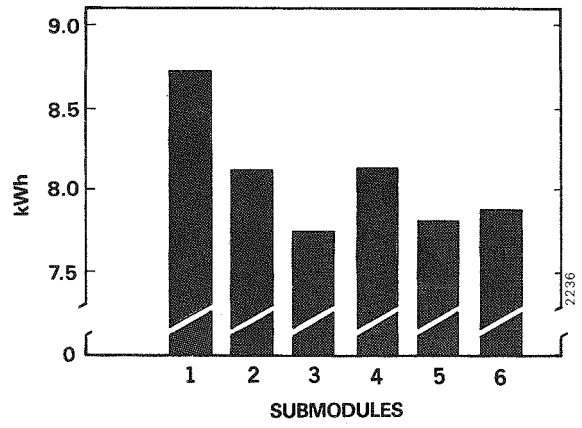

Figure 15-11. Delivered energy data for Phase I submodules after modification.

ment are presented in Figure 15-12. These data indicate that although the formation of these zinc growths was not completely eliminated, they were present to a lesser extent. Of probably greater significance is the fact that they no longer accumulated to cause a deterioration in performance as additional cycles were taken. This indicated that improved cleanup between cycles had been accomplished.

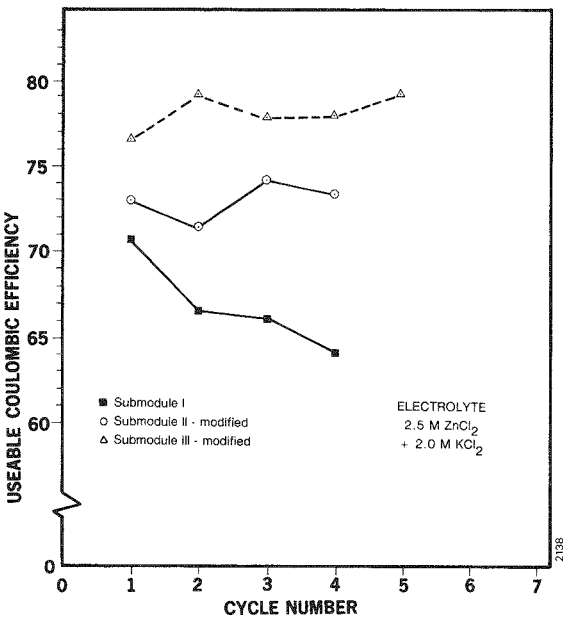

Figure 15-12. Effect of modification on cycle-test data for Phase I submodules.

REFERENCES

1. Development of the Zinc-Chloride Battery for Utility Applications. Palo Alto, Calif.: Electric Power Research Institute, April 1979. EM-1051.

Section 16

REFURBISHING AND TESTING OF THE 45-kWh MODULE

ABSTRACT

A program conducted in 1978-79 to upgrade the delivered energy and to improve the electrochemical energy efficiency of the 45-kWh module led to a significant improvement in performance. During initial testing, the electrochemical energy efficiency of the module averaged 48.4% -- well below the 63% targeted. Major contributors to the poor performance were found to be: (1) zinc growths under and around intercell graphite buses short circuiting the normal flow of current in the battery stack, and (2) low stack vacuum which resulted in a higher concentration of dissolved chlorine in the electrolyte, and consequently decreased coulombic efficiency. Refurbishment of the module, involving reconfiguration of components and modifications to the battery stack, upgraded performance to delivery of 50 kWh at 60% electrochemical energy efficiency, on the average. The maximum delivered energy was 53.6, and the maximum electrochemical energy efficiency observed was 60.3%.

INTRODUCTION

The 45-kWh battery module built and tested during Phase I of RP226-3 met the 45-kWh delivered energy goal and exhibited good operational characteristics, including repeatability of performance over consecutive charge/discharge cycles. However, the average electrochemical energy efficiency, at 48.4%, was significantly lower than the expected 63%(1).

To improve the module efficiency and to upgrade the delivered energy to 50 kWh -- a basic design point for Mark 4 battery modules -- a module-refurbishing program was initiated in Phase II. Apart from the 50-kWh delivered energy goal, the electrochemical energy efficiency target for this program was set at 63%. This refurbishing program was carried out under the following subprograms:

- Submodule Improvement: To modify the six individual submodules such that 8.3 kWh could be delivered from each submodule at a 63%+ electrochemical energy efficiency.
- Module Configuration: To increase the capacity of the battery system from 45 kWh to 50 kWh and to minimize heat transfer between stack and store compartments.
- Module Test: To evaluate performance of the refurbished module.

SUBMODULE IMPROVEMENT

Single-cell development programs led to the development of high-conductivity electrolytes for maximum efficiency in load-leveling battery applications. Use of these electrolytes in the Phase I submodules, however, led to a loss in efficiency due to shorting caused by zinc growths within and, to some extent, between cells. This efficiency problem was not evident when lower-conductivity electrolyte, zinc chloride with a lesser amount of supporting electrolyte, was used for the initial qualification of the submodules. As part of

the refurbishing program, an effort was made to make the submodules more tolerant to the more conductive electrolytes. To deactivate all exposed graphite areas other than the actual working surfaces, the top and bottom edges of the chlorine electrodes and the bus areas between the electrodes were coated with Boltaron PVC. Masking and the technique for installing it were redesigned to further reduce the potential for development of zinc growths in poorly masked areas.

The original method of making electrical contact between the graphite end buses in the 10-cell submodules and the titanium current collectors proved unreliable from a voltage drop and repeatability standpoint. This terminal design involved a through-bolt and clamp-down type connection. As part of the refurbishing operation, the terminal arrangement was changed from a clamped connection to a connection similar to that used between the graphite buses and electrodes, i.e., an interference-type connection. Using this press-contact technique, the voltage drop at the terminal was reduced to 20 mV at the design current of 100 amperes.

Following these modifications, the submodules were subjected to qualification testing. This testing showed that while the performance had certainly improved on the initial cycle, consecutive cycles resulted in a progressive decrease in efficiency, as shown in Figure 16-1.

This observation led to initiation of submodule studies, reported upon in Section 15 of this report, which ultimately identified the problem of zinc growth activity underneath the buses and at the extreme outside edges of the submodules. Because these areas were in stagnant electrolyte zones, it appeared likely that these growths had accumulated from cycle to cycle. Methods devised to create electrolyte flow in these stagnant zones were quite effective. Retesting of the submodules showed that these changes had significantly improved efficiency and had eliminated the progressive loss in performance from cycle to cycle. The average performance of the six submodules was 8.07-kWh delivered energy, 72.2% coulombic efficiency, and 86.2% voltaic efficiency. The resulting 61.8% electrochemical energy efficiency was just 1.2% short of the target. These results should be contrasted with the 61.6% coulombic and 53% electrochemical energy efficiency results for the submodules before refurbishing.

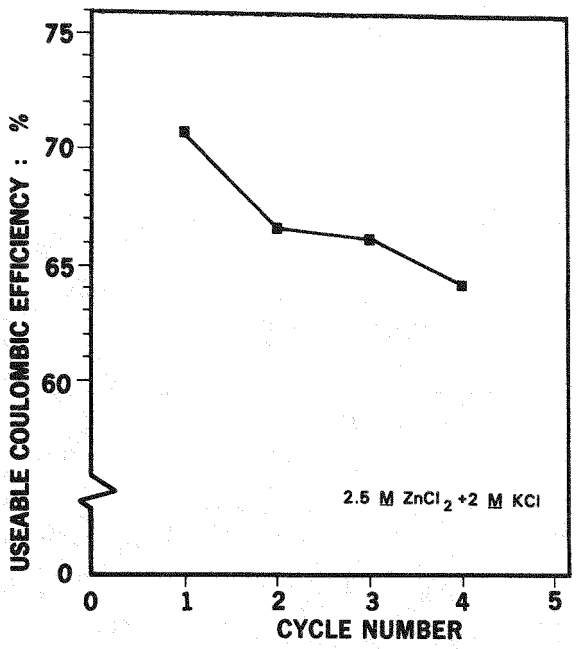

Figure 16-1. Effect of consecutive cycling on submodule coulombic efficiency.

MODULE RECONFIGURATION

A major task in refurbishing the 45-kWh module was to relocate the electrolyte sump compartment. In the original design, the sump sat within the confines of the store. Because of the Kynar construction, insulation of this sump proved difficult and a significant heat transfer between stack and store occurred through the sump walls during battery operation. This caused additional hydrate decomposition, and the chlorine evolved resulted in a higher than anticipated load on the gas/hy-

drate-former pump. To correct this problem, an additional section was added to the case to locate the sump above the store where it is thermally isolated from the store compartment by a chlorine gas space. The original testing had also shown that the hydrate storage volume within the store was limited to the 45-kWh level. To give a measure of over-capacity for this development battery, the store volume was increased to hold 440 liters of water as opposed to the 268 liters in the original design. In conjunction with increasing the capacity of the store, the filter area within the store was more than doubled. The reconfigured battery case, compared to the original case, is shown in Figure 16-2.

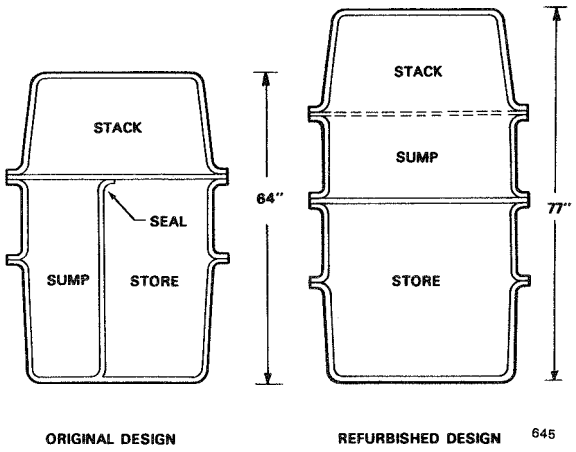

Figure 16-2. Comparison of original and refurbished cases.

Other changes involved the main electrolyte manifold, the fluorescent-light hydrogen-chlorine reactor, and the busing to the external terminals. The main electrolyte manifold was changed from an end-feed method to a center-feed method to give better flow distribution. The hydrogen-chlorine reactor light was changed from an enclosed unit within the gas flow system to a convective arrangement. In this arrangement, the light is simply located in the gas space within the stack compartment. This change was made to return hydrogen chloride back to the electrolyte and not to the store. In addition, this ensured hydrogen recombination when the battery was in a stand mode and the gas pump was not operating. The busing connecting the submodules to the external terminals was changed by greatly increasing the mass of titanium to lower the resistance. These changes, and the relocation of the sump are illustrated by Figures 16-3 and 16-4, exploded views of the module before and after refurbishment.

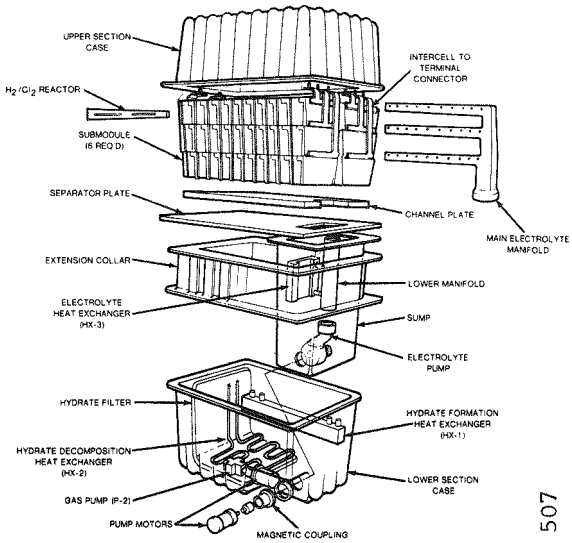

Figure 16-3. Original configuration of the 45-kWh module. Note location of sump in store compartment, end-feed manifold and strip busing for submodule connections.

TESTING OF THE REFURBISHED MODULE

As of April 6, 1979, a total of 31 cycles had been accumulated on the module. Apart from the first cycle, which was a cleaning cycle for which zinc-chloride solution was used as the electrolyte, an electrolyte of zinc chloride, potassium chloride, and a proprietary leveling agent at a pH of 0.1 was used for all module testing. This electrolyte was not changed throughout the cycling. Cycles 1 through 26 were taken to optimize operational conditions, maximize charge vacuum, and fully define the control sequence. This done, five consecutive cycles at greater than 50-kWh delivered

energy were run on the battery. These cycles demonstrated stability of performance and showed the extent to which the overall performance of the battery had been improved over the original design. The results of this five-cycle test are compared in Table 16-1 to the average performance before refurbishing.

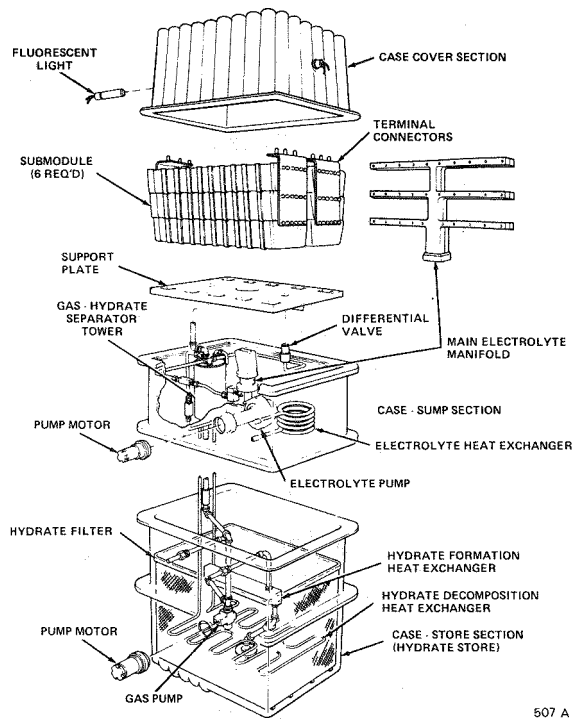

Figure 16-4. Refurbished 45-kWh module. Note relocation of the sump above the store, center-feed manifold and heavier busing for submodule connections.

The significant values in these results were the increase in average delivered energy from 43.2 to 51.6 kWh (53 kWh delivered on the last cycle), the improvement in electrochemical energy efficiency from 48.4% to 57.2%, and the coulombic efficiency improvement from 58.7% usable to 70.8% usable. The only apparent loss in performance was in voltaic efficiency -- 80.6% for the refurbished module, compared to 82.4% for the original module. This did not, however, represent a real loss in voltaic efficiency, but reflected the fact that after refurbishing, terminal voltages were used for all voltage readings. In the original module, because of the high contact resistances between the graphite buses and titanium connectors, probe voltages rather than terminal voltages were used to compute the voltaic efficiency.

Although these results demonstrated a significant improvement in module performance, further improvement was sought. The gas/hydrate-former pump was overhauled in an attempt to achieve a higher stack vacuum, and heavier section titanium busing was installed to interconnect the submodules. This done, the goal was set to demonstrate consistent delivery of 50 kWh at 60% electrochemical energy efficiency. The average results for nine consecutive cycles are compared with the earlier five-cycle test results in Table 16-2.

For practical purposes, the goal of consistent delivery of 50 kWh at 60% electrochemical energy efficiency had been met. During testing of the refurbished module, the maximum energy delivered was 53.6 kWh, and the maximum electrochemical energy efficiency observed was 60.3%.

DISCUSSION

A significant improvement in module performance was realized through the refurbishing program. One program goal, consistent delivery of 50 kWh, was reached; and the coulombic and electrochemical energy efficiencies of 71.2% and 59.4%, respectively, approached the 73% and 63% goals set for the refurbishing program. The higher capacity (53.6 kWh) and higher electrochemical energy efficiency (60.3%) observed for individual cycles suggest that the criteria set for modules to be tested at the BEST Facility -- 52.3 kWh at 65% electrochemical energy efficiency -- can be satisfied.

A major reason for the 1.8% shortfall in coulombic efficiency was the inability of the gas/hydrate-former pump to

Table 16-1

45-kWh MODULE PERFORMANCE BEFORE AND AFTER REFURBISHMENT

Module Parameter	10-Cycle Average Before Refurbishing	5-Cycle Average After Refurbishing
Current density, mA/cm^2		
Charge	30.0	32.8
Discharge	33.0	32.8
Stack pressure, psig		
Charge	-0.60	-1.65
Discharge	--	-3.80
Coulombic efficiency, %		
Full power	53.9	65.5
Usable	58.7	70.8
Voltaic efficiency, %	82.4	80.6
Energy efficiency, %	48.4	57.2
Usable energy delivered, kWh	43.2	51.6

reach the stack pressure design value of -5 psig. Because of this, more chlorine remained dissolved in the electrolyte and the resulting zinc corrosion reduced the coulombic efficiency. Success in programs underway to increase the capacity of this pump should result in higher stack vacuum and higher coulombic efficiency.

From an operational standpoint, only one element of battery operation showed excessive sensitivity and that was the hydrate formation system involving the gas/hydrate-former pump, the hydrate-formation heat exchanger and the hydrate discharge coil. Minor fluctuations in glycol temperature or store pressure resulted in heat exchanger freeze-up. This required very careful control of glycol temperature and store pressure. The operation of the hydrate formation heat exchanger had to be made more forgiving if multi-module battery systems were to be operated successfully. Programs to accomplish this were initiated.

Table 16-2

45-kWh MODULE PERFORMANCE BEFORE AND AFTER GAS-PUMP OVERHAUL AND BUSING IMPROVEMENT

	Before	After
Stack pressure in charge, psig	-1.7	-3.5
Coulombic efficiency, %	70.8	71.2
Voltaic efficiency, %	80.6	83.4
Energy efficiency, %	57.2	59.4
Delivered energy, kWh	51.6	50.0

Hydrogen levels during all phases of battery operation stayed very low indicating success with the convective flow fluorescent light arrangement. However, carbon dioxide levels did accumulate to the 1% level within the gas space suggesting that an inerts-rejection device may be needed.

The 45-kWh module refurbishment program was productive toward advancing the zinc-chloride battery technology. Beyond increasing the delivered energy from 43 to 50 kWh and the electrochemical energy efficiency from 48% to 60%, the program resulted in development of new assembly techniques and increased understanding of operational details.

REFERENCE

1. Development of the Zinc-Chlorine Battery for Utility Applications. Palo Alto, Calif.: Electric Power Research Institute, April 1979. EM-1051.

Section 17

COMPUTER MODELING OF MODULE OPERATION

ABSTRACT

A computer program was written to simulate the behavior of a zinc-chloride battery module, the basic element of a load-leveling battery plant. The methodology used to develop the computer model is discussed, and the method of verifying the model is presented. Comparison of data from simulated operation with data obtained during operation of the 45-kWh battery module has verified that the accuracy of the computer model is at least 95%. The computer model is a timesaving tool for predicting the effects of proposed design changes and for optimizing the design and performance of the battery module.

INTRODUCTION

Although there is no substitute for actual testing of battery modules, computer simulation of battery behavior often can be used to expedite developmental efforts. A computer model of the battery can be used to evaluate proposed design changes and to optimize design and performance. Such a computer model based upon the operation of the 45-kWh module has been developed. An overview of the construction of this computer model and its operation is given in this section along with the results of verifying simulated operation against actual performance of the 45-kWh module.

Although this discussion of the model is not heavily dependent upon knowledge of the battery operation, a brief review will be presented. A more detailed discussion is found in Section 3. The module is represented schematically in Figure 17-1.

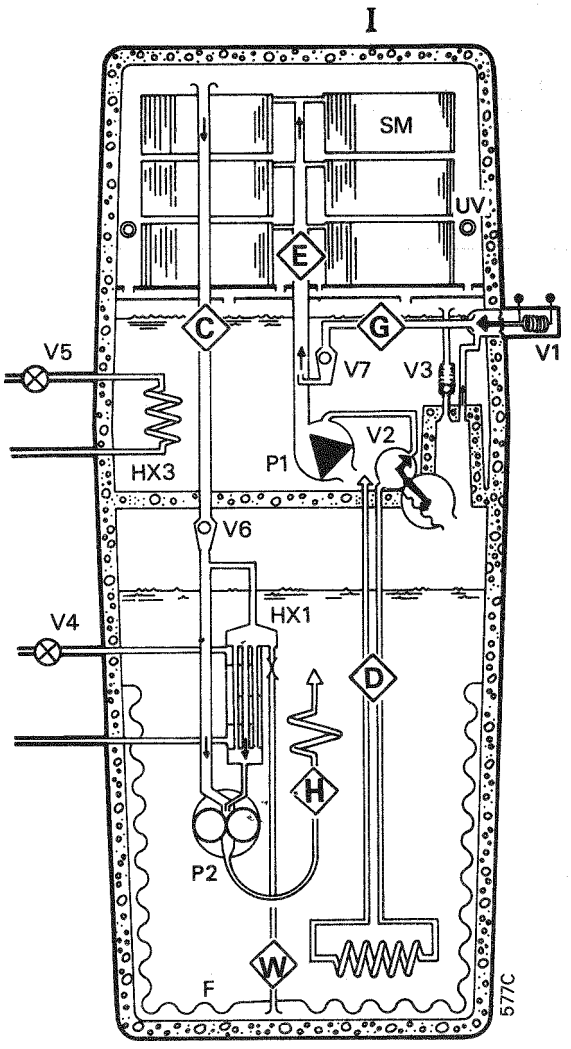

Figure 17-1. Load-leveling module schematic.

During charge, current is driven through the six battery submodules. Within a submodule SM, aqueous zinc chloride solution (electrolyte) is elec-

trolyzed with zinc being plated on the negative electrodes and chlorine gas evolved on the positive electrodes. The chlorine gas is pumped to the store through flow line C by pump P2 which also pumps water from the store up flow line W and through heat exchanger HX1 where it is chilled. The chlorine gas and chilled water are mixed as they flow into line H forming chlorine hydrate. The hydrate leaves line H and settles into the store water. Before the water enters line W the hydrate is separated out by a filter F. In the submodule, the zinc chloride removed during the charging process is replenished using pump P1 to move electrolyte from the sump area through flow line E to the submodule. Heat exchanger HX3 is used to control the temperature of the electrolyte both during charge and discharge.

During discharge, current is delivered by the electrochemical reaction of zinc metal and dissolved chlorine to form zinc chloride. The process of supplying chlorine for this reaction is as follows: (a) warm electrolyte is pumped through heat exchanger HX2 via flow line D when pressure controlled valve V2 is open (the condition for this valve being open is that the store pressure is lower than a certain set point), (b) the heat from HX2 causes hydrate to disassociate releasing chlorine gas, and (c) the chlorine gas flows through solenoid valve V1 (which is open during discharge and closed during charge), through flow line G and E on its way to the submodules.

As the operation of the module is very dependent on fluid flow, several valves are required. Valves V6 and V7 are check valves used to eliminate back flow. Valve V3 is a relief valve which opens when the difference between store and stack pressure is too great. Valves V4 and V5 control the flow of external coolant to the heat exchangers. During battery operation a small amount of hydrogen is evolved. An ultraviolet (UV) lamp (identified by the pair of concentric circles in Figure 17-1) causes the hydrogen to combine with chlorine gas to form HCl. Lastly, the entire battery is enclosed in a thermally and electrically insulated case I.

MODEL CONSTRUCTION

To develop the computer model of the battery, it was first necessary to gain a detailed understanding of the operation of the battery and to develop quantitative expressions for the physical processes involved. A time iterative approach was used for the modeling. The state of the battery is defined at time t_o by initializing a set of variables (state variables) including pressures, temperatures, moles of chlorine, and many others. The first iteration of the program calculates the values of the state variables at a time $t_1 = t_o + \Delta t$ using equations that depend on the state variables at time t_o. For the second iteration, the values of the state variables at a time $t_2 = t_1 + \Delta t$ are calculated using the state variables at time t_1, and so on. This iterative approach is illustrated by Table 17-1 where the arrow indicates the flow of calculated data from iteration to iteration.

The following equation for the store pressure (P2) is an example of one of the calculations made during an iteration.

$$P2_i = (MCL2_{i-1} - LMCL2_{i-1}) \cdot R \cdot (T2_{i-1} + 273)/VOL2_{i-1}$$

Here, using the ideal gas law, the pressure of the store on the i-th iteration $P2_i$ is given as a function of state variables calculated during the i-1th iteration. These variables are chlorine gas in the store area MCL2, moles of chlorine gas in the store liquid, LMCL2, the temperature of the store, T2, the volume of the store gas space, VOL2, and the ideal gas constant, R.

Table 17-1

TIME ITERATIVE APPROACH TO MODELING

	INITIAL STATE AT START	FIRST ITERATION	i-TH ITERATION
TIME	$t_o = 0$	$t_1 = t_o + \Delta t$	$t_i = t_{i-1} + \Delta t$
STATE VARIABLES	P_o	P_1	P_i
	T_o	T_1	Ti_i
	VOL_o	VOL_1	VOL_i
	MCL_o	MCL_1	MCL_i
	$MHYD_o$	$MHYD_1$	$MHYD_i$
	ETC.	ETC.	ETC.

To understand how the calculations made during an iteration of the program relate to what is happening in a battery module, it is illustrative to examine the flow processes in the battery. Figure 17-2 shows the flow pattern of chlorine in a module. In the stack area, chlorine gas is released from the submodules during charge and reacted during discharge as represented by double arrow A; gas pumped from the stack area to the store area is represented by arrow B; while arrows C and D represent gas transferred from the store to the stack through relief valve V3 and solenoid valve V1, respectively. Arrows E through I are concerned with hydrate processes. The amount of hydrate formed when mixing chilled water I from the store and chlorine gas B from the stack is represented by E. The gas above the store liquid changing to hydrate and vice versa is shown by F. The amount of hydrate disassociated due to external heating is G and due to heating from heat exchanger HX2 is H. By keeping track of changes in the amount of chlorine in the stack and store, the change in pressure in both these regions can be calculated from iteration to iteration.

The heat flow into both the stack and store is shown in Figure 17-3. Heat enters the stack area from electrochemical processes A and from outside the case C. Removal of heat B and D is via heat exchangers HX3 and HX2, respectively. In the store, heat is created due to hydrate formation F and enters from outside the case G as well as via heat exchanger HX2 as represented by arrow D. Arrow E represents the heat extracted by heat exchanger HX1. From the net heat flow during an iteration, the temperature change in both the stack and store can be calculated. Many other processes are also included in the model.

The success of this modeling approach depends on how accurately the equations used to calculate the state variables during an iteration reflect the true behavior of a battery module. Two

inherent problems limit the accuracy of this approach: (1) round-off errors, and (2) the inaccuracies associated with calculations of a continuous process using finite time increments. There is a round-off error associated with every computer calculation, and after many iterations of the program, the cumulative error can become large. Use of double-precision calculations will reduce the error but the present program has modeled the battery accurately without the use of double precision. The time-iterative approach approximates a continuous process by calculating the value of a variable at time t_i using the value of the state variables at time $t_i-\Delta t$ rather than at time t_i. If the state variables have changed significantly between $t_i-\Delta t$ and t_i, there will be a significant error in the calculation. Although this error can be reduced by making Δt smaller, decreasing Δt will increase the number of calculations needed to simulate a given time period of battery operation and thus will increase the round-off error.

The structure of the program is shown in Figure 17-4. The vertical column of boxes on the left shows the flow of

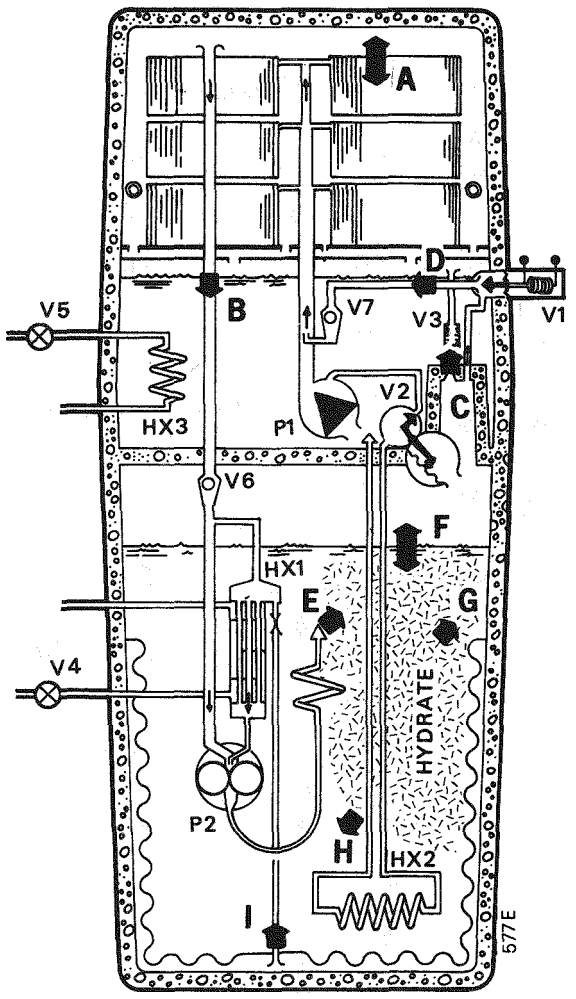

Figure 17-2. Chlorine gas, chlorine hydrate, and water mass flow in a module during battery operation.

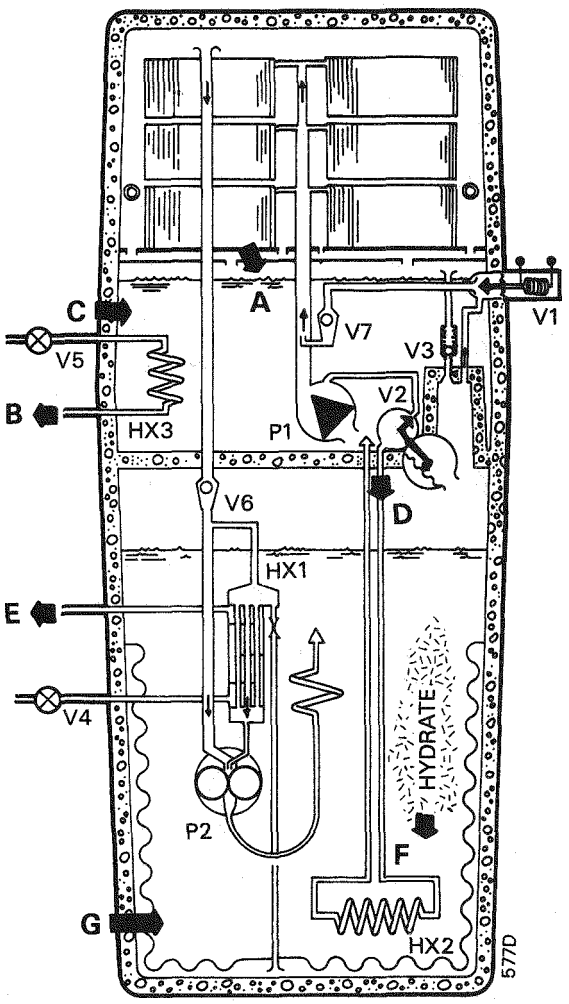

Figure 17-3. Heat flows in a module during battery operation.

calculations in the main section of the simulation program. The vertical column of boxes on the right shows the subroutines that are called by the main program.

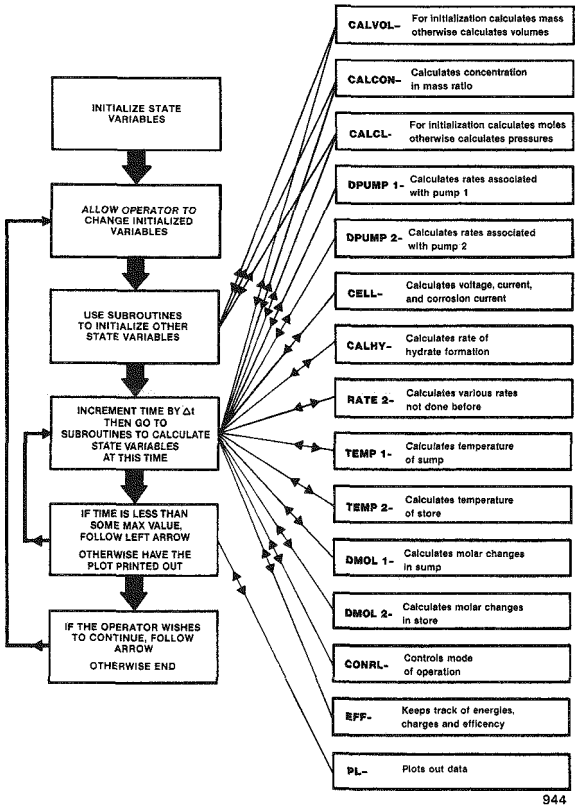

Figure 17-4. Flow diagram of simulation program.

The sequence of execution for the main program is as follows. First, over a hundred variables are given an initial predetermined value. These variables define the initial state of the battery, the mode of control for the battery, and the time variables associated with the modeling. The operator of the program is then allowed to change any of these variables to test the effect of the changes. The program then takes the initial variables and calculates additional state variables by calling the subroutines CALVOL, CALCON, and CALCL. Now the iteration process begins. Each iteration requires the sequence of subroutines shown in Figure 17-4 to be called so that the value of all the state variables will be calculated. The first sequence of iterations is completed when the desired time period of battery operation has been simulated. During the iteration process, selected state variables are recorded as a function of time. A plot of some of these variables is printed out after the iteration process is completed. Finally, the operator is given the option of continuing the program or ending the run. If the program is continued, iteration will begin using the values of the state variables at the end of the first sequence of iterations, unless the operator chooses to change the value of any of these variables.

MODEL VERIFICATION

The purpose of the computer model is to accurately simulate the performance of an actual zinc-chloride battery module. To verify the model, its output was compared to data taken from a test run of the 45-kWh module.

At the time the comparison was made, the 45-kWh module was the only module in operation designed for load-leveling applications. The major difference between a simulated run by the model and an actual run of the 45-kWh module is the way the flow of fluid in the heat exchangers HX2 and HX3 is controlled. The model assumes that the flow in HX2 is controlled by the pressure in the store, whereas in actual operation of the module, the valve is manually controlled. For HX3, the model assumes the flow to be constant but in actual operation it is varied manually.

Comparisons between the output of the model and actual data from the module should, to first order, provide a good basis for verification of the model. Since it is impossible to program the human factor involved in the actual operation of the battery, differences

will exist between the actual data and the output of the model. The verification process started by determining as accurately as possible the initial parameters needed in the model to represent the battery module. Then, the results of a computer run using those parameters were compared with data from an actual battery run.

For comparison, run #33 of the 45-kWh module was selected as representative. During this run, made on May 2, 1979, the battery was charged to full capacity and delivered 53-kWh of electrical energy during discharge. The output of the simulation run, shown in Figure 17-5, is a plot that shows the value of selected variables as a function of time. In the plot, time increases in the down direction and the value of the variables increases going to the right. As the plot takes several minutes to type out, many variables were shown on one plot rather than having a separate plot for each variable. In the plot, P stands for the stack pressure; 2 stands for the store pressure; T stands for the stack temperature; @ stands for the store temperature; V stands for the battery voltage; and H stands for the moles of hydrate. The plot with a time scale of sec x 10^4 shows 50,000 seconds of battery running time. Besides the plot, the output includes a table of electrical charges, energies, and efficiencies associated with the battery's simulated performance. These values were transferred from the bottom of Figure 17-5 to Table 17-2 for comparison with results from the actual module run. The comparison shows a match which is significantly better than 95%.

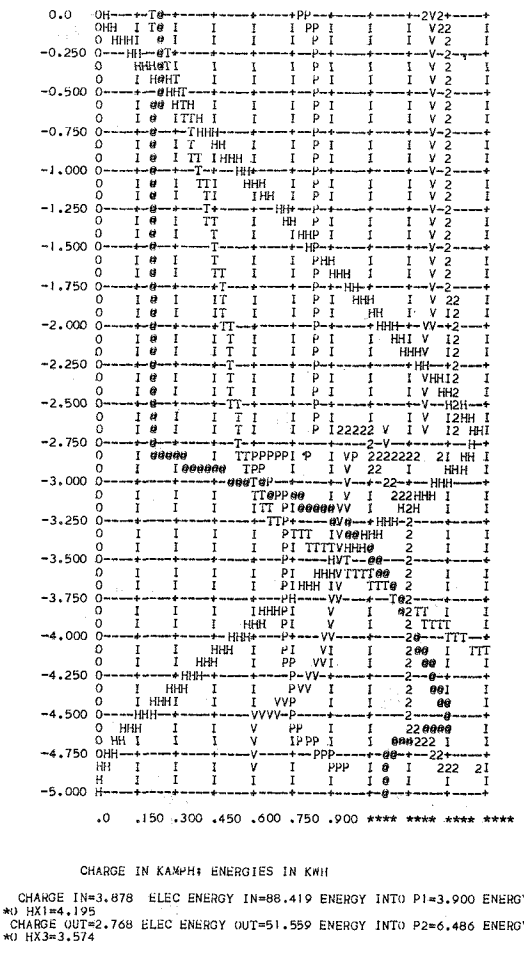

CHARGE IN KAMPH; ENERGIES IN KWH

CHARGE IN=3.878 ELEC ENERGY IN=88.419 ENERGY INTO P1=3.900 ENERGY INT
*O HX1=4.195
CHARGE OUT=2.768 ELEC ENERGY OUT=51.559 ENERGY INTO P2=6.486 ENERGY INT
*O HX3=3.574

ELEC EFF=0.583 COU EFF=0.714 VOLT EFF=0.817 945
TYPE 1 TO CONTINUE, 0 TO STOP

Figure 17-5. Output of computer run which simulates run #33 of the 45-kWh module. The plot is of battery variables as a function of time. A more detailed breakdown of the plot is found in Figures 17-6 through 17-9.

To verify that the behavior of the variables in the model as a function of time follows the same behavior as the data from the battery, Figures 17-6 through 17-9 may be examined. Each figure contains the computer graphic output with one or two variables highlighted by thick solid lines. The corresponding data from run #33 of the module is represented by dots. In Figure 17-6, the battery cell voltage is highlighted showing an excellent match. Figure 17-7 shows the pressure in the store and in the stack. During charge, there is good agreement between the actual data and simulation. The deviation during discharge is a result of valve V2 being manually controlled during operation of the module. Looking at the temperature of the store shown in Figure 17-8, it can be seen that again there is excellent agreement. As expected, the stack temperature (shown in Figure 17-9) does not show a good correlation. This is due

to the manual manipulation of the flow in heat exchanger HX3 during actual operation.

Ample verification of the computer simulation model is provided by Table 17-2 and Figures 17-6 through 17-9. The major discrepancies are due to the manual operation of the module. When control of battery operation becomes automatic as planned, the model should more accurately simulate operation of the battery module.

Table 17-2

COMPARISON OF CHARGE, ENERGY, AND EFFICIENCY BETWEEN SIMULATION RUN AND RUN #33 OF THE 45-kWh MODULE

	Coulombic Input (kAh)	Coulombic Discharge (kAh)	Energy Input (kWh)	Energy Output (kWh)	Energy Efficiency (%)	Coulombic Efficiency (%)	Voltaic Efficiency (%)
Simulation Run	3.878	2.768	88.419	51.559	58.3	71.4	81.7
Run #33 of 45-kWh module	3.886	2.798	90.000	53.240	59.2	72.0	82.2
Difference	0.2%	1.1%	1.8%	3.2%	1.5%	0.8%	0.6%

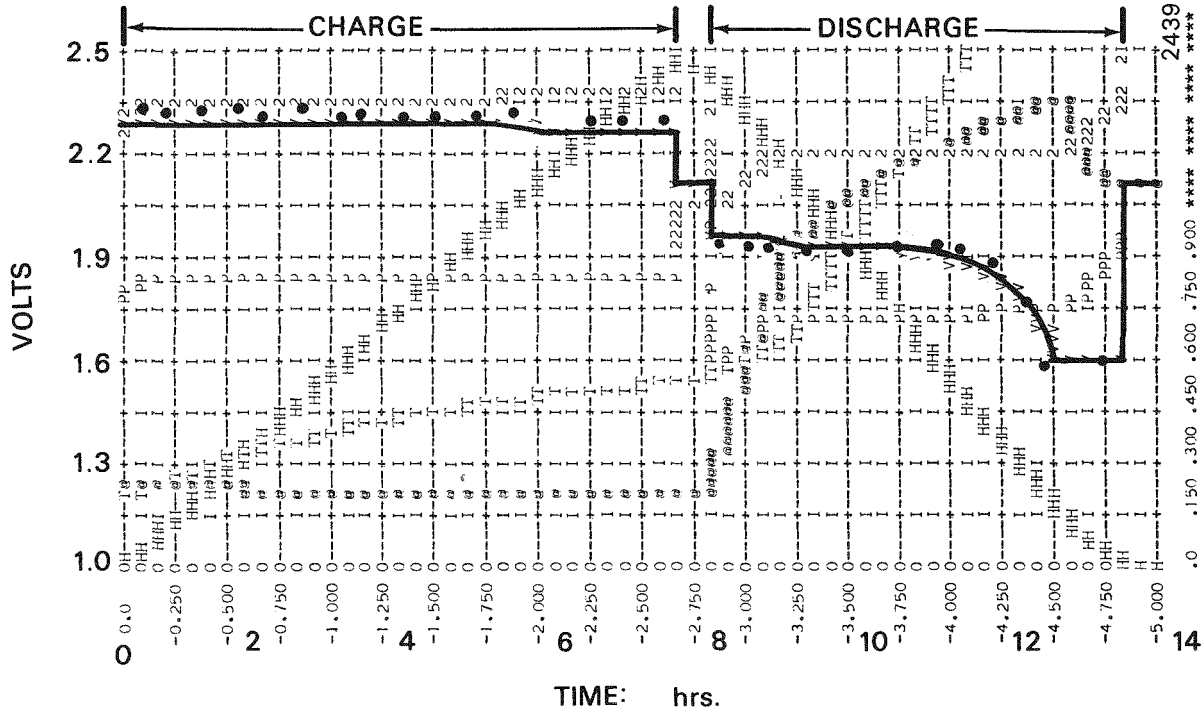

Figure 17-6. Cell voltage vs. time - computer output of model with the simulated voltage shown by the broad solid line and data from cycle #33 of the 45-kWh module represented by the dots.

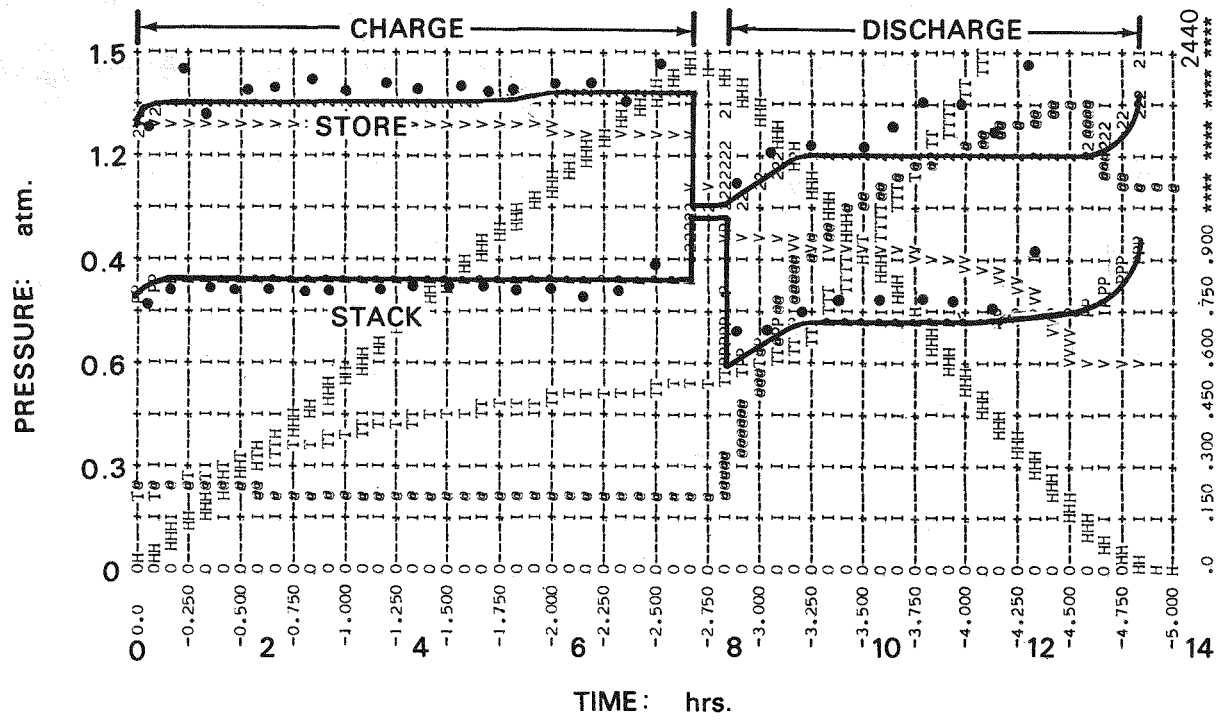

Figure 17-7. Stack and store pressure vs. time - computer output of model with the simulated pressures shown by the broad solid lines and data from cycle #33 of the 45-kWh module represented by the dots.

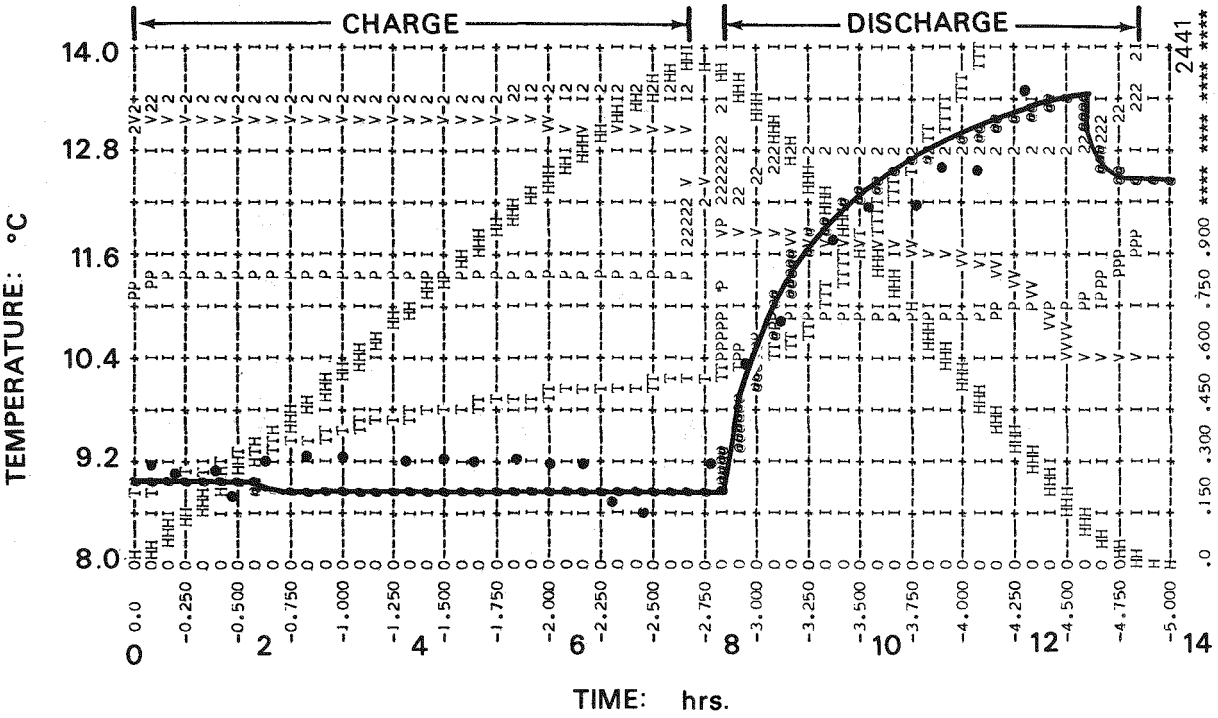

Figure 17-8. Store temperature vs. time - computer output of model with the simulated temperature shown by the broad solid line and data from cycle #33 of the 45-kWh module represented by the dots.

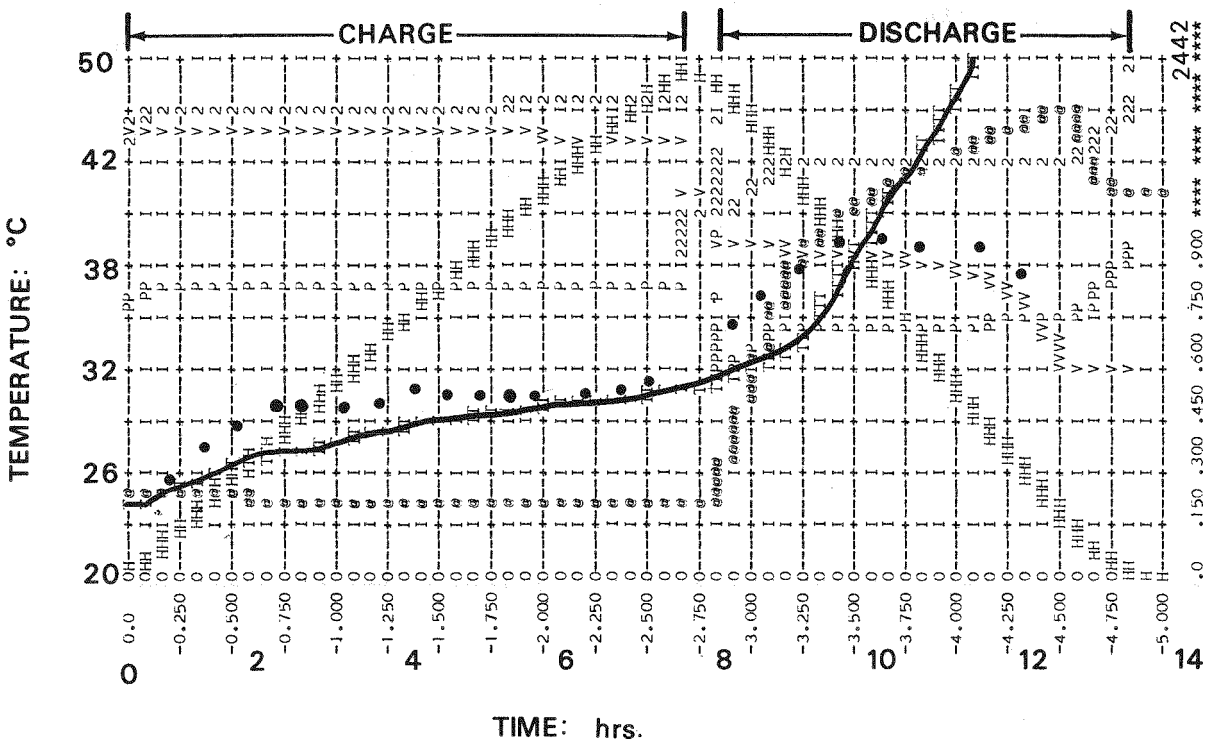

Figure 17-9. Stack temperature vs. time - computer output of model with the simulated temperature shown by the broad solid line and data from cycle #33 of the 45-kWh module represented by the dots.

DISCUSSION

The computer model developed to accurately simulate operation of the zinc-chloride battery module is of great value to the battery development program because:

- It provides a better understanding of the inter-relationships between components of the module.
- It yields information needed to help design the battery control system.
- It allows one to predict the consequences of battery module design changes.
- It allows one to predict the effects of a certain component failure within the module.
- It provides a basis for the modeling of a battery system made up of many modules.
- It provides a centralized location for information about the module as well as indicating areas where knowledge is lacking.
- It can be used to optimize the performance of the module.

The model has already been used for several specific purposes. Through a simulation, it was found that the battery can operate effectively if valve V3 is replaced by an orifice. A plan to eliminate valves V1 and V3 by keeping V3 always closed and V1 always open, was found not to be feasible. The amount of zinc remaining on the electrodes after a charge-discharge cycle was determined by the model.

In the future, the computer simulation model can be used for a multiplicity of applications because of its flexibility. The following can be varied when running the program: (1) operating time in each battery mode, (2) molarity of the electrolyte, (3) volumes of gas and liquid in stack and store, (4) pressures in stack and store, (5) temperatures in stack and store, (6) heat exchanger properties, (7) current into and voltage of the battery, (8) electrode configuration, (9) flow through orifices, (10) pump characteristics, (11) heat flow rates, (12) heat input from pumps, (13) control parameters, and (14) amount of carbon dioxide in stack and store of the battery.

This simulation model, although it reflects fairly accurately the performance of a real module, must be used with the awareness that it is only a model and is not completely accurate. The model is being continually improved in an attempt to reflect reality more accurately and thus, expand its use.

Section 18

45-kWh MODULE FAILURE MODES AND EFFECTS ANALYSIS

ABSTRACT

A failure modes and effects analysis (FMEA) was performed which treats the battery module as a system. In addition to the stack subsystem, major mechanical components of the sump and store subsystems were selected for analysis. All major mechanical components were found to be critical to module operation. Those components identified for follow-up study are pumps, valves, the hydrogen-chlorine reactor system, the submodule, the case, and seals. This study has provided direction for component design and development, a methodology for the collection of test data, and a basis for future FMEA efforts.

INTRODUCTION

System effectiveness is defined as the overall ability of the system to perform its intended function. Reliability is one of the major attributes that determines system effectiveness, and it can be defined as the probability that a system will perform its intended function satisfactorily for a given time period under specified operating conditions. This FMEA will provide a qualitative input into the study of total system reliability.

FMEA is a formalized study intended to identify the modes by which a system can fail, the causes of each failure, and the effects that each failure can have on the system. The system may be a single component, an assembly made of a few components, or a complex assembly of many components. In this study, under the general heading of reliability studies, Energy Development Associates (EDA) has undertaken FMEA of the load-leveling zinc-chloride battery module.

FMEA is a valuable design evaluation tool because it can provide a basis for selection of design alternates, indicate priorities for test and evaluation, and help to specify maintenance schedules. It can call attention to inherent design weaknesses and be of assistance in the objective evaluation of design requirements. The study reported herein represents an initial thrust into what is intended to be an ongoing FMEA program.

The objectives of this study were to:

- Identify failures critical to module performance.
- Guide component selection and development.
- Provide information for design of monitoring and control systems.
- Develop criteria for the testing program and module maintenance schedules.
- Initiate an FMEA data bank as a basis for ongoing FMEA updates.

The module was treated as a mechanical system. Eighteen major components in the store and sump were identified for analysis based on the assumption that a malfunction would result in the break-

down of the system. The stack subsystem was analyzed as five subassemblies, each consisting of one to several individual components. A subjective rating system was established for both probability of occurrence and severity of consequence for each failure mode. All possible types of failures and the consequence of each were estimated for each individual component.

DESIGN OF FMEA STUDY

The battery module was chosen as the unit of study for this FMEA because it is the largest replaceable component of the battery system. It was necessary to establish some definitions, assumptions, and limitations in order to create boundaries for the study. These conditions were:

- Select a module schematic to represent the concept of the refurbished 45-kWh module. It is shown in Figure 18-1.
- Preselect 18 of the mechanical components in the store and sump for detailed study based on their likelihood of suffering a failure that would result in module shutdown. These 18 components are identified in Figure 18-1.
- Divide the stack subsystem into five subassemblies which are illustrated in Figure 18-1.
    1. Submodule Set. Major components of a submodule are illustrated in Figure 18-2.
    2. Electrical Connection System (connector plates and terminals).
    3. H_2/Cl_2 Reactor System.
    4. Case including seals.
    5. Electrolyte Distribution System (electrolyte, manifolding, support plate).
- Consider single failures only. Multiple or sequential failures were not included. However, it was assumed that, for subassemblies containing multiples of the same component (e.g.,submodule as a subassembly, chlorine electrode as component), a component failure mode will occur on the average to all similar components over a given time period, and can therefore have a cumulative effect on the subassembly and, by extension, on the module itself.
- Exclude failures caused by incorrect assembly or installation procedures so as to concentrate on design-related, and materials-related failures.
- Take the qualitative approach because sufficient data are not yet available for quantitative reliability work.

For each component studied all possible failure modes were recorded. Also enumerated were the cause of each failure mode, the effect of each failure mode on the module as a whole, the criticality of a failure effect, the probability of a failure mode occurring, methods for detection of the presence of a failure mode, and recommendations for corrective action. Probability and criticality (severity) were rated on a subjective scale from one to three. The rating values are explained in Table 18-1. Evaluation of failures represents the informed judgment of EDA's engineering staff, and is based on historical evidence, test results, and on expectation for future design iterations.

RESULTS

Detailed FMEA reports are filed for each component analyzed. It is intended that these form the basis for ongoing FMEA work. Several general observations were made in the data analysis process:

- There was consensus that all 18 store and sump components chosen for analysis are critical. In this instance, critical means

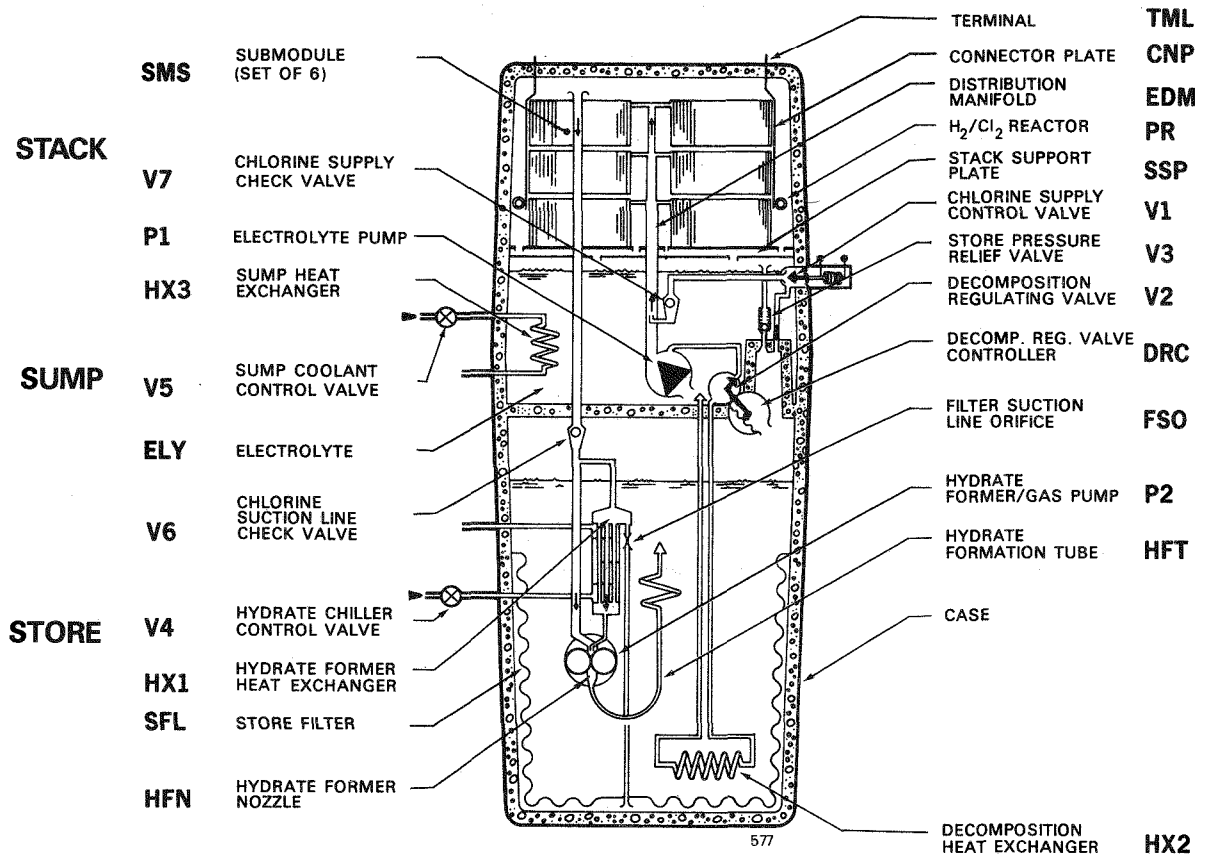

Figure 18-1. Schematic showing general arrangement of the mechanical components in refurbished 45-kWh load-leveling module.

Table 18-1

FAILURE RATING SCALE

PROBABILITY OF OCCURRENCE	ASSIGNED VALUE	SEVERITY OF EFFECT ON PERFORMANCE
Slight chance	1	Negligible effect
Some probability	2	Performance is degraded
High expectations	3	Module can no longer function or it presents a safety hazard.

that the component can suffer a major (Table 18-1 [2]) or critical (Table 18-1 [3]) failure. With the exception of the electrolyte distribution system, all subassemblies in the stack are also critical.

- There was also consensus that all critical failures result in a condition that must not be allowed to progress. Both the timely sensing of the failure and subsequent shutdown of the module were requirements for each critical failure.

- Failures suffered by components in the stack subsystem, which has no moving parts, tend to be related to degradation or aging of materials. Those of components in the store and sump subsystems, which have moving parts, are related to mechanical failures.

- The materials-dependency of stack failures leads to analysis of stack FMEA data by materials type, principally plastics, graphites, case composition, seals, and electrolyte.

- The mechanical-dependency of sump and store failures leads to analysis of sump and store FMEA data by component type, principally pumps, valves, and heat exchangers.

The first two observations lead to the proposal of a series reliability model for the module, because the failure of any one component or subassembly leads directly to failure of the module. Therefore, the series model defines the mathematics of possible reliability calculations. In order to identify and prioritize the most unreliable components for follow-up action, an "Importance Number" was defined. The Importance Number is the sum of the severity rating and the probability of occurrence rating and, therefore, can range from two to six.

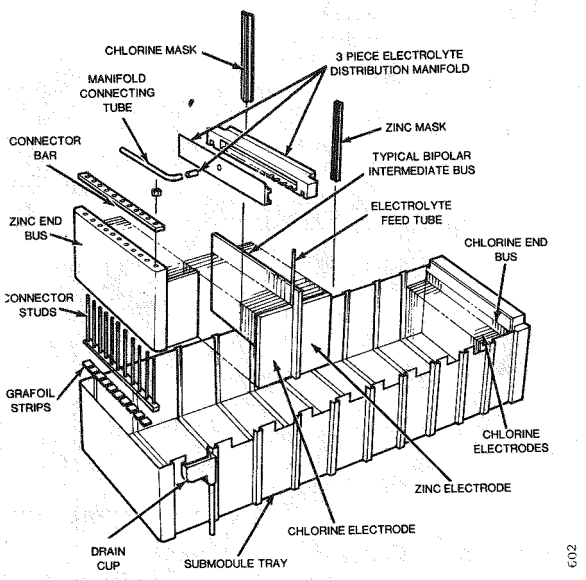

Figure 18-2. Major components of a submodule.

IMPORTANCE NUMBER = PROBABILITY RATING + SEVERITY RATING

Components that experienced failures rating the highest Importance Number, 6, became candidates for intensive design and life study.

Analysis of data for failures that rated Importance Number 6 shows that three of the components in this category are valves. Valves, by failing to open or close appropriately, can create critical effects in operating pressures. Pump and valve failures dominate those failures with Importance Number 5. Case failures associated with breakage of the seal also rated 5, as did failures of components that communicate with the exterior through the case (e.g., terminals) where seal breakage was the critical effect. The fragile nature of the porous-graphite chlorine electrode material was evident in the rating of 5 given to cracked or broken electrodes in the submodule.

The possible safety hazard from hydrogen buildup that could result from a failure of the hydrogen-chlorine reactor (PR) system resulted in a rating of 3 in severity and 3 in prob-

ability for PR failures. In the submodule, failures leading to impeded flow to the chlorine electrode pair rated Importance Number 6 since electrochemical competence of the cell is thereby compromised.

From Analysis of the most common symptoms associated with critical failures, it became apparent that, except for the sump coolant control valve (V5) and the electrolyte pump (P1), all critical failures of store and sump components and the H_2/Cl_2 reactor system (PR) have an effect on the store pressure, the stack pressure, and/or the differential pressure. In the case of V5, an increase in sump temperature can be expected to result in some pressure effect as well. Although a pressure effect was not mentioned in failures of P1, because pumps are used to create pressure differentials, failure of P1 also should result in a pressure effect.

Common causes of pump failure include interruption of the power supply, primary motor failure, decoupling due to flow surge or sudden loading, primary internal pump failure, and bearing failure. Direct detection of the operational status of pumps was recommended so that, at pump failure, the module could be shut-down before secondary effects were manifested.

Valves suffer three failure modes: fail to close, fail to open, and leakage. These modes tend to have common causes such as collection of debris and dried electrolyte, corrosion from the environment or grounding, aging stress, mechanical deformation, and failures of the valve-actuating systems and power supplies. Recommendations by the analysts for improving valve performance included protecting the valves from debris by using filters, overdesign and testing valves under stress, providing a backup power supply which possibly could be part of the battery system itself, and using latching valves wherever possible.

Heat exchangers in general are relatively reliable since they have no moving parts. Blocking and breakage are the most serious problems together with a decrease in heat exchange capacity caused by hydrate coating the tubes. Suggestions for improvement included care in selecting materials, employing a design that prevents both rubbing contact and electrical grounding, and the use of filters to protect them from blockage.

Plastics are used extensively in the submodules for framing, trays, and electrolyte flow channels. They are also used for manifolding, plumbing, the stack support plate, and in the case composition. Deterioration or aging of plastics with time can result in blistering of the surface, cracking, or breaking. Blistering is the most common failure mode. Cracking and breaking of plastic components, although likely to cause immediate severe effects such as massive leakage of electrolyte from stack to sump (if SSP is involved), are judged very unlikely to occur. When blistering occurs in a large-bore electrolyte flow channel such as the stack support plate (SSP), the effect is minimal. When blistering occurs in a small-bore flow channel such as those that feed the chlorine electrode pairs, the effect (i.e., impeded flow) is likely to be severe: depletion of zinc chloride in charge, reverse plating in discharge; electrode shutdown and gas lock if the vent is involved. The most current design utilizes for components in the small-bore flow channels a plastic that exhibits improved resistance to blistering.

Graphites are used in the submodule for electrodes and buses. In the sump and store graphitic material is used in pump bearings. With time, these materials can deteriorate, especially the porous graphite used for the chlorine electrode pairs, releasing graphite sludge into the electrolyte. The resultant electrolyte contamination is discussed below. The effects of electrolyte flow impedance by sludge in small-bore flow channels is as described

above for blistering of plastics. Mechanical failures of graphite parts (such as cracks, breaks, or bowing) can result in creation of extraneous liquid paths, shorting, and formation of parasitic currents. The fragile, porous-graphite chlorine electrode pair is especially susceptible to mechanical failures resulting in shorts, dendritic growth, non-uniform flow, and, ultimately, decreased efficiency. Major research effort is currently addressed to the qualification of cost-effective, high-performance graphites.

Two electrolyte failure modes are considered serious: impurities and pH changes. Impurities can be introduced by accumulation of graphitic sludge from deterioration of graphites, and from leaching-out of plastic degradation products. The results are increased hydrogen evolution and dendritic growth. A pH above the specified normal range can result in increased rate of graphite deterioration and increased CO_2 formation. A pH below the normal range can result in increased hydrogen evolution. Both electrolyte failure modes can lead to reduced module efficiency.

All major failures of the case are related to breakage of the seal. The module case provides isolation from the environment and is designed to operate, in the stack area, at negative pressure. In addition to cracking from gradual aging of the plastics utilized in case composition, the section joints and various through-case assemblies are sites for possible leakage of air into the module and leakage of electrolyte and chlorine into the environment. A safety hazard can result from release of chlorine; however, this is seen as unlikely since the failure scenario would lead first to module shutdown. Various plastic sealants and mechanical compression systems are utilized to effect case-joint and case-assembly seals.

The most common symptom of failures of stack components is decreased module efficiency. Direct detection of the failures is presently possible only through destructive examination of shutdown modules.

DISCUSSION

If, as it appears from this FMEA, the load-leveling module can be described by a series model, the reliability of the module is the product of the reliabilities of the subsystems:

$$R_{MODULE} = R_{STORE} \cdot R_{SUMP} \cdot R_{STACK}$$

Based on this relationship, the reliability of the module will be less than that of its least reliable component.

One common measure of the reliability of a component is failure rate, or the number of failures suffered by the component in a given time period. Failure rate data on a large number of components have been compiled by the Reliability Analysis Center (RAC), Rome Air Development Center at Griffiss Air Force Base in New York. This information can be valuable for relative or comparative purposes, or to indicate the best performance that should be expected of a specific class of components.

According to RAC data, the failure rate for centrifugal pumps exceeds the failure rate of the least reliable valve. Failures of the centrifugal electrolyte pump (P1) are rated Importance Number 5. This, coupled with the critical function of P1 in the module, suggests that design effort be concentrated here. A pump development program is currently underway.

The FMEA analysts chose the two solenoid valves, chlorine supply control valve (V1), and the decomposition regulating valve (V2), plus the store pressure relief valve (V3) as those

requiring follow-up action. The Importance Number, 6, for failures of these valves reflects this priority. The chlorine-suction line check valve (V6) was judged not as critical in application and, therefore, does not appear in the top-priority list.

In the most recent design iteration of the battery module, solenoid valves V1 and V2 are replaced by pneumatic valves. Due to the critical nature of its function, the store pressure relief valve (V3) is being redesigned. It may possibly be replaced by an orifice in a later design iteration.

The ultraviolet bulbs currently used as the hydrogen-chlorine reactors have a manufacturer-projected mean life of 6000 hours, or a failure rate of 167 failures per 10^6 hours of operation. The present design increases the PR system reliability by allowing access for preventative maintenance and by providing redundancy.

CONCLUSIONS

This FMEA study served to increase understanding of present module operation and to provide input for future design reviews. Conclusions drawn from this study are:

1. Classification of failures by Importance Number made it possible to identify components for major design consideration because of their function in module safety or basic module operation, or because of demonstrated unreliability. These components are ranked in descending order of importance:
   - Valves, V1, V2, and V3
   - The hydrogen-chlorine reactor system
   - The hydrate-formation nozzle
   - Pumps
   - Submodule flow channels to chlorine electrode pairs
   - Case and seals
   - Chlorine electrodes
2. The consensus that all of the components or subassemblies analyzed are critical components leads to the conclusion that the sensor and control subsystems also will be critical to battery operation. A module must be taken safely out of the electrical network whenever a failure of any one of its critical components occurs.
3. All but three critical failures of sump and store components are signaled by changes in store, stack, and/or differential pressure.
4. Since the stack subsystem contains no moving parts, it is relatively reliable in that effects of materials-related failures manifest themselves cumulatively with time. In contrast, a valve failure will have a more immediate effect on module performance.

RECOMMENDATIONS

Based on the results of this study, the following recommendations for further work are made:

1. Perform an FMEA at the next lower indenture level for some of the components analyzed in this study. In other words, in this study a valve was considered the end item. In the next indenture level, a valve will be the system composed of mechanical and electronic parts, all of which must receive an FMEA.
2. Analyze the module components that were not considered in this study for criticality, and perform FMEA.
3. Maintain an ongoing FMEA study to be updated for each design iteration.

4. Perform an FMEA on the design of a complete battery system including auxiliaries and control systems. The sensor and control subsystems require immediate and major logistical engineering effort. This includes treatment of the subsystems as critical components of the total system in reliability modeling, and in the performance of subsystem FMEA.

5. Systematically bank failure data from the various experimental programs to create mathematical inputs for reliability calculations and modeling.

6. Perform accelerated life-testing of materials and mechanisms in the module environment.

7. Give special attention to the sensing and recording of pressures in experimental work. This recommendation is based on the observation that all critical failures of sump and store components are signaled by pressure effects. Module performance and operational status can be monitored by pressure sensors. Temperatures also were mentioned as status indicators. Temperature-sensing and recording are also suggested for the purpose of establishing operating limits.

8. Investigate those areas referred to as suggested improvements in the filed FMEA reports for possible design modifications.

9. Perform a detailed FMEA, by examining each component, on those areas in the sump and store which may affect the operation of the stack.

10. Specify torque requiremenmts for all nuts and bolts and other installation procedures.

11. Specify maintenance periods and maintenance procedures for inspecting components external to the case.

Section 19

45-kWh MODULE: SUPPLEMENTARY STUDIES

ABSTRACT

Following successful testing of the 45-kWh battery module, three additional studies were conducted: (a) a charge-stand experiment to evaluate the performance of a module fully charged awaiting a demand for delivery of energy, (b) short-circuit testing to determine whether the resulting high current would result in damage to the module, and (c) reconfiguration of the module to improve maintenance accessibility. The charge-stand experiment showed that electrolyte cannot be allowed to drain from the stack during the charge-stand state. During the short-circuit tests, the peak current of 9200 amperes, 17 times the normal 540 amperes, decayed to 400 amperes within seconds causing no damage to the module. As a side benefit of increased maintenance accessibility, the reconfiguration improved the utility of the module as a test bed for new components.

INTRODUCTION

Cycle-testing of the 45-kWh module was conducted primarily to demonstrate the feasibility of combining the stack, store, sump, and all auxiliary components into a self-contained, integrated system. Although this role was most important, the module has been useful for other supplementary studies as well. Simulation of a 24-hour cycle in a utility environment was started by using the 45-kWh module to evaluate the charge-stand state; and a short-circuit test was conducted to determine the effects of high currents due to accidental or deliberate short circuits during battery plant operation. These supplementary studies, or experiments, are discussed in this section, along with a description of a modification made to improve the usefulness of the module for future studies.

CHARGE STAND EXPERIMENT

This experiment was conducted as part of a general plan to use the 45-kWh battery module to evaluate the operational states proposed for future modules operating in a utility environment. One of these is the charge stand state when the modules of a battery plant are fully charged awaiting the demand for delivery of energy. In this state, the electrolyte and gas/hydrate-former pumps are turned off, coolant flow is stopped, the chlorine supply valve controlling gas access to the electrolyte stream is open, the hydrate decomposition regulating valve is closed, and the hydrogen-chlorine reactor lights remain on. These components may be identified by reference to the schematic representation of the 45-kWh module included as Figure 19-1.

Because of modifications made during refurbishment of the module in early 1979, the electrolyte drains out of the cells when the electrolyte pump is off. This became an important factor during the experiment.

Experimental Procedure and Results

For the purpose of this experiment, a two-hour charge at the normal 33 mA/cm^2 charging current was chosen to deposit

sufficient zinc and to save time. The electrolyte was the standard load-leveling electrolyte formulation of zinc-chloride, supporting electrolytes, and leveling agent. The pH was adjusted to 0.1. The intended charge stand duration was 5.4 hours, the time estimated in the analysis of a 24-hour cycle in the utility application.

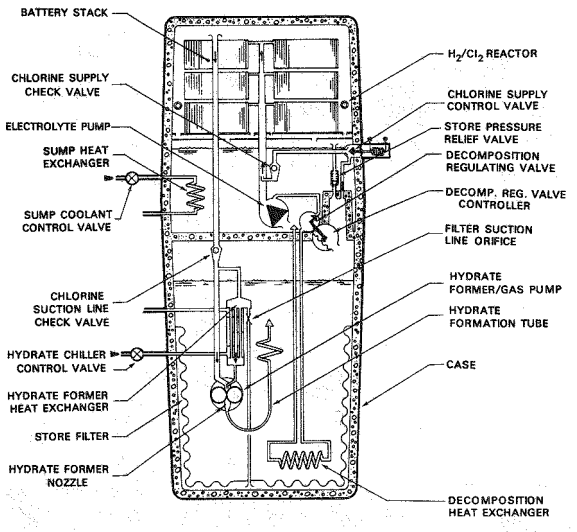

Figure 19-1. Refurbished 45-kWh module. During charge stand, the chlorine supply valve is open to allow gas access to the electrolyte stream. The decomposition regulating valve is closed to prevent electrolyte flow through the hydrate-decomposition heat exchanger. Both pumps are off.

The 45-kWh module was charged for two hours and then put into the charge-stand state. In a short time (15-20 minutes) the temperature at the hydrogen-chlorine reactor increased dramatically from 38°C to 75°C. The experiment was stopped because of possible harmful thermal effects on plastic components of the module. Flushing the stack compartment with air produced an immediate reduction of the temperature to 35-40°C. This was due not only to the fact that a colder gas was brought in to flush the system but that one of the reacting species, chlorine gas, was being removed at the same time. The module was then discharged in the normal manner. This experiment was repeated several times with similar results.

The source of this excessive heat was hypothesized to be either:

- Heat generated due to the exothermic hydrogen-chlorine recombination.

- Heat generated by the direct reaction of zinc with chlorine. This is possible in the 45-kWh module because electrolyte drains out of the cells when the electrolyte pump is turned off.

To distinguish between these two reaction mechanisms, another trial was made during which the hydrogen-recombination reactor light was turned off to eliminate the contribution of the hydrogen-chlorine reaction. All other conditions for charge stand remained the same.

Again the module was charged for two hours and then placed in charge stand. As shown in Figure 19-2, the sump temperature of the electrolyte was 34.0°C at the end of charge, and the gas-space temperature measured at the reactor was 38.4°C. The store pressure was at 8.8 psig and the stack at -2.5 psig. At this point the chlorine supply valve was opened and the stack and store pressures equilibrated at +2.5 psig. This took six minutes. At that time the reactor light was turned off (see Figure 19-2).

At the six-minute mark, the temperature of the gas space had increased from 38.4°C to 42.2°C. After the reactor was turned off (six minutes into stand), the temperature of the gas dropped to 39.6°C in two minutes at the eight-minute mark. This drop in temperature indicated the effect of the net heat contributed to the system by the hydrogen and chlorine recombination. The overall temperature of the gas, however, continued to climb until 60°C was reached in 25 minutes. Instead of flushing with air to bring the temperature to normal levels, the elec-

trolyte pump was turned on to fill the stack with electrolyte.

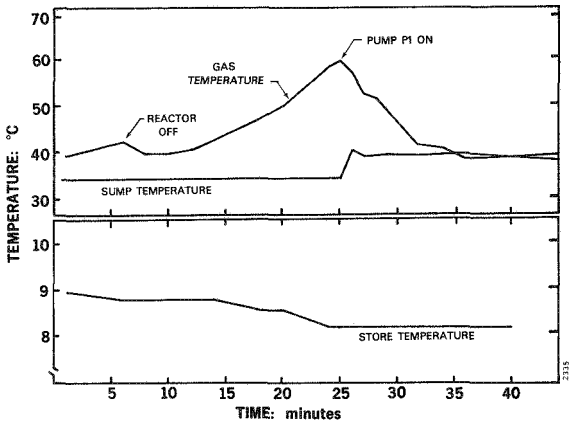

Figure 19-2. Temperature excursions within the module as a function of time in the charge-stand state. When the hydrogen-recombination light was turned off after six minutes, elimination of the hydrogen-chlorine reaction caused the stack gas temperature to drop slightly but the zinc-chlorine reaction caused the temperature to continute to rise. At the 25-minute mark, turning on the electrolyte pump flooded the cells with electrolyte curtailing the zinc-chlorine reaction and transferring heat to the sump. The store temperature decrease is attributed to heat absorbed by chlorine hydrate decomposition to supply chlorine to the stack.

Immediately the temperature started to decrease and in about five minutes dropped to a near-normal level of approximately 40°C. At the same time, when the electrolyte pump was turned on the temperature of the electrolyte in the sump rose from 34.6°C to 39.2°C due to mixing of the "hot" electrolyte remaining in the partially-drained stacks with the bulk electrolyte in the sump (see Figure 19-2.) This observation is consistent with the hypothesis that most of the heat being generated in the stack area was due to the reaction of the exposed zinc surfaces with chlorine gas. Further examination showed that chlorine gas was being consumed rapidly as indicated by the decrease in the pressures of both the store and stack from +2.5 psig to -1.2 and -1.4 psig, respectively. The decrease in the store temperature from 9.0°C to 8.1°C can be attributed to the rapid consumption of chlorine in the stack, since the heat absorbed in decomposing chlorine hydrate to replace the chlorine would produce cooling of the store.

Analysis and Discussion

The following calculations attempt to quantify these observations assuming that most of the heat generated during charge stand is the result of the zinc-chlorine recombination. These calculations are based on the observed temperature changes of the electrolyte before and after mixing at the 25-minute mark. These figures indicate the moles of reacting species needed to generate the heat released due to the zinc-chlorine reaction in the stack compartment.

1. $Q = c.m.\Delta T$

   where

   Q = heat in kCal

   c = specific heat, kCal/kg-°C

   m = mass of material, kg

   ΔT = change in temperature, °C

2. $$Q = \frac{0.95 \text{ kCal}}{\text{kg°C}} \times 260\,\ell\ ZnCl_2 \times 1.325 \frac{\text{kg}}{\ell} \times 4.6°C$$

   $$= 1505 \text{ kCal}$$

3. $\Delta H_{ZnCl_2} = 112$ kCal/mole

4. $$\frac{1505 \text{ kCal}}{112 \text{ kCal/mole}} = 13.4 \text{ moles}$$

   of $ZnCl_2$ formed

The quantity of heat required to liberate 13.4 moles of chlorine from hydrate in the store is:

1. (13.4 moles chlorine) x (18.6 kCal/mole of hydrate decomposed) = 250 kCal heat removed from store

2. $\Delta T = \frac{(250\ \text{kCal})}{(1.0)(400\ell H_2O)} = 0.6°C$

The experimental value is 0.8°C $\pm$0.1°C which compares favorably with the calculated results of 0.6°C.

To convert the amount of chlorine reacted with zinc to a coulombic loss on stand with drained or partially drained stacks, the calculations are as follows:

1. 13.4 moles x 65.37g Zn/mole = 876g Zn lost

2. 1.21g Zn/amp-hour by Faraday's law

3. $\frac{876g\ \text{Zn lost}}{1.21g\ \text{Zn/amp-hour}} = 724$ amp-hrs.

4. $\frac{724\ \text{amp-hours} \times 100}{27{,}000\ \text{amp-hours discharge}}$

   = 2.7% coulombic loss/25 minutes

The hydrogen level during the time the reactor was turned off rose from 0.2% to 10.0%. The higher hydrogen level is to be expected since the kinetics of hydrogen evolution are accelerated by higher temperatures. The net contribution of heat that would have been added by the hydrogen-chlorine reaction would be as follows:

1. $H_{2(g)} + Cl_{2(g)} \rightarrow 2\ HCl_{(g)}$

2. $H_{react} = (2)(22.06)$

   = 44.12 kCal/mole of H_2

3. 60ℓ (volume of stack) x 0.10 = 6.0ℓ of hydrogen

4. $\frac{6.0\ell}{24.2\ell/\text{mole}} \times 44.12$ kCal/mole

   = 10.9 kCal

The ratio of this heat to that calculated for the zinc-chlorine reaction is:

$$\frac{10.9\ \text{kCal}\ (H_2/Cl_2)}{1500\ \text{kCal}\ (Zn/Cl_2)} \times 100\% = 0.7\%$$

From this one must conclude that the heat added by the hydrogen-chlorine reaction is insignificant compared to the heat generated by the zinc-chlorine reaction.

It appears conclusive that the dramatic temperature increase in the stack compartment during charge stand was due to the zinc-chlorine reaction made possible because the electrolyte drained from the stack exposing zinc to the chlorine environment. It is concluded therefore that a nondraining stack is essential to limit the direct reaction of zinc with chlorine by maintaining an electrolyte barrier covering the deposited zinc.

SHORT-CIRCUIT TESTS

As part of the battery plant design, module-bypass switches are being considered for short-circuiting any defective module to remove it from a string of series-connected modules. With this concept, any module that exhibits performance variations beyond pre-set limits will be eliminated from its string by: (a) closing its bypass switch, (b) opening the valve controlling chlorine supply to the electrolyte stream, and (c) turning off the electrolyte and gas/hydrate-former pumps. This procedure accomplishes safe shut down of the module and allows the series string to continue charge or discharge without interruption by shunting the current around the defective module. The short-circuit current through

the module is limited by the amount of chlorine dissolved in the electrolyte when the bypass switch is closed. To evaluate the feasibility of this concept, low-resistance short circuits were imposed on the 45-kWh module with a twofold purpose: (a) to determine whether a short circuit would result in damage or performance degradation, and (b) to obtain short-circuit data for use in bypass switch design.

The electrical circuit for the experiment, Figure 19-3, comprises a 0.5 milliohm short-circuit path when the knife switch is closed. An oscilloscope is used to measure the initial current peak because of the slow response time of the chart recorders. The following characteristics of the module were monitored:

- Stack pressure
- Store pressure
- Stack temperature (UV light area)
- Sump temperature
- Electrolyte pH
- Electrolyte specific gravity
- Stack gas composition

A total of ten short circuit experiments were conducted during a three day period. One short circuit was imposed with the electrolyte pump on for a short time to simulate a failure of the protective device which turns the pumps off when the bypass switch is closed. Each short circuit test was followed by a short period of discharge or charge operation to stabilize operating temperatures and pressures.

The converter was turned off during the experiments to avoid any possibility of converter damage. In order to simulate actual conditions, the knife switch was closed as quickly as possible after turning off the converter and the electrolyte and gas/hydrate-former pumps. The chlorine supply valve was closed during these short-circuit tests to prevent gas flow into the electrolyte stream.

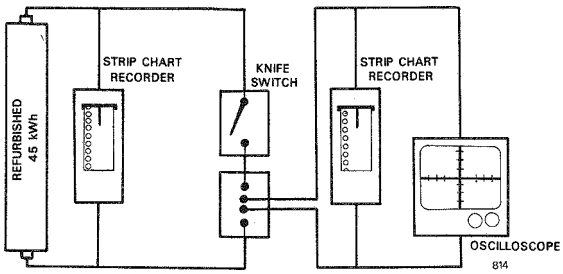

Figure 19-3. The electrical circuit used for monitoring current and voltage when the 45-kWh module was shorted.

The results indicate that there were no temperature or pressure increases threatening damage to the module. Gas analyses and changes in hydrogen-chlorine reaction temperature indicate that no significant rise in hydrogen concentration results from short-circuiting. The pH and specific gravity of the electrolyte were measured on the first day, but these measurements were discontinued thereafter because of the negligible changes observed.

Current and voltage curves are shown in Figures 19-4, and 19-5. The current reached a peak of 9200 amperes approximately four milliseconds after the knife switch was closed and decayed to approximately 400 amperes in 15 seconds, while the voltage decreased from 20.8 to 4.2 volts in half a second. Recovery of the terminal voltage after the knife switch was opened is shown in Figure 19-6. The slow rise in voltage diminishes the possibility of restrike fault currents.

When the module was shorted with the electrolyte pump on, a greater decrease in stack pressure and increase in sump temperature was observed, but the degree of these changes was of no consequence relative to module safety. The peak current was identical to the other tests; however, the decay time was

longer. The current decreased to 1200 amperes in 30 seconds at which time the electrolyte pump was turned off. The module performance data presented in Table 19-1 reveal no unexpected behavior trend.

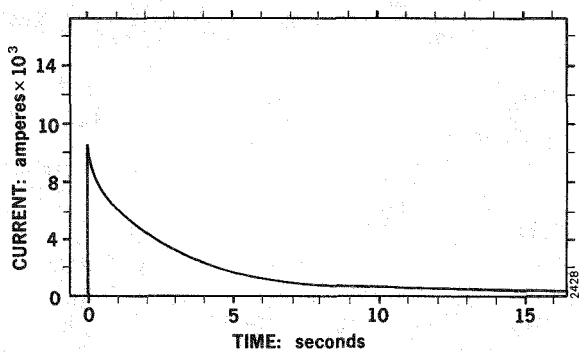

Figure 19-4. Plot of current peaking when the 45-kWh module was shorted with the pumps off.

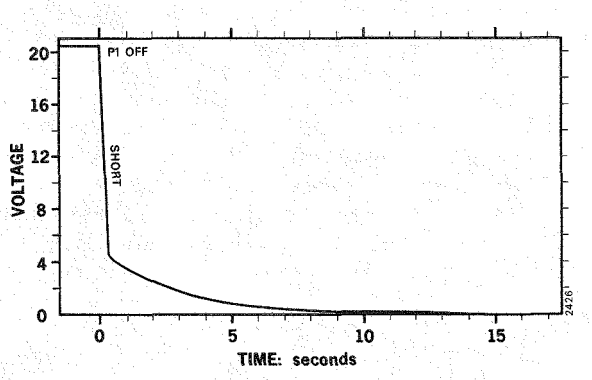

Figure 19-5. Plot shows the change in voltage with time when the 45-kWh module was shorted with the pumps off.

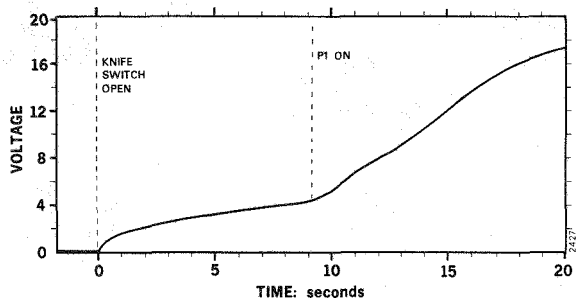

Figure 19-6. Recovery of terminal voltage when the switch on a shorted module is opened.

Table 19-1

45-kWh MODULE PERFORMANCE
BEFORE AND AFTER SHORT CIRCUIT

EFFICIENCY	BEFORE	AFTER
Coulombic	73%	71%
Voltaic	78%	83%
Energy	57%	59%

The experiment demonstrated that a module can be short circuited safely with no immediate effect on performance, and no long term effect discernible at this time. The 9200 ampere maximum short-circuit current was approximately half that expected from extrapolating results of submodule short-circuit tests. As the titanium buses in the 45-kWh module have approximately double the resistance of the BEST prototype busing, the extrapolated higher peak current should be used for bypass-switch design.

MODULE RECONFIGURATION

In November 1979, to improve its utility as a test bed, the 45-kWh module was reconfigured by relocating the gas/hydrate-former pump, the hydrate heat exchanger, all valves and most of the plumbing outside the battery case. As shown in Figure 19-7, components other than submodules, the electrolyte pump, the sump heat exchanger and the hydrate decomposition heat exchanger, are now accessible from the outside for maintenance and substitution of new components for testing. Within limits, piping can be modified easily to evaluate alternative flow concepts or to accommodate new components not included in the original design. Component failures since the reconfiguration have already demonstrated the benefits of maintenance accessibility. Also, use of the module for preliminary evaluation of an inerts rejection device points to its utility as a test bed.

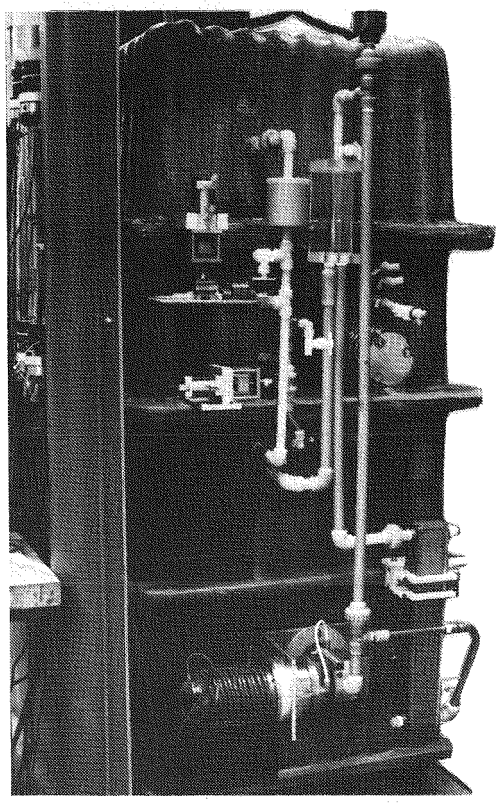

Figure 19-7. 45-kWh module reconfigured with all valves, the hydrate heat exchanger, and the gas/hydrate-former pump outside the case.

DISCUSSION

With the advent of second-generation technology, any further major overhaul of the 45-kWh module would not be worthwhile. However, the module will continue to be useful as a test bed for new concepts and components, particularly in its new configuration with most of the auxiliary components mounted outside the case. Plans for the future include:

- Continuing the simulation of a 24-hour cycle to evaluate performance under normal and fault conditions anticipated in the utility environment.
- Conducting a high-voltage test to determine the effect (if any) of the high voltage at the end of a string of modules in a battery plant.
- Evaluating alternative discharge profiles to simplify operation.

PART IV

CYCLE TESTING OF 1.7-kWh BATTERY

Section 20

PROGRAM STATUS: 1.7-kWh SYSTEM

The 1.7-kWh battery, shown in Figure 20-1, has been undergoing testing since April of 1976 to determine the life of the battery stack. Even though it was built in early 1976, the dense-graphite zinc electrodes, the porous-graphite chlorine electrodes, and the interference fit between the electrodes and the graphite buses are features of current submodule design. The chlorine electrodes are of particular interest because this battery includes the first porous-graphite chlorine electrodes in the EDA load-leveling battery development program.

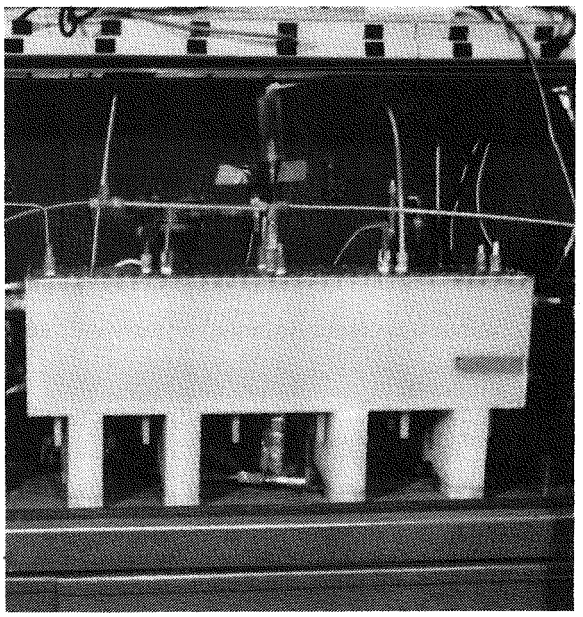

Figure 20-1. Photograph of the 1.7-kWh battery stack.

During RP226-2, when some development work was continuing after testing had started, the system accumulated 54 cycles (1). Operation of the system was then shifted from manual to automatic control. By the end of Phase I of RP226-3, the cycle count had increased to 446 (2). During Phase II of RP226-3, the 1000-cycle milestone was reached in June 1979; and the test objective of 2500 cycles was half-realized on March 15, 1980 when the system had accumulated 1250 cycles without significant performance degradation.

The original system used through cycle 1112 to support testing of the 1.7-kWh battery stack is shown schematically in Figure 20-2. This system, intended to simulate the operation of a complete battery, included provisions for forming, storing, and decomposing chlorine-hydrate. As a consequence, the system was quite complex in terms of gas and liquid lines, fittings, and auxiliary components. Unfortunately, repeated failures of auxiliary components and recurring leaks in fittings resulted in a significant loss of battery cycling time. Because of this, the system was modified as described in Section 23 to improve its reliability.

Testing began with the system under manual control. Then the pace of the testing was accelerated in March 1977, when the battery operation was shifted to 24-hour unattended computer control, starting with cycle #63. The computer was programmed to step the battery system repeatedly through the prescribed charge/discharge cycle and to collect, record, and display performance data. The program also includes preset limits for failure detection and procedures for safe shutdown of the battery under fault conditions. The computer functions are more fully described in Section 21.

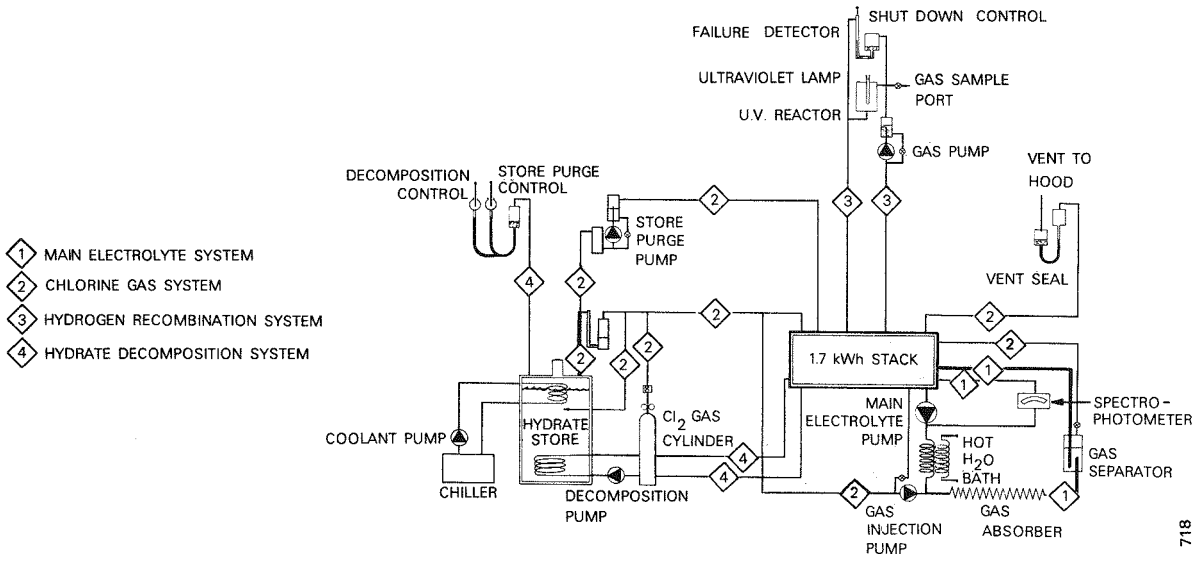

Figure 20-2. Schematic diagram of the original system used to test the 1.7-kWh battery stack. This system included a separate loop for hydrogen-chlorine recombination and provisions for forming, storing, and decomposing chlorine hydrate.

Along with the shift to computer control came the need for an efficient method for handling the large amount of data collected. As the computer was programmed to record a three-line data set at five-minute intervals, approximately 400 lines of data are recorded for each run. One can readily perceive the need for a computer-based system for organizing, reducing, and analyzing the data to be accumulated over the 2500-cycle life of the test. The NOMAD data-base management system available through a computer time-sharing service offered by National CSS, Inc., was chosen for this purpose. The 1.7-kWh system performance data, recorded on magnetic tape at EDA, is transferred routinely via telephone link to the NCSS computer where it is stored in three forms: as raw data on magnetic tape, a complete data base filed on tape, and a condensed data base filed on disk. This file structure, which evolved through efforts to reduce cost, has served well. The condensed data base, containing the data most frequently of interest is readily accessible, and all data can be recalled from tape to disk for processing at any time by means of relatively simple NOMAD commands. The system, more fully described in Section 22, includes provisions for computation, statistical analysis, construction of summary lists, and graphical presentations.

Because of the continual maintenance difficulties encountered with the original system, that system was modified in November of 1979 to eliminate components that had contributed most to the loss of cycling time. Removal of the chlorine-hydrate store and associated components was the principal feature of the modification. To compensate for this, chlorine evolved during charge is now vented into the hood exhaust, and chlorine required for discharge is supplied by cylinder chlorine. Comparison of the modified system shown in Figure 20-3 with the original system, Figure 20-2, shows the degree of simplifica-

tion effected without changing operating conditions for the battery stack. This modification and its positive effect on accelerating the life test are discussed in Section 23.

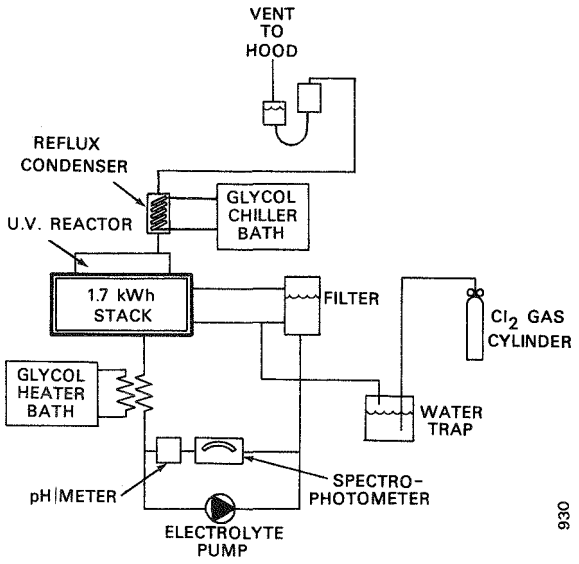

Figure 20-3. Schematic of the 1.7-kWh test system modified to improve reliability. The hydrate store was removed and the hydrogen-chlorine recombination loop was incorporated into the case top.

Test results through 1250 cycles -- halfway toward the 2500-cycle targeted life -- are shown by the plot of efficiencies in Figure 20-4. In this figure, the pattern of 100-cycle increments of averaged data is broken at cycle 1112, the last cycle of the original system, to indicate the performance trend before and after the modification. A more detailed comparison of recent before-and-after test history is included in Section 23, while a discussion of the original battery system and its performance through the first 1000 cycles will be found in Section 21.

The modified system offers good potential for increasing the rate of accumulation of cycles. Also, elimination of

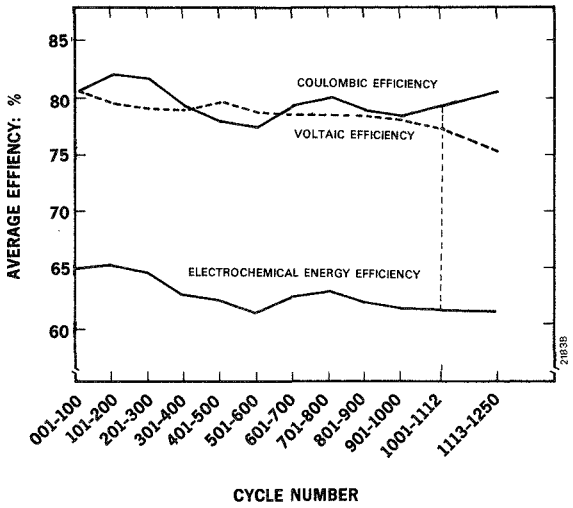

Figure 20-4. Efficiency data for the 1.7-kWh battery stack shown as averages for the groups of cycles indicated. The dotted line marks the last cycle of the original test system and the start of testing with the modified system.

failure-prone components that often were the cause of electrolyte changes enhances the potential for exceeding the record of 138 cycles without electrolyte maintenance. With over four years of testing gone by, there is ample evidence that the goal of 2500 cycles will be reached.

REFERENCES

1. Development of High-Efficiency, Cost-Effective Zinc-Chlorine Batteries for Utility Peak-Shaving, 1976. Palo Alto, Calif.: Electric Power Research Institute, March 1978. EM-711.

2. Development of the Zinc-Chlorine Battery for Utility Applications. Palo Alto, Calif.: Electric Power Research Institute, April 1979. EM-1051.

Section 21

1.7-kWh BATTERY SYSTEM: THE FIRST 1000 CYCLES

ABSTRACT

Life testing of a 1.7-kWh cell system was initiated in 1976 as part of a joint EPRI-EDA program to develop the zinc-chloride battery for utility load-leveling. The battery stack in this system is of particular interest in that it embodies many of the design concepts utilized in present EDA technology, e.g., porous-graphite chlorine electrodes. From early 1977 onwards, cycle-testing of this system was conducted with a microprocessor-based data acquisition and control system. As of June 1979, the system had accumulated 1000 charge-discharge cycles. As indicated by the constancy of the voltaic efficiency, the performance deterioration through 1000 cycles was negligible. EDA plans to continue testing through 2500 cycles -- the life target for commercialization of load-leveling batteries.

INTRODUCTION

Early in the joint EPRI-EDA program to develop the zinc-chloride battery for utility load-leveling, a number of test cells were designed and cycled to test the feasibility of the battery system. The first was built in mid-1974. It was a 1-kWh cell with chlorine electrodes made of ruthenia-catalyzed titanium. The second design, an upgraded version of the 1-kWh cell rated at 1.4 kWh, was tested beginning in early 1976. Concurrently, a 1.7-kWh cell, which employed porous-graphite chlorine electrodes, was assembled and put on test. Due to the low cost, ease of control, and inherent safety of the graphite material, the main test focus was placed on the 1.7-kWh system and the titanium system was retired (1). In June 1979, this system, shown in Figure 21-1, reached the milestone of accumulating 1000 charge/discharge cycles yielding an electrochemical energy efficiency of 60% or greater.

Because the porous-graphite electrodes are considered to be the life-limiting components of the load-leveling battery, the 1.7-kWh battery system has been operated continuously to demonstrate the stability of the electrodes over the targeted 2500-cycle life of a commercial load-leveling system -- 1 cycle/day, 5 days/week, 50 weeks/year for 10 years. Concern over their life arose because similar electrodes used in the chlor-alkali industry have experienced a short life of several months. Several differences in the operating parameters of the 1.7-kWh system -- principally the electrolyte pH -- are theorized to aid in prolonging electrode longevity and, therefore, the targeted life of the system (2). Another goal of this test program is to demonstrate that zinc-chloride systems can operate for an extended period with no electrolyte maintenance.

SYSTEM DESCRIPTION

Although the 1.7-kWh cell was built in early 1976, several components in the battery stack represent state-of-the-art zinc-chloride technology. These components are the dense-graphite zinc-electrode substrates, the Union Carbide PG-60 porous-graphite chlorine-electrode substrates, the dense-graphite buses, and the interference fit between the electrode substrates and the bus.

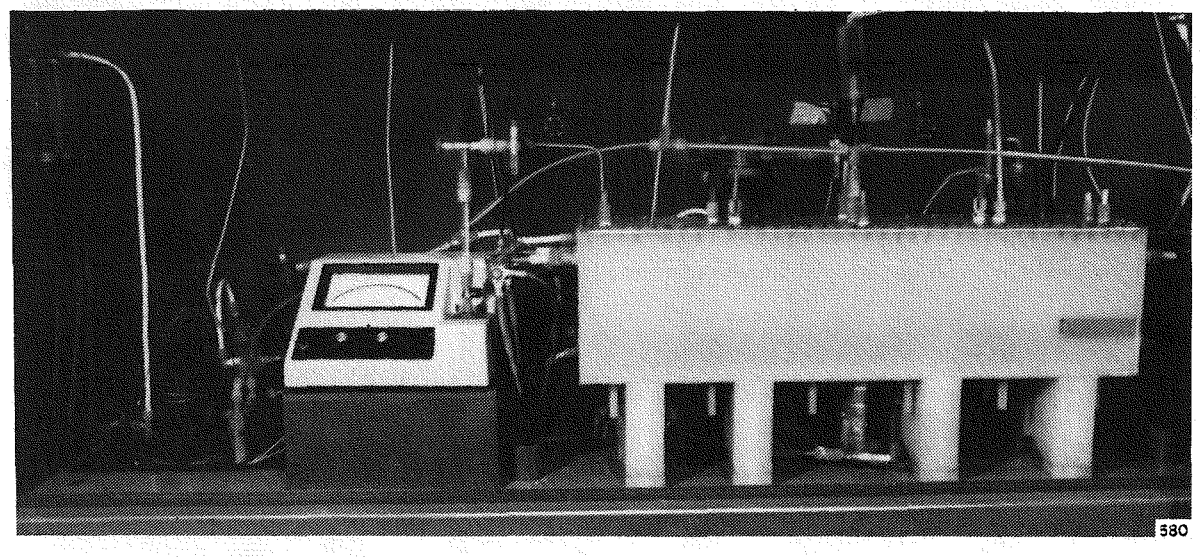

Figure 21-1. Photograph of 1.7-kWh battery system installed in laboratory hood.

The 1.7-kWh system simulates a full-scale battery module in that it is compartmentalized into a stack and a store. The stack shown in Figure 21-2 is the site of the electrochemical reaction. The outer case forms the electrolyte sump at the bottom, holds the two cell trays, and defines the system's major gas space at the top. Each tray of 48 cells is made up of 48 chlorine-electrodes and 25 zinc-electrodes. Twenty-three of the zinc electrodes are active on both sides, while the two electrodes at either end of the cell assembly are active only on the inside face. The total area for the chlorine electrodes is 6194 cm^2 and the inter-electrode cell gap is 0.33 cm (3).

As illustrated in Figure 21-3, the inactive faces of the chlorine electrodes are mated in pairs to form a cavity for the distribution of the electrolyte to the active faces of the cells. Electrolyte flows from the sump, through an external loop into the manifold, through the pairs of chlorine electrodes, and past the zinc electrodes. It then overflows the stack area and falls back by gravity into the sump. This flow pattern allows the liberation of a constant supply of zinc and chlorine from the electrolyte for the electrochemical reaction in the stack area during charge, and it introduces the chlorinated electrolyte during discharge to permit the electrochemical recombination of the two elements.

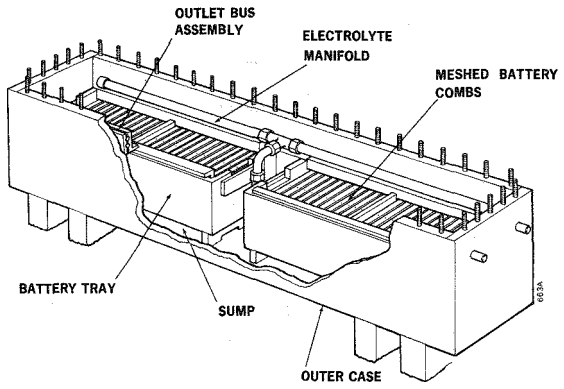

Figure 21-2. Cutaway drawing of the 1.7-kWh stack unit. Outer case serves as electrolyte sump and defines major gas space in system. Outer case cover not shown.

Figure 21-4 is a photograph of a section of the stack area that shows the chlorine electrode pairs, with gas vents to prevent gas locking, and the zinc electrodes. Figure 21-5 is a diagram of a similar portion of the stack area showing both the buses and a por-

tion of the electrolyte manifold, in addition to the electrodes.

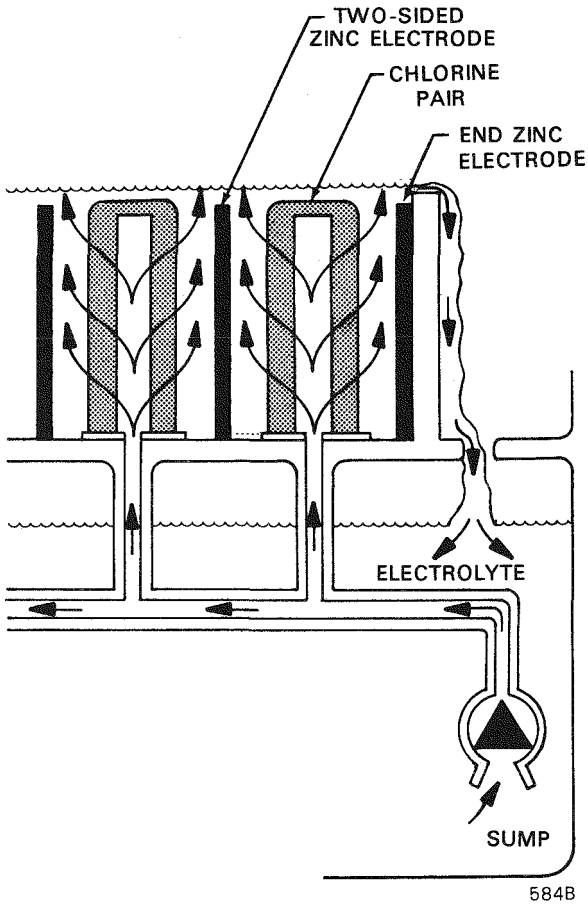

Figure 21-3. Schematic representation of chlorine electrode pair and zinc electrode showing electrolyte flow path.

The operation of the 1.7-kWh system is contingent upon a network of auxiliary components. The system schematic diagram in Figure 21-6 illustrates the relationships of these components to the stack. Their operation can best be characterized by describing the four main loops: the electrolyte loop, the gas loop, the hydrogen recombination loop, and the hydrate decomposition loop.

Electrolyte, Loop 1. The main electrolyte loop begins at the bottom of the case where the electrolyte flows out of

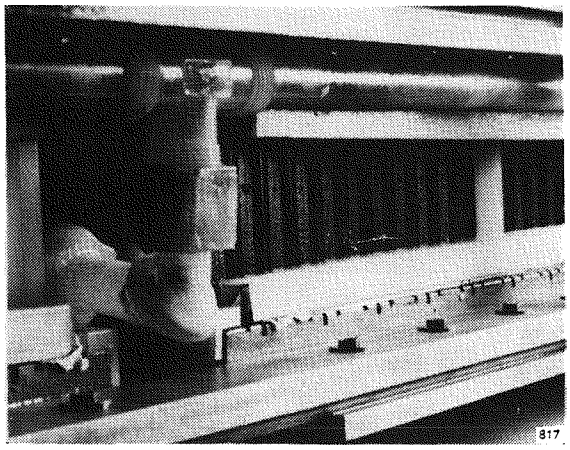

Figure 21-4. Photograph of a section of the 1.7-kWh battery stack area showing zinc and chlorine electrodes. Note vent holes in chlorine electrode pairs.

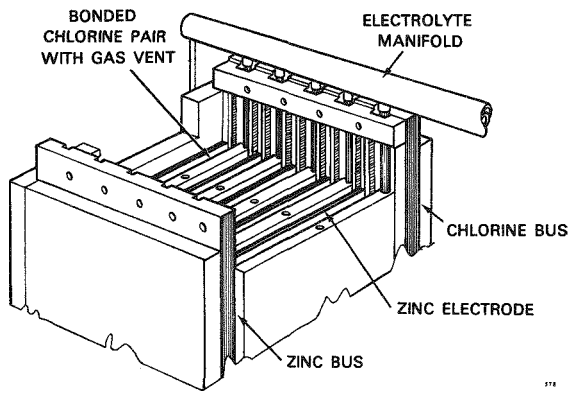

Figure 21-5. Section of 1.7-kWh battery stack showing construction details.

the sump through the electrolyte pump and into a heat exchanger to establish isothermal flow. During discharge only, chlorine gas is injected into the stream by a micropump. The flow then enters a mixer (gas absorber) to chlorinate the electrolyte and passes through a gas separator that removes the excess chlorine, which returns to the stack gas space. The chlorinated electrolyte re-enters the battery case into the distribution manifold. A small amount of electrolyte is continuously pumped through a spectrophotometer that measures the chlorine concen-

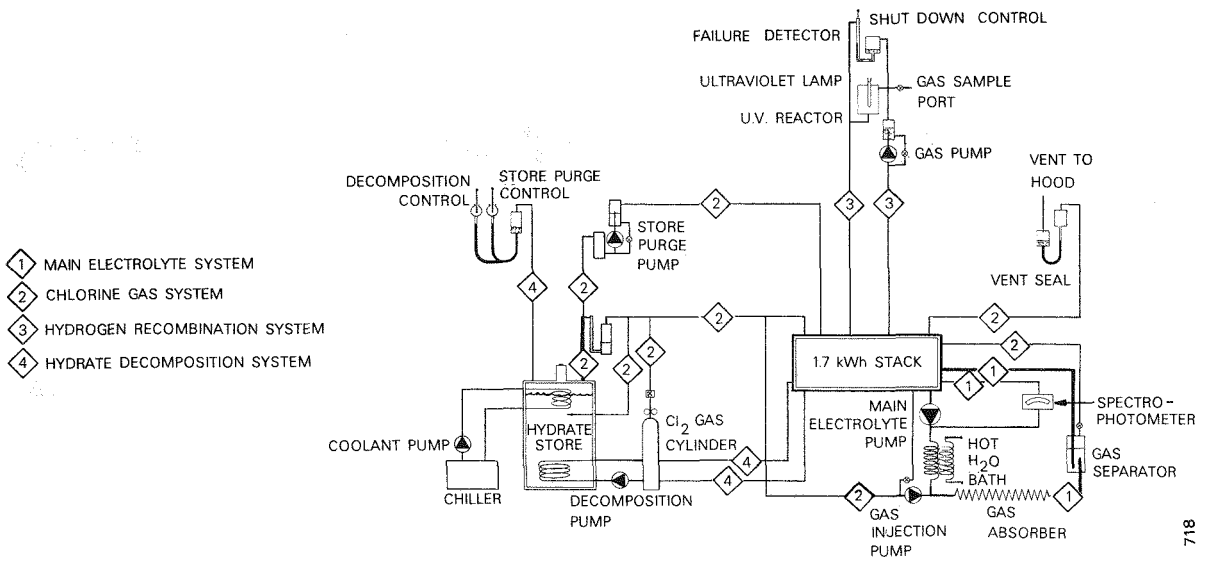

Figure 21-6. Schematic diagram of the 1.7-kWh battery system with four numbered subsystems.

tration. The electrolyte capacity required to maintain the desired range of zinc molarity for a 5-hour charge is 15 liters. The electrolyte flow rate is 1.86 ml/min-cm^2 (12 ℓ/min).

Gas Systems, Loop 2. During charge, gas leaves the top of the stack and flows into the store via the inlet tube located below the liquid level. The store purge pump, controlled by a manometer, runs as necessary during charge to maintain a differential pressure between the stack and the store. The heated chlorine inlet tube is positioned above an agitator that mixes the chlorine with cold store water to form chlorine-hydrate which settles to the bottom as it is formed. On discharge, chlorine evolved from decomposition of the chlorine-hydrate passes through the upper exit tube, through the differential manometer, and back toward the stack where it is drawn to the gas absorber by the gas injection pump. An auxiliary chlorine tank is tied directly to this gas line for use during the latter stages of discharge when hydrate is no longer available. A second differential manometer is connected to the gas space area of the stack to prevent excessive pressure on the stack case. The total gas volume of the system is 18 liters.

Hydrogen Recombination, Loop 3. A micropump draws gas from the battery case at the rate of 10 ℓ/minute and pumps the gas through a chamber containing two ultraviolet lights. These lights recombine any free hydrogen evolved from the zinc electrode, with the chlorine.

Chlorine Storage, Loop 4. During discharge, warm electrolyte from the battery is circulated through a coil in the bottom of the store by a micropump to heat and thereby decompose the hydrate. Store pressure is sensed by a manometer to actuate a switch which controls the micropump to sustain the proper rate of hydrate decomposition.

SYSTEM OPERATION

Since initial testing of the 1.7-kWh system in early 1976, battery cycling has been conducted using the test conditions shown in Table 21-1. These conditions continue to be employed in order to generate a consistent data base of test results.

Table 21-1

1.7-kWh SYSTEM TEST CONDITIONS

	Charge	Discharge
Current, A	220	190
Curr. Dens., mA/cm^2	35.5	30.8
Time, h	5.0	5.8
[Cl_2], g/ℓ	1.3	1.4
Flow, ml/min-cm^2	1.86	1.86
Temp., °C	40	40
Pressure	ambient	ambient

A cycle was defined as a five-hour charge yielding an electrochemical energy efficiency of 60% or greater. A charge of less than 5 hours or an energy efficiency below 60% becomes a "run" that does not qualify toward meeting the life target of 2500 cycles. The standard cycling regime established at the onset of testing consists of the following phases:

1. Cooldown
2. Constant current charge
3. Turnaround
4. Constant current discharge
5. Constant voltage discharge
6. Cleanout

The cooldown phase precedes the five-hour charge phase in order to chill the store in preparation for chlorine storage. In the turnaround phase, the cell stands for a short period of time with the gas injection and main electrolyte pumps running to chlorinate the system preparatory to discharge. After a two-hour constant current discharge, the terminal voltage is maintained at 1.69 volts or above by reducing the current as necessary. This phase is terminated when the current has been reduced to 15 amperes. The battery is short-circuited in the cleanout phase to strip any plated zinc remaining on the zinc electrodes because zinc-on-zinc plating is not desirable in the load-leveling battery system. At first a stand phase was included after cleanout, but this was eliminated when operation was shifted from manual to automatic control.

DATA ACQUISITION AND CONTROL SYSTEM

The 1.7-kWh system was cycled manually for about one year until early 1977 when a microprocessor-based data acquisition and control system (DACS) was installed. The manual cycling regime was conducted for 8-10 hours a day, five days a week. Under automatic control, the system was expected to cycle 24 hours a day, 7 days a week with a minimum of human interference. Thus, in order to maintain a consistent data base, the controller had to be programmed to continue cycling in the mode established under manual control. It also had to provide for any contingencies that might arise when the system was unattended. A major concern was the failure of cell components or subsystems that could cause damage to the cell.

In addition to failure capabilities, the automatic controller was programmed to record data every five minutes. Under manual control, data such as current and voltage, was recorded once an hour. Other advantages of the DACS include a visual display and the ability to reduce and manipulate some of the data to provide additional information.

The data acquisition system consists of a standard 19-inch relay rack containing a microprocessor, a cathode ray tube (CRT) for data display, and all interfacing between the battery and its components. A printer terminal also is included in the system to retrieve data as hard copy for instant use and to record data on cassette tapes for later insertion into a data base, as discussed in Section 22. The tasks of this system are: cycling and auxiliary subsystem control; monitoring of operating parameters; collection and display of data; detection of and response to failures; and reduction of time, current, and voltage to amp-hours, watt-hours, and efficiencies. Figure 21-7 is a photograph of a CRT data display page that shows most of the important

parameters monitored. The top two-thirds of the display shows temperatures, voltages, currents, cumulative amp-hours and watt-hours, phase number, time remaining in that phase, time of day, and the date. The bottom of the screen is a display of the active components such as level detectors, pumps, solenoids, and heaters.

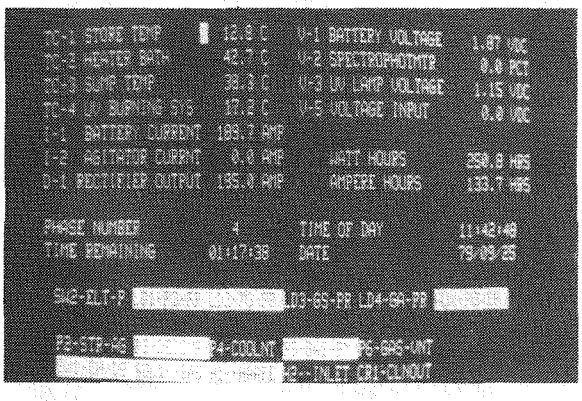

Figure 21-7. Photograph of a CRT data display page showing most of the important parameters monitored by the data acquisition and control system.

Figure 21-8 is a photograph of the CRT display page for efficiency. The current cycle energy efficiency is derived by dividing current cycle discharge watt-hours by current cycle charge watt-hours. It is low in this display because the photograph was taken early in the discharge phase. The microprocessor also calculates and maintains a record of the accumulated electrochemical energy, coulombic and voltaic efficiencies.

RESULTS AND DISCUSSION

A plot of efficiency as a function of cycle number for the first 1000 cycles is shown in Figure 21-9. The performance parameter of greatest interest in this program is voltaic efficiency because it can indicate degradation of the chlorine electrodes. As can be seen, over the duration of cycles, there has been an apparent decline in voltaic efficiency of 1%. Secondly, there is a reciprocal relationship

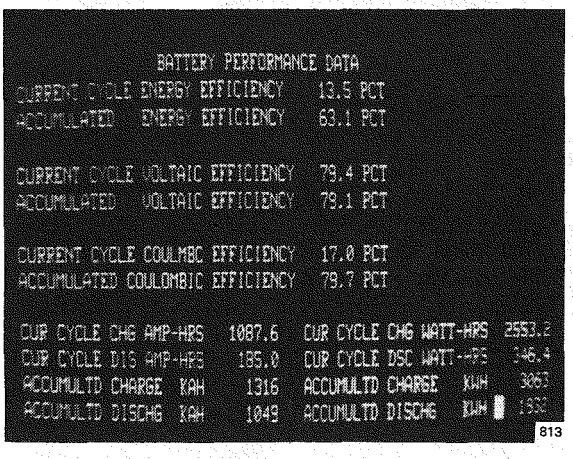

Figure 21-8. Photograph of a CRT data display page showing efficiencies monitored by the data acquisition and control system.

between the coulombic and voltaic efficiencies. This occurs because conditions that tend to optimize one of them tend to decrease the other in the zinc-chloride battery. As can be seen in the figure, a slight loss in electrochemical energy efficiency has occurred over the period of 1000 cycles. Therefore, bivariate linear regressions were run comparing energy efficiency to the voltaic and coulombic efficiencies to attempt to make a correlation for this 2% loss (from 65-63%). It was found that there was a greater correlation between energy efficiency and coulombic efficiency than there was with voltaic efficiency. Therefore, it is felt that most of the losses in energy efficiency (ε_e) were due to coulombic efficiency (ε_c) losses rather than voltaic efficiency (ε_v) losses. The average efficiencies for the first 1000 cycles are: electrochemical energy - 63.1%, voltaic - 79.1%, and coulombic - 79.7%.

Late in 1979 another test was performed to ascertain the stability of the system's voltaic performance by comparing it to a single-cell design incorporating the flat-plate technology of 1979. Figure 21-10 compares cell voltage versus current density for the two systems, whose voltages were taken by

probe at their respective chlorine electrodes. As can be seen, the voltaic performance of the 1.7-kWh system made with 1976 technology is almost equivalent to the single cell. One possible explanation for this near-equivalent performance is that the electrodes have become more active as they have aged. Interestingly, the electrode activation process for the 1.7-kWh electrodes was only one-fourth of the time that is now considered optimal. It has been concluded that the apparent 1% loss in voltaic efficiency in the 1.7-kWh system is probably due to deterioration of the electrode-to-bus contact. An important measure of the system is the fact it has consistently delivered an average energy of 1.62 kWh over the entire 1000 cycles. A graph of this performance parameter is included as Figure 21-11.

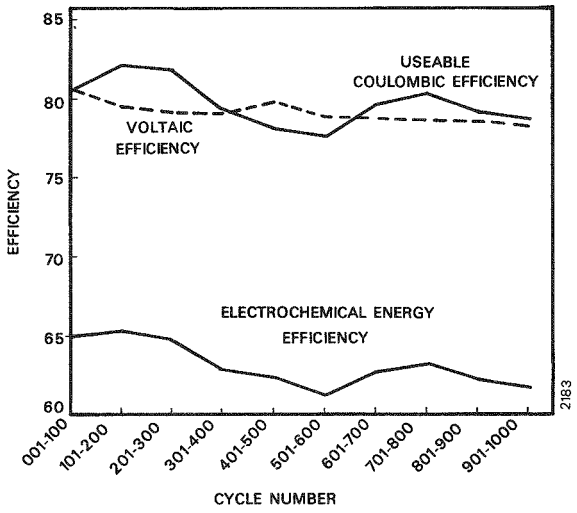

Figure 21-9. Performance efficiencies of the 1.7-kWh system plotted against cycle number.

During almost four years of cycling, only one performance degradation mode has been identified in the system. It has occurred six times and in each case the gas vent holes in some chlorine-electrode pairs became plugged with an unknown substance. These occurrences were accompanied with an average decrease in energy efficiency of 3.3%. However, the energy efficiency regained its previous level after removal of the plugs. Several types of analyses were run to determine the composition of the blockage material and Table 21-2 shows the results of the elemental analysis. It was concluded that the source of the substance was probably one or more of the plastic materials used in the battery. This conclusion is based on the fact that fluorine is the only element identified that would not be expected to occur within the system during normal battery operation.

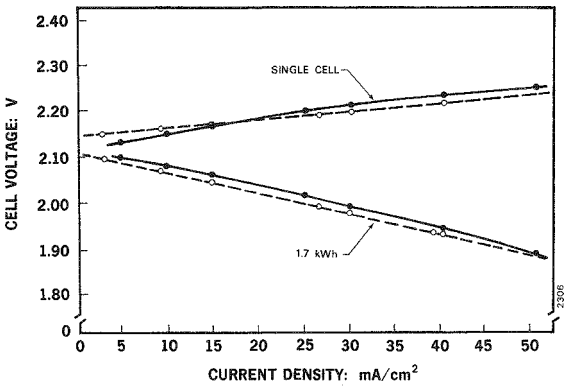

Figure 21-10. Comparison of voltaic performance of the 1.7-kWh system utilizing early 1976 technology and a single-cell incorporating 1979 technology.

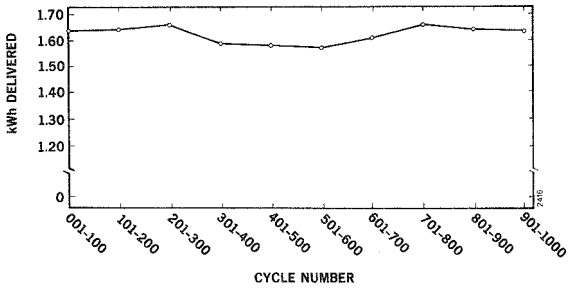

Figure 21-11. Delivered energy of the 1.7-kWh battery system as a function of cycle number.

There are three possible sources of fluorine: polyvinylidene fluoride (manufactured under the tradename Kynar), which is used for the stack-sump case as well as for tube connectors; polytetrafluoroethylene (tradename Teflon, TFE), which is used for tubing and pump gears; and a specialized form of TFE, Gortex, which is used as the top inside seal for the battery case.

Table 21-2

ELEMENTAL ANALYSIS OF UNKNOWN MATERIALS

Material	Percent of Material
Carbon	16.5
Hydrogen	00.8
Nitrogen	00.5
Fluorine	06.6
Chlorine	32.0

During the 1000 cycles, the electrolyte was changed 35 times, either to improve battery performance or to correct conditions resulting from failures of auxiliary components. Most of the changes were forced by auxiliary component failures. However, 138 of these cycles were completed without requiring a change of electrolyte.

The first thousand cycles of the 1.7-kWh battery system represented 40% of the cycle life targeted for a commercial load-leveling battery and was a significant demonstration of the stability of the porous-graphite chlorine electrodes. The demonstration continues with over 50% of the life goal having been reached at this writing. By internal inspection and by inspection of electrode voltage data, it is known that the chlorine electrodes are still sound; and there is every reason to believe that the target life of 2500 cycles will be achieved.

REFERENCES

1. Development of the Zinc-Chlorine Battery for Utility Applications. Palo Alto, Calif.: Electric Power Research Institute, April 1979. EM-1051, Part I, Section 1, p. 3.

2. Ibid., Part IV, Section 28, pp. 2-3.

3. Development of High-Efficiency, Cost-Effective, Zinc-Chlorine Batteries for Utility Peak-Shaving, 1976. Palo Alto, Calif.: Electric Power Research Institute, March 1978. EM-711, Part III, Section 3, pp. 2-8.

Section 22

DATA-BASE MANAGEMENT SYSTEM FOR THE 1.7-kWh SYSTEM

ABSTRACT

Continuous acquisition of data by the microprocessor controlling life testing of the 1.7-kWh cell system presented an immediate need for a standardized method of data organization, reduction, and analysis. To meet this need, a data base using the data-base management system (DBMS) of National CSS has been established. This report describes the application of this system to the organization, maintenance, and analysis of the data acquired from the 1.7-kWh cell system. Examples are included to demonstrate its capabilities. Favorable experience with the system has led to the planning of similar data bases for the 45-kWh EPRI module, the BEST prototype modules, and those to be produced in the pilot production plant in Greensboro, North Carolina.

INTRODUCTION

Extensive testing of the zinc-chloride load-leveling battery module is required before commercial production of the system can begin. The large amount of data generated from this testing will be used to characterize the operation of the battery, determine optimum operating conditions, and provide reliability information about components within the battery module. Use of the acquired data to accomplish these goals will be facilitated by a data-base management system (DBMS).

In the past, computer-assisted methods of storing and analyzing large amounts of data isolated the user from his data. The user's access to his data files was always through the services of a computer programmer who developed specialized programs to produce the reports desired. Further, the lack of central data management led to independent data files and duplication of data among these files.

The appearance of data-base management technology in the early 1970s was a response to the need for a closer interaction between the end-user, his data, and the computing system resources. With a DBMS, all the data is contained in one centralized data-base file which the user can access with simple commands. This enables efficient management of data directly by the end-user who may have little knowledge of computer programming.

This presentation describes the application of a DBMS to the organization and analysis of scientific data related to testing and evaluation of the 1.7-kWh zinc-chloride battery. This battery system is naturally suited for a demonstration of the capabilities of a DBMS because of the large amount of data continually generated by its microprocessor controller.

The data management facility of National CSS, Inc. was chosen by EDA for this application. Referred to as NOMAD, this software package is one of several data-base management systems offered by the remote-computing industry. NOMAD operates within the IBM 360/370 environment and contains its own high-level command language with a procedural facility for complex processing requirements.

The NOMAD data-base management system can be discussed in relation to the three main areas of data-base manage-

ment: organization, maintenance, and report generation. Data-base organization refers to the data structure, which is the order of storing data items in relation to each other. Maintenance refers to entering, rearranging, or deleting data in the data base. Finally, report generation refers to data access, which is the process whereby the end-user obtains selected information from the data base in various forms of computer printout, such as tables and graphs.

DATA-BASE ORGANIZATION

The first step in the construction of a data base is the determination of the data items to be included in the data base. This step will be illustrated by examining the data-collection methods used in the 1.7-kWh system.

For this system, a microprocessor-based data acquisition and control system cycles the battery repeatedly through runs consisting of six phases as shown in Table 22-1. Once the hydrate store has cooled to the required temperature, the microprocessor terminates phase 1 and initiates phase 2 to charge the battery for five hours. After a short turnaround period, phase 3, the microprocessor initiates discharge of the battery at constant current, phase 4, and then continues discharge at constant voltage, phase 5, until a preset battery current and voltage is reached. Any remaining zinc deposits are then removed during phase 6.

Not only does the microprocessor control the battery operation, but it also performs the task of data acquisition. A set of data is recorded at the occurrence of every phase change and at five-minute intervals within each phase. The format for these two types of data sets is shown in Table 22-2. A phase change data set is denoted by the letter P and time data sets by the letter T. The data items that are sampled in each type of data set and their corresponding abbreviations in the printout can be found in Table 22-3. Since approximately 5000 data points are recorded in a 24-hour period, the task is to reduce and organize this collection of data in a way that will facilitate effective analysis.

Table 22-1

PHASE SEQUENCE FOR 1.7 kWh-BATTERY RUN

Phase Number	Description	Time
1	Hydrate store cooled to 5°C	6 min
2	Constant current charge - 35.5 mA/cm^2	5 h
3	Turnaround	6 min
4	Constant current discharge - 30.8 mA/cm^2	2 h
5	Variable current discharge (constant voltage)	2.5 h
6	Cleanout	1.5 h

The next step in the construction of the data base is to determine the data structure, or the manner in which the data will be stored. This structure may be defined as relational or hierarchical. Figure 22-1 shows that the data from cycling battery systems naturally leads to a combination of these two forms. The data is divided into three classes, and these classes form the hierarchy. Data that characterize a particular run are on the highest level. Items such as the run number (RN) and system efficiencies (CE, EE, WE) are members of this class. The next level consists of information that characterizes each phase in the run such as the phase number (PH) and the time of day (TM) at the start of the phase. Finally, information that characterizes each five-minute interval is contained in the lowest level.

Table 22-2

DATA PRINTOUT
FROM 1.7-kWh MICROPROCESSOR

```
P
PH=   1     V1=  0.01   I1=   0.2   D1=79/03/21 TM=03:36:29 CK=  3548
RN=1082     HC=   0.0   HD=   0.0   CW=   0.0   DW=   0.0   DK=  2195
CE=   0.0   EE=   0.0   WE=   0.0   AC=  1505   AD=  1186

T
TM=03:37:32 V1=  0.01   I1=   0.3   D1=79/03/21 PH=   1     T1=   9.4
TR=00:00:00 HC=   0.0   HD=   0.0   V2=   5.1   V3=  1.46   V5=   4.5
CE=   0.0   EE=   0.0   WE=   0.0   T3=  35.0   T2=  40.6

P
PH=   2     V1=  0.01   I1=   0.2   D1=79/03/21 TM=03:41:47 CK=  3548
RN=1082     HC=   0.0   HD=   0.0   CW=   0.0   DW=   0.0   DK=  2195
CE=   0.1   EE= 100.0   WE=   0.1   AC=  1505   AD=  1186

T
TM=03:42:32 V1=  2.38   I1= 221.2   D1=79/03/21 PH=   2     T1=   5.1
TR=04:59:15 HC=   2.7   HD=   0.0   V2=   5.3   V3=  1.45   V5=   4.5
CE=   0.0   EE=   0.1   WE=   0.0   T3=  34.6   T2=  40.5

T
TM=03:47:32 V1=  2.38   I1= 221.2   D1=79/03/21 PH=   2     T1=   5.1
TR=04:54:16 HC=  21.1   HD=   0.0   V2=   4.8   V3=  1.46   V5=   4.6
CE=   0.0   EE=   0.1   WE=   0.0   T3=  34.7   T2=  40.8

T
TM=03:52:32 V1=  2.39   I1= 221.0   D1=79/03/21 PH=   2     T1=   5.3
TR=04:49:15 HC=  39.6   HD=   0.0   V2=   4.8   V3=  1.46   V5=   4.6
CE=   0.0   EE=   0.1   WE=   0.0   T3=  34.8   T2=  40.6

T
TM=03:57:32 V1=  2.39   I1= 221.7   D1=79/03/21 PH=   2     T1=   5.2
TR=04:44:16 HC=  58.0   HD=   0.0   V2=   5.1   V3=  1.45   V5=   4.6
CE=   0.0   EE=   0.1   WE=   0.0   T3=  34.7   T2=  40.5

T
TM=04:02:32 V1=  2.39   I1= 221.7   D1=79/03/21 PH=   2     T1=   5.3
TR=04:39:15 HC=  76.5   HD=   0.0   V2=   4.8   V3=  1.45   V5=   4.6
CE=   0.0   EE=   0.1   WE=   0.0   T3=  35.0   T2=  40.7

T
TM=04:07:32 V1=  2.39   I1= 221.4   D1=79/03/21 PH=   2     T1=   5.0
TR=04:34:15 HC=  94
>
```

The three levels in the hierarchy are linked through the use of a key item which has values that are unique within the data base. Each key item is dependent upon the one in the level above it. On the highest level, the key item is the run number. For example, there can be only one run #1000 in the data base. On the next level, the key item is phase number. There can be only one phase 1 corresponding to cycle #1000. On the lowest level, the key item is an index number assigned sequentially to each five-minute interval data set in each phase.

The relational aspect of the data-base structure arises from the fact that all items on the same level possess a one-to-one correspondence with their key item. That is, for run #1000 there is only one date, one energy efficiency, etc.

The design of a data base is a trade-off between data storage space and data retrieval times. The disadvantage of a hierarchical database becomes obvious when information is constantly requested from the lowest levels. For access to the lowest levels, NOMAD must search through each level, from the highest to the lowest, to obtain the data. This approach uses more computer process time than would be the case with a relational data base, and this translates into increased costs.

Table 22-3

1.7-kWh DATA PRINTOUT SYMBOLS
FOUND IN PHASE AND TIME DATA SETS

PHASE

PH	Phase
V1	Voltage
I1	Current
D1	Date
TM	Time
CK	Accumulated Charge kWh
RN	Run Number
HC	Charge Ah
HD	Discharge Ah
CW	Charge Wh
DW	Discharge Wh
DK	Acc. Discharge kWh
CE	Coulombic Eff.
EE	Voltaic Eff.
WE	Energy Eff.
AC	Acc. Charge kAh
AD	Acc. Discharge kAh

TIME

TM	Time
V1	Voltage
I1	Current
D1	Date
PH	Phase
T1	Store Temp.
TR	Time Remaining in Phase
HC	Charge Ah
HD	Discharge Ah
V2	Spectrophotometer
V5	UV Lamp Voltage
CE	Electrolyte pH
EE	Coulombic Eff.
WE	Voltaic Eff.
T3	Energy Eff.
T2	Electrolyte Temp.
T2	Heater Bath Temp.

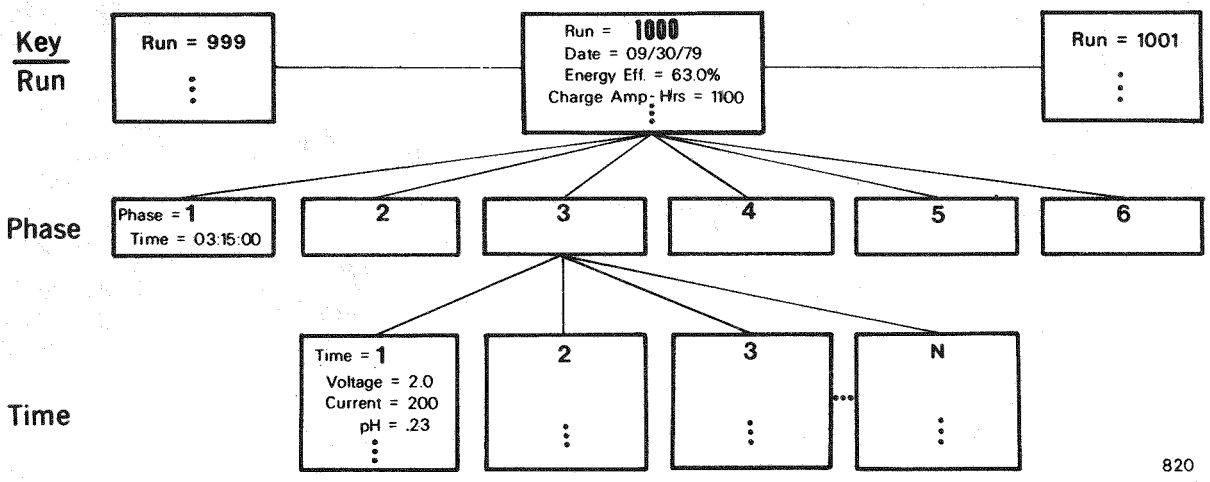

Figure 22-1. Hierarchical structure of 1.7-kWh data base showing key items (run, phase, time) and typical data items for each of the three levels.

In a relational data base, there are no levels to be searched. However, substantially more data storage space, and thereby higher cost, is required to obtain the same data information. Since there are no key items to link a particular five-minute data set to a particular phase and run, a value for phase and run along with the other data, such as efficiency and phase start-time, must be stored along with the information contained in each data set. That is, complete identification of the information is required for each set of data.

Since the data base for the 1.7-kWh battery cell system is a combination of the hierarchical and relational forms, it represents a compromise between the data storage costs and database search time. Once the data-base structure is fixed, it is formulated in a file which is called the schema in data-base terminology. In this schema, the data items are specified in item statements while the logical and structural relationships of these items are defined in segment and master statements.

DATA-BASE MAINTENANCE

Data contained in computer files may be stored on a disk or on magnetic tape, the choice being a compromise between ready access to data on a disk and the much lower cost of tape storage. Because files can be manipulated or edited only when they reside on the disk, any file stored on tape must be moved to the disk to be used.

Two forms of the 1.7-kWh data base have been created to take advantage of the low cost of tape storage while providing easy access to data most frequently needed. A complete data base containing all of the 1.7-kWh data is stored on tape while a condensed form of the data base is stored on the disk. The condensed data base contains averages, maximums, minimums, and standard deviations of the monitored parameters for each phase of each run, whereas the complete data base includes the values for all parameters at five-minute intervals throughout a run. The comparatively small amount of storage space required by the condensed data base makes disk storage economically practical.

Entering data into both forms of the 1.7-kWh data base involves the transfer and storage of data as shown in Figure 22-2. Raw data obtained by the microprocessor is initially recorded on digital cassette tape and then transmitted to the NCSS disk system. Although each cassette tape contains information

characterizing several runs of the battery system, a separate temporary raw data file is established on the disk for each run.

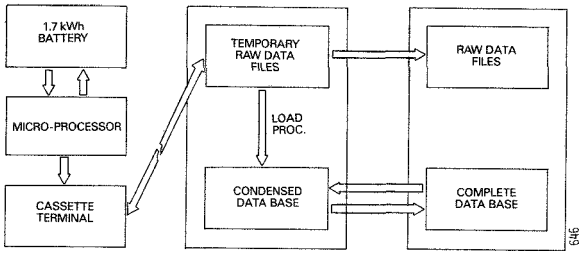

Figure 22-2. Flow of data for maintenance of data base.

The complete data base is moved to the disk, and then a load procedure, acting upon the temporary raw data file, is used to enter data from the raw data file into both versions of the data base. This procedure consists of a series of logical commands that are understood by NOMAD. Values for data items defined in the schema are obtained from each data set in the data file and placed into the data base according to the schema structure. While the schema gives the data base form, the load procedure gives it content.

The load procedure also performs the task of data reduction. For example, the microprocessor records the run date in every data set. The load procedure extracts the date only once and then ignores it in the following data sets.

As the load procedure duplicates the data it places into the data base the raw-data file remains intact. This raw-data file and the updated complete data base which are no longer of immediate use, are copied onto less costly NCSS tape and erased from the disk space. In this way these files are retained for future reference at a lower cost, while the condensed data base is immediately available.

REPORT GENERATION

The principal objective of a DBMS is to allow the end-user to easily manipulate and examine a large collection of data so that it becomes a valuable tool in data analysis. Several brief examples, using the data base for the 1.7-kWh battery system, will serve to illustrate the ease with which data can be accessed and analyzed using the Nomad system.

Example 1: One important use of a DBMS for battery testing is to provide an information summary for each run. Using the LIST command, Table 22-4, giving summary information for each phase and for the entire run, can be easily produced. A printout summarizing the entire data base also is easily obtainable. For example, Table 22-5 gives such a summary characterizing the runs contained in the entire data base. In addition to the average efficiencies and the number of runs, the maximum and minimum values also are displayed.

Table 22-4

RUN 1020 SUMMARY

CYCLE NO.	ENRGY EFF	VOLT EFF	COUL EFF	FULL PWR ENRGY EFF	FULL PWR VOLT EFF	FULL PWR COUL EFF	DIS AMP-HR	CHARGE AMP-HR
861	61.4	78.4	78.3	58.2	78.6	74.0	863.2	1101.8

PHASE	PHASE START TIME	MAXIMUM BATT VOLT	MINIMUM BATT VOLT	MAXIMUM BATT CURR	MINIMUM BATT CURR	AVG STORE TEMP.	AVG SUMP TEMP.	AVG PH
1.0	07:42:56	0.00	0.00	0.4	0.2	8.5	35.9	0.63
2.0	07:49:38	2.38	2.35	221.0	219.9	5.1	37.8	0.38
3.0	12:49:39	2.14	2.14	0.0	0.0	10.9	34.1	0.43
4.0	12:55:40	1.91	1.86	189.5	188.8	12.5	35.2	0.52
5.0	14:55:41	1.88	1.71	189.7	10.0	13.1	39.1	0.60
6.0	18:05:20	1.22	0.00	0.4	0.1	14.3	37.6	0.62

Table 22-5

DATA-BASE SUMMARY

AVG ENRGY EFF	MAX ENRGY EFF	MIN ENRGY EFF	AVG VOLT EFF	MAX VOLT EFF	MIN VOLT EFF	AVG COUL EFF	MAX COUL EFF	MIN COUL EFF	CNT NO. RUNS
62.5	64.7	55.7	78.6	79.6	76.2	79.5	81.9	71.2	94

Example 2: A useful NOMAD feature allows the definition of items that are not contained in the data base. For example, Table 22-6 shows the range of full power efficiencies which were defined and then calculated from information in the data base. The range was defined in the LIST command as the difference between the maximum and minimum values.

Table 22-6

FULL POWER EFFICIENCY

AVERAGE FULL PWR ENRGY EFF	RANGE OF FULL PWR ENRGY EFF	AVERAGE FULL PWR VOLT EFF	RANGE OF FULL PWR VOLT EFF	AVERAGE FULL PWR COUL EFF	RANGE OF FULL PWR COUL EFF
58.9	13.4	78.8	3.4	74.7	17.8

Example 3: Logical groups of data can be formed easily, as shown in Table 22-7. First, there is a list of runs that did not qualify as cycles because the energy efficiency of the battery system was below the required 60%. Next, there is a list of runs in which a failure occurred, and the time of occurrence is recorded. Finally, the last column shows those runs in which there was a pH adjustment.

Table 22-7

LOGICAL GROUPS

RUNS WITH ENRGY EFF BELOW 60.0%	RUNS WITH FAILURE OCCURENCE	TIME OF FAILURE	RUNS WITH PH ADJUST
1181	840	21:12:34	910
1182	903	03:09:22	924
1183	904	14:53:52	928
1184	920	14:07:01	947
	961	12:00:05	951
	961	08:57:27	955
	1010	08:34:03	971
	1051	17:29:54	975
	1051	17:28:41	1010
	1051	17:30:32	1014
	1203	16:28:37	1020
	1204	04:29:04	1070
	1204	10:25:12	1073
	1205	16:53:18	

Example 4: Another powerful feature of NOMAD makes it possible to selectively access certain portions of the data base that meet specified criteria. As previously shown in Table 22-6, the average full-power coulombic efficiency for all the data-base runs is 74.7%. Dividing the data base into two groups results in the output found in Tables 22-8 and -9. Table 22-8 contains information on those runs with the full-power coulombic efficiency greater than the average. Table 22-9 contains information on those runs with full-power coulombic efficiency equal to or less than the average.

In Tables 22-8 and -9 the average ampere-hours delivered during three intervals during discharge are displayed. While there is no difference between the two groups in the number of ampere-hours delivered two hours into discharge (first column), there is a noticeable difference in the full-power and total ampere-hours delivered. This is expected since the groups are segregated by full-power coulombic efficiency and the average number of ampere-hours acquired during charge is the same for both groups.

Table 22-8

RUNS WITH FULL POWER COULOMBIC EFFICIENCY ABOVE AVERAGE

AVERAGE PHA 4 AMP-HRS	AVERAGE FULL PWR DIS AMP-HRS	AVERAGE DISCH AMP-HRS	AVG DIFF	AVERAGE CHARGE AMP-HRS	AVERAGE FULL PWR COUL EFF	AVERAGE COUL EFF
380.8	838.6	887.3	48.7	1106.1	75.8	80.2

Table 22-9

RUNS WITH FULL POWER COULOMBIC EFFICIENCY EQUAL TO OR BELOW AVERAGE

AVERAGE PHA 4 AMP-HRS	AVERAGE FULL PWR DIS AMP-HRS	AVERAGE DISCH AMP-HRS	AVG DIFF	AVERAGE CHARGE AMP-HRS	AVERAGE FULL PWR COUL EFF	AVERAGE COUL EFF
379.8	808.4	868.1	59.7	1106.5	73.1	78.5

It is interesting to note that, while a 2.7% difference exists in the average full-power coulombic efficiencies between the groups, only a 1.7% difference is found in the average total coulombic efficiency. This means that the group of runs with the lower full-power coulombic efficiencies gained 1% in coulombic efficiency during variable current discharge, which is the period between full power and total discharge. This is shown in the number of ampere-hours delivered (AVG DIFF) during this period. The runs with the lower than average full-power coulombic efficiencies tend to deliver more ampere-hours during variable current discharge than those runs with a higher average full-power coulombic efficiency. Data-base systems assist greatly in making observations such as this which characterize the operation of the battery.

NOMAD INTERFACES

NOMAD also interfaces with a statistical software package to permit using the data base for a wide range of statistical and correlation studies. This can be demonstrated by the following example: Dividing the data base into two groups, above and below the average full-power voltaic efficiency, results in the output shown in Tables 22-10 and -11. Since the pH is consistently higher in the group with the lower average full-power voltaic efficiency, a correlation between pH and voltaic efficiency is a possibility. In addition, the pH range in each phase is very nearly the same for both groups indicating no correlation between range and full-power voltaic efficiency. To test these assumptions, the correlation matrix in Table 22-12 is easily produced. The first column of this table shows that the correlation coefficients for voltaic efficiency (VEFF) relative to several pH parameters range from 0.06 to 0.108. As correlation coefficients may range from 1.00 (perfect correlation) to -1.00 (perfect inverse correlation) with values close to 0.00 indicating an absence of correlation, the low values in this table signify that there is no correlation between voltaic efficiency and pH.

Table 22-10

RUNS WITH VOLTAIC EFFICIENCY ABOVE AVERAGE

AVERAGE FULL PWR VOLT EFF	PHASE	AVG PH FOR ALL RUNS DURING PHA	AVERAGE MAX PH	AVERAGE MIN PH	AVERAGE RANGE
79.2	1	0.33	0.33	0.33	0.01
	2	0.36	0.41	0.32	0.09
	3	0.40	0.40	0.39	0.00
	4	0.38	0.47	0.30	0.17
	5	0.41	0.48	0.35	0.13
	6	0.43	0.47	0.40	0.08
		0.39	0.43	0.35	0.08

Table 22-11

RUNS WITH VOLTAIC EFFICIENCY AT OR BELOW AVERAGE

AVERAGE FULL PWR VOLT EFF	PHASE	AVG PH FOR ALL RUNS DURING PHA	AVERAGE MAX PH	AVERAGE MIN PH	AVERAGE RANGE
78.5	1	0.44	0.44	0.44	0.00
	2	0.44	0.50	0.37	0.12
	3	0.46	0.46	0.46	0.00
	4	0.45	0.54	0.33	0.21
	5	0.49	0.59	0.40	0.19
	6	0.53	0.57	0.51	0.06
		0.47	0.52	0.42	0.10

Table 22-12

CORRELATION MATRIX

CORRELATION MATRIX

VEFF	1.000				
AVGPH	0.108	1.000			
MAXPH	0.108	0.917	1.000		
MINPH	0.093	0.859	0.694	1.000	
RANGEPH	0.060	0.446	0.719	-.001	1.000
	VEFF	AVGPH	MAXPH	MINPH	RANGEPH

VARIABLE	MEAN	STANDARD DEVIATION
VEFF	78.82446	0.50090
AVGPH	0.39106	0.15614
MAXPH	0.52904	0.19337
MINPH	0.24755	0.13568
RANGEPH	0.28149	0.14067

IMAS:>

NOMAD also interfaces with a program which gives the user a plotting capability. Table 22-13 was obtained by dividing the first 1000 cycles into 10 groups of 100 cycles each and computing the average efficiency for each group. This data was then displayed in graphical form in Figure 22-3 by using a single PLOT command. This command not only produces a graph of the data, but also allows the user great flexibility in labeling and axes size.

Table 22-13

1.7-kWh SUMMARY EFFICIENCIES

CYCLES	AVG ENRGY EFF	MAX ENRGY EFF	MIN ENRGY EFF	AVG VOLT EFF	MAX VOLT EFF	MIN VOLT EFF	AVG COUL EFF	MAX COUL EFF	MIN COUL EFF
001-100	64.9	68.2	60.3	80.6	84.1	77.7	80.5	84.2	73.0
101-200	65.3	67.3	61.1	79.5	83.6	78.0	82.1	84.9	77.1
201-300	64.7	67.4	61.1	79.1	81.9	75.7	81.8	85.2	78.4
301-400	62.8	66.0	59.8	79.0	80.5	75.3	79.4	85.0	75.0
401-500	62.3	64.3	60.0	79.8	80.7	78.4	78.1	80.7	74.8
501-600	61.2	68.4	60.0	78.9	80.0	75.0	77.6	87.0	75.3
601-700	62.7	66.8	60.1	78.7	81.9	76.2	79.6	84.5	74.7
701-800	63.2	65.7	60.4	78.7	79.8	77.0	80.3	83.7	75.9
801-900	62.2	63.7	60.0	78.6	79.4	76.8	79.2	81.2	76.6
901-1000	61.7	63.4	60.0	78.3	79.1	76.5	78.7	81.0	76.0
	63.1	66.1	60.3	79.1	81.1	76.7	79.7	83.7	75.7

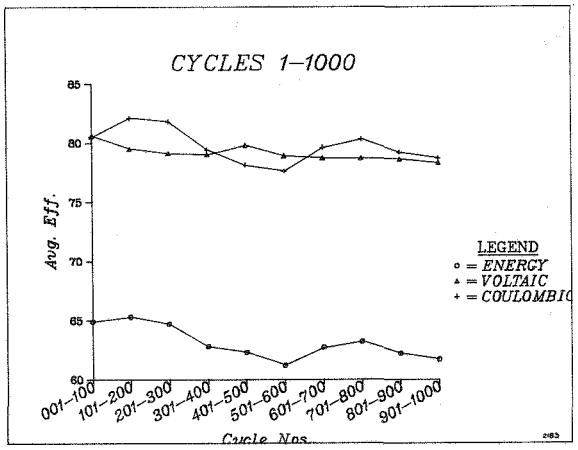

Figure 22-3. 1.7-kWh system efficiencies for cycles 1-1000.

DISCUSSION

A DBMS is a powerful tool that allows flexible and efficient analysis of large amounts of data. It is quite useful in the battery testing program for providing immediate summary information on a single run or over many runs to determine the operating characteristics of the battery. While using raw data and manual search in any of the previous examples would be extremely time consuming, relatively little effort was required with the DBMS.

The NOMAD data-base management system has been applied to the 1.7-kWh battery system not only to benefit from better management of data but also to gain experience in data-base management concepts. Confidence in the utility of a DBMS has led to planning for establishing data bases for the EPRI 45-kWh module, the BEST prototype modules, and the modules to be produced at the pilot plant in Greensboro, North Carolina.

Section 23

THE 1.7-kWh SYSTEM: CYCLES 1000-1250

ABSTRACT

In December 1979, the cycling rate of the 1.7-kWh battery stack was accelerated by a system modification to eliminate mechanical components that had, through repeated failure, caused an unacceptable loss of cycling time during the first 1000 cycles. By eliminating the hydrate store and relocating the hydrogen-chlorine recombination light to a new case top, many failure-prone components were removed from the system without altering test conditions for the stack. Comparison of cycling data before and after the modification shows a significant increase in operating time and in the percentage of runs that qualify as cycles toward the 2500-cycle life goal.

INTRODUCTION

After experiencing long-term continual maintenance difficulty caused by failures unrelated to cell performance, the decision was reached to modify the 1.7-kWh system to improve its reliability. System leaks and failures of auxiliary components had accounted for excessive downtime seriously impeding progress toward reaching the 2500-cycle goal of the life test. Except for occasional blocking of chlorine-electrode vent holes (see Section 21), some electrolyte degradation, and leaks in the case top seal, the stack had been essentially trouble-free compared to the other components of the system. As many of the failure-prone components and many of the fittings that were difficult to seal were associated with the hydrate formation process, elimination of the hydrate store offered the main opportunity to remove components that contributed nothing to the purpose of the test -- life testing of graphite electrodes.

Therefore, elimination of the hydrate store was the basic approach taken to increase system reliability without changing the test conditions for the stack. The modified system employs venting of evolved chlorine during charge and supplying cylinder chlorine during discharge as the substitute for the hydrate formation and decomposition process.

The modified system is described in this section with appropriate reference to the original system for comparison. Results in terms of operating experience since the modification in November-December 1979 are compared with prior data for operating time and cycling rate.

MODIFIED SYSTEM

The photograph of the modified system, Figure 23-1, can be compared to a similar view of the original system included as Figure 21-1 in Section 21. Schematic diagrams of both the original and the modified 1.7-kWh system are presented in Figures 23-2 and 23-3 for ready comparison and a quick appreciation of the simplification effected by the modification. The modified system is discussed in this section in terms of its three main features: the stack, the electrolyte loop, and chlorine management. Comparison references to the original system are included without attempting a detailed description, as a complete description of the original system is given in Section 21.

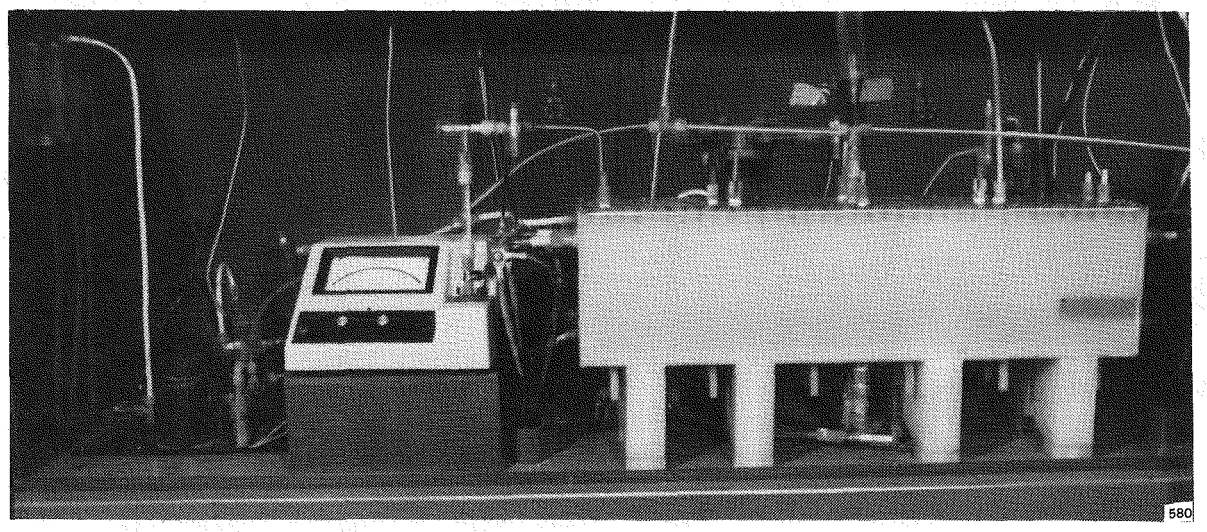

Figure 23-1. Photograph of the modified 1.7-kWh, battery stack test system.

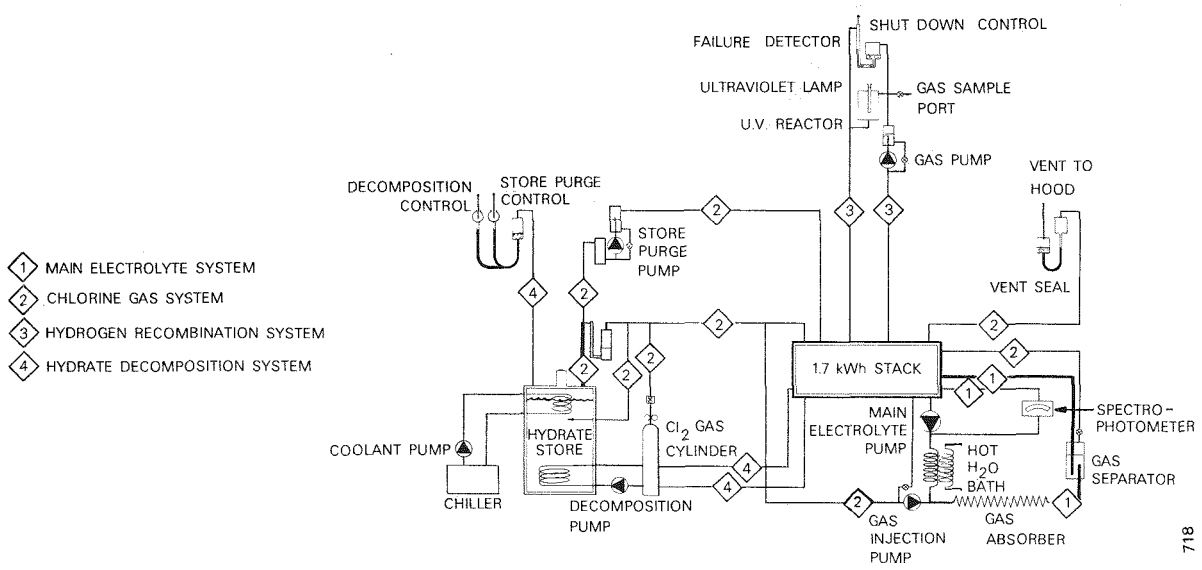

Figure 23-2. Schematic diagram of the original 1.7-kWh system. This system accumulated 1112 cycles from April 1976 to November 1979 when the system was simplified.

Stack

A new battery case top was designed to incorporate a fluorescent light, improve the seal, and facilitate removal and reinstallation. Including the fluorescent light in the case top eliminated the hydrogen-chlorine recombination loop with its associated pump and its troublesome leaky fittings.

The original case top was installed with many bolts, inserted through the top into threaded holes in the case wall. This design, with a flat Teflon gasket, proved to be ineffective for sealing the battery case. A new frame insert, set with studs (fewer than before) and machined to accept an O-ring gasket, was welded to the case top to restore a flat surface. The new top is

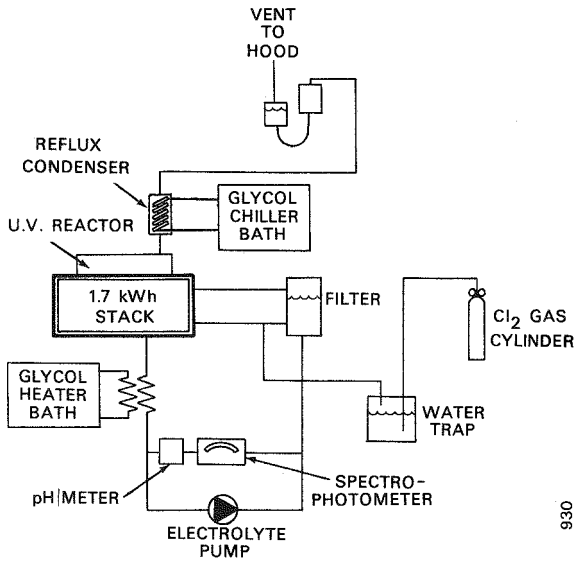

Figure 23-3. Schematic of the 1.7-kWh system modified in November 1979 to eliminate failure-prone components not essential to the purpose of life testing of the battery stack.

now much easier to install and remove; and the O-ring seal has proved to be much superior to the original. While the top was removed, titanium wires were attached to the graphite buses for use as voltage probes in future testing to determine busing losses. Deteriorating bus contact surfaces may be responsible for the long-term slow degradation of voltaic efficiency. No other changes were made to the cell assembly or busing inside the stack.

Electrolyte Loop

The electrolyte flows from the bottom of the sump through a heat exchanger, the electrolyte pump, a filter, and then back to the electrolyte distribution manifold in the stack. An auxiliary loop is used to supply electrolyte to a spectrophotometer for measurement of chlorine concentration. The heat exchanger maintains the electrolyte temperature at 40°C as in the original system and is of similar design. The new electrolyte pump is a substantial improvement over the pump previously used. The magnetic coupling of this new pump eliminates the mechanical sealing problems which, with the old pump, were a common cause of system failure, often forcing a change of the electrolyte.

Chlorine Management

The decision to eliminate formation, storage, and decomposition of chlorine-hydrate as the method for handling chlorine required an alternate approach. During charge, the chlorine gas evolved is vented through a glycol-cooled reflux condenser into the hood exhaust. The reflux condenser prevents the chlorine gas from removing water from the electrolyte and thereby altering the electrolyte concentration. During discharge, cylinder chlorine is supplied through a bubbler and inserted into the electrolyte stream through a gas sparger located immediately after the filter.

Microprocessor Controller Adjustments

Operation of the system remained as before except that phase 1, the cool-down phase, was eliminated because there is no longer a store to cool. Software changes to the control program were minimal as most of the system hardware changes could be accommodated by adjusting the control limits for deleted components outside their range of operation. That is, operating set points were adjusted so as to have the control program unaffected by the disappearance of components previously controlled. Sensor inputs which were necessary for operation and control of the store and supporting components were no longer needed and were therefore eliminated.

RESULTS AND DISCUSSION

Comparison of the battery data for four months (August-November) preceding modification with the data for three months (December-February) after modification shows that the goal of accelerating the accumulation of cycles has been achieved.

Battery operation data for each month from August 1979 through February 1980 is presented in Table 23-1. In column 1, the maximum number of runs possible in each month is listed. As one run requires slightly less than 12 hours, the maximum was calculated by assuming continuous cycling at the rate of two cycles each day. November and December were shortened months because the system was being modified and therefore not operating for portions of these months.

The actual number of runs in each month is listed in column 2; and column 3 lists the actual number of runs as a percentage of the total possible. Before modification, the system was operating approximately 50% of the time, the vast majority of downtime being due to auxiliary component failures. In the three months following the modification, the system was operating almost 75% of the time. This percentage would be higher (close to 90%) except for the low percentage in December when the microprocessor unit was being calibrated and the electrolyte was being replaced. Electrolyte replacement occurred several times following the modification in an attempt to cleanse the system of any impurities that might have been introduced at that time. As shown, the system was operating 90% of the time in January and February.

Similarily, column 4 shows the number of cycles acquired in each month while column 5 shows these cycles as a percentage of the total possible in column

Table 23-1

COMPARISON OF OPERATING TIME AND CYCLES ACQUIRED BEFORE AND AFTER MODIFICATION OF THE 1.7-kWh SYSTEM

Month	Maximum Number of Runs Possible	Actual Runs	% of Possible Runs	Cycles Acquired	% of Possible Cycles	% of Runs Qualified as Cycles
Aug. '79	62	33	53	19	31	58
Sept.	60	32	53	27	45	84
Oct.	62	27	44	15	24	56
Nov.	40	15	38	0	0	0
Average before refurbishment:			47	-	25	50
Dec.	52	21	40	17	33	81
Jan. '80	62	57	92	55	89	97
Feb.	56	49	88	46	82	94
Average after refurbishment:			73	-	68	91

1. Again, the after modification figures are substantially higher.

Column 6, like column 3, is a good indicator of the success of the modification. This column shows for each month the percentage of runs that qualified as cycles (electrochemical energy efficiency equal to or above 60%). After the modification, 90% of the runs qualified as cycles, whereas previously only one-half of the runs met the requirement.

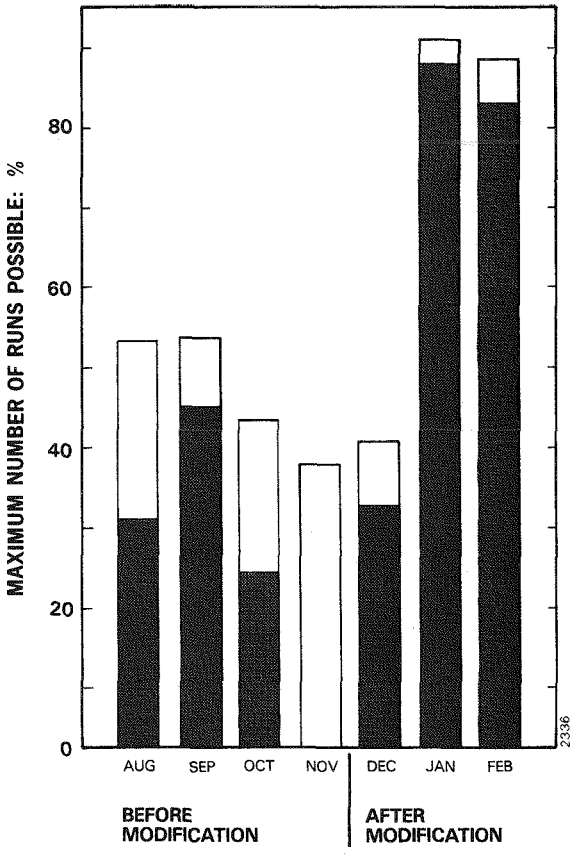

Figure 23-4. Comparison of runs and cycles for the 1.7-kWh system before and after modification. The open bars represent runs as a percentage of the maximum number of runs possible. The shaded bars represent cycles (runs yielding 60% or greater electrochemical energy efficiency) as a percentage of the maximum number of runs possible.

The operating time and cycle acquisition data presented in Table 23-1 are summarized graphically in Figure 23-4. This figure shows clearly that the system modification has produced a remarkable increase in running time. Also apparent in Figure 23-4 is an increase in the percentage of runs that qualify as cycles by yielding 60% or greater electrochemical energy efficiency. This unexpected benefit may be attributable to more stable operating conditions established by the system modification.

The efficiency data plotted in Figure 23-5 for cycles 1001 through 1250 show that the electrochemical energy efficiency is the same after the modification as it was before. The decrease in voltaic efficiency and corresponding increase in coulombic efficiency indicate the need for further adjustment of the chlorine flow rate during discharge.

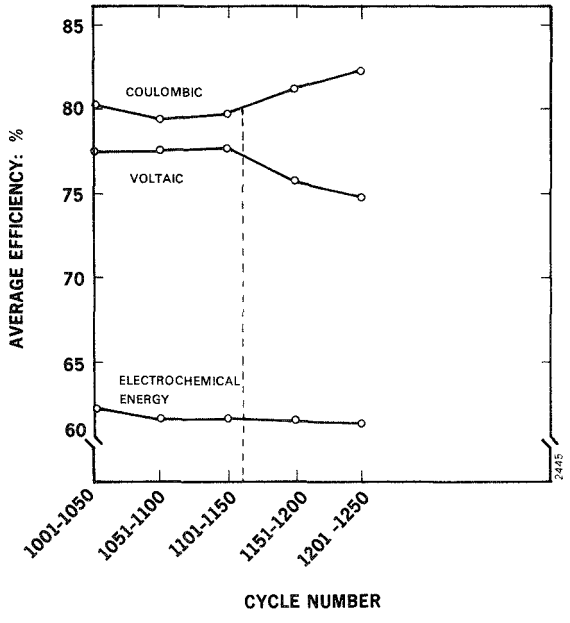

Figure 23-5. Efficiency data for the 1.7-kWh battery stack. Note that the electrochemical energy efficiency has been unaffected by the system modification made after cycle 1112 (dotted line).

Although experience with the modified 1.7-kWh system has been rather short compared to the time spent working with the original system, the evidence so far clearly justifies the modification. The system has been operating close to 90% of the time possible and 90% of the runs made are qualifying as cycles. This performance improvement suggests that more stable operating conditions have resulted from effective sealing of the system. Measurements of specific gravity, pH, and chlorine concentration support this conclusion.

There is no doubt that reliability and maintainability have been improved, but a claim of high reliability would be premature based upon such a short operating period. Nevertheless, results to date encourage the expectation of more rapid accumulation of cycles with minimum maintenance required.

PART V

DEVELOPMENT OF BEST-BATTERY TECHNOLOGY

Section 24

PROGRAM STATUS: BEST-BATTERY TECHNOLOGY

INTRODUCTION

At the beginning of Phase II of RP226-3 -- April, 1978 -- EDA was negotiating a contract with the U.S. Department of Energy (DOE) to build a 4-MWh zinc-chloride battery system to be tested at the Battery Energy Storage and Test (BEST) Facility in Hillsborough Township, New Jersey. This contract was signed in September 1978, and the DOE-EDA BEST-Battery Program began January, 1979. This is a 33-month program, with delivery of the 4-MWh zinc-chloride battery system scheduled for mid-1981.

Prior to the initiation of the BEST-Battery Program, it was agreed upon by EPRI, DOE, and EDA that the EPRI-EDA research, development, and engineering program -- RP226-3 Phase II -- would be integrated with the DOE-EDA advanced-engineering and pilot-production program. Since the BEST-Battery Program began, the EPRI-EDA battery-stack and auxiliary-component development programs have been conducted almost entirely in support of the BEST-Battery Program.

MODULE DESIGN

The EPRI 45-kWh battery module, built during Phase I of RP226-3, is the pre-prototype for the BEST-battery modules. Part III describes refurbishment and testing of this module during Phase II. As illustrated in Figure 24-1, this integrated battery module contains most of the auxiliary components and subsystems required for continuous closed-system operation. These include: (a) the six submodules, which comprise the battery stack; (b) two pumps -- one for electrolyte circulation and one for gas transfer/hydrate formation; (c) three heat exchangers -- one for hydrate formation, one for hydrate decomposition, and one for temperature control of the electrolyte; (d) two fluorescent lights, for photochemically catalyzing the reaction between hydrogen and chlorine; and (e) a variety of valves for controlling module operation.

Although these components and subsystems perform their respective operations in the refurbished 45-kWh module, they are suboptimal for one or more reasons dealing with cost, manufacturability, reliability, and/or per-

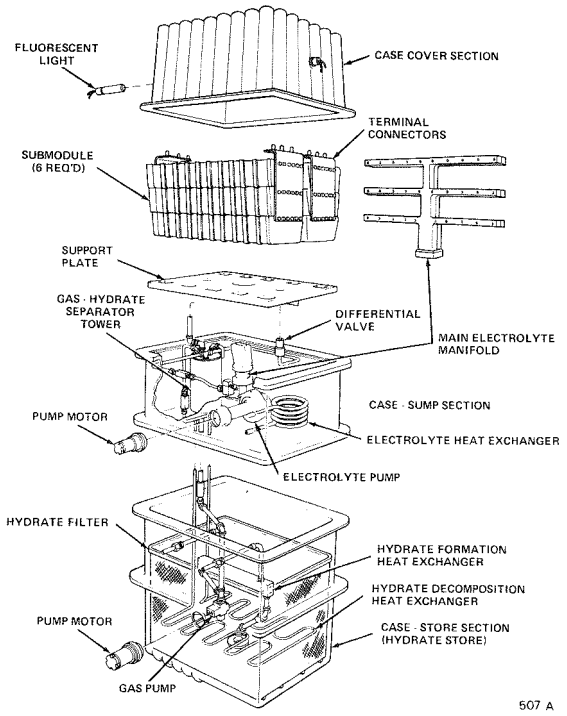

Figure 24-1. Exploded view of the refurbished EPRI 45-kWh module illustrating the major auxiliary components and subsystems.

formance. Also, the 45-kWh battery module does not incorporate an inert-gas rejection subsystem. This subsystem is required to routinely cleanse the chlorine gas of foreign ("inert") gases, such as air or carbon dioxide, which would otherwise accumulate to a level where module operation would be impaired.

The design of the BEST-battery modules is based on the EPRI 45-kWh battery module. The specifications for the components and subsystems are almost identical. In fact, the increase in delivered dc energy from 50 kWh to 52.3 kWh for the BEST-battery modules -- as described in Section 25 -- is due to projected improvements in electrochemical energy efficiency, rather than to specific design or operational changes.

EPRI-EDA PROGRAM SUPPORT

At the beginning of Phase II, development programs were established in the areas of submodules, pumps, hydrogen-chlorine reactor, and inert-gas rejection device. The objective was to develop more optimal prototype components and subsystems than those employed in the 45-kWh module. Also programs to qualify low-cost materials for use in zinc-chloride batteries were continued and expanded early in Phase II. These programs were conducted in anticipation of the BEST-Battery Program.

Since the initiation of the BEST-Battery Program, the EPRI-EDA Phase II Program has continued to provide developmental support in these areas. Three specific programs were emphasized: (a) flat-plate chlorine-electrode submodule design and development; (b) low-cost materials qualification; and (c) inert-gas rejection subsystem design and development.

Submodule Design and Development

The design of a more cost-effective and manufacturable submodule, employing flat-plate chlorine electrodes, was initiated at the beginning of Phase II in anticipation of the BEST-Battery Program. As the sources of problems with the Phase I design submodules were identified -- Section 15 -- the objective of achieving better cell balance in the new submodules was also emphasized.

The new submodule design is illustrated in Figure 24-2. It employs a variety of injection-molded parts. This feature was made possible by the successful qualification of a low-cost plastic which lends itself to this type of processing. The development of this design proceeded at different levels. The injection-molded flat-plate chlorine-electrode frames were successfully developed at the cell level, while development of the other design features proceeded at the two-cell, 4-volt and the submodule (ten-cell, 20-volt) levels. These activities are reviewed in detail in Sections 28 and 29.

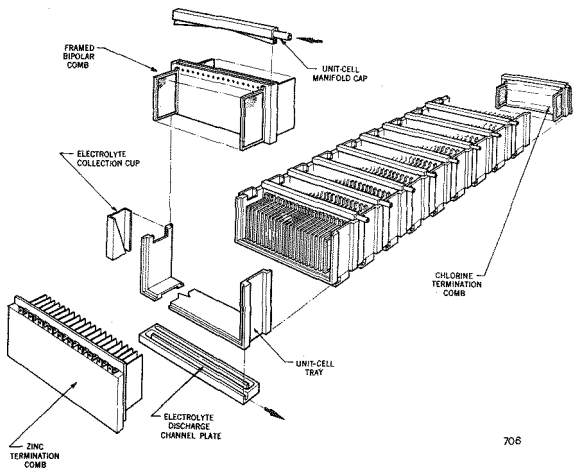

Figure 24-2. Perspective view of the BEST-battery submodule design. Note the injection-molded plastic components and the flat-plate chlorine electrodes.

Qualification of Low-Cost Materials

As mentioned above, the use of low-cost injection-molded plastic parts in the Phase II submodule design was made possible by the qualification of a suitable plastic for this application.

During Phase II, two polyvinyl chloride formulations, from two different suppliers, were qualified for use in the battery. Also qualified were a glass-reinforced polyester formulation and a polypropylene formulation. The polyester is being used in the fabrication of cases for the prototype BEST-battery modules. Details are provided in Section 26.

Another materials program was initiated early in Phase II to qualify low-cost porous and dense graphites for use as electrode substrates and bus bars in the battery. Four alternative porous graphites and at least one dense graphite were qualified. These low-cost graphites are also being employed in the submodules going into the prototype BEST-battery modules. Details of this program appear in Section 27.

Inert-Gas Rejection Subsystem

In order for a BEST-battery module to operate as a sealed system during evaluation at the BEST Facility, it is necessary to occasionally reject foreign gases from the gas spaces of the module to ambient. The accumulation of CO_2 formed by the slow oxidation of graphite, and air diffusing and leaking through the battery case, would eventually hinder normal battery operation. Accordingly, a subsystem is required which will separate these foreign gases from chlorine and routinely reject them from the gas space of the module.

During Phase II a prototype inert-gas rejection subsystem for 50-kWh battery modules was developed. A photograph of the breadboard prototype device for the 45-kWh module is shown in Figure 24-3. In this device -- a three-stage chlorine-chlorine electrolytic cell -- the chlorine is electrochemically processed to separate it from the electrochemically inert gases. The purified chlorine is returned to the gas space of the module, while the inert gases are vented to the ambient. Three separate phases of this development program are discussed in Sections 33-35.

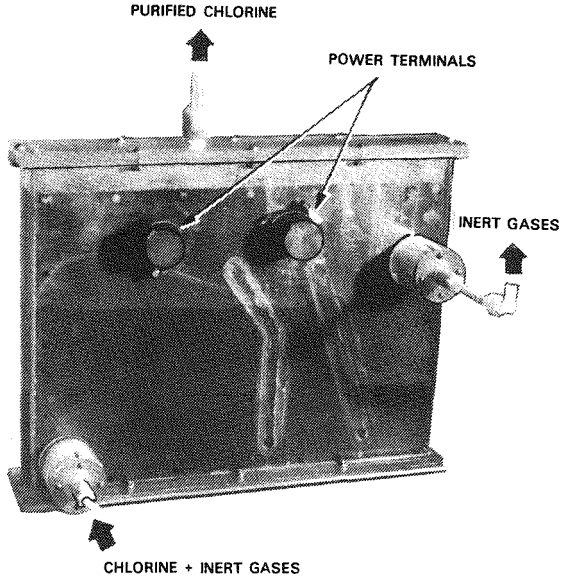

Figure 24-3. Photograph of the prototype inerts-rejection device for the 45-kWh battery module. This device processes chlorine at rates in excess of 0.5 ℓ/min.

Other Development Programs

During the 24-month period of Phase II, other component-development efforts were conducted in support of the BEST-Battery Program. These development efforts were in the areas of: (a) passive hydrogen/chlorine reactor; (b) gas/hydrate-former and electrolyte pumps; and (c) hydrate-former heat exchanger. These programs are reviewed in Sections 30, 31, and 32, respectively. Of major importance to the BEST-Battery Program is the nearly completed effort to develop a hydrate-former heat exchanger which utilizes direct-cooling with liquid Freon. A heat exchanger, presently being fabricated and using commercially available titanium plate-coils, should meet the specification for the BEST-battery modules.

BEST-BATTERY SYSTEM

The detailed design of this 4-MWh zinc-chloride test system is in final preparation at this time -- March 1980. Figure 24-4 is an artist's rendition of the battery system in bay no. 2 at the BEST Facility. It is comprised of

eighty integrated zinc-chloride battery modules assembled into two 2.1-MWh battery strings; two cooling subsystems; a ventilation/scrubber subsystem; a control subsystem; and the associated electrical wiring and plumbing. The forty 22.6/19.2-volt (charge/discharge) battery modules, comprising each string, will be mounted on a rack and electrically connected in series to form a 904/768 volt system which will interface with the BEST-Facility power-conditioning system. The rack structure -- containing the battery modules, coolant manifolding, control wiring, and microprocessor module controllers -- will be enclosed and connected to a ventilation/scrubbing subsystem. This subsystem will automatically ventilate the rack structure in the case of chlorine leakage from one or more battery modules. The ventilation-exhaust scrubber and the cooling/chilling subsystems will be located on a concrete pad adjacent to the building. The two direct-cooling Freon subsystems will be used to form and store chlorine hydrate and to provide temperature control of battery electrolyte.

The EDA-supplied control subsystem will feature a central controller to monitor and regulate the battery strings, the chilling/cooling subsystems, and the power-conditioning equipment. It will communicate directly with the BEST-Facility computer -- through which it will access the power-conditioning equipment -- and with the individual microprocessor-based battery-module controllers. The module controllers will perform local control actions, maintain checks on module operation, and acquire information for transmission to the central data processor.

Each battery module will deliver 52.3-kWh of dc energy, making the delivered capacity of each string 2.1 MWh. The electrochemical energy efficiency target for this battery is 65%. Additional specifications and the operational design of these BEST-battery modules are described in the next section -- Section 25.

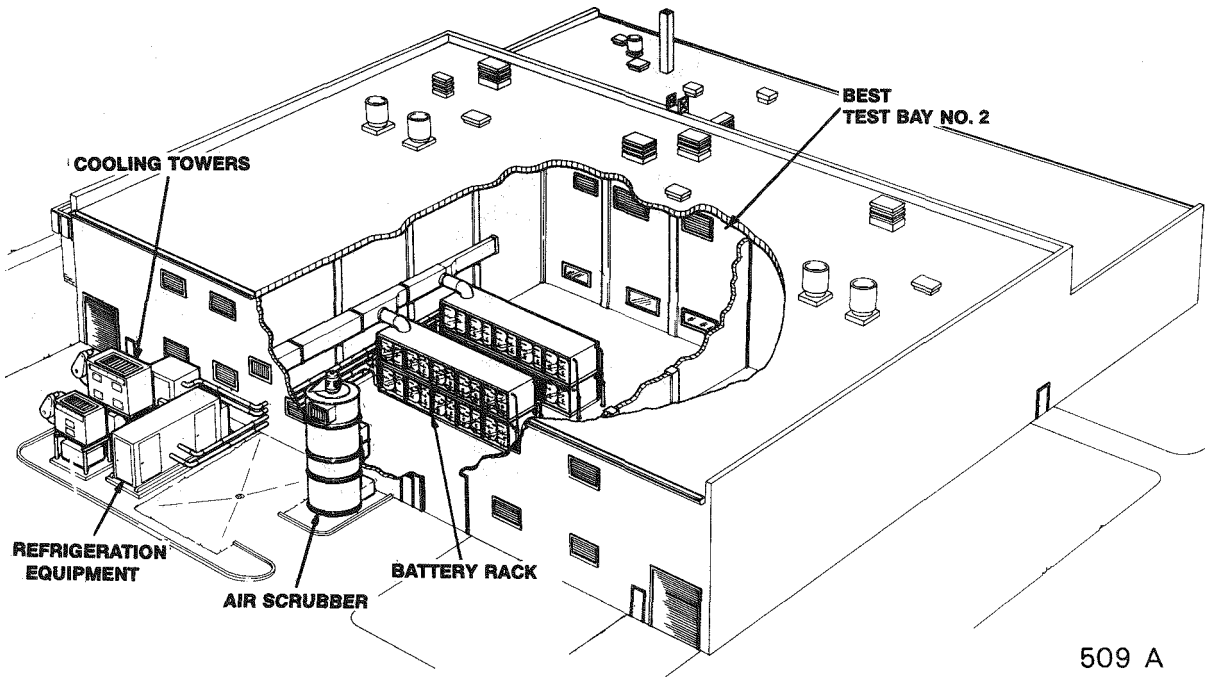

Figure 24-4. Artist's rendition of the 4.2-MWh zinc-chloride battery system in bay no. 2 at the BEST-Facility. Note the rack-mounted 52.3-kWh battery modules which form the basic building blocks of the system.

Section 25

SPECIFICATION AND DESIGN OF THE BEST-BATTERY MODULE

ABSTRACT

The basic unit of the 4-MWh zinc-chloride BEST-battery system is the integrated battery module. It incorporates a stack compartment -- which contains the battery stack and electrolyte sump -- and a store compartment -- where chlorine hydrate is formed, stored, and decomposed. The BEST-battery modules are designed with auxiliary components and subsystems to allow continuous closed-system operation. The functions of these components and subsystems are described. The module performance specification calls for 52.3 kWh of delivered dc energy at a fractional electrochemical energy efficiency of 0.65.

INTRODUCTION

As stated in Section 24, the objective of the DOE-EDA BEST-Battery Program is to design, build, and deliver a 4-MWh zinc-chloride battery system for testing at the BEST Facility by mid-1981. In this program, the capability of large-scale zinc-chloride batteries will be demonstrated for the electric-utility load-leveling application in a variety of areas including: manufacturability, cost-effectiveness, reliability, and performance. The detailed design of this 4-MWh battery system is currently in preparation. It is based on the use of approximately 80 battery modules, each of which will deliver ∿52 kWh of dc energy. Prototype battery modules are presently being built and tested in this program.

This section briefly reviews the specifications, general design, and operation of the BEST-battery modules. The specific development areas addressed as part of the EPRI-EDA Program are identified. Progress on the individual component development programs are discussed in the subsequent sections of this report.

ELECTROCHEMICAL SPECIFICATIONS

The design, operation, and specification of the BEST-battery modules are based on those of the EPRI 45-kWh module. Table 25-1 compares the electrochemical specifications of the BEST-battery module with the demonstrated operational and performance characteristics of the 45-kWh module. Under similar operating conditions, the BEST-battery modules are projected to demonstrate about a 5-point improvement in the usable coulombic efficiency and a 1.5-2.0 point improvement in voltaic efficiency. Improved chlorine-electrode activation and internal busing will provide the voltaic-efficiency gains. The improved battery-stack design and increased level of vacuum on the stack during charge will provide the coulombic-efficiency gains. The increase in delivered energy projected for the BEST-battery modules is due entirely to the improved efficiency.

Table 25-1

OPERATIONAL AND PERFORMANCE PARAMETERS

	45-kWh	BEST
CHARGE:		
t, hours	6.8	6.6
i, mA/cm^2	33	33
V, volts/cell	2.29	2.26
DISCHARGE (5 h):		
i, mA/cm^2	33	33
V, volts/cell	1.85	1.91
EFFICIENCIES:		
Coulombic		
Total	0.77	0.80
Unusable	0.06	0.04
Usuable	0.71	0.76
Voltaic	0.83	0.85
Energy	0.59	0.65
DELIVERED ENERGY (kWh)	50	52.3

DESIGN AND OPERATION

Figure 25-1 is a positional and operational schematic of the BEST-battery module. It illustrates the relative positioning of major components and subsystems in the module. The operation of the module will be controlled on the basis of the pressure in the stack compartment of the module. An average 5-psi pressure differential will be maintained between the store and the stack during both charge and discharge using a gas pump (P2) to transfer gas from stack to store via line 5. Pressure relief of the store is accomplished via valve V3. Absolute pressure control is accomplished during charge by controlling the rate of chlorine hydrate formation and during discharge by controlling the rate of chlorine hydrate decomposition. The hydrate-formation rate on charge is controlled by the rate of heat rejection from the store fluid in the hydrate formation heat exchanger, HX1. The hydrate-decomposition rate on discharge is controlled by the rate of heat transfer from the battery electrolyte to the store fluid in the decomposition heat exchanger, HX2.

During charge the electrolyte pump (P1) feeds electrolyte to the chlorine electrodes in the battery stack via line 1. Electrolyte overflows from the cells of the battery stack, collects in separate return channels molded into the bottom plate of each cell, and returns by gravity to the sump. The chlorine gas generated during charge is pumped from the stack, via line 5, by the gas pump (P2) where it is mixed with prechilled store fluid from HX1 to form chlorine hydrate. The store operates at approximately ambient pressure, while the stack is maintained at -5 psig. The -5 psig vacuum accomplishes dechlorination of the electrolyte during charge.

During discharge the electrolyte pump feeds chlorinated electrolyte to the chlorine electrodes in the battery stack via line 1. Again, electrolyte overflows from the cells and returns by gravity to the sump through separate return channels. Chlorination of the electrolyte is accomplished by injecting gaseous chlorine at 3 psig, via line 7, into the electrolyte feed line 1. Chlorine gas is formed in the store by transferring heat from the electrolyte to the store fluid in HX2 and decomposing chlorine hydrate. Absolute pressure control of the stack at about -2 psig is accomplished by controlling the rate of heat transfer to the store fluid. Again, P2 is used to maintain the 5 psi pressure differential between the store and the stack.

Two additional subsystems are required for continuous closed-system operation of the BEST-battery modules. Two fluorescent lights are employed in the gas space of the battery stack to photochemically catalyze the reaction between hydrogen and chlorine gases. This subsystem is necessary in order to prevent the accumulation of chemically and/or

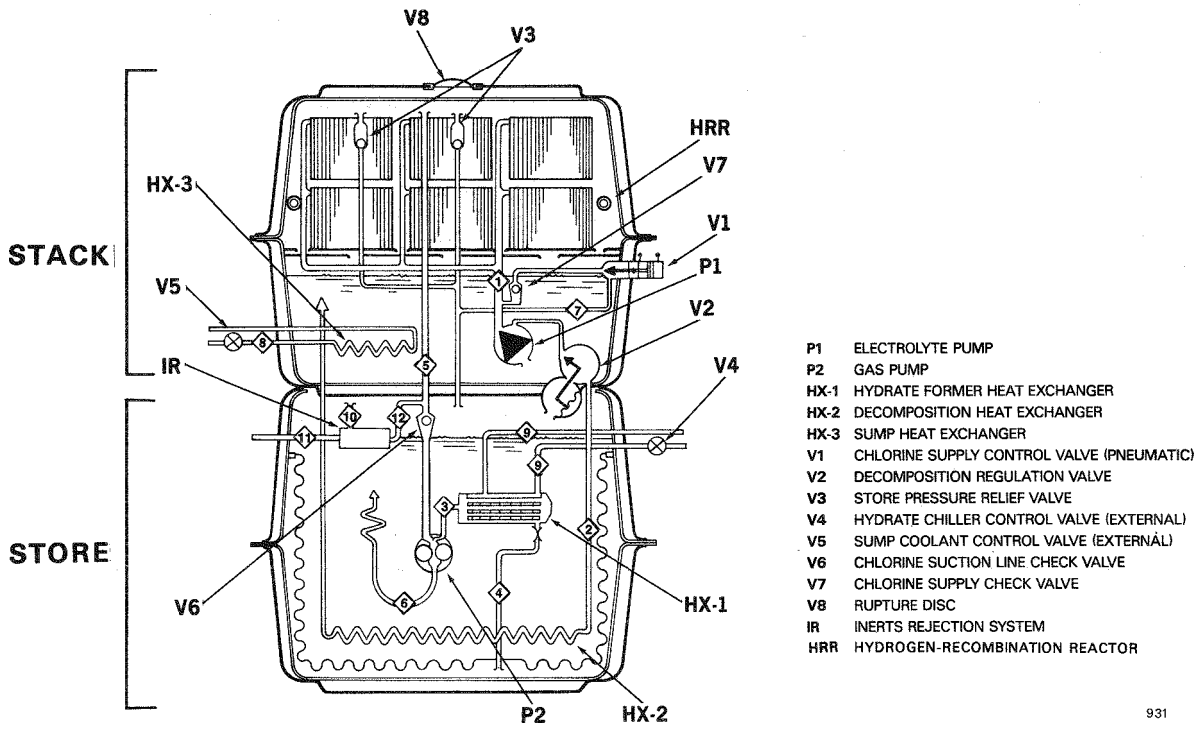

Figure 25-1. Operational schematic of the BEST-battery module illustrating the components and subsystems required to allow continuous closed-system operation.

electrochemically formed hydrogen to a concentration level where it would react spontaneously with chlorine. This subsystem operates continuously through charge, standby, and discharge.

The other subsystem, an inerts-rejection device, is employed in the gas space of the battery store. It is operated subsequent to the useful discharge of the module for the purpose of separating undesirable foreign gases -- so-called "inerts" -- from chlorine and rejecting them to the environment. The mixture of chlorine and foreign gases enters the device via line 10 at the rate of about 0.5 ℓ/min. After being processed and separated from the foreign gases, the purified chlorine is returned to the battery module proper, via line 12, while the foreign gases are rejected to the outside environment via line 11. Without this subsystem ambient gases drawn into the module, and carbon dioxide formed at a low rate internally, would accumulate to concentration levels where they would eventually deleteriously affect hydrate formation during charge or chlorine dissolution during discharge.

PROGRAM INTEGRATION

At the end of Phase I of RP226-3 -- March 31, 1978 -- EDA had built and initially tested its first integrated battery module for the electric-utility load-leveling application, i.e., the 45-kWh battery module. This battery module incorporated all of the auxiliary components and subsystems to allow closed-system operation, with the exception of the inerts-rejection subsystem. For a variety of reasons, however, some of the auxiliaries incorporated into this pre-prototype BEST-battery module were suboptimal.

At the beginning of RP226-3 Phase II -- April 1978 -- development programs were established in the areas of (a) electrolyte pump, (b) gas/hydrate-former pump, (c) passive hydrogen/chlorine reactor,

and (d) inerts-rejection subsystem. These programs were initiated with the objectives of cost-reduction, improved manufacturability, higher efficiency, and improved reliability in anticipation of the DOE-EDA BEST-Battery Program. A subcontract was let to a pump development company to design improved pumps of low-cost plastics for both the electrolyte-circulation and gas/hydrate-former applications. Another subcontract was let to evaluate and develop a long-life self-powered light for use as a passive hydrogen/chlorine reactor subsystem. A low-level in-house effort was initiated to develop an inerts-rejection subsystem. Also, new and existing in-house programs were pursued in order to qualify more costeffective plastics and graphites for use in the battery environment.

Ten months into RP226-3 Phase II -- January 1979 -- the DOE-EDA BEST-Battery Program formally started. At the request of both DOE and EPRI the two programs at EDA were integrated, with the EPRI Program providing developmental support to the DOE BEST-Battery Program. At this time, the pump design and development programs were transferred from the EPRI Program to the BEST Program, as prototype pumps were being scheduled for fabrication. After promising results were reported by the subcontractor, the self-powered passive-reactor development program was picked-up in-house about 15 months into the Phase II Program. About 18 months into the program, efforts were initiated to design and develop a hydrate-former heat exchanger for the BEST-battery module, which uses liquid Freon as the coolant.

In addition to the component and materials development programs, the EPRI Phase II Program has provided the BEST-battery module stack design, and support in the evaluation and development of this design. This design incorporates flat-plate chlorine-electrodes; injection-molded PVC chlorine-electrode frames, bus frames, unit-cell trays, and a number of other features designed to reduce cost and improve performance. This design and developmental effort was initiated at the beginning of Phase II and has continued over its 24-month duration. All the above mentioned developmental efforts have been performed during Phase II of RP226-3 in support of the BEST-Battery Program. The next 10 sections -- 26 through 35 -- review the progress on these EPRI-EDA sponsored programs.

Section 26

MATERIALS QUALIFICATION: I. PLASTICS

ABSTRACT

The development of cost-effective materials for use in zinc-chloride batteries is important to commercializing this technology. The materials-qualification program was continued during Phase II to develop low-cost plastics to replace Kynar (polyvinylidene fluoride) and Teflon (polytetrafluoroethylene). Chemical and electrochemical screening tests -- involving exposure to chlorinated zinc chloride solution and to the zinc-chloride cell environment, respectively -- were employed in the qualification of these plastics. One glass-reinforced polyester, one polypropylene, and two polyvinyl chloride compounds passed these screening tests during Phase II. These materials are being employed in the prototype BEST-battery modules.

INTRODUCTION

The program for the selection and qualification of plastics is involved in the development of cost-effective materials for use in the zinc-chloride battery. Initially, the battery case and many other component parts were fabricated from high cost fluorine-based plastics such as Kynar and Teflon (1). These stable polymers permitted control of leached contamination and degradation so that other battery parameters could be studied to determine optimum operating conditions. Concurrently, a materials evaluation program was undertaken to identify and qualify more cost-effective materials for use in commercial batteries.

Though the zinc-chloride battery offers attractive electrochemical properties, the presence of wet chlorine poses a challenging materials problem because of its strongly corrosive nature. The advent of modern plastics with wide-ranging chemical and physical properties has made the handling of wet chlorine more feasible. Chemical stability, mechanical properties, and material and processing costs form the basis for the selection of candidate materials. The materials program was initiated in 1976, during RP226-2 (1). This program was continued during Phase I of RP226-3 (2). This section reports work performed in Phase II of RP226-3.

With the advent of the BEST-Battery Program at EDA, successful development of more cost-effective materials for use in battery modules took on new importance. In addition to demonstrating acceptable performance at the BEST-Facility, this program contains criteria in the areas of cost-effectiveness and manufacturability of the technology. Therefore, the qualification of low-cost plastics, which lend themselves to mass-production processing techniques, could significantly impact on the success of the BEST-Battery Program.

During Phase II of RP226-3 efforts focused upon the development of five principal groups of compounds: glass-reinforced polyesters, polyvinyl chlorides, high density polyethylenes, polypropylenes, and vinylidene fluoride-based elastomers. This section summarizes the results of qualification tests performed on these compounds. In addition, fabrication techniques and

their effects on material properties are examined. Finally, evaluation of other candidate battery materials is discussed.

CHEMICAL SCREENING TESTS

A chemical screening test was established according to ASTM D543, Resistance of Plastics to Chemical Reagents. Materials were screened for blistering, weight and dimensional changes, solution pH stability, and extraction of metal components that would contaminate the battery system. Screening tests were performed using the system shown in Figure 26-1 which simulates the chemical conditions in the zinc-chloride battery. Candidate plastics were placed in 4-neck flat flange type resin reaction flasks containing aqueous zinc chloride. Hot plates underneath the flasks keep the contents at the desired temperature. Dry chlorine gas from the cylinder flows into the gas manifold via a gas-washing bottle that wets the gas. The gas manifold delivers wet chlorine gas to each flask, thus minimizing loss of water from the electrolyte solution by evaporation. An individual chlorine gas inlet and outlet is provided for each flask. This eliminates contamination from samples elsewhere in the screening system. Saturation of the solution with chlorine is assured by continuous sparging.

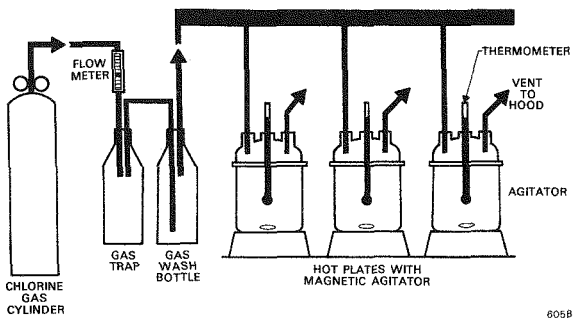

Figure 26-1. Diagram of laboratory system used for chemical screening tests. The flasks contain the plastics under test and the chlorinated zinc chloride solution.

A set of standard test parameters was selected and maintained throughout this degradation testing. Conditions were chosen to simulate the battery environment and to ensure continuity of test results. They included temperatures of 25° and 50°C, respectively, a 30% zinc-chloride solution having a specific gravity of 1.295 and a pH of 1.0.

All plastic samples were examined microscopically and photographed prior to testing. Initially, test specimens were exposed to the chlorinated zinc chloride solution for 30 days at ambient temperature. Standard measurements were made on each test specimen and test solution to determine whether degradation had occurred. Physical measurements, performed prior and subsequent to degradation testing, included specimen weight and dimensions, blisters/mm^2 of surface area, and blister diameter. Solution specific gravity and pH changes were recorded and an atomic absorption analysis was performed to check for leached metal contaminants. If the specimens and their test solutions appeared unaffected by this initial exposure, the tests were continued for another 30 days at 50°C. If a sample appeared inert after tests at 25°C and 50°C, it was passed on for electrochemical evaluation.

ELECTROCHEMICAL TESTS

The purpose of the electrochemical evaluation program is to qualify a material for use in the battery. Materials evaluated in this program have already passed chemical screening tests and are believed to be stable. The electrochemical test is the final evaluation performed on a material prior to its more widespread use in the battery. A material is electrochemically evaluated by placing it in a zinc-chloride cell having an established baseline performance. Here it is exposed not only to chlorinated zinc chloride but also to the electrochemical environment. Any effect on the performance of the cell due to the presence of the material is carefully monitored. An exploded view of the test cell used for electrochemi-

cal qualification of plastics is shown in Figure 26-2.

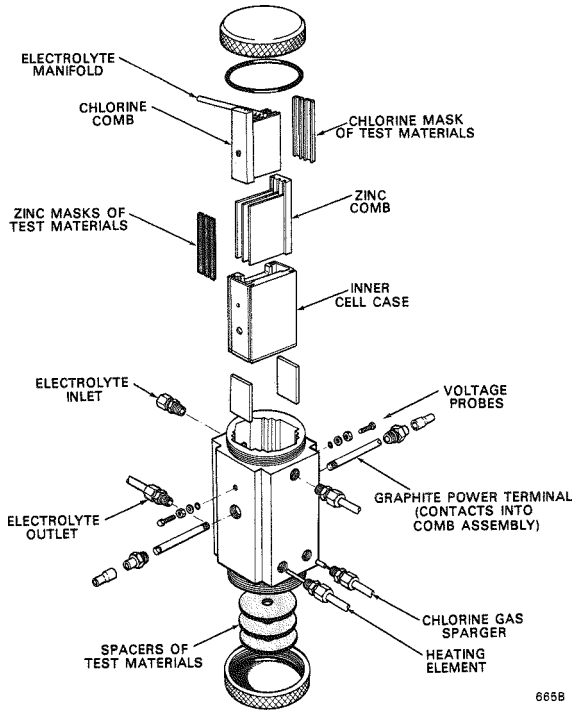

Figure 26-2. Exploded view of the test cell used for electrochemical testing. The spacers, masks, and the inner-cell case may be made of the test materials. This cell design permits maximum exposure of the test materials to the most active electrochemical treatment.

The test cell consists of two comb-type buses containing two chlorine electrodes and three zinc electrodes, respectively. The spacers, masks, or inner-cell case may be made from test materials. The spacers and inner case provide a large surface area for exposure to the electrolyte, and are in close proximity to the chlorine sparger and the heating elements. The masks serve to expose the material to the most active electrochemical environment within the cells.

Initially, five cells were constructed. After initial debugging, fresh electrolyte was placed in each cell and circulated over zinc rods to remove any metal impurities. Samples were retained for atomic absorption analysis. The cells were cycled daily and data recorded until stable performances were established. Next, a test material was introduced for evaluation into each cell except one which was retained as a control. It contained only qualified materials. All cells were subjected to a number of uniform charge-discharge cycles and all pertinent data recorded. Performances of cells containing test materials were compared to that of the control cell.

Gas analyses for nitrogen, oxygen, hydrogen, and carbon dioxide were made during the charge cycles and recorded daily along with variations in the pH of the electrolyte. Any adjustments made to the electrolyte were recorded. Usable coulombic efficiencies for each cell were plotted against the cycle number. Periodically, atomic absorption and total organic carbon analyses were made to detect leached metal contaminants and possible breakdown of the polymer chains, respectively. If the cell performance is not significantly altered by the presence of the test specimen after 15 cycles, the test material is believed to be stable in the cell environment. Additional life testing may be performed subsequent to this electrochemical screening.

RESULTS AND DISCUSSION

The discussion of test results is divided into six categories: (1) polyesters, (2) polyvinyl chlorides, (3) polyethylenes, (4) polypropylenes, (5) Vitons and perfluoroelastomers, and (6) others. In the areas where candidate materials have passed both types of screening tests and were recommended for widespread use within EDA, the results of use-testing will also be discussed.

Polyester

The battery case material must have high strength and rigidity. Glass-rein-

forced polyesters offer good mechanical properties and low material and fabrication costs relative to Kynar and Teflon. Therefore, the stability of polyesters in the battery environment was investigated. A discussion of the results to date and problems encountered follows.

Several types of polyester resins, including vinyl esters, were chemically tested during Phase I. A corrosion resistant resin, Pes-16, was the most stable in the battery environment. The importance of the glass-reinforcing component was also recognized. A number of possible veil and mat combinations were evaluated using the stable corrosion-resistant resin, and a specific polyester resin and glass composite was chemically qualified.

Electrochemical testing of the composite was undertaken in Phase I and concluded in Phase II (2). A cell containing spacers constructed from the polyester resin and glass composite completed 93 cycles. The electrochemical performance of the cell, hydrogen evolution rate, and electrolyte pH were compared with those of a cell of the same design constructed from only qualified materials. The results were statistically analyzed using analysis of variance to determine if the material had any effect on cell performance. Results showed that at the 95% confidence level the presence of the polyester composite did not adversely affect cell performance.

Following completion of chemical and electrochemical screening tests, fabrication techniques for the necessary battery components were considered. Test results provided guidelines for proper fabrication techniques as well as the modes of polyester degradation. All polyester cases for the larger battery systems were fabricated by hand layup. The complex lamination, layup, and cure procedures required for a fiberglass reinforced polyester resulted in problems during the scale-up fabrication of battery cases for an 8.3-kWh submodule and the 45-kWh module. Those surfaces in direct contact with the mold during layup showed no deterioration. However, flaking occurred at surfaces containing voids which had been repaired by brushing on extra resin. This resulted from the inhibition of polymerization by oxygen and subsequent exposure of monomer to the chemical environment. The incorporation of an additive to prevent air inhibition in the surface layer, and sanding unpolymerized areas of this layer, eliminated the flaking. Another problem involved the formation of cracks in resin-rich areas of the case. The use of a low-viscosity prepromoted resin to improve the flexibility of such areas remedied this problem.

Polyvinyl Chloride

The development of polyvinyl chloride (PVC) compounds to replace Kynar and Teflon in such battery components as the case liner, electrode frames, masks, and manifolds has continued during Phase II. They have emerged as the most promising class of materials to meet the requirements of good chemical resistance, processibility, and low-cost. Results to date are summarized in this section.

Two polyvinyl chlorides, PVC-56 and PVC-68, were chemically qualified during Phase I (2). These materials were then subjected to electrochemical testing during Phase II. Electrolyte pH, hydrogen gas evolution rate, voltaic efficiency, and usable coulombic efficiency were monitored in cells containing test materials and in the Kynar control cell. Analysis of variance was performed on these data to determine if the test materials had statistically significant effects on any of these variables. Both PVC-56 and PVC-68 had no statistically significant effects at the 95% confidence level. Due to variations in the coulombic efficiency of the control cell, the statistical insignificance of the test material on this observable was questionable. However, similar cells with PVC-56 masks have been cycled for more than a year with repeatable and reproducible coulombic efficiencies in the high-70% to low-80% range.

Following electrochemical screening, two entire standard test cells were constructed from PVC-56 and PVC-68, respectively for life testing. Day-to-day cycling variations were encountered with the Kynar control cell, as well as the cells constructed from PVC. Efforts to reduce these variations continue. Data thus far indicate no adverse effects resulting from the use of PVC in the cells.

After chemical and electrochemical qualification, fabrication, and processing techniques for specific battery components were considered. These components are subject to different chemical, physical, and structural requirements. The most economical mass-production techniques available for a specific component also must be considered. PVC as such, or with a certain degree of mechanical reinforcement, may be a suitable material for a number of components.

Because of its low modulus of elasticity, PVC is not a desirable candidate material for battery parts requiring strength and rigidity such as the battery case and pump impellers and gears. However, it is suitable for a number of other components. These include submodule trays, manifolds, pipes, pipe fittings, and case liners. PVC pipes and pipe fittings can be produced by extrusion or injection molding. Pipes are commercially available and pipe fittings have been successfully injection molded from PVC-68. Vacuum-formed PVC-68 case liners also have been produced successfully.

The flat-plate chlorine electrode frames are critical elements in the production of the zinc-chloride battery. Hundreds of these frames are required for each battery. Since injection molding is the most economical method of producing them, molding trials were conducted to study the feasibility of injection molding frame-halves from PVC-68. However, in early trials the compound proved difficult to injection mold. Modification of the PVC-68 formulation was required to facilitate injection molding. The modified injection molding compound, PVC-88, was used in subsequent molding trials. PVC-88 chlorine electrode frame-halves were successfully injection molded in March 1979. The injection molded frame-halves were assembled using ultrasonic welding and solvent-bonding techniques. However, blistering and swelling of the electrolyte feed channels in the test cells made it necessary to injection mold the feed channel as a separate part from Kynar.

Efforts to develop an optimum molding compound continue. Test results indicating an inverse relationship between the amount of processing history and compound stability suggested injection-molding trials using dry blend rather than granulated sheet. To prove this concept, PVC-68 dry blend and PVC-68 granulated sheet were injection molded. As expected, the temperature required to mold dry blend was lower than that needed to mold granulated sheet. To further reduce the temperature and shear required for injection molding, a lower molecular weight PVC would be required. Frames were injection molded from a PVC-68-based formulation containing a lower molecular weight PVC resin. However, these frames blistered in chlorinated zinc chloride. Chemical testing of other PVC compounds, based on the original PVC-68 formulation, is in progress. Preliminary screening tests of six recently injection molded PVC compounds indicate that a modified formulation of PVC-68, PVC-108, has emerged as the most stable molding compound to date.

The development of alternate PVC compounds has been proceeding concurrently with the development of an optimum molding compound based on PVC-68. The PVC-56 compound previously qualified is no longer commercially available. The manufacturer was contacted regarding the possibility of obtaining a similar replacement compound. A compound having the same additive system as PVC-56 was sent. This material, PVC-82, contained a lower molecular weight resin than PVC-56, and therefore was believed to be more injection moldable. Two PVC-82 sample coupons were subjected to

chemical resistance tests in chlorinated zinc chloride at 25°C and 50°C, respectively. No blistering was observed in either sample. Following an additional 30 days of testing at 50°C, the surface of the coupon tested only at 50°C appeared mottled, while that of the second coupon remained unaffected except for some etching. A third 30 days of testing at 50°C was performed to resolve the discrepancy in test results between the two coupons. Blistering of both coupons resulted.

Electrochemical evaluation of a third PVC-82 coupon in a Kynar test cell was performed concurrently. Following the completion of 15 cycles, the coupon was removed and blistering observed. A statistical analysis of the results for the 15 cycles showed that at 95% confidence level, the presence of the compound had adversely affected cell performance. Additionally, pH values for the cell containing PVC-82 were found to be different from that of a Kynar control cell at the 95% confidence level.

Efforts to qualify other PVC compounds continue. A number of PVC manufacturers were contacted regarding test samples. An injection molded PVC check valve did not blister in initial chemical tests. Further tests of this material are planned. Chemical tests of three rigid injection-molding PVC compounds will proceed upon receipt of test samples.

Polyethylene

Polyethylene also was considered for injection-molded components. Polyethylene not only is less costly than PVC but also is more easily injection-molded. However, it is generally less resistant to oxidizers than PVC. Therefore, studies have focused upon high density polyethylene compounds. These compounds not only exhibit greater chemical resistance and reduced permeability to liquids and gases than lower density polyethylenes but also show increased tensile strength and hardness.

Over 25 polyethylene compounds have been chemically tested but none have passed the chemical screening tests. Initially, compression-molded polyethylene samples compounded with various stabilizer components were tested in order to find an optimum stabilizer system. Copolymers were studied in preference to homopolymers due to the susceptibility of the latter to stress-cracking. A synergistic, three-component stabilizer system is frequently used in these compounds. These three components were evaluated individually and collectively in chlorinated zinc chloride at 25°C. The high density polyethylene resin with no added stabilizers was also evaluated and showed numerous tiny blisters. The sample containing all three stabilizers appeared unchanged at 25°C, as did two of the three coupons containing only one of the stabilizers. The coupon containing the third stabilizer, however, blistered after exposure at 25°C. This suggested the possibility of eliminating the unstable component from this formulation to produce a more inert material. A sample containing only the two low-volatility stabilizer components blistered in testing at 50°C, but fewer blisters were observed.

It was concluded that the resin must necessarily be stabilized, preferably with a stabilizer of low volatility. Subsequent samples included an extruded formulation with a stabilizer of this type. Atomic absorption analyses of the test solutions showed no leached contamination, but pronounced increases in the solution pH values were noted. Furthermore, blistering was still observed, though to a lesser degree than noted in previous samples.

Some possible causes of this blistering have been investigated. The use of silicone mold-release agents did not affect blistering. The surface of a copolymer sample was abraded to determine if a relationship exists between blistering and the physical condition of the surface. A mechanically-abraded surface appeared to be less inert than one left as processed, i.e., extruded, thus indicating a relationship between

surface tension and stability. The blistering of the abraded surface indicated further that this type of copolymer degrades in the battery environment.

Other types of polyethylenes were also evaluated. Ultra-high molecular weight polyethylenes were screened despite their increased cost and lower fabrication versatility, but results showed obvious degradation. Five of the compression-molded copolymers were post-fluorinated producing a Kynar-like surface layer of molecular thickness on these samples. However, no significant improvement was achieved with this treatment in comparison to the unfluorinated compounds.

Polypropylene

Polypropylene was also considered as an alternate material to PVC for injection molded parts. Like polyethylene, it is more easily injection molded and less costly than PVC. Its chemical resistance is substantially the same as polyethylene. The main differences in the chemical resistance properties of the two polyolefins are related to the higher melting point of polypropylene and to the absence of environmental stress cracking as a problem.

Nine polypropylene compounds have been chemically tested. Investigations included both homopolymers and copolymers. A talc-filled polypropylene and two propylene-ethylene copolymers were unstable in chlorinated zinc chloride. The surface of another polypropylene compound P.P.-6, appeared bleached, more opaque, and less glossy following testing in chlorinated zinc chloride for 30 days at 25°C and 30 days at 50°C. Small surface stains also were detected, but no blisters were observed.

Electrochemical evaluation of a P.P.-6 spacer in a Kynar test cell was pursued. After the completion of 15 cycles, the results were statistically analyzed to determine if the material had any effect on cell performance. Results showed that at the 95 % confidence level the presence of the polypropylene compound did not adversely affect cell performance. Unfortunately the manufacturer has discontinued marketing this formulation. A discussion with the manufacturer revealed that a similar polypropylene is commercially available. Chemical and electrochemical testing of injection molded tensile bars of this compound, P.P.-9 is in progress.

Vitons and Perfluoroelastomers

Efforts toward the development and qualification of elastomeric polymers for nonrigid battery components such as gaskets, 'O' rings, seals, tubing, and filter materials have continued during Phase II. Vitons, elastomeric copolymers containing vinylidene fluoride, have emerged as the most promising class of materials to meet the requirements of good chemical resistance and relative low cost. Perfluoroelastomers based on the copolymerization of tetrafluoroethylene, perfluoro (methyl vinyl ether) and a third monomer (perfluoro vinyl ether grouping with an active cure site monomer) have also been studied but are more costly (2).

Fifteen Viton fluoroelastomers have been chemically tested. A Kel-F copolymer of vinylidene fluoride and chlorotrifluoroethylene also was tested but found to be unacceptable. Evaluation of compound stability was based primarily on weight and dimensional changes because the projected total surface area of elastomer in the battery is small compared to the electrolyte volume, thus reducing the significance of metal leachings and pH changes from these materials. Following a review of the physical and chemical test data from the 15 Viton samples, the four most stable were identified. Two of these compounds will undergo electrochemical qualification testing upon the arrival of additional test samples from DuPont. Unfortunately, the other two were dropped from commercial production. Chemical screening tests of two recently introduced Viton compounds,

similar to those no longer produced, are in progress.

As mentioned previously, perfluoroelastomers have also been evaluated. The relative high cost of these materials has limited the extent of their development. Two perfluoroelastomers were found to be stable in the battery environment. At present, these compounds are being used as seals and seats in pressure differential valves.

Others

A variety of other materials were studied in addition to those reviewed above. These materials were considered for a wide range of applications including adhesives, battery case, pump components, bearings, and bearing coatings. A tetrahydrofuran-activated solvent-based adhesive emerged as the most stable formulation. An allyl diglycol carbonate polymer and an acrylic-based multipolymer were investigated as possible battery case materials, but neither were stable in chlorinated zinc chloride. Polyphenylene sulfide (Ryton, Phillips™), Mono Cast (The Polymer Corp.™) nylon compounds, and poly amide-imide compounds (Torlons, AMOCO ™) were investigated as possible materials for pump components, but chemical resistance tests indicated they were unstable in the battery environment. A family of carbon-graphite products also were considered for pump component applications. Two of the eight grades tested were chemically qualified. One, EDA code G-26, twice failed electrochemical qualifications tests performed in a zinc-chloride test cell. Electrochemical evaluation of the other chemically qualified grade, EDA code G-31, is still in progress and preliminary results appear encouraging.

STATUS

Prior to Phase I, battery components were constructed chiefly of Kynar and Teflon, both high cost plastics. The status of various materials are summarized in Table 26-1. A glass-reinforced polyester, Pes-16, has been chemically and electrochemically qualified for use as the battery case material. Two polyvinyl chloride compounds, PVC-56 and PVC-68, were chemically and electrochemically qualified. PVC-68 electrode and busbar frames have been successfully injection molded and are in use. PVC-108, a modified formulation of PVC-68, has emerged as the most stable molding compound to date. Development of high density polyethylene and polypropylene compounds received increased emphasis. Chemical and electrochemical testing of a polypropylene is in progress. Vitons have emerged as the most promising class of elastomers for nonrigid components. Electrochemical evaluation of two chemically qualified Vitons will proceed upon the receipt of test samples from DuPont. A family of carbon-graphite products were evaluated for possible pump component applications. Electrochemical testing of one of these materials is now in progress. Efforts to qualify additional materials continue.

Table 26-1

MATERIALS QUALIFICATION PROGRAM STATUS
(AS OF 3/31/80)

MATERIAL		Chemically	Electrochemical Qualification		
EDA Code	Description	Qualified	Awaiting	In Progress	Qualified
Pes-16	Glass-reinforced polyester	x			x
PVC-56	Medium molecular weight polyvinyl chloride	x			x
PVC-68	Medium molecular weight polyvinyl chloride	x			x
PVC-99	Injection molded polyvinyl chloride check valve	In progress			
PVC-108	Medium molecular weight polyvinyl chloride	In progress			
P.P.-6	Polypropylene	x			x
P.P.-9	Polypropylene	In progress		x	
V-4	Viton fluoroelastomer	x	x		
V-8	Viton fluoroelastomer	x	x		
G-31	Carbon-graphite material	x		x	

REFERENCES

1. Development of High-Efficiency, Cost-Effective Zinc-Chlorine Batteries for Utility Peak-Shaving, 1976. Palo Alto, Calif.: Electric Power Research Institute, March 1978. EM-711.

2. Development of the Zinc-Chlorine Battery for Utility Applications. Palo Alto, Calif.: Electric Power Research Institute, April 1979. EM-1051.

Section 27

MATERIALS QUALIFICATION: II. GRAPHITES

ABSTRACT

Graphite is the only material presently used for both electrodes and buses in the zinc-chloride battery. Through Phase I of RP226-3, ATJ, EBP, and PG-60, three graphites manufactured by Union Carbide, were the only graphites qualified for use in the battery. These are relatively expensive materials whose prices have risen in recent years. Therefore, a program was implemented to qualify low-cost graphites for use in the battery. Fourteen dense and nine porous materials were evaluated. At least four of the porous materials were qualified on the basis of these tests. All but one of the dense materials passed preliminary screening tests. In further testing, one of the lower-priced materials performed well in test cells and submodules of the BEST-battery design.

INTRODUCTION

Criteria for the development of the zinc-chloride battery for the commercial electric-utility load-leveling applications include utilization of low-cost and readily available materials for battery components. Because it fulfills these criteria as well as offering a high degree of chemical inertness and good cycle-life, graphite is presently used as the zinc and chlorine electrode substrate material as well as the bus material in the EPRI 45-kWh battery module and the prototype BEST-battery modules.

The unique design of the zinc-chloride battery requires the positive, or chlorine electrode, to be made of a porous material so that the electrolyte can flow through it. Chlorine electrodes were first made of porous graphite in 1971-72 in a 60-kWh demonstration system for an electric vehicle. While the demonstration system successfully exhibited the feasibility of the zinc-chloride battery concept, relatively low voltaic performance was demonstrated by the porous-graphite electrodes (1).

Subsequently, excellent voltaic performance was achieved in batteries operating with ruthenia-catalyzed, porous-titanium chlorine electrodes (2). Although the current price of ruthenized titanium is comparable to (though higher than) that of porous graphite, large-scale demand for ruthenium could result in prohibitive costs for this type of chlorine electrode. Furthermore, the sensitivity in the performance of ruthenia-catalyzed electrodes to electrolyte pH and the reduced overpotential for hydrogen formation, create additional operational limitations and problems when compared to porous-graphite electrodes for this application.

During the last four years, techniques have been developed that decrease the overpotential for the chlorine reaction on the porous graphite and thereby improve battery voltaic performance (3). Thus, porous graphite again became the chlorine-electrode substrate material because of its low cost and availability. At the beginning of Phase II, Union Carbide porous graphite, grade 60 (PG-60) was the only porous-graphite chlorine-electrode material qualified for use in the battery. This material, however, is a

relatively expensive porous graphite. Accordingly, it has been necessary to search for alternate less-expensive porous graphites.

Until now only two dense graphites have been used in the zinc-chloride battery. These two graphites, ATJ and EBP are two molded, fine-grained graphites produced by Union Carbide. The latter is a purified grade of the former. These graphites have desirable properties and are known to perform well in the zinc-chloride battery system. These high-quality graphites are also relatively expensive.

For these reasons, a program of graphite evaluation was implemented to determine the feasibility of using other less-costly graphites in the zinc-chloride battery. This study deals with the qualification program for 9 candidate porous and 14 dense graphite materials. The materials selected for qualification have physical properties similar to those of PG-60 and EBP. Criteria for selection also included low-cost and availability from the manufacturer for use on a commercial basis in the near future.

Testing of the porous materials concentrated on voltaic performance and the effect of the materials on coulombic efficiency. Other tests were conducted to determine the stability of these potential chlorine-electrode materials under extremely corrosive conditions. Dense graphites were also tested for coulombic efficiency effects as well as the performance which could be anticipated when utilizing the materials as zinc electrodes. The latter test included measurements on capacity density, zinc-plate adhesion, and zinc-plate morphology.

EXPERIMENTAL DETAIL

Materials Evaluated

Fourteen dense-graphite materials were evaluated in this study. They were selected using cost and availability as the criteria. These graphites as well as their manufacturers and cost are listed in Table 27-1 along with the ATJ and EBP graphites used as test controls. The graphites are produced by four different manufacturers. As can be seen from this table, all of these materials are less expensive than Union Carbide grade ATJ and EBP graphites presently used in the zinc-chloride batteries.

Table 27-1

DENSE GRAPHITES TESTED IN MATERIALS-EVALUATION PROGRAM

Designation	Status	1977 Cost ($/lb)
SRA	Commercial	0.90
SXA	"	1.13
ATJ	"	3.82
JVB	"	NA
SQC	"	1.03
EBP	"	5.44
CLD	"	2.15
CE	Experimental	--
LMF	Commercial	1.29
HG	"	3.74
HI	"	2.79
LJ	"	2.00
20K	"	3.50
26L	"	1.20
99M	"	3.42
26N	"	3.71

The nine porous-graphite materials were chosen, in part, because they have physical properties similar to PG-60. The physical properties and costs of these materials and of PG-60, are listed in Table 27-2. While the other graphites are commercially available, the 19C porous graphites are experimental materials that can be produced on a commercial basis in the near future. All candidate graphites were less expensive than PG-60. The PG-60 material was used as a control graphite for all of the tests.

Table 27-2

PHYSICAL PROPERTIES AND PRICE OF POROUS GRAPHITES SELECTED FOR EVALUATION

Graphite Designation	Apparent Density (g/cm^3)	Electrical Resisitivity ($m\Omega$-cm)	Flexural Strength (psi)	Cost ($/lb)
PG-60	1.05	3.0	400	5.67
24A	1.04	NA	300	5.39
23B	1.00	3.0	250	4.21
13D	1.05	3.8	400	4.31
19C	1.36	1.6	1480	2.00
19C-1	1.30	1.6	1740	2.00
19C-2	1.20	2.0	1110	2.00
19C-3	1.20	2.1	1000	2.00
19C-5	1.06	3.1	510	2.00
19C-6	1.15	2.4	720	2.00

Test Equipment

The test cell used in this study is shown in Figure 27-1 in an exploded view. This cell was selected as it allows easy removal and replacement of the zinc and chlorine electrodes. Electrolyte pressure drop through the chlorine-electrode was monitored by reading the height of electrolyte in the stand pipes during cell operation. The test system is shown schematically in Figure 27-2. Temperature was maintained with an electronic temperature controller, a silicone diode temperature probe, and a 100-watt quartz immersion heater. This combination is capable of controlling temperature in this system with an accuracy of ±1°C. Electrolyte flow rate was monitored with a Brooks R2-15B rotameter calibrated with the test electrolyte. A Teflon and glass needle valve was used to control the rate of electrolyte flow.

Voltages were monitored using a digital voltmeter. Changes in charge and discharge voltage were signaled by an electronic analog voltage detector. Ampere-minutes of charge and discharge were measured using electronic analog counters calibrated to an accuracy of ±0.5%. Because the same counter was used for both charge and discharge, however, the error in coulombic-efficiency measurements attributable to these instruments is likely to be much smaller.

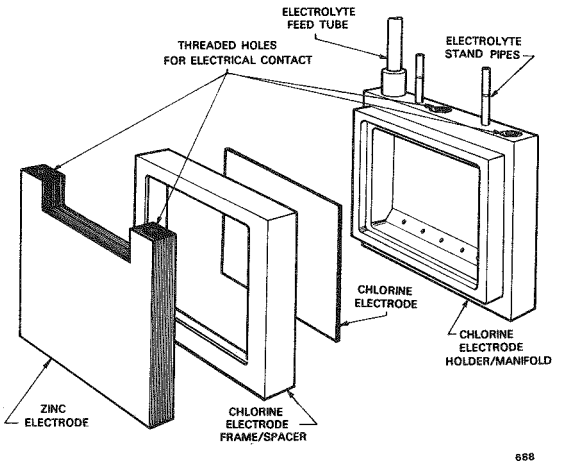

Figure 27-1. Exploded view of the test cell. Pressure drop across the porous-chlorine electrode is indicated by the height of electrolyte in a stand-pipe. The entire cell fits into a case/clamp (not shown) to ensure electrical contact and liquid seal.

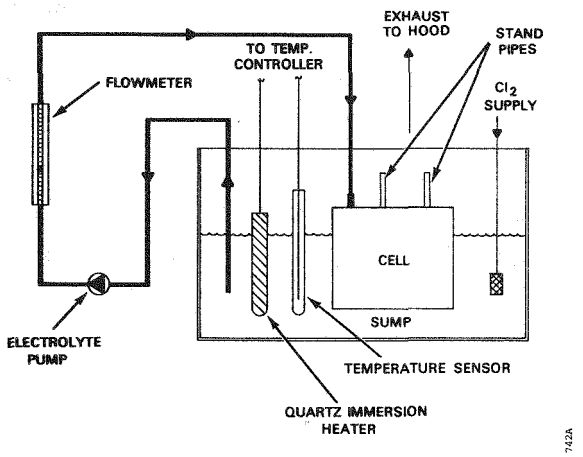

Figure 27-2. Schematic representation of the test system. Temperature is maintained with a quartz immersion heater, thermocouple, and temperature controller.

Chlorine was dissolved in the electrolyte by feeding cylinder chlorine to a gas-dispersion tube located in the sump. The electrolyte was chlorine saturated whenever chlorine was used in a particular test. Components of the system which came into contact with the electrolyte were made of graphite, Teflon, Kynar, glass, titanium, and quartz exclusively. Tantalum wires were used for electrical contact because this material offers lower electrical resistance than titanium.

Qualification Testing Procedures

The qualification testing of the dense graphites is divided into two basic categories: measurements of the effects of impurities in the graphites on cell coulombic efficiency, and measurements of the zinc plating characteristics of the materials such as battery capacity, zinc adhesion, and zinc morphology when employing the various test materials as the zinc electrode. The qualification testing of the porous-graphite electrodes can be broken down into three distinct classifications: measurement of voltaic performance characteristics (including polarization data and voltage versus flow-rate profiles), coulombic efficiency tests to determine the effect of contaminants that will leach from the graphites, and electrode-stability measurements on graphites.

Effect on Coulombic Efficiency. The purpose of this qualification test is to determine if the candidate graphites contain appreciable quantities of leachable impurities which will affect the coulombic efficiency of zinc-chloride cells during extended cycling. In lieu of an actual use test, requiring extensive cycle testing to qualify candidate materials, a screening test was developed to determine the effect of leachable contaminants on coulombic efficiency. It has been demonstrated in the past that several chemical species are capable of lowering the hydrogen overpotential on zinc to the point where hydrogen gas is formed at a rate which significantly affects coulombic efficiency (4).

One electrode of each material was placed in 500 ml of concentrated reagent-grade hydrochloric acid (37.7% by weight) to leach the contaminants for one month at ambient temperature. The beakers were manually agitated each working day. After one month, 106 ml of each hydrochloric acid solution were added to six liters of 2M $ZnCl_2$. This quantity is the volume of hydrochloric acid required to lower the pH of this solution to approximately 0.1. Repeatable coulombic efficiency baseline data were achieved on all test cells. The same electrolyte formulation was used with pH adjusted, using uncontaminated reagent-grade hydrochloric acid. Following the baseline control cycles, the cells were cycled using the contaminated test electrolytes. Unactivated PG-60 electrodes were used in all cells to minimize the effects of contamination and to standardize the tests. Current densities during charge and discharge were 45 and 40 mA/cm^2, respectively. The period of charge was three hours. The electrolyte flow rate was 2 ml/cm^2-min on both charge and discharge.

All coulombic efficiencies were determined under a test regime in which the cells were discharged at constant current until the cell voltage dropped to 1.6 volts and then discharged at constant voltage until the current density dropped to 5 mA/cm^2. At this point, coulombic efficiency measured in the discharge is defined as the usable coulombic efficiency.

Voltaic Performance. The purpose of this qualification test is to determine the level of activation and the corresponding electrolytic processing requirements for the various candidate porous graphites. After electrolytic activation, acceptable materials should demonstrate voltaic characteristics similar to PG-60.

All porous materials were machined into flat-plate electrodes. They were machined with an end-mill finish which prevents loose graphite from being ground into the pores of the material. Two electrodes of each material were tested.

The electrolyte chosen for this phase of testing was 3M $ZnCl_2$ + 2M KCl, pH = 0.1. Temperature was maintained at 30°C. The electrolyte flow rate was maintained at 2.0/3.5 ml/cm^2-min for charge/discharge. This high discharge flow rate prevents slight variations in the flow rate and/or the chlorine concentration from significantly affecting the discharge voltage. Tests were made with the electrolyte saturated with chlorine (~2.7 g/ℓ). A two-hour charge period was used for all cycles. Two hours is adequate charge time to prevent the occurrence of changes in voltage attributable to the zinc plate.

Polarization data were taken near the end of charge and approximately 15 minutes into discharge. This is enough time to allow discharge voltages to properly stabilize. Voltage versus electrolyte flow-rate data were recorded immediately following polarization measurements. All voltages reported are working-cell voltages. This assumes small (<30 mV at 40 mA/cm^2) and repeatable overpotentials on the zinc electrode. These voltages eliminate the need for a reference electrode.

Consecutive activation steps were performed on each type of porous graphite. Each step involved electrolytic activation of the chlorine electrodes for a total of 300 mAh/cm^2 in 1% zinc chloride solution. The above described voltaic performance measurements were performed on virgin materials. After each activation step, both the practical limit of activity achievable and the amount of electrolytic processing required to achieve this limit were determined.

Chlorine Electrode Stability. One of the most important requirements placed on chlorine-electrode materials is dimensional stability during electrochemical cycling in the potentially corrosive environment of the zinc-chloride battery. Once again, measurement of this property with a use test would require extensive cycling. Therefore, a test was designed in which corrosive battery conditions were exaggerated to hasten the degradation phenomenon.

In these tests, electrodes were anodically treated in dilute hydrochloric acid (pH = 0.7) at 60 mA/cm^2 for approximately 21 hours. Before electrolysis, the electrodes were treated by heating them in an oven to 250°C and then plunging them into boiling water. This process removes any loose graphite left on the surface by the machining process. The electrodes were then oven-dried at 100°C and weighed to five significant figures on a Mettler beam balance every hour until their weight stabilized. After electrolysis, the electrodes were rinsed by flowing deionized water through them for one hour. They were next oven-dried and weighed in the same manner as described above. Finally, the percentage weight loss was calculated. Comparison of the weight-loss data indicates the relative degradation rates of the porous-graphite materials.

Zinc Electrode Performance. The loading (charge capacity density) of the zinc electrode has a direct influence on the cost of the battery ($/kWh). The relationship between capacity density and the zinc electrode graphite substrate is not well understood. Nevertheless, this aspect of the dense materials was investigated with the hope of screening those candidates which demonstrated grossly negative results with respect to capacity density. Related to the charge capacity density is the zinc plate morphology. Therefore, qualitative measurements were made of the type of zinc plate obtained when utilizing the various materials as the zinc electrode. Also important to capacity and coulombic efficiency is the adherence of the zinc to the graphite substrate. A significant lack of adhesion can result in peeling or flaking of the zinc plate which gives rise to cell inefficiency. Therefore, adhesion strength was also used to screen each material. Lastly, incidental to this adhesion strength measurement, the zinc plate was weighed and the charge coulombic efficiency, ε_c^c was calculated as the ratio of the measured weight and the weight expected on the basis of Faraday's Law. This measurement of the charge coulombic efficiency was to be used to substantiate data obtained from the other tests as well as to validate differences observed in these tests.

To measure these four zinc-electrode parameters, a standardized test was developed. All dense materials were machined into zinc electrodes and employed in the cells shown in Figure 27-1. All electrodes were machined with a grind-finish. The cells were charged at 45 mA/cm^2. Temperature was maintained at 30°C and electrolyte flow rate at 2 ml/cm^2-min. Cells were charged in this manner until heavy dendriting occurred on the zinc plate. A voltage detector was set to automatically terminate the charge mode when it had sensed a voltage excursion of greater than approximately 200 mV. This is used as the operational definition of a dendrite. The product of the period of charge and current density is termed the charge capacity density of the battery and is usually expressed in mAh/cm^2.

After charge was terminated, the cell was removed from the sump and disassembled. The zinc plate obtained was then inspected with respect to zinc morphology. The brightness and porosity of zinc plates and the quantity and location of dendrites were the types of observations made. After the electrode was inspected, the zinc plate was peeled from the electrode using a spring scale. The maximum force required to remove the zinc plate from the graphite substrate in this way was measured. The zinc plate was then rinsed with deionized water, dried, and weighed on a Mettler analytical balance to five significant figures with an accuracy of ±0.1%. This weight was then used to determine the charge coulombic efficiency obtained when utilizing the materials as zinc electrodes.

These tests were performed five times on each material. The electrodes were then reverse-charged for three hours at 10 mA/cm^2. This process involves reversing the polarity of the cell and charging in the normal manner. Chlorine is evolved at the zinc electrode during this process. This reversal is designed to simulate longer-term cycling of an electrode. Subsequent to the reverse charging, the cell was charged once more in the same manner as before using the same zinc electrode. The purpose of this is to determine the performance which can be anticipated from the candidate materials after a significant period of battery operation. All measurements were repeated during this last test.

EXPERIMENTAL RESULTS AND DISCUSSION

These tests were performed over approximately a one-year period. Chronologically, the porous-graphite materials were evaluated first, followed by the dense-graphite materials. Where both types of graphites were subjected to the same type of qualification test, the results will be reported and discussed together.

Effect on Coulombic Efficiency

Since coulombic efficiency testing is time-intensive, requiring long charge periods and the generation of an extensive data base, testing of this aspect of candidate porous materials was limited to a narrowed field. Materials 19C-3 and 19C-5 were chosen using cost, voltaic performance, and physical properties as the major criteria. Material 19C-5 also was chosen because of its physical similarity to PG-60. Conversely, 19C-3 was chosen for its higher density and strength characteristics, as well as its lower electrical resistivity. PG-60 was tested as the control against which the other porous materials were compared. Coulombic efficiency test results are given in Figure 27-3 for PG-60, and 19C-3 and 19C-5. As can be seen in Figure 27-3, no effect on coulombic efficiency was observed for any of the materials.

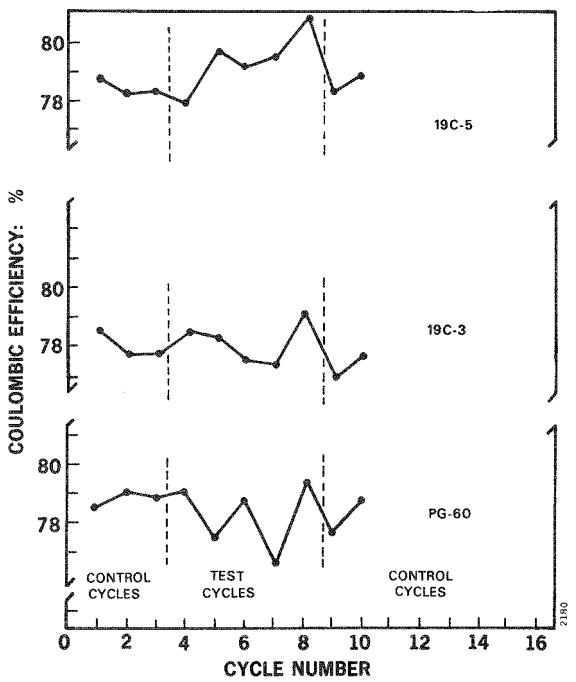

Figure 27-3. Results of the coulombic efficiency screening test for porous graphites showed no difference between test cycles accomplished using electrolyte pH adjusted with acid, contaminated by the graphite, and control cycles.

These tests were repeated after the porous graphites were exposed to the acid for two additional months. Once again no effect was observed. It is difficult to draw concrete conclusions from this test, but it appears that 19C-3, 19C-5, and PG-60 do not measurably affect coulombic efficiency via the leaching of deleterious contaminants.

Analysis of variance was performed on the coulombic efficiency data recorded for cycles 1-10 on the three cells. The results indicate statistically significant differences between cells over the 10 cycles at the 90% confidence level. However, no significant differences were identified between control cycles and test cycles on individual cells. This can be stated with relative certainty due to small variations within each group of data. Therefore, contamination from the graphites at these levels does not appear to adversely affect coulombic efficiency.

All dense materials except CLD were tested in this same manner. CLD was not tested in this phase of the study due to the unavailability of this material at the time of testing. Tests were performed, however, on graphite SQC, the material from which CLD is purified. Therefore, results obtained from tests on SQC could be used as the "worst-case" for CLD.

Results given in Table 27-3 indicate that very little difference exists between test cycles made with the electrolyte contaminated with the various test materials and those cycles accomplished with control electrolyte. Analysis of variance performed on these data indicate that although differences exist from cell to cell, no difference exists between control cycles and test cycles made with any material at the 95% confidence level. It can be concluded then, that leached contaminants from these materials do not adversely affect coulombic efficiency.

Chemical analyses were performed on samples of the contaminated acids used in adjusting the pH of the zinc-chlo-

ride electrolyte used in these tests. A Spectrametrics Spectranspan IIIA emission spectrometer was used to make a qualitative determination of contamination present in these solutions. The uncontaminated control hydrochloric acid did exhibit contamination by several elements. However, about three times as many elements were present in most samples of contaminated acid.

Table 27-3

RESULTS OF THE COULOMBIC EFFICIENCY SCREENING TESTS ON DENSE GRAPHITES

Cell No.	Material	Cycle No. 1	2	3	4	5
1	SQC	77.7	77.8	77.4	77.9	78.5
2	ATJ	78.0	79.4	79.3	79.0	80.1
3	SRA	78.4	78.2	78.0	78.2	78.4
1	Control	77.6				
2	Control	79.8				
3	Control	78.2				
1	LJ	78.4	77.3	77.2	76.2	77.4
2	20K	78.8	79.1	79.3	78.5	78.7
3	SXA	79.2	78.6	78.4	78.8	78.4
1	Control	78.7				
2	Control	80.2				
3	Control	79.3				
1	CE	78.0	77.9	77.0	78.1	77.7
2	JVB	79.6	79.5	79.5	79.5	79.6
3	EBP	79.1	77.9	78.6	78.6	78.4
1	Control	77.9				
2	Control	79.9				
3	Control	78.6				
1	HI	78.1	77.7	77.9	78.4	77.6
2	CLD	79.1	78.7	79.6	79.6	79.0
3	LMF	78.4	78.7	78.7	79.2	78.7
1	Control	77.6				
2	Control	79.0				
3	Control	78.0				
1	26N	78.5	78.3	78.1	77.9	77.7
2	99M	79.2	78.6	79.0	79.1	78.4
3	26L	77.9	79.1	79.0	79.4	79.4
1	Control	78.4	77.7	77.7		
2	Control	78.8	78.1	78.3		
3	Control	78.5	79.0	78.7		
4	Control	73.5	77.4	74.4	75.2	74.6
4	HG	72.5	74.8	73.4	75.3	73.8

Furthermore, several of these elements such as titanium and calcium are typically found in graphite materials. Again, it is difficult to draw concrete conclusions from these results due to the qualitative nature of the measurement and the presence of background contamination in the control acid. Moreover, since all materials were found to have no effect on coulombic efficiency in this screening test, determination of the levels of elements which are detrimental to coulombic efficiency based on this test would be virtually impossible.

It is worthy of note that although no effect on coulombic efficiency was observed in these tests, several of the hydrochloric acid samples were seen to demonstrate a pronounced color change after prolonged exposure to the graphites. Even after the addition of samples of these contaminated acids to unacidified electrolyte the color change was apparent. Color changes of this magnitude are not generally associated with normal cell cycling.

It is difficult to extrapolate these coulombic efficiency results to actual contamination levels in the 45-kWh battery modules due to differences in geometry and conditions. Furthermore, synergism between contaminants leaching from these graphites and from other materials that may be included in the BEST-battery modules may have an effect on performance. For these reasons, this test is valid only as a screening tool. Final coulombic-efficiency qualification can only come after use-testing at the two-cell or submodule level.

Voltaic Performance

Polarization data for various porous-graphite materials are given in Figure 27-4 for the unactivated electrodes and in Figure 27-5 for the electrodes after the activation process. As can be seen, PG-60 achieves a significantly higher discharge voltage ($\sim$60mV at 40 mA/cm^2) than the other materials in the unactivated state. However, after activation, the difference in discharge voltage between PG-60 and 19C-5, the best-performing of the candidate materials, is less than 5mV at 40 mA/cm^2. It should be noted that there is a difference in the degree of electrolytic activation required to make these materials perform equivalently. For example, to obtain equivalent voltages on discharge, 19C-5 requires twice the degree of activation as PG-60. The quantities of activation required by test materials to achieve optimum voltages are given in Table 27-4. As can be seen from this table, most of the candidate materials require about the same degree of electrolytic activation. Differences in the extent of electrolytic activation required to impart maximum voltaic efficiency to a PG-60 electrode reported here and previously could be related to the differences in evaluation conditions. No attempt will be made in this section to explain these differences.

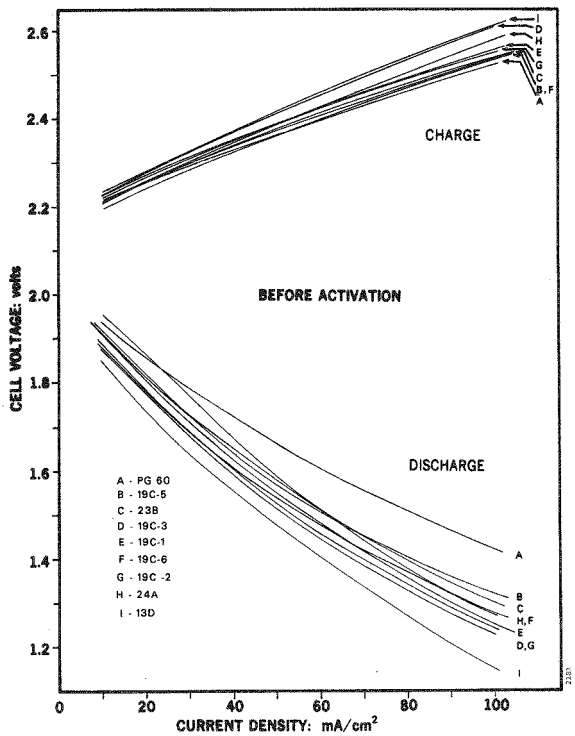

Figure 27-4. Working cell polarization curves before activation (as received from machine shop) for the various candidate porous materials. Note the differences in voltaic performance among the porous materials is accentuated during discharge.

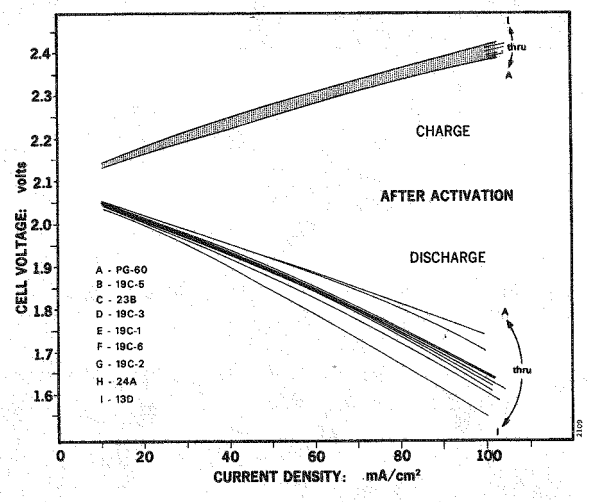

Figure 27-5. Polarization curves for the candidate porous materials after complete activation. Under battery operating conditions (<50 mA/cm^2), a number of candidate graphites are capable of achieving voltages comparable to those of PG-60.

Table 27-4

ELECTROLYTIC ACTIVATION REQUIRED TO OBTAIN OPTIMAL VOLTAIC PERFORMANCE

Material	Degree of Activation (mAh/cm^2)
PG-60	450 - 600
24A	900 - 1200
23B	900 - 1200
13D	1500 - 1800
19C	1500
19C-1	900 - 1200
19C-2	600 - 900
19C-3	1200
19C-5	900 - 1200
19C-6	900

Small differences in voltages (< 20 mV) can be accounted for by slight variations in the conductivity of the electrolyte caused by differences in temperature (2-3°C), variations in the composition of the electrolyte, and differences from cell to cell in the electrolyte flow rate.

Under selected conditions, the maximum voltaic efficiencies attained with electrodes manufactured from the various test materials are reported in Table 27-5. These data again illustrate the relative similarity in chlorine-electrode activity demonstrated by both the activated candidate materials and activated PG-60.

Table 27-5

VOLTAIC AND PRESSURE CHARACTERISTICS OF FULLY-ACTIVATED POROUS ELECTRODES

Electrode Material	Pressure Drop (cm of electrolyte)	Maximum Voltaic Efficiency(%)
PG-60	1.0 - 2.2	87.1
24A	1.0 - 3.7	85.6
23B	1.0	86.3
13D	1.0 - 2.0	84.3
19C	1.0 - 13.0	86.1
19C-1	1.0 - 8.7	86.0
19C-2	1.0 - 3.7	85.8
19C-3	1.0 - 2.2	86.5
19C-5	1.0	87.2
19C-6	1.0	86.4

The pressure drops developed by flowing electrolyte through the electrodes at 2 ml/cm^2-min are also reported in Table 27-5. The pressure drops through all materials are low -- a few centimeters of electrolyte. Precise measurement of these low pressure drops could not be obtained due to cell geometry and the presence of opaque Kynar fittings in the electrolyte standpipes. However, it can be stated that all of the graphites tested possess, to varying degrees, little resistance to the flowing electrolyte. The hydraulic resistance of all the electrodes is small compared to the resistance of the chlorine-electrode feeder tubes employed in both the EPRI 45-kWh and BEST-battery modules.

At least four porous-graphite materials, 19C-1, -3, -5, and -6, as well as, 23B achieved voltages comparable to PG-60 under standard test conditions. All the materials are capable of performing within 20 mV of PG-60 on discharge at 40 mA/cm^2. The differences are even less during charge.

As can be seen from Figure 27-5, PG-60 exhibits the most linear discharge polarization curve and out-performs the candidate materials in voltage by ∿100 mV at 100 mA/cm^2. Under this higher current density condition the electrochemical reaction is driven deeper into the pores of the electrode resulting in increased overpotential on the electrode. The magnitude of this increase could depend on the thickness of the activated surface layer and/or the physical properties of the unactivated bulk-electrode material. If the activated surface layer is thicker for PG-60 than it is for the candidate porous graphites, then it will demonstrate improved voltaic performance at higher current densities. Similarly if the unactivated PG-60 bulk-electrode material incorporates a more optimal pore-size distribution, or other pertinent physical characteristics, it will also demonstrate improved voltaic performance as the reaction penetrates beyond the activated surface layer. It is believed that these phenomena account for the linear discharge polarization characteristic demonstrated by PG-60 porous-graphite electrodes.

A plot of electrolyte flow rate versus cell discharge voltage for materials in the fully-activated state is given in Figure 27-6. Under these conditions, all of the materials exhibit curves of similar shape with the voltage drop-off point occurring around 1 ml/cm^2-min. This indicates that, despite differences in physical properties, all the materials possess virtually the same mass-transfer limitation characteristics. The experimental points corresponding to 0.5 ml/cm^2-min in Figure 27-6 are connected to the other points with a broken line indicating that these are unstable voltages that could be in error by more than one volt. Very low electrolyte flow rates are difficult to control due to the limitations of the Teflon needle valves used in these systems to regulate flow. With respect to this measurement, there appear to be very few differences between the materials.

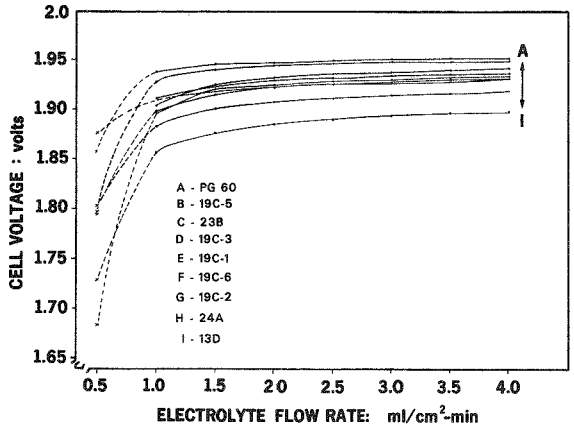

Figure 27-6. Voltage versus electrolyte flow rate profile at 40 mA/cm^2 for the porous materials tested. All materials demonstrate essentially the same characteristics with respect to this measurment. Experimental points corresponding to 0.5 ml/cm^2-min are connected to the other points with a broken line to indicate that these lower values are unstable voltages.

Chlorine Electrode Stability

The relative rates of physical degradation of graphites 19C-3, 19C-5, and PG-60 under the exaggerated conditions described in the previous section are given in Table 27-6. Of the three materials listed, PG-60 has the highest rate of physical deterioration. Although only a few tests were conducted, it appears that a relationship could exist between density and stability. This implies that, during degradation or activation, the layer of degraded or activated material could be thinner for the denser materials than it is for the less dense PG-60 material. The mechanism of physical deterioration that determines the finite life of the chlorine electrode during the operation

of the battery is not well understood. It is believed to be related to oxidation of the graphite electrode substrate, as is the case under these exaggerated test conditions. However, it is difficult to correlate these data with expected electrode life. Assuming the mechanisms are similar, the data suggest that either of the two test materials will have a longer life under battery operating conditions than PG-60.

Zinc Electrode Performance

Achievable charge capacity densities varied appreciably, both within each set of tests performed on each material and between test materials. The greatest average value of 251 mAh/cm^2 was obtained for material HI. The lowest average value of 167 mAh/cm^2 was obtained for SRA, a coarse-grained inexpensive material. Excluding this lower value, capacity for all other materials is in the range of approximately 200-250 mAh/cm^2. In results from tests on ATJ, capacity varied from 200 to 228 mAh/cm^2 when tests were made on different electrodes machined from the same material. This indicates that normal statistical distribution could be responsible for the range exhibited by the materials tested. Only one electrode of each material was generally tested because of time considerations. Variations within groups are large relative to differences between groups, therefore the differences observed between materials cannot be considered significant on the basis of this test. In any case, it can be concluded that gross difference between materials with respect to capacity obtained when employing the materials as the zinc electrode, do not exist, with the possible exception of SRA graphite.

The strength of the physical bond (adhesion) between the electrodeposited zinc and the substrate also demonstrated variability, ranging from a low of 16×10^3 dynes for graphite CE to a high value of 178×10^3 dynes for material LJ. There appears to be a relationship between grain size in the graphite and adhesion strength between the graphite and zinc plate based on these data. The finer-grained materials such as ATJ and CE exhibit a lower force of adhesion while coarser-grained graphites such as SQC and CLD demonstrate a greater adhesion force. This is probably related to the greater porosity of these coarse-grained materials. Graphite ATJ, which has performed favorably for some time as the zinc electrode, achieved one of the lowest adhesion values. Therefore, the significance of the differences observed in these tests is probably not great. These values will increase with time as the surface of the electrode is altered by the plating process.

Table 27-6

RESULTS OF ELECTRODE-STABILITY TESTS

Electrode Material	Test No.	Weight Loss, % Exptl.	Weight Loss, % Average	Apparent Density, g/cm^3 Manufacturer	Apparent Density, g/cm^3 Measured at EDA
PG-60	1	36.6	33.2	1.06	0.96 - 0.99
	2	29.7			
19C-5	1	26.9	28.6	1.06	0.96 - 1.06
	2	30.4			
19C-3	1	22.9	21.4	1.20	1.12 - 1.24
	2	20.0			

The effect of substrate morphology on zinc plate morphology is not well understood. Prominences in the substrate will, however, lead to dendrite formation. A quantitative understanding of the effect of porosity of the substrate and hence, irregularities of the plate, on dendrite formation, however, does not exist. In any case, measurements of charge coulombic efficiency made incidental to other measurements by weighing the peeled zinc plates are difficult to interpret. Average values of this property lie in the range of 80-85%. Attempts to correlate these values with adhesion strength or zinc plating capacity were unsuccessful due to large variations between groups as well as possible differences in the baselines of each of three cells used in this study. Comparison was made in each cell between the test material and ATJ, the control graphite. Differences between test and control cycles do not appear great.

The type of zinc plate obtained (bright, dull, dendrites, etc.) when using each material as the zinc electrode was qualitatively determined. Zinc plates were classifed and categorized with these results being analyzed for possible differences from material to material. Plates obtained were generally moderately bright with scattered dendrites. Differences in porosity of the zinc plate, brightness of zinc, and location of dendrites were observed in tests on many materials. These occurrences were randomly distributed in tests on a particular material. These differences are attributed to normal experimental error associated with test conditions, electrolyte formulation, and slight physical differences from cell to cell.

Due to the randomness of these results, it appears that a statistically designed experiment requiring the generation of a rather large database would be necessary to completely qualify a material with respect to this particular property. The fact that these values are randomly distributed and not repeatable in any one group of tests, however, does indicate that gross effects resulting from surface differences do not exist. More subtle differences which remain undetected by these tests may, however, be present. Further testing would, however, have to be limited to a narrowed field of candidate materials due to the degree of data required on each material.

Additional Dense Graphite Qualification

Graphite CLD was selected for further qualification testing in cells of the Phase II battery design. These cells contain three chlorine electrode pairs and two zinc electrodes, of exactly the same dimensions as those employed in the battery submodule. The zinc electrodes were cut from CLD billets with a wafer-saw. Materials of construction were idential to those in use in the modules: PVC, Kynar, glass, Teflon, graphite, and titanium. Test conditions were also the same. Current densitites on both charge and discharge were 33 mA/cm^2. Temperature was usually maintained at 30°C during charge and 40°C on discharge.

Results from these tests show CLD to be comparable to ATJ chemically and electrochemially when utilized as the zinc electrode. Although most cycles included only a four-hour charge, a few seven-hour charge cycles were accomplished. The occurrence of dendrites in these tests was comparable to that during tests of ATJ. Coulombic efficiency results were similar for the four-hour charge cycles, however, a slight difference was observed for the seven-hour charge cycle. This difference is not thought to be significant at this time due to the limited quantity of data available. Furthermore, differences in the surface finish may contribute to this result.

REFERENCES

1. P. C. Symons and P. Carr. "Chlorine Electrodes in the Zinc-Chlorine Battery System." Proceedings of the Eighth Intersociety Energy Conversion Engineering Conference Philadelphia, Pa., August 13-17, 1973.

2. P. C. Symons and M. J. Hammond. Evaluation of a 1-kWh Zinc-Chloride Battery System. Palo, Alto, Calif.: Electric Power Research Institute, 1976. EM-249.

3. A. F. Laethem and G. E. Sussman. "Activation of Porous-Graphite Chlorine Electrodes for Zinc-Chlorine Hydrate Batteries." In Proceedings of the 154th Electrochemical Society Meeting. Vol. 78-2, 1978, pp. 193-5.

4. Development of High-Efficiency Cost-Effective, Zinc-Chlorine Batteries for Utility Peak-Sharing, 1976. Palo Alto, Calif.: Electric Power Research Institute, 1978. EM-711.

Section 28

BATTERY STACK: CELL DEVELOPMENT

ABSTRACT

The objective of this study was to develop a flat-plate chlorine-electrode frame design which, when employed in zinc-chloride cells and submodules, would allow achievement of the BEST-battery performance specifications. These specifications are delivery of $\geq$165 mAh/cm^2 at $\geq$65% electrochemical energy efficiency. Two frame designs were evaluated in twenty-five cells of 80-Wh size. With minor modifications, one of these designs was developed to consistently meet and exceed these performance targets at the cell level.

INTRODUCTION

The stack design of the EPRI 45-kWh battery module, i.e., the Phase I submodule design, was discussed in Sections 15 and 16. This design incorporated profiled porous-graphite chlorine electrodes. These assemblies were formed by glueing together two machined-cavity porous-graphite plates. The processing costs associated with this design feature prompted the establishment of a submodule design and development program early in Phase II. This submodule design and development effort was also stimulated by the need to develop a more manufacturable design in anticipation of the BEST-Battery Program. In general, this new -- Phase II -- submodule design was to be more cost-effective and manufacturable than the Phase I design.

Early in Phase II, a set of specifications were established for the design. The more significant of these were: (a) low-cost materials (plastics and graphites); (b) plastic components designed for mass-production fabrication techniques; and (c) flat-plate chlorine electrodes. With the signing of the contract for the BEST-Battery Program, performance specifications were also established for the Phase II submodules. Table 28-1 compares these performance specifications with the

Table 28-1

BEST BATTERY OBJECTIVES COMPARED WITH PHASE I SUBMODULE PERFORMANCE

	BEST OBJECTIVE	REFURBISHED PHASE I Low	High
Delivered Energy, kWh	8.7	7.8	8.7
Electrochemical Energy Efficiency, %	65.0	59.4	66.7
Coulombic Efficiency, %	76.0	69.2	78.2
Voltaic Efficiency, %	85.0	85.9	85.4

performances demonstrated by the Phase I submodules. To consistently meet or exceed these objectives, the Phase II submodule design must also effectively isolate unit cells and achieve good coulombic efficiency balance.

Sections 26 and 27 addressed the qualification of low-cost plastics and graphites for use in the Phase II submodule. The following section -- Section 29 -- describes the submodule design and the development of the design at the submodule level. This section deals with the development of one of the main components -- the flat-plate chlorine-electrode frame. Two designs were evaluated in small zinc-chloride test cells. One of these designs was developed to provide consistent performances at the cell level which exceeded the BEST-battery performance objectives.

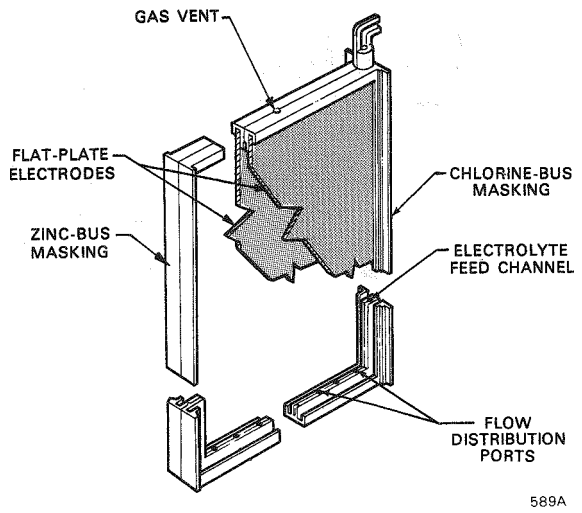

Figure 28-1. Two-piece "clamshell" frame design. The injection-molded frame halves -- mirror images of each other -- are joined to form the completed frame shown.

FRAME DESIGNS

Two different frame designs were evaluated in the course of these studies. They both incorporated essentially the same features, but differed significantly in achieving these features.

The first and original frame concept was the all-PVC two-piece "clamshell" unit, which is shown in Figure 28-1. An ultrasonic welding technique was employed to join the two injection molded PVC frame halves. A noteworthy feature of this frame, which testing revealed to be unacceptable, is the formation of the electrolyte feed-channel from PVC. Flow-uniformity to the chlorine-electrode pairs is governed by this hydraulically resistive channel. Any changes in pressure drop through these channels can materially affect a cell's performance, i.e., lead to flow imbalances and result in poor voltage-time discharge profiles. Degradation of the PVC in this channel by the chlorinated electrolyte was discovered during testing.

Because the success of this new stack design depended quite heavily on the successful development of a chlorine-electrode frame, a second frame was designed on the BEST-Battery Program. The development of this design was conducted in parallel with the above effort. This design, referred to as the four-piece frame, is shown in Figure 28-2. Again, inexpensive PVC was used to form the more massive frame members. Kynar was employed in those components where its enhanced chemical inertness was considered desirable, i.e., the electrolyte channel and

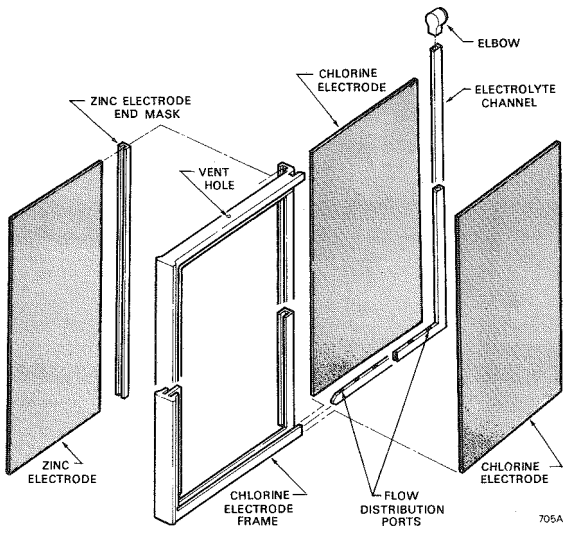

Figure 28-2. Four-piece frame design.

manifold elbow. Smaller parts with critical tolerances were more readily injection moldable in Kynar than PVC. For this reason, the zinc-electrode end-mask was also made of Kynar. The impact on cost was negligible, as these components are much less massive than the PVC frame member. Still cost-effective, these more technically sound four-piece frames are now employed in all Phase II submodules. The ability to injection mold these frame assemblies/components is a major accomplishment in the manufacturability of the zinc-chloride battery.

EXPERIMENTAL DETAILS

Cell/System Design

Chlorine-electrode termination is employed in these Phase II test cells as shown in Figure 28-3. Three framed chlorine packs are mated with two zinc electrodes. In this manner non-active graphite-surface area, which is an extension of the zinc plate, has been minimized. By employing chlorine-electrode termination, improved coulombic-efficiency repeatability was expected. These cells also employ a 0.2 cm inter-electrode gap.

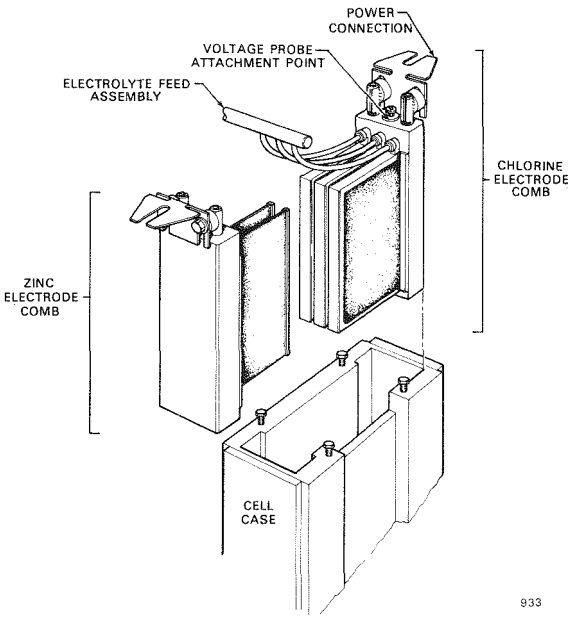

Figure 28-3. The Phase II test cell.

This test program employed an integrated cell/system assembly basically equivalent in design to the Phase I test cell/system described in Section 14. A view of the Phase II system appears in Figure 28-4. A small gear-pump is used to circulate electrolyte. Flow control is accomplished by varying pump speed; it is monitored with the rotameter shown. The electrolyte temperature is controlled using a proportional controller, quartz heating element, and glass-sheathed temperature probe. Provision is also made for sparging chlorine into the electrolyte sump. All case penetrations are properly sealed to allow vacuum operation. Not shown is the vacuum source. Vacuum was accomplished by pumping water in a closed loop through an aspirator.

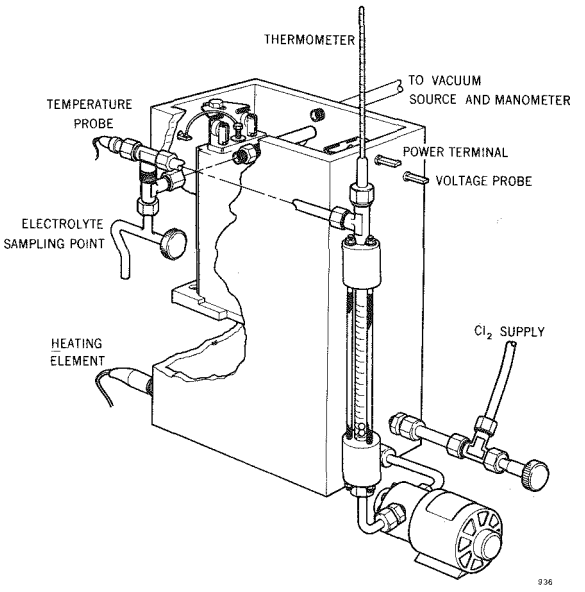

Figure 28-4. The Phase II test system. A glass-plate and gasket (not shown) are used to cover and seal the assembly.

By making electrical connections at the top of the buses, penetrations of the inner cell case are avoided. This prevents spurious flows due to draining of the inner cell case as was encountered in the study of the Phase I cells (see Section 14). Coulombic efficiency is determined with a digital coulo-

meter. A digital watt-hour meter is used to monitor cycle energy efficiency. Cell voltage is taken at the buses off current-free probes as shown in the figures.

Operational Conditions

The standard operating conditions employed, with the exception of system pressure and electrolyte volume, follow the BEST-battery module specifications. A 2.5M $ZnCl_2$ + 2.0M KCl, pH 0.2 electrolyte was employed. Charge/discharge temperatures were controlled at 30/40°C (±1°C). Electrolyte flow-rate was 2 ml/cm^2-min. Both the volume of electrolyte and level of vacuum (during charge) were greater in these tests than those specified for the modules. The larger electrolyte volume was nearly compensated for in the full-charge cycles by charging for 7 hours instead of 6.6 hours. The level of vacuum averaged about -6 psig and was employed only during charge. Although different, this should compare with typical module conditions of -4 to -5 psig during both charge and discharge. A current density of 33 mA/cm^2 was employed on both charge and discharge. A charge duration of 3.5 to 4 hours was employed in the majority of cycles taken. Periodically, longer (7-hour) charges for capacity were performed.

Activation

Each newly assembled cell was activated electrolytically using conditions developed for the 19C-5 porous-graphite electrode material. With the exception of a slightly longer processing time, the process is similar to that reported previously (1).

RESULTS AND DISCUSSION

To date in this program, a total of 25 small test cells have been assembled and evaluated. Due to the type of testing employed, none of these cells accumulated an extensive number of cycles. Performance data from selected cells are presented and compared with the BEST-battery performance objectives in Table 28-2. Demonstrated performances can be seen to meet or exceed the targets.

Performance repeatability for a given cell and reproducibility from cell to cell to date has not been as good as anticipacted. Variability in coulombic efficiency was primarily responsible. Two factors, neither of which are design related, are thought to have influenced cell operation and led to this type of behavior. Firstly, and most importantly, none of these cells have undergone the extensive testing

Table 28-2

PERFORMANCE OF PHASE II CELLS

FRAMING	CELL NO.	NUMBER OF CYCLES	PERFORMANCE RANGE ε_c	ε_v	ε_e
Two Piece	IV	16	74-81	86-88	65-70
Two Piece	V	15	75-82	87-88	65-72
Four Piece	XII	14	79-82	85-86	67-70
Four Piece	XIII	9	76-79	85-87	65-67
Four Piece	XV	20	75-82	84-87	65-70
BEST-Battery Requirements	--	--	76	85	65

which the Phase I cells had. For this reason, satisfactory "clean-up" of the cells had not been accomplished. Difficulties encountered in control of vacuum level may also have played a role.

Voltaic efficiency generally exceeded the targeted 85% value. Although newly activated cells demonstrated 88-89% voltaic efficiency on the first cycle or two, this would drop as additional cycles were taken. They would routinely level-out at 85-87%.

The bulk of this data was obtained on short four-hour charge cycles. Capacity, however, was periodically evaluated. Although seven-hour charge capacity was not achieved on every attempt, cell performance in this regard would in general improve with continued cycling and reach this objective.

Two-Piece Frame Evaluation

Evaluation of the two-piece frame design began in April 1979. As shown in Table 28-2, these frames met and exceeded the targeted objectives for a reasonable number of cycles. Eventually, however, performance of these cells began to deteriorate. This was manifested by a significant increase in the differential between full-power and usable coulombic efficiencies. The initial 0.5-1% differential rose to over 5%. Flow testing of the frames revealed a significant flow imbalance among the chlorine-electrode pairs. This created maldistribution in current sharing between the paralleled zinc plates during discharge and increased the differential between the full-power and usable coulombic efficiencies.

Blistering and swelling of the injection-molded PVC electrolyte-feed channels was identified as the source of the flow imbalance. A brief discussion of this topic appears in Section 26. Prior to the development of these flow imbalances, however, the performance of cells with these two-piece chlorine electrode frames met and surpassed the BEST-battery performance objectives.

Four-Piece Frame Evaluation

This evaluation was initiated when the four-piece frames became available in early August 1979. The use of Kynar for the fabrication of the electrolyte-feed channel prevented the eventual development of electrolyte flow imbalances as observed with the two-piece design. As indicated by the data in Table 28-2, cells which employed this four-piece chlorine-electrode frame design demonstrated performances which also met or exceeded the objectives. These frames are now employed in the submodules being fabricated for the prototype BEST-battery modules.

Cells operating with both the two-piece and four-piece frames typically demonstrated good voltage-time discharge profiles as shown in Figure 28-5. The slope of the profile before the "knee" is at least as good as that obtained with Phase I cells.

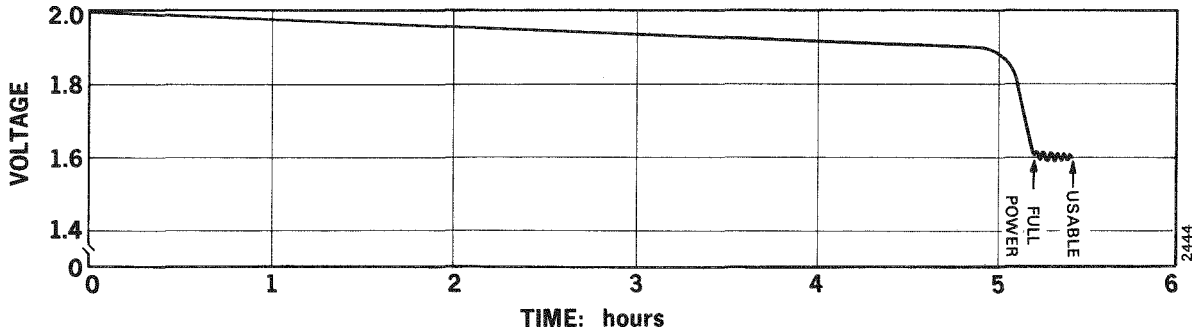

Figure 28-5. Discharge voltage-time profile of Phase II cell.

The differential between the full-power and usable coulombic efficiency data points for the Phase II cells was somewhat larger than with the Phase I units. This is thought to reflect a slightly poorer electrolyte flow balance between the chlorine packs.

Design Modifications

Attainment of the performance objectives at the cell level necessitated two minor design modifications. These were successfully accomplished, and are now employed in submodules.

The first modification resulted from masking deficiencies at the chlorine-bus. This problem was encountered early in the program and was readily overcome as shown in Figure 28-6. In the original design, overlap of adjacent frames resulted in a narrow path -- exaggerated for clarity in the figure -- through which zinc grew and short-circuited to the chlorine bus. The consequence of this deficiency -- i.e., capacity limitation -- led to the modification shown. This modification alleviated the problem.

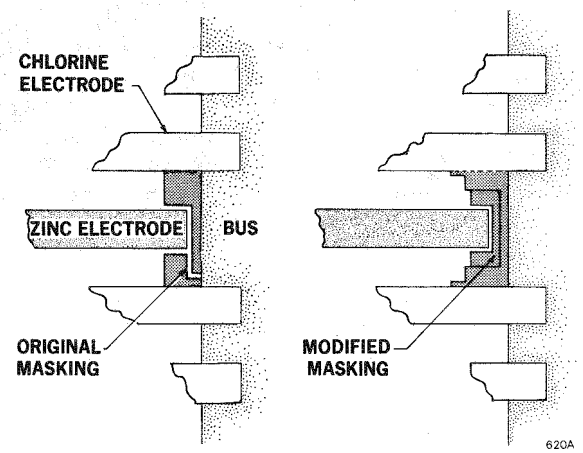

Figure 28-6. Correction of masking deficiency. In the original masking format, a gap -- the size of which has been exaggerated for clarity -- allowed zinc to plate and short to the chlorine bus.

The second modification resulted from the bowing and breakage of a few PG-60 chlorine electrodes during activation of pre-prototype submodules. This problem was never observed at the cell level, but the design modification -- emanating from the BEST Program -- was tested here to evaluate its effect on efficiency and capacity. A PVC pin was incorporated in the center of the chlorine-electrode pair for support as illustrated in Figure 28-7. The ends of the pin are flattened to form retainer buttons.

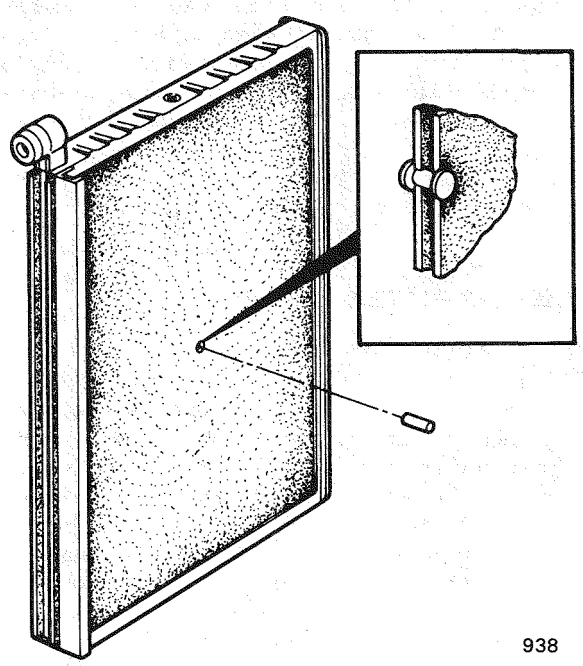

Figure 28-7. Central support of the flat-plate chlorine electrodes. A PVC pin is inserted through holes in the flat-plate electrodes; the ends of this pin are then flattened.

It was believed that the center masking of the chlorine electrode, by these retainer buttons, would affect zinc-plate uniformity in the corresponding region of the zinc electrode. The plate in this region was thinner, but coverage remained complete and continuous. No adverse effect on performance has been seen. Retaining pins are now employed in all submodules.

Program Status

A suitable injection-molded chlorine-electrode frame design has been developed. Cells employing these frames achieve and surpass the performance objectives established for the BEST-battery modules. Electrochemical energy efficiencies in the range of 66-69% are typical.

The following section (Section 29) discusses other aspects of the flat-plate chlorine-electrode submodule design. The objective there is to retain a similar level of performance as cells are assembled in parallel and series to form 20-volt, 90-ampere sub-modules.

REFERENCES

1. Development of the Zinc-Chlorine Battery for Utility Applications. Palo Alto, Calif.: Electric Power Research Institute, April 1979. EM-1051.

Section 29

BATTERY STACK: SUBMODULE DEVELOPMENT

ABSTRACT

At the beginning of Phase II of RP226-3, a more cost-effective and manufacturable submodule design was sought for the stack of the BEST-battery modules. To consistently achieve the electrochemical energy efficiency target of 65%, the design also had to provide improved unit-cell isolation and coulombic-efficiency balance relative to Phase I submodules. A new -- Phase II -- submodule was designed which incorporates low-cost graphites, low-cost injection-molded PVC components, flat-plate chlorine electrodes, and PVC-framed bus bars. This design has been developed to the level where it achieves electrochemical energy efficiencies in the range of 62-64%.

INTRODUCTION

The design and performance of the Phase I submodules were discussed in Section 15. They incorporated profiled porous-graphite chlorine electrodes. Even in pilot-production quantities, this design feature would be quite impractical and not cost-effective. The Phase I submodules also suffered from design faults which caused appreciable coulombic efficiency imbalances among unit cells.

Early in Phase II, a program was initiated to design and develop a more cost-effective and manufacturable submodule in anticipation of the BEST-Battery Program. The approach was to incorporate (a) more cost-effective materials of construction, (b) plastic components designed for mass-production fabrication techniques, and (c) flat-plate chlorine electrodes. Also the design was to address the isolation of unit cells in order to improve the coulombic efficiency balance.

Sections 26 and 27 reviewed the progress made in the qualification of low-cost plastics and graphites for use in this new submodule design. The previous section -- Section 28 -- reviewed the successful development of a flat-plate chlorine-electrode frame, fabricated by the injection-molding process. This section discusses the progress made in the development of this new design, designated the Phase II submodule. Incorporated in the design are low-cost flat-plate chlorine electrodes and injection-molded PVC plastic components. Submodules of this design are evaluated with respect to meeting the performance objectives detailed in Table 29-1. The effectiveness of the design in achieving balanced coulombic efficiencies among unit cells is emphasized. Developmental testing leading to the achievement of 62-64% electrochemical energy efficiency is also discussed.

SUBMODULE DESIGN

The objective of this effort was to conceive and develop a new submodule design which was both more manufacturable and less costly to produce than the Phase I submodules. The approach was to reduce the number of component parts, design them for mass production, and incorporate flat-plate chlorine electrodes as discussed in Section 28. As pilot-scale production quantities are required for the BEST-battery modules, practicality of assembly is also of significance.

Table 29-1

PHASE II SUBMODULE PERFORMANCE TARGETS

Charge/Discharge Current	90.8 A
Charge Duration	6.6 h
Discharge Duration	5.0 h
Coulombic Efficiency	76%
Charge Voltage	22.6 V
Discharge Voltage	19.2 V
Voltaic Efficiency	85%
Electrochemical Energy Efficiency	65%
Delivered Energy	8.7 kWh
Submodule Active Area,	2.75 m^2

To meet performance targets, the new design must effectively overcome the deficiencies identified in the Phase I submodules. Isolation of unit cells must be sufficient to ensure against the formation of the intercell zinc growths discussed in Section 15. To accomplish this objective, the Phase II design encapsulates the graphite bus bars in a two-piece PVC picture frame to provide a better bus-to-case seal and isolate adjacent unit cells.

The full submodule design is shown in Figure 29-1. Ten unit cells are series-connected using the comb-type bipolar design. The unit is much less complicated than its predecessor in that fewer parts are employed. Important features include:

- The unit-cell electrolyte manifold is incorporated into the plastic bus-framing. A simpler, more structurally sound assembly results.
- The electrolyte collection cup and a resistive outlet channel-plate are part of the unit-cell-tray subassembly.

Details of electrolyte feed and distribution are readily seen in Figure 29-2. Incorporation of the unit-cell manifolding into the bus-framing is readily seen here. With the four-piece chlorine-electrode frames, described in the previous section, the elbow is pressed or snapped into its manifold port. This is accomplished at the same time that the electrode pair is press-fit into the bus.

The new design retains zinc-electrode termination in the unit cells. This decision was based upon the conviction that the bus sealing technique employed would provide the isolation necessary, thereby avoiding the need to switch to chlorine-electrode termination.

This submodule design is less complicated than its predecessor, the Phase I submodule. Fewer and generally more massive components are employed. Ease of assembly was a design criterion. Of major significance is the use of commercially available PVC which allows standard joining techniques -- solvent bonding and ultrasonic welding -- to be employed.

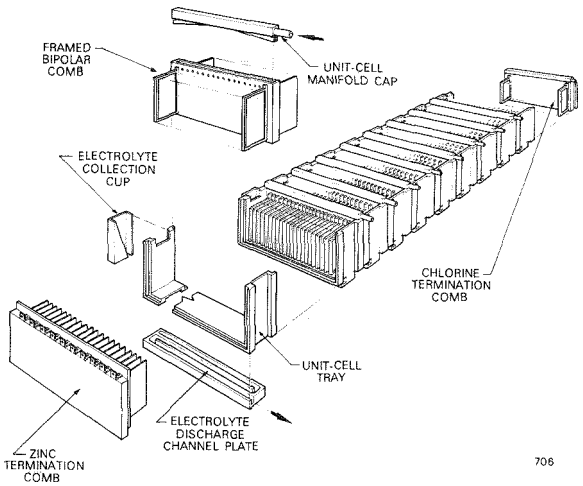

Figure 29-1. Exploded view of Phase II submodule.

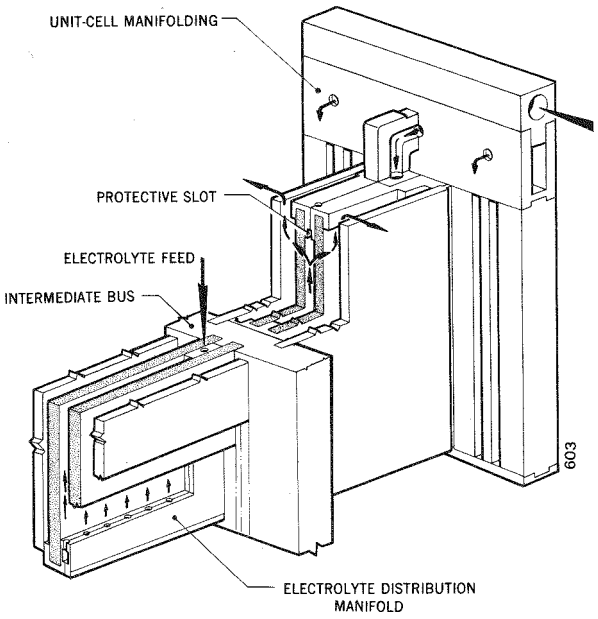

Figure 29-2. Section of Phase II submodule design showing electrolyte flow.

EXPERIMENTAL DETAILS

Test Stand

Figure 29-3 is a schematic of the test system currently employed in test and evaluation of the Phase II design submodules. This test stand design, developed over the past few years at EDA, has become standard due to its flexibility and the presence of certain special diagnostic capabilities.

Using a gear-type gas pump, reduced stack pressures can be established during charge or discharge to approximate module operating conditions. A mercury manometer is used to monitor system pressure. System temperature is maintained by use of glycol heating and cooling baths which reject or accept heat from the electrolyte in the in-line heat exchanger. Coulombic efficiency is determined with the aid of a digital coulometer, while the energy efficiency is determined with the aid of a digital watt-hour meter.

For diagnostic purposes, electrolyte sampling points are provided. Chlorine concentration, specific gravity and pH are therefore easily attainable. With the above described system, chlorine is injected into the electrolyte stream on the high-pressure side of the electrolyte pump during discharge. The in-line filter also serves to separate undissolved gas from the electrolyte stream. This gas is then vented through a separate line to the gas space of the submodule test stand.

The qualification testing of Phase II submodules for the prototype BEST-battery modules has been performed on similar, but somewhat different, test systems. Because much of the data reported in this section were obtained on those systems, the differences are briefly described. The two major differences involve the absence of the filter/gas separation device, and the discharge chlorine being injected on the low-pressure side of the electrolyte pump. The former detail does not adversely affect operation or performance because a provision for venting undissolved chlorine is incorporated into the chlorine-electrode frames and represents the normal operating mode in the module. The later difference, however, of injecting chlorine into the pump inlet, did lead to certain concerns about the dissolved-chlorine levels on discharge. These levels tended to be abnormally high and difficult to control.

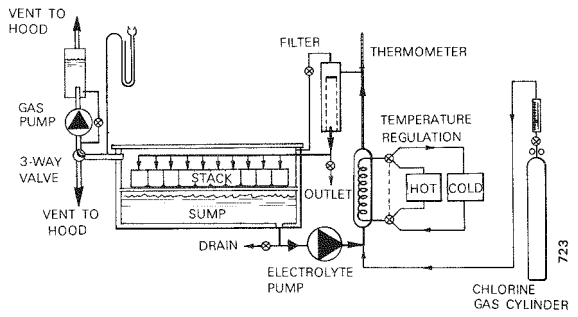

Figure 29-3. Schematic of submodule test stand.

Operational Conditions

The standard operating conditions employed in the evaluation of submodule units are dictated by the operational specifications of the battery module. These are detailed in Table 29-2. These conditions were adhered to throughout the majority of tests. Wherever deviation from these fixed conditions occurred, the conditions employed are detailed as part of the discussion.

The 2.5M $ZnCl_2$ + 2.0M KCl electrolyte system was employed in the majority of tests conducted. A proprietary leveling agent was used to achieve needed plate capacity. Concentrated reagent grade HCl is used to adjust pH to the 0.1-0.2 range prior to each charge.

Table 29-2

STANDARD OPERATING CONDITIONS
SUBMODULE TEST AND EVALUATION

Current density	33 mA/cm^2
Charge duration	7 h
Temperature	30/40°C
System pressure	-4 psig
Electrolyte flowrate	2 ml/cm^2-min
$[Cl_2]$	satd. soln.

Submodule Activation and Processing

Difficulties encountered in the in-situ activation of chlorine electrodes plagued the processing of the first eight submodules which were fabricated with PG-60 chlorine electrodes. Experience indicated that the electrode bowing and breakage which occurred during this period was at least partially, if not completely, related to the material used (this batch of PG-60 graphite).

When the 19C-5 porous graphite -- low-cost material qualified for battery use as described in Section 27 -- became available, it did not possess the same sensitivity to the standard processing that PG-60 demonstrated. Process modifications had already been developed, however, for PG-60 and these modifications were continued with the new material to minimize the electrode stress generated during processing.

An overnight tap-water rinse was routinely employed between activation and evaluation. As difficulties were encountered during test, due to particulate graphitic debris generated during activation, a procedure for flushing water between the electrodes was employed. With more recent units, partial disassembly and flushing was employed.

RESULTS AND DISCUSSION

At the time of this writing, eleven submodule units have been fabricated with 19C-5 chlorine electrodes. These are in addition to the eight initial units employing PG-60 chlorine electrodes which were produced due to the unavailability of the 19C-5 early in the program.

The production of the PG-60 units was undertaken to allow test and evaluation of the system aspects of the first prototype BEST-battery module, thereby avoiding delay in that area. Because these units did not contain the specified porous-graphite chlorine electrodes, their performance characteristics are not covered in any detail here.

Of the eleven submodule units employing 19C-5 chlorine electrode material, only two units to date have received any level of extensive testing, i.e., beyond a few evaluative cycles. These

two units -- 79J003, which has accumulated in excess of forty cycles, and L80A5, which has at present accumulated 15 cycles -- provide the bulk of data reported. Other units contribute to a lesser degree.

Four major areas have been addressed in the evaluation and development of the submodule design for the BEST-battery modules. These areas are: (1) effectiveness of the design in preventing inter-cell zinc growths, (2) achieving the usable coulombic efficiency target of 76%, (3) achieving the voltaic efficiency target of 85%, and (4) identifying and overcoming failure modes. These areas are now addressed separately.

Design Effectiveness

Of major concern was the avoidance of zinc growths between unit-cells in the Phase II submodule design. This phenomenon was responsible for the excessive coulombic efficiency imbalance in the Phase I design submodules (Section 15). The balance in coulombic efficiency among unit cells is easily determined by inspection of the recorder trace showing its voltage - time discharge profile. Such a trace from submodule L80A5 is reproduced in Figure 29-4.

As a general rule, all Phase II submodules displayed discharge profiles which indicate good balance among unit cells. The figure of merit in this regard is the absence of "steps" in the discharge profile. Although steps on occasion were observed, the imbalances they represented were at most 5-7%. The Phase I submodules had shown in excess of 30% imbalance occasionally. The imbalances observed in these Phase II submodules were found to result from a subassembly failure, and were not the result of short-circuiting between unit cells. Correction of this deficiency is described later in this section. The effectiveness of the Phase II design in preventing the zinc growth phenomenon was then confirmed by disassembly and visual inspection of fully-charged submodules.

Both the slope of the discharge profile and the differential between the full power coulombic (16 volts at 33 mA/cm^2) and the usable coulombic (16 volts at 5 mA/cm^2) efficiencies are of major importance to overall battery performance. A typical voltage-time profile for discharge is shown in Figure 29-4. From this, it may be deduced that the Phase II submodules appear at least equivalent to their Phase I predecessors.

Coulombic Efficiency

Despite the good cell balance described above, the coulombic efficiency (ε_c) of the new submodules consistently fell 6-10% below the expected level (∿78%), based upon Phase I submodule experience and Phase II cell test data. The exact magnitude of this shortfall did not

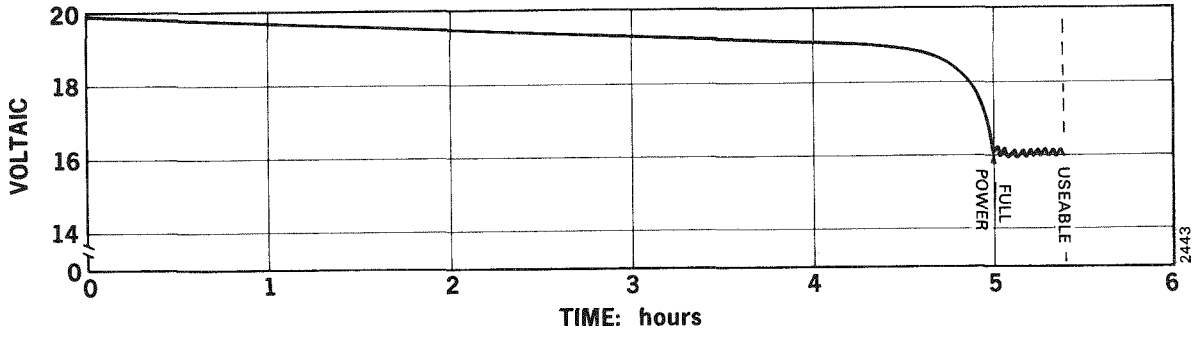

Figure 29-4. Discharge voltage-time profile of a Phase II submodule. Unit-cell balance is demonstrated by the absence of any "steps" in the profile.

become evident until the subassembly failures described below had been identified and corrected.

The cause of the shortfall was not identified until the last quarter of Phase II. In a study using a bipolar comb (4-volt) test assembly (as described in Section 15), excessive levels of hydrogen were found. Tests performed at ambient pressure revealed hydrogen gas concentration levels in the range of 1-6% during charge. The resultant ε_c of the two unit cells ranged from 63-65%. This contrasts with the 67-71% and the 0.1-0.2% H_2 levels obtained in small test cells.

The addition of a known hydrogen suppressant to the electrolyte was successful in significantly lowering the hydrogen formation rate and leading to increases in ε_c. The ε_c increased to the 70% level at ambient pressure, and to the 74-78% range under a vacuum of 0.5 atm (charge only). These ε_c levels are comparable to those obtained in the small test cells.

Not yet understood is the source of the hydrogen observed. The electrolyte pH did not undergo a change corresponding to the quantity of hydrogen evolved. This suggests a source other than the free HCl which is used to adjust the starting pH of the electrolyte. Surprisingly, high levels of CO_2 were found in addition to the H_2 present. These data further suggest an organic or carbonaceous source for this apparent electrolyte contamination which led to H_2 and CO_2 cogeneration.

At the submodule level, similar results have been obtained. Suppression of hydrogen by use of an additive has resulted in an increased coulombic efficiency.

Voltaic Efficiency

In contrast to the results obtained with test cells, submodules to date have not exhibited any detectable decay in their voltaic efficiency (ε_v). This statement reflects the data for the two units which have accumulated a reasonable number of test cycles -- L80A5 with 15 cycles and 79J003 with close to 40. An ε_v of 85-86% is anticipated based upon results obtained with these two units.

In addition to being relatively stable over these cycles, the voltaic efficiencies of these submodules are about 3-4% lower than those obtained with newly activated test cells. After cycling, however, test cells stabilize at a voltaic-efficiency level comparable to these submodules.

The ε_v stability described above was obtained in testing with the electrolyte system of choice -- 2.5M $ZnCl_2$ + 2.0M KCl. When 79J003 was tested for 8 cycles with an alternate electrolyte -- 2.0M $ZnCl_2$ + 0.5M KCl -- a 2% drop in ε_v was encountered as of the sixth cycle. By polarizing the unit, this loss was recovered. Sensitivity to chloride ion concentration in the electrolyte may be indicated.

Failure Modes

Two submodule failure modes, both attributable to the failure of PVC joining techniques, have been identified. The corrective actions taken to date have proven satisfactory.

A few of the early submodules, including 79J003, were found to exhibit or develop steps in their discharge profiles. Coulombic efficiency imbalances between unit cells of 5-7%, were the cause of concern regarding zinc-growth accumulations in these units.

Assistance was provided the BEST-Battery Program in identifying the problem as a flow imbalance caused by the failure of an ultrasonic weld on the PVC bus-frame assembly. Figure 29-5 illustrates the failure of this joint as it was observed during disassembly and inspection. The ultrasonically-welded frame sections were supposed to provide a reasonable seal

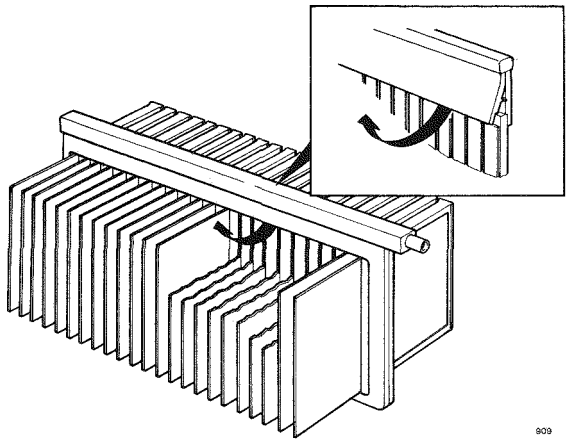

Figure 29-5. Failure of bus-framing weld resulted in electrolyte-flow imbalances.

to the graphite bus and a leak-tight seal to one another, as they formed the unit-cell electrolyte distribution manifold. When the leak-tight seal failed, electrolyte was diverted from the chlorine electrodes of one unit cell directly into its neighboring unit cell.

A solvent bonding technique has proved successful in repairing all submodule units produced. Adequate to excellent unit-cell balance was again achieved. With subsequent submodules produced, the practice of solvent bonding in addition to welding of the PVC bus-framing halves has been adopted.

A second and more catastrophic failure mode was encountered with one of the initial PG-60 units. The unit-cell manifold cap (see Figure 29-1) separated from the framed comb assembly. Massive flow imbalances developed, making discharge virtually impossible. With attention to assembly detail, and improvements in the solvent bonding technique employed, failures of this nature have not occurred since.

PROGRAM STATUS

The major objective -- design and development of a cost-effective battery stack using flat-plate chlorine electrodes and low-cost graphite materials -- has been successfully accomplished. From a performance standpoint, the new design is technically sound. Most importantly, the design effectively prevents formation of intercell zinc-growths.

Although the source of electrolyte contamination has not yet been identified, contamination leading to excessive hydrogen formation has been established as the cause of suppressed coulombic efficiency. This has been partially overcome by the addition of a hydrogen-suppressing additive to the electrolyte. Only a single unit -- L80A5 -- has undergone test since this development. Four cycles accomplished to date have given the results presented in Table 29-3.

Table 29-3

PHASE II SUBMODULE PERFORMANCE

	Test No.			
	9	12	14	15
Full-Power Coulombic Efficiency (%)	70.0	71.3	70.6	69.6
Usable Coulombic Efficiency, ε_c (%)	73.0	73.8	74.0	73.6
Voltaic Efficiency, ε_v (%)	85.2	86.2	85.7	85.2
Electrochemical Energy Efficiency, ε_e (%)	62.2	63.6	63.4	62.7

These usable coulombic efficiencies are still falling a little short of the targeted efficiency of 76%. The demonstrated voltaic efficiencies are meeting the target of 85%. State-of-the-art electrochemical energy efficiencies are about 1-3% short of the 65% target. As of this writing, studies directed towards meeting this target continue. These include: (a) development of an improved electrolyte formulation; (b) optimization of operational conditions; and (c) secondary activation of submodule chlorine electrodes in order to recover the shortfall in coulombic efficiency as a voltaic-efficiency increase.

Section 30

PASSIVE HYDROGEN-RECOMBINATION REACTOR DEVELOPMENT

ABSTRACT

The recombination of hydrogen -- formed chemically and/or electrochemically during normal battery operation -- with chlorine is presently catalyzed by fluorescent-light reactors to maintain hydrogen concentrations in the module gas-space below hazardous levels, i.e., 5%. Although the hydrogen formation rate is very low -- less than 0.5% of chlorine formation rate during charge -- it could accumulate to hazardous levels in the event of bulb or power failure. This study deals with the experimental evaluation of self-powered tritium lights, based on beta-excitation of phosphor, as a backup passive reactor for the continuous and safe operation of the battery. Experiments conducted with several different types of tritium lights at hydrogen levels up to 9% under stagnant conditions and up to 18% under steady-state flow conditions proved that such a reactor is unsuitable for the battery application due to insufficient light intensity.

INTRODUCTION

In the zinc-chloride battery, some hydrogen is produced as an undesirable by-product of the electrolysis of aqueous zinc-chloride during normal operation of the battery. Hydrogen evolution rates, and the reaction of hydrogen with chlorine via photochemical catalysis were studied in previous years at EDA (1). The photochemical reactor was found to be the most suitable for the zinc-chloride battery application.

The photochemical catalysis of the hydrogen/chlorine reaction is presently facilitated by fluorescent-light reactors. An 8-watt fluorescent light source, Sylvania, F8T5/Black Light, was chosen from among other similar types of lights due to its better performance (1). These lights require ac power, last about 6000 hours, and cost $6.30 each. Each BEST-battery module will contain two of these light sources in the stack gas space.

If the ac power to the lights is interrupted during any battery cycle, potentially hazardous conditions could develop if the hydrogen concentration rises above 5%. Therefore, hydrogen concentrations at all times should be maintained below this limit, preferably by means other than those requiring an ac power supply. An alternative reactor was sought which would not require any external power, cost less than $20, last at least 10 years, and be capable of reacting 150 ml/min of hydrogen at the 0.5% level in chlorine.

Due to the success of the fluorescent light reactor, the development of a passive photochemical reactor was undertaken. Use of Self-Powered tritium lights as a back-up safety reactor was investigated. These lights do not require any external power, and have life in excess of seven years. Tritium lights are manufactured by Self-Powered Lighting Ltd. and consist of phosphor-coated glass tubes filled with tritium gas ($^3H_1$) as the excitation source for the phosphor material.

As radioactive materials were involved, the initial testing and development of the passive reactor was given to a subcontractor. The "subcontractor

investigation" subsection covers the work done and data obtained by this subcontractor. Subsequent testing was performed at EDA to qualify the tritium lights as a back-up reactor in the BEST-battery module.

REACTION OF HYDROGEN AND CHLORINE

The combination of hydrogen and chlorine was observed as early as 1801 by Cruikshank. The first investigation was performed by Draper during the 1840s and repeated by Bunsen and Rascoe during 1855-1859 (2). Due to its complicated kinetics, it was investigated extensively during the period of 1920-1940 (3). The reaction is known to be a chain reaction involving the formation of free radicals (4).

The efficiency of a photochemical reactor for hydrogen recombination with chlorine is determined, therefore, by the following parameters: (a) Intensity of light, (b) the wavelengths of radiation emitted by the light source, (c) the contact time that the gases have with the radiation, (d) the hydrogen concentration entering or present in the reactor, (e) the temperature inside of the reactor, (f) gas pressure and wall effects, and (g) inhibitors present in the system.

The reaction rate is directly proportional to the fractional power of the absorbed light intensity where the power varies from 0.5 to 1.0 (2,5,6,7). The intensity of the light source should be at least 10^{14} quanta/sec. It is also very desirable to have a monochromatic source (8).

Chlorine gas molecules absorb light radiation continuously at wavelengths (λ) of 479 nm or below, which covers the blue and violet color band regions as well as the ultraviolet region (7,9). By absorption of light, chlorine molecules disassociate into free radicals and the chain reaction starts.

The quantum yield of the reaction is defined as:

$$\phi = \frac{\text{no. of molecules of HCl formed/sec}}{\text{no. of quanta absorbed/sec}}$$

Values quoted in the literature range from 2×10^4 to 6×10^5 molecules per quantum (10,11,12). Relative quantum yields at various wavelengths are reported as follows: 0.10 at 260 nm, 0.49 at 313 nm, 0.53 at 365 nm, 1.00 at 405 nm, 0.67 at 436 nm, and 0.22 at 546 nm (13).

An indefinite induction period is very likely, during which extremely slow or undetectable chemical change occurs (14). This induction period could be shortened by previous illumination of the gases (2). Traces of ammonia produces long induction periods. Nitric oxide (but not nitrous oxide) and chlorine dioxide also inhibit the reaction (15). The hydrogen chloride produced in the reaction has itself a retarding effect on the reaction rate. The presence of moisture does not affect the quantum yield of the reaction (7).

It was found that, in the absence of oxygen, the reaction is of the first order with respect to the H_2 pressure (7). Also, the reaction rate diminishes as a result of decreasing the total gas pressure. With increasing hydrogen pressures, the quantum yield rises through a maximum. The quantum yield is also reduced by inert gases (16).

The reaction is sensitive to reactor dimensions. Reaction at the wall was suggested by Chapman and Grigg (17), for destroying the Cl atoms because the reaction was slower in capillary tubes than when conducted under the same light intensity in tubes of wider bore, especially at low pressures (15).

SUBCONTRACTOR INVESTIGATION

Self-powered tritium lights are essentially phosphor-coated glass tubes containing tritium ($^3H_1$) gas as the excitation source. The light is shown schematically in Figure 30-1. The beta rays emitted by tritium excite the phosphor molecules and cause the phosphor coating to fluoresce. Light radiation passes through the glass to the environment.

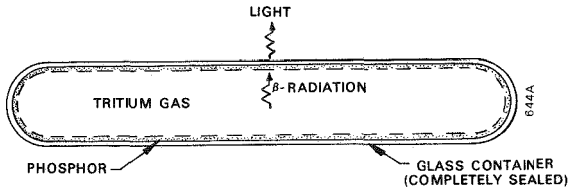

Figure 30-1. Self-powered tritium light. The β-radiation excites the phosphor coating on the inside of the glass ampule to emit light to the environment.

These tubular lights, manufactured by Self-Powered Lighting Ltd., have an outside diameter of of 0.64 cm and are 15.2 cm in length. The wall thickness of the borosilicate glass container, 1 mm, is sufficient to stop the beta rays emitted by tritium gas. The wavelength of the light radiation is determined by the type of phosphor material used. The intensity is varied by varying the tritium pressure. Due to absorption of the beta particles in the tritium gas itself, the brightness of the lights does not increase linearly with tritium pressure.

Preliminary tests to establish the feasibility of tritium-light reactors were conducted by a subcontractor for EDA. Tests were performed using three different types of tritium lights. The reaction vessel used was provided by EDA and is described in the next subsection of this report.

Equal volumes of hydrogen and chlorine were measured in Plexiglass cylinders and were transferred into the reactor vessel with the aid of pressurized nitrogen gas. Therefore, the reaction mixture in the vessel was combination of three gases, i.e., 2.5% Cl_2 + 2.5% H_2 + 95% N_2. The lights were placed in the glass reactor tube and gas samples were taken from the sampling ports. The hydrogen concentration in the sample mixture was monitored by a Bacharach Model G hydrogen sniffer, which measures combustible gases only in the presence of oxygen. Results of tests conducted with two and three lights at 2.5% and 1.8% hydrogen levels under stagnant conditions are given in Figure 30-2. Performance of a F8T5/BL light at the 1.8% hydrogen level, using the same procedure, is also shown on the same graph. From this graph it appears that the tritium lights are effective in catalyzing the hydrogen-chlorine reaction.

EDA STUDIES

Following this demonstration of the proof-of-concept, a study to qualify these lights as a backup reactor for the BEST-battery module was undertaken. This subsection describes the experimental details and the results of the qualification testing.

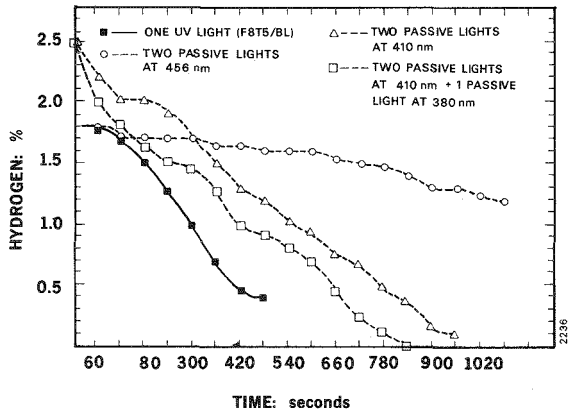

Figure 30-2. Test results obtained by the subcontractor under stagnant conditions in a three-component gas mixture. The data indicate photochemical catalysis of the H_2/Cl_2 reaction.

The reactor system was designed to be used as either a batch or steady-state flow reactor. Figure 30-3 illustrates the reactor system used throughout this study. Both the gas mixing and the reaction vessels were made out of PVC. Dimensions of the main reaction vessel were 6 by 12 by 24 inches (volume: 1 cf) and of the mixing chamber were 6 by 6 by 6 inches with four PVC plate baffles inside, to channel and mix the gases. Hence, a homogeneous gas mixture entered the main reaction vessel where the reaction takes place.

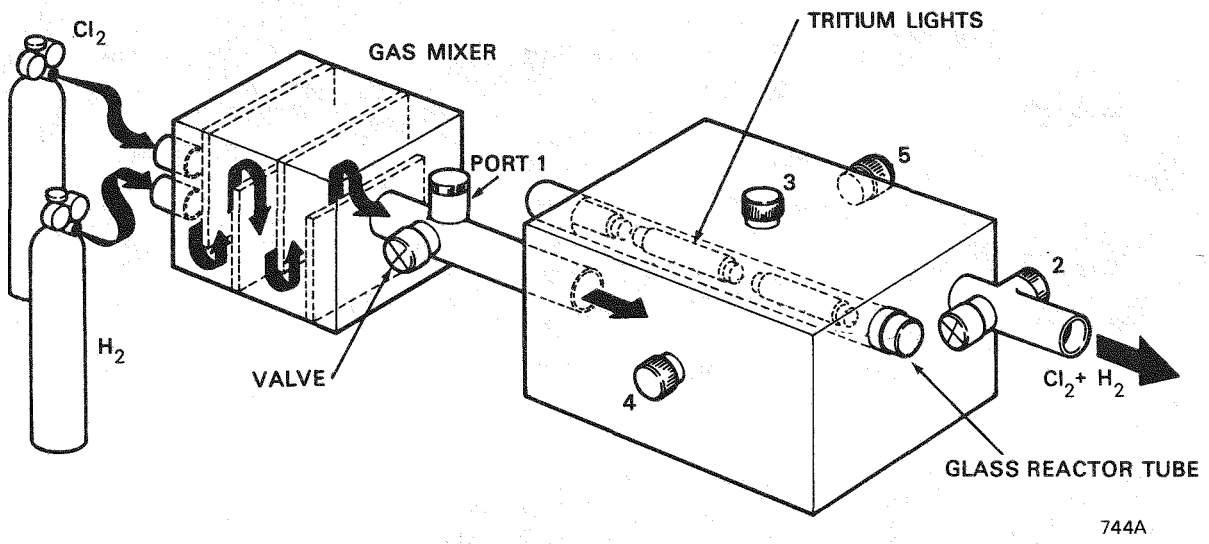

Figure 30-3. Reaction vessel system used in this study. The reactor volume is approximately half of the gas-space volume in the stack of a 50-kWh module.

A glass tube -- 3/4-inch diameter, 26-inch long, and wall thickness of 0.1 inch -- was placed 9 inches below the top, 3 inches from the bottom, and 3 inches from the side walls in the reaction vessel. Light sources were placed in this glass tube during the experiments. The glass tube transmits radiation in 350-3000 nm range which covers the wavelength region of interest for the reaction.

The gas mixing chamber was connected to the inlet of the reaction vessel. A valve was placed in this line. Another valve was placed at the other end of the reaction vessel. The whole system was provided with five gas sampling ports. Three of the ports were on the main reaction vessel, one at the inlet to the vessel after the mixing chamber, and one at the outlet of the reaction vessel after the gases have swept past the lights.

Both hydrogen and chlorine gases were supplied from pressurized cylinders to the mixing chamber. The concentration and the flow rate of the mixture was adjusted by varying the flow rate of the individual gas streams which were monitored using rotameters. All tubes were covered with black tape to avoid external light radiation. Sampling ports were connected to a multi-position valve with thin Teflon tubing. The outlet of this valve was either connected directly to a thermal conductivity gas analyzer, or gas samples were taken with syringes for analysis by gas chromatography, depending on the nature of the testing.

A thermometer was immersed in the vessel one inch above the glass tube, and a manometer was connected to monitor the pressure of the gases in the vessel. For stagnant condition experiments, the reaction vessel was purged with the desired gas mixture of hydrogen and chlorine for 30 minutes; then valves 2 and 1 were closed in such a way so that the gases would have approximately 53.6 mmHg (above ambient) pressure, which would allow sampling during the testing. Lights were inserted in the glass tube and gas samples were taken at certain time intervals from ports 3, 4, and 5. Mostly port 5 was used, because it was the closest port to the reactor tube. Gas samples were taken with syringes and analyzed with a Carle Analytical

Gas Chromatograph, Model 111H. In most experiments, more than one light was used. Lights were placed end-to-end in the glass reactor tube along the length.

In the steady-state flow experiments, ports 3, 4, and 5 were closed. Lights were placed in the glass reactor tube and gas samples were taken only from ports 1 and 2. The sampling ports were directly connected, via the multi-position valve, to a Caldos 4T, Thermal Conductivity Gas Analyzer (Ethyl Intertech Corporation, Princeton, N.J.). This is a continuous measuring unit based on the differences in the thermal conductivity of gas components.

A tritium monitoring device, Triton Model 955B (Johnston Laboratories, Inc., Cockeysville, Maryland) which can detect beta rays around 5×10^{-6} μ Ci/ml of air (maximum permissible dose for tritium) was located adjacent to the experimental set-up. This instrument was to be used only in the case of accidental breakage of the tritium lights. Normally the tritium lights are safe because the beta rays cannot penetrate the 1-mm thick walls of the glass case. The presence of the tritium monitoring device was required by the Nuclear Regulatory Commission.

The tests were conducted using 14 different tritium lights. The lights differ from one another depending on the type of phosphor material and tritium pressure used. Changing the phosphor material and the tritium pressure changes the wavelength and intensity of the radiation emitted, respectively. The phosphor materials were supplied to Self-Powered Lighting by Sylvania. They were selected by EDA on the basis of their wavelength and efficiency characteristics. The phosphor materials used in these tests are listed in Table 30-1.

Table 30-1

TYPES OF PHOSPHOR MATERIAL USED IN THE TRITIUM LIGHTS

Type (Sylvania)	Characteristics	Activity (∿Ci/Light)	Wavelength (λ, nanometer)	Band Width (nanometer)
RH48-22B2 Lanthanum Oxybromide	Blue*	4-6	380	--
SF95-33BB Calcium Tungstate: $CaWO_4$	Blue*	4-6	410	--
RH48-71B1 Lanthanum Oxybromide: Tl	Blue*	4-6	410	--
372	Blue**	17	450	--
2011 Barium Silicate	*	4-6	350	45
2051 Strontium Borate	*	4-6	370	30
2041 Ba, Mg, Sr, Zn Silicate	*	4-6	370	40
217 Ba, Mg Silicate	Violet*	4-6	400	30
1320 ZnS: Ag	Blue**	17	450	30
1250 ZnCdS: Cu	Green**	17	520	-
145 ZnS: Cu	Green**	17	520	36
RH48-22B2 Lanthanum Oxybromide	Blue**	17	380	--
217 Ba, Mg Silicate	Violet**	17	400	30

*Unpressurized (0.65 atm)
**Pressurized (2.5 atm)

Tests were performed at 3-9% hydrogen concentration levels under stagnant conditions, where hydrogen concentrations were monitored as a function of time. Tables 30-2 and 30-3 contain representative test data. As can be seen from these tables there is no decrease in the hydrogen concentration with time, indicating that the lights are not catalyzing the reaction at any detectable rate. The negligible increase in temperature supports the lack of detectable reaction between hydrogen and chlorine which is exothermic.

A test was conducted under stagnant conditions to study the effect of direct contact of the lights with the gas mixture to avoid the possibility of any loss of radiation through the glass reactor tube. This was not expected, as ordinary glass transmits light radiation in the wavelength region of interest. The test results indicated that no detectible reaction was occuring.

Another type of test was conducted under stagnant conditions in order to evaluate the ability of the self-powered lights to sustain the reaction between hydrogen and chlorine once it was initiated by a F8T5/BL fluorescent light. This test was a simulation of the conditions which would exist in the battery module if the fluorescent lights were lost due to a power outage or bulb failure. It would also shorten the induction period which is more apparent at low intensities. The passive lights -- 7 lights at 372-410 nm region -- did not sustain the

Table 30-2

STAGNANT CONDITIONS

Passive Lights: 3 at 450 nm (17 Ci/Light #1320) + 2 at 400 nm (17 Ci/Light #217) + 1 at 400 nm (6 Ci/Light #217)

Time (min)	Port	T°C	H_2%	O_2%	N_2%	CO_2%	CO%
0	5	25.1	4.918	0.016	0.075	N.D.	N.D.
			4.754	0.019	0.668	N.D.	N.D.
			5.082	0.071	0.203	N.D.	N.D.
5	5	25.2	5.443	0.022	0.085	N.D.	N.D.
			4.688	0.635	2.016	N.D.	N.D.
			5.131	0.111	0.341	N.D.	N.D.
15	5	25.2	5.246	0.048	0.146	N.D.	N.D.
			5.197	0.141	0.390	N.D.	N.D.
			5.361	0.072	0.195	N.D.	N.D.
30	5	25.3	5.197	0.112	0.351	N.D.	N.D.
			4.260	0.645	3.772	N.D.	N.D.
45	5	25.3	5.213	0.106	0.341	N.D.	N.D.
			3.770	1.503	4.907	N.D.	N.D.
75	5	25.4	5.164	0.088	0.314	N.D.	N.D.
			5.295	0.074	0.249	N.D.	N.D.

Table 30-3

STAGNANT CONDITIONS

Passive Lights: 4 at 450 nm (17 Ci/Light) + 2 at 400 nm (6 Ci/Light #217) + 1 at 380 nm (6 Ci/Light RH48-22B2)

Time (min)	Port	T°C	H_2%	O_2%	N_2%	CO_2%	CO%
0	5	24.2	8.792	N.D.	0.03	N.D.	N.D.
			9.374	N.D.	0.08	N.D.	N.D.
1	5	24.2	9.248	N.D.	0.10	N.D.	N.D.
3	5	24.2	9.172	N.D.	0.075	N.D.	N.D.
6	5	24.2	8.412	0.33	4.12	N.D.	N.D.
10	5	24.3	9.248	N.D.	0.03	N.D.	N.D.
30	5	24.4	8.234	0.37	2.10	N.D.	N.D.
			8.969	N.D.	0.11	N.D.	N.D.
60	5	24.5	9.121	N.D.	0.07	N.D.	N.D.
			9.146	N.D.	0.105	N.D.	N.D.
90	3	24.6	9.146	N.D.	0.12	N.D.	N.D.
	4		9.501	N.D.	0.05	N.D.	N.D.
210	3	25.4	9.248	N.D.	0.06	N.D.	N.D.
	5		8.994	N.D.	0.08	N.D.	N.D.
240	5	25.6	8.994	N.D.	0.08	N.D.	N.D.
			9.273	N.D.	0.05	N.D.	N.D.

reaction which terminated upon the elimination of the fluorescent light.

Additional tests were conducted under steady-state flow conditions -- 3 ℓ/min and 7.5 ℓ/min flow rates -- using gas mixtures containing as much as 18% hydrogen entering the reactor chamber. Table 30-4 contains some of the data obtained. Statistical analysis of these data confirmed the absence of a measurable reaction rate even at the highest hydrogen concentration levels.

EDAs data were in obvious disagreement with the preliminary results obtained by the subcontractor. As illustrated in Figure 30-2, the subcontractor's data suggested easily measurable reaction rates between chlorine and hydrogen due to photochemical catalysis as apparently achieved via the self-powered lights.

t was conducted to essen-
cate the subcontractor's
f-powered lights. A gas

Table 30-4

STEADY-STATE FLOW

Passive Lights: 4 at 450 nm (17 Ci/Light) + 2 at 400 nm (6 Ci/Light #217) + 1 at 380 nm (6 Ci/Light #RH48-22B2)

Total Flow Rate: 7.5 ℓ/min

	Port	T°C	H_2%	O_2%	N_2%	CO_2%	CO%
Entering the reactor	1	24.0	12.161	N.D.	0.27	N.D.	N.D.
			12.668	0.10	1.27	N.D.	N.D.
Leaving the reactor	2	24.0	12.415	N.D.	0.16	N.D.	N.D.
			10.135	1.88	4.80	N.D.	N.D.
Entering the reactor	1	24.09	14.442	0.015	0.36	N.D.	N.D.
			14.188	0.11	1.33	N.D.	N.D.
Leaving the reactor	2	24.0	15.202	N.D.	0.06	N.D.	N.D.
			11.655	1.33	4.80	N.D.	N.D.
Entering the reactor	1	24.0	17.482	0.01	0.36	N.D.	N.D.
			18.090	N.D.	0.06	N.D.	N.D.
Leaving the reactor	2	24.0	15.861	0.76	3.64	N.D.	N.D.
			18.546	N.D.	0.21	N.D.	N.D.
Total Flow Rate: 3 ℓ/min							
Entering the reactor	1	23.6	8.184	0.02	0.46	N.D.	N.D.
			8.792	N.D.	0.10	N.D.	N.D.
Leaving the reactor	2	23.6	7.956	0.42	2.00	N.D.	N.D.
			8.513	<0.01	0.14	N.D.	N.D.
Entering the reactor	1	23.6	12.719	0.01	0.23	N.D.	N.D.
			12.567	N.D.	0.05	N.D.	N.D.
Leaving the reactor	2	23.6	11.047	0.33	2.02	N.D.	N.D.
			11.959	N.D.	0.12	N.D.	N.D.

mixture of 2.5% H_2 + 2.5% Cl_2 + 95% N_2 was employed under stagnant conditions. Unlike the data appearing in Figure 30-2, EDAs data indicated no measurable change in the hydrogen concentration with time when the same tritium lights were utilized. The discrepancy apparently arises from the hydrogen detection method employed by the subcontractor. The hydrogen sniffer is a device for measuring combustible gases in the presence of oxygen. As it was employed, it provided false readings in this application.

DISCUSSION

Results of tests conducted at EDA proved that self-powered tritium lights were not catalyzing the reaction at any detectable rate. A study was undertaken to investigate the reason. As mentioned previously, the two major requirements of a photochemical reactor were the intensity and the wavelength of the light radiation. Given that the wavelength region of the phosphor material used was correct, the only remaining factor was insufficient intensity. Despite the high quantum yield of this chain-propogation reaction, the intensities of these lights were evidently too low to initiate or sustain the reaction.

Spectral radiance as well as uniformity of some of these lights were measured by Optronic Labs Inc. Results of these tests are given in Figure 30-4.

The F8T5/BL fluorescent light is presently used in battery modules as the recombination reactor. Figure 30-5 shows the intensity versus wavelength distribution of a 40-watt light of the same type. From this figure, the power output of an 8-watt (F8T5/BL) light in the 300-480 nm spectral region is calculated to be 1.84 watt. Whereas the brightest tritium light source attainable in the same region has a power output of 3.47×10^{-5} watt. The radiation emitted at the peak intensity corresponds to 3.3×10^{18} quanta/sec (at 356 nm) and 7.8×10^{13} quanta/sec (at 450 nm), respectively. This indicates that the rate of reaction with the tritium light will be 4.2×10^{4} times slower than the fluorescent light.

From this fact it is concluded that self-powered tritium lights are not suitable as a backup reactor to the fluorescent-light reactor in zinc-chloride battery modules.

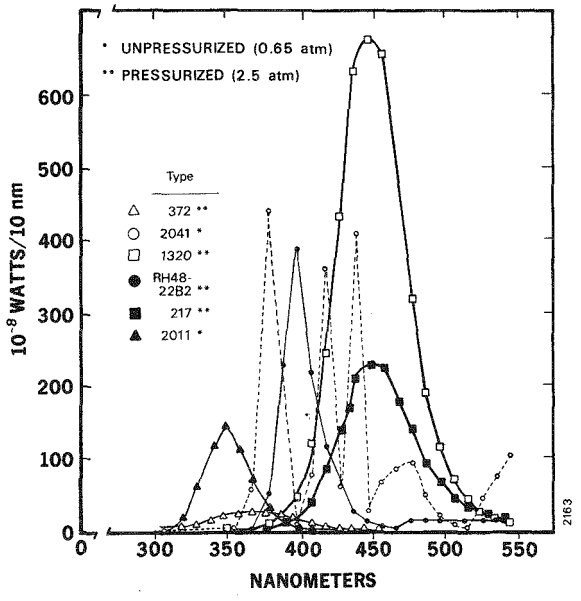

Figure 30-4. Spectral energy distribution and power outputs (below the threshold limit of 480 nm) of some of the tritium lights tested.

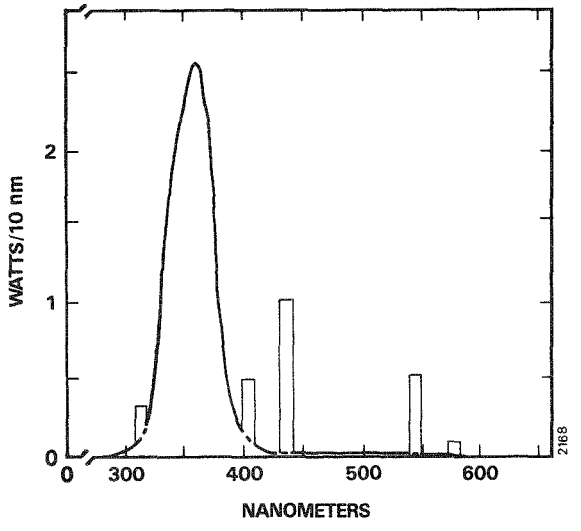

Figure 30-5. Spectral energy distribution of a Sylvania F40/BL black light. (These data were obtained from GTE Sylvania Engineering Bulletin 0-306.)

REFERENCES

1. Development of the Zinc-Chloride Battery for Utility Applications. Palo Alto, Calif.: Electric Power Research Institute, April 1979. EM-1051, Parts 1-3.

2. N. R. Dhar. The Chemical Action of Light. London: Blackie & Son Ltd., 1931.

3. W. Nernst. Z. Electrochem., 24, 335, 1918.

4. E. A. Moelwyn-Hughes. Physical Chemistry, Second Revised Edition, Chap. XXIII. Pergamon Press, Oxford, London, New York, Paris, 1964.

5. R. O. Griffith and A. McKeown. Photo-Processes in Gases and Liquid Systems. London: Longmans, Green & Co., 1929.

6. W. A. Noyes, and P. A. Leighton. The Photochemistry of Gases. New York: Dower Publications, Inc., 1941.

7. Mellor. Comprehensive Treatise on Inorganic and Theoretical Chemistry. London and New York: Longmans, Green & Co., 1956, Vol. 2, Supplement 2, Part I.

8. W. A. Noyes, G. S. Hammond, J. N. Pitts. Advances in Photochemistry. New York and London: Interscience Publishers, 1964, Vol. 3, 161.

9. P. G. Ashmore, F. S. Dainton, T. M. Sugden. Photochemistry and Reaction Kinetics. London: Cambridge University Press, 1967.

10. Max Bodenstein. Z. Physikal Chem. 85, 351, 1913.

11. G. Kornfeld and H. Muller. Z. Physikal Chem. 117, 242, 1925.

12. L. Harris. Nat. Acad. Sci., 14, 110, 1928.

13. A. J. Allmand and E. Beesley. J. Chem. Soc., 2693-2709, 1930.

14. Burgess and Chapman. J. Chem. Soc. 89, 1299, 1906.

15. C. Ellis and A. A. Wells. The Chemical Action of Ultraviolet Rays. New York: Reinhold Publishing Corporation, 1941.

16. M. Ritchie. J. Chem. Soc., 857, 1937.

17. D.L. Chapman and P. P. Grigg. J. Chem Soc., 3233, 1928.

Section 31

PUMP DEVELOPMENT

ABSTRACT

In BEST-battery modules, two pumps are required. One, the electrolyte pump, recirculates electrolyte through the porous-graphite chlorine electrodes. A second pump is required for transferring chlorine gas and mixing it with cold water to form chlorine hydrate during charge. Development work on the electrolyte pump was done through an EDA subcontractor. This subcontractor provided a detailed design for the pump and the pump-motor magnetic coupling assembly. Development work on the gas/hydrate former pump was performed at EDA. A vane pump was designed, built, and tested during the first nine months of the Phase II Program. These pump programs were initiated in April 1978 -- the beginning of Phase II of RP226-3 -- and transferred to the DOE-EDA BEST-Battery Program in January 1979.

INTRODUCTION

In the design of the zinc-chloride BEST-battery module, described in Section 25, two pumps are required per module. One pump is required to provide electrolyte to the flow-through chlorine electrodes in the battery stack. This pump is referred to as the electrolyte pump and is required during charge as well as discharge. A second pump is required to transfer chlorine gas, which is generated electrochemically during charge, from the stack compartment and to maintain this compartment at a specified level of vacuum. In addition, this pump also mixes the cooled store liquid with chlorine gas to form chlorine hydrate. This pump is referred to as gas/hydrate-former pump. It may, or may not, operate during the discharge phase of the battery cycle.

The electrolyte pump used in the 45-kWh EPRI battery module was an end-suction, closed-impeller, horizontal centrifugal pump (1). A 48-volt Bosch dc motor was used to drive the pump. The pump was constructed almost entirely of titanium.

The gas/hydrate-former pump used in the 45-kWh EPRI battery module was a gear pump (1). It was a modified version of ECO G-10 gear pump designed for magnetic coupling and battery through-wall mounting. This pump had glass-filled Teflon spur gears and a titanium body. It was designed primarily for pumping liquids. In the present application, it ingested a gas-liquid mixture. This pump was also driven using a Bosch dc motor.

Table 31-1 compares the overall efficiencies of the pump/motor combinations used on the 45-kWh EPRI module with the target efficiencies for commercial modules. The pump/motor combinations used in the BEST-battery modules should demonstrate efficiency improvements, as well as progress in the areas of manufacturability, cost, and reliability.

In this section the work done on pump development during Phase II of RP226-3 is presented. The work on the development of a more-efficient and cost-effective electrolyte pump was subcontracted to GEC Associates of Troy, Michigan. GEC designed a pump that will meet the efficiency requirement of the battery module. Work on a gas/hydrate former pump was done in-house at EDA. This

involved the study of a vane pump/compressor as an alternative to the gear pump used in the 45-kWh module. The study involved tests on commercially available pumps and compressors using air-water mixtures at the inlet. A modified design was fabricated of suitable materials and tested with chlorine-water mixtures under conditions similar to the battery.

Table 31-1

PUMP/MOTOR EFFICIENCIES

	Demonstrated in 45-kwh Module	Projected for Commercial Modules
Electrolyte Pump	40%	60%
Gas/Hydrate-Former Pump	12%	25%

ELECTROLYTE PUMP

Pump Requirements

The zinc-chloride battery utilizes porous-graphite flow-through chlorine electrodes. Flow of electrolyte through chlorine electrodes is required during charge as well as discharge. Electrochemical considerations indicate that optimal battery performance is obtained at a fluid flux of 2 ml/cm^2-min through the chlorine electrodes. This determines the capacity of the pump. This single pump feeds electrolyte to 1320 chlorine-electrode pairs which are located in cells at different voltages. This mode of operation allows for parasitic (shunt) currents to flow through the common electrolyte loops. The resistance of these loops is engineered to minimize these currents by providing high length to cross-sectional area ratios in both the inlet and outlet flow channels to each cell. This leads to an increase in hydraulic resistance, however, which means more energy is required to pump the fluid. The pressure head to be developed by the pump is determined from this criterion.

The electrolyte pump is a critical component in the module, and therefore its reliability is of utmost importance. This pump must have a life in excess of 10 years, which is 30,000 hours of operation with 5,000 starts and stops. Because of the potential for leakage of chlorine, no rotary seals and penetrations are permissible in the module case. The pump should, thus, either be a magnetically-coupled design or a submersible motor-driven design. Materials of construction must be stable in the battery environment. Thus, only those materials qualified for use in the environment can be used.

The pump requirements for commercial battery modules are summarized in Table 31-2.

Table 31-2

REQUIREMENTS FOR COMMERCIAL ELECTROLYTE PUMP

Flow	330 ℓ/min
Pressure Head	3.5 psi
Inlet Pressure	10 psia
Pump Motor Efficiency	60%
Life	$\geq$30,000 h
Cost	$\leq$\$150 (1977\$)

Pump Design

A subcontract for the electrolyte-pump design was awarded to GEC Associates of Troy, Michigan. The subcontract required GEC to design the pump to meet the pumping requirements listed in Table 31-2. The subcontract also required that GEC design the total package: pump, motor, coupling, and mount-

ing hardware. Plastic, as well as, metal designs were to be considered.

GEC studied the problem and recognized that an off-the-shelf pump design would not be appropriate for this application. Professor G. Edmonson of the University of Michigan was contracted as a consultant on this project. Professor Edmonson has developed a computer code for pump design. The computer code contained design data, design methodology, a library of available pump designs, and additional fundamental design information. Once the pumping requirements and the fluid properties were fed into the computer, the program first determined if a commercially available pump was adequate for the given application. If so, it provided the manufacturer's name and model number. If not, then it indicated that a special design effort was required and if instructed to do so, it developed a new design.

For this particular specification, no existing design was appropriate, and thus, a new design was generated. It is a mixed-flow single-stage pump. The impeller is closed and has relatively long vanes which have three-dimensional curvature. It is shown in Figure 31-1. This configuration is not suitable for injection molding; it can, however, be produced by investment casting from titanium.

The case is a single volute-type designed to efficiently convert the velocity head into pressure and minimize the radial thrust. The pump assembly is schematically shown in Figure 31-2.

GAS/HYDRATE FORMER PUMP

Requirements

In the present module design, this pump has two functions. First, it transfers the chlorine gas that is generated electrochemically in the stack during charge to the store and maintains the stack at a specified level of vacuum. Secondly, it functions as a hydrate former by mixing the prechilled store fluid with the chlorine gas. The pump ingests a gas-liquid mixture and pumps it into the store. Under the specified conditions, chlorine hydrate is formed at the pump outlet. The fluid flowing out of the pump is a slurry containing liquid, gas, and hydrate particles. For a commercial battery module the requirements of the pump are given in Table 31-3.

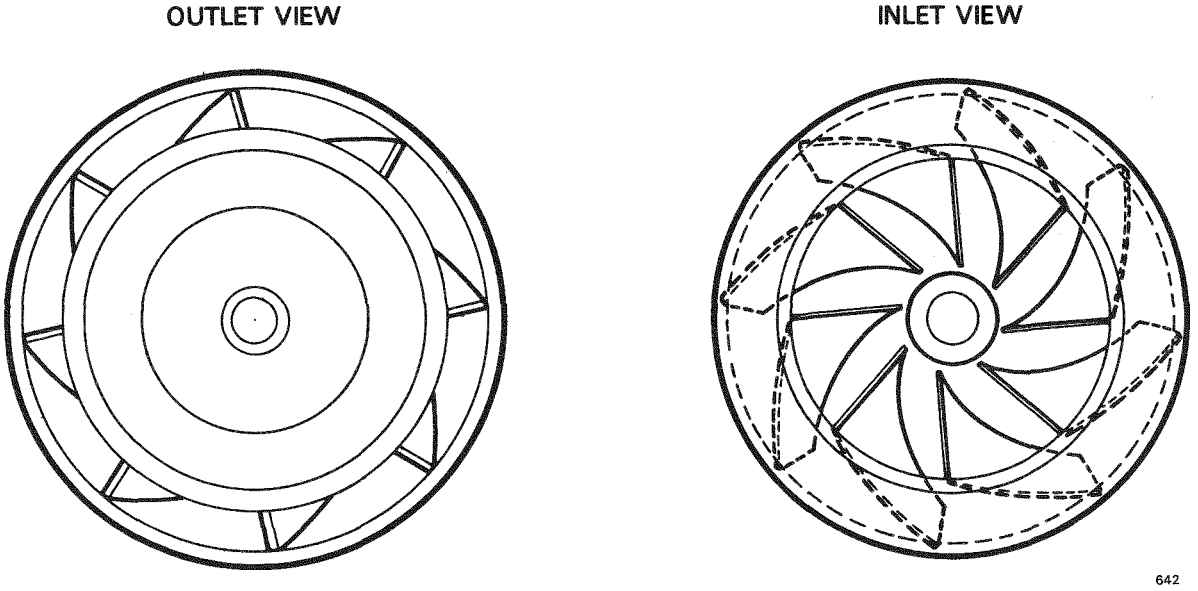

Figure 31-1. Electrolyte pump impeller.

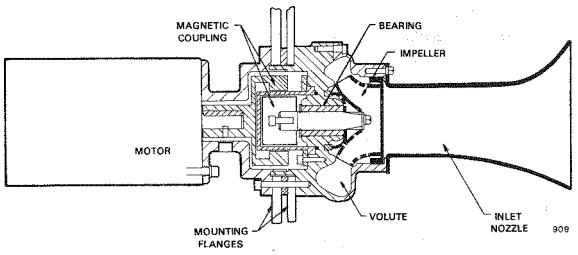

Figure 31-2. Assembly schematic of the electrolyte pump.

Table 31-3

REQUIREMENTS FOR COMMERCIAL GAS/HYDRATE-FORMER PUMP	
Liquid Flow	11.5 ℓ/min
Gas Flow	45 STP ℓ/min
Inlet Pressure	9 psia
Outlet Pressure	25 psia
Power Input	≤300 W
Life	≥30,000 h
Cost	≤$100 (1977$)

Development Work

From the considerations of the pumping requirements, a positive-displacement pump is appropriate for this application. Gear pumps, vane pumps, piston pumps, liquid-ring pumps, diaphragm pumps, and internal gear pumps are examples of positive-displacement pumps. In the 45-kWh EPRI module, a gear pump is used as the gas/hydrate-former pump. In this program, alternative positive displacement pumps were studied. The vane pump offered the potential of design simplicity, higher efficiency, and lower cost.

In the first phase of the study, some commercially available vane pumps and compressors were tested with air-water mixtures to determine their pumping characteristics. Vane pumps are designed for pumping liquids and have no built-in compression ratio. Vane compressors are designed for handling gases only and have a built-in compression ratio. The present application involves pumping of liquid-gas mixture and in addition to that, the pump is also required to maintain an inlet vacuum. These characteristics determine the configuration of inlet and outlet ports.

The compressor concept was selected for further development because the internal compression offers the potential for higher efficiency. The efficiency is also quite strongly dependent on the inlet conditions: namely, the ratio of liquid to gas that enters the pump. The compression ratio is correct for only the design mixture. For mixtures with different ratios, the compression ratio will be different from design, resulting in inefficiency.

Operation of the vane pump is shown schematically in Figure 31-3. As the rotor moves, the centrifugal force acting on the vanes cause it to move radially outward. Thus, the vanes are always scraping against the fixed housing. The fluid is trapped between the vanes on the inlet side and is compressed until it reaches the outlet port where it is discharged. The vanes also provide a seal between the inlet

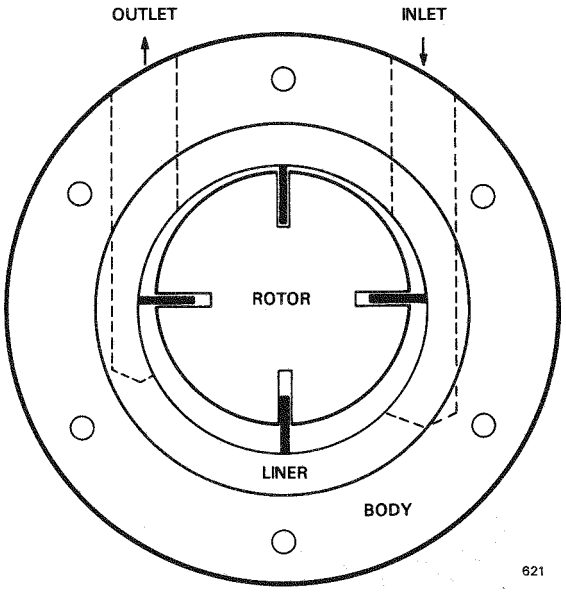

Figure 31-3. Schematic of the vane pump.

and outlet ports. An advantage of the vane pump is that the vanes are the elements subject to maximum wear. Although prone to wear, there is enough vane length available so that as the vane wears, it keeps moving further out. Thus, the action is self-correcting and the pump is less prone to failure.

Using the test data, a vane pump was designed for the present application. No lubricant was permissible in the system, so the materials selected were such that no lubrication is needed. Proper selection of materials was a key factor in the life expectancy of the pump. Graphitar has been successfully used for vanes and bearing materials.

The test setup used for testing the pump with air and water is shown schematically in Figure 31-4. Tests conducted using air and water showed that the pump was able to pump 10 ℓ/min water and 39 STD ℓ/min of air at an inlet pressure of 10 psia, and at an outlet pressure of 20 psia.

The pump was then tested with chlorine gas and water to evaluate its performance as a hydrate former. The results showed that the vane pump did not work efficiently as a hydrate former. To verify the experimental conditions, a gear pump was used, and it performed well as a hydrate former. To improve the efficiency of the vane pump as a hydrate former, several parameters were studied. Inlet configurations were changed so the gas and liquid could either be premixed outside or they could be separately injected into the pump. The effect of this change was inconclusive. Also, the number of vanes was increased from four to eight and the effect of this change on hydrate formation was observed.

The results of this study show that a vane pump can be used for pumping gas-liquid mixtures. The pump efficiency is reduced by use of two-phase mixture at the inlet. In tests conducted using air-water mixtures, an overall pump/motor efficiency near 20% was achieved. The vane pump tested was not very effective as a hydrate former and this aspect needs further investigation. Adequate mixing of gas and liquid phases is required for hydrate formation. It appears that high centrifugal forces acting on the liquid and low centrifugal forces on the gas may induce some separation resulting in inadequate mixing inside the pump. Thus, most of the mixing may be taking place external to the pump. In the gear pump, the clearance and cavity size are small so there is more potential for mixing. Also, in a gear pump there is no internal compression. All of the compression occurs at the outlet port which is a region of violent mixing. The vane pump designed and tested as a hydrate-former was based on the compressor concept, i.e., the compression takes place internal to the pump. From hydrate formation considerations, a vane pump with little or no internal compression, similar to the gear pump, may be preferable. The considerations of life and cost also require further investigation.

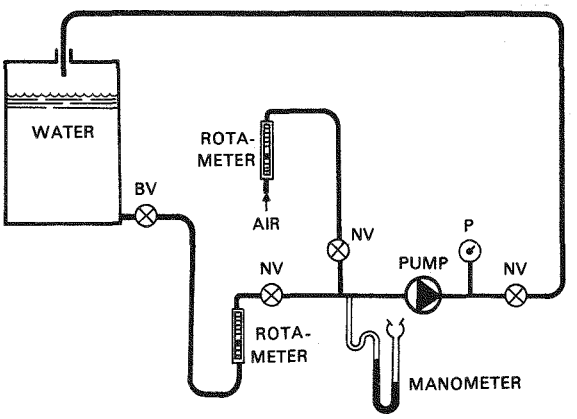

Figure 31-4. Schematic of the test setup for pump tests with air and water mixture.

PROGRAM STATUS

The above described pump development efforts were conducted between April 1978 and December 1978 -- as part of Phase II of RP226-3. Extensions of these efforts -- prototype pump design and manufacturing programs -- are now

being conducted as part of the DOE-EDA BEST-Battery Program. The subcontract with GEC Associates was transferred to the DOE-EDA BEST-Battery Program in January 1979. GEC is providing prototype pump designs for both the electrolyte-circulation and the gas/hydrate-former applications. A prototype pump design and manufacturing subcontract was also established with Ingersoll-Rand very early in the BESTBattery Program. Prototype and preprototype pumps for both applications are also scheduled for near-term delivery from this subcontractor.

Cost reductions are being emphasized in these programs by designing and building prototype pumps of low-cost plastics, as well as titanium. Plastic versions of centrifugal, liquid-ring, and gear pumps are being produced for evaluation and possible incorporation into prototype BEST-battery modules. Present estimates indicate that the commercial cost targets presented in Tables 31-2 and 31-3 can be achieved with mass-produced plastic pumps.

REFERENCE

1. Development of the Zinc-Chlorine Battery for Utility Applications. Palo Alto, Calif.: Electric Power Research Institute, April 1979. EM-1051, Part III, Section 17.

Section 32

HYDRATE-FORMER HEAT EXCHANGER DEVELOPMENT

ABSTRACT

In the zinc-chloride battery, chlorine is stored in the form of chlorine-hydrate. The removal of heat from the battery to form chlorine-hydrate is accomplished by means of a heat exchanger. A program for developing cost-effective designs for this heat exchanger was undertaken. Designs were developed for water/glycol cooled as well as direct refrigerant-cooled heat exchangers. A direct-cooling liquid-overfeed refrigeration system was set up and used for evaluating heat-exchanger designs. Test results were used to design a plate-coil heat exchanger which should meet the requirements for BEST-battery modules.

INTRODUCTION

During the charge phase of the zinc-chloride battery, gaseous chlorine is evolved at the chlorine electrodes. The chlorine gas is transferred from the battery stack to the store where it is mixed with cooled store liquid to form chlorine hydrate. Because the formation of chlorine hydrate is an exothermic process, continuous removal of heat from the store is required for steady-state operation of the module. This is accomplished through a heat exchanger identified as the hydrate-former heat exchanger. A chilled aqueous solution of glycol or a refrigerant is used to provide cooling. The heat exchanger and chiller are not required during module discharge.

In the 45-kWh battery module, a shell-and-tube heat exchanger is used. This heat exchanger has 150 titanium tubes each 0.125-inch in diameter. Because mixing of battery and cooling fluids is not permissible, the tubes are welded to the tube sheet. This heat exchanger represents a major cost item. Cost analyses show that even at high production rates, this design may not meet the cost guidelines. Also, for the BEST module, direct-Freon cooling instead of indirect-glycol cooling is being considered. The development of cost-effective hydrate-former heat exchangers were, therefore, undertaken in this program.

This section first develops the requirements for the hydrate-former heat exchanger. These requirements are developed on the basis of chiller system and module considerations. Specifications on the coolant side are presented for each type of cooling system.

Next, design analyses are presented for both the water-glycol solution-cooled heat exchanger and the direct refrigerant-cooled heat exchangers. Use of unaugmented unenhanced surfaces yields a design that is bulky and large. Enhanced surfaces are thus considered. Use of Union Carbide high-flux surface on the refrigerant side and sand-grain roughness on the water side produces a much more compact design.

A direct-cooling liquid-overfeed refrigeration system was set up for the test and evaluation of heat exchangers. Four types of heat exchangers were acquired for testing. These include: plate-coil type (made by Tranter, Inc.), tube-in-tube type with Union Carbide high-flux coating, shell-and-tube type, and spiral type made of stainless steel. Testing of the first two heat exchangers has been completed.

REQUIREMENTS FOR HYDRATE-FORMER HEAT EXCHANGER

In the operational design of the BEST-battery module -- Section 25 -- chlorine-hydrate is formed by mixing chlorine gas and water in a gear pump. The water used for hydrate formation is first cooled to a temperature below the equilibrium temperature for hydrate formation. This liquid is then mixed with chlorine gas and the mixture is slightly pressurized to form hydrate. The amount of water used and the degree of chilling is such that heat released during hydrate formation is absorbed by the mixture and the temperature is raised to the equilibrium value. Thus, the heat load, liquid flow rate, and temperatures are determined from hydrate-formation considerations. Because the store fluid is already saturated with dissolved chlorine, the temperature of the heat exchanger surface on that side should not fall below the equilibrium hydrate formation temperature. If it does, hydrate formation may occur at the heat exchanger surface and its accumulation can significantly reduce the heat transfer. The flow through the heat exchanger is provided by the liquid head available in the battery store. This determines the pressure-drop constraint.

Specification

The total heat to be removed by the heat exchanger consists of the following components:

- heat released due to hydrate formation (1.45 g-moles of Cl_2/min)
- heat due to the gas/hydrate former pump and motor inefficiency
- heat transferred through the module case from ambient and battery stack
- heat released due to condensation of the water vapor carried over from the stack
- heat from the warm gas coming over from the stack

These heat loads are given in Table 32-1 for the BEST-battery module.

Table 32-1

HEAT LOAD FOR HYDRATE-FORMER HEAT EXCHANGER

Heat-Load Components	kCal/min
Heat of Hydrate Formation	27.00
Pump Heat	7.20
Condensation	0.72
Heat Transfer	0.63
Warm Gas from Stack	0.29
Total Heat Load	35.84

The heat load and other specifications for the hydrate-former heat exchanger are given in Table 32-2. The amount of water to be cooled in the heat exchanger, as determined by the hydrate-formation considerations, is 11.5 ℓ/min. The water to be cooled enters the heat exchanger at the store temperature which is at 10°C. The bulk mean outlet temperature is ∿ 6.9°C. As indicated earlier, the heat-exchanger surface temperature on the warm side should not fall below 5.9°C. The pressure head available to drive the flow through heat exchanger is the height of the liquid column in the battery store. This is limited to about 1 psi.

Coolant Selection: Two alternative cooling concepts received consideration. One concept uses indirect glycol cooling, in which a water-glycol solution is used as coolant in the heat exchanger. The other concept uses direct liquid-overfeed cooling in which liquid Freon directly from the chiller is used as the coolant. The coolant flow rate is selected such that about

one-third of the Freon entering the heat exchanger is boiled.

The heat exchanger design is sensitive to the coolant used. Thus, specifications were developed for glycol, as well as, Freon cooled systems. These are given in Tables 32-3 and 32-4.

Table 32-2

HEAT EXCHANGER REQUIREMENTS (Warm Side)

Heat Load	35.84 kCal/min
Water Flow	11.5 ℓ/min
Pressure Drop	≤1 psi
Water Inlet Temperature	10°C
Heat Exchanger Wall Temperature	≥5.9°C

Table 32-3

COOLANT-SIDE SPECIFICATIONS USING GLYCOL

Coolant Flow Rate	10 ℓ/min
Pressure Drop	<5 psi
Coolant Inlet Temperature	4°C

Other Considerations: Materials of construction must be compatible with the battery environment. Titanium and qualified plastics are the only available materials. No leakage of coolant into battery or battery fluid into coolant is permissible. This means that all joints must be prepared using techniques that assure zero leak. A maintenance-free operating life of 10 years is desired. The present cost guidelines indicate that heat exchangers should cost less than $120 (1979 dollars) when produced in annual quantities of 25,000 or more.

Table 32-4

COOLANT-SIDE SPECIFICATIONS USING FREON

Freon Flow into Heat Exchanger	2.0 ℓ/min
Liquid Freon Leaving Heat Exchanger (rest vaporizing)	1.3 ℓ/min
Inlet Temperature	4°C
Pressure Drop	<1 psi

DESIGN OF WATER/GLYCOL COOLED HEAT EXCHANGER

A subcontract for the development of cost-effective hydrate-former heat-exchanger designs was given to Dr. Wen-Jei Yang, Professor of Mechanical Engineering, University of Michigan, Ann Arbor, Michigan. The work was divided into two parts. Part I was concerned with the selection of the most feasible concepts for the present application. In Part II the feasible concepts were optimized to produce a cost-effective heat-exchanger design.

Preliminary Selection: Four types of heat exchangers are suitable for liquid-to-liquid service. They are: (1) spiral type, (2) flat-plate type, (3) graphite heat exchangers, and (4) shell-and-tube type. Of these, graphite heat exchangers may not be suitable because fluid-tight joints are difficult to achieve. Thus, the spiral type, flat-plate type, and shell-and-tube type heat exchangers were analyzed using the heat transfer coefficient limit designs. The results of the analysis show that:

- The spiral-type heat exchanger is the best choice for this service. Both titanium and PVC can be used. The PVC heat exchanger would, however, be bulky and large.

- Flat-plate type heat exchanger is the next best candidate. Titanium should be used, while PVC plates of about 0.02-inch thickness would be marginally acceptable.

- Shell-and-tube heat exchanger is feasible but bulky and, thus, may not be a good choice. Only titanium is feasible; PVC cannot be used.

Design Optimization: A design-optimization study for the spiral and plate-type heat exchangers was carried out. Important geometrical parameters were selected and expressions for overall heat transfer coefficient and pressure drop were developed in terms of these parameters. By varying the parameters, a number of different designs can be generated. For spiral-type heat exchanger the channel width, channel height (plate spacing), and plate thickness are the important geometrical parameters. By selecting these parameters, the overall heat transfer coefficient and pressure drop can be determined. From the knowledge of the overall heat transfer coefficient, the log-mean temperature difference, and heat load (the last two are determined from the specification), the required heat exchanger surface area is calculated. The heat exchanger volume, channel length, mass, and diameter can then be calculated.

Figure 32-1 shows the results of an optimization analysis for the spiral-type heat exchanger for plate spacing of 0.125 inch and plate thickness of 0.049 inch. The channel width is varied and is plotted on the abscissa. Heat-exchanger volume (V), channel length (L), mass (m), diameter (D_o), pressure drop (Δp) and minimum surface temperature to avoid freeze-up (T_{wo}) are plotted as functions of the channel width. Half of the heat exchanger mass (m/2) is plotted because this produces a convenient scaling factor. The two vertical lines represent the design constraint. Left of the first vertical line, the pressure drop exceeds the maximum permisible value, while, towards the right of the second vertical line, the flow becomes laminar, reducing the heat transfer coefficient. Thus, for a given plate spacing and thickness, the channel width could be varied from 4.25 to 11 inches. Looking at the volume and mass curves, the narrower the channel, the lighter and more compact the unit will be. Similar curves were generated for a plate spacing of 0.250 inch. The results show that reducing the plate spacing produces a more compact design. Figure 32-2 shows the results of a similar optimization analysis for the plate-type heat exchanger.

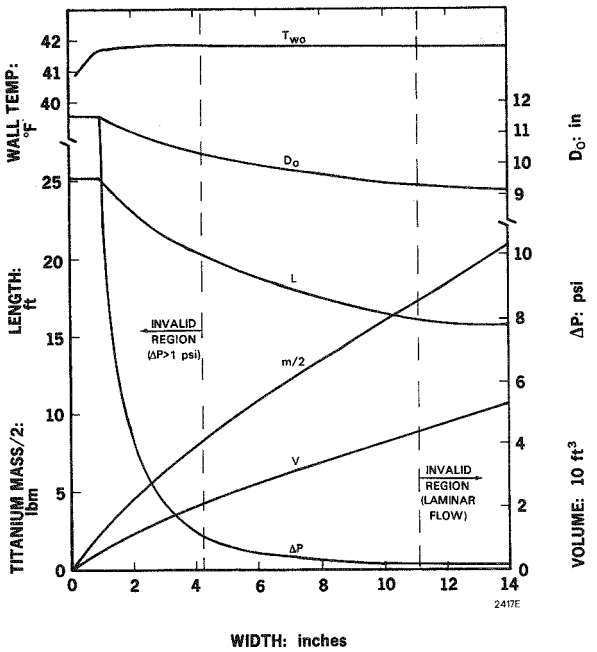

Figure 32-1. Optimization of spiral-type heat exchanger for plate spacing of 0.125 inch and plate thickness of 0.049 inch.

DESIGN OF DIRECT REFRIGERANT-COOLED HEAT EXCHANGER

Analysis of the cooling system required for the 4.2-MWh zinc-chloride battery system for the BEST Facility indicates that a direct refrigerant cooling system has many advantages over an indi-

rect liquid-cooling system. Battery modules fabricated and tested at EDA have only used the indirect liquid-cooling concept. Use of boiling Freon as a coolant has a major impact on the design of the hydrate-former heat exchanger.

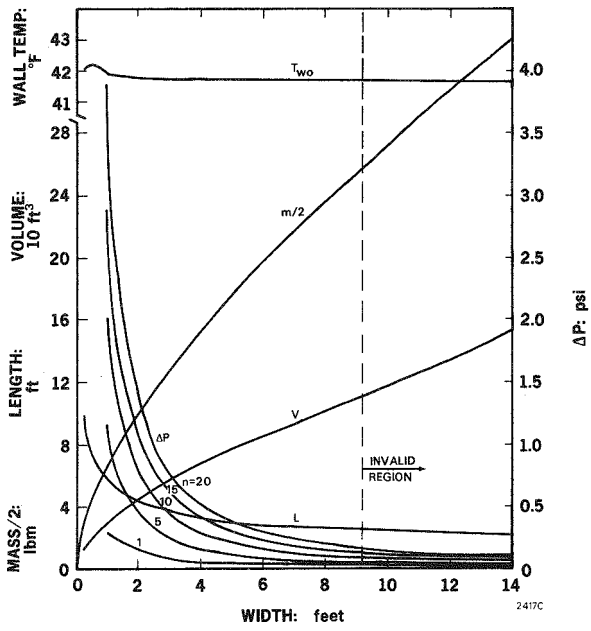

Figure 32-2. Optimization of flat-plate type heat exchanger for plate spacing of 0.250 inch and plate thickness of 0.049 inch. (Width plotted on abscissa is plate width times the number of plates.)

A subcontract for the development of designs for cost-effective hydrate-former heat exchanger was also awarded to Dr. Wen-Jei Yang. This work was also carried out in two parts. The first part was concerned with preliminary selection in which various feasible concepts were studied and evaluated. In the second part, the concepts found to be most promising were further analyzed to produce optimized designs.

In the case of heat exchangers using boiling Freons, augmentation is frequently used on the boiling side to improve the heat transfer coefficient. The augmented surfaces are not readily available in titanium. Thus, both augmented and unaugmented surfaces were considered but the latter was emphasized.

Preliminary Selection: In this portion of the work, three types of heat exchangers were first considered and analyzed, based on the heat transfer coefficient limit design: spiral type, shell-and-tube type, and flat-plate type. Augmentation or enhancement was not considered, only plane surfaces were used. The results of the analysis indicated that the spiral type was the best suited for this application. The analysis indicated that the design range in this case was quite limited and depended upon the quality change occurring in the heat exchanger.

Design Optimization (Unaugmented Unenhanced Surfaces): The spiral-type heat exchanger was analyzed. First, the overall heat transfer coefficient and pressure drop expressions were developed. Geometrical characteristics and quality change of Freon were used as parameters in the above expressions. By varying these parameters individually, their effects on the heat exchanger size and weight were studied. From these considerations, the optimal design was selected. The results of the analysis are shown graphically in Figure 32-3. Compared to water-glycol cooled heat exchanger, the design range for the direct Freon-cooled heat exchanger is quite limited. The results of the optimization study indicate the following:

- The best overall heat transfer performance which yields the most compact size is under the condition that the heat transfer coefficient on both sides are equal. This condition is most probably achieved in the range of quality change less than 10 percent.

- The design constraint due to the warm-side pressure drop is overcome by selecting the warm-side channel height to be 0.25 inch, twice the cold side.

- The lowering of the quality change yields higher refrigerant flow, thus relaxing the restriction of refrigerant flow on the exchanger width and reducing the exchanger size and weight by adding piping and pumping cost. The quality change of 0.05 (or 5 percent) appears to be the lowest limit below which the warm-side wall surface will be overcooled.

- The heat exchanger width (upper limit) is restricted to be less than 11.2 inches under the given operating conditions in order to keep the warm fluid in turbulent flow.

- The lower limit of the heat exchanger width is restricted by the pressure drop on the warm-fluid side.

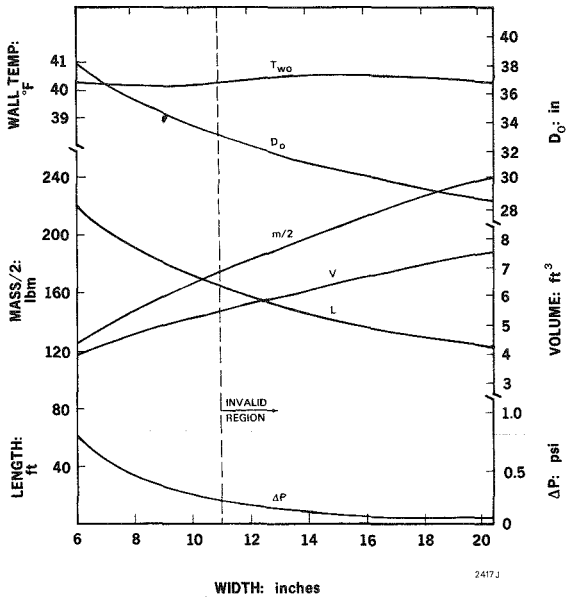

Figure 32-3. Optimization of spiral-type heat exchanger for plate thickness of 0.049 inch, plate spacing on Freon side 0.125 inch, and plate spacing on water side is 0.25 inch (33% quality change).

Design Optimization (Enhanced Surfaces): The heat exchanger designed using unaugmented unenhanced surfaces produces a design which is quite bulky and the material cost, as well as fabrication cost, will be high. Thus, the use of enhanced surfaces was considered on the spiral type heat exchanger.

On the Freon side, Union Carbide high-flux surface was selected. High-flux surface is a matrix of metallic particles brazed to the outside of a base tube. The matrix is about 0.007-inch thick and has a 60% void fraction (1). The surface promotes high-turbulent nucleate boiling, the degree of wall super-heat is reduced, and high heat-transfer coefficients are realized.

Sand-grain roughness was selected for enhancement on the water side. This type of enhancement in tubes is produced by electroplating. For flat surfaces, it could be produced either by electroplating or machining. The heat-transfer coefficient can be increased up to two-fold by this type of enhancement (2).

The design optimization using the above enhancement techniques was carried out. Results for plate spacing of 0.125 inch and plate thickness of 0.049 inch are presented in Figure 32-4. Pressure drop, heat exchanger weight, and other dimensions are plotted as a function of the channel width. As can be seen (Figure 32-4), the use of enhancement produces a much more compact and lightweight design.

EXPERIMENTAL

Emphasis was placed on the development of a heat exchanger design for use with Freon. This subsection describes the equipment and procedures used to evaluate two heat exchanger designs for use with Freon. A direct-cooling liquid-overfeed refrigeration system was set up for the test and evaluation of heat exchangers. The schematic of the refrigeration unit is shown in Figure 32-5. The unit was designed and built at EDA in consultation with Mr. R. A. Johnson of Ray Johnson and Associates,

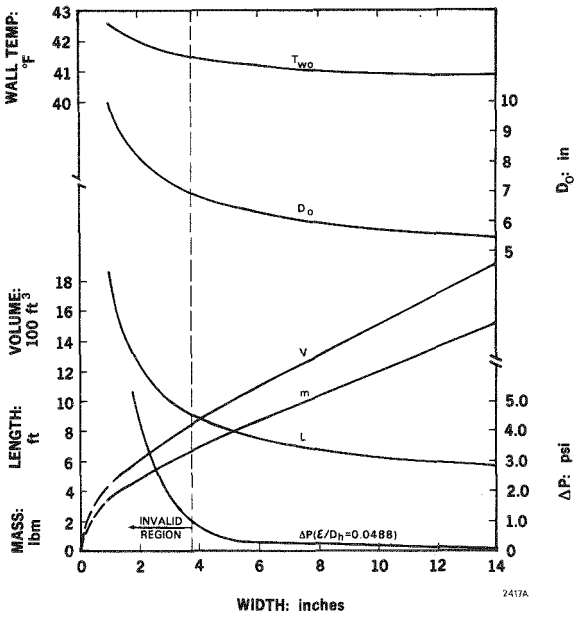

Figure 32-4. Optimization of spiral-type heat exchanger for plate spacing of 0.125 inch, plate thickness of 0.049 inch, high-flux surface on Freon side sand-grain roughness on water side, and quality change of 33%.

Inc., Royal Oak, Michigan. The system was built around an existing Tecumseh Model CG4075 condensing unit. Freon, at required temperature, is held in a low-pressure receiving tank. A Procon vane pump is used to pump the liquid Freon from the receiving tank into the heat exchanger and through a fixed orifice. In the refrigeration system for the commercial battery plant a number of heat exchangers are connected in parallel and to ensure uniform distribution of refrigerant in each heat exchanger, an orifice is added before each heat exchanger. In the present system, it is used to simulate the conditions that will exist in the commercial or BEST-battery system. After the Freon enters the heat exchanger, the heat transferred to it from the water first raises its temperature and causes some boiling to take place. The flow of liquid refrigerant is selected such that at the design level one-third of the Freon is evaporated and the rest leaves the heat exchanger as liquid. This liquid gas mixture goes to a liquid-gas separator, from where the liquid is returned to the low pressure Freon holding tank and the vapor flows into the compressor. The vapor is compressed and condensed in the air cooled condenser, from where it flows into the low-pressure holding tank. Before entering the holding tank, it flows through an expansion valve which reduces the pressure to the desired level. In the present system, the expansion valve also controls the Freon level in the low-pressure receiver tank by using a level-master level sensor.

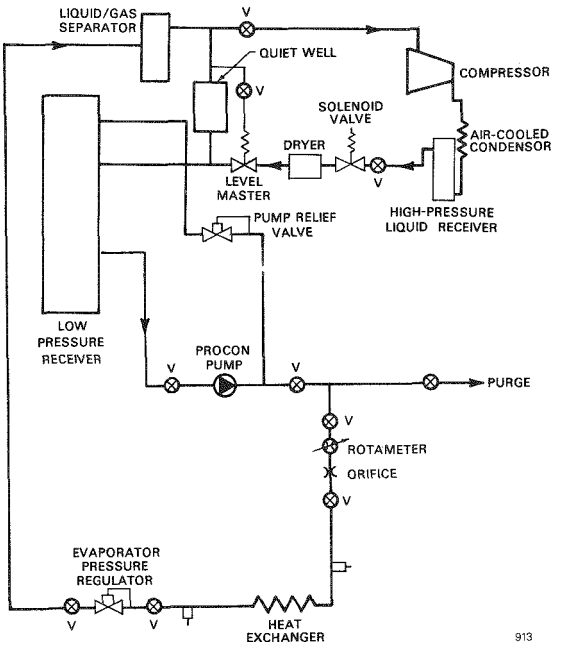

Figure 32-5. Schematic of the direct cooling liquid overfeed system set up for heat exchanger evaluation.

The system is instrumented for heat exchanger testing. A rotameter is used in the liquid-Freon loop, downstream of the pump, to measure the flow of liquid Freon entering the heat exchanger. Thermocouples are used to measure the Freon temperature at the inlet and outlet of the heat exchanger. Pressure gauges are also used at the heat exchanger inlet and outlet. Figure 32-6 shows the instrumentation used for the

heat exchanger tests. A constant temperature bath is used to provide water for the heat exchanger. A rotameter is used to measure the water flow rate and two matched mercury-in-glass thermometers are used to measure the temperature of water entering and leaving the heat exchanger.

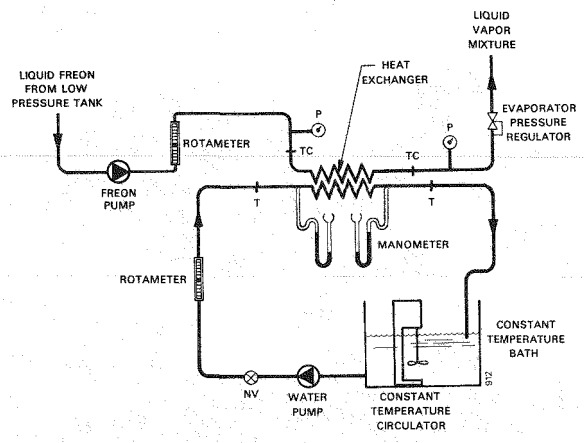

Figure 32-6. Schematic of test set up showing instrumentation used for heat exchanger testing.

Procedure

To start the test, the refrigeration unit is turned on and Freon in the holding tank is allowed to cool down to the required temperature of near 4°C. The flow of water through the heat exchanger is started and the constant temperature circulator is turned on. Freon pressure at the heat exchanger outlet is controlled by varying the evaporator pressure regulator setting; Freon flow rate is controlled by varying the pump rpm. The water bath is maintained near 10°C. Temperature and pressures are monitored and recorded in steady-state.

RESULTS AND DISCUSSION

The design analysis suggests that spiral-type and flat-plate type heat exchangers are the best suited for the present application. Two manufacturers of spiral type heat exchangers were contacted: American Heat Division of Alfa-Laval Thermal, Inc., Somerville, N.J., and Spirec, a division of Portescap U.S., Inc., New York, N.Y. Both companies have the capabilities to make titanium heat exchangers but currently only on a custom basis. Two commercially available spiral-type stainless steel heat exchangers were selected for testing.

Tranter, Inc., makers of titanium plate-coil (Econocoil) heat exchangers were contacted. These Econocoil banks are primarily used for heating or cooling of solution baths. The plates are immersed in the solution and cooling or heating fluid flows through the plate coil. Tranter representatives recommended use of a three-plate Econocoil bank in which each plate is 12-inches wide by 24-inches long and 0.375-inch thick. Units of this type would cost about $230 or about $4.5/kWh in quantities of 10,000-20,000. Freon flows through the Econocoil and water to be cooled flows on the outside. Titanium parts were provided by Tranter, Inc, and a PVC enclosure to facilitate the water flow was designed and built at EDA.

A tube-in-tube heat exchanger was also designed and built. A titanium tube, 0.625-inch in outside diameter and 19-feet in length, was coated with Union Carbide high-flux surface to provide enhanced surface for boiling. This tube was contained in 1-inch O.D. titanium tube. The tubes were rolled in a helical coil of about 14-inches diameter. Proper connections were welded at the ends to provide flow of Freon and water.

Testing of Tranter Econocoil and tube-in-tube heat exchangers with Union Carbide's high-flux surface was completed. Test results for the Tranter Econocoil heat exchanger are presented in Table 32-5. The test results indicate that with water flow of 11 ℓ/min entering the heat exchanger at 10°C with a Freon flow rate of 1.2 ℓ/min entering the heat exchanger at 4°C, a

Table 32-5

TEST DATA ON TRANTER PLATE-COIL HEAT EXCHANGER FOR WATER AND FREON FLOW RATES OF 11 AND 1.2 LITERS/MINUTE, RESPECTIVELY

Water Temp., °C		Freon Temp., °C		Heat Transfer	
Inlet	Outlet	Inlet	Outlet	kCal/min	kCal/h-m^2-°C
10.0	7.8	3.7	4.2	24.2	276
10.0	7.7	3.6	4.2	25.3	288
10.1	7.9	3.8	4.3	24.2	230
10.0	7.8	3.6	4.2	24.2	273
10.2	8.0	3.9	4.7	24.2	284
10.0	8.0	4.6	4.7	22.0	284
10.0	7.9	4.0	4.6	23.1	280
				Mean=23.9 =1.03	Mean=273 =19.8

heat transfer rate of 23.9 kCal/min and overall heat transfer coefficient of 273 kCal/h-m^2-°C was obtained. As discussed earlier, the required heat transfer rate for the hydrate-former heat exchanger is 35.84 kCal/min. It was ascertained that the refrigeration system was not limiting the heat exchanger performance. Based on these results, a plate-coil heat exchanger that meets the battery requirements is being built.

Test results on the tube-in-tube heat exchanger are presented in Table 32-6. This heat exchanger has a heat transfer surface of 3.1 ft^2. The mean overall heat transfer coefficient obtained for this heat exchanger was 1652 (±43) kCal/h-m^2-°C. A heat transfer rate of 33.2 kCal/min was obtained with a flow of water at 11 ℓ/min entering the heat exchanger at 10°C and Freon flow of 1.8 ℓ/min entering at 4°C. The test data given here are for a quality change of 0.37 (37%). The design overall heat transfer coefficient was 3198 kCal/h-m^2-°C because of the use of an enhanced surface on the boiling side. Even though the specified heat transfer coefficient was not achieved, it did demonstrate the attractiveness of enhanced surfaces in increasing the average heat transfer coefficient from 288 to 1652 kCal/h-m^2-°C (see Tables 32-5 and 32-6). This increase will lead to the development of a more compact heat exchanger.

PROGRAM STATUS

The development of a cost-effective hydrate-former heat exchanger for BEST-battery modules was undertaken during Phase II of RP226-3. Designs were developed for heat exchangers utilizing indirect-glycol cooling as well as for direct-refrigerant cooling. System optimization studies indicate that use of direct cooling would be more efficient and cost effective. Because of no previous experience at EDA in the use of direct-refrigerant cooled heat exchangers in the battery module, the development of direct refrigerant-cooled heat exchangers was emphasized. Design optimization was performed through the use of a subcontractor. A liquid-overfeed refrigeration system was set up for the testing of heat exchangers. Commercially available heat exchangers were acquired for testing and one heat exchanger was designed at EDA.

Table 32-6

TEST DATA ON TUBE-IN-TUBE HEAT EXCHANGER FOR WATER AND FREON FLOW RATES OF 11 AND 1.8 LITERS/MINUTE, RESPECTIVELY

Water Temp., °C		Freon Temp., °C		Heat Transfer	
Inlet	Outlet	Inlet	Outlet	kCal/min	kCal/h-m^2-°C
10.0	7.0	4.3	4.6	33.0	1694
9.9	6.9	4.1	4.4	33.0	1667
10.0	7.0	4.3	4.7	33.0	1717
10.0	7.0	4.3	4.4	33.0	1671
10.0	7.0	4.1	4.4	33.0	1627
10.0	7.0	4.1	4.4	33.0	1606
10.0	7.0	4.2	4.3	33.0	1671
10.0	7.0	4.2	4.6	33.0	1671
10.0	6.9	3.8	4.2	34.1	1595
10.0	6.9	4.1	4.3	34.1	1679
				Mean=33.2 =0.46	Mean=1652 =43

Test results from the Tranter platecoil heat exchanger were used to design a platecoil heat exchanger which should meet the specifications for the BEST-battery module. This heat exchanger is presently being built and should be available for testing in April. Tests conducted on a heat exchanger utilizing Union Carbide high-flux boiling surface indicated that this surface was highly effective in enhancing the heat transfer coefficient on the Freon side. Use of this coating will significantly reduce the required surface area and, hence, the cost. At present, the high-flux surface is being used only on the outside surface of tubes. It is not commercially used on flat surfaces. Thus, for the present heat exchanger designs, use of tubes is being considered.

REFERENCES

1. K. E. Starner and R. A. Cromis. "Energy Savings Through use of High-Flux Evaporator Surface in Centrifugal Chillers. In Proceedings of the Central Water Chiller Conference. Purdue University, Nov. 1976.

2. D. F. Dippery and R. H. Sabersky. "Heat and Momentum Transfer in Smooth and Rough Tubes at Various Prandtl Numbers." Int. J. Heat Mass Transfer, 1963, Vol. 6, pp. 329-353.

Section 33

INERTS-REJECTION DEVICE: I. PROOF OF CONCEPT

ABSTRACT

In order to allow continuous closed-system operation of zinc-chloride battery modules at the BEST Facility, it is necessary to prevent the accumulation of foreign -- "inert", e.g., carbon dioxide, air -- gases in the gas spaces of the modules. This section describes the design and testing of a small chlorine-chlorine cell which electrochemically removes chlorine from a gas mixture containing chlorine, carbon dioxide, and air. The inert gases pass through the cathode compartment of the cell unprocessed, for rejection to the environment. The test results indicate that the gas separation is virtually complete, and that this concept for the inerts-rejection device is practical.

INTRODUCTION

The operational design of the BEST-battery module is described in Section 25 of this report. As indicated there, the continuous closed-system operation of the module requires the prevention of foreign-gas accumulation so that the gas phase remains primarily chlorine. However, the battery will be under reduced pressure during the charge cycle and some air will likely be drawn into the system. Also, a small amount of carbon dioxide is electrochemically produced at the chlorine electrode. These gases, if allowed to accumulate in the battery system, will eventually impair the performance of the system due to their dilution effects on the partial pressure of chlorine. Therefore, it will be necessary to periodically remove air and carbon dioxide from the chlorine gas phase.

The selection of the method to separate the foreign gases from chlorine involves several important considerations. First, the method and associated hardware must be compatible with the battery design and operation. Second, because it is employed as a battery subsystem, it must be highly reliable and low in cost. Third, the energy required to perform this operation must be small in comparison to the delivered energy of the module on a per-cycle basis. Finally, if it is assumed that air and carbon dioxide will be rejected to the atmosphere, then the separation of chlorine from the contaminant gases must be virtually complete in order to prevent chlorine release into the atmosphere.

In a previous report (1), four methods for inerts rejection were proposed and analyzed. The proposed methods were membrane permeation, gaseous diffusion, hydrate formation for partial separation of chlorine, and electrochemical separation of chlorine. The results of this study indicated that the electrochemical separation of chlorine was the most promising option.

This section of the report briefly describes the design and operational characteristics of a small chlorine-chlorine cell which was built and tested to experimentally evaluate the electrochemical separation concept for inerts rejection. The favorable results obtained from this proof-of-concept device led to the subsequent analysis of how and when a device based on this concept should operate and the actual development of a prototype device sized for 50-kWh zinc-chloride

battery modules. These studies are described in Sections 34 and 35 of this report.

EXPERIMENTAL DETAIL

Conceptually, the electrochemical separation of chlorine from contaminant gases is quite simple. The impure chlorine from the battery is admitted to a cathode compartment where the chlorine is dissolved in the catholyte and reduced to chloride ion. The contaminant gases, being electrochemically inert, pass through the cathode compartment and vent to the atmosphere. At the anode, chloride ions migrating from the catholyte to the anolyte are reoxidized to form pure chlorine which is returned to the battery.

A conceptual design of a chlorine-chlorine cell is shown in Figure 33-1. The essential components of the cell are the anode, cathode, separator, and electrolyte. The use of a packed bed cathode and separator is necessary because the cathode must accommodate both gas and liquid flow. The packed bed provides a tortuous path for the mixing of two-phase flow. The separator allows for liquid transfer and ion migration between the anode and cathode compartments but maintains gas separation.

The first experimental cell design is shown in Figure 33-2. A small-bore cylindrical packed-bed cathode was chosen to minimize potential problems associated with gas channeling. The cell was evaluated using the test apparatus shown in Figure 33-3.

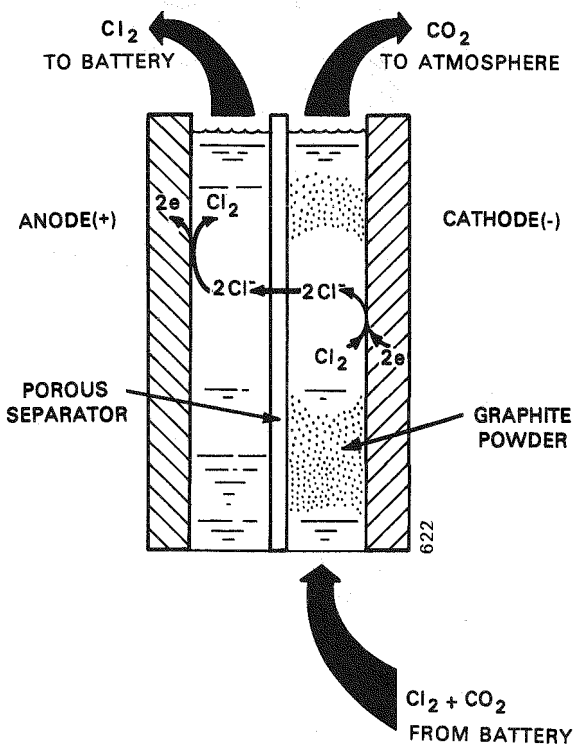

Figure 33-1. Conceptual design of chlorine-chlorine inerts-rejection cell.

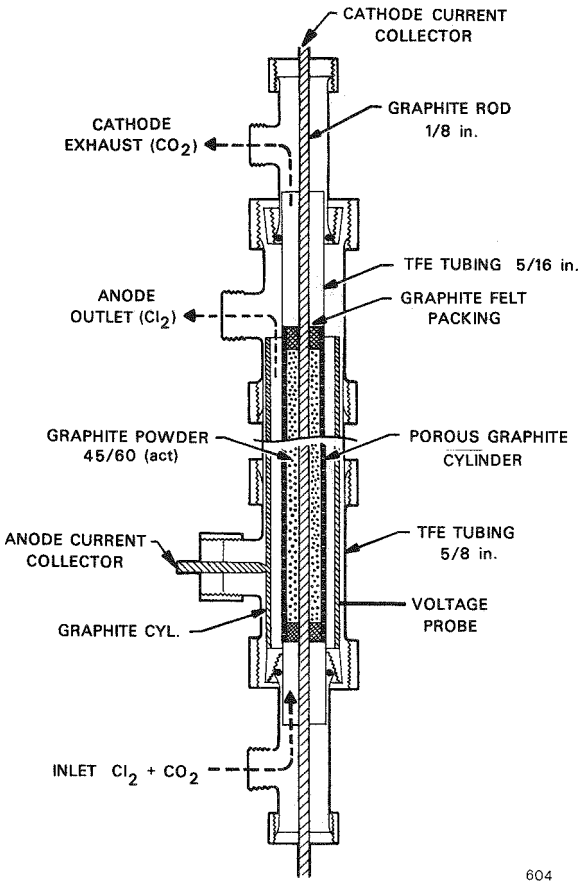

Figure 33-2. Schematic of cylindrical chlorine-chlorine cell.

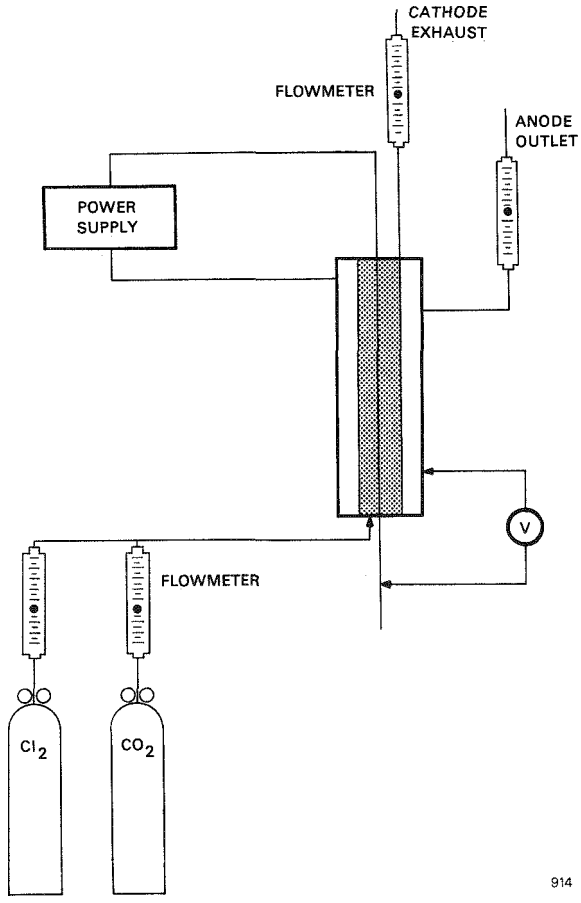

Figure 33-3. Laboratory test apparatus for chlorine-chlorine cell.

RESULTS AND DISCUSSION

The current-voltage characteristics of the cell were evaluated using four different electrolytes. For these tests, the inlet chlorine flow rate was held constant at 26 ml/min. The resulting polarization curves are shown in Figure 33-4. The best results were obtained using a 25% HCl solution as the electrolyte. Using the HCl electrolyte, the performance of the cell was considered adequate. The power requirements were not excessive and, considering the size of the cell, it was capable of processing chlorine at an acceptable rate.

The next phase of testing was to evaluate the completeness of gas separation. For this test, an equal volume mixture of chlorine and carbon dioxide was fed into the cathode inlet at a total flow rate of 50 ml/min. The cathode exhaust rate was monitored on the flowmeter. At an applied potential of 1.2 volts, the exhaust rate was 25 ml/min, indicating complete separation of chlorine from the carbon dioxide.

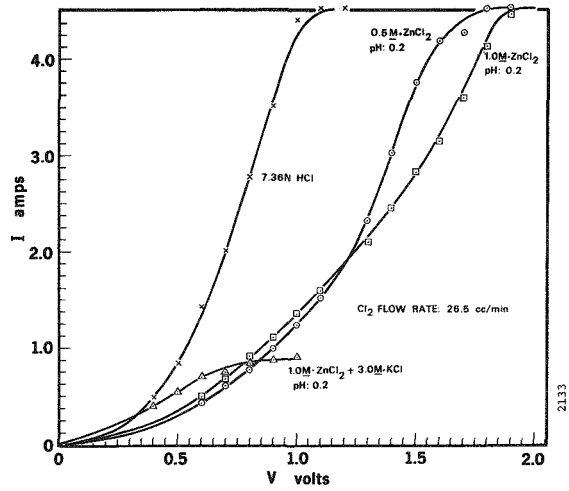

Figure 33-4. Current voltage curves for cylindrical chlorine-chlorine cell.

These results provide the proof-of-concept for utilizing a chlorine-chlorine cell for inerts rejection. The device is compatible with the zinc-chloride battery environment, is operationally simple, and is capable of virtually complete separation of chlorine from foreign gases. The data further suggest an energy requirement of ~5 Wh/ℓ of chlorine processed. Depending on the quantity of gas to be processed per module-cycle, this energy requirement could also prove to be acceptable.

Based on these favorable results, parallel programs were established to pursue the development of a prototype inerts-rejection device for 50-kWh battery modules. Section 34 describes the developmental status of a mathematical model for predicting the accumulation of inert gases in the stack and store gas spaces of the module during continuous closed-system operation. This model, in combination with gas data from the EPRI 45-kWh module, are

used to establish the capacity and operational specifications for an electrochemical chlorine-chlorine inerts-rejection device for battery modules. Based on these specifications, Section 35 describes the design and development of a prototype inerts-rejection subsystem for the BEST-battery modules.

REFERENCES

1. Development of the Zinc-Chloride Hydrate Battery for Utility Applications. Palo Alto, Calif.: Electric Power Research Institute, April 1979. EM-1051.

Section 34

INERTS-REJECTION DEVICE: II. HOW AND WHEN WILL IT OPERATE?

ABSTRACT

An inert-gas rejection device is required for continuous closed-system operation of 50-kWh zinc-chloride battery modules at the BEST Facility. Modeling of carbon dioxide accumulation in the gas spaces of 50-kWh battery modules is performed for the purpose of determining how and when an inerts-rejection subsystem should operate. Gas-analysis data from the EPRI 45-kWh module are used to refine the model. The model predicts that a subsystem capable of processing gas mixtures at the rate of 0.5 ℓ/min for two hours during cleanout will maintain the carbon dioxide concentration below 1% by volume in the critical gas spaces and thereby allow continuous operation.

INTRODUCTION

There are two separate compartments, each having its own gas space, in zinc-chloride battery modules. One compartment contains the battery stack -- where the electrochemical reactions occur -- and the electrolyte sump -- where the bulk of the electrolyte is retained for circulation through the cells of the battery stack. The other compartment is the store, in which chlorine hydrate is formed and stored during the charge mode and decomposed during discharge. The gas spaces of these two compartments are effectively isolated from one another. However, controlled transfer of gases during operation is possible, as described in Section 25. The nominal volumes of the gas spaces are 60ℓ and 30ℓ for the stack and store, respectively.

During operation of the battery, hydrogen, carbon dioxide, nitrogen, and oxygen accumulate in the gas spaces of these two compartments. Hydrogen and carbon dioxide are by-products of the electrochemical reactions within the system. Air may accumulate in the system because the battery stack operates under reduced pressure. With the exception of hydrogen, these gases are categorized as inert gases because the reactions and methods by which they occur are not reversible in the electrochemical processes of the battery (1). As discussed in Section 33, these inert gases must be removed from the system to prevent their accumulation which will eventually interfere with normal operation of the battery.

The rate of air leakage into the battery through the battery case is unknown and therefore was not considered in this preliminary study. A fluorescent light reactor facilitates the reaction of evolved hydrogen with chlorine in the battery system.

This analytical study is one part of a program to develop a device to separate carbon dioxide from a gas mixture of carbon dioxide and chlorine, and reject it to the environment. In this investigation, modeling work was conducted to characterize the accumulation and distribution of carbon dioxide produced in the system. A coupled pair of first-order linear-differential equations were developed which, together with the appropriate initial conditions, describe the concentration of carbon dioxide in the stack and store at any time during battery operation. The model also can simulate the operation

of the inerts-rejection device. The solutions of the governing equations were programmed on the computer. Using this program, the carbon dioxide concentration and its variation with time can be predicted for each phase of battery operation over any number of consecutive cycles. This analysis provides a basis for determining the timing and duration of operation for an inert-gas rejection device, and the location and capacity of this device, in a battery module.

INITIAL MODEL

During normal battery operation, carbon dioxide is produced by the slow oxidation of the porous-graphite chlorine electrodes and a small amount enters due to air leakage through the battery case. A schematic of the battery module used for modeling is shown in Figure 34-1. Carbon dioxide and chlorine generated in the stack are transferred to the store during charge. The chlorine is combined with the prechilled store fluid to form chlorine hydrate, and it is assumed that carbon dioxide accumulates in the store gas space. The carbon dioxide and chlorine from the store are transferred back to the stack during discharge, and carbon dioxide accumulates in the stack gas space. For this study, it was assumed that a 1% volume concentration of carbon dioxide in the stack gas space during charge and in the store gas space during discharge was an upper limit.

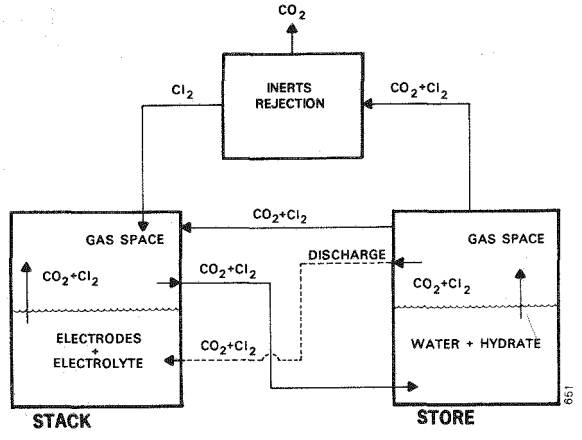

Figure 34-1. Schematic of battery module illustrating carbon dioxide generation, distribution, and rejection.

It is projected that carbon dioxide is produced at a rate of 0.006 ℓ/min during charge, i.e., 0.02% of the chlorine evolved (2,3), and half of that, or 0.003 ℓ/min, during discharge. The corresponding rate of chlorine generation during charge is 33 ℓ/min. This gives a carbon dioxide level at the end of a typical cooldown charge/discharge sequence of almost 4% by volume of the total gas volume.

The nomenclature shown in Table 34-1 was used in the mathematical development of the models.

Table 34-1

NOMENCLATURE USED IN MATHEMATICAL MODELS

Nomenclature

m = mass of CO_2 at any given instant (g)

V = volume of gas space (ℓ)

$\dot{V}$ = volumetric gas-flow rate (std ℓ/min)

$\dot{m}$ = mass flow rate (g/min)

$x = \frac{m}{V}$ = concentration of CO_2 (g/ℓ)

q = rate of generation of CO_2 (g/min)

Subscripts:

1 = stack

2 = store

3 = rejection device

12 = from stack to store

21 = from store to stack

23 = from store to rejection device

Governing Assumptions and Relationships

In this study attention was focused on analysis of carbon dioxide accumulation in the stack and store gas spaces during the battery module operation. Models for operation with and without inert-gas rejection are developed on the basis of the following assumptions:

- there is no dissolution of carbon dioxide in the store fluid or in the electrolyte in the stack.
- there are constant gas-flow rates during any particular phase of the battery cycle.
- there is a constant volume of gas in the gas spaces, 60 liters in the stack and 30 liters in the store, due to the fact that liquid volumes remain constant.
- gas is thoroughly mixed in the gas spaces, i.e., there is no spatial variation in gas concentrations.
- the generation of carbon dioxide is constant during a given phase of battery operation.

Using the above assumptions and nomenclature, as well as the principle of conservation of mass, the mass balance equations for carbon dioxide in the battery-stack and store gas spaces can be written as:

$$\underline{\text{Stack}}: \quad \frac{dm_1}{dt} = q_1 + \dot{m}_{21} - \dot{m}_{12} \qquad (34\text{-}1)$$

$$\underline{\text{Store}}: \quad \frac{dm_2}{dt} = \dot{m}_{12} - \dot{m}_{21} - \dot{m}_{23} \qquad (34\text{-}2)$$

where $\dot{m}_{12} = x_1 \dot{V}_{12}$

$\dot{m}_{21} = x_2 \dot{V}_{21}$

$\dot{m}_{23} = x_2 \dot{V}_{23}$

For the case without inert-gas rejection, $\dot{V}_{23} = 0$ and the $\dot{m}_{23}$ term drops out of Eq. 34-2. Eq. 34-1 and 34-2 can be rewritten in terms of carbon dioxide concentration in the stack and store:

$$\underline{\text{Stack}} \quad \frac{dx_1}{dt} = \frac{q_1 + x_2\dot{V}_{21} - x_1\dot{V}_{12}}{V_1} \qquad (34\text{-}3)$$

$$\underline{\text{Store}} \quad \frac{dx_2}{dt} = \frac{x_1\dot{V}_{12} - x_2\dot{V}_{21} - x_2\dot{V}_{23}}{V_2} \qquad (34\text{-}4)$$

The following initial conditions are used in the solution of Eq. 34-3 and 34-4:

$$\text{at } t = 0; \; x_1 = x_1^\circ \text{ and } x_2 = x_2^\circ$$

i.e., x_1° and x_2° are the initial concentrations of carbon dioxide in the stack and store gas spaces, respectively.

The simultaneous solution of Eq. 34-3 and 34-4, for the case where gas mixtures of carbon dioxide and chlorine from the store gas space are processed at a constant volumetric flow rate by an inert-gas rejection device, results in the relationships presented here as Eq. 34-5 and 34-6:

$$x_1 = Ce^{k_1 t} + \left(x_1^\circ - C - \frac{f}{d}\right) e^{k_2 t} + \frac{f}{d} \qquad (34\text{-}5)$$

$$x_2 = p_1 Ce^{k_1 t} + p_2 \left(x_1^\circ - C - \frac{f}{d}\right) e^{k_2 t} + \frac{f\dot{V}_{12} - dq_1}{d\dot{V}_{21}} \qquad (34\text{-}6)$$

where

$$C = \frac{1}{(p_1 - p_2)} \left[x_2^\circ - p_2 x_1^\circ + \frac{f p_2 \dot{V}_{21} - f\dot{V}_{12} + dq_1}{d\dot{V}_{21}} \right] \quad (34\text{-}7)$$

$$c = \frac{\dot{V}_{12}}{V_1} + \frac{\dot{V}_{21} + \dot{V}_{23}}{V_2} \quad (34\text{-}8)$$

$$k_1 = -\frac{c + \sqrt{c^2 - 4d}}{2} \quad (34\text{-}9)$$

$$k_2 = -\frac{c - \sqrt{c^2 - 4d}}{2} \quad (34\text{-}10)$$

$$P1 = \frac{V_1 k_1 + \dot{V}_{12}}{\dot{V}_{21}} \quad (34\text{-}11)$$

$$P2 = \frac{V_1 k_2 + \dot{V}_{12}}{\dot{V}_{21}} \quad (34\text{-}12)$$

$$d = \frac{\dot{V}_{12}\dot{V}_{23}}{V_1 V_2} \quad (34\text{-}13)$$

$$f = \frac{\dot{V}_{21} q_1 + \dot{V}_{23} q_1}{V_1 V_2} \quad (34\text{-}14)$$

Model Predictions and Module Data

To obtain the numerical results for the equations derived from the mass balance, appropriate values for various parameters were substituted in the equations. The equations were then solved by computer.

The model predicts that steady-state levels of carbon dioxide are attained after two to four cycles when the inert gases are rejected, and that the steady-state concentration level depends on the rejection rate. Table 34-2 gives the numerical results.

The results suggest that a reasonable rejection rate will lead to an acceptable level of carbon dioxide during normal battery operation. Based on the computer simulation, if an inerts-gas rejection device processes store gas at the rate of 200 ml/min during cooldown and charge, the volume percentage of carbon dioxide would not exceed the 1% level in either the stack during charge or in the store during discharge.

The initial model was developed to simulate the operation of the EPRI 45-kWh battery module. Gas sampling data were taken from the 45-kWh battery module during normal system operation in order to evaluate the model and, if necessary, aid in its refinement. Due to problems encountered, in both the gas sampling and the module operation, only a limited number of runs produced data that were usable for purposes of this evaluation. Although there were slight numerical variations in carbon dioxide concentration from run to run, all followed essentially the same pattern over a charge/ discharge sequence. In view of this, one run was chosen as a representative cycle for purposes of evaluating the initial model. Figure 34-2 shows both the data from the initial model and the actual data from the representative cycle over a normal charge/discharge cycle (7-hour charge, 5-hour discharge). As can be seen from this figure, the model predicted much higher carbon dioxide concentrations in both the stack and store throughout an entire cycle. It was necessary to refine the model in view of the discrepancy between the predicted carbon dioxide concentrations over the cycle and the actual concentrations encountered in the module.

Table 34-2

PREDICTED CONCENTRATIONS OF CARBON DIOXIDE IN STACK AND STORE GAS SPACES WITH AND WITHOUT REJECTION OF INERTS

Cycle #	Concentration of Carbon Dioxide (%) Stack (end of charge)	Store (end of discharge)	Flow Rate Through Rejection Device (ml/min)
1	2.02	0.61	0
	0.70	0.29	200
	0.31	0.20	500
2	4.09	1.10	0
	0.78	0.31	200
	0.31	0.20	500
3	6.16	1.59	0
	0.79	0.31	200
	0.31	0.20	500
4	8.22	2.08	0
	0.79	0.31	200
	0.31	0.20	500
5	10.29	2.57	0
	0.79	0.31	200
	0.31	0.20	500

REFINED MODEL

Revised Assumptions and Relationships

In order to derive a model that more nearly represented actual module operation, it was necessary to re-evaluate the governing assumptions used. One assumption, that there was no dissolution of carbon dioxide in the store fluid or in the electrolyte in the stack, was found to be in error by examination of the available gas-sampling data. From Figure 34-2 it can be seen that the model, which utilized the assumption, shows an accumulation of carbon dioxide in both the stack and store, with the major accumulation of carbon dioxide in the store during charge and in the stack during discharge due to the direction of the major gas flow during a cycle phase. During the actual cycle there is no accumulation of carbon dioxide in either the stack or store during charge and the accumulation in the stack and store during discharge is only one-fourth of that predicted. In light of these data, the assumption was revised as follows:

- There is dissolution of carbon dioxide in the store fluid during charge and release of the accumulated carbon dioxide from the store during discharge.

Using four of the original assumptions and one rewritten assumption, the mass balance equations for carbon dioxide in the battery stack and store gas spaces with inert-gas rejection from the store can be written as:

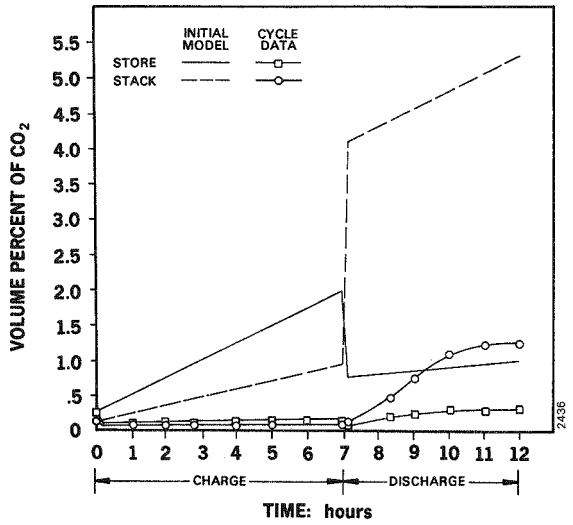

Figure 34-2. Comparison of computer simulation using initial model and actual data showing volume (%) of carbon dioxide for one battery cycle with no rejection device and with identical initial volume concentrations of carbon dioxide.

$$\underline{\text{Stack}}: \frac{dm_1}{dt} = q_1 + \dot{m}_{21} - \dot{m}_{12} \qquad (34\text{-}1)$$

$$\underline{\text{Store}}: \frac{dm_2}{dt} = (1\text{-}a)\,\dot{m}_{12} - \dot{m}_{21} + q_2 - \dot{m}_{23} \qquad (34\text{-}15)$$

where $\dot{m}_{12} = x_1 \dot{V}_{12}$

$\dot{m}_{21} = x_2 \dot{V}_{21}$

$\dot{m}_{23} = x_2 \dot{V}_{23}$

For the case without inert-gas rejection, $\dot{V}_{23} = 0$ and the $\dot{m}_{23}$ term drops out of Eq. 34-15. During charge the release term (q_2) drops out of Eq. 34-15. During discharge the accumulation term (a) = 0 and the m_{12} term becomes simply $\dot{m}_{12}$ as in Eq. 34-2.

Eq. 34-1 and 34-15 can be rewritten in terms of carbon dioxide concentration in the stack and store:

$$\underline{\text{Stack}} \quad \frac{dx_1}{dt} = \frac{q_1 + x_2\dot{V}_{21} - x_1\dot{V}_{12}}{V_1} \qquad (34\text{-}3)$$

Store: Charge

$$\frac{dx_2}{dt} = \frac{(1\text{-}a)\,x_1\dot{V}_{12} - x_2\dot{V}_{21} - x_2\dot{V}_{23}}{V_2} \qquad (34\text{-}16)$$

Store: Discharge

$$\frac{dx_2}{dt} = \frac{x_1\dot{V}_{12} - x_2\dot{V}_{21} + q_2 - x_2\dot{V}_{23}}{V_2} \qquad (34\text{-}17)$$

The following initial conditions are used in the solution of Eq. 34-3 and 34-16 and Eq. 34-3 and 34-17:

$$\text{At } t = 0;\ x_1 = x_1^\circ \text{ and } x_2 = x_2^\circ$$

i.e., x_1° and x_2° are the initial concentrations of carbon dioxide in the stack and store gas spaces, respectively.

The simultaneous solution of Eq. 34-3 and 34-16 for charge and Eq. 34-3 and 34-17 for discharge for the case where gas mixtures of carbon dioxide and chlorine from the store gas space are processed at a constant volumetric flow rate by an inert-gas rejection device, results in the relationships presented earlier as Eq. 34-5 through 34-12,

and where

$$d = \frac{\dot{V}_{12}\left(\dot{V}_{23} + a\dot{V}_{21}\right)}{V_1 V_2}$$

$$f = \frac{\dot{V}_{21}q_1 + \dot{V}_{23}q_1}{V_1 V_2}$$

for Eq. 34-3 and 34-16 (charge with accumulation in store)

and

$$d = \frac{\dot{V}_{12}\dot{V}_{23}}{V_1 V_2}$$

$$f = \frac{\dot{V}_{21}q_1 + \dot{V}_{23}q_1 + \dot{V}_{21}q_2}{V_1 V_2}$$

for Eq. 34-3 and 34-17 (discharge with release from store).

To obtain the numerical results for the equations derived from the mass balance, appropriate values for various parameters were substituted in the equations. The equations were then solved by computer.

COMPARISON OF MODULE DATA AND MODEL

Figure 34-3 shows the carbon dioxide concentration data from the representative cycle and the carbon dioxide concentrations predicted by the refined model. The refined model provides a fairly accurate fit to the module data.

An inerts-rejection device operates most efficiently when its feed gas is richest in inerts. From Figure 34-3, it can be seen that carbon dioxide reaches its maximum concentration in the stack gas space at the end of discharge. However, the store operates at positive pressure and would provide a driving force for the gas entering the inerts rejection device, whereas the stack operates below ambient pressure and an external driving force would have to be provided. Thus, the optimum time to reject inerts would be after discharge and the appropriate site would be the store. A computer simulation of the refined model providing for rejection from the store after discharge (during cleanout) was run. Based on the computer simulation, the refined model predicts that steady-state levels of carbon dioxide are attained after 9 cycles when the inert gases are rejected at the rate of 500 ml/min, and after 14 cycles when inert gases are rejected at the rate of 200 ml/min. In addition, at the 200 ml/min rejection rate, steady-state concentrations of carbon dioxide in the stack during charge and in the store during discharge are very close to the 1% limit. With a 500 ml/min rejection rate, the steady-state concentrations are less than 0.5%. In order to minimize the steady-state carbon dioxide concentrations, the 500 ml/min rejection rate was chosen. Table 34-3 gives the numerical results of carbon dioxide concentration as a function of rejection rate when inerts are rejected for two hours.

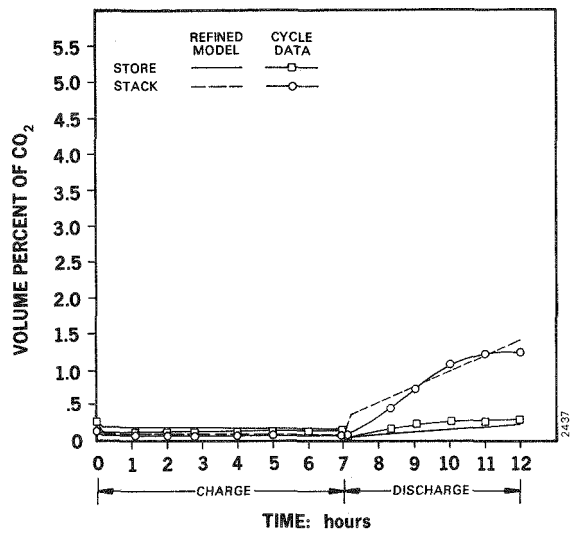

Figure 34-3. Comparison of computer simulation using refined model and actual data showing volume (%) of carbon dioxide for one battery cycle with no rejection device and with identical initial volume concentrations of carbon dioxide.

Table 34-4 gives the numerical results from the computer simulation of carbon dioxide concentration as a function of rejection time. If inerts were rejected for one hour, steady-state would not be reached until the fourteenth cycle and the concentrations of carbon dioxide in the stack during charge and the store during discharge would be very close to the 1% limit. However, if inerts were rejected for three hours

Table 34-3

PREDICTED CONCENTRATIONS OF CARBON DIOXIDE IN THE MODULE GAS SPACES WITH AND WITHOUT REJECTION OF INERTS

Cycle #	Concentration of Carbon Dioxide (%) Stack (end of charge)	Store (end of discharge)	Flow Rate Through Rejection Device (ml/min)
1	0.07	0.25	0
	0.07	0.25	200
	0.07	0.25	500
2	0.23	0.39	0
	0.19	0.36	200
	0.14	0.31	500
3	0.40	0.54	0
	0.30	0.45	200
	0.19	0.36	500
4	0.56	0.69	0
	0.40	0.53	200
	0.23	0.39	500
5	0.73	0.84	0
	0.47	0.60	200
	0.25	0.41	500
6	0.89	0.98	0
	0.53	0.66	200
	0.27	0.42	500
7	1.06	1.13	0
	0.59	0.71	200
	0.28	0.43	500
8	1.22	1.28	0
	0.64	0.76	200
	0.29	0.44	500
9	1.39	1.43	0
	0.68	0.80	200
	0.29	0.45	500
10	1.55	1.57	0
	0.72	0.83	200
	0.29	0.45	500

Table 34-4

PREDICTED CONCENTRATIONS OF CARBON DIOXIDE IN THE MODULE GAS SPACES AT A FEED RATE OF 500 ml/MIN TO THE INERTS-REJECTION DEVICE

Cycle #	Concentration of Carbon Dioxide (%) Stack (end of charge)	Store (end of discharge)	Rejection Time (hours)
1	0.07	0.25	1
	0.07	0.25	2
	0.07	0.25	3
2	0.18	0.35	1
	0.14	0.31	2
	0.11	0.28	3
3	0.28	0.43	1
	0.19	0.36	2
	0.13	0.30	3
4	0.36	0.51	1
	0.23	0.39	2
	0.15	0.32	3
5	0.42	0.56	1
	0.25	0.41	2
	0.15	0.32	3
6	0.47	0.61	1
	0.27	0.42	2
	0.16	0.33	3
7	0.52	0.65	1
	0.28	0.43	2
	0.16	0.33	3
8	0.55	0.68	1
	0.29	0.44	2
	0.16	0.33	3
9	0.58	0.71	1
	0.29	0.45	2
	0.16	0.33	3
10	0.61	0.73	1
	0.29	0.45	2
	0.16	0.33	3

steady-state would be reached only three cycles earlier (cycle number 6) than if inerts were rejected for two hours. The actual carbon dioxide concentrations for the two- and three-hour rejection times are well below the 1% limit in the gas spaces of interest. In order to minimize time of operation, the two-hour rejection time was chosen. From Table 34-4 it can be seen that if a rejection device processes store gas at the rate of 500 ml/min during a two-hour cleanout, the volume percentage of carbon dioxide would not exceed the 1% level in either the stack during charge or in the store during discharge.

STATUS

Based on a computer simulation utilizing the refined model it has been predicted that an inerts-rejection device, processing store gas at a rate of 500 ml/min for two hours during cleanout, would maintain stack gas during charge and store gas during discharge at levels below 1%. The model also predicts that steady-state would be reached in nine cycles at this rate and duration of rejection.

Single-cycle predictions of this refined model agree with gas-analysis data from the 45-kWh battery module. Experimental verification of the continuous closed-system cycling predictions, however, is currently not possible due primarily to leaks through the flange areas of the module. Despite this inability to completely verify the refined model, its predictions are used to establish the mode of operation and capacity of an inerts-rejection device for battery modules. Based on these specifications, a prototype device is designed and developed, as described in Section 35.

It is recommended that complete experimental verification of the model be pursued. This means accumulation of gas-analysis data during sequential cycles on a closed-system module: This should be performed on either the 45-kWh module, after elimination of existing leaks, or on one of the prototype BEST-battery modules. Similarly, it is recommended that the maximum tolerable levels of foreign gases during charge and discharge be determined experimentally. These data would allow more accurate specification of the design and operation of an inerts-rejection device.

REFERENCES

1. Development of the Zinc-Chlorine Battery for Utility Applications. Palo Alto, Calif.: Electric Power Research Institute, April 1979. EM-1051, Part V, Section 36, pp. 1-14.

2. Ibid., Part IV, Section 28, pp. 4-5.

3. Ibid., Part V, Section 37, p. 15.

Section 35

INERTS-REJECTION DEVICE: III. PROTOTYPE FABRICATION AND TESTING

ABSTRACT

An inerts-rejection device is needed to routinely cleanse the gas spaces of the BEST-battery modules of impurity gases. A full-scale device was developed for removing air and carbon dioxide from chlorine gas. This three-stage chlorine-chlorine cell is capable of processing impure chlorine gas at a rate >0.5 ℓ/minute. Chemical analysis indicates that the separation of gases is virtually complete, with less than 0.2% chlorine by volume remaining in the impurity gases after separation. A breadboard device is operational on the 45-kWh module and a refined design, for integration into the BEST-battery modules, has been prepared.

INTRODUCTION

The successful operation of an electrochemical inerts-rejection device was described in Section 33. Using a chlorine-chlorine cell of cylindrical design, complete separation of chlorine from foreign gases was achieved at reasonable chlorine-processing rates. This cylindrical device demonstrated proof of concept and provided a solid technical basis for the development of a prototype inerts-rejection subsystem sized for 50-kWh battery modules.

In conjunction with this experimental program, computer modeling studies were performed to determine when the inerts-rejection system should operate in a battery module and what chlorine processing rates would be required. As described in Section 34, the initial model was refined with the input of experimental data taken from the 45-kWh module. From the refined model, an operational sequence for the inerts-rejection device was defined. The modeling results indicate that this device should operate at a chlorine-gas processing rate of 0.5 ℓ/minute for two hours during the clean-out phase of operation, i.e., immediately following discharge.

In this section, a chlorine-chlorine cell design is described which allowed scale-up of this electrochemical processing device. Two large cells -- 100 cm^2 and 300 cm^2 electrode area -- were built and characterized. Based on this successful scale-up, a three-stage prototype device was built, bench tested, and connected to the EPRI 45-kWh module for evaluation as a full-scale subsystem. A similar device was designed for integration and incorporation into the third prototype BEST-battery module.

CELL STUDIES

Design

A cylindrical cell design was used for the proof-of-concept device described in Section 33. The cylindrical design, however, did not prove practical for scale-up. The thin-walled graphite cylinder, employed as the membrane or separator, was very friable and fragile. Attempts to produce larger-diameter cylinders were generally unsuccessful. Also, resistance problems with the cathode current collector were anticipated with currents on the order of 75-100 amperes.

To avoid difficulties associated with scaling up the cylindrical cell, a flat-plate cell was designed and built. Its construction is shown in Figure 35-1. This cell had a central common-cathode and two end anodes. The electrodes were 5-inches tall and 1.625-inches wide. The working electrode area was about 52 cm^2 per face. A major problem with this design was that entering gas would not divide uniformly between the two cathode packed beds. Gas channeling was also prevalent. This created current imbalances and generally poor performance. Due to these difficulties, the design was abandoned.

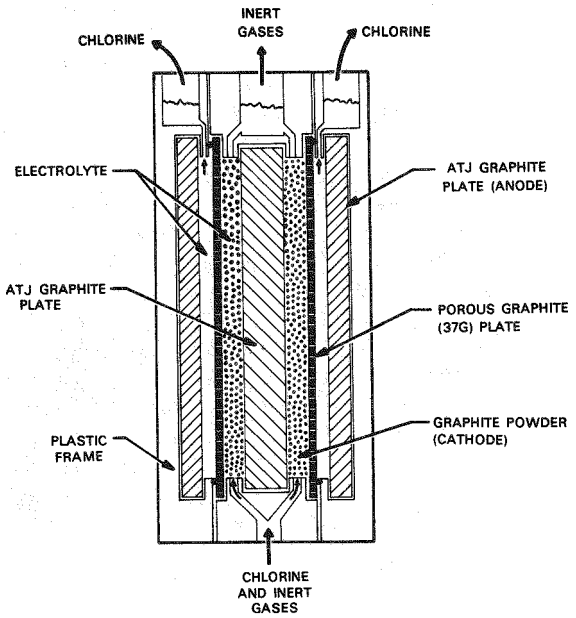

Figure 35-1. Schematic of chlorine-chlorine cell for processing chlorine. Note the common-cathode design feature.

The problem associated with the first two designs, capacity and gas channeling, were overcome with a third design. This cell design, shown in Figure 35-2, is a flat-plate design, but the cathode is fabricated to a proprietary design. The gas flow is directed through the entire cathode. Accordingly, electrodes of considerable area and gas processing capacity can be constructed.

The electrodes were machined from dense graphite. Screw threads were tapped in the backs of the electrodes for current collectors and voltage probes. The gas ports were made using tapped holes and Kynar fittings. The graphite separators were machined from porous graphite. The separator was bonded to the dense graphite. The spacers were machined from both Lucite and PVC plastic. The electrodes were bonded to the spacer with silicone rubber. The graphite particles used in the packed beds were all 25/60 mesh.

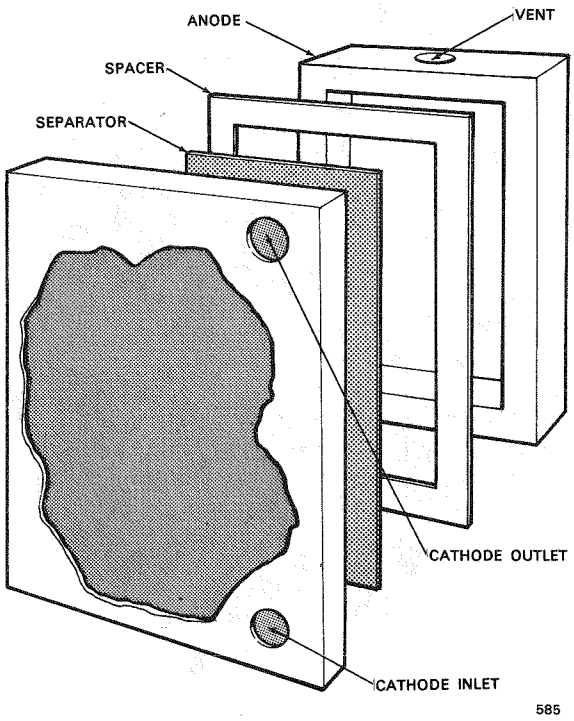

Figure 35-2. Improved chlorine-chlorine cell.

Test Equipment and Procedure

A schematic of the laboratory test equipment is shown in Figure 35-3. Appropriately sized flowmeters were used to monitor gas flow rates into the cells, as well as, the exhaust flow rates. The flowmeters were extremely sensitive to moisture condensation and it was necessary to install liquid traps in the exhaust lines. The power supply used in the testing was capable of operating in either a constant current or constant voltage mode. The

reference voltmeter could be read to one millivolt.

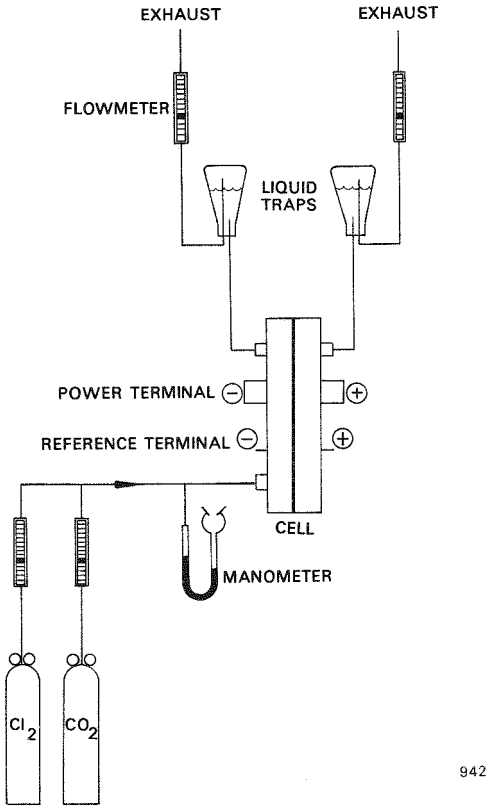

Figure 35-3. Schematic of laboratory test apparatus. This system was used to evaluate gas-processing rates, as well as gas-separation capabilities.

The performance of the cell was evaluated after the cell had several hours of operating time. This initial time served as a breaking-in period to ensure that the separator was thoroughly wetted with the 10% HCl electrolyte. The cell was characterized by obtaining polarization curves at different chlorine flow rates. For these performance evaluations, only pure chlorine was used.

Performance

100-cm^2 Cell: Polarization curves for a cell with an active cathode area of 100-cm^2 cell are shown in Figure 35-4. The polarization of the cell is not greatly affected by the chlorine flow rate. For these curves, no attempt was made to consume all the chlorine entering the cathode. The current efficiency (fraction of current used to reduce the entering chlorine) may be evaluated as shown in Table 35-1. The internal transfer current, column 7, arises from the transfer of anodically generated chlorine back to the cathode where it is electrochemically reduced to chloride ion. This process represents the current inefficiency in the cell and varies from 2 to 4 amperes. Due to this relatively constant parasitic current, the current efficiency of the cell increases with increasing applied current.

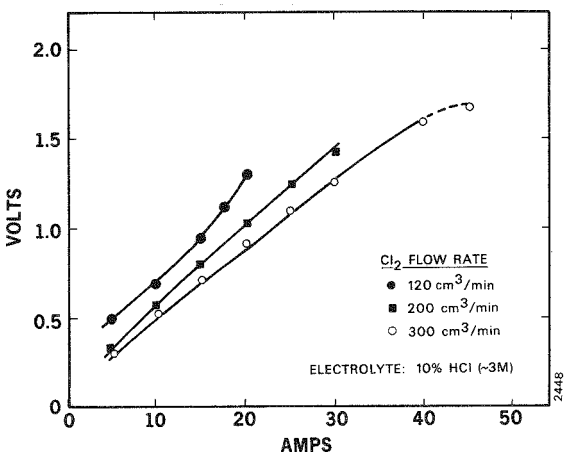

Figure 35-4. Polarization curve for 100-cm^2 chlorine-chlorine cell.

This relationship is shown graphically in Figure 35-5. The experimentally-determined chlorine processing rates are plotted as a function of the applied current. For reference, the faradaic equivalent current is also plotted. This curve would be obtained if there were no transfer of chlorine from the anode back to the cathode. From the two curves, the current efficiency at any current can be determined as the ratio of the experimental chlorine processing rate divided by the theoretical processing rate. From the equation in Figure 35-5, the calculated current efficiency at 30 amperes is 89%, in good agreement with the experimental value (Table 35-1) of 90%.

Table 35-1

CURRENT EFFICIENCY OF 100-cm^2 CELL

(1) Inlet Cl_2 Flow (ml/min)	(2) Exit Cl_2 Flow (ml/min)	(3) Chlorine Processed (1 - 2) (ml/min)	(4) Current Used to Process Cl_2 (3) x 0.144 (A)	(5) Cell Current (A)	(6) Current Efficiency (4÷5)x100% (%)	(7) Internal Chlorine Transfer Current (5 - 4) (A)
100	45	55	7.9	10	79	2.1
100	5	95	13.7	15	91	1.3
120	65	55	7.9	10	79	2.1
120	25	95	13.7	17.5	78	3.8
160	80	80	11.5	15	77	3.5
200	45	155	22.3	25	89	2.7
200	10	190	27.4	30	91	2.6
300	225	75	10.8	15	72	4.2
300	115	185	26.6	30	89	3.4
300	5	295	42.5	45	94	2.5

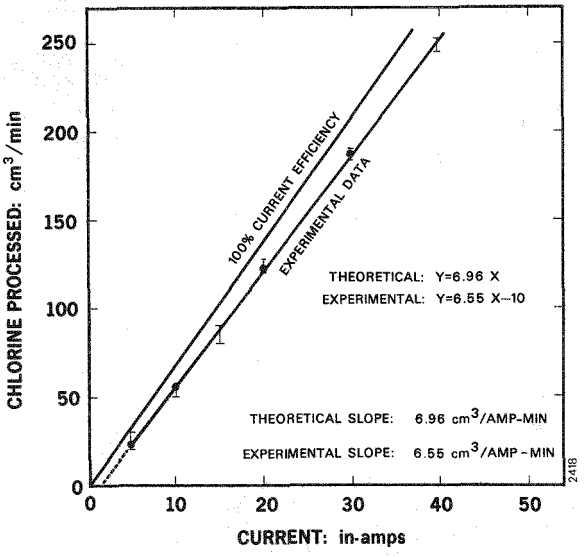

Figure 35-5. Chlorine-processing rate as a function of applied current. The parasitic current is relatively independent of the applied current.

In Figure 35-6, the power input to the cell is plotted as a function of the chlorine processing rate. The power consumed by the cell during its operation is an important parameter as this power consumption is an energy penalty for the zinc-chloride battery. A nearly linear relationship exists between the power input and the chlorine processing rate.

<u>300-cm^2 Cell</u>: The construction of the 300-cm^2 cell is identical to that of the 100-cm^2 cell. To increase the

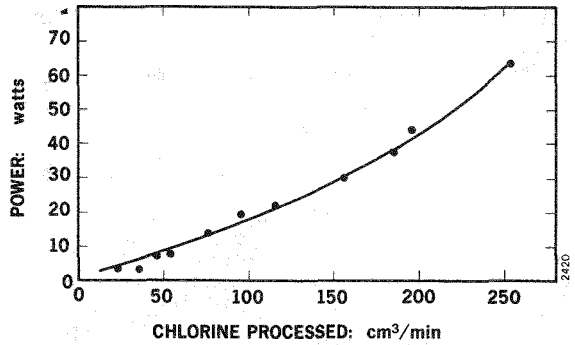

Figure 35-6. Power consumption of a 100-cm^2 cell as a function of chlorine-processing rate.

working area from 100 cm^2 to 300 cm^2, only the width was increased. For the 300-cm^2 cell, the dimensions of the electrode were 20 cm high by 18.5 cm wide.

A typical polarization curve for the 300-cm^2 is shown in Figure 35-7. Some increased polarization is noted above 80 amperes for a flow rate of 0.5 ℓ Cl_2/min. However, at this current level, the cell is near its limiting current, consuming virtually 100% of the entering chlorine.

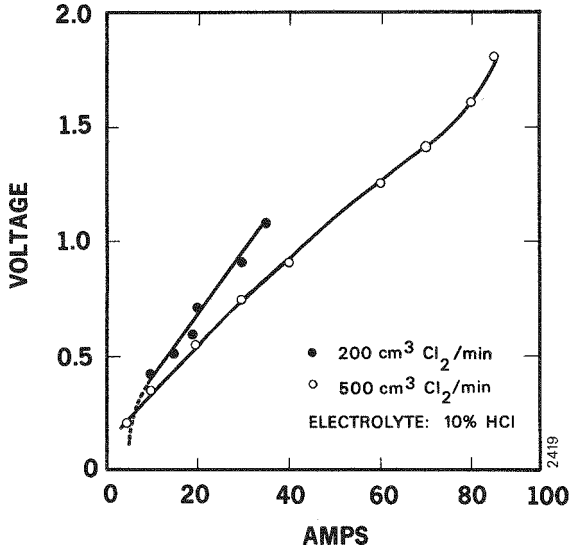

Figure 35-7. Polarization curve for 300-cm^2 cell. This cell is capable of processing about 0.5 ℓ/min of chlorine.

In Figure 35-8, the current efficiency of the 300-cm^2 cell is shown. When compared to the efficiency of the 100-cm^2 cell, Figure 35-5, the 300-cm^2 cell is very similar. For the 100-cm^2 cell, the experimental line slope is 6.6 ml Cl_2/ampere and for the 300-cm^2 cell, the line slope is 6.2 ml Cl_2/ampere.

In Figure 35-9, the power requirements for the 300-cm^2 cell are shown as a function of the chlorine processing rate. From this curve it can be seen that approximately 150 watts of input power are required to process 0.5 ℓ Cl_2/min. This processing rate meets the design criteria and energy requirements for the subsystem. For a two-hour duty cycle, the energy requirement is approximately 0.3 kWh.

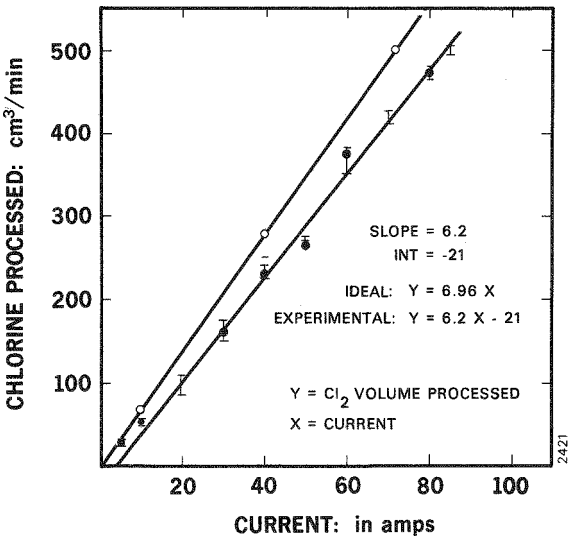

Figure 35-8. Chlorine processing rate as a function of applied current for 300-cm^2 cell.

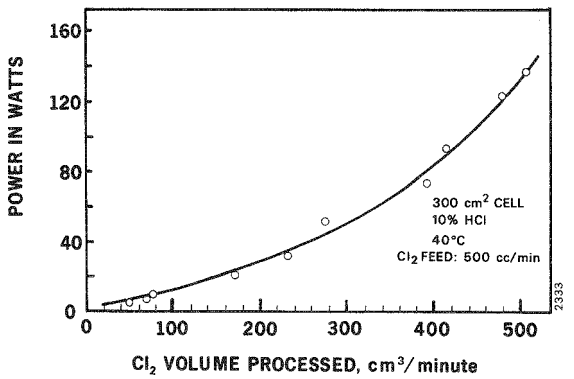

Figure 35-9. Power requirements for a 300-cm^2 cell as a function of chlorine-processing rate.

Foreign Gas Separation and Side Reactions: Long-term unattended operation of the inerts-rejection subsystem requires that foreign gases in the cell behave as electrochemically inert gases. If any of the foreign gases undergo electrode reactions, compositional changes in the electrolyte will occur. The common impurity gases in the stack are oxygen, nitrogen, hydro-

gen, and carbon dioxide. Of these gases, only oxygen and hydrogen typically show any electrochemical activity and therefore must be evaluated at the cathode. Also, the production of CO_2 at the anode could alter the electrolyte composition.

The electrochemical inertness of carbon dioxide was confirmed by feeding a standard CO_2-Cl_2 gas mixture into the cathode and analyzing the CO_2 content of the cathode exhaust at different exhaust rates. By doing this, it was confirmed that the concentration of CO_2 in the exhaust was directly proportional to the amount of chlorine consumed in the cathode. Under conditions of complete chlorine removal, the exhaust flow rate equalled the CO_2 inlet flow rate and was virtually pure CO_2 by gas analysis.

To determine the inertness of oxygen, air was admitted into the cathode at a measured flow rate while the exhaust flow rate and the ratio of the nitrogen/oxygen content in the cathode exhaust were measured at different cell potentials. The nitrogen/oxygen ratio remained constant at all applied potentials. Assuming that nitrogen is inert, the constancy of the nitrogen/oxygen ratio implies that oxygen is neither formed nor consumed in the cell.

Hydrogen may be formed by reduction of protons at the cathode at sufficiently negative potentials. Also, if admitted with the chlorine gas stream, it may be oxidized to protons depending upon the cathode potential. The formation of hydrogen by proton reduction occurs at a cell voltage of about 2.1 volts. At lower cell potentials, the oxidation of hydrogen should be spontaneous, but test results indicate that very little, if any, conversion of hydrogen to protons occurs during cell operation. This lack of reactivity may be ascribed to the high overpotentials associated with hydrogen reactions on graphite under these test conditions.

Analysis of the anode gas under varying conditions of temperature and current density indicate that the rate of carbon-dioxide evolution is rather constant at about 0.03%. For a two-hour operation at 90 amperes, this translates to 0.1 Ah of carbon dioxide, or about 15 millimoles of hydrochloric acid added to the electrolyte. Thus, about 60-70 cycles are required to produce one mole of hydrochloric acid. Therefore, the acidity of the electrolyte will increase at a negligible rate if the electrolyte volume is on the order of 1-2 liters.

Long-term unattended operation of the device depends upon electrolyte stability, foreign gas inertness, and water transfer to and from the cell. As described in this section, the foreign gases are inert. The vapor pressure of hydrogen chloride above a 10% hydrochloric acid solution is negligible and loss of hydrogen chloride through the vapor phase is not expected. Water transfer to and from the cell is expected but the net rate of transfer will depend on the operating temperature of the cell. If the operating temperature is near that of the chlorine-gas stream entering the cathode, then water transfer should also be negligible.

PROTOTYPE INERTS-REJECTION SUBSYSTEM

Design

The interfacing of the inerts-rejection subsystem with a module imposed several important requirements on the subsystem. Because the subsystem vents the inert gases to the atmosphere, chlorine emissions had to be extremely low. This consideration suggested a multiple-stage device, the first stage to process most of the chlorine, and additional stages to serve as polishing units to remove trace amounts of chlorine contained in the inert-gas stream.

A second requirement was that the unit be totally self-contained and effectively isolated from the module. This suggested that the unit be housed in a container utilizing leak-proof gas fittings and power connections.

It was anticipated that the gas flow rate through the subsystem would be variable, and therefore a constant-current mode of operation could not be used. For a controlled potential device, it is desirable to have all stages of the device operate at the same potential. Also, for a controlled potential device, the need for remote voltage sensing/control can be eliminated if the electrical resistance of the external circuit is minimal. The cell voltage at any current, I, is related to the power supply voltage by the expression $E = V - IR$ where E is the cell potential, V is the voltage at the power supply terminals, and R is the electrical resistance between the power supply and the cell. To maintain a constant cell voltage to within 0.2 volts over a current range of 0-100 amperes, R is calculated to be 2 milliohms.

To satisfy the first requirement, a three-stage device was designed which consisted of a 300-cm^2 cell for the first stage, followed by two 100-cm^2 cells to serve as polishing units. To minimize the number of power connections and simplify the gas connections, all three cathode chambers were machined into a single piece of graphite.

The requirement of a low-resistance power contact for the cell was solved with the development of a contact which has about 2 milliohms of resistance. Thus, by using two contacts on each electrode, the total resistance for the contacts is equivalent to two milliohm. The lead resistance in the conductors is kept negligible by the appropriate selection of wire gauge.

A case was also designed so that the subsystem would be self-contained. Both the gas fittings and the power connections through the case were designed to be leak-proof. A photograph of the fully assembled subsystem is shown in Figure 35-10.

Performance

Before interfacing the completed subsystem with a module, the performance of the cell was evaluated using previously described procedures. First, the power characteristics of the three-stage device were determined using cylinder chlorine. These results are shown in Figure 35-11. As can be seen, the power requirements are slightly lower than those of a single-stage 300-cm^2 cell.

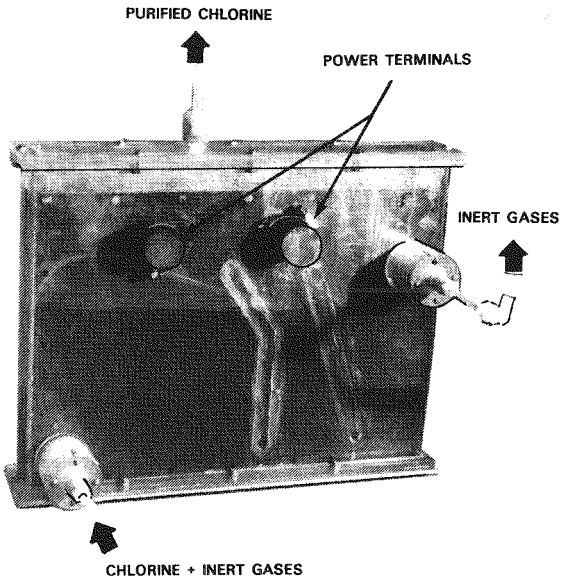

Figure 35-10. Prototype inerts-rejection subsystem. This three-stage chlorine-chlorine cell can process impure chlorine at rates in excess of 0.5 ℓ/min.

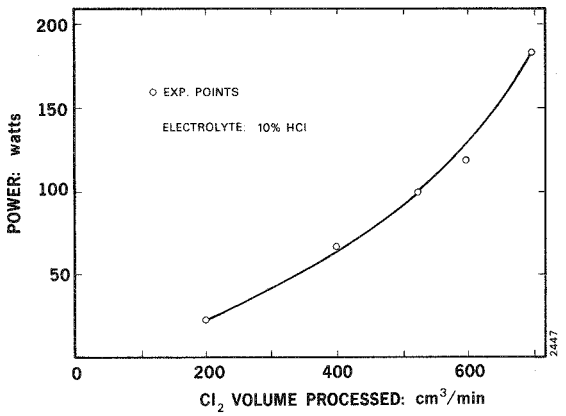

Figure 35-11. Power consumption of a three-stage 500-cm^2 inerts-rejection subsystem as a function of chlorine processing rate.

A second test was performed to determine what cell potential was necessary to minimize chlorine emissions in the inerts gas stream. For this testing, a short column, packed with potassium iodide, was inserted in the cathode exhaust stream and the rate of color change of the column was noted as the cell was operated at different potentials. The cathode inlet gas was chlorine which contained 6.5% CO_2 so that venting was continuous at all potentials.

At an applied potential of 1.8 volts, the visual color change of the potassium-iodide column was slight, and the cell was operated at this potential for one hour. The inlet flow rate was maintained at 0.5 ℓ/minute and the current was nearly constant at 75 amperes. The vent rate from the cathode was about 30 ml/minute. At the end of one hour, the entire contents of the potassium-iodide column were dissolved in hydrochloric acid, and the iodine was titrated with standard thiosulfate. From the titration, it was determined that 0.6 ml of chlorine gas was vented in the one-hour interval, during which a total volume of 1800 ml of carbon dioxide was vented. The calculated chlorine content of the cathode vent gas is 0.6 ml Cl_2/1800 ml total x 100 = 0.03% by volume. This low value of chlorine emissions to the atmosphere is believed to present no environmental problems.

The subsystem was then externally interfaced to the 45-kWh module as shown schematically in Figure 35-12. After completing the interfacing, pretest results demonstrated that the anode exhaust pressure (stack) must be the same as the cathode exhaust pressure (atmospheric) or the electrolyte would transfer in accord with the pressure differential. Thus, if the stack pressure exceeded the atmospheric pressure, the electrolyte was pumped out of the cathode exhaust. The store pressure exceeds atmospheric pressure, and this pressure is used to drive the gas through the subsystem. The inlet gas flow rate was controlled by means of a throttling valve.

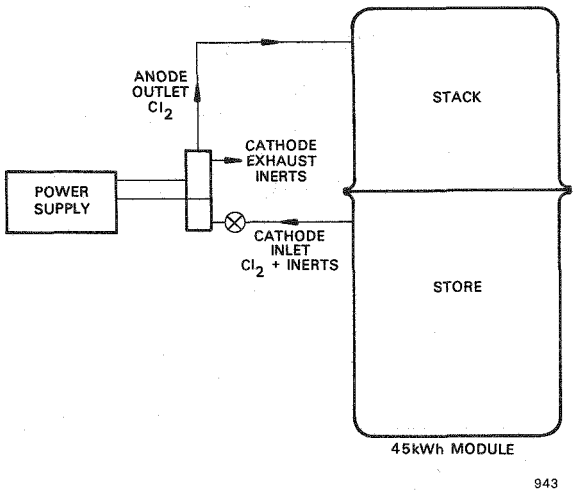

Figure 35-12. Interfacing of inerts-rejection subsystem to module. The pressure differential between the store and the stack is utilized to feed the inert-gas rejection subsystem.

After the test conditions were established, the inerts subsystem was operated for one hour on the module. The inlet flow rate to the subsystem was maintained at about 0.5 ℓ/minute and contained 5% inerts by gas analysis. The subsystem operating voltage was 1.83 volts, and the current was nominally 85 amperes. A potassium iodide column was again placed in the cathode exhaust for chlorine analysis. After one hour of operation, the potassium iodide was analyzed, and the chlorine content of the exhaust gas was calculated to be 0.2% by volume.* Gas analysis of the module revealed that the inert-gas content had increased from the initial 5% to 10%. This unexpected result was later traced to an air leak in one of the seals on the module. The results of the subsystem performance are very satisfactory and demonstrate the viability of the approach used to remove foreign gases from a module.

*More correctly, this is an iodine equivalent. For this calculation, it is assumed that all iodide oxidation is due to chlorine, while in fact, oxygen in the exhaust may cause some oxidation of the potassium iodide.

Discussion

Although the performance and reliability of the subsystem are very good, further simplification of the design is necessary to reduce manufacturing costs. However, it should be noted that the materials cost, principally for graphite, are less than $50 for the unit, i.e., less than $1/kWh. Analysis of the design indicates that most dimensional tolerances are not critical for reliability of operation. Thus, manufacturing costs may be reduced considerably by using low-tolerance production procedures.

Some difficulties have been encountered in obtaining a gas-tight seal between the porous-graphite separator and the dense-graphite channeled cathode. Further development of bonding techniques are warranted so that a suitable production technique can be established.

PROGRAM STATUS

The development of the inert-gas rejection subsystem has been conducted in three stages. The first stage -- proof-of-concept demonstration -- was completted early in Phase II. The other two stages -- modeling of inert-gas accumulation and scale-up of the chlorine-chlorine electrolytic cell -- proceeded in parallel during the last year of Phase II. These two efforts are also nearly complete.

The modeling studies may require some additional refinement as more experimental data become available on the accumulation of CO_2 and air in a better scaled system than the 45-kWh module. Present model predictions -- extrapolated primarily from single-cycle data on the 45-kWh module -- indicate that a gas-processing rate of 0.5 ℓ/min for a two-hour period at the end of each cycle is the proper operational mode for this device.

In the cell scale-up studies, an improved cell design was developed. Utilizing this design, a full-scale three-stage device was built which met and exceeded the specified gas-processing rate in bench tests. This device is presently connected in breadboard manner to the 45-kWh module. A similar device has been designed for incorporation and integration into the third prototype BEST-battery module.

PART VI

ADVANCED-TECHNOLOGY STUDIES

Section 36

PROGRAM STATUS: ADVANCED TECHNOLOGY DEVELOPMENT

INTRODUCTION

As described in Parts III and V of this report, major efforts were conducted during Phase II of RP226-3 in the areas of evaluating and improving the 45-kWh battery module and in developing improved module technology for the BEST battery. In addition to these hardware-oriented development programs, more fundamental efforts were conducted to provide the basis for advanced-technology zinc-chloride battery modules. During Phase II advanced-technology development programs were directed at improving efficiency and reducing battery-stack costs.

Table 36-1 compares the demonstrated performance of the 45-kWh battery at the end of Phase I with the performance targets established for it, the BEST-battery technology, and commercial technology. At the end of Phase I, the coulombic efficiency of the 45-kWh battery module fell 13 points short of the target. At the beginning of Phase II, this was a major concern at EDA.

Table 36-1

DEMONSTRATED AND TARGETED MODULE-PERFORMANCE LEVELS

	EFFICIENCIES,%		
TECHNOLOGY	ε_c	ε_v	ε_e
EPRI 45-kWh Battery			
Demonstrated (2/78)	59	82	48
Target	72	83	60
BEST-Battery	76	85	65
Commercial Battery	85	88	75

As the results of the studies reported in Section 14 became available, it was apparent that advances were also needed in the area of increasing the delivered capacity density (mAh/cm^2). Both the 45-kWh battery module and the BEST-battery module technologies appear to be limited to about 165-170 mAh/cm^2. To a first approximation, the capital cost of the battery stack ($/kWh) is inversely proportional to the delivered capacity density.

The concerns over the limitations of the technology at the beginning and initial stages of Phase II, as well as the desire and need to improve the technology in these areas, dominated the philosophy used in the development of advanced technology during Phase II. In the area of efficiency, it is apparent from the analysis presented in Section 9, that an electrochemical energy efficiency of 75% for a commercial zinc-chloride battery will result in a load-leveling battery plant which operates at a net efficiency of $\geq$ 65%. It is also apparent that increasing the delivered capacity density will result in significant battery-stack cost advantages.

EFFICIENCY

Early in Phase II the main concern was coulombic efficiency. Previous EDA studies indicated that the major source of coulombic inefficiency at the cell

level was the mass-transfer-limited reaction between dissolved chlorine and electrodeposited zinc at the zinc electrode. Cell data also suggested that the rate of this reaction was higher during charge than during discharge.

Modeling efforts, conducted during Phase II, confirmed that the reaction of dissolved chlorine at the zinc electrode was the major source of coulombic inefficiency during charge. These efforts identified the three major sources of fluid motion which control the mass transport of chlorine to the zinc electrode during charge. Figure 36-1 illustrates the electrolyte flow patterns established in the inter-electrode cell gap if each convective source existed by itself. Forced convection of electrolyte through the porous-graphite chlorine electrode and vertically upwards between the zinc and chlorine electrodes is the preferred mode of operation in the cell or battery. Natural convection of electrolyte is due to the formation of a low-density electrolyte layer adjacent to the zinc electrode created by the cathodic depletion of zinc-ion species. Bubble-induced convection of electrolyte is created by the anodic generation of chlorine gas at the chlorine electrode. These three convections couple to establish a steady-state fluid-dynamic pattern in the inter-electrode gap which controls the rate of chlorine transfer to the zinc electrode during charge.

Coulombic efficiency (ε_c) data of the type illustrated in Figure 36-2, suggest that the optimal cell gap for coulombic-efficiency maximization during charge is greater than 3 mm. When combined with the predicted voltaic efficiency, (ε_v), the optimal cell gap for energy efficiency (ε_e), maximization during charge is also greater than 3 mm. These results suggest some efficiency gains, at least during charge, by increasing the inter-electrode cell gap from 2 mm for the 45-kWh and BEST-battery modules, to 3 mm or greater for advanced-technology modules.

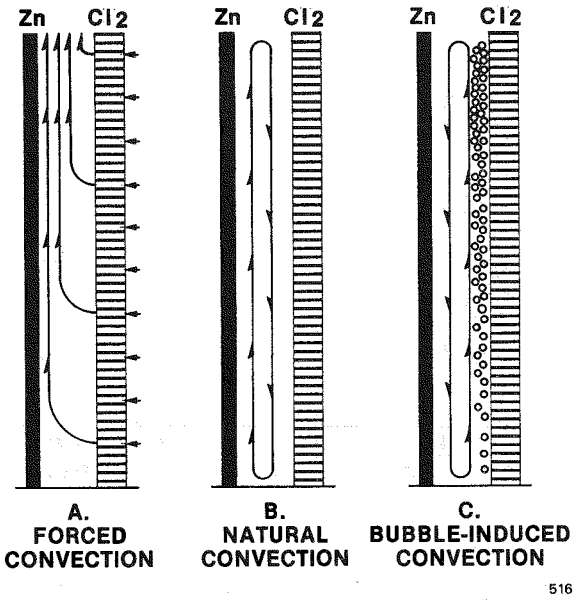

Figure 36-1. Schematic illustration of the individual electrolyte-flow patterns established in the cell gap by the three major sources of fluid convection during charge.

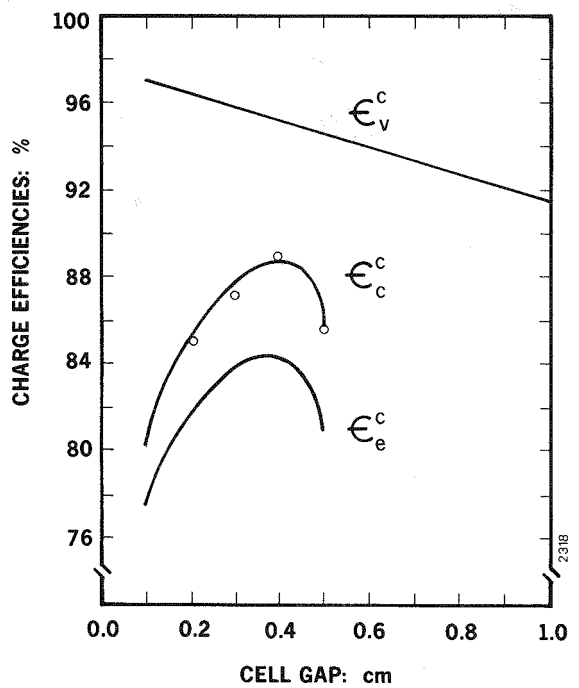

Figure 36-2. The dependence of the coulombic, voltaic and energy efficiencies during charge on the cell gap. Note the optimal gap under these conditions is >0.3 cm.

A well-known approach to increasing the usable coulombic efficiency of zinc-chloride cells and batteries is to increase the applied current density. This phenomenon is discussed in Section 9 and illustrated here in Figure 36-3. This approach does not provide much of an improvement in electrochemical energy efficiency, however, unless it is accompanied by improved voltaic performance.

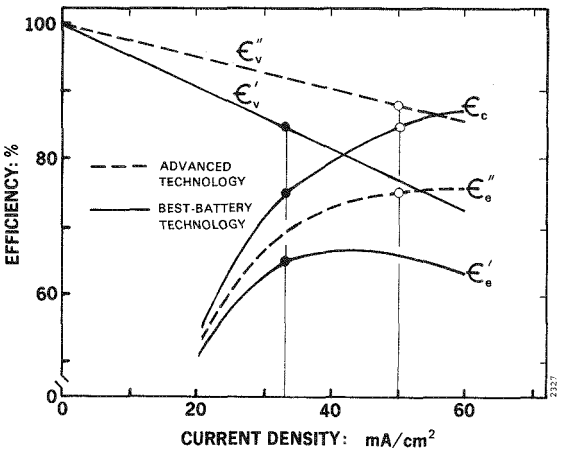

Figure 36-3. The dependence of the coulombic, voltaic, and energy efficiencies on the applied current density. Note the projected improvement in electrochemical energy efficiency (ε_e) due to combining operation at 50 mA/cm^2 with improved voltaic performance.

An obvious way to improve the voltaic efficiency of zinc-chloride cells and batteries is to improve the activation of the porous-graphite chlorine electrodes. Studies in this area were conducted during Phase II. Figure 36-4 illustrates the voltaic performance achieved by cells which were activated using a new proprietary activation process for the porous-graphite chlorine electrodes.

When cells employing more highly activated chlorine electrodes were operated at a current density of 50 mA/cm^2, electrochemical energy efficiencies greater than 74% were observed. The relationships illustrated in Figure 36-3 were essentially confirmed by this study.

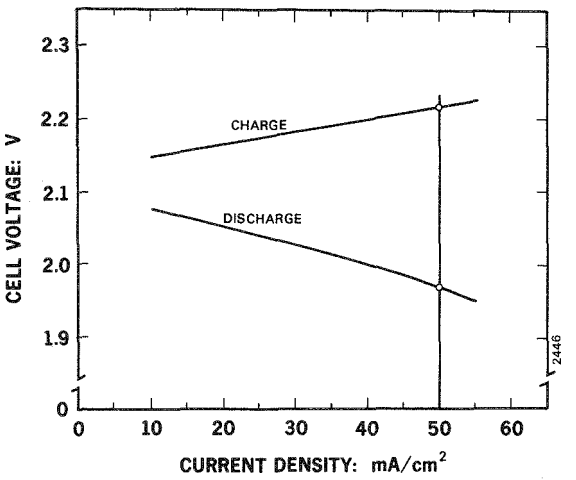

Figure 36-4. Polarization curve for a zinc-chloride cell employing chlorine electrodes activated by new process. At 50 mA/cm^2, the discharge voltage is 89% of the charge voltage.

CAPACITY DENSITY

As previously mentioned, the cost of the battery stack is essentially inversely proportional to the delivered capacity density. By doubling the capacity density, the same electrode area (quantity of graphite) will deliver double the energy (mWh/cm^2) and the cost ($/kWh) of the battery stack will essentially be cut in half.

Previous experience with cells containing the 2 mm cell gap indicated that use of a higher current density during charge would result in reduced zinc loading (charge capacity density) and therefore, a reduction in delivered capacity density. This would quite probably negate the improvements realized in the area of efficiency.

It was known, however, that increasing the inter-electrode cell gap improves the zinc loading capabilities of zinc-chloride cells. The studies also indicated that the electrochemical energy efficiency would not suffer, and could improve, if the inter-electrode gap were increased to greater than 3 mm.

Four test cells were built and tested with cell gaps in the range of 2.5-4 mm.

These larger-gap cells not only demonstrated electrochemical energy efficiencies in excess of 70%, but they consistently delivered more than 200 mAh/cm^2 when operated at 45 mA/cm^2 with selected electrolytes. When operated at 50 mA/cm^2 current density, one of the cells demonstrated an ε_e of 74.3% and delivered in excess of 250 mAh/cm^2. This is a 50% increase over the 165-170 mAh/cm^2 delivered capacity achievable with the 2 mm gap technology. To a first approximation, this corresponds to a 33% reduction in the active area of electrodes in the battery stack.

INTRODUCTION TO PART VI CONTENT

A number of programs were conducted to supplement and support efforts to improve the efficiency and the delivered capacity of zinc-chloride cells. Sections 37-41 review these support efforts in the area of developing a data base on the physicochemical properties of aqueous electrolyte solutions containing $ZnCl_2$, KCl, NaCl, and HCl. Density, conductivity, viscosity, chlorine solubility, and the transference number for zinc were determined in solutions of interest as electrolytes in the zinc-chloride battery.

These data have been useful in the coulombic-efficiency modeling effort and in the interpretation of existing empirical relationships and phenomena. An example of the latter is a temperature coefficient which was used to account for the temperature dependence of the rate of the chlorine/zinc corrosion reaction. The viscosity data at different temperatures were used in the Stokes-Einstein relationship to calculate the temperature dependence of the diffusion coefficient for dissolved chlorine. To a large extent, the temperature dependence of the diffusion coefficient accounts for the empirically obtained temperature coefficient.

These physical properties have been used extensively in the modeling of the inter-electrode fluid dynamics, which control the transport of chlorine to the zinc electrode during electrodeposition.' These coulombic efficiency modeling efforts, directed at developing a mathematical model which quantitatively predicts coulombic efficiency, are reviewed in Sections 42-47. Although these efforts have not yet culminated in the successful development of this quantitative model, they have resulted in a much more fundamental and thorough understanding of the processes which control the transport of dissolved chlorine to the zinc electrode. They have also provided qualitative and even semi-quantitative interpretations of experimentally observed phenomena. One of these phenomena is the observed difference between the normalized rate (at 1 g/ℓ $[Cl_2]$) of the chlorine/zinc corrosion reaction during charge and discharge. This interpretation is explained in Section 42.

In Sections 48 and 49, the effects of cell gap and electrolyte composition on electrochemical energy efficiency are discussed. In Section 48, experimentally determined charge coulombic efficiency data on the effect of cell gap are combined with a mathematical voltaic efficiency model to predict the optimal cell gap for energy-efficiency maximization during charge. In Section 49, four cell gaps in the range of 2.5-4 mm and nine electrolyte compositions are experimentally evaluated for the purpose of maximizing the electrochemical energy efficiency at delivered capacity densities of $\sim$200 mAh/cm^2.

Two supplemental studies are reviewed in Sections 50 and 51. The transient discharge characteristics of a zinc-chloride cell are discussed in Section 50. A preliminary equivalent circuit for the cell is developed to predict the transient response of the battery in the event of an accidental short circuit. Section 51 reviews the status of an experimental effort to establish the technical feasibility of utilizing

larger electrodes in zinc-chloride cells and battery stacks. This program is also directed at reducing battery-stack costs.

These programs have combined to provide electrochemical energy efficiencies in excess of 74% for delivered capacity densities of 250 mAh/cm^2 at the cell level. Not discussed in detail in this report is a pre-prototype advanced-technology submodule, which was built and tested near the end of Phase II. This pre-prototype submodule demonstrated 70% electrochemical energy efficiency and provided preliminary verification of the technology at the submodule level.

Section 37

ELECTROLYTE PROPERTIES: I. DENSITY

ABSTRACT

A comprehensive data base on the physicochemical properties of zinc-chloride battery electrolytes -- containing the chloride salts of zinc, potassium, and sodium -- is important in the optimization of the battery system. This section presents experimentally determined densities of aqueous solutions containing 0.5-4.0$\underline{m}$ $ZnCl_2$ + 0-4$\underline{m}$ KCl + 0-4$\underline{m}$ NaCl at 25°C, 40°C, and 55°C. The experimental data are fitted to empirical relationships for predicting solution density (ρ, g/ml) as a function of composition ($\underline{m}$, molality or $\underline{M}$, molarity) at each temperature (T_i):

$$\rho(T_i) = a_i + b_i C_{ZnCl_2} + c_i C_{KCl} + d_i C_{NaCl}$$

The values of the empirical constants (a_i, b_i, c_i, and d_i) depend on the temperature and the concentration units employed. These relationships can be used to monitor the state of charge or discharge of zinc-chloride cells and batteries.

INTRODUCTION

One of the characteristics of the zinc-chloride battery is its demonstrated ability to perform over wide concentration ranges of aqueous zinc chloride electrolytes. Potassium chloride, sodium chloride, or combinations of the two are often added to the zinc chloride as supporting electrolytes. Addition of these electrolytes depresses the chlorine solubility, thereby enhancing coulombic efficiency. Supporting electrolytes reduce the solution resistivity, and hence increase the voltaic efficiency of the battery. Furthermore, the addition of salts changes the solution density and viscosity and, therefore, can alter the fluid dynamics of the cell in the interelectrode gap. In order to improve battery performance, it is important to have a good understanding of the physical chemistry of the mixed electrolytes.

This report is the first in a series of reports dealing with the physical properties of mixed salt solutions in the concentration ranges of interest for the zinc-chloride battery. It deals with the development of empirical relationships that relate solution densities to solution concentrations. The concentration ranges are 0.5-4.0 moles/kg H_2O ($\underline{m}$) zinc chloride, 0-4$\underline{m}$ potassium chloride, and 0-4$\underline{m}$ sodium chloride. The densities of the $ZnCl_2$ + KCl + NaCl + H_2O system were determined by pycnometry at 25°, 40°, and 55°C. With the use of a computer, these data were fitted to an equation of state relating density to composition on the thermodynamic molal scale. These equations are generally accurate to ±0.003 density units, for zinc-chloride concentrations at or above 0.5$\underline{m}$. The equation of state has also been converted to the molar scale. The transformation from the molal to molar scale results in a simple, linear equation.

Density is defined as the solution weight divided by its volume (W/V). The solution density of the battery electrolyte has two primary effects on the battery system: it can influence the fluid dynamic patterns in the interelectrode cell gap, and it affects the power required to pump electrolyte through the battery. The availability of accurate density data also permits determination of the battery state-of-

charge. These data can be used for both theoretical and experimental models to evaluate charging efficiency at various stages of charge by appropriate differentials.

A survey of the literature revealed no information on the four-component system $ZnCl_2$ + KCl + NaCl + H_2O (1), but systems such as $ZnCl_2$ + KCl + H_2O and $ZnCl_2$ + NaCl + H_2O have been studied. Shevchuch and Moshinski (2) constructed a two-coordinate solubility isotherm of the $ZnCl_2$ + NaCl + H_2O solution at 25°C. Figure 37-1 is a weight percent ternary phase diagram which was constructed using their data. A similar diagram for the system $ZnCl_2$ + KCl + H_2O at 25°C is shown in Figure 37-2. It was constructed from the solubility data of the system $ZnCl_2$ + KCl + H_2O (3). Note that any composition in the area above the solubility curve has

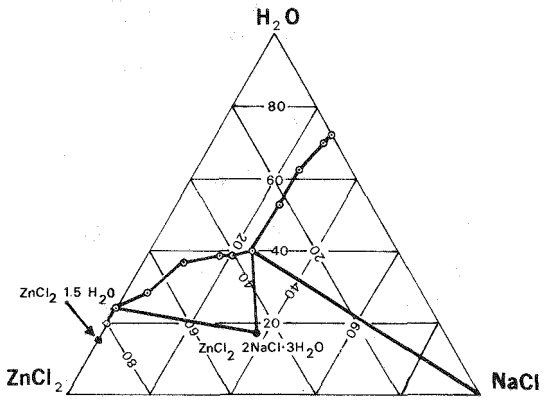

Figure 37-1. Ternary phase diagram of zinc chloride + sodium chloride + water (weight percent) at 25°C.

only one phase and that all salts are soluble in the solutions.

The solubility limits of potassium chloride and sodium chloride in various zinc chloride solutions have been calculated from these diagrams. The results are plotted in Figure 37-3. During charge, zinc chloride is depleted from the solution to a concentration of not lower than 0.5M. The energy efficiency decreases below this concentration. From Figure 37-3 it is evident that ∿5 molar is the upper limit of concentration for supporting electrolytes in battery applications, since that is the solubility limit of these species in 0.5M zinc chloride solutions.

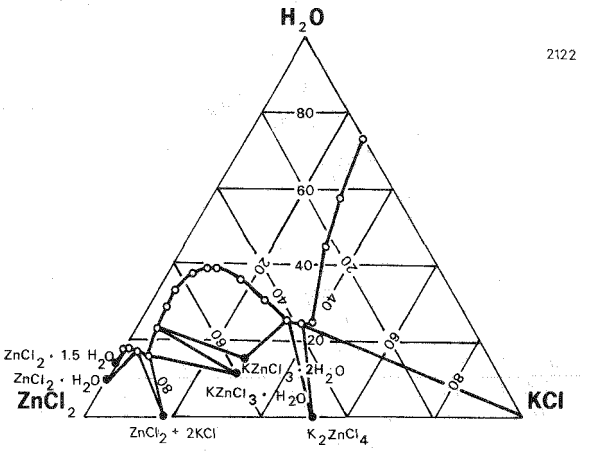

Figure 37-2. Ternary phase diagram of zinc chloride + potassium chloride + water (weight percent) at 25°C.

EXPERIMENTAL

Materials

The sodium chloride and potassium chloride salts used in this study are analytical reagent grade and they were used without further purification. The zinc chloride stock solution (5M) was prepared at EDA by the reaction of chlorine gas with high-purity zinc metal. The zinc chloride standard solution was prepared by dissolving a known weight of cleaned pure zinc rod in concentrated hydrochloric acid. Antimony (>1 ppm) was added to accelerate the reaction.

Equipment and Procedure

The test solutions are made up in molalities. The percentage compositions of zinc chloride and water in the zinc chloride stock solutions are calculated from the molarity and density of the stock solutions. The quantities of water, zinc chloride stock solution, potassium chloride, and sodium chloride required to make up each test solution were weighed-out on a single-pan electric balance, Sartorius Model 2442.

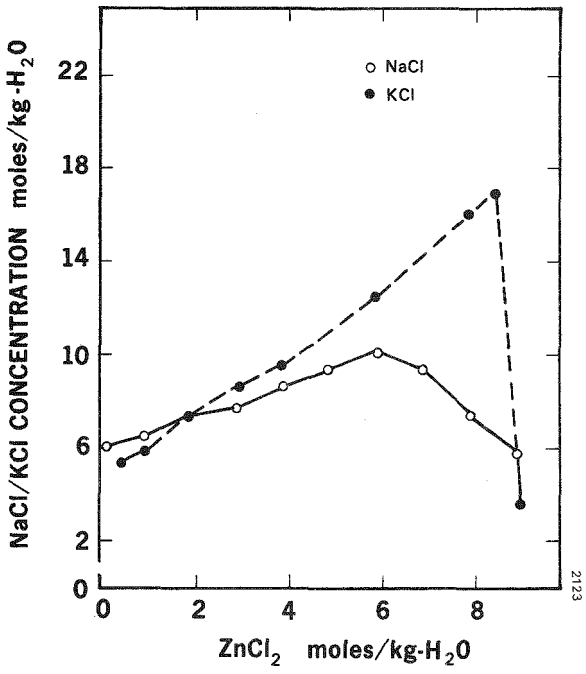

Figure 37-3. The solubilities of KCl and NaCl in $ZnCl_2$ solutions at 25°C. Note that 5m KCl or NaCl is the solubility limit in 0.5m $ZnCl_2$ and that 5m total supporting electrolyte is therefore an upper limit.

Six Gay Lussac bottle pycnometers with individual volumes of approximately 25 ml were used for the density measurements. Using distilled water, the volumes were calibrated at the three temperatures of 25°, 40°, and 55°C. A Blue M Model MW-1120-1 constant temperature bath was used to regulate the temperature at 25 ±0.2°, 40 ±0.2°, and 55 ±0.2°C. The thermometer used to calibrate the constant temperature bath was calibrated against standards certified by the National Bureau of Standards.

The concentration of the zinc chloride stock solution was determined by potentiometric titration, to ±0.3%, using 0.1 N potassium ferrocyanide as the titrant. The zinc chloride standard was used to check the $K_4Fe(CN)_6$ concentration prior to every zinc chloride titration. Both the calomel reference electrode and the Model 12 Research pH meter used were made by Corning. The platinum indicator-electrode was made out of a platinum wire sealed in a glass tubing with approximately one-cm length of platinum wire exposed.

EXPERIMENTAL RESULTS

The measured densities and calculated volumes of the salt solutions at specified molalities ranging from 0-4m are tabulated in Table 37-1 for the three temperatures. The calculated volumes are plotted in Figures 37-4 through 37-8 as a function of the molal concentration of each salt in the various media. The slope of each line represents the partial molal volume of one of the salts in the presence of a particular concentration of the other salts. Since Figures 37-4 through 37-7 show a series of parallel straight lines, it is apparent that both potassium chloride and sodium chloride have rather constant partial molal volumes in the different media. Figure 37-8 indicates that linear relationships for zinc chloride exist only above concentrations of one molal. Slopes for the straight lines are listed in Tables 37-2 through 37-4 with the average partial molal volumes of each salt at the three temperatures.

Table 37-1

SOLUTION DENSITIES AND SOLUTION VOLUMES OF MIXED ELECTROLYTES

Molality, m			Density, g/ml			Solution Volume, ml/1000g-H_2O		
$ZnCl_2$	KCl	NaCl	25°C	40°C	55°C	25°C	40°C	55°C
0.49	0	0	1.0565		1.0420	1009.7		1023.8
0.49	2.00	1.01	1.1546		1.1386	1104.2		1119.7
0.49	3.10	1.07	1.1869		1.1715	1146.1		1161.2
0.49	2.03	1.97	1.1841		1.1686	1126.0		1140.9
0.49	3.04	2.00		1.2031	1.1950		1172.1	1180.1
1.00	0	0	1.1055			1027.9		
0.98	0	0	1.1063	1.0983	1.0890	1024.7	1032.1	1040.9
1.96	0	0	1.1944	1.1845	1.1742	1069.9	1069.8	1079.2
2.95	0	0	1.2739	1.2628	1.2521	1100.6	1110.3	1119.8
1.96	1.00	0	1.2210	1.2105		1098.8	1108.3	
1.96	3.00	0	1.2691	1.2591		1174.6	1183.9	
1.96	5.00	0	1.3046	1.2954		1256.8	1265.7	
2.95	1.00	0	1.2944	1.2831		1140.7	1150.8	
2.95	2.94	0	1.3327	1.3190		1216.4	1229.0	
2.95	4.93	0	1.3631	1.3518		1298.0	1308.9	
1.00	2.00	1.01	1.1897			1130.0		
1.00	1.00	2.01	1.1863			1119.8		
2.00	0	0	1.1974	1.1875	1.1775	1062.8	1071.1	1080.8
2.00	1.06	0	1.2238	1.2132	1.2032	1104.4	1114.1	1123.3
2.00	2.00	0	1.2445	1.2340	1.2243	1142.3	1152.0	1161.2
2.00	3.00	0	1.2663	1.2554	1.2456	1181.5	1191.7	1201.1
2.00	4.00	0	1.2874	1.2767	1.2669	1220.0	1230.2	1239.7
2.00	0	1.01	1.2192	1.2081	1.1979	1092.3	1102.3	1111.7
2.00	3.00	2.00	1.3038	1.2942	1.2844	1237.2	1246.4	1255.9
2.00	0.99	0.99	1.2413	1.2303	1.2184	1131.3	1141.4	1152.6
2.00	2.00	1.00	1.2636	1.2527	1.2409	1171.3	1181.5	1192.8
2.00	3.00	1.03	1.2856	1.2749	1.2636	1210.6	1220.8	1231.7
2.00	0	2.00	1.2389	1.2275	1.2155	1121.6	1132.1	1143.2
2.00	0	3.00	1.2580	1.2467	1.2355	1151.1	1161.5	1172.1
1.99	0	3.99	1.2766	1.2652	1.2539	1178.6	1189.3	1200.0
2.00	0	0	1.1976	1.1873	1.1761	1062.6	1071.8	1082.1
1.99	0	0	1.1964	1.1864	1.1756	1062.6	1071.5	1081.4
1.94	0	0	1.1926	1.1827	1.1716	1060.2	1069.1	1079.2
1.88	0	0	1.1895	1.1796	1.1687	1056.1	1065.0	1074.9
2.00	2.00	2.00	1.2800	1.2688	1.2572	1202.0	1212.6	1223.8
2.00	2.00	3.00	1.2992	1.2887	1.2781	1229.3	1239.3	1249.6
2.00	2.00	4.01	1.3195	1.3099	1.2993	1255.2	1264.4	1274.7
2.00	1.01	2.00		1.2478	1.2365		1173.9	1184.7
3.00	0	0	1.2742	1.2627	1.2509	1105.7	1115.8	1126.3
3.00	1.00	0	1.2943	1.2827	1.2707	1146.1	1156.5	1167.4
3.00	0	1.00	1.2915	1.2797	1.2672	1136.2	1146.7	1158.0
3.00	0	2.00	1.3081	1.2954	1.2824	1166.5	1177.9	1189.9
3.00	1.00	2.00	1.3261	1.3137	1.3013	1206.8	1218.2	1229.8
3.00	2.00	2.00	1.3435	1.3314	1.3189	1246.7	1258.0	1269.9
3.00	0	3.01	1.3241	1.3111	1.2983	1197.0	1208.9	1220.8
3.00	1.00	3.00	1.3416	1.3291	1.3168	1236.5	1248.1	1259.8
3.00	2.00	3.00	1.3587	1.3468	1.3346	1275.8	1287.1	1298.8
4.00	0	0	1.3467	1.3345	1.3218	1147.4	1157.9	1169.0
4.00	2.00	1.00	1.3914	1.3786	1.3659	1259.7	1271.4	1283.2
4.00	1.00	2.00	1.3895	1.3767	1.3633	1249.9	1261.5	1273.9
0.50	1.00	1.00	1.1207	1.1127	1.1031	1071.8	1079.5	1088.9
0.50	0	0	1.0553	1.0491	1.0408	1012.2	1018.2	1026.3
0.50	4.01	0	1.1865	1.1794	1.1712	1152.0	1159.0	1167.1

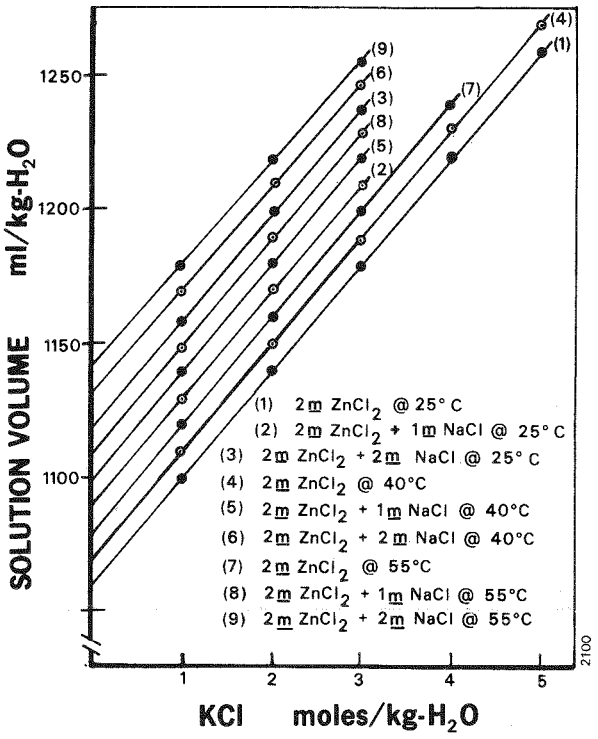

Figure 37-4.

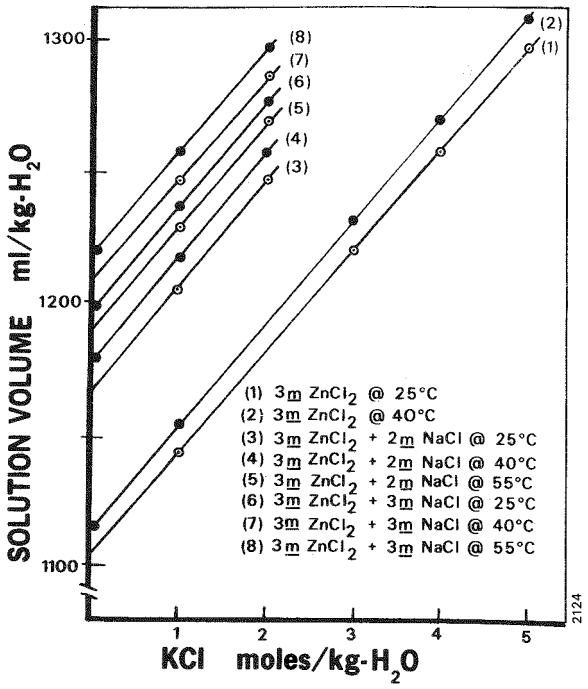

Figure 37-5.

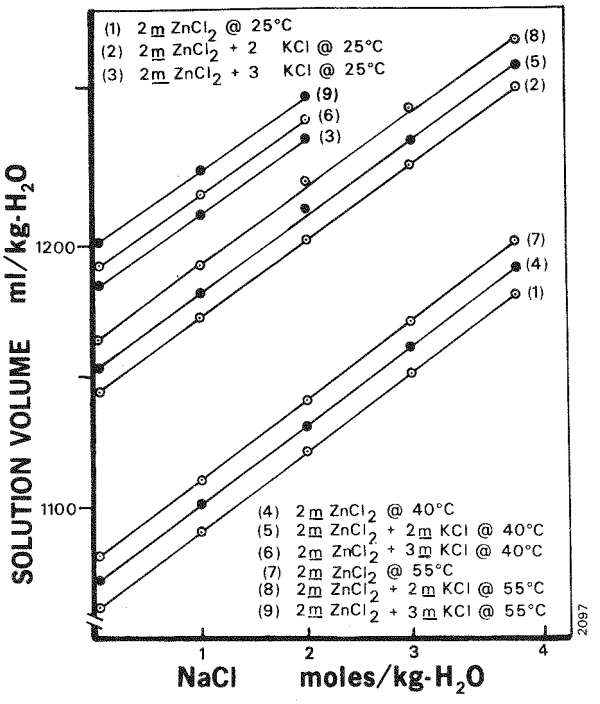

Figure 37-6.

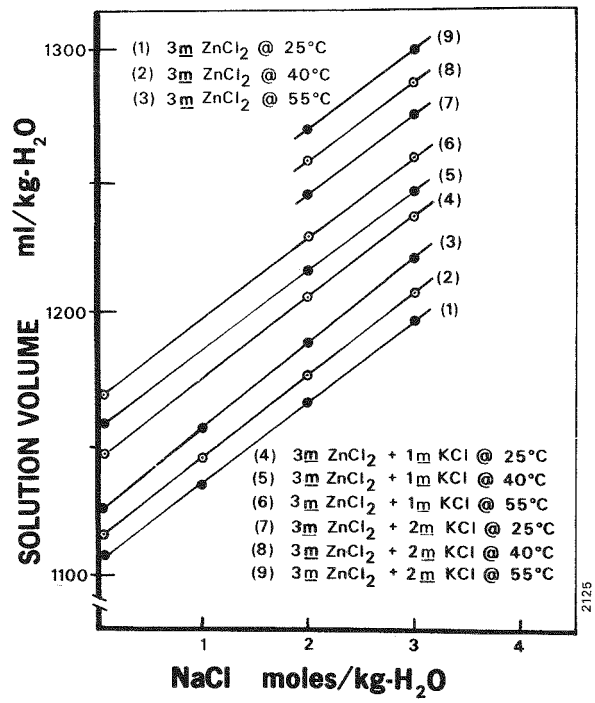

Figure 37-7.

Figures 37-4 through 37-7. Solution volume of mixed electrolytes as a function of salt concentrations at 25°, 40°, and 55°C. Note the slopes of the lines ($\partial V/\partial n$) are the partial molal volumes for the salts in the various media at the three temperatures.

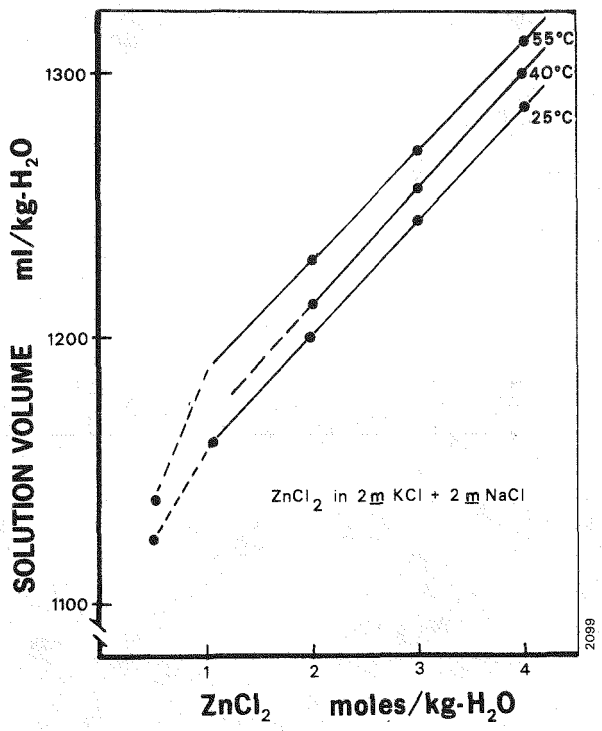

Figure 37-8. Solution volumes of 0.5-4.0m $ZnCl_2$ in electrolyte solutions containing 2m KCl and 2m NaCl at the three temperatures.

Table 37-2

PARTIAL MOLAL VOLUMES OF KCl (ml/mol)

Medium	Temperature 25°C	40°C	55°C
2m $ZnCl_2$	39.7	39.8	40.0
2m $ZnCl_2$ + 1m NaCl	39.1	39.2	39.7
2m$ZnCl_2$ + 2m NaCl	38.8	38.2	38.8
3m $ZnCl_2$	39.3	39.6	--
3m $ZnCl_2$ + 2m NaCl	40.1	40.1	40.0
3m $ZnCl_2$ + 3m NaCl	39.4	39.1	39.0
Molal volume avg. ±σ	39.4 ±0.4	39.3 ±0.7	39.3 ±0.9

Table 37-3

PARTIAL MOLAL VOLUMES OF NaCl (ml/mol)

Medium	Temperature 25°C	40°C	55°C
2m $ZnCl_2$	29.5	29.8	30.2
2m $ZnCl_2$ + 2m KCl	28.3	28.2	28.2
2m $ZnCl_2$ + 3m KCl	27.9	27.4	27.4
3m $ZnCl_2$	30.4	31.1	31.5
3m $ZnCl_2$ + 1m KCl	30.2	30.6	30.9
3m $ZnCl_2$ + 2m KCl	29.1	29.1	28.9
Molal volume avg. ±σ	29 ±1	29 ±1	30 ±2

Table 37-4

PARTIAL MOLAL VOLUMES OF $ZnCl_2$ (ml/mol)

Medium	Temperature 25°C	40°C	55°C
2m KCl + 2m NaCl	43.4	44.4	44.7

EMPIRICAL DENSITY RELATIONSHIPS FOR MOLAL SCALE

The general expression for the density of a solution is the weight of the solution, W, divided by the volume, V. For a multi-component solution, the solution weight is the sum of the weight contributions of each component as shown in Eq. 37-1.

$$W = n_1(MW)_1 + n_2(MW)_2 + \ldots n_j(MW)_j \qquad (37\text{-}1)$$

where

n_j = number of moles of the jth component

$(MW)_j$ = molecular weight of the jth component

Similarly, the volume of the solution is equal to the sum of the contribution of each component:

$$V = n_1 \bar{v}_1 + n_2 \bar{v}_2 + n_3 \bar{v}_3 + \ldots + n_j \bar{v}_j \qquad (37\text{-}2)$$

where

n_j = number of moles of the jth component

$\bar{v}_j = \left(\frac{\partial V}{\partial n}\right)_{n_1, n_2, n_3 \ldots T, P}$ = partial molal volume

T = temperature

P = pressure

There is no difficulty in determining the weight of a solution of known composition. However, $\bar{v}_j$ is, in general, a function of n_j, and has a different value at different concentrations of j. For a multi-component system, where there are interactions between species, $\bar{v}_j$ also can be a function of the concentration of the other constituents.

Because of the above described complications associated with the partial molal volumes, the density of a multi-component system must be determined experimentally. After having experimentally determined the densities of a number of solutions, the $(\partial V/\partial n_j)$ terms can be calculated to generate a density equation such as:

$$\text{density} = \frac{n_1(MW)_1 + n_2(MW)_2 + \ldots n_j(MW)_j}{n_1\bar{v}_1 + n_2\bar{v}_2 + \ldots n_j\bar{v}_j} \qquad (37\text{-}3)$$

If the volume expression of the solution is nearly linear with increasing n_j, then $\bar{v}_j$ is nearly a constant and, for solutions containing 1000 g of water, Eq. 37-3 may be simplified to:

$$\text{density} = \frac{1000 + n_1(MW)_1 + n_2(MW)_2 + n_3(MW)_3 + \ldots n_j(MW)_j}{1000 + an_1 + bn_2 + \ldots jn_j} \qquad (37\text{-}4)$$

where

1000 = weight (g) of water in 1000 ml.

n_j = number of moles of the jth component.

$(MW)_j$ = molecular weight of the jth component.

1000 = approximate volume of 1 kg of water in ml.

a,b,c, = coefficients which represent the volume contributions of each component. The coefficients are approximate values of partial molal volumes.

In this study, the linearity of the data contained in Figures 37-4 through 37-8 suggests that they can be fit to Eq. 37-4. The resultant empirical equation is given by:

$$\text{density} = \frac{1000 + 136.3\, n_{ZnCl_2} + 74.5\, n_{KCl} + 58.5\, n_{NaCl}}{1000 + a\, n_{ZnCl_2} + b\, n_{KCl} + c\, n_{NaCl}} \qquad (37\text{-}5)$$

In Tables 37-2 through 37-4, the partial molal volumes for potassium chloride, sodium chloride, and zinc chloride are given for different electrolyte compositions. The values

are only approximately constant and, to obtain a best fit to Eq. 37-5, a multi-linear regression computer program was used to determine the values of a, b, and c. An equation of the following form was used.

$$V(exp) = V_o + a\,\underline{m}_{ZnCl_2} + b\,\underline{m}_{KCl} + c\,\underline{m}_{NaCl} \qquad (37\text{-}6)$$

where

V(exp) = experimentally-determined volume of solution, dependent variable

V_o = intercept, a constant

a,b,c, = volume coefficients, constants

$\underline{m}_j$ = molality, independent variable

The results of the regression analysis are given in Table 37-5. The average $\overline{v}_j$ values also are listed.

Comparison of the results indicates that the computer-derived coefficients do not differ significantly from the experimentally-determined partial molal volumes. Because the best-fit empirically-determined intercepts differ from 1000 ml, the equations will not be accurate at zinc chloride concentrations lower than $0.5\underline{m}$.

Substitution of the coefficients and intercepts into Eq. 37-5, yields Eq. 37-7, -8, and -9 for the three temperatures.

at 25°C,

$$\text{density} = \frac{1000 + 136.3\underline{m}_{ZnCl_2} + 74.5\underline{m}_{KCl} + 58.5\underline{m}_{NaCl}}{972.3 + 44.7\underline{m}_{ZnCl_2} + 39.2\underline{m}_{KCl} + 29.7\underline{m}_{NaCl}} \qquad (37\text{-}7)$$

at 40°C,

$$\text{density} = \frac{1000 + 136.3\underline{m}_{ZnCl_2}}{981.0 + 45.7\underline{m}_{ZnCl_2}}$$

Table 37-5

REGRESSION ANALYSIS RESULTS

Multi-linear Regression Analysis of Equation

$$V = V_o + a\,\underline{m}_{ZnCl_2} + b\,\underline{m}_{KCl} + c\,\underline{m}_{NaCl}$$

Component	Regression Coefficient			$\left(\frac{\partial V}{\partial n}\right)$ avg. ±s		
	25°C	40°C	55°C	25°C	40°C	55°C
$ZnCl_2$	44.7	45.7	47.7	43.4	44.4	44.7
KCl	39.2	38.1	38.3	39.4 ±0.4	39.4 ±0.4	39.3 ±0.9
NaCl	29.8	29.7	29.0	29.0 ±1.0	29.0 ±1.0	29.0 ±2.0
Intercept	972.3	981.0	989.0			

$$+ \frac{74.5\underline{m}_{KCl} + 58.5\underline{m}_{NaCl}}{38.1\underline{m}_{KCl} + 29.7\underline{m}_{NaCl}}$$

(37-8)

at 55°C

$$\text{density} = \frac{1000 + 136.3\underline{m}_{ZnCl_2}}{989.5 + 47.7\underline{m}_{ZnCl_2}} + \frac{74.5\underline{m}_{KCl} + 58.5\underline{m}_{NaCl}}{38.3\underline{m}_{KCl} + 29.0\underline{m}_{NaCl}}$$

(37-9)

These equations relate density to electrolyte composition on the molal scale and are generally accurate to ±0.003 density units which is roughly ±0.1 molal.

EMPIRICAL DENSITY RELATIONSHIPS FOR MOLAR SCALE

An expression based on molar concentrations may be derived from the following equation:

$$\text{density} = \frac{1000 + 136.3\ n_1}{1000 + n_1\bar{v}_1} + \frac{74.5\ n_2 + 58.5\ n_3}{n_2\bar{v}_2 + n_3\bar{v}_3}$$

(37-10)

where subscript: 1 = $ZnCl_2$
2 = KCl
3 = NaCl

For simplicity, the density of water is assumed to be 1.000 g/ml. Eq. 37-10 is limited to a solution containing 1 kg of water. Under this condition, $n = \underline{m}$ and Eq. 37-10 can be rewritten:

$$\text{density} = \frac{1000 + 136.3\ \underline{m}_1}{1000 + \underline{m}_1\bar{v}_1} + \frac{74.5\ \underline{m}_2 + 58.5\ \underline{m}_3}{\underline{m}_2\bar{v}_2 + \underline{m}_3\bar{v}_3}$$

(37-11)

where subscript: 1 = $ZnCl_2$
2 = KCl
3 = NaCl

The molality-to-molarity ratio can be used to convert the molal expression to a molar expression:

$$\frac{\underline{m}_j}{\underline{M}_j} = \frac{1000\ g}{g \text{ of water in one-liter solution}}$$

(37-12)

Using Eq. 40-2, setting V = 1000 ml, and letting the volume contribution of water = V_4, then:

$$1000 = n_1\bar{v}_1 + n_2\bar{v}_2 + n_3\bar{v}_3 + V_4$$

where n_1, n_2, n_3 are the number of moles of components 1, 2, 3 in a solution volume of 1000 ml. They are numerically equal to $\underline{M}_1$, $\underline{M}_2$, $\underline{M}_3$ so that:

$$V_4 = 1000 - \underline{M}_1\bar{v}_1 - \underline{M}_2\bar{v}_2 - \underline{M}_3\bar{v}_3$$

and the weight of water (g) in one liter of solution is 1.000 x V_4 = V_4

Therefore,

$$\frac{\underline{m}_j}{\underline{M}_j} = \frac{1000}{1000 - \underline{M}_1\bar{v}_1 - \underline{M}_2\bar{v}_2 - \underline{M}_3\bar{v}_3}$$

and

$$\underline{m}_1 = \frac{1000\underline{M}_1}{1000 - \underline{M}_1\bar{v}_1 - \underline{M}_2\bar{v}_2 - \underline{M}_3\bar{v}_3}$$

(37-13)

$$\underline{m}_2 = \frac{1000\underline{M}_2}{1000 - \underline{M}_1\bar{v}_1 - \underline{M}_2\bar{v}_2 - \underline{M}_3\bar{v}_3}$$

(37-14)

$$\underline{m}_3 = \frac{1000\underline{M}_3}{1000 - \underline{M}_1\bar{v}_1 - \underline{M}_2\bar{v}_2 - \underline{M}_3\bar{v}_3} \qquad (37\text{-}15)$$

By substituting Eq. 37-13, -14, and -15 into Eq. 37-11, Eq. 37-16 is obtained.

$$\text{density} = \left[1000 + (136.3 - \bar{v}_1)\,\underline{M}_1 + (74.5 - \bar{v}_2)\,\underline{M}_2 + (58.5 - \bar{v}_3)\,\underline{M}_3\right]/1000 \qquad (37\text{-}16)$$

If $\bar{v}_1$, $\bar{v}_2$, $\bar{v}_3$ are constants, Eq. 37-16 may be simplified to:

$$\text{density} = 1 + a\,\underline{M}_1 + b\,\underline{M}_2 + c\,\underline{M}_3 \qquad (37\text{-}17)$$

Concentrations expressed in molalities from Table 37-1 were converted to molarities and multi-linear regression was performed to obtain the following empirical equations at the three temperatures:

at 25°C,

$$\text{density} = 1.029 + 0.091\underline{M}_1 + 0.034\underline{M}_2 + 0.027\underline{M}_3 \qquad (37\text{-}18)$$

at 40°C,

$$\text{density} = 1.022 + 0.089\underline{M}_1 + 0.035\underline{M}_2 + 0.028\underline{M}_3 \qquad (37\text{-}19)$$

at 55°C,

$$\text{density} = 1.010 + 0.088\underline{M}_1 + 0.026\underline{M}_2 + 0.029\underline{M}_3 \qquad (37\text{-}20)$$

Eq. 37-18, -19, and -20 relate solution density to composition on the molar scale and are generally accurate to ±0.003-density units (g/ml).

In order to further validate these equations, six solutions were made up in molar concentrations and duplicate specific gravity (22°/22°C) measurements were made. The experimentally-determined specific gravities were converted to densities and compared to the densities calculated using Eq. 37-18. These values are listed in Table 37-6. In four of the six solutions, the agreement is within 0.004 density units, or less than one division (0.005) on a conventional hydrometer. Therefore, Eq. 37-18 through 37-20 are suitably accurate in predicting the density of solutions from their molarities. In addition, they can be used to estimate the zinc content of an electrolyte to about ±0.1$\underline{M}$ while a battery is in the charging or discharging mode.

DISCUSSION

The precision in this work is nominally ±0.001 mole of the listed value. This is the nominal precision associated with weighing, transferring, and pipetting samples. For the three components being transferred, this would lead to an accuracy of approximately 0.0003 density units in the pycnometric results. Duplication testing on the pycnometers demonstrated a precision of 0.0001 to 0.0002 density units. Therefore, the accuracy of the equations is not affected by the experimental error.

The accuracy of the fundamental equation, density vs. molality, depends on the constancy of the partial molal volume terms. Multi-linear regression curve-fitting of the data to obtain the best constants for the partial molal volume terms resulted in a constant other than 1000 for the volume of water. Because of this, large deviations are to be expected for electrolytes containing low salt concentrations. For solutions containing at least 2-molal supporting electrolyte

and 0.5-molal zinc chloride, the derived expressions are quite accurate.

Each molar expression in Eq. 37-18, -19, and -20 was derived from more than 30 data points. From the computer expression, the calculated density agreed to within ±0.003 density units of the experimental value with a mean standard error of 0.2%. Confidence bands generated at the 0.99 confidence level produced an interval width of 0.01 or less for all points. Based on the experimental data and the computer analysis, the molar equation is expected to meet or exceed the accuracy of conventional hydrometers. That is, the equation can be used to predict the density of a mixed electrolyte to within ±0.005 units.

Table 37-6

COMPARISON OF CALCULATED AND MEASURED DENSITIES

($\underline{M}_1$, $\underline{M}_2$, and $\underline{M}_3$ refer to Molar Concentrations of $ZnCl_2$, KCl, and NaCl, respectively)

Solution Composition	Experimental Specific Gravity 22°C/22°C	Experimental Density at 22°C	Calculated Density at 25°C	Density Deviation Exptl. - Calcd.
$2\underline{M}_1 + 4\underline{M}_2 + 1\underline{M}_3$	1.381	1.378	1.374	+0.004
$2\underline{M}_1 + 3\underline{M}_2 + 2\underline{M}_3$	1.372	1.375	1.367	+0.008
$2.5\underline{M}_1 + 2\underline{M}_2 + 3\underline{M}_3$	1.406	1.403	1.406	-0.003
$2.5\underline{M}_1 + 2\underline{M}_2$	1.327	1.324	1.325	-0.001
$0.6\underline{M}_1 + 2.2\underline{M}_2$	1.156	1.154	1.158	-0.004
$0.5\underline{M}_1 + 2.1\underline{M}_2 + 3.2\underline{M}_3$	1.251	1.248	1.232	+0.016

REFERENCES

1. Chem. Abs., 1928 to 1978.

2. V. G. Shevchuk and A. S. Moshinski. "The $ZnCl_2 + ZnSO_4 + H_2O$ and NaCl + $ZnCl_2 + H_2O$ Systems at 25°C." Russian, J. of Inorg. Chem. 14, 1969, pp. 1316-1318.

3. W. F. Linke. Solubility: Inorganic and Metal-Organic Compounds. Princeton, N.J.: Van Nostrand, 1965.

Section 38

ELECTROLYTE PROPERTIES: II. CONDUCTIVITY

ABSTRACT

The voltage drop across the electrolyte in the inter-electrode gap can amount to 30-50% of the internal voltage loss in zinc-chloride cells and batteries. This section presents experimentally determined conductivities of aqueous solutions containing 0.5-4.0$\underline{m}$ $ZnCl_2$ + 0-4$\underline{m}$ KCl + 0-4$\underline{m}$ NaCl at 25°C, 40°C, and 55°C. The experimental data are fitted to a generalized empirical relationship for predicting solution conductivity (k, mho/cm) as a function of temperature (T, °C) and composition ($\underline{M}$, molarity):

$$k = (0.0967 + 0.0017T) - (0.014 + 0.0002T)\ \underline{M}_{ZnCl_2} + (0.026 + 0.0007T)\ \underline{M}_{KCl} + (0.004 + 0.0006T)\ \underline{M}_{NaCl}$$

The results can be used to help select electrolyte compositions which minimize internal voltage losses and improve the voltaic efficiency of zinc-chloride cells and batteries.

INTRODUCTION

Optimization of the zinc-chloride battery system requires that optimum voltaic efficiency is attained. The loss of voltaic efficiency is partly due to the ohmic voltage drops in the electrolyte gap and those in the graphite electrodes, conductors, and contacts. Some of the voltaic efficiency loss is also due to the polarization losses at the electrodes. It is estimated that the ohmic voltage drop in the electrolyte gap accounts for up to 50% of the internal voltage losses. Hence, the knowledge of the conductivity of the battery electrolytes is important in selecting the proper electrolyte.

This is the second in a series of sections on the physical properties of mixed electrolytes for the zinc-chloride battery. It covers the conductivities of mixed electrolytes. The conductivity is dependent on the concentration of the electrolyte. For a multicomponent mixed electrolyte, the conductivities of component ionic species are sometimes additive while the resistivities (reciprocal of conductivity) of the component species are not. The additive nature of the component conductivities holds if: (1) the viscosity of the electrolyte remains relatively constant with concentration, and (2) there is no complexation among the various ionic species, or there are no changes in existing complexes as different species are added. It has been demonstrated that the mixed electrolyte solutions within the ranges of this study have relatively constant viscosities (see Section 39). Therefore, conductivity should be a linear function of the concentration of each of the components provided there is no change in complexation upon the addition of salts.

The conductivities are measured for solutions of zinc chloride and zinc chloride with varying concentrations of the supporting electrolytes of potassium chloride and sodium chloride in the range of 0-4 $\underline{m}$ each. In a limited study, the conductivities also are investigated for zinc chloride solutions containing different concentrations of hydrochloric acid. HCl is added to the battery electrolyte to achieve the desired initial pH value of 0.1.

Since, in most cases, the conductivity of a solution increases 1-2% for each degree rise in temperature, the solution temperature is an important parameter to be considered in the conductivity measurements. In this study, solutions were prepared in molalities and their conductivities were measured at 25°C, 40°C, and 55°C. Relationships between the conductivities and the molalities of the salts at the three temperatures are established by best-fit calculations. Using density data already available (Section 37), conductivity relationships for molar concentrations also are established. Further, temperature is introduced into a general conductivity expression by combining the empirical formulas for the three temperatures

EXPERIMENTAL

Materials

The sodium chloride and potassium chloride salts used in this study are analytical reagent grade and they were used without further purification. The zinc chloride stock solution (5 moles/liter) was prepared by the reaction of chlorine gas with high-purity zinc metal. The pH of battery electrolyte solutions is normally maintained around 0.1. To achieve this pH value, concentrated hydrochloric acid of reagent grade was used.

Equipment and Procedure

Test solutions and temperature control devices used in this study are the same as those described in Section 37. A fill-type conductivity cell with a cell constant of approximately 10 was used to measure solution conductivity. It was first cleaned, coated with platinum black, and then calibrated with 1.205 m potassium chloride that was dried prior to the preparation of the solution. The standard solution of potassium chloride had a specific conductivity of 0.111 mho/cm at 25°C. A YSI Model 31 conductivity bridge was used to measure the resistance, R, of the cell filled with the standard solution of potassium chloride. The cell constant was then calculated as the product of the cell resistance, R, and the conductivity of the potassium chloride, k.

The cell was rinsed several times with each test solution and the cell resistances were measured at the three temperatures of 25°C, 40°C, and 55°C. The conductivity of each solution, k, was calculated as the ratio of the cell constant and the measured cell resistance.

EXPERIMENTAL RESULTS

Using the procedure described above, the conductivities of more than 30 solutions were determined experimentally. The results are listed in Table 38-1. Since the resistance reading of the conductivity bridge is reproducible to ±2% and the specific resistances of all solutions measured are between 4.9 and 8.3 ohm-cm, the results for conductivity have an error of approximately ±0.01 mho/cm.

The conductivity data in Table 38-1 are plotted in Figures 38-1 through 38-4 to illustrate the dependence of conductivity on the concentration of sodium chloride, potassium chloride, and temperature. In Figure 38-1, solution conductivities are plotted for 2m zinc chloride with 0.0-4.0m sodium chloride. In Figure 38-2, solution conductivities are plotted for 2m zinc chloride + 2m potassium chloride and 3m zinc chloride solutions with different sodium chloride concentrations. Figures 38-3 and 38-4 show the dependence of solution conductivity on the potassium chloride concentration. In Figure 38-3, the medium is 2m zinc chloride, and in Figure 38-4 the medium is 2m zinc chloride and 1m sodium chloride.

Solution conductivities at the three temperatures are shown in Figure 38-5 as a function of hydrochloric acid concentration for 2m $ZnCl_2$ solutions. The slope of the lines in Figure 38-5 are much steeper than those in Figures 38-1 through 38-4 for salt concentrations of sodium chloride and potassium chloride. This indicates that hydrochloric acid is more effective in increasing the conductivity of a solution than the salts. The influence of hydrochloric acid on conductivity is approximately 10 times greater than sodium chloride and five times greater than potassium chloride.

Table 38-1

EXPERIMENTALLY DETERMINED CONDUCTIVITIES OF MIXED ELECTROLYTE

Solution			Conductivity, k (mho/cm)		
m $ZnCl_2$	+ m KCL	+ m NaCl	25°C	40°C	55°C
2.00	0	0	0.10	0.12	0.14
2.00	1.06	0	0.14	0.17	0.20
2.00	2.00	0	0.18	0.21	0.25
2.00	3.00	0	0.21	0.26	0.31
2.00	4.00	0	0.25	0.31	0.35
2.00	0	1.01	0.12	0.15	0.17
2.00	0.99	0.99	0.16	0.20	0.23
2.00	2.00	1.00	0.19	0.24	0.29
2.00	3.00	1.03	0.23	0.28	0.33
2.00	3.00	2.00	0.24	0.30	0.37
2.00	0	2.00	0.14	0.17	0.21
2.00	0	3.00	0.16	0.20	0.24
1.99	0	3.99	0.17	0.22	0.27
2.00	0 (pH=3.3)	0	0.07	0.12	0.14
2.00	0 (pH=1.6)	0	0.07	0.12	0.14
1.99	0 (pH=0.6)	0	0.12	0.14	0.16
1.94	0 (pH=0.1)	0	0.17	0.21	0.23
1.88	0 (pH=0.4)	0	0.23	0.27	0.33
2.00	2.00	2.00	0.21	0.26	0.31
2.00	2.00	3.00	0.23	0.28	0.34
2.00	2.00	4.01	0.24	0.30	0.37
3.00	0	0	0.10	0.13	0.15
3.00	1.00	0	0.13	0.16	0.19
3.00	0	1.00	0.12	0.15	0.17
0.5	4.01	0	0.31	0.38	0.43
0.5	1.00	1.00	0.17	0.21	0.25
0.5	2.00	2.00	0.26	0.31	0.38
0.5	0	4.00	0.20	0.26	0.32
1.00	2.00	1.01	0.21	0.27	0.31
1.00	1.00	2.01	0.19	0.23	0.29
3.00	0	3.00	0.14	0.18	0.22
3.00	1.00	3.00	0.17	0.21	0.26
3.00	2.00	3.00	0.20	0.25	0.30
3.00	0	2.00	0.13	0.16	0.20
3.00	1.00	2.00	0.16	0.20	0.23
3.00	2.00	2.00	0.19	0.24	0.27
4.00	2.00	1.00	0.16	0.20	0.23
4.00	1.00	2.00	0.14	0.18	0.22

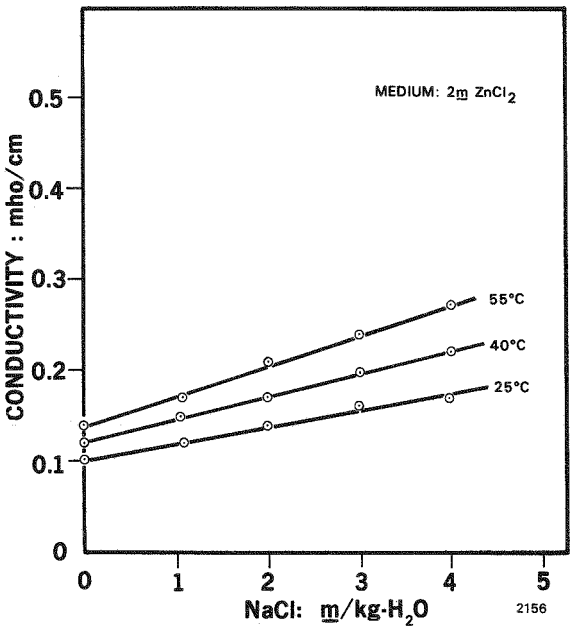

Figure 38-1. Electrical conductivity of $ZnCl_2$ + NaCl solutions as a function of NaCl concentration at 25°C, 40°C, and 55°C. $ZnCl_2$ molality was maintained constant at 2m concentration.

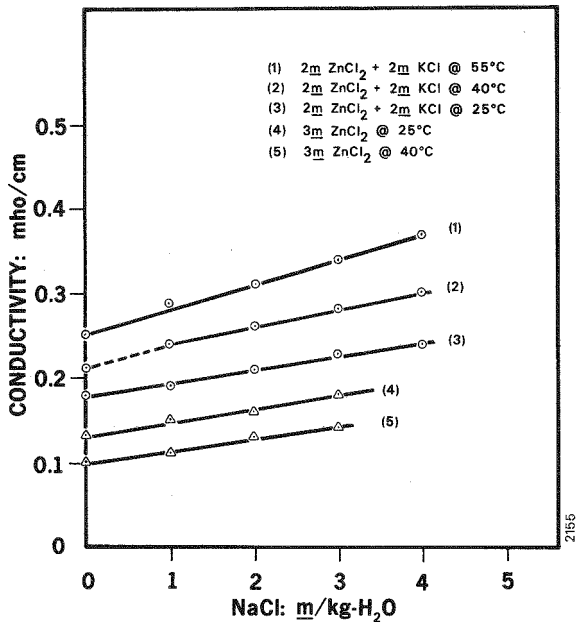

Figure 38-2. Electrical conductivity of $ZnCl_2$ + KCl + NaCl concentration at 25°C, 40°C, and 55°C. $ZnCl_2$ and KCl concentrations were held constant for a given set of measurements, as indicated in the figure.

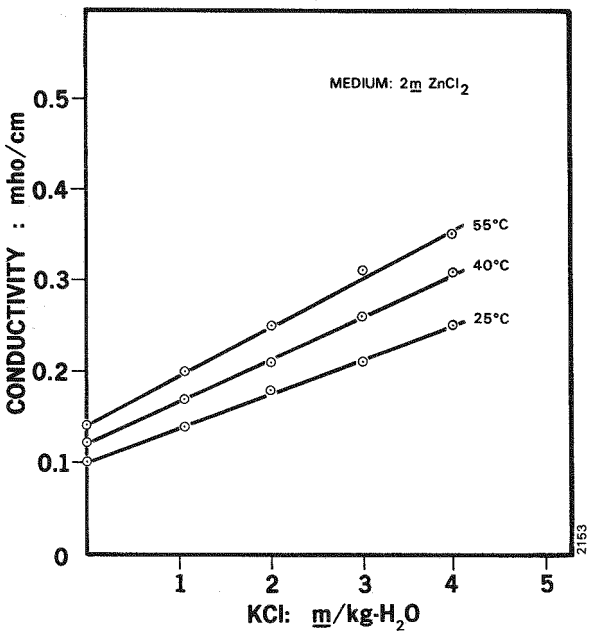

Figure 38-3. Electrical conductivity of $ZnCl_2$ + KCl solutions as a function of KCl concentration at 25°C, 40°C, and 55°C. $ZnCl_2$ concentration was held constant at 2m.

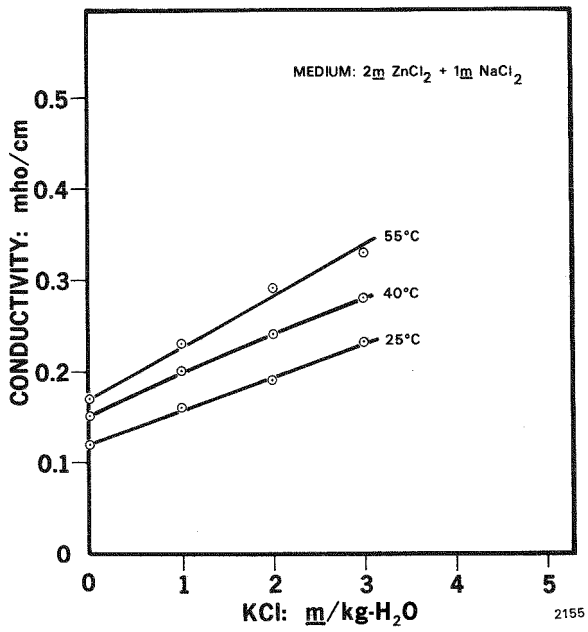

Figure 38-4. Electrical conductivity of $ZnCl_2$ + NaCl + KCl concentrations at 25°C, 40°C, and 55°C. $ZnCl_2$ and NaCl concentrations remained constant at 2m and 1m, respectively.

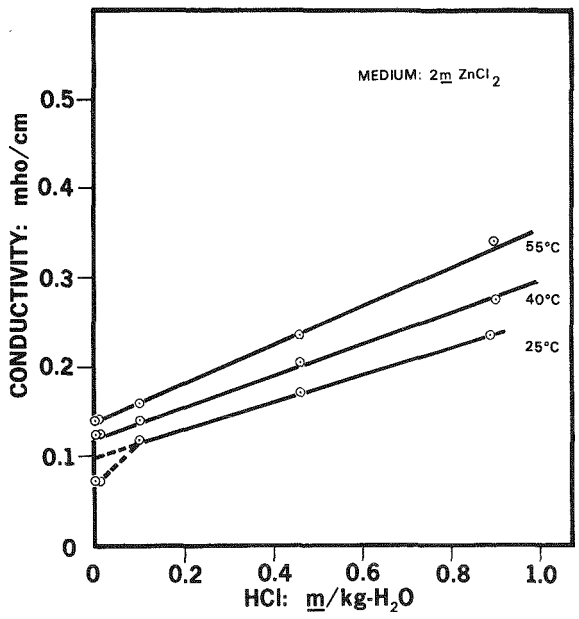

Figure 38-5. Solution conductivity of 2$\underline{m}$ zinc chloride as a function of hydrochloric acid concentration at the three temperatures. Note the molality coordinate is expanded.

EMPIRICAL CONDUCTIVITY RELATIONSHIPS FOR MOLAL SCALE

Assuming a linear relationship between conductivity and molality, a multi-linear regression was used in the form:

$$k = a + b\underline{m}_1 + c\underline{m}_2 + d\underline{m}_3$$

where k = solution conductivity (mho/cm)

$\underline{m}_1$ = molality of zinc chloride

$\underline{m}_2$ = molality of potassium chloride

$\underline{m}_3$ = molality of sodium chloride

and a, b, c, d, are constants.

The experimentally determined values for the conductivities of the approximately 30 solutions listed in Table 38-1 were used in best-fit computations to find the coefficients a, b, c, and d at the three different temperatures. The results are:

$$\text{at } 25°C,\ k = 0.149 - 0.020\ \underline{m}_1 + 0.036\ \underline{m}_2 + 0.015\ \underline{m}_3 \qquad (38\text{-}1)$$

$$\text{at } 40°C,\ k = 0.182 - 0.024\ \underline{m}_1 + 0.044\ \underline{m}_2 + 0.021\ \underline{m}_3 \qquad (38\text{-}2)$$

$$\text{at } 55°C,\ k = 0.211 - 0.028\ \underline{m}_1 + 0.051\ \underline{m}_2 + 0.029\ \underline{m}_3 \qquad (38\text{-}3)$$

Table 38-2 lists the results of calculations using Eq. 38-1. For comparison purposes, the experimentally determined conductivities are listed in parenthesis. Since the experimental data are accurate only to $\pm$0.01 mho/cm, the two sets of values can be assumed to be identical. The only exception is for the 0.5$\underline{m}$ $ZnCl_2$ + 4.0$\underline{m}$ KCl solution. For no obvious reason, the conductivity of this particular solution is higher than the value predicted by the empirical equation.

EMPIRICAL CONDUCTIVITY RELATIONSHIPS FOR MOLAR SCALE

For practical applications, conductivity as a function of electrolyte molarity was derived. This was accomplished by first converting the solution concentrations from molalities to molarities using the solution density relationships. Multi-linear regression for best-curve fit then was applied to find the coefficients using the linear equation of the form:

$$k = a' + b'\underline{M}_1 + c'\underline{M}_2 + d'\underline{M}_3$$

where k = solution conductivity

$\underline{M}_1$ = molarity of zinc chloride

$\underline{M}_2$ = molarity of potassium chloride

$\underline{M}_3$ = molarity of sodium chloride

and a', b', c', and d' are constants.

Table 38-2

CALCULATED AND EXPERIMENTAL (BRACKETS) DATA FOR THE CONDUCTIVITIES OF MIXED ELECTROLYTES AT 25°C, IN mho/cm (SALT CONCENTRATION IN moles/kg-H_2O)

NaCl \ KCl	0	1	2	3	4	$ZnCl_2$
		0.18	0.21	0.25	0.28 (0.31)	0.5
		0.17	0.20	0.24	0.27	1.0
0		0.15 (0.14)	0.18 (0.18)	0.22 (0.21)	0.25 (0.25)	2.0
		0.13 (0.13)	0.16	0.20	0.23	3.0
		0.11	0.14	0.18	0.21	4.0
	0.15	0.19 (0.17)	0.23	0.26	0.30	0.5
	0.14	0.18	0.22 (0.21)	0.25	0.29	1.0
1	0.13 (0.12)	0.16 (0.16)	0.20 (0.19)	0.23 (0.23)	0.27	2.0
	0.11 (0.12)	0.14	0.18	0.21	0.25	3.0
	0.09	0.12	0.16 (0.16)	0.19	0.23	4.0
	0.17	0.21	0.24 (0.26)	0.28	0.31	0.5
	0.16	0.20 (0.19)	0.23	0.27	0.30	1.0
2	0.14 (0.14)	0.18	0.21 (0.21)	0.25 (0.24)	0.28	2.0
	0.12 (0.13)	0.16 (0.16)	0.19 (0.19)	0.23	0.26	3.0
	0.10	0.14 (0.14)	0.17	0.21	0.25	4.0
	0.18	0.22	0.26	0.29	0.33	0.5
	0.18	0.21	0.25	0.28	0.32	1.0
3	0.16 (0.16)	0.19	0.23 (0.23)	0.26	0.30	2.0
	0.14 (0.14)	0.17 (0.17)	0.21 (0.20)	0.24	0.28	3.0
	0.12	0.15	0.19	0.22	0.26	4.0
	0.20 (0.20)	0.24	0.27	0.31	0.34	0.5
	0.19	0.23	0.26	0.30	0.34	1.0
4	0.17 (0.17)	0.21	0.24 (0.24)	0.28	0.32	2.0
	0.15	0.19	0.22	0.26	0.30	3.0
	0.13	0.17	0.20	0.24	0.28	4.0

The results are given in Eq. 38-4, -5, and -6.

$$\text{at } 25°C,\ k = 0.139 - 0.019\ \underline{M}_1 + 0.044\ \underline{M}_2 + 0.019\ \underline{M}_3 \qquad (38\text{-}4)$$

$$\text{at } 40°C,\ k = 0.165 - 0.022\ \underline{M}_1 + 0.055\ \underline{M}_2 + 0.026\ \underline{M}_3 \qquad (38\text{-}5)$$

$$\text{at } 50°C,\ k = 0.190 - 0.026\ \underline{M}_1 + 0.065\ \underline{M}_2 + 0.036\ \underline{M}_3 \qquad (38\text{-}6)$$

Eq. 38-4, -5, and -6 were used to compute the conductivity values for solution temperatures of 25°C, 40°C, and 55°C where salt concentrations are expressed in moles/liter.

GENERAL CONDUCTIVITY RELATIONSHIP ON MOLAR SCALE

Based on a comparison of the coefficients in the Eq. 38-4, -5, and -6, it is apparent that they are functions of the solution temperature. That is, their absolute values increase with increasing temperature. More than three data points are required to establish the temperature dependence of the coefficients. For a first approximation, a linear relationship was assumed based on three data points. The best-fit method is used to calculate the change of the coefficients as a function of temperature.

Therefore, a', b', c', and d' are

$$a' = 0.0967 + 0.0017T$$

$$b' = -(0.014 + 0.0002T)$$

$$c' = 0.026 + 0.0007T$$

$$d' = 0.004 + 0.0006T$$

where T is the solution temperature in degrees Celsius.

As a result, k is a function of not only salt concentrations but also of temperature in the range of 25-55°C and:

$$k = (0.0967+0.0017T) - (0.014+0.0002T)\underline{M}_1 + (0.026 + 0.0007T)\underline{M}_2 + (0.004+0.0006T)\underline{M}_3 \qquad (38\text{-}7)$$

and will predict solution conductivity within ±0.02 mho/cm or better.

DISCUSSION

The empirical equations derived in this study are based on experimentally measured solution conductivities. Since the accuracy in predicting conductivity is approximately ±0.01 mho/cm, the accuracy in predicting the resistivity of solutions depends on the actual value of solution conductivity. For instance, a solution having a specific conductivity of 0.11 ±0.01 mho/cm may have a specific resistivity of 9.2 ±0.8 ohm-cm, while a solution having a conductivity of 0.25 ±0.01 mho/cm has a resistivity of 4.0 ±0.2 ohm-cm, i.e., a much smaller deviation.

The empirical relationships developed herein are suitable for predicting the conductivity of mixed electrolyte solutions that contain $\geq 0.5\underline{m}$ zinc chloride over the temperature range of 25-55°C. As such, they span the salt concentration and temperature ranges that are presently considered acceptable for the load-leveling battery application. Beyond these ranges the relationships may or may not be valid. Regions where they are not valid include:

- Mixed electrolyte solutions containing $<0.5\underline{m}$ zinc chloride.
- Electrolyte solutions containing zinc chloride salt only, with no potassium chloride or sodium chloride added.

Data on the resistivity of solutions that contain only zinc chloride have been generated previously at EDA and are reproduced in Figure 38-6. It is apparent from the results of the present study that, in mixed electrolyte solutions, increases in zinc chloride concentration have an adverse effect on solution conductivity in the range of 0.5-4.0m. From the data in Figure 38-6, this is not obvious for solutions that contain only zinc chloride. The difference is most likely the result of complex-ion formation in the mixed electrolyte solutions, i.e., as more zinc chloride is added to the mixed electrolyte solutions, more chloride ions are tied up as $ZnCl_4^=$ and $ZnCl_3^-$.

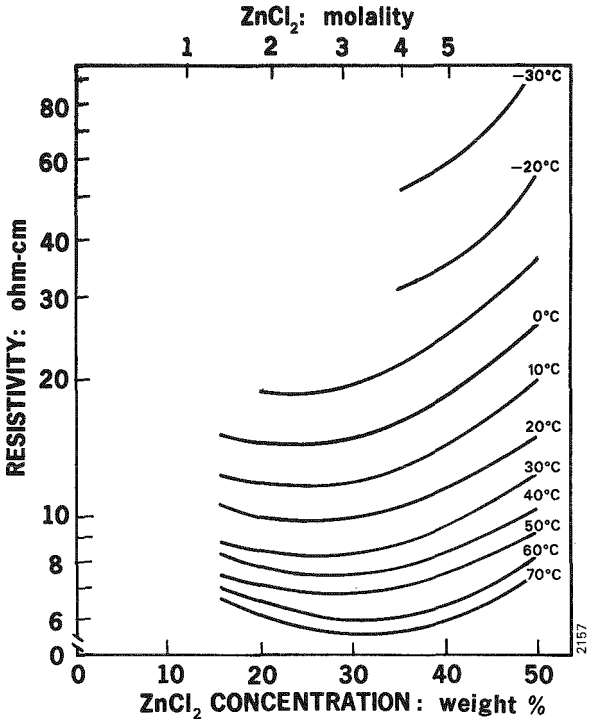

Figure 38-6. Resistivity of zinc chloride solutions at various temperatures and concentrations. It can be seen there is a minimum resistivity for each temperature.

The dramatic effect of hydrochloric acid on the electrolyte conductivity is most likely due to the relative mobility of the hydronium ion (H_3O^+). It is obviously the most mobile of the cations in solution and therefore has a dramatic effect on the conductivity of the solution. It should be noted that for normal battery applications, relatively small quantities of hydrochloric acid are added (0.1-0.2 moles/liter). These quantities are sufficient, however, to alter the conductivity of pure zinc chloride solutions by several hundredths of a mho/cm and most likely will account for similar effects in mixed electrolyte solutions.

CONCLUSIONS

1. The following equation can be used to calculate solution conductivity at a specific temperature and solution concentration to ±0.02 mho/cm:

$$k = (0.0967 + 0.0017T) - (0.014 + 0.0002T)\,\underline{M}_1 + (0.026 + 0.0007T)\,\underline{M}_2 + (0.004 + 0.0006T)\,\underline{M}_3$$

   where 1, 2, and 3 are the subscripts for zinc chloride, potassium chloride, and sodium chloride, respectively and T is the temperature in °C.

2. The conductivity of zinc chloride solutions containing supporting electrolytes increases with increasing concentrations of potassium chloride and sodium chloride, and decreases with increasing concentrations of zinc chloride, for the concentration ranges applicable to the zinc-chloride battery.

3. Potassium chloride is more effective than sodium chloride in increasing the conductivity of a solution, either in weight per unit volume of salt or moles per unit volume of salt.

Section 39

ELECTROLYTE PROPERTIES: III. VISCOSITY

ABSTRACT

The viscosity of battery electrolytes affects the fluid dynamics and mass transport in the inter-electrode gap, as well as the requirements for the electrolyte pump in zinc-chloride batteries. This section presents experimentally determined viscosities of aqueous solutions containing 0.5-2.0$\underline{m}$ $ZnCl_2$ + 0-5$\underline{m}$ KCl + 0-4$\underline{m}$ NaCl at 25°C, 40°C, and 55°C. The experimental data are fitted to empirical relationships for predicting solution viscosity (η, centipoise) as a function of composition ($\underline{m}$, molality) at each temperature (T_i):

$$\eta(T_i) = \frac{a_i + b_i \underline{m}_{ZnCl_2} + c_i \underline{m}_{KCl}}{A_i + B_i \underline{m}_{ZnCl_2} + C_i \underline{m}_{KCl}} \frac{+ d_i \underline{m}_{NaCl}}{+ D_i \underline{m}_{NaCl}}$$

The values of the empirical constants (a_i, b_i, . . . C_i, and D_i) depend on the temperature. The results can be used to help understand the effects of electrolyte composition and temperature on the fluid dynamics and mass transport in the inter-electrode gap with a view to coulombic-efficiency maximization.

INTRODUCTION

This section is the third of a series on the physical properties of mixed electrolytes. It addresses the property of solution viscosity, which is the resistance of a solution to flow or a measure of its internal friction. Knowledge of solution viscosity is basic to the study of fluid dynamics in the inter-electrode cell gap. The viscosity of the electrolyte also is an important factor in determining the power requirements of the electrolyte pump that circulates electrolyte to the battery stack.

An Ostwald viscometer was used to measure viscosity because it is capable of an accuracy that exceeds the needs of cell modeling studies. The viscosity of a solution was calculated from the density of the solution, a constant that is a function of viscometer dimensions, and the time required for the solution meniscus to flow between two preset heights on the viscometer.

Twenty-seven solutions of mixed electrolytes of the form $ZnCl_2$ + KCl + NaCl with varying combinations of concentrations were prepared. Their viscosities were measured at 25°C, 40°C, and 55°C to obtain the temperature dependence of the solutions over the temperature range of interest for the zinc-chloride battery. By combining the experimental results for viscosity and conductivity, empirical formulas were derived for viscosity as a function of salt molality.

EXPERIMENTAL

Materials

The zinc chloride stock solution, having a concentration of approximately 5 moles/liter, was prepared by the reaction of chlorine with high-purity zinc metal. The sodium chloride and potassium chloride salts were analytical reagent grade and they were used without further purification.

Equipment and Procedure

Ostwald viscometers were used to measure the viscosities of the electrolyte solutions. The volume of the reservoir of the viscometer was approximately six milliliters. A transparent constant temperature bath, Blue-M Model

MW-1162SSA-1, was used to control the temperature accurately to ±0.1°C. The viscometer was cleaned using acid-dichromate, followed by a thorough rinsing with distilled water, and then dried by passing acetone vapor through it.

Distilled water was used to calibrate the viscometer and obtain the cell constants at the three temperatures of 25°C, 40°C, and 55°C. A fixed volume of distilled water was introduced into the viscometer which was totally immersed vertically in the water bath, except for one centimeter of the top portion. Suction was applied to one side of the viscometer opening to raise the liquid level above the two permanently marked lines. The liquid was then allowed to flow by gravity back to its original level. The time (t_o) required for the liquid meniscus to pass between the two marks was recorded using a stop watch, Scientific Products Model C6570. At least four replicate measurements were taken on each sample and the mean measurements were used in subsequent calculations.

The cell constant (A) for each viscometer was calculated using the following equation:

$$A = \eta_o / (d_o \cdot t_o) \qquad (39\text{-}1)$$

Where η_o = viscosity of water,

d_o = density of water,

t_o = measured time in seconds.

Each cell was calibrated at the different temperatures of 25°C, 40°C, and 55°C. A volume of solution, equal to the volume of distilled water used for calibration, was introduced into the viscometer to obtain the viscosity of the sample solution. After the temperature of the solution equilibrated with the temperature of the bath, the same procedure used for cell calibration was followed to obtain the time (t) for each solution.

Using the solution densities determined in Section 37 and the appropriate cell constant, the viscosity of each sample was calculated using Eq. 39-2.

$$\eta = A.d.t \qquad (39\text{-}2)$$

In order to achieve highly reliable measurements of viscosity using an Ostwald viscometer, the following precautions should be noted. The position of the viscometer should be exactly vertical. The viscometer should be dry and clean before the test solution is introduced. The standard solution used to calibrate the viscometer should have a viscosity close to that of the test solutions. The pressure drop in the reservoir should be kept to a minimum between the beginning and the end of the measurements, which means the liquid level in the reservoir should be filled slightly higher than, but close to, the widest portion of the glass bulb.

Duplicate readings using the same solution and the same viscometer are reproducible to within 0.5%. Reproducibility of the viscosity measurement using two different viscometers also is about 0.5%. Empirically calculated solution viscosities have a standard error of 4%.

EXPERIMENTAL RESULTS

The measured viscosities of the various mixed salt solutions are listed in Table 39-1. Many attempts were made to correlate the experimentally determined viscosities with the compositions of the solutions. The following relationships were examined:

- viscosity versus $(\text{molality})^2$
- viscosity versus molality
- viscosity versus $(\text{molality})^{1/2}$
- fluidity $(1/\eta)$ versus $(\text{molality})^2$
- fluidity versus molality

Figure 39-1 is an example of the relationships that were examined, and it

Table 39-1

MEASURED SOLUTION VISCOSITIES AT THREE TEMPERATURES*

Solution Concentration $\underline{m}ZnCl_2$ + $\underline{m}KCl$ + $\underline{m}NaCl$			Viscosity (cp) at 25°C	40°C	55°C
0.49	0.00	0.00	1.05		0.58
0.49	2.00	1.00	1.06(0.23)**		0.63(0.33)**
0.49	3.10	1.07	1.09(0.27)**		0.66(0.39)**
0.49	2.03	1.97	1.19(0.24)**		0.71(0.36)**
0.49	3.04	2.00		0.92(0.35)**	0.74(0.41)**
0.98	0.00	0.00	1.20	0.84	0.65
1.96	0.00	0.00	1.42	1.01	0.76
2.95	0.00	0.00	1.82	1.19	0.90
1.96	1.00	0.00	1.33(0.15)**	0.95(0.18)**	
1.96	3.00	0.00	1.20(0.22)**	0.89(0.27)**	
1.96	5.00	0.00	1.18(0.29)**	0.90(0.35)**	
2.00	0.00	0.00	1.45(0.10)	1.02(0.12)	0.78(0.14)
2.00	1.06	0.00	1.34(0.14)	0.96(0.17)	0.74(0.20)
2.00	2.00	0.00	1.26(0.18)	0.92(0.21)	0.71(0.25)
2.00	3.00	0.00	1.22(0.21)	0.90(0.26)	0.72(0.31)
2.00	4.00	0.00	1.19(0.25)	0.89(0.31)	0.71(0.35)
2.00	0.00	1.01	1.45(0.12)	1.03(0.15)	0.78(0.17)
2.00	0.99	0.99	1.37(0.16)	0.99(0.20)	0.76(0.23)
2.00	2.00	1.00	1.31(0.19)	0.96(0.24)	0.75(0.29)
2.00	3.00	2.00		1.02(0.30)	0.82(0.37)
2.00	3.00	1.03		0.95(0.28)	0.76(0.33)
2.00	0.00	2.00		1.06(0.17)	0.80(0.21)
2.00	0.00	3.00		1.09(0.20)	0.84(0.24)
2.00	0.00	4.00	1.61(0.17)	1.15(0.22)	0.88(0.27)
2.00	2.00	2.00	1.38(0.21)	1.01(0.26)	0.79(0.31)
2.00	2.00	3.00	1.47(0.23)	1.09(0.28)	0.86(0.34)
2.00	2.00	4.01	1.61(0.24)	1.20(0.30)	0.94(0.37)

*Corresponding solution conductivity (mho/cm) is included in the parenthesis.

**Indicates calculated conductivity, others are experimental values.

illustrates the effect of the molality of the potassium chloride and sodium chloride salts, on the solution viscosity. It is clear that a simple linear relationship between the viscosities and the molalities of the solutions does not exist. The same conclusions are drawn for all of the other relationships that were examined.

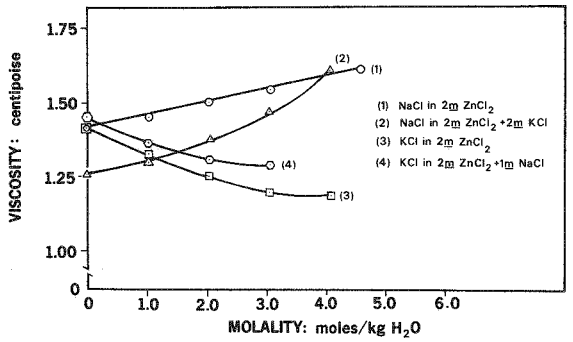

Figure 39-1. Solution viscosity at 25°C as a function of salt molalities.

However, a linear relationship was closely approximated for the solution composition and the product of solution viscosity (η) and conductivity (k). This linear relationship was derived as a result of the plots of η x k versus molality of one component for a series of solutions.

Figure 39-2 shows the effect of sodium chloride or potassium chloride concentrations on this product at a solution temperature of 25°C. Figures 39-3 and 39-4 illustrate similar relationships at the solution temperatures of 40°C and 55°C, respectively. Each line stands for the effect of sodium chloride or potassium chloride on the product of viscosity and conductivity in the different media.

Table 39-2 shows the product of η x k for the solutions listed in Table 39-1. Wherever experimental conductivities were not available, previously derived empirical equations (Section 38) were used to calculate the conductivity. The data listed in Table 39-2 were used in multi-linear regression computations to obtain empirical relationships of the form:

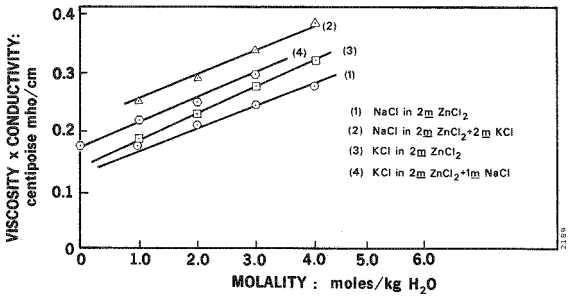

Figure 39-2. Product of viscosity and conductivity is a linear function of concentration of NaCl or KCl at 25°C in $ZnCl_2$ electrolytes.

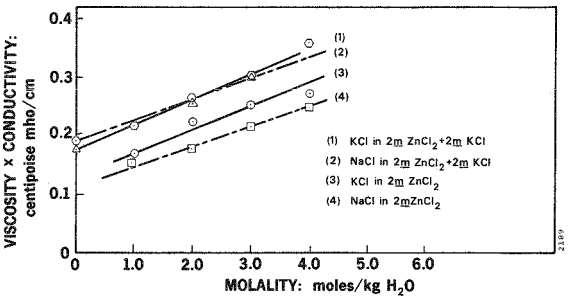

Figure 39-3. Product of viscosity and conductivity variation with the concentrations of KCl or NaCl at 40°C in $ZnCl_2$ electrolytes.

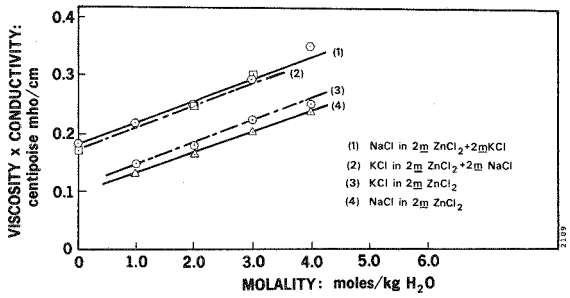

Figure 39-4. Effect of KCl or NaCl concentration on the product of viscosity and conductivity at 55°C in $ZnCl_2$ electrolytes.

$$(\eta \times k) = a + b\underline{m}_1 + c\underline{m}_2 + d\underline{m}_3 \quad (39\text{-}3)$$

where $\underline{m}_1$ = molality of zinc chloride

$\underline{m}_2$ = molality of potassium chloride

$\underline{m}_3$ = molality of sodium chloride

and a, b, c, and d are constants.

The results are given by Eq. 39-4, -5, and -6 for the three different temperatures:

$$\text{at } 25°C, \quad \eta \times k = 0.126 + 0.008\underline{m}_1 + 0.040\underline{m}_2 + 0.037\underline{m}_3 \quad (39\text{-}4)$$

$$\text{at } 40°C, \quad \eta \times k = 0.134 - 0.008\underline{m}_1 + 0.040\underline{m}_2 + 0.036\underline{m}_3 \quad (39\text{-}5)$$

$$\text{at } 55°C, \quad \eta \times k = 0.097 - 0.0003\underline{m}_1 + 0.041\underline{m}_2 + 0.037\underline{m}_3 \quad (39\text{-}6)$$

By substituting the empirical relationships for conductivity (Section 38) in Eq. 39-4, -5, and -6, Eq. 39-7, -8, and -9 are obtained for the viscosity relationships at the three different temperatures.

at 25°C:

$$\eta = \frac{0.126 + 0.008\underline{m}_1 + 0.040\underline{m}_2 + 0.037\underline{m}_3}{0.149 - 0.020\underline{m}_1 + 0.036\underline{m}_2 + 0.015\underline{m}_3} \quad (39\text{-}7)$$

at 40°C:

$$\eta = \frac{0.134 - 0.008\underline{m}_1 + 0.040\underline{m}_2 + 0.036\underline{m}_3}{0.182 - 0.024\underline{m}_1 + 0.044\underline{m}_2 + 0.021\underline{m}_3} \quad (39\text{-}8)$$

at 55°C:

$$\eta = \frac{0.097 - 0.0003\underline{m}_1 + 0.041\underline{m}_2 + 0.037\underline{m}_3}{0.211 - 0.028\underline{m}_1 + 0.051\underline{m}_2 + 0.029\underline{m}_3} \quad (39\text{-}9)$$

Eq. 39-7 was used to calculate the viscosity values reported in Table 39-3. The experimentally-determined viscosities, shown in parentheses in Table 39-1, are included for comparison. The differences between the two sets of values average ±0.03 centipoise or less.

DISCUSSION

The observed effects on viscosity due to the addition of zinc chloride, sodium chloride, and potassium chloride salts to the solution follow the same trends in the mixed salt media as they do in pure water. The viscosity increases with increasing zinc chloride and/or sodium chloride concentrations, but decreases with increasing potassium chloride concentrations. The usual relationship between temperature and viscosity holds in this study, the viscosity decreases about 2% for each degree rise in temperature.

These data are of practical importance in two areas of current development work: the design of the main electrolyte pump, as well as modeling studies of coulombic efficiency. In the first area, the viscosity, or resistance to flow, of the fluid is an important parameter in determining the hydraulic requirements for the pump and manifolding system that are used to circulate and distribute electrolyte to the battery stack. A more thorough knowledge of the pertinent fluid viscosities will allow more accurate specification of the hydraulic requirements of this subsystem.

In the area of modeling studies of coulombic efficiency, the viscous forces balance the bouyant forces in the inter-electrode cell gap. An increase in the viscous forces retards fluid motion or convection, resulting in decreased convective transport of dissolved chlorine to the zinc electrode and possibly a higher coulombic efficiency for the cell.

Table 39-2

PRODUCT OF MEASURED VISCOSITY AND CONDUCTIVITY AT THREE TEMPERATURES

Solution Concentration			Viscosity x Conductivity (cp x mho/cm) at		
$\underline{m}ZnCl_2$ +	$\underline{m}KCl$ +	$\underline{m}NaCl$	25°C	40°C	55°C
0.49	2.00	1.00	0.244		0.208
0.49	3.10	1.07	0.294		0.257
0.49	2.03	1.97	0.286		0.256
0.49	3.04	2.00		0.322	0.303
1.96	1.00	0.00	0.200	0.171	
1.96	3.00	0.00	0.264	0.240	
1.96	5.00	0.00	0.342	0.315	
2.00	1.06	0.00	0.188	0.163	0.148
2.00	2.00	0.00	0.227	0.193	0.178
2.00	3.00	0.00	0.256	0.234	0.223
2.00	4.00	0.00	0.298	0.276	0.249
2.00	0.00	1.01	0.174	0.155	0.133
2.00	0.99	0.99	0.219	0.198	0.175
2.00	2.00	1.00	0.249	0.230	0.218
2.00	3.00	2.00		0.306	0.303
2.00	3.00	1.03		0.266	0.251
2.00	0.00	2.00		0.180	0.168
2.00	0.00	3.00		0.218	0.202
2.00	0.00	4.00	0.274	0.253	0.238
2.00	2.00	2.00	0.290	0.263	0.245
2.00	2.00	3.00	0.338	0.305	0.292
2.00	2.00	4.01	0.386	0.360	0.348

Table 39-3

CALCULATED AND EXPERIMENTAL (PARENTHESES) VISCOSITIES (cp) OF MIXED ELECTROLYTES AT 25°C
SALT CONCENTRATIONS IN MOLES/kg-H_2O

NaCl \ KCl	0	1	2	3	$ZnCl_2$
		0.97	1.00	1.01	0.5
0		1.05	1.06	1.07	1.0
		1.25(1.34)	1.23(1.26)	1.21(1.22)	2.0
		1.52	1.43	1.37	3.0
	1.08	1.09	1.09(1.06)	1.09(1.09)	0.5
1	1.18	1.17	1.16	1.15	1.0
	1.44(1.45)	1.36(1.37)	1.32(1.31)	1.29(1.29)	2.0
	1.79	1.61	1.51	1.44	3.0
	1.20	1.19	1.18(1.19)	1.17	0.5
2	1.30	1.27	1.24	1.23	1.0
	1.54(1.50)	1.46	1.40(1.38)	1.36	2.0
	1.87	1.69	1.58	1.51	3.0
	1.30	1.27	1.25	1.23	0.5
3	1.40	1.35	1.32	1.29	1.0
	1.63(1.54)	1.53	1.47(1.47)	1.42	2.0
	1.93	1.76	1.64	1.57	3.0

CONCLUSIONS

Major findings of this study are:

1. Solutions of mixed electrolytes, $ZnCl_2$ + KCl + NaCl, in the concentration ranges generally applicable to the zinc-chloride battery have viscosity values close to 1.0 centipoise at ambient temperature. Viscosity increases slightly with increasing zinc chloride and sodium chloride concentrations and decreases with increasing concentrations of potassium chloride. For all salt concentrations, the viscosity decreases as the temperature increases.

2. The following equations can be used to calculate solution viscosity over the concentration ranges applicable to the operation of the zinc-chloride battery:

$$\eta = \frac{a + b\underline{m}_1 + c\underline{m}_2 + d\underline{m}_3}{a' + b'\underline{m}_1 + c'\underline{m}_2 + d'\underline{m}_3}$$

where the subscripts, 1, 2, 3 refer to $ZnCl_2$, KCl, NaCl, respectively.

The values of coefficients are:

Coefficient x 1000	Temperature (°C) 25	40	55
a	126	134	97
b	8	-8	-0.3
c	40	40	41
d	37	36	37
a'	149	182	211
b'	-20	-24	-28
c'	36	44	51
d'	15	21	29

Section 40

ELECTROLYTE PROPERTIES: IV. CHLORINE SOLUBILITY

ABSTRACT

The solubility of dissolved chlorine in the electrolyte is important because the major source of coulombic inefficiency in zinc-chloride cells is the first-order reaction of dissolved chlorine with electrodeposited zinc. This section presents experimentally determined chlorine solubilities in aqueous solutions containing 0.5-3M $ZnCl_2$ + 0-4.4M KCl + 0-4.4M NaCl at 25°C, 40°C, and 55°C. All data are obtained at an equilibrium chlorine partial pressure of one atmosphere. The results indicate that chlorine solubility is inversely proportional to the concentrations of both KCl and NaCl, with NaCl having the largest effect. Chlorine solubility also decreases with increasing temperature and approaches a value of 1 g/ℓ at 55°C regardless of electrolyte composition.

INTRODUCTION

Energy Development Associates (EDA) is developing a zinc-chloride battery for use as a load-leveling system by the electric-utility industry. It is necessary to maximize coulombic efficiency in an effort to meet the targeted electrochemical energy efficiency of 75% for this application. The major source of coulombic inefficiency is the direct reaction of dissolved chlorine with the zinc electrode. During the charge mode, zinc is deposited at the cathode and chlorine gas is produced at the anode. The chlorine dissolves in the battery electrolyte and reacts with the deposited zinc. Ideally, the chlorine should not come in contact with the zinc plated at the cathode. However, the reaction between the zinc metal and the dissolved chlorine cannot be totally eliminated because both electrodes are immersed in the same solution. One way of reducing this corrosion reaction is to minimize the solubility of chlorine in the electrolyte. This can be achieved by either decreasing the partial pressure of chlorine in the battery stack or by adding supporting salts to the battery electrolyte.

The physicochemical properties of zinc-chloride battery electrolytes are being investigated in order to develop a more thorough understanding of their influence on electrochemical energy efficiency. This section -- the fourth in a series on properties of battery electrolytes -- addresses chlorine solubility in aqueous solutions containing the chloride salts of zinc, potassium, and sodium. Solubility is defined as the maximum quantity of chlorine dissolvable in a unit volume of electrolyte in equilibrium with a given partial pressure of chlorine, and is expressed in units of grams of chlorine per liter of electrolyte.

The solubility of chlorine in single salt solutions has been studied rather extensively (1-6). Goodwin (4) tested the dependence of chlorine solubility on temperature (-3°C to 35°C) in potassium chloride and sodium chloride solutions. He concluded that the chlorine-solubility curves for both salt solutions were almost identical, except that the solubility of chlorine in the sodium chloride solution is slightly lower than in the potassium chloride solution. When sodium chloride was substituted for potassium chloride on a mole-for-mole basis, the solubility

curve did not differ significantly, indicating no complex formation between potassium chloride and sodium chloride in the presence of dissolved chlorine. Mandella (2) studied chlorine solubility in sodium chloride solutions at 20°C in the concentration range of 0.8-3.6M and found that chlorine solubility decreases with increasing concentration of salt.

Bott and Schulz (3) measured the chlorine solubility of a 4.3M sodium chloride solution at 50-75°C in a pH range of 1.0-2.5. They found that, for solutions having a pH lower than 1.5, chlorine solubility decreases slightly when the pH of the sodium chloride solution is increased. When the pH is in the range of 1.5-2.5, the solubility of chlorine increases with increasing pH.

Hine and Inuta (4) studied chlorine solubility in hydrochloric acid in the concentration range of 2-10M. Their results show that chlorine solubility is proportional to the partial pressure of chlorine in the gas phase, while the slope is a function of both the concentration of hydrochloric acid and temperature.

Other studies include Yokotu's study (5) on the effect of pressure (0.1-1 atm), temperature (30-70°C), salt concentration (3.6-5.0M), and pH (1-5) on the solubility of chlorine in sodium chloride solutions. Sherrill and Izard (6) determined chlorine solubility in solutions of hydrochloric acid, potassium chloride, and sodium chloride at 25°C and one atmosphere.

Chlorine solubility in zinc chloride solutions has been determined at 30°C in the concentration range of 1-4M in earlier studies at EDA (7). A few zinc chloride solutions in the presence of supporting electrolytes also were studied. However, no systematic study of chlorine solubility was made for zinc-chloride battery electrolytes containing the mixed chloride salts of zinc, potassium, and sodium. The electrolytes tested in this study include acidified zinc chloride concentrations of 0.5-2.5M with concentration ranges of 0-4M for both sodium chloride and potassium chloride. The solubility of chlorine was measured at the three temperatures of 25°C, 40°C, and 55°C, which span the temperature range of interest for zinc-chloride battery operation. Chlorine concentration was determined by the iodine-thiosulfate method, which is capable of an accuracy of better than ±0.1 g/ℓ.

EXPERIMENTAL

Materials

The zinc chloride stock solution, which has a concentration of approximately 5M was prepared by the reaction of zinc metal with chlorine gas. The potassium chloride and sodium chloride salts and concentrated hydrochloric acid were all reagent grade. They were used with no further purification. Liquefied chlorine gas was supplied by the Matheson Company and was used directly from the cylinder.

The chemicals used in the chlorine concentration measurements included reagent-grade granular potassium iodide and sodium thiosulfate crystals. Potassium iodate, an analytical reagent purchased from the Baker Company, was also used. It was dried in an oven at 110°C for three hours and stored in a desiccator. The starch indicator solution was supplied by Anachem Chemicals Ltd.

Preparation of Reagents

Potassium Iodide. Eighty grams of granular potassium iodide were dissolved in distilled water to make 400 ml of the solution and stored in a constant-volume dispensing dark plastic bottle. A 10-milliliter aliquot of this solution, which contained two grams of potassium iodide, was used in each titration. For the titration of a sample solution at elevated temperatures, the reagent was refrigerated prior to use so that the titration could be performed near to room temperature.

Starch Indicator Solution. The contents of the aliquot were poured into a one-liter volumetric flask and diluted to the mark with distilled water.

Sodium Thiosulfate Solution. This solution was used as the standard titrant in the analysis of chlorine concentration. Prior to the preparation of this standard solution, distilled water was boiled for five minutes, and allowed to cool to room temperature. This sterilized water was used to prepare the 0.05N sodium thiosulfate standard solution. A very small quantity of sodium carbonate was added to make the solution slightly basic in order to enhance the stability of the standard solution.

Potassium Iodate Standard Solution. 2.8 grams of the dried potassium iodate were weighed to ±0.1 milligram and dissolved in 500 milliliters of water in a volumetric flask. Ten to twenty-five milliliters of this standard solution were used to standardize the sodium-thiosulfate solution.

Dilute Hydrochloric Acid. Forty-three milliliters of concentrated reagent-grade hydrochloric acid were used to prepare a 500-milliliter 1.0N hydrochloric acid solution. This reagent was added to make sure that the titration was carried out in an acidic medium.

Preparation of Test Solutions

A total of 36 solutions were tested. These covered the zinc chloride concentration range of 0.5-2.5M and the potassium chloride and sodium chloride concentration ranges of 0-4M. The molarity of the zinc chloride stock solution was determined through its specific gravity. The plot of specific gravity (20°C/60°F) versus the molarity of zinc chloride is shown in Figure 40-1. In the preparation of a 500-milliliter test solution, the required quantities of potassium chloride and sodium chloride supporting electrolytes were weighed on a Ohaus-Triple-Beam balance that was accurate to ±0.05 grams, and transferred into a 500-milliliter volumetric flask. The required volume of stock solution of zinc chloride was added. The solution cooled down considerably during preparation, which led to an initial contraction in volume. For this reason the make-up volume of water was added after the solution reached room temperature.

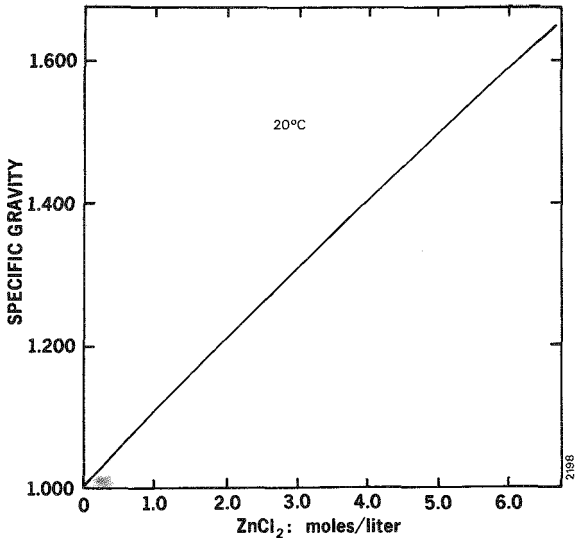

Figure 40-1. Zinc chloride concentration as a function of its specific gravity (20°C/60°F).

Equipment and Procedures

Figure 40-2 is a schematic of the apparatus used in the chlorine-solubility measurements. Chlorine gas from the cylinder was bubbled through distilled water to equilibrate it with water vapor. A chlorine manifold then distributed the wet chlorine gas among six separate flasks that contained six different test solutions and were immersed in a constant-temperature water bath. A more detailed schematic of the solution flask is shown in Figure 40-3. Chlorine gas from the chlorine manifold was introduced under the surface of the solution by a chlorine sparger. The sparger also served as a stirrer. Excess chlorine escaped the flask through a vent tube. To withdraw a test sample from the flask, the vent was closed, and a 10 ml graduated pipette was placed tightly over the capillary tube, until the desired volume was obtained.

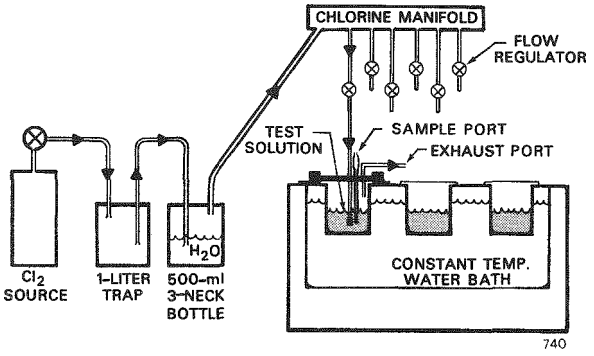

Figure 40-2. Apparatus used in chlorine solubility measurements.

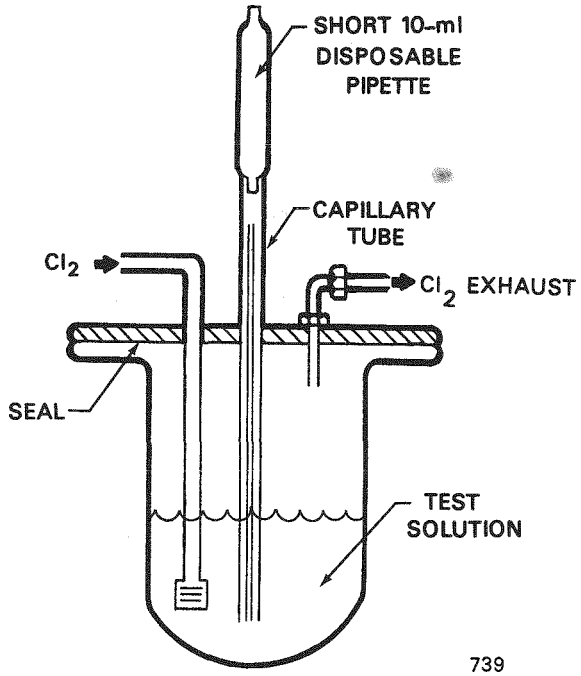

Figure 40-3. Detail of flask used in chlorine solubility measurements.

739

In order to establish a standard procedure for achieving chlorine saturation in the test solution, a preliminary test was performed on five solutions: four mixed-salt solutions and a 20% potassium chloride solution. The latter was tested because its chlorine solubility has been reported in the literature. The results of the test revealed that the solutions reached chlorine saturation in one hour. Analysis of the chlorine concentration in the solutions taken after one and one-half and after two hours showed no change from the measurements taken after one hour.

The method used to obtain measurements at the three temperatures involved establishment of equilibrium at each temperature, beginning with the lowest temperature. After achieving 25°C in the water bath, chlorine was sparged through the solutions for two hours to ensure saturation prior to sampling. Next the temperature was increased to 40°C and chlorine sparging was continued for one hour subsequent to temperature stabilization and prior to sampling. The same procedure was followed for measurements at 55°C.

Determination of Chlorine Solubility

Dissolved chlorine in the electrolyte exists in the form of several species according to the following reactions:

$$Cl_2\ (aq) + H_2O \rightleftharpoons HOCl + H^+ + Cl^-$$

$$Cl_2\ (aq) + Cl^- \rightleftharpoons Cl_3^-$$

Determination of these dissolved chlorine species was made by the standard iodometric procedure. To an excess of acidified potassium iodide solution, 10 ml of the test solution were added. The liberated iodine was titrated by a sodium thiosulfate solution. The sodium thiosulfate solution was standardized by using a primary potassium iodate solution as a standard.

RESULTS

This study was performed to quantify the effects of the following parameters on the solubility of chlorine:

Table 40-1

EXPERIMENTAL RESULTS OF CHLORINE SOLUBILITY MEASUREMENTS

Solution Composition (M)			Solution	Cl_2 Solubility (g/ℓ)		
$ZnCl_2$	KCl	NaCl	pH	25°C	40°C	55°C
2.5	2.00	0	0.15	2.5	1.6	1.1
1.5	2.10	0	0.46	2.7	1.7	1.1
0.5	2.20	0	0.68	3.1	1.9	1.2
2.5	4.00	0	0.15	2.2	1.4	1.0
1.5	4.22	0	0.24	2.3	1.5	0.9
1.0	4.43	0	0.29	2.3	1.5	1.2
2.5	2.00	2.00		1.9	1.3	0.9
1.5	2.10	2.10		2.0	1.4	0.9
1.0	2.20	2.20		2.1	1.5	1.0
2.5	3.01	2.00		1.7	1.2	1.0
1.5	3.50	2.11		1.9	1.2	1.0
2.5	0	2.00		2.2	1.5	1.0
1.5	0	2.12		2.5	1.6	1.1
0.5	0	2.23		2.7	1.7	1.1
2.5	0	3.99		1.7	1.2	0.8
1.5	0	4.24		1.8	1.2	0.8
1.0	0	4.41		1.8	1.2	0.8
2.5	1.00	1.01		2.2	1.6	1.1
1.5	1.05	1.05		2.5	1.7	1.1
0.5	1.11	1.12		2.8	1.8	1.1
2.5	1.00	2.00		2.0	1.4	1.0
1.5	1.06	2.12		2.2	1.5	1.0
0.5	1.11	2.22		2.3	1.5	1.0
3.0	0	0		2.8	1.8	1.2
3.0	0	0	-0.02	2.6	1.8	1.2
2.5	0	0	0.13	2.8	1.9	1.3
2.5	0	0	2.55	2.9	2.0	1.3
1.5	0	0	0.43	3.1	2.0	1.2
1.0	0	0	0.57	3.3	2.1	1.3
0.5	0	0	0.74	3.4	2.2	1.4
2.5	2.00	1.00	2.35	2.1	1.5	1.0
2.5	2.00	1.00	0.24	2.2	1.5	1.0
2.5	2.00	1.00	-0.03	2.1	1.5	1.0
2.5	2.00	1.00	-0.13	2.2	1.5	1.0
2.5	2.00	1.00	-0.22	2.2	1.5	1.1
2.5	2.00	1.00	-0.25	2.2	1.5	1.0

- Concentrations of potassium chloride and sodium chloride as supporting electrolytes.
- Concentration of zinc chloride, corresponding to different states of charge and discharge.
- Concentration of hydrochloric acid.
- Temperatures of 25°, 40°, and 55°C.

The experimental results on chlorine solubility obtained at ambient pressure are summarized in Table 40-1. These data are accurate to ±0.1 g/ℓ.

Under fully discharged conditions, the 2.5-3.0M chloride electrolytes used in the zinc-chloride battery typically have a pH in the range of 0.1-0.2. For the first two 500-milliliter test solutions prepared -- 2.5M $ZnCl_2$ + 2M KCl and 2.5M $ZnCl_2$ + 4M KCl -- the addition of 65 millimoles of hydrochloric acid (HCl) lowered their pH into this range. Hence, all subsequent test solutions were also made 0.13M in HCl.

Effect of Potassium Chloride on Chlorine Solubility

The change in chlorine solubility for pure $ZnCl_2$ and $ZnCl_2$ + 2.0M NaCl solutions as a function of potassium chloride concentration at the temperatures of 25°C, 40°C, and 55°C are illustrated in Figures 40-4 and 40-5. The resulting straight lines indicate that the decrease in chlorine solubility is proportional to the potassium chloride concentration for both the zinc chloride and the zinc chloride plus sodium chloride media. At any particular temperature, the zinc chloride concentration solely determines the slope of the linear relationships. The slope increases as the zinc chloride concentration decreases, indicating that the addition of potassium chloride decreases chlorine solubility more effectively at lower concentrations of zinc chloride.

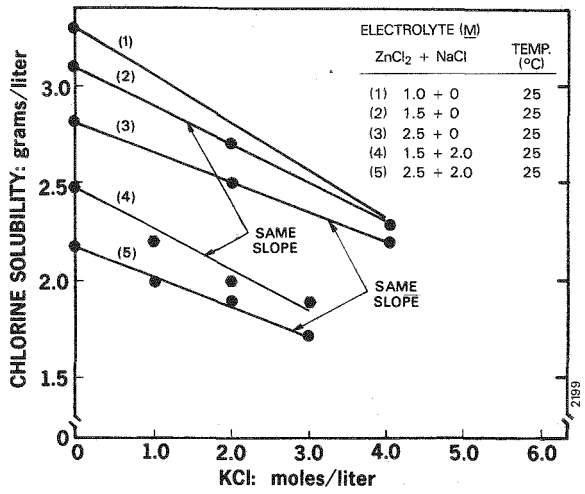

Figure 40-4. Effect of potassium chloride on chlorine solubility in zinc chloride and zinc chloride + sodium chloride solutions at 25°C.

Effect of Sodium Chloride on Chlorine Solubility

The addition of sodium chloride salts to the pure zinc chloride solution depresses the solubility of chlorine in a manner similar to that of adding potassium chloride salts to the solution. This effect is shown in Figure 40-6.

However, if potassium chloride is also present in the zinc chloride medium when sodium chloride is added, there is a greater decrease in chlorine solubility as the first mole of sodium chloride is added to the solution. The further addition of sodium chloride beyond one mole tends to depress chlorine solubility to a lesser extent. This phenomenon is illustrated in Figure 40-7.

Effect of Temperature on Chlorine Solubility

Consistent with the behavior of most soluble gases in a solution, chlorine solubility decreases with increasing temperature, as illustrated in Figures 40-8, 40-9, and 40-10. The plots as a

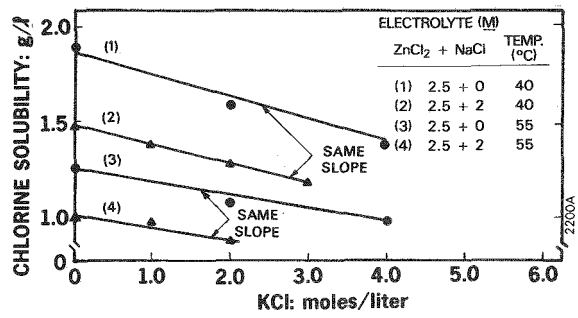

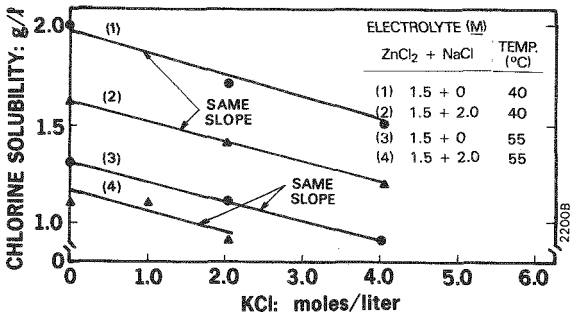

Figure 40-5 (a,b). Effect of potassium chloride on chlorine solubility in zinc chloride and zinc chloride + sodium chloride solutions at 40°C and 55°C.

general rule show that the solutions with relatively high chlorine solubilities also have higher temperature coefficients. Regardless of the solution composition, all solutions tested appear to approach a limiting chlorine solubility at 55°C of about 1 gram per liter (g/ℓ).

The chlorine solubility data for pure zinc chloride solutions as a function of temperature are plotted in Figure 40-10. As the zinc chloride concentration is increased, the slope of the line (solubility versus temperature), is somewhat lowered. Chlorine solubility versus zinc chloride concentration at various temperatures is shown in Figure 40-11. Zinc chloride suppresses the chlorine solubility, as expected. However, at elevated temperatures, the variation in chlorine solubility with zinc chloride concentration is relatively small compared to that at 25°C.

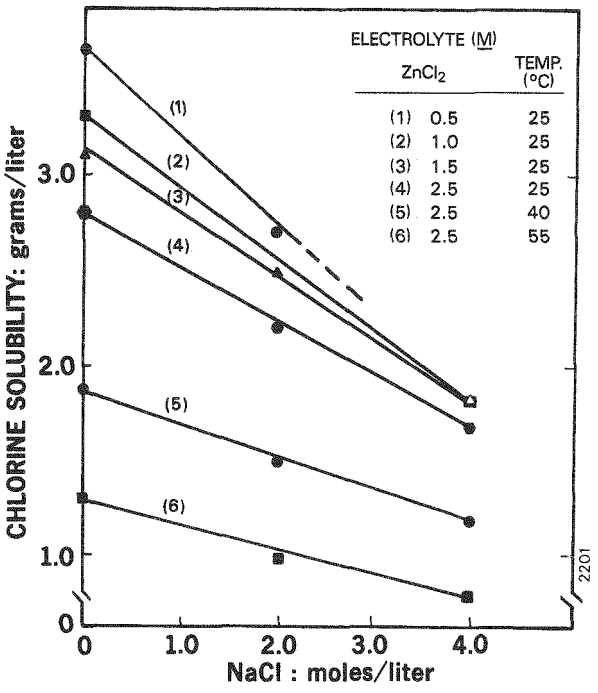

Figure 40-6. Effect of sodium chloride on chlorine solubility in a pure zinc chloride solution at 25°C, 40°C, and 55°C.

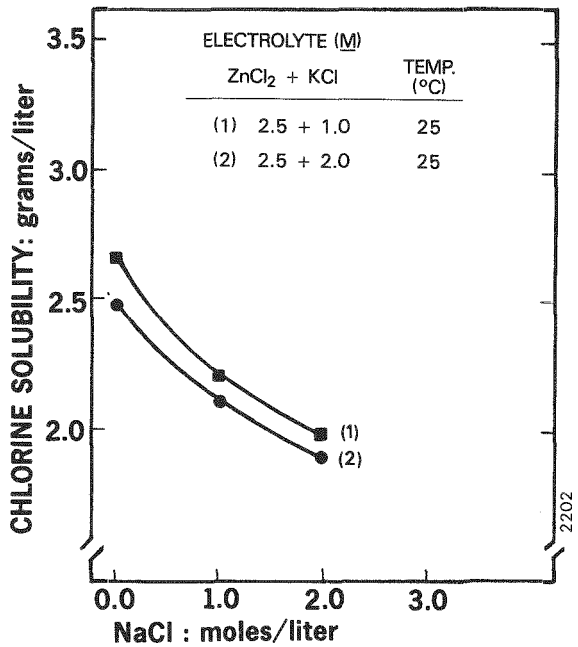

Figure 40-7. Chlorine solubility at 25°C when sodium chloride is added to zinc chloride + potassium chloride solution.

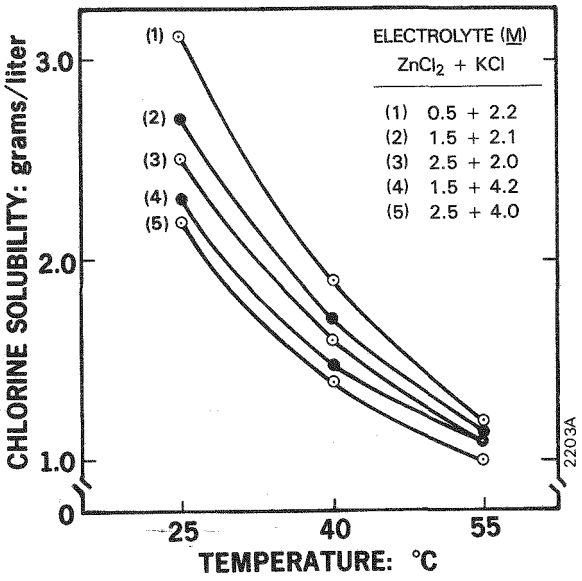

40-8 (a)

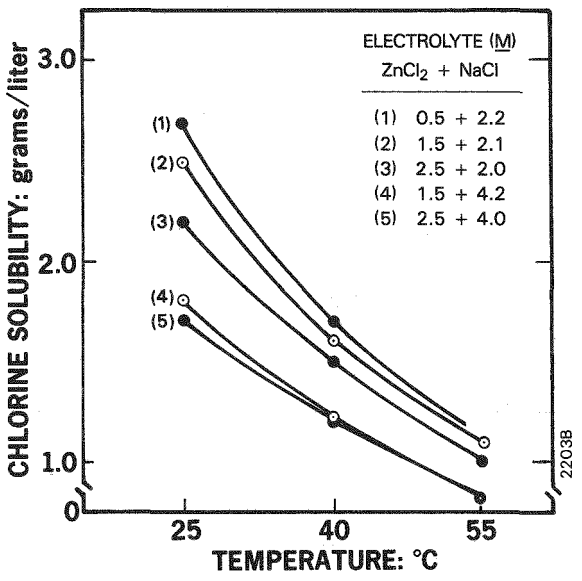

40-8 (b)

Figure 40-8 (a,b). Graphs depicting the decrease in chlorine solubility in various mixed-salt solutions as temperature increases.

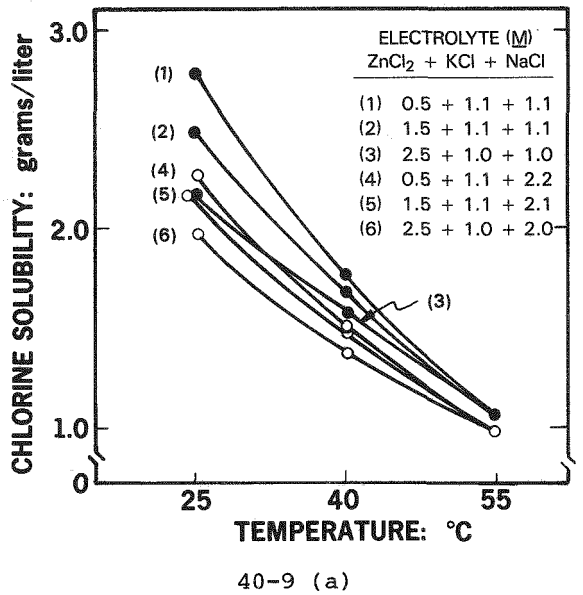

40-9 (a)

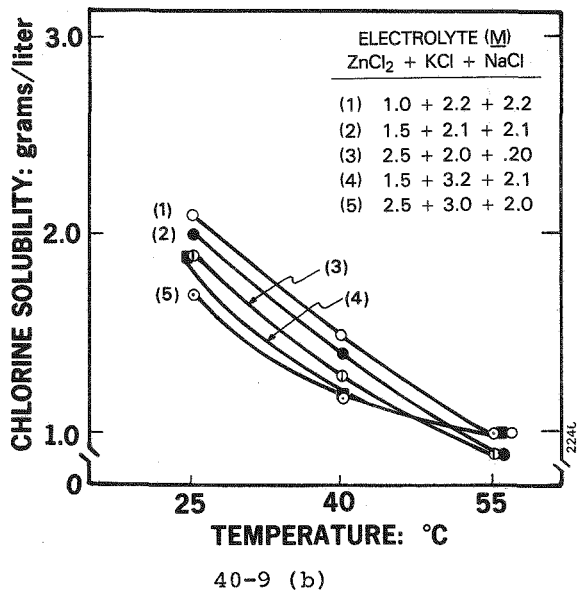

40-9 (b)

Figure 40-9 (a,b). Decreasing chlorine solubility in mixed-salt solutions as temperature increases.

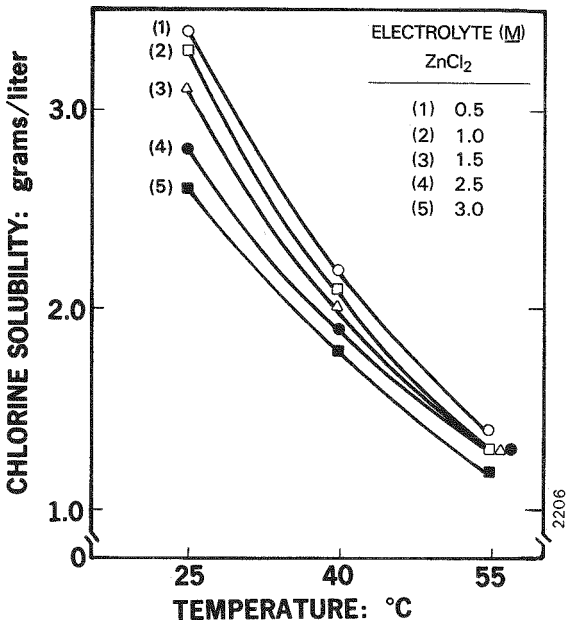

Figure 40-10. Graph depicting decrease of chlorine solubility with temperature increase in pure zinc chloride solutions.

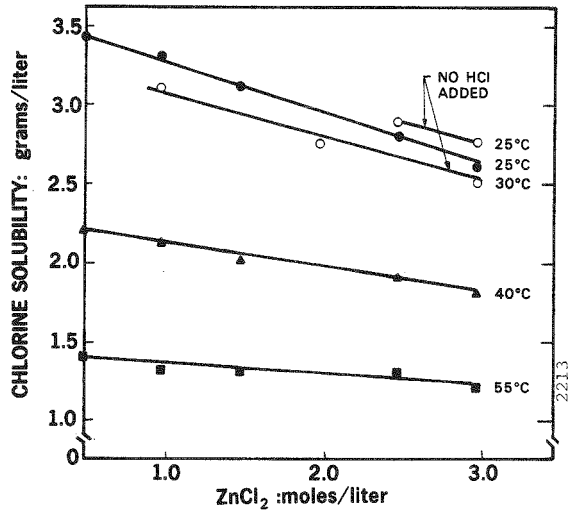

Figure 40-11. Chlorine solubility of acidified (0.13M HCl) zinc chloride at four temperatures.

Effect of Acidity on Chlorine Solubility

As one would expect, chlorine solubility in an acidified zinc-chloride solution decreases with increasing concentration of zinc chloride, as shown in Figure 40-11. Plots of the chlorine solubility at 25°C, for zinc chloride with no added hydrochloric acid, are also shown in Figure 40-11, as well as the results of an earlier EDA study made at 30°C. There is a slight decrease in chlorine solubility due to the presence of 0.13M hydrochloric acid.

The effect of acidity on the chlorine solubility for the solution 2.5M $ZnCl_2$ + 2M KCl + 1M NaCl, where supporting electrolytes are present, was also studied. With reference to the data listed in Table 40-1, the overall difference is within the 0.1 g/ℓ experimental error. Based on these data, addition of HCl does not affect chlorine solubility in mixed salt electrolytes.

Effect of Battery State-of-Charge on Chlorine Solubility

In Figures 40-12 and 40-13, plots are given of chlorine solubility as a function of zinc chloride concentration -- which corresponds to different stages of charge and discharge -- in eight different mixed electrolyte compositions. It can be seen that chlorine solubility increases with the depth of the charging process. The increase is greater for solutions with lower concentrations of supporting electrolytes and lower temperatures, and smaller for solutions with higher concentrations of supporting electrolytes and higher temperatures.

DISCUSSION

The results of this study indicate that the solubility of chlorine is inversely proportional to the concentration of both sodium chloride and potassium chloride in the electrolyte. For all mixed-electrolyte compositions evaluated, the concentration of zinc chloride has a similar effect on chlorine solubility. Individually, sodium chloride has the greatest effect on reducing the solubility of chlorine.

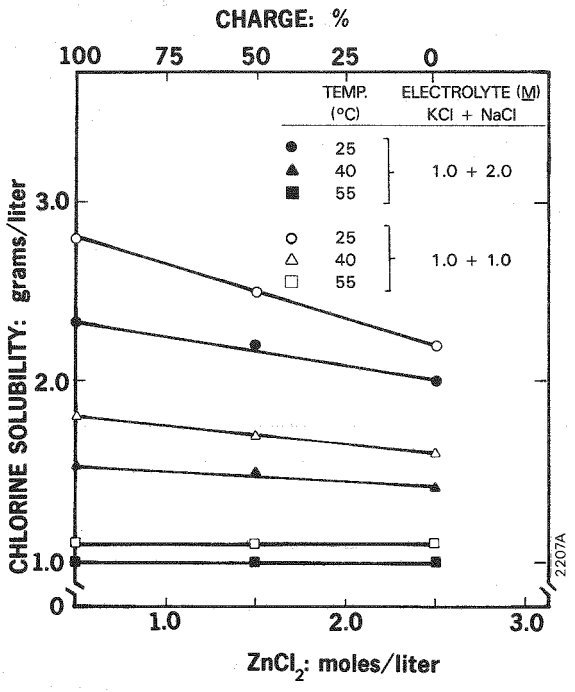

40-12 (a)

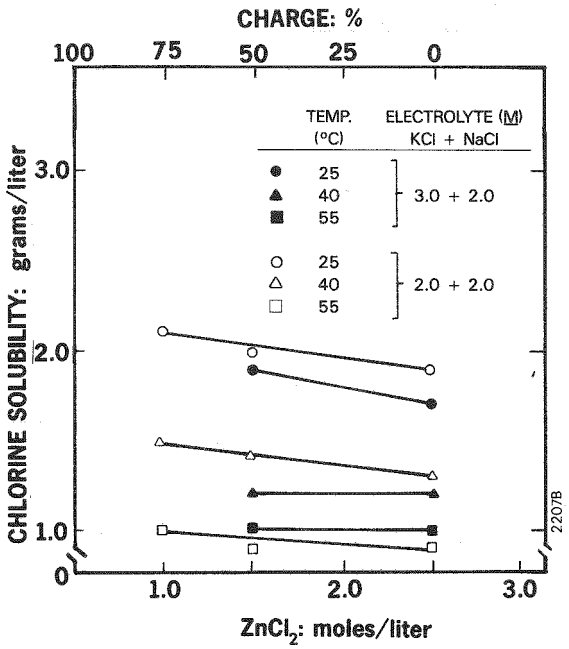

40-12 (b)

Figure 40-12 (a,b). Effect of battery state-of-charge (zinc chloride concentration) on chlorine solubility in four mixed-salt elctrolytes at three temperatures.

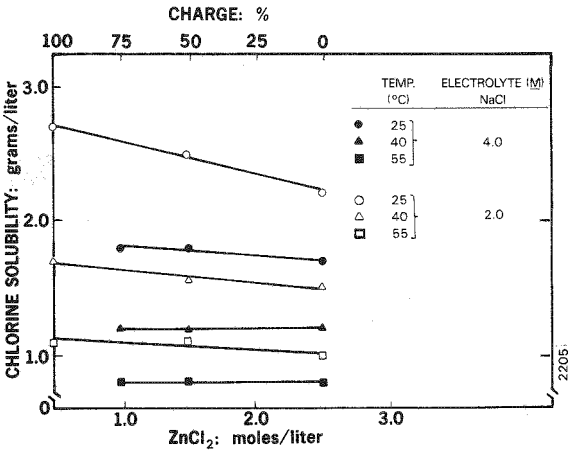

40-13 (a)

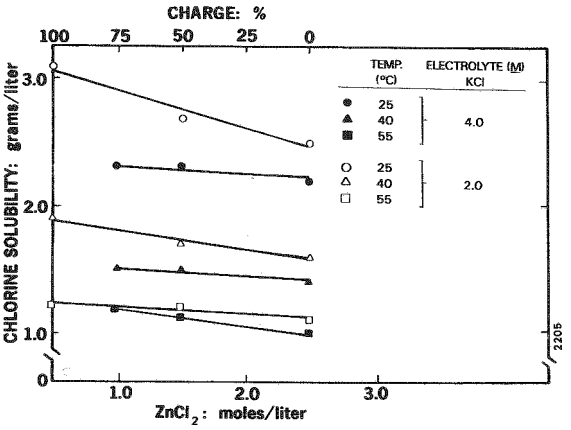

40-13 (b)

Figure 40-13 (a,b). Effect of battery state-of-charge on chlorine solubility in four mixed-salt electrolytes at three temperatures.

The effect of supporting electrolytes on reducing chlorine solubility are most significant at low temperature and low zinc chloride concentration. Their effect is minimized at elevated temperature, where all mixed-electrolyte compositions appear to approach the same chlorine solubility limit of 1 g/ℓ at 55°C.

These results suggest the use of ≥3M supporting electrolyte concentrations and elevated temperatures for the purpose of controlling chlorine solubility and thereby improving the coulombic efficiency of zinc-chloride cells and batteries. However, the apparent advantage in operating at elevated temperature, i.e., in the range of 50-55°C, is not realized due to the effect of temperature on the transport rate of dissolved chlorine to the zinc electrode. The increased diffusivity for dissolved chlorine and the reduced thickness of the diffusion boundary-layer, resulting from increasing the temperature, appear to counterbalance the effect of reduced chlorine solubility.

In terms of specifying optimal electrolyte compositions for use in the zinc-chloride battery, the results of this study can be combined with those of the study on solution conductivity (Section 38). Zinc chloride solutions of ≥3M supporting salts in the form of potassium chloride and sodium chloride have both high ionic conductivity and low chlorine solubility. This combination of mixed electrolytes should result in both higher voltaic and coulombic efficiencies.

CONCLUSIONS

1. Addition of potassium chloride lowers the solubility of chlorine in zinc chloride solutions linearly with potassium chloride concentration. The slope of the line is determined by the zinc chloride concentration.

2. Addition of sodium chloride lowers the chlorine solubility of zinc chloride solutions. For $ZnCl_2$ + KCl electrolytes, the rate of decrease of solubility decreases with NaCl concentration. Sodium chloride is more effective in reducing the chlorine solubility than potassium chloride.

3. As the temperature is raised, the chlorine solubility decreases. At 55°C for all mixed electrolytes the chlorine solubility reaches a limit of ∿1 g/ℓ.

4. Based on chlorine-solubility and conductivity data, zinc chloride electrolytes containing ≥3M (KCl + NaCl) salts should yield higher voltaic and coulombic efficiencies.

REFERENCES

1. W. L. Goodwin. "The Nature of Solutions." Trans. Roy. Soc. (Edin), 30, 1882, p. 587.

2. E. Olideri Mandella. "Sulla Solubilita Degli Alogeni Negli Idracide E. Sal I Alcaline Corrispendenti." Gazz. Chem. Ital., 50, 1920, p. 89.

3. T. R. Bott and S. Schulz. "Solubility of Chlorine in a Brine Solution at Different pH Values." J. Appl. Chem. (London), 17 (12), 1967, pp. 356-8.

4. F. Hine and S. Inuta. "Solubility of Chlorine in Hydrochloric Acid." Bull. Chem. Soc. Jap., 41 (1), 1968, p. 75.

5. N. Yokotu. "Solubility of Chlorine in Concentrated Sodium Chloride Solution." Kagaku Kogaku, 22, 1958, pp. 476-82.

6. M. S. Sherill and E. F. Izard. "The Solubility of Chlorine in Aqueous-Solutions of Chloride and the Free Energy of Trichloride Ion." J. Amer. Chem. Soc., 53, 1931, pp. 1667-74.

7. Development of High-Efficiency, Cost-Effective Zinc-Chlorine Batteries for Utility Peak Shaving, 1976. Palo Alto, Calif.: Electric Power Research Institute, March 1978. EM-710.

Section 41

ELECTROLYTE PROPERTIES: V. TRANSFERENCE NUMBERS OF ZINC

ABSTRACT

Migration of zinc-ion species affects the local zinc chloride concentration and solution density in the electrolyte layer adjacent to the zinc electrode and thereby influences natural convection at this electrode during both charge and discharge. This section presents experimentally measured transference numbers for ionic-zinc species in aqueous solutions containing 1.5-3m $ZnCl_2$ + 0-5m KCl + 0-3m NaCl + 0-0.4m HCl at 30°C using the Hittorf method. Negative transference numbers for zinc are obtained in most mixed-salt solutions with minimums of -0.2 to -0.3 occurring in the chloride ion concentration range of 6-8m. The data support the presence of anionic zinc complexes such as $ZnCl_3^-$ and $ZnCl_4^{2-}$, which account for the negative transference numbers.

INTRODUCTION

The zinc-chloride battery utilizes zinc-chloride electrolyte with the addition of supporting electrolytes such as potassium chloride, sodium chloride and hydrochloric acid. The purpose of the supporting electrolyte is mainly to improve the voltaic efficiency by increasing the conductivity, and to improve the coulombic efficiency by depressing the chlorine solubility. The operating characteristics of the battery, such as coulombic efficiency, voltaic efficiency and energy storage density do not bear a simple correlation with the composition of the electrolyte. Hence, determination of the various physical properties of the mixed electrolytes is essential. This section, which is the fifth in a series on electrolyte properties, deals with the transference numbers of zinc in the battery electrolytes.

The transference number of zinc indirectly affects the performance of the battery. The transference number of zinc affects the local concentration of zinc chloride near the zinc electrode during charge and discharge. The zinc chloride concentration at the surface affects the morphology of the zinc deposit and the magnitude of hydrogen evolution at the zinc electrode (1). In addition, the resultant density variations adjacent to the zinc surface cause natural convection which enhances the transport of dissolved chlorine to the zinc surface and lowers the coulombic efficiency of the battery (2,3). Therefore, the transference number of zinc in various mixtures of $ZnCl_2$ + KCl + NaCl + HCl solutions were measured under the practical range of compositions. It is also expected that these measurements will shed light on the complicated solution equilibria of zinc and chloride ions.

Several methods are available for the measurement of transference numbers in electrolyte solutions. These include Hittorf's method, direct moving boundary method, indirect moving boundary method, analytical boundary method, e.m.f. measurements using cell with transference, e.m.f. method using cell in force field, and isotope method. In the present work, the Hittorf method is used because of its direct and relatively simple approach. The Hittorf method is based on the con-

centration changes of the species concerned in the anode and cathode compartments after the passage of a known quantity of electricity. The Hittorf method (4) has been used since 1853 to measure transference numbers in dilute solutions (5), concentrated solutions (6) and in mixed electrolytes (5-9).

Even though the Hittorf method suffers from some limitations such as water transport, accuracy of analytical measurements, and electrode coulombic efficiency, it is still one of the most commonly used methods for the measurement of transference numbers of ions in concentrated solutions. The Hittorf method has been used to investigate systems such as mixtures of hydrochloric acid and potassium chloride (8), hydrochloric acid and sodium chloride (8), and potassium chloride and sodium chloride (7). Furthermore, Hittorf transference data are available for zinc-chloride solution at different concentrations and temperatures, and comparison can be made without required adjustment of the individual technique. Based on the above considerations, the Hittorf method was chosen for the measurement of the transference number of zinc in the various ($ZnCl_2$ + KCl + NaCl + HCl) electrolytes being considered for the zinc-chloride battery.

Transference numbers of zinc in zinc-chloride solutions are reported by Harris and Parton (10) for up to 13m $ZnCl_2$ concentration at 25° and 35°C. The data are presented in Figure 41-1 and the transference number of zinc ions decreases from +0.4 to -0.6 where minimum can be observed at 8-9m $ZnCl_2$. The transference number of zinc changes sign at about 2m $ZnCl_2$. The negative sign of the transference number of zinc indicates that at higher $ZnCl_2$ concentrations most of the zinc is in the form of anionic complexes:

$$Zn^{2+} + nCl^- = ZnCl_n^{2-n} \qquad (41\text{-}1)$$

where n varies from 1 to 4. The most common complex is believed to be $ZnCl_4^{2-}$.

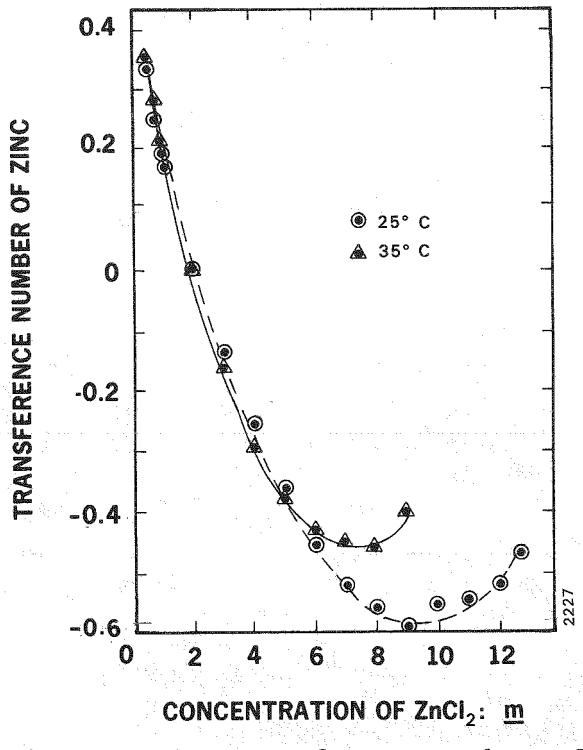

Figure 41-1. Transference number of zinc in zinc-chloride solutions, after Harris and Parton (10).

EXPERIMENTAL

Cell Design

A sketch of the experimental Hittorf cell is shown in Figure 41-2. The design is essentially that of MacInnes (5,8). The cell was designed in such a way as to minimize disturbing effects such as natural convection, diffusion, local heating, and electro-osmosis. The cell allows easy access to samples of different compartments of the cell, especially the junction compartment.

The cell is made of Pyrex glass, and the internal diameter of the cell is 8 mm. The volume of each compartment is 17 cm^3 allowing about 5 cm^3 for the silver/silver chloride electrode. This provides roughly 10-15% change in zinc concentration upon passing 0.03 faraday of electricity without significant mixing between compartments. In fact, mixing became noticeable only when the

silver/silver chloride electrode had been regenerated over five times. The anode and cathode compartments are made of graduated tubing which allows direct reading of the compartment volume without weighing the entire compartment.

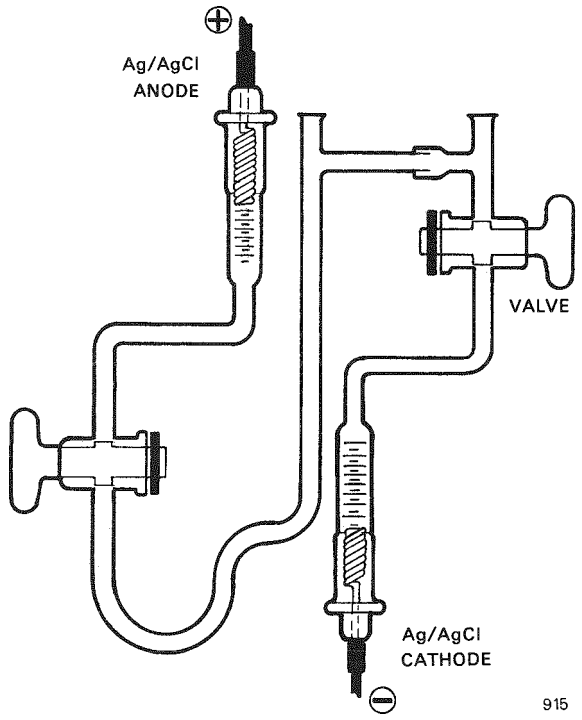

Figure 41-2. Cell for measurement of transference numbers based on Hittorf mehtod. The cell is molded after the apparatus of MacInnes (5, 8).

Materials

All chemicals are reagent grade and were used without further purification. The zinc-chloride stock solution was prepared by direct reaction of chlorine gas with high- purity zinc metal (New Jersey Zinc, 99.99%). Hydrochloric acid, potassium chloride and sodium chloride were supplied by Fisher Scientific Company, and the silver wire (99.999%) by Alfa Ventron.

Analysis for Zn^{2+} and H^{+} ions

The analysis of the electrolytes in the anode, cathode, and middle compartments was done by titration. Hydrogen-ion concentration was determined potentiometrically by sodium carbonate using pH meter (Orion Research Model 701 A). Subsequent titration of zinc was carried out upon addition of ammonia/ammonium chloride buffer and Eriochrome Black T indicator. The latter analysis is accurate to within 0.2% under the experimental conditions. All concentrations are reported on molality basis (mole/kg water) unless otherwise stated. All measurements were made at constant temperature 30.0°C $\pm$ 0.1°C.

The concentrations in the middle compartment, and in the compartments between the anode and the middle, and between the cathode and the middle, were analyzed only for comparison among themselves, and this serves as an indication of the degree of mixing between compartments.

The Silver/Silver Chloride Electrode

The use of two zinc electrodes was considered first. However, because the coulombic efficiency of zinc electrode was in the 98-100% range and was not reproducible enough, the use of two silver/silver chloride electrodes was adopted successfully. The electrodes were prepared from 1 mm diameter silver wire. Because of the need for large surface area, 80 cm of wire was wound into compact coils which served as the electrodes. In most experiments, the length of the experiments was limited by the usable amount of silver chloride on the electrode. The silver/silver chloride electrodes were prepared by anodizing the silver coils in zinc chloride solution. The quantity of electricity passed was twice the number of coulombs passed during the transference experiments.

Measurement of Quantity of Electricity

The quantity of electricity passed during the transference experiment was determined by multiplying the constant current by the time of electrolysis. A constant current of 40 mA was main-

tained by Precision Current Source Model CS-111 (North Hills Electric Company, Inc.). The current was calibrated against a silver coulometer which consisted of a silver anode and concentric platinum cylinder cathode. The weight of the silver electrodeposited on the platinum electrode was used to measure the actual number of faradays passed. The average time of each experiment was about 24 hours.

Theoretical Calculation of the Transference Number of Zinc From Experimental Data

i) Without water transport: Zinc balance at anode is given by

$$\Delta n_{A,Zn} = - t_{Zn}\, Q/F \qquad (41\text{-}2)$$

where

$$\Delta n_{A,Zn} = 2\,(m_i - m_{f,A})\, W/1000 \qquad (41\text{-}3)$$

Zinc balance at cathode:

$$\Delta n_{C,Zn} = t_{Zn}\, Q/F \qquad (41\text{-}4)$$

where

$$\Delta n_{C,Zn} = 2\,(m_{f,C} - m_i)\, W/1000 \qquad (41\text{-}5)$$

where m_f and m_i are the final and initial molality of zinc, respectively, W is the weight of water and Q/F is faradays of electricity passed. Subscript A and C represent anode and cathode, respectively.

ii) With water transport: The equations are presented under the assumption that the hydration number of zinc is larger than that of chloride.

Zinc balance at anode is given by

$$\Delta n_{A,Zn} = - t_{Zn}\, Q/F \qquad (41\text{-}6)$$

where

$$\Delta n_{A,Zn} = 2(m_i\, W/1000 - m_{f,A}\, W/1000 - m_i X/1000) \qquad (41\text{-}7)$$

where X is the weight of water transferred.

Zinc balance at cathode

$$\Delta n_{C,Zn} = t_{Zn}\, Q/F \qquad (41\text{-}8)$$

where

$$\Delta n_{C,Zn} = -2\,(m_i\, W/1000 - m_{f,C}\, W/1000 - m_i X/1000) \qquad (41\text{-}9)$$

Since

$$(m_i - m_{f,A}) = -\,(m_i - m_{f,C}) \qquad (41\text{-}10)$$

therefore

$$-\Delta n_{A,Zn} = n_{C,Zn} \qquad (41\text{-}11)$$

and the transference number from the anode should be equal to that calculated from the cathode.

Neglecting the water transport results in slightly larger transference number for zinc, and substantial differences between anodic and cathodic transference numbers can be due only to differences of the coulombic efficiencies of the anode and the cathode.

RESULTS AND DISCUSSION

The transference numbers of zinc have been calculated for the cathode and anode compartments according to equations 41-2 through 41-5. The effects of changes in HCl, NaCl, and KCl concentrations are reported in mixed $ZnCl_2$ electrolytes over the practical range of operation. The concentrations are reported in molality. The data points in the figures for mixed electrolytes are characterized by parenthesis (x,y), where x and y are the molalities of KCl and NaCl, respectively.

The effect of change in concentration of hydrogen ion on the transference number of zinc, t_{Zn}, is presented in Figure 41-3. It should be noted that the concentration of hydrogen ion at the anode in most cases was negligible,

while at the cathode, it increased by almost 100%. This is due to the large transference number of hydrogen ion. This change in hydrogen ion concentration is unavoidable in transference measurements of zinc species. In order to measure the transference number of hydrogen ion, separate experiments should be conducted where the quantity of electricity is much smaller. The transference number of zinc is very low and changes from positive to negative at an HCl concentration of 0.3m.

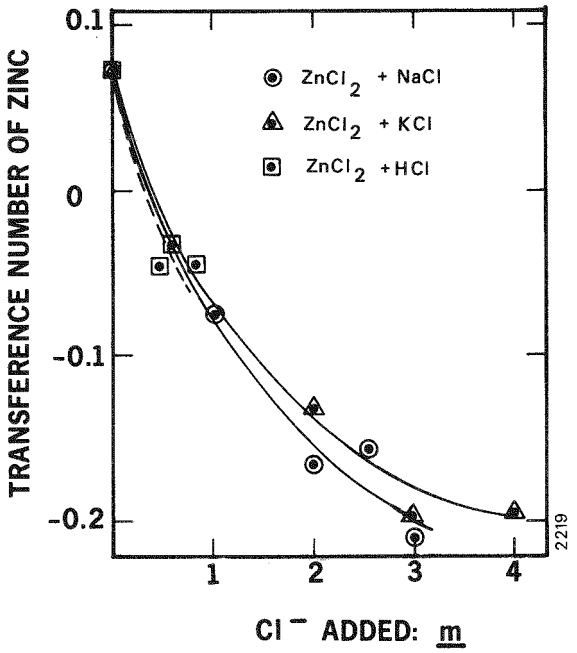

Figure 41-3. Effect of change in concentration of supporting electrolytes on t_{Zn} in 1.500m $ZnCl_2$ electrolyte.

The effect of change in concentration of KCl and NaCl on t_{Zn} is also plotted in Figures 41-3. The transference number of zinc generally decreases with increasing concentration of the supporting electrolytes. The effects of HCl, NaCl, and KCl are compared in Figure 41-3. It is observed that the effect of supporting electrolyte on t_{Zn} depends only on the total chloride content and is almost independent of the nature of the cation below 1m Cl^- concentration and only very weakly dependent at higher Cl^- concentration. The negative sign of the transference number of zinc also indicates that at higher chloride content, most of the zinc is in the form of anionic complexes, such as $ZnCl_4^{2-}$. The results suggest that all comparative effects of supporting electrolytes should be made on a constant chloride basis and the chloride derived from the hydrochloric acid cannot be neglected.

At high chloride concentration, the decrease in the transference number of zinc is smaller in the presence of KCl than in NaCl, indicating that the mobility of K^+ is higher than Na^+, a well-documented phenomenon, which is due to the higher solvation of the Na^+ ion. At high electrolyte concentrations, the anionic zinc chloride complex probably forms ion-pairs with available cations. Also, the zinc chloride complexes can form polymeric networks in the solution.

The effect of KCl on the transference number of zinc in $ZnCl_2$ + KCl, with and without HCl added, is shown in Figure 41-4. It can be seen that at a constant chloride content, t_{Zn} is higher in the adjusted pH = 0.15 solution.

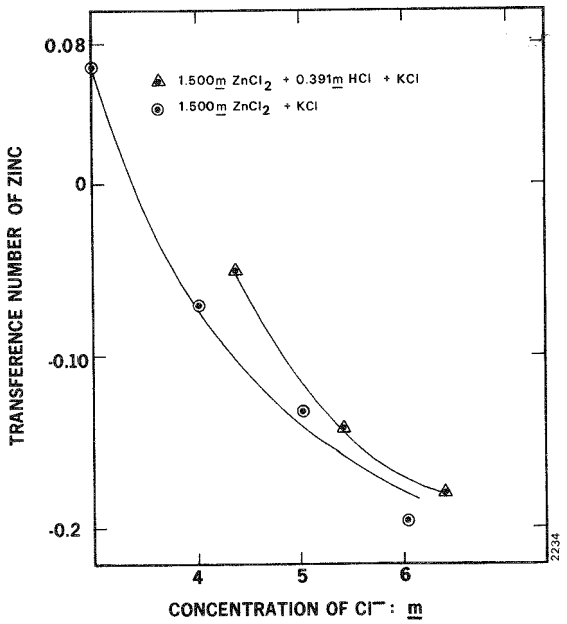

Figure 41-4. Effect of change in HCl concentration on t_{Zn} in electrolytes containing 1.500m $ZnCl_2$ + KCl.

This is probably due to higher mobility of H_3O^+ compared to K^+ ions.

The effect of NaCl and KCl on t_{Zn} in electrolytes containing 1.500m $ZnCl_2$ + 0.391m HCl (pH = 0.15) are compared in Figures 41-5 and 41-6. In general, the transference number of zinc initially decreases with increasing total chloride content. Then, it starts to increase at high Cl^- concentrations. A minimum is observed at total chloride content of about 6-7m. The transference number of zinc is generally higher when the concentration of sodium ion is larger than that of potassium ion under the same total chloride content. The increase in t_{Zn} upon the addition of NaCl, as shown in Figure 41-5 (IV), is due to the fact that the total chloride content is already high and lies in the region where t_{Zn} increases with addition of more chloride.

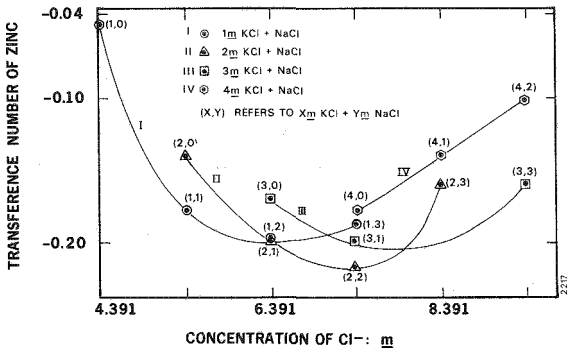

Figure 41-5. Effect of change in NaCl concentration on t_{Zn} in electrolyte containing 1.500m $ZnCl_2$ + 0.391m HCl + NaCl + KCl.

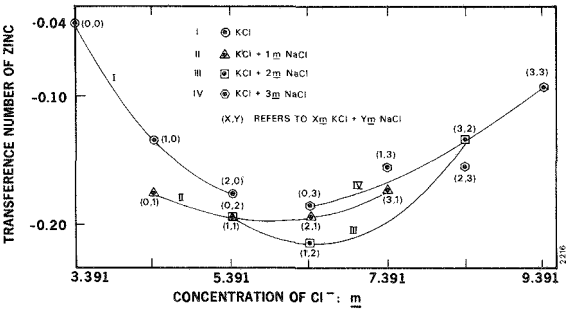

Figure 41-6. Effect of change in KCl concentration on t_{Zn} in electrolyte containing 1.500m $ZnCl_2$ + 0.391m HCl + NaCl + KCl.

The effects of $ZnCl_2$ concentration on the transference number of zinc in mixed electrolytes containing various concentrations of HCl, NaCl, and KCl are presented in Figures 41-7 through 41-9. In all cases, a steady decrease in the transference number of zinc can be observed upon the addition of $ZnCl_2$ up to 3.2m $ZnCl_2$. In the presence of higher concentrations of supporting electrolyte, the transference number of zinc decreases faster with $ZnCl_2$ concentration. This behavior is again related to the formation of anionic chloro-complexes of zinc.

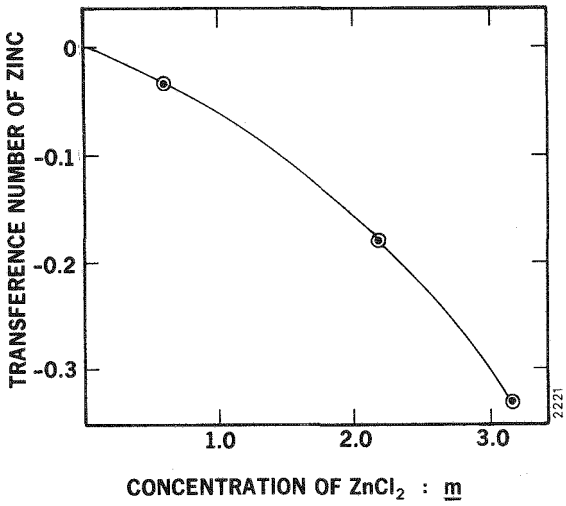

Figure 41-7. Effect of change in $ZnCl_2$ concentration on t_{Zn} in electrolyte containing $ZnCl_2$ + 2.500m KCl + 0.391m HCl.

CONCLUSIONS

The transference number of zinc, t_{Zn}, in mixed $ZnCl_2$-KCl-NaCl-HCl electrolytes has been measured. It varies around the zero value and depends on the total chloride content of the solution. The transference number generally decreases and becomes negative with the addition of supporting electrolytes. This trend is believed to be due to the shift in the solution equilibrium toward the formation of anionic zinc-complexes, such as $ZnCl_4^{2-}$. The effect of various cations on the transference number of zinc is noticeable only at high concentrations. How-

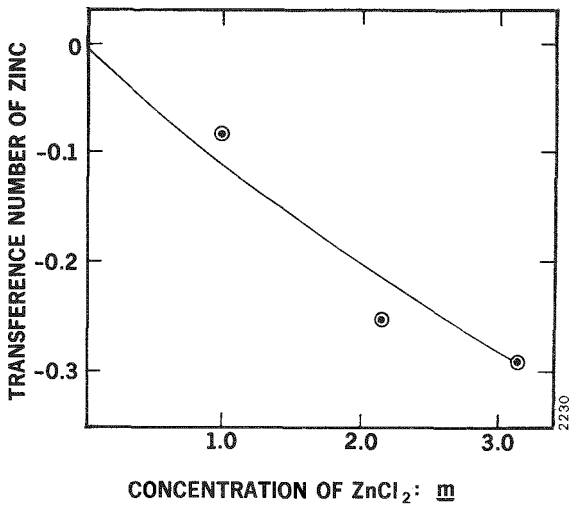

Figure 41-8. Effect of change in $ZnCl_2$ concentration on t_{zn} in electrolyte containing $ZnCl_2$ + 3.75m KCl + 2.50m NaCl + 0.130m HCl.

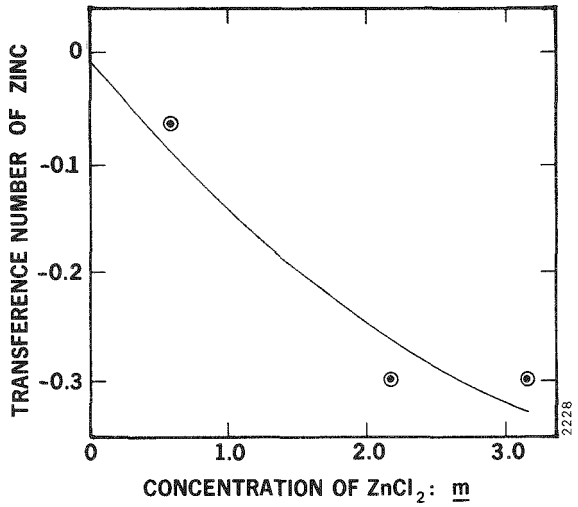

Figure 41-9. Effect of change in $ZnCl_2$ concentration on t_{zn} in electrolyte containing $ZnCl_2$ + 5.00m KCl + 1.25m NaCl + 0.184m HCl.

ever, this effect is small. The relative change in the transference number of zinc with the addition of the supporting electrolyte increases in the order: HCl > KCl > NaCl. This is due to the fact that as the mobility of the cation increases, the relative contribution of the zinc ion to the overall ionic transport becomes smaller.

Negative transference number of zinc implies that the concentration gradient of zinc-chloride at the zinc surface is higher because the migration flux opposes the diffusion flux. This phenomenon has some impact on the magnitude of natural convection at the zinc electrode during both charge and discharge. The significance of this contribution should be evaluated and the transference number of zinc should be considered in the selection of the optimal electrolyte composition for the battery.

REFERENCES

1. D. Kralik. "Hydrogen Evolution and Nodular Zinc Growth in the Zinc-Chloride Battery" M.S. Thesis, Wayne State University, 1978.

2. G. L. Henriksen, S. Kodali, J. Jorne and C. J. Warde. "Zinc Electrode Current Efficiency in Zinc-Chlorine Hydrate Batteries: I. Theoretical Aspects." 155th Meeting of the Electrochemical Society, Abs. 378, Boston, May 1979.

3. S. Kodali, J. Jorne and G. L. Henriksen. "Zinc Electrode Current Efficiency in Zinc-Chlorine Hydrate Batteries: III. Natural Convection During Electrodeposition." 155th Meeting of the Electrochemical Society, Abs. 375, Boston, May 1979.

4. W. Hittorf. Pogg. Ann., 89, 77, Germany, (1853).

5. D. A. MacInnes J. of American Chemical Society, 47, 1922 (1925).

6. M. D. Monica, G. Petrella, A. Sacco, and S. Bufo. Electrochim Acta, 24, 1013 (1979).

7. P. J. Van Rysselberge. J. of American Chemical Society, 55, 790 (1933).

8. D. A. MacInnes, T. Shedlowsky, and L. G. Longsworth. Chem. Rev., 13, (1933).

9. R. L. Kay. "Transference Number Measurements" in Techniques of Electrochemistry. ed. A. J. Salkind, and E. Yeager, New York: Wiley-Interscience, 1973, Vol. 2, pp. 61-116.

10. A. C. Harris and H. N. Parton. Trans. Faraday Soc., 35, 758 (1938).

Section 42

COULOMBIC EFFICIENCY: I. THEORETICAL BACKGROUND

ABSTRACT

For a voltaic efficiency of 0.87-0.88 usable coulombic efficiencies $\geq$0.85 are required in order to achieve the electrochemical energy efficiency target for commercialization of $\geq$0.75. Modeling studies are conducted to quantitatively predict the effects of operational and geometrical parameters on the coulombic efficiency of zinc-chloride cells during charge. This section establishes that three fluid-convection sources combine to control the mass-transfer limited reaction of dissolved chlorine with electrodeposited zinc, i.e., the major source of coulombic inefficiency. These three sources are: (a) forced convection of electrolyte through the porous-graphite chlorine electrodes and upwards between the electrodes, (b) natural convection due to zinc ion depletion at the zinc electrode, and (c) bubble-induced convection due to chlorine gas evolution at the chlorine electrode. Using typical operating conditions and relationships from the literature, fractional inefficiencies of 0.03-0.07 are calculated for individual contributions. Accordingly, none of the sources appears to be dominant. This initial investigation forms the basis for additional studies in which refined relationships are developed for the operational and geometrical conditions typically employed in zinc-chloride cells.

INTRODUCTION

In the development of the zinc-chloride battery for the electric-utility load-leveling application, EDA has established a fractional energy efficiency target of $\geq$0.65 for the battery plant. On the basis of previous studies (1), this translates to an electrochemical energy efficiency target of $\geq$0.75 for the battery. In order to meet this target, the voltaic and coulombic efficiencies of the battery must be $\geq$0.87, assuming an equal split. At practical current densities, voltaic efficiencies of 0.90 have been demonstrated (2). Coulombic efficiencies in the mid-to-upper 0.80 range are still required in order to meet or exceed the electrochemical energy efficiency target.

Coulombic efficiency can be defined as the ratio of delivered capacity (Ah) from the cell or battery during discharge to the input capacity during charge. Mathematically, the fractional usable coulombic efficiency (ε_c) can be expressed as:

$$\varepsilon_c = \frac{\text{Usable delivered capacity (Ah)}}{\text{Capacity charged (Ah)}} \qquad (42\text{-}1)$$

The usable coulombic efficiency can be split into a charge coulombic efficiency (ε_c) and a discharge coulombic efficiency (ε_c) where:

$$\varepsilon_c = \varepsilon_c^c . \varepsilon_c^d \qquad (42\text{-}2)$$

The charge and discharge coulombic efficiencies can be expressed in terms of average corrosion current densities (i_{cor}) and applied current densities (i_a) during charge and discharge, where the superscripts, c and d, refer to charge and discharge, respectively:

$$\varepsilon_c^c = \frac{i_a^c - i_{cor}^c}{i_a^c} \qquad (42\text{-}3)$$

$$\varepsilon_c^d = \frac{i_a^d}{i_a^d + i_{cor}^d} \qquad (42\text{-}4)$$

In the early 1970s, a study was performed at EDA to develop an empirical relationship for the average corrosion current density in zinc-chloride cells which utilized flow-by chlorine electrodes. Figure 42-1 illustrates this flow-by mode of operation, and contrasts it to the present flow-through mode of operation. In the flow-by mode of operation a single chlorine-electrode plate is utilized. Electrolyte is supplied to the cell at the bottom of the inter-electrode cell gap and forced vertically upwards between the chlorine and zinc electrodes. In the flow-through mode of operation, a pair of chlorine-electrode plates are assembled to form an intra-electrode cavity utilizing top, bottom, and side framing to seal the cavity. Electrolyte is supplied to this cavity and forced through the porous-graphite chlorine-electrode plates into the inter-electrode cell gaps formed on either side of the chlorine-electrode pair. Again the electrolyte is forced upwards between the chlorine and zinc electrodes in the inter-electrode gap.

The study performed on flow-by chlorine-electrode cells indicated a linear dependence of the corrosion current density on the concentration of chlorine dissolved in the electrolyte on both charge and discharge. The average corrosion current density was also found to depend on the temperature and flow velocity of the electrolyte between the electrodes. The resultant empirical relationship for the average corrosion current density can be presented as:

$$i_{cor} = K \cdot C_o \cdot C_v \cdot C_t \qquad (42\text{-}5)$$

where K is a constant which is different for charge and discharge, C_o is the concentration of dissolved chlorine in

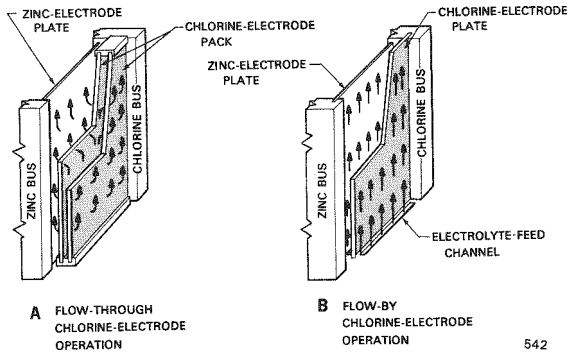

Figure 42-1. Schematic illustration of flow-through and flow-by modes of chlorine-electrode operation. Note that in the flow-through mode of operation, chlorinated electrolyte is forced through the porous-graphite chlorine-electrode substrates, while in the flow-by mode of operation it is forced past the faces of the chlorine-electrode substrate.

the bulk electrolyte, C_v is the electrolyte velocity coefficient, and C_t is the temperature coefficient.

Prior work at EDA has indicated that the chlorine concentration and electrolyte temperature were coupled such that $C_o \cdot C_t$ is approximately constant when temperature was used to effect a change in the chlorine concentration, while all other conditions were held constant. Eq. 42-5 also suggests that the corrosion current density is due entirely to the reaction of dissolved chlorine with electrodeposited zinc:

$$Zn(s) + Cl_2(aq) = ZnCl_2(aq) \qquad (42\text{-}6)$$

Recent work by Kim and Jorne has shown that the rate-determining step in this reaction is the mass transfer of dissolved chlorine to the zinc electrode (3).

In 1977 this model was applied to data obtained from a 400-Wh zinc-chloride cell utilizing flow-through chlorine electrodes. For the geometrical and operational conditions employed in these tests, the values for the normalized corrosion current density (K) during charge and discharge were 1.9 and

1.1 $(mA/cm^2)/(g/\ell)$, respectively. It was postulated at that time that the difference was due to different convective effects during charge and discharge.

Based on these EDA studies, it was decided to pursue the development of a more fundamental coulombic-efficiency model for flow-through chlorine-electrode cells. In this preliminary analytical study: (a) the sources of coulombic inefficiency during charge are presented, (b) contributions to the major source are analyzed using relationships from the literature, and (c) the results of the analysis are presented and discussed in terms of developing a desired model.

SOURCES OF COULOMBIC INEFFICIENCY

In zinc-chloride cells, there are essentially four independent sources that cause coulombic inefficiency. They can be summarized as follows:

- Internal electrical short-circuits caused by zinc dendrites.
- Chemical and/or electrochemical formation of hydrogen at the zinc electrode.
- Electrochemical corrosion couples on the zinc electrode or extensions of it.
- Corrosion of electrodeposited zinc by chlorine dissolved in the electrolyte.

Electrolyte formulation studies, performed over the last several years (4,5), have resulted in the identification of electrolyte additives and conditions which control zinc-dendrite and hydrogen formation at acceptably low levels. In a similar manner, edge dendrites and electrochemical corrosion couples can be controlled by the proper design of the cell, as well as the proper selection of electrolyte and operating conditions. As was the case for the flow-by chlorine-electrode cells, the major source of coulombic inefficiency in flow-through chlorine-electrode cells is the direct chemical reaction of dissolved chlorine with metallic zinc.

As stated previously, it has been shown that the rate-determining step in this reaction is the mass transfer of dissolved chlorine to the zinc electrode (3). In a completely stagnant cell this transport would occur by molecular diffusion across the cell gap. The rate of this reaction can be expressed in terms of the corrosion current density as:

$$i_{cor} = \frac{nFD\ (C_o - C_w)}{d} \qquad (42\text{-}7)$$

where i_{cor} is the limiting current density for chlorine transport by molecular diffusion $(amps/cm^2)$, n is the number of electrons transferred, 2, in the reaction, F is Faraday's constant (96,500 coulombs/equivalent), D is the diffusion coefficient for dissolved chlorine $(1x10^{-5}\ cm^2/sec)$, C_o is the bulk concentration of dissolved chlorine $(moles/cm^3)$, C_w is the concentration of dissolved chlorine at the electrode-electrolyte interface (zero), and d is the inter-electrode cell gap (cm).

For practical cell gaps (0.2-0.4 cm) and chlorine concentrations $(1.4x10^{-5}$ to $2.8x10^{-5}\ moles/cm^3)$ the corrosion current density would be in the range of 0.14-0.54 mA/cm^2. At an applied current density of 35 mA/cm^2 during charge, the coulombic inefficiency due to molecular diffusion is in the range of 0.004-0.015. In an actual operating zinc-chloride cell, however, the observed corrosion density is an order of magnitude larger than that for molecular diffusion across the gap. It is speculated that mass-transfer enhancement of dissolved chlorine to the zinc electrode occurs due to fluid motion (convection) in the inter-electrode cell gap.

Figure 42-2 schematically illustrates the affect of fluid motion on the diffusion-layer thickness (δ) for dissolved chlorine. Without convection, δ is equal to the inter-electrode cell gap (d). The diffusion-layer thickness

decreases with increasing convection resulting in much steeper chlorine concentration gradient. If δ is substituted for d in Eq. 42-7, it can be seen that the corrosion current density is inversely proportional to the diffusion-layer thickness.

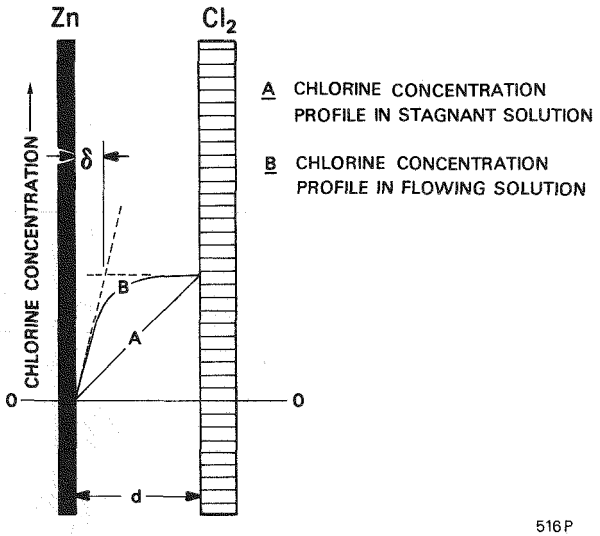

Figure 42-2. Effect of fluid motion on the chlorine concentration profile and the diffusion boundary-layer thickness (δ). In the absence of fluid motion the boundary-layer thickness equals the inter-electrode cell gap (δ=d).

The possible sources of convection in the inter-electrode cell gap during charge can be summarized as follows:

- Forced Convection of bulk electrolyte due to the forced circulation of electrolyte through the porous-graphite chlorine electrodes and vertically upwards between the zinc and chlorine electrodes.
- Natural Convection of electrolyte in the layer adjacent to the zinc electrode due to the electrolyte-density gradient created by the depletion of ionic-zinc species.
- Bubble-Induced Convection established by the anodic generation of chlorine gas at the porous-graphite chlorine electrode.
- Thermally-Induced Convection created by differential heating or cooling within the inter-electrode cell gap.

Both thermally-induced and natural convections occur as a result of establishing electrolyte-density variations in the inter-electrode cell gap. The relative magnitude of these variations established by these two processes provides a basis for determining their respective contributions to the total fluid motion and mass transfer of dissolved chlorine.

Thermally-Induced Electrolyte-Density Gradient

The influence of thermal effects on inducing convection is determined by the differential heating or cooling that occurs at or immediately adjacent to the zinc electrode. There are three thermal processes occurring simultaneously at this location during charge. These processes are:

- Heat Generation due to the enthalpy of the chemical corrosion reaction (ΔH_{cor}) which occurs at the electrode- electrolyte interface.
- Thermodynamic Cooling due to the entropy of the electrochemical half-cell reaction ($\Delta S_{electrochem}$):

$$Zn^{++}(complex) + 2e \longrightarrow Zn(s)$$

- Heat Generation due to the total polarization (η) at and immediately adjacent to the zinc electrode.

The combined influence of these effects determines the net heat-release or absorption rate and therefore the extent of thermally-induced convection.

The heat generation rate due to the corrosion reaction was calculated on the basis of a reaction rate corresponding to 3.3 mA/cm^2 corrosion current density and a ΔH_{cor} of 112 kCal/mole at 25°C. The thermodynamic cooling rate

due to the entropy of the electrochemical half-cell reaction was calculated on the basis of a reaction rate corresponding to 33 mA/cm^2 applied current density and a $T\Delta S_{electrochem}$ of 10.6 kCal/mole at 25°C. The entropy of the half-cell reaction ($\Delta S_{electrochem}$) was calculated on the basis of absolute entropy values (S^o) for $Zn^{++}_{(aq)}$ and $Zn_{(s)}$ of -25.5 Cal/deg-mole and 10 Cal/deg-mole, respectively (6). Although the absolute entropy value for Zn^{++} (complex) may differ from that of $Zn^{++}(aq)$, it should not dramatically affect the resultant value for $\Delta S_{electrochem}$. Finally, a rather large cathodic polarization, of 40 mV at the zinc electrode, was assumed in the calculation of the heat generation rate due to this source.

Table 42-1 summarizes the calculated heat-release and absorption rates for the individual processes. The net heat release rate of 2.1 Cal/cm^2-hr can account for less than a 2°C temperature rise in a 0.3 mm-thick electrolyte-boundary layer. This in turn can account for a local change in electrolyte density of only 0.002 g/cm^3. This local electrolyte density variation is very small in comparison to that created by natural convection, as will be demonstrated below.

Table 42-1

HEAT RELEASE AND ABSORPTION RATES

Source	Q(Cal/cm^2-hr)
ΔH_{cor}	-7.5
$\Delta S_{electrochem}$	6.5
η	-1.1
Net	-2.1

ANALYSIS OF MAJOR INEFFICIENCY SOURCES

Figure 42-3 illustrates the electrolyte flow patterns in the inter-electrode cell gap that would be established by the individual convective sources if they existed by themselves. For both forced and natural convections during charge, there is an upward flow of electrolyte adjacent to the zinc electrode. For bubble-induced convection, there is a downward flow of electrolyte adjacent to the zinc electrode. In all cases, the resultant fluid motion enhances the mass transport of dissolved chlorine to the zinc electrode.

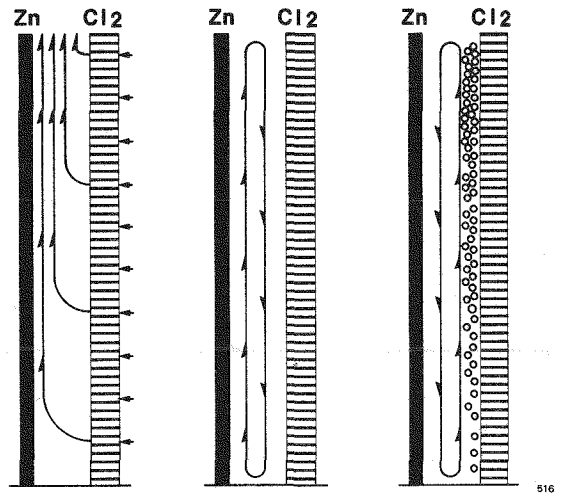

Figure 42-3 (A-C). Vertical sections of cell illustrating the flow patterns created by each convective source. Note that A and B reinforce one another with an upward flow of electrolyte adjacent to the zinc electrode, while C opposes A and B with a downward flow in that region.

Forced Convection

The imposed flow of electrolyte through the porous-graphite chlorine-electrode substrate results in the flow pattern illustrated in Figure 42-3(A). In the analysis of the contribution due to this source, fully-developed laminar flow was used to approximate the flow in the inter-electrode gap. The rate of mass transfer of chlorine to the zinc electrode, expressed in terms of a limiting (corrosion) current density, resulting from this type of convection is given by Newman (7):

$$i_{cor}^{c} = 0.9783 \frac{nFDC_o}{s_i} \left(\frac{\bar{U}_x}{dDx} \right)^{1/3} \qquad (42\text{-}8)$$

where S_i is the stoichiometric coefficient for chlorine in the reaction (2), U_x is the average local flow velocity of electrolyte in the cell gap (cm/sec) at height x, and x is the height along the electrode (cm).

The average vertical velocity of electrolyte in the cell gap at height x is given by:

$$\bar{U}_x = \left(\frac{x}{d}\right) V_o \qquad (42\text{-}9)$$

where V_o is the apparent velocity of electrolyte through the porous-graphite electrode, i.e., the flow rate per projected unit area of the porous electrode. Substitution of Eq. (42-9) into Eq. (42-8) gives:

$$i^c_{cor} = 0.9783 \frac{nFDC_o}{S_i} \left(\frac{V_o}{Dd^2}\right)^{1/3} \qquad (42\text{-}10)$$

Inspection of Eq. 42-10 reveals that the corrosion current density due to forced convection alone is independent of electrode height. However, it is dependent on cell gap -- a halving of the gap value results in an increase of 60% in corrosion current density. Under typical operating conditions, the i^c_{cor} value is about 2.4 mA/cm^2. (See Results and Discussion).

Natural Convection

Natural convection of electrolyte in the layer adjacent to the zinc electrode is created by the depletion of zinc-ion species from this layer which reduces its density with respect to the bulk electrolyte. The flow induced by this process results in the flow pattern illustrated in Figure 42-3(B). Several methods for estimating the interfacial-electrolyte density are reported in the literature (7,8). For the assumed electrolyte composition -- 2M $ZnCl_2$ + 3M KCl + 2M NaCl -- the analysis is complex due to variations in K^+, Na^+, and zinc-species concentrations. The simplified approach used here to estimate the interfacial-electrolyte density incorporates the following assumptions:

(a) Non-complexed zinc ions, i.e., Zn^{++}(aq) only

(b) Ionic mobilities of all cationic species (Na^+, K^+, and Zn^{++}) are the same.

(c) The Cl^- concentration at the electrode-electrolyte interface is the same as in the bulk electrolyte, i.e., 9M.

Using these assumptions the relative transport numbers of the three cationic species were calculated by:

$$t_i = \frac{Z_i C_i}{\sum_{j=1}^{3} Z_j C_j} \qquad (42\text{-}11)$$

where t_i is the transport number of species i, Z_i is the number of charges on species i, C_i is the concentration of species i, Z_j is the number of charges on each cationic species present, and C_j is the concentration of each cationic species present in the bulk electrolyte.

At limiting current density, the interfacial concentration of Zn^{2+} at the zinc electrode is zero. The resulting K^+ and Na^+ concentrations at limiting current would be 5.4M and 3.6M, respectively. The corresponding interfacial-electrolyte density is 1.200 g/cm^3. Using the diffusion coefficient of Zn^{2+} obtained by Kim and Jorne (10) and Grashof, Sherwood, and Schmidt numbers, a limiting current density (i_L) for zinc deposition of 0.227 A/cm^2 was calculated. Using this value, the Zn^{2+} interfacial concentration (C_w) at the normal current density (i^c_a) of 0.035 A/cm^2 was calculated using the expression,

$$C_w = C_O \cdot \left(1 - \frac{i^c_a}{i_L}\right) \qquad (42\text{-}12)$$

where C_w and C_o are Zn^{++} concentrations at the zinc electrode and in the bulk, respectively. The corresponding Zn^{2+} interfacial concentration under these conditions is 1.7M. The corresponding K^+ and Na^+ interfacial concentrations are 3.4M and 2.2M and the interfacial-electrolyte density is 1.280 g/cm^3. The difference in the bulk and interfacial electrolyte density is found to be 0.08 g/cm^3.

The Sherwood number (Sh) which describes the rate of mass transfer of a species under limiting current to a vertical electrode can be utilized to calculate a corrosion current density due to natural convection:

$$i^c_{cor} = \frac{nFDC_o}{h} \quad (Sh) \qquad (42\text{-}13)$$

where h is the electrode height (cm).

The Sherwood number is usually expressed in terms of the mass-transfer coefficient (k_m):

$$Sh = \frac{k_m h}{D} \qquad 42\text{-}(14)$$

For a vertical electrode, in either an infinite medium or a vertical slot geometry, it has been shown that the general correlation for the Sherwood number under natural convection conditions is given by:

$$Sh = a\ (Sc \cdot Gr)^b \qquad (42\text{-}15)$$

where a and b are empirical constants, Sc is the Schmidt number, and Gr is the Grashof number.

The Schmidt and Grashof numbers are defined as:

$$Sc = \nu/D \qquad (42\text{-}16)$$

$$Gr = g\frac{\Delta\rho}{\rho} \cdot \frac{h^3}{\nu_2} \qquad (42\text{-}17)$$

where ν is the kinematic viscosity (poise), $\Delta\rho$ is the density difference between the bulk electrolyte and the electrolyte adjacent to the zinc electrode (g/cm^3), ρ is the density of bulk electrolyte (g/cm^3), and g is the gravitational constant (cm/sec^2).

The values of a and b for our particular geometry, however, are not available. For a vertical electrode in an infinite medium and under laminar flow conditions, the values of a and b are 0.66 and 0.25, respectively (11). For the interfacial concentrations of 1.7M Zn^{2+}, 3.4M K^+, 2.2M Na^+, and 9M Cl^- (calculated above) the Grashof and Schmidt numbers are 1.22×10^7 and 581, respectively. These yield a Sherwood number for chlorine mass transport of 192. The corrosion current density calculated under these conditions is 1.0 mA/cm^2.

Bubble-Induced Convection

Bouyancy-induced convection, similar to that of natural convection at the zinc electrode, is created by the anodic generation of chlorine-gas bubbles at the porous-graphite chlorine electrode. Figure 42-3(C) illustrates the flow pattern induced by this source. A search of existing literature provided no satisfactory relationship for the enhancement of chlorine transport due to this source. Its contribution is approximated here using the relationship developed by Mohanta and Fahidy (12) for the effect of anodic gas evolution on the mass transfer of a species to the cathode during copper deposition:

$$\Delta(Sh) = \alpha \cdot (Re_g) \cdot \beta \cdot (Sc)^{0.25} \cdot (h/d) \cdot \gamma \qquad (42\text{-}18)$$

where $\Delta(Sh)$ is the increase in the Sherwood number and Re_g is the Reynolds number based on gas velocity. For their geometry and conditions, the values of α, β, and γ were 3.09, 0.77, and 0.33, respectively. Using Eq. 42-13 and -18, and these values for α, β, and γ, a corrosion current density due to bubble-induced convection was estimated at 1.1 mA/cm^2.

RESULTS AND DISCUSSION

For a specific set of conditions, the contributions from the individual convective sources were calculated using the previously discussed relationships. The conditions used were:

Design Parameters

- Electrode height (h) = 10 cm
- Inter-electrode gap (d) = 0.2 cm

Operational Parameters

- Electrolyte flow velocity (V_o) = 0.03 cm/sec
- Bulk chlorine concentration (C_o) = 2×10^{-5} mole/cm^3
- Applied current density (i_a^c) = 0.035 A/cm^2
- 2M $ZnCl_2$ + 3M KCl + 2M NaCl electrolyte at 40°C

Table 42-2 summarizes the results of these calculations.

Table 42-2

INDIVIDUAL CONVECTIVE-SOURCE CONTRIBUTIONS TO COULOMBIC INEFFICIENCY

Convective Source	i^c_{cor} (mA/cm^2)	Fractional Inefficiency
Forced	2.4	0.069
Natural	1.0	0.029
Bubble-Induced	1.1	0.031

The results suggest that none of the convective sources is dominant, despite the fact that the contribution from forced convection is a factor of 2 larger than the individual contributions from the other two sources. Using the above-described relationships from the literature, which are not directly applicable to the zinc-chloride cell geometry and conditions, an order of magnitude difference in the individual contributions would be required to establish a dominant source. The contribution from forced convection is the only value for which experimental data are available for comparison (5). The experimental data obtained at 30°C suggests a normalized corrosion current density of 1.3 (mA/cm^2)/(g/ℓ) due to forced convection at an electrolyte flow velocity of 0.03 cm/sec. Eq. 42-10 predicts a normalized corrosion current density of 1.7 (mA/cm^2)/(g/ℓ) due to this rate of forced convection at 40°C. Using a ratio of the temperature coefficients established in accordance to Eq. 42-5, to adjust the predicted value to 30°C, results in a normalized corrosion current density of 1.2 (mA/cm^2)/(g/ℓ). This value compares favorably to the experimental value. The individual contributions from natural and bubble-induced convections are more difficult to check experimentally.

In view of the apparent fact that all three sources of convection contribute significantly to the transport of dissolved chlorine to the zinc electrode, it appears necessary to combine their individual contributions in order to develop a satisfactory mathematical model. Initially, one might consider direct summation of the individual contributions. This results in a corrosion current density during charge of 4.5 mA/cm^2, which is larger than that observed experimentally under the assumed conditions. The predicted corrosion current density should not exceed the measured corrosion current density, due to the complicating factors of increasing zinc-plate roughness, decreasing cell gap, etc., which occur experimentally.

A simple approach which accounts for the opposing flow of bubble-induced convection during charge is the algebraic summation of the individual contributions, where the sign of the bubble-induced contribution is negative. In a similar manner the sign of the natural convection contribution during discharge would also be negative, due to a downward movement of higher density electrolyte in the layer immediately adjacent to the zinc electrode. Using this approach, the normalized corrosion current densities during charge and discharge are predicted to be 1.6 and 1.0 $(mA/cm^2)/(g/\ell)$, respectively. These values agree reasonably well with those previously measured experimentally and reported earlier for 400 Wh zinc-chloride cells -- 1.9 and 1.1 $(mA/cm^2)/(g/\ell)$ for charge and discharge, respectively. Also, the ratio of charge-to-discharge values agrees quite well -- 1.6 predicted versus 1.7 obtained experimentally. Although no claims are made concerning the validity of this simple approach, it does provide qualitative agreement with the limited experimental data. Perhaps most significant, however, is the establishment of a plausible explanation for the discrepancy observed between the normalized corrosion current densities during charge and discharge.

Upon completion of this initial analytical study, concurrent programs were established to continue the development of a mathematical model for quantitatively predicting the effects of operational and geometrical parameters on coulombic efficiency. The next five sections -- Sections 43-47 -- review these programs. They involve experimental approaches for refining the individual convective-source expressions for EDAs cell geometry and operating conditions. In addition, studies were performed to determine the combined effects of these three convective sources on the coulombic efficiency during charge.

REFERENCES

1. Development of the Zinc-Chlorine Battery for Utility Applications. Palo Alto, Calif.: Electric Power Research Institute, April 1979. EM-1051.

2. A. F. Laethem and G. E. Sussman. "Activation of Porous-Graphite Chlorine Electrodes for Zinc-Chlorine Hydrate Batteries." 154th Meeting of the Electrochemical Society, Abs. 73, October 1978.

3. J. T. Kim and J. Jorne. "Mass Transfer of Dissolved Chlorine to a Rotating Zinc Hemisphere in $ZnCl_2$ Solutions." J. Electrochem. Soc., 125, 89-94 (1978).

4. Development of the High-Efficiency, Cost Effective, Zinc-Chlorine Batteries for Utility Peak-Shaving, 1976. Palo Alto, Calif.: Electric Power Research Institute, March 1978. EM-711

5. Development of the Zinc-Chlorine Battery for Utility Applications. Palo Alto, Calif.: Electric Power Research Institute, April 1979. EM-1051.

6. F. T. Wall. Chemical Thermodynamics. 2nd Edition. W. H. Freeman and Company. 1965.

7. J. Newman. Electrochemical Systems. New York: Prentice-Hall, Inc., 1973.

8. C. W. Tobias, M. Eisenberg, and C. R. Wilke. "Diffusion and Convection in Electrolytes - A Theoretical Review." J. Electrochem. Soc., 99, (1952).

9. J. R. Selman and J. Newman. "Free-Convection Mass Transfer with a Supporting Electrolyte," J. Electrochem. Soc., 118, (1971).

10. J. T. Kim. Ph.D. Thesis. Wayne State University, 1978.

11. C. R. Wilke, M. Eisenberg, and C. W. Tobias. "Correlation of Limiting Currents and Free Convection Conditions." J. Electrochem. Soc., 100, (1953).

12. S. Mohanta and T. Z. Fahidy. "The Effect of Anodic Bubble Formation on Cathode Mass Transfer Under Natural Convection Condition." J. App. Electrochem. 7, 235-38 (1977).

Section 43

COULOMBIC EFFICIENCY: II. EFFECT OF FORCED CONVECTION ON CHLORINE TRANSPORT

ABSTRACT

The convective transport of dissolved chlorine to the zinc electrode determines the coulombic efficiency of zinc-chloride cells. In this section, the contribution due to forced convection is investigated experimentally using a cell with a segmented zinc electrode. In the absence of applied current, chlorinated electrolyte is circulated through the cell. Weight loss data are obtained for cell gaps in the range of 0.25-0.50 cm and flow rates in the range of 1-6 cm^3/cm^2-min. Results obtained over the bulk of the electrode surface compare favorably with the mathematical model for fully-developed laminar flow in a cumulative flow channel. The model and the data indicate that forced convection accounts for 40-50% of the total chlorine transport rate to the zinc electrode of a cell during charge.

INTRODUCTION

In the zinc-chloride battery one of the active materials, chlorine, is stored in a separate compartment and chlorine-saturated electrolyte is circulated through the battery stack in order to assure the adequate supply and removal of chlorine at the porous graphite electrode during discharge and charge, respectively. This forced convection of electrolyte during the discharge period minimizes the mass transfer overpotential and improves the voltaic performance of the chlorine electrode. Similarly, it enhances the transport of zinc ion-rich electrolyte to and away from the zinc electrode. However, via this process dissolved chlorine also gets transported to the zinc electrode where the two react chemically, resulting in coulombic efficiency losses (1). This adverse effect is especially critical during the charging process and limits the charge coulombic efficiency and the overall energy efficiency.

There are two other sources of fluid motion in the interelectrode gap:

- Natural Convection, due to the density variation of the electrolyte generated by depletion of zinc ions adjacent to zinc electrode (2,3).
- Bubble-induced Convection, due to uneven distribution of electrochemically evolved chlorine bubbles on the chlorine electrode (2).

Earlier work at EDA (2) suggested that no single convective mechanism was responsible for the total coulombic inefficiency of the cell. The contribution of each source to the overall rate of chlorine transfer to the zinc electrode is significant, as discussed in Section 42. In order to establish a mathematical model for the overall corrosion current, it is necessary to study each mechanism separately. The superimposition of the three mechanisms is probably non-linear due to opposing flow interactions (2). However, identifying and measuring the individual convections separately is the first step in understanding the overall convective transport of chlorine in the inter-electrode gap.

This section is the second in the series of sections on coulombic efficiency and deals with the effect of forced convection on the mass transport of dissolved chlorine to the zinc electrode. In Section 42, the theoretical analysis of the three convective mechanisms was based on literature data.

In the present section a more detailed analysis of forced convection, directly applicable to the EDA zinc-chloride battery, is presented. Experiments were designed to simulate a situation where only forced convection exists. To this end, experiments were carried out in the absence of applied current to eliminate bubble-induced convection and to minimize natural convection. Two phenomena -- the enthalpy of the corrosion reaction and the zinc-chloride formed in this reaction -- will have minor and opposing effects on the interfacial electrolyte density which could induce a minor amount of natural convection. This contribution is second-order in these experiments and quite small in comparison to the forced convection.

MODEL DEVELOPMENT

Nomenclature

The following nomenclature is used in the development and discussion of a mathematical model which describes the mass transport of chlorine to the zinc electrode under forced convection.

a constant

b constant

C_b bulk concentration [mole/cm^3]

d interelectrode gap [cm]

d_h equivalent hydraulic diameter [cm]

D diffusion coefficient [cm^2/sec]

F Faraday's constant 96,487 [coulombs/equiv.]

F_g geometrical factor

h height [cm]

i_{cor} corrosion current density [mA/cm^2]

$i_{cor(local)}$ local corrosion current density [mA/cm^2]

k mass transfer coefficient [cm/sec]

n number of electrons

S_i stoichiometric coefficient

t time [sec]

U velocity [cm/sec] in the x direction

V_o apparent velocity through the porous graphite [cm/sec] in the y direction

X height [cm]

X_e entrance length [cm]

y Distance from the zinc electrode [cm]

GREEK SYMBOLS

ν Kinematic viscosity [cm^2/sec]

ρ density [g/cm^3]

DIMENSIONLESS NUMBERS

Sh Sherwood number, $\frac{kd}{D}$

Sh_{av} Average Sherwood number

Re Reynolds number, Ud/ν

Sc Schmidt number, ν/D

Mathematical Model

The convective diffusion of dissolved chlorine to the zinc-electrode determines the rate of corrosion and consequently, the coulombic efficiency of the battery (1). The forced convection of the electrolyte represents one of the three convective mechanisms which enhance the transport of dissolved chlorine to the zinc-electrode.

The fluid mechanics of the forced convection is presented in Figure 43-1. The chlorinated electrolyte is uniformly fed through the porous graphite electrode and then flows upward in the inter-electrode gap. The flow in the inter-electrode gap is somewhat unique in that the average velocity increases linearly with the height and reaches its maximum at the top of the cell.

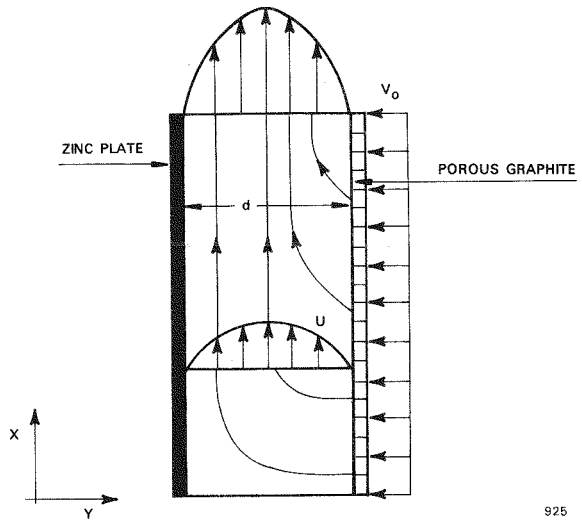

Figure 43-1. Schematic illustration of electrolyte flow pattern and velocity profile in the inter-electrode gap due to forced convection.

The velocity distribution inside the gap can be determined by solving the continuity and momentum equations for a two-dimensional incompressible flow (4). A closed-form analytical solution to this problem, however, is not possible due to nonlinearity of the mass and momentum conservation equations. The assumption of fully-developed laminar flow in a cumulative flow channel is therfore adopted.

If the flow in the inter-electrode gap is assumed to be a fully developed laminar flow between two parallel plates, then the average rate of mass transfer of dissolved chlorine to the electrode is given by (5):

$$Sh_{av} = 1.62\ [(F_g)\ (Re)\ (Sc)\ d_h/h]^{1/3} \qquad (43\text{-}1)$$

where F_g is a geometrical factor given by $F_g = 1.5$ for infinite parallel flat plates, h is the electrode height and d_h is the hydraulic diameter which is equal to twice the inter-electrode gap, $d_h = 2d$.

The rate of mass transfer of dissolved chlorine is given by (5):

$$Sh_{av} = 1.85 \left[(Re)\ (Sc)\ \frac{2d}{h} \right]^{1/3} \qquad (43\text{-}2)$$

and the average corrosion limiting current is:

$$i_{cor} = 1.467\ \frac{nFDC_b}{S_i} \left(\frac{U}{dDh} \right)^{1/3} \qquad (43\text{-}3)$$

Because the flow in the inter-electrode gap is cumulative, the average velocity in the gap U is a linear function of the height h:

$$U = \left(\frac{h}{d} \right) V_o \qquad (43\text{-}4)$$

where V_o is the apparent velocity through the porous electrode. Substituting Eq. 43-4 in Eq.43-3 gives

$$i_{cor} = 1.467\ \frac{nFDC_b}{S_i} \left(\frac{V_o}{Dd^2} \right)^{1/3} \qquad (43\text{-}5)$$

Equation 43-5 reveals that the corrosion current density for the forced convection case is independent of the electrode height and is inversely proportional to $d^{2/3}$. This result, although based on a simplified assumption, reveals that in a cumulative flow channel, under laminar conditions, the limiting current distribution is uniform. This is a unique situation of a flow system uniformly accessible to mass transfer. Similar property can be found only in the rotating disk and the rotating cylinder electrodes.

EXPERIMENTAL

The local and average corrosion currents due to forced convection alone were determined by measuring weight losses of zinc plates exposed to a circulation of chlorinated zinc-chloride solution. The single cell consisted of a flow-through porous graphite (PG-113, Union Carbide) and a flat zinc plate, 10 x 10 cm, (New Jersey Zinc, 99.99%). The weight of the zinc plate was measured before and after circulating chlorinated 1.5M $ZnCl_2$ solution under various operating conditions. The average corrosion current was calculated according to Faraday's law.

In some experiments, a segmented zinc plate was used in order to measure the local distribution of the corrosion current. The segmented zinc plate, made of ten horizontal strips 1.0 cm wide, was placed facing the porous graphite, and the weight loss of each segment was measured. The cell with the segmented zinc plate is shown in Figure 43-2, and the associated flow circuit is shown in Figure 43-3. The cell, constructed of Kynar, was clamped together and placed in a large glass jar which served as the electrolyte sump. The chlorine-saturated electrolyte was circulated from the sump into the cell by a pump (Micropump Corporation) and back to the sump by overflowing it above the zinc plate. The temperature was maintained at 35°C±1°C by a constant temperature bath (Haake E52). The electrolyte flow rate was measured by a Brook flowmeter (R-6-15-B tube size) which was calibrated at different temperatures and electrolyte compositions with an accuracy of ±5%.

The electrolyte consisted of 1.5M zinc-chloride, and the pH of the solution was adjusted at pH = 0.5-0.7 by adding HCl. The solution was saturated with chlorine by sparging chlorine gas in the electrolyte sump. The solubility of chlorine at 35°C in 1.5M zincchloride solution is about 2.25 g/ℓ. The chlorine concentration was checked every fifteen minutes by taking 1 cm^3 sample, adding it to a KI solution and titrating it with 0.01 N $Na_2S_2O_3$, using starch as an indicator.

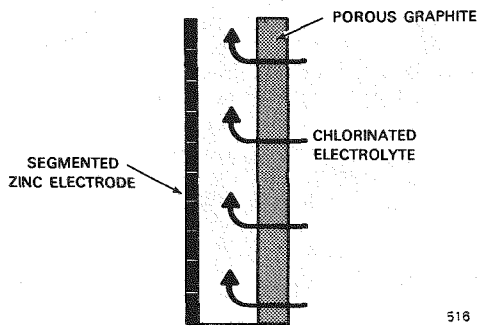

Figure 43-2. Schematic illustration of the inter-electrode gap showing the segmented zinc electrode used to study the corrosion current distribution along the height of the electrode.

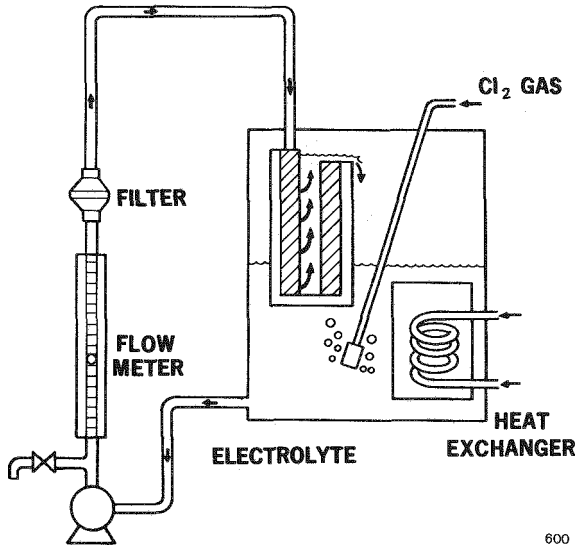

Figure 43-3. Schematic diagram of the experimental apparatus used to study forced convection. Flow through the cell was controlled using a speed controller on a small capacity gear pump.

RESULTS AND DISCUSSION

Average Corrosion Rate

The average corrosion current density (mA/cm^2) was calculated from the weight

loss of the zinc (mg/cm^2 sec) using Faraday's law. The effects of flow rate and cell gap on average corrosion current density are shown in Figure 43-4. Raising the flow rate or decreasing the cell gap both result in increasing the average velocity in the cell gap and, consequently, the corrosion current density.

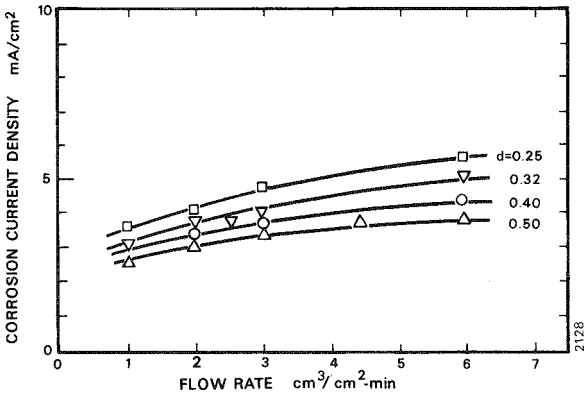

Figure 43-4. Effect of flow rate on the average corrosion current density. Increasing the flow rate or decreasing the cell gap increases the average corrosion current density.

A comparison between the experimental results and the theoretical model is shown in Figure 43-5. Considering the general correlation for convective mass transport to be:

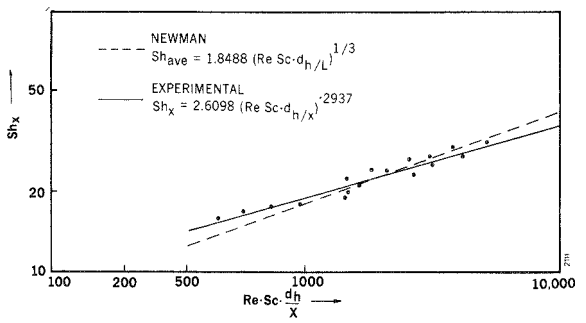

Figure 43-5. Comparison between experimental mass transfer rates and theoretical model based on fully-developed laminar flow.

$$Sh = a\,[(Re)\,(Sc)\,d_h/x)]^b \qquad (43\text{-}6)$$

The constant a and the exponent b were found from Figure 43-5 using the least-squares method:

$$a = 2.61 \pm .22$$

$$b = .294 \pm .026$$

Theoretical values for fully developed laminar flow between two infinite parallel plates are given by equation 43-2:

$$a = 1.85$$

$$b = 0.33$$

The agreement between the experimental data and the theoretical model is quite good (91% confidence) considering the simplified assumption in adopting a fully developed laminar flow of a cumulative nature.

The experimental mass transfer rates are slightly higher than the theoretical line as shown in Figure 43-5. This is expected because the convective effect of the velocity component vertical to the wall (V) has been neglected in the approximated solution. In addition, the assumption of a fully developed laminar flow is not applicable to the real situation at the bottom of the cell where entrance effects are quite important. The length of the entrance region X_e is given by Landau (6) for flow between two parallel plates:

$$\frac{X_e}{d_h} = a\,Re^{-b} \qquad (43\text{-}7)$$

where a and b are positive constants, and their numerical values are not known for the specific nature of the present flow.

The average Reynolds number in the present experiments is about Re=50. The low value of the Reynolds numbers is probably the reason for the generally good agreement between the

experimental data and the theoretical correlation for fully developed laminar flow in a channel.

Another reason for higher mass transfer rates could be the effect of natural convection in the vicinity of the corroding zinc plate. The zinc-chloride formed at the zinc plate, gives rise to a density variation and natural convection in the downward direction. This is counterbalanced by the heat (enthalpy) of the corrosion reaction which would reduce the density of the interfacial electrolyte and induce natural convection in the upward direction. The net contribution is likely to be negligible. At the bottom of the zinc plate where the forced convection is very low, the formation of local vortices is possible due to the coupling of flows causing higher corrosion rates for the bottom section.

Despite the above factors which can cause deviations from the theoretical model, the results obtained are in overall agreement with the theoretical model, and the simplified model of fully developed laminar flow can serve for an estimation of the contribution of the isolated forced convection.

Local Distribution of the Corrosion

The local distribution of the corrosion current density under different operating conditions is shown in Figures 43-6 and 43-7, where the local corrosion current is plotted vs. the electrode height. The effect of cell-gap on the corrosion current distribution is shown in Figure 43-6 where the distribution is more uniform at the smaller cell gap. Similarly, the corrosion current distribution is more uniform at higher flow rates as shown in Figure 43-7. Both figures indicate that the local distribution of mass transfer rates of chlorine tends to be more uniform at higher velocities where the forced convection is dominant and the natural convection and entrance effects are relatively insignificant.

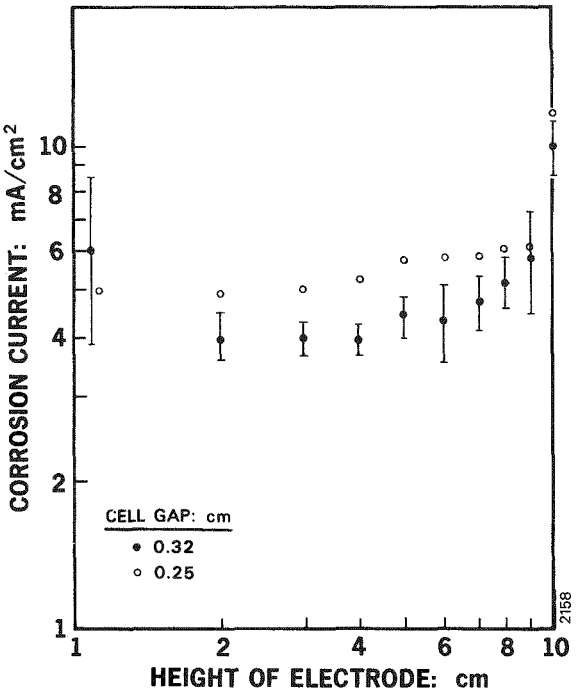

Figure 43-6. Effect of cell gap on the local corrosion current distribution at 3 cm^3/cm^2-min flow rate, 35°C, and a dissolved chlorine concentration of 2.25 g/ℓ.

In both figures, 43-6 and 43-7, the corrosion current at the top of the electrode is considerably higher than its average value. This sharp increase of the corrosion rate is probably due to: (a) Higher velocity of the electrolyte and formation of local vortices due to narrowing of the gap at the top of the cell; or (b) The overflow of the chlorinated solution at the top of the zinc plate.

It was also observed that the corrosion rate was considerably higher at the lowest section of the segmented zinc plate. This is probably due to the entrance effects. Higher mass transport rates in the entrance region is mainly due to a thinner boundary layer. The obtained results show that the transport rate in the entrance section is about 20-40% higher than the average value.

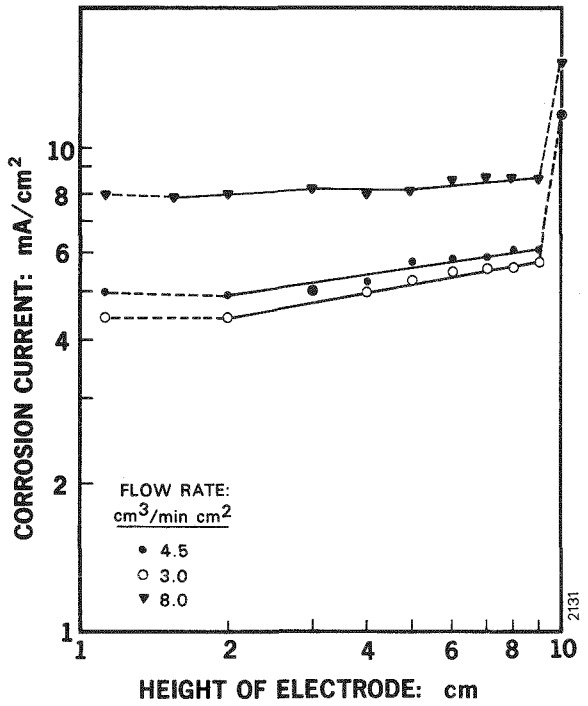

Figure 43-7. Effect of flow rate on the local corrosion current distribution at 35°C and a dissolved chlorine concentration of 2.25 g/ℓ in a cell with a gap of 0.26 cm.

The dependence of the local corrosion current density on the height was calculated from the average distribution of seventeen experiments. The distribution is shown in Figure 43-8, where the normalized corrosion current density is plotted vs. the electrode height. The corrosion current density is normalized according to the approximated model of fully developed laminar flow in a cumulative flow channel (Eq. 43-19).

$$i_{cor}\ (\text{Normalized}) = \frac{i_{cor}\ (\text{local})}{V_o^{1/3}\ d^{-2/3}} \qquad (43\text{-}8)$$

The slope of the line in Figure 43-8, excluding the bottom and top sections, indicates that the local corrosion current density is proportional to the 1/6th power of the electrode height, and for all practical purposes, the local corrosion distribution is fairly uniform along the electrode height.

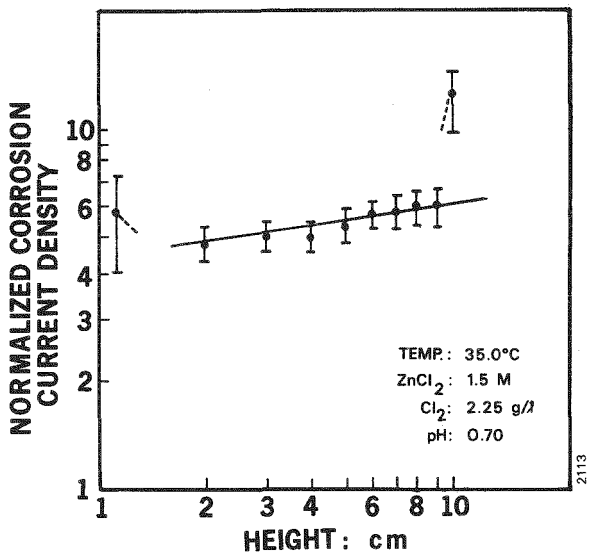

Figure 43-8. Height dependiency of the normalized corrosion current density showing $i_{cor} \propto h^{1/6}$.

The simplified model can predict the average and local corrosion losses due to forced convection within 91% confidence. The local distribution of the corrosion rate is practically uniform although a weak dependence, $i_{cor(local)} \propto h^{1/6}$, has been established. The high corrosion rates at the bottom and the top sections are probably due to entrance effect at the bottom and narrowing and overflow effects at the top.

STATUS

A mathematical model was developed for the mass transport of dissolved chlorine to the zinc electrode under forced convection. This model assumes fully developed laminar flow in a cumulative flow channel, i.e., the inter-electrode gap.

The model agrees quite well with the results of seventeen experiments con-

ducted under a variety of conditions. The prediction of uniform corrosion current density along the height of the electrode is verified experimentally with $i_{cor} \propto h^{1/6}$, i.e., a very weak dependence on height.

The model and the experimental data indicate that forced convection can account for only about 40-50% of the corrosion current density observed during actual cell operation. This suggests that the net corrosion current density is also dependent on other sources of convection; namely natural and bubble-induced convections.

REFERENCES

1. J. T. Kim and J. Jorne. "Mass Transfer of Dissolved Chlorine to a Rotating Zinc Hemisphere in $ZnCl_2$ Solution". J. Electrochemical Society, 125, 89-94 (1978).

2. G. L. Henriksen, S. Kodali, J. Jorne and C. J. Warde. "Zinc-Electrode Current Efficiency in Zinc-Chlorine Hydrate Battery: I. Theoretical Aspects". Extended Abstract No. 374, The Electrochemical Society Meeting. Boston, 1979.

3. S. Kodali, J. Jorne and G. L. Henriksen, "Zinc-Electrode Current Efficiency in the Zinc-Chlorine Hydrate Battery: III. Natural Convection During Electrodeposition". Extended Abstract No. 375, The Electrochemical Society Meeting. Boston, 1979.

4. H. Schlichting. Boundary-Layer Theory, 6th ed., New York: McGraw Hill, 1968.

5. J. Newman. Electrochemical Systems. Englewood Cliffs: Prentice Hall, 1973. pp. 316-322.

6. Landau, U. "Distribution of Mass Transport Rates Along Parallel Plane Electrodes in Forced Convection". Ph.D. Thesis, University of California, 1976. LBL 2702.

Section 44

COULOMBIC EFFICIENCY: III. EFFECT OF NATURAL CONVECTION ON MASS TRANSPORT OF CHLORINE

ABSTRACT

The convective transport of chlorine to the zinc electrode determines the coulombic efficiency of zinc-chloride cells. In this section, the contribution due to natural convection at the zinc cathode in a vertical slot -- cell gap -- is investigated experimentally using a zinc/zinc electrolytic cell. A 2 mm-thick porous diaphragm and cupric ions at a concentration of ∿50 mg/ℓ are used to simulate the chlorine electrode and dissolved chlorine, respectively. Mass-transfer limited electrodeposition rates for copper are used to establish a Nernst diffusion-layer thickness of 0.28 mm and develop a mathematical model for mass transfer in a 2-5 mm vertical slot under 30 mA/cm^2 uniform applied current density. This model predicts that natural convection accounts for only about 15-30% of the total chlorine transport rate during charge.

INTRODUCTION

As described in Section 42, the major source of coulombic inefficiency in zinc-chloride cells is the reaction of chlorine, dissolved in the electrolyte, with electrodeposited zinc. This reaction has also been shown to be mass-transfer limited (1). During charge there exist three major sources of convection which combine to control the rate of chlorine transport to the zinc electrode. These three sources are: (a) forced convection due to the forced flow of electrolyte through the porous chlorine electrodes, (b) natural convection due to zinc ion depletion and the creation of a lower-density electrolyte layer adjacent to the zinc electrode, and (c) bubble-induced convection due to the anodic generation of chlorine gas at the chlorine electrode.

Using relationships available in the literature, an analysis of the contribution from these three sources in transporting chlorine to the zinc electrode was performed in Section 42. The results indicated that none of the three sources dominated the mass transport of chlorine to the zinc electrode. Due to the unique geometry and operation of zinc-chloride cells, the validity of the relationships used in the analysis were questioned and programs were established to either verify or refine them for application to zinc-chloride cell operation. The previous section -- Section 43 -- reviewed the program which verified the relationship used for forced convection. This section describes the program which was conducted to verify or refine the relationship for natural convection.

A brief review of available relationships for heat-transfer phenomena in this type of geometry and for mass transfer to a vertical electrode in an infinite medium is presented first. Similarities in these phenomena are used to establish relationships for mass-transfer to an electrode in a vertical-slot geometry under uniform current density conditions. Cationic tracer experiments were conducted to verify these relationships. A value is obtained for the empirical constant, which allows refinement of the mathematical model.

THEORETICAL BACKGROUND

The zinc-chloride inter-electrode cell gap consists of a rectangular vertical slot as shown in Figure 44-1. During the charge cycle zinc ions are consumed at the zinc electrode. Because of the depletion of zinc ions, the concentration of zinc chloride in the electrolyte and its density at this electrode is lower than that of the bulk. Because of the buoyancy effects, the lower density electrolyte at the electrode surface starts moving upwards, and the hydrodynamic cell as shown in Figure 44-1 is established. For any given hydrodynamic cell, if the density difference between the bulk electrolyte and that at the electrode surface exceeds a certain limit, secondary hydrodynamic cells within the primary cell are established. At even larger density differences the flow can become turbulent.

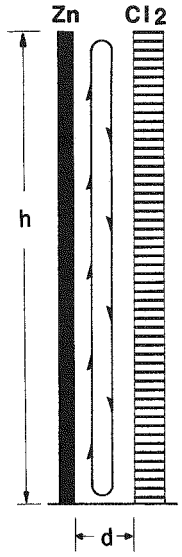

FLOW PATTERN
NATURAL CONVECTION

Figure 44-1. Inter-electrode gap of a zinc-chloride cell. Under natural convection a hydrodynamic cell as depicted is established.

There are no analytical expressions or experimental correlations in the literature for uniform current density (mass transfer) in a vertical-slot geometry of this type. Review articles by Ostrach (2) and Catton (3) include results of analytical and experimental work on heat transfer between vertical plates in this type of geometry. This work deals mainly with uniform wall temperatures which does not necessarily lead to uniform heat flux along the height of the plates. In the present operation the superposition of forced flow, as described and analyzed separately in Section 43, leads to a rather uniform bulk electrolyte concentration along the height of the electrodes (plates) which is similar to electrodeposition on a vertical plate in an infinite medium.

The close-form analytical solution to this problem is not possible due to the nonlinearity of the mass, momentun, and species conservation equations. Analogies to the heat transfer relationships for this type of geometry and to the mass transfer relationships for a vertical electrode in an infinite medium are therefore used to develop a mathematical relationship for mass transfer to an electrode in a vertical-slot geometry.

In these discussions the following terms are employed:

- The Grashof Number (Gr) arises from the force balance in the momentun equation and is given by:

$$Gr = g \frac{\Delta\rho}{\rho} \frac{h^3}{\nu 2} \qquad (44\text{-}1)$$

where g is the gravitational constant (cm/sec^2), $\Delta\rho$ is the density difference between the bulk electrolyte and the interfacial electrolyte (g/cm^3), ρ is the bulk electrolyte density, h is the electrode height (cm), and is the kinematic viscosity (poise).

- The Schmidt Number (Sc) is the ratio of the momentum and molecular diffusion and is given by:

$$Sc = \frac{\nu}{D} \qquad (44\text{-}2)$$

where D is the diffusion coefficient (cm^2/sec).

- The Rayleigh Number (Ra) is the product of the Grashof and the Schmidt numbers:

$$Ra = (Gr)(Sc) \qquad (44\text{-}3)$$

- The Sherwood Number (Sh) compares convective transfer to a vertical electrode to that of diffusional transfer and is given by:

$$Sh = \frac{i\,h}{nFD\Delta C} = \frac{k_m h}{D} \qquad (44\text{-}4)$$

where i is the current density (amperes/cm^2), n is the number of electrons transferred in the reaction (2), F is Faraday's constant (96,487 coulombs), ΔC is the concentration difference in the species of interest between the bulk electrolyte and the interfacial electrolyte (moles/cm^3), and k_m is the mass transfer coefficient (cm/sec).

For very low Grashof numbers (<1000), the process is simple diffusion. In Batchelor's analysis (4) of heat transfer in a vertical slot for higher Gr in the boundary layer regime, the heat transfer rate yielded the following relationship between Sh and Gr:

$$Sh = k_1 (Gr)^{1/4} \qquad (44\text{-}5)$$

where k_1, is a constant. Sparrows and Gregg (5) obtained the same relationship for uniform heat flux (similar to uniform current density) from a vertical plate. In their analysis the fluid properties at half the vertical plate height (h/2) are used to determine Gr. In mass transfer to a vertical electrode in an infinite medium, the exponent of the Grashof number is also identical (6).

Sparrows and Gregg extended their study to include the properties of the medium, i.e., the Schmidt Number, and also local convective transport rates. The local convective transport at any height, x, on the vertical plate was given by:

$$Sh_x = k_2 \left[(Gr_x) \left(\frac{Sc^2}{0.8 + Sc} \right) \right]^{1/5} \qquad (44\text{-}6)$$

where k_2 is another constant. For large Sc this relationship becomes:

$$Sh_x = k_2 (Gr_x\, Sc)^{1/5} = k_2 (Ra_x)^{1/5} \qquad (44\text{-}7)$$

Assuming the analogies between heat transfer and mass transfer continue to hold, the average Sherwood number is related to the Rayleigh number (Ra) by:

$$Sh_{av} = k_3 (Ra)^{1/4} \qquad (44\text{-}8)$$

where k_3 is a new constant. This relationship should describe mass transfer to an electrode in a vertical-slot geometry under constant current density, if the anologies hold. These relationships are now tested experimentally and an empirical value for k_3 obtained for this geometry.

EXPERIMENTAL

Apparatus

The experimental apparatus for the natural convection analysis consists of a dense graphite zinc electrode substrate (cathode), a diaphragm, and a zinc rod anode (Figure 44-2). The electrolyte is a 1.5M aqueous zinc-chloride solution containing a cationic tracer which is more noble than zinc. Copper ion as $CuCl_2$ was used here at a concentration of about 50 mg/ℓ . No supporting electrolyte was used in this study. This negates the complexity in the ionic redistribution and the associated density variation at the zinc electrode during the charge cycle.

During these experiments, zinc is transferred from the zinc rod to the zinc electrode electrolytically. The diaphragm is a porous graphite, PG-60. The distance between the zinc electrode and the diaphragm, d, is a variable. The active height of the zinc electrode is 100mm, the same height as used presently in the battery. The diaphragm is a few mm taller, the additional height being masked by Kynar paint to eliminate any flow-through above the active height. The electrode width is 100mm, and along with the diaphragm it is fixed in a Lucite box with a predetermined, but variable gap between them. The Lucite box is filled with electrolyte as shown in Figure 44-2. The electrolyte flows over the zinc electrode into the back space (to the left of the electrode in Figure 44-2) and transferred to the main body of the electrolyte using a pump. This creates a flow through the porous diaphragm, into the gap, and up through it over the zinc electrode. This is an imposed forced convection through the gap between the zinc electrode and the diaphragm. This flow rate is low enough not to have any significant effect on the natural convection in the gap. The method of transferring zinc from a zinc rod anode to a dense graphite cathode eliminates the generation of chlorine gas in the cell gap. Because this experiment is designed to study the effects of only natural convection, other forms of convection are to be eliminated. Elimination of chlorine-gas evolution eliminates bubble-induced convection and the normal flow through the diaphragm is reduced to a trickle in order to limit forced convection to insignificant levels. However, a small flow is required to eliminate startification in the cell gap. Hence, the only major source of convection present in the cell is natural convection at the zinc electrode. The dc power for the charge operation was supplied by a Udylite PC10 power supply.

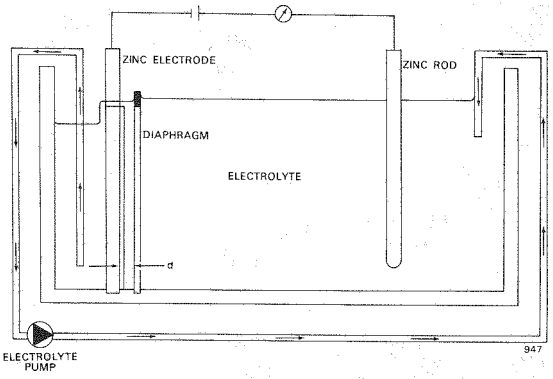

Figure 44-2. Experimental apparatus for studying natural convection. The concentration of the cationic tracer is uniformly maintained in the gap by a slow forced flow of bulk electrolyte through the diaphrahm.

Procedure

At the beginning of each experiment, the zinc electrode was fly-cut on a milling machine with a clean dry cutter. This process removed the previously exposed contaminated layer and exposed a fresh new surface each time for electroplating zinc. It was observed during the course of these experiments that this step eliminated flaky zinc deposition on the surface. The zinc electrode was positioned in the Lucite box to provide the desired gap width and all the necessary electrical connections were made. Zinc-chloride electrolyte of 1.5M concentration with a known level of the copper tracer was transferred from a storage container to the Lucite test vessel. The pump, used to transfer electrolyte from the back section into the sump, was turned on and the flow adjusted to the desired rate. The charge current was turned on and adjusted to give a current density of 30 mA/cm^2.

The charging voltage and the voltage between the zinc electrode and the diaphragm were continuously monitored. The latter was not allowed to exceed the open circuit voltage of the zinc-chloride cell (2.12 V), in order to prevent chlorine generation on the diaphragm. The temperature of the electrolyte was also monitored. Observations with the naked eye indicated boundary layer development at the zinc electrode. This boundary layer in all cases appeared within a few seconds from the start of the charging process. In each experiment, electrodeposition

lasted for about two hours. At regular intervals, samples of electrolyte from the bulk and the cell gap were taken to analyze for the concentration of copper.

At the end of the electrodeposition, the pump and the electrical leads were disconnected and the electrolyte was transferred to a holding container. The quick transfer of electrolyte eliminated any exchange reactions between metallic zinc and copper ion. The electrodes were rinsed with distilled water. Zinc electrode was removed from the Lucite box and allowed to dry. The plated zinc was carefully peeled off from the electrode and samples of 0.635-cm diameter were cut at locations shown in Figure 44-3. These samples were weighed and analyzed for the content of the tracer element. Knowing the time of deposition and the quantity of tracer deposited, the average local current density (i) at each location for the tracer deposition was obtained. The entire procedure was repeated for three different gap widths (0.20, 0.32, and 0.50 cm).

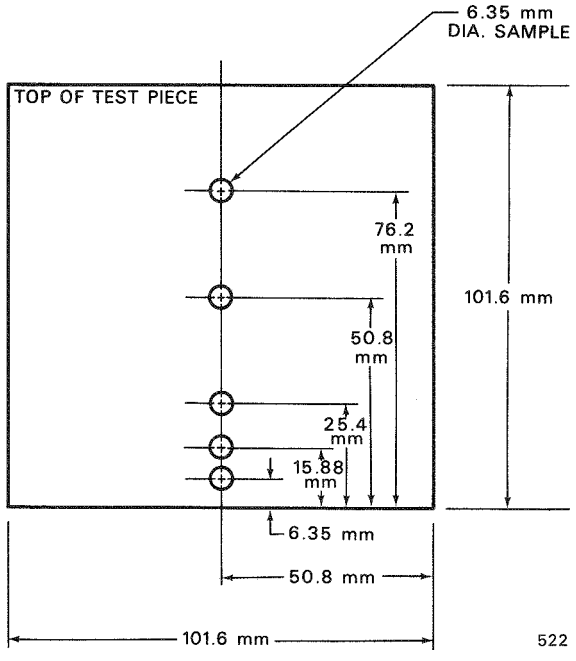

Figure 44-3. Location of samples analyzed for tracer. Samples taken at these locations were analyzed for the tracer content and the mass transfer distribution was established.

RESULTS AND DISCUSSION

As described in the experimental subsection, the local current densities (i) for tracer deposition were obtained at different heights from the bottom of the electrode. These currents in each experiment were normalized using the value of the tracer current density at 0.635-cm height from the bottom in each experiment. Table 44-1 gives these normalized values of current density at different heights for different gap widths. They are plotted against the height in Figure 44-4. The slope of the line passing through the data points indicates clearly that the current density is inversely proportional to the 1/5th power of the height. Sparrow and Gregg (5) in their theoretical analysis and experimental work proved such a distribution for the case of uniform heat flux on a vertical plate in an infinite medium. The uniform heat flux in their case has to be compared with uniform current density for zinc deposition in the

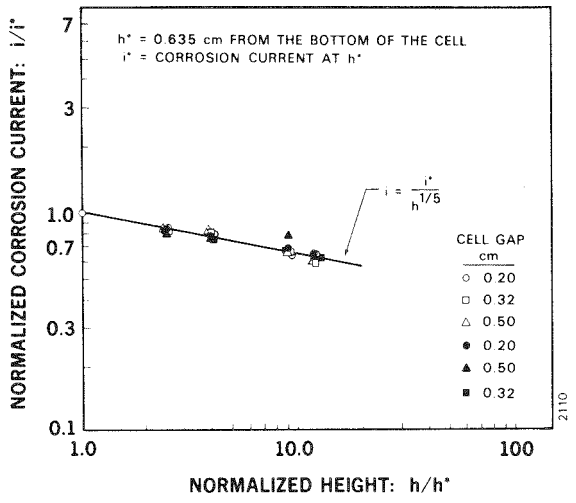

Figure 44-4. Variation of corrosion current with height. These data agree well with heat-transfer relationship of Sparrows and Gregg.

Table 44-1

CORROSION CURRENT DISTRIBUTION WITH HEIGHT

Cap Width (cm)	Normalized Corrosion Current (i_x/i_x^*) At Different Heights				
	x/x*=1.00	x/x*=2.50	x/x*=4.00	x/x*=8.00	x/x*=12
0.20	1.00	0.82	0.75	0.68	0.64
0.32	1.00	0.81	0.80	0.65	0.58
0.50	1.00	0.80	0.76	0.64	0.62
0.20	1.00	0.84	0.78	0.69	0.64
0.32	1.00	0.80	0.75	0.79	0.62
0.50	1.00	0.83	0.76	0.66	0.60

i_x = corrosion current at height x
i_x^* = corrosion current at x = 0.63 cm

present case. The zinc deposition and the resultant concentration change establish the flow pattern with a boundary layer at the zinc electrode in the cell gap. The concentration of the tracer in the bulk is uniform, and its concentration at the wall is zero because its deposition is mass-transfer limited. Hence, only the boundary layer thickness controls its deposition rate. The boundary layer thickness distribution with height obtained here is similar to that obtained by Sparrow and Gregg (5).

It appears reasonable from the similarities in the two transport phenomena to assume that such similarity will extend to the mass transport as well. Hence, the same relationship given in Eq. 44-8 with a different constant should be applicable to the present case. Using the tracer deposition experiments, the value of this constant can be calculated.

Boundary Layer Thickness

Under mass-transfer limited current conditions we know that the current density 'i_L' is given by (7):

$$i_L = \frac{nFD\ (C_b - C_w)}{\delta} \qquad (44\text{-}9)$$

where δ is the Nernst diffusion layer.

In the experiment the values of i_L, D, n, F are known, C_b is the concentration of the tracer in the cell gap and Cw concentration on the wall is zero. Substituting these values in Eq. 44-9, the diffusion-layer thickness 'δ' is obtained as:

δ= 0.28 mm

Empirical Relation for Natural Convection

The complexes formed by the zinc ions and the copper (tracer) ions in the solution are expected to be very similar and hence, their transport properties are assumed to be identical. Under these conditions, their concentration boundary layers will also be the same. The zinc deposition current density used in these experiments was 30 mA/cm^2. Ignoring migration and substituting the values of current density, boundary layer thickness, diffusion coefficient, F and n in Eq. 44-9, the change in concentration of zinc chloride between the bulk and the wall is obtained as:

$$C_b - Cw = \frac{\delta i}{nFD} = 0.39\underline{M}$$

The Grashof number, Gr, for this case given by Eq. 44-1 is 7.45×10^8. Using the properties of the electrolyte used

in the experiment (1.5M zinc-chloride) its Schmidt number is calculated to be 910. From the Gr and Sc numbers, the Rayleigh number, Eq. 44-3, was obtained. From Eq. 44-4, the Sherwood number for the transport in the vertical slot was obtained. Substituting Sh and Ra in Eq. 44-8, the empirical constant k_3 was calculated to be 0.36.

Hence, the generalized equation for the calculation of corrosion losses in the cell gap is

$$Sh_{av} = 0.36\ (Ra)^{1/4} \qquad (44\text{-}10)$$

Using this relationship in Eq. 44-4 allows a refined prediction of the average chlorine corrosion current density attributable to natural convection in a vertical slot. At 1 g/ℓ chlorine concentration the calculated corrosion current density is 0.7 mA/cm^2 for an applied current density of 30 mA/cm^2 in a 1.5M $ZnCl_2$ electrolyte. This is about 15-30% of the total corrosion current density observed during actual cell operation (see Section 46).

STATUS

From the literature described in the theoretical background subsection, it was assumed that natural convection phenomena are similar at a vertical electrode in an infinite medium and in a vertical slot. The mass-transfer limited copper-deposition rates measured along the height of the electrode confirmed this analogy.

Within the range of cell gaps studied -- 0.2-0.5 cm -- there was no measurable effect of cell gap on the mass-transfer rates for copper deposition. Using the experimentally obtained data a Nernst diffusion layer thickness for copper ions was calculated to be 0.28 mm. Assuming the diffusion-layer thickness to be same for zinc ions, the zinc chloride concentration change across the diffusion-layer was calculated to be 0.39M under the conditions investigated.

These results were then used to obtain a value for the empirical constant, k_3, in Eq. 44-8 of 0.36. This relationship describes natural convection controlled heat and mass transfer to a vertical plate in a vertical slot under conditions of uniform flux.

REFERENCES

1. J. T. Kim and J. Jorne. "Mass Transfer of Dissolved Chlorine to a Rotating Zinc Hemisphere in Zinc-Chorine Solution." J. Electrochemical Society, January 1978, pp. 89-94.

2. Simon Ostrach. "Natural Convection in Enclosures." Advances in Heat Transfer, Vol. 8, 1972.

3. I. Catton. "Natural Convection in Enclosures." In Proceedings of the Sixth International Heat Transfer Conference, Vol. 6, 1978, pp. 13-81.

4. G. W. Batchelor. J. Fluid Mechanics, 1956, 1,177.

5. E. M. Sparrow and J. L. Gregg. "Laminar Free Convection From a Vertical Plate With Uniform Surface Heat Flux." Transactions of the ASME, February 1956, pp. 435-440.

6. C. R. Wilke, M. Eisenberg, and C. W. Tobias. "Correlation of Limiting Currents and Free Convection Conditions." J. Electrochem. Soc., 100, (1953).

7. J. Newman. Electrochemical System. New York: Prentice-Hall, Inc., 1973, p. 327.

Section 45

COULOMBIC EFFICIENCY: IV. DETERMINATION OF $ZnCl_2$ CONCENTRATION PROFILES UNDER NATURAL CONVECTION

ABSTRACT

Holographic interferometry -- double-exposure photography of interference fringe patterns produced by refractive-index variations in the electrolyte -- is used to experimentally determine steady-state electrolyte-concentration and density profiles established by natural convection at a zinc cathode. Interferograms obtained at a zinc cathode operating in a 0.4 cm vertical slot (cell gap) containing 1.5M $ZnCl_2$ electrolyte at applied current densities of 3-30 mA/cm^2 are analyzed using an iterative computer code to construct concentration profiles. These profiles are analyzed to obtain values for diffusional and convective transport parameters under the above conditions: (a) a Nernst diffusion-layer thickness of 0.15-0.20 mm, (b) an effective diffusion coefficient for zinc-ion species of 1.75×10^{-5} cm^2/sec, and (c) a normalized chlorine corrosion current density due to natural convection of 0.4 $(mA/cm^2)/(g/\ell)$.

INTRODUCTION

As discussed in the three previous sections -- Sections 42 through 44 -- the mass transfer rate of dissolved chlorine to the zinc electrode controls the coulombic inefficiency of zinc-chloride cells. The analysis performed in Section 42 revealed that three sources of fluid convection control the mass transport of chlorine to the zinc electrode during charge: (1) forced convection of bulk electrolyte through the chlorine electrodes; (2) natural convection of electrolyte in the layer adjacent to the zinc electrode resulting from zinc-ion depletion; and (3) bubble-induced convection of electrolyte resulting from chlorine gas evolution at the chlorine electrode. In an effort to maximize the coulombic efficiency of zinc-chloride cells during charge, these three convective sources are being analyzed individually to determine their respective contributions to the mass transport of chlorine to the zinc electrode.

In Section 43, the contribution from forced convection was established experimentally and a mathematical model which assumes fully-developed laminar flow in a cumulative flow channel was verified. In Section 44 cationic tracer experiments resulted in a refined mathematical model for the contribution due to natural convection at a zinc cathode operating under constant current density in a vertical-slot geometry. Using this model a diffusion boundary-layer thickness of 0.28 mm and a zinc-chloride concentration difference of 0.39 moles/ℓ were predicted for operation at 30 mA/cm^2 current density in a 1.5M $ZnCl_2$ electrolyte.

In this section, holographic interferometry is employed to establish the concentration profiles for zinc chloride at a zinc cathode as a function of applied current density in a cell operating with only natural convection. The results of this study are used to supplement those of the previous section in analyzing the contribution natural convection makes in the net transport of dissolved chlorine to the zinc electrode during electrodeposition.

Interferometry is a method by which variations of refractive index of fluids are manifested as interference fringe patterns. Because the refractive index of the electrolyte used in

these experiments is a known function of the concentration of $ZnCl_2$, interferograms (photographs of the fringe patterns) can be analyzed to determine the concentration profiles. Holographic interferometry is a special type of interferometry in which the optical waves which interfere are recorded by double-exposure, off-axis holography. This technique has two unique features which were important for these measurements. First, it is possible to vary the location of the plane on which a camera is focused when the interferograms are photographed. Second, requirements for the optical quality of the windows of the electrolyte cell are moderate.

In the experiments reported here, the boundary layers were extremely thin (approximately 0.50 mm), and refractive index gradients were large. This caused appreciable bending, or refraction, of the light rays as they passed through the cell. When refraction is strong, the classical methods of analyzing interferograms are not valid and significant errors result if they are used. The interferometric data recorded during these experiments were analyzed with a new computer code which iteratively corrects the measurements until the errors due to refraction become negligible.

EXPERIMENTAL

Equipment and Procedures

Figure 45-1 is a schematic drawing of the electrolytic cell. The main body of the cell was a rectangular tank manufactured from plexiglas. Two flat quartz optical windows were mounted so that they formed the ends of the active portion of the cell. The cathode was a machined and polished rectangular graphite bar held vertically by a plexiglas electrode-holder which fit snugly into the space between the quartz windows. A thin porous diaphram was mounted in a similar manner opposite the cathode. The natural convection under study took place in the 3 mm wide slot between the cathode and the diaphram. This slot was 100 mm high and the widths of the cathode and diaphram were 5 mm. The cathode and diaphram were physically more than 110 mm high, but an impermeable coating was placed on the top 10 mm of the diaphram. A large amount of fresh electrolyte resided on the other side of the porous diaphram, so that a small forced flow through the diaphram into the slot could be maintained to reduce vertical density stratification in the slot. The cathode graphite bar and the zinc rod anode inserted in the bulk electrolyte were connected to a Hewlett Packard model 6201B direct-current power supply through a circuit which included a milliammeter.

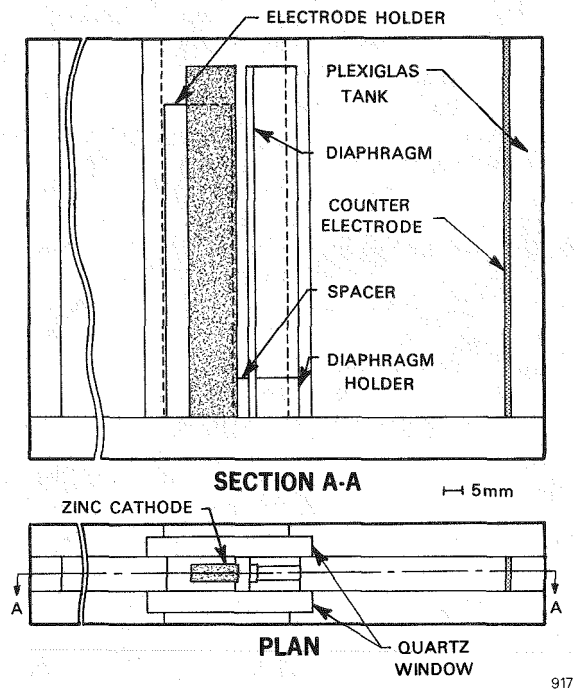

Figure 45-1. Electrolytic cell. Natural convection takes place in the vertical slot formed by the electrode and the diaphragm; and the object beam of the interferometer passes though the quartz windows.

For each test run the electrodes were cleaned and fresh $ZnCl_2$ was placed in the cell. A small, gravity-driven, flow of fresh electrolyte into the bulk fluid to the right of the diaphram was maintained at a rate determined empirically to reduce stratification. The

power supply was adjusted to attain the desired current density at the electrode surface, and the cell was operated for 5 minutes in order to achieve steady natural convection before a hologram of the boundary layer was recorded.

The optical apparatus is shown schematically in Figure 45-2. The components of this holographic interferometer were assembled on a massive, flat, granite block. The granite block rested on inflated inner tubes. This high mass, low spring constant system had a natural frequency of approximately 1 Hz and therefore effectively isolated the interferometer from building vibrations.

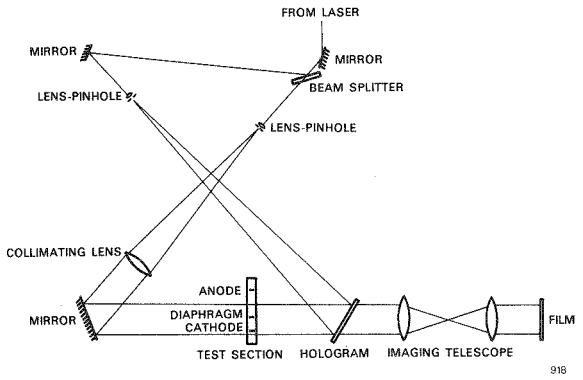

Figure 45-2. Optical apparatus. Interferograms of the natural convection boundary layer are recorded by two-exposure holography and are viewed or photographed through a two-element telescope.

A continuous beam of light from a Spectra-Physics model 125, 50 mW helium-neon laser was divided into two beams by a variable-ratio beam splitter. One beam was expanded by a microscope objective lens and filtered with a 10 μm diameter pinhole spatial filter. The resultant diverging spherical wave formed the reference wave of an off-axis holographic system. The second beam was expanded and filtered in the same manner but then passed through a 128 mm diameter, 629 mm focal length, collimating lens. The resultant plane wave was reflected by an optically flat, adjustable, mirror through the electrolytic cell. This wave is referred to as the object wave of the holographic system.

The object wave and reference wave both impinge on a photographic plate consisting of Agfa-Gavaert type 10E75 emulsion coated on a rigid 10 cm x 13 cm glass plate held in a rigid fixture. After development, this plate is referred to as a hologram. Recorded on the hologram is a complex, microscopic, interference pattern formed by optical interference between the reference and object waves at the time of recording. When the hologram is illuminated by the reference wave alone, it diffracts light into the propagation direction of the object wave. This diffracted light is a precise replica of the original object wave, which had passed through the electrolytic cell.

To form a holographic interferogram, a single photographic plate is exposed twice. The first exposure, which is referred to as the reference exposure, is recorded before the current is turned on. The electrolyte is quiescent and has a homogeneous density during this exposure. The second exposure is recorded while natural convection is occurring. When this double-exposure hologram is illuminated by the reference wave, the two object waves (with and without convection) are reconstructed simultaneously and interfere with each other. This interference forms a fringe pattern which can be photographed. The interference pattern was photographed on high resolution film by using a telecentric telescope formed by two imaging lenses as shown schematically in Figure 45-2. The object plane on which the telescope is focused must be determined accurately; hence, the film holder was mounted on a high-precision, micrometer-driven, translation stage. The object plane was chosen based on criteria dictated by the fringe analysis scheme, which is described in the following subsection.

Computer Analysis of Data

When concentration gradients within a boundary layer are small, no appreciable refraction occurs, and fringe interpretation is straightforward. In this case, all optical rays through the electrolytic cell can be considered to be straight lines parallel to the surface of the cathode. As indicated in Figure 45-3(a), the light interfering at any point in an interferogram is contributed by two rays which follow the same straight path through the cell. One ray passes through the electrolyte with homogeneous refractive index n_o at the time of the first holographic exposure. The second ray passes through the boundary layer which, at a given height in the cell, has a refractive index n(x), which is to be measured. By examining the fringe pattern, one can determine the optical path length difference of these two rays. This difference is denoted by $\Delta\bar{\Phi}(x)$ and can be expressed mathematically as:

$$\Delta\bar{\Phi}(x) = \int_A^B [n(x) - n_o]\, dz = \overline{AB}\,[n(x) - n_o] = W_m\,[n(x) - n_o] \qquad (45\text{-}1)$$

where W_m is the width of the cathode. Since $\Delta\bar{\Phi}(x)$ is measured by using the interferogram, the refractive index distribution in the boundary layer is

$$n(x) - n_o = \Delta\bar{\Phi}(x)/W_m \qquad (45\text{-}2)$$

Once $[n(x) - n_o]$ is determined, the concentration profile can be computed by using the following relation which was determined by refractometer measurements made at EDA:

$$C(x) - C_o = 52.63\,[n(x) - n_o] \qquad (45\text{-}3)$$

where C_o is the concentration in the bulk electrolyte outside the boundary layer at 20°C (1.5 moles/ℓ). The corresponding refractive index n_o is 1.3695.

As the current density is increased, the refractive index gradients increase and the analysis of interferograms becomes much more complex. In this case, two light rays which meet at a point in the interferogram travel significantly different paths through the test cell. A typical ray passing through the boundary layer is shown as a solid curve in Figure 45-3(b). This ray is continuously curved as it passes through the boundary layer and is discontinuously bent as it passes through the test cell window. The interferogram formed when refraction is significant depends strongly on the telescope or camera lens which is used. In Figure 45-3(b), the interferogram is formed when object plane $\overline{aa}$ is imaged onto the film plane. Point P' in the interferogram is the image of point P in the boundary layer. (For simplicity, the hologram, which would be located between the test cell and the lens is omitted from this figure.) The second ray which contributes to the interference pattern at point P' is shown as a straight dotted line. Light following this ray traveled through the electrolyte with homogeneous refractive index n_o at the time of the first holographic exposure. The optical path length difference of these two rays is denoted by $\Delta\tilde{\Phi}(x')$ and can be expressed mathematically as:

$$\Delta\tilde{\Phi}(x') = \int_A^B n(x)\, ds + n_o\,(\overline{BB_o} - W_m - W_s) + n_w\,(\overline{B_oC_o} - W_w) - n_a\,\overline{CC_o} \qquad (45\text{-}4)$$

where ds is the differential length of the curved ray, W_m is the width of the cathode, W_s is the width of the gap between the cathode and the cell window, W_w is the thickness of the window, n_w is the refractive index of the window, and n_a is the refractive index of the ambient air.

It is difficult to invert equation 45-4 to determine n(x) because the ray path through the test cell is not known. In fact, this path is related to the refractive index distribution n(x) by

the following nonlinear differential equation:

$$\frac{(d^2x/dz^2)dx}{1+(dx/dz)^2} = \frac{dn}{n} \qquad (45\text{-}5)$$

and $ds = [1 + (dx/dz)^2]^{1/2}\, dz.$ (45-6)

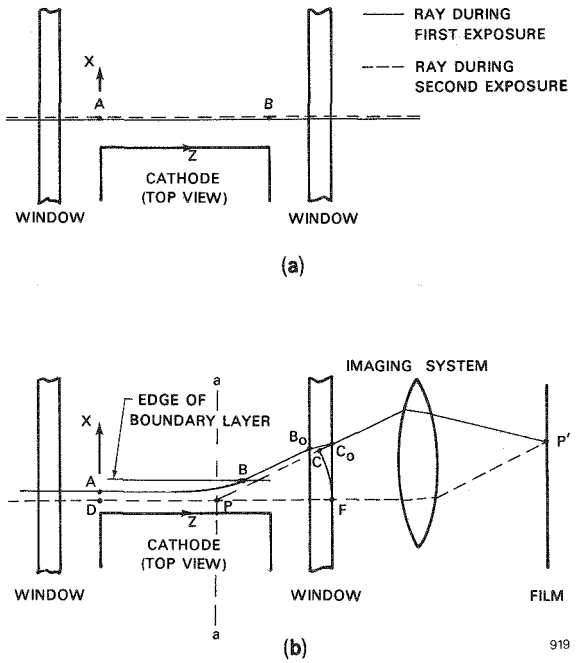

Figure 45-3. Optical paths through test cell. (a) When refraction is negligible, the interfering optical rays travel along the same straight-line path during both holographic exposures. (b) When refraction is strong, the interfering optical rays travel along different paths, and the imaging geometry plays an important role.

Equations 45-4, 45-5 and 45-6 form a nonlinear inversion problem whose solution is not known. In order to analyze the data from these experiments, a computer code was written which enabled inversion of the data with good accuracy. The algorithm is an iterative one in which successive approximations to n(x) are computed. The solution is first approximated by making an initial estimate of n(x) by applying equation 45-2. An efficient computational ray tracing code is then used to solve equations 45-5 and 45-6.

This enables calculation of an approximate path length difference $\Delta\tilde{\Phi}'(x)$ using equation 45-4. The calculated path length difference $\Delta\tilde{\Phi}'(x)$ is compared with the measured difference $\Delta\tilde{\Phi}(x)$ at several points on the interferogram. If the two are not in close agreement, the estimated distribution n(x) is corrected and the procedure is repeated iteratively until good agreement between computed and measured optical path length differences is obtained.

Prior to designing the electrolytic cell computer simulations of experiments with strongly refracting boundary layers were made. It was shown that data which yielded 50 percent errors when inverted by the usual procedure, equation 45-2, could be accurately inverted using this code.

With reference to Figure 45-3(b), it should be noted that when refraction is extremely strong, it is necessary to focus on planes such that point P is below the electrode surface. In this case the experimental procedure must be changed so that the cathode is physically removed during the first exposure, enabling light to pass through this region. Analysis of data recorded in this format required significant alteration of the computer code.

RESULTS

A total of 32 holographic interferograms were recorded during this investigation. Many of these contributed to the development of the experimental technique but were not analyzed. Successful interferograms were recorded in the current density range $3.0 < i < 30.0$ mA/cm^2. Figure 45-4 is an interferogram recorded at the lowest current density, 3.0 mA/cm^2. This figure is greatly enlarged. The physical distance from the cathode to the outermost dark fringe is only 0.5

mm. Refraction is negligible, so this interferogram could be analyzed by using equation 45-2; however, the computer code was used because it yielded a more accurate estimate of the concentration gradient near the wall. Figure 45-5 is an interferogram recorded at 10 mA/cm^2. This interferogram requires some correction by the computer code because refraction is significant. At higher current densities, it is necessary to use the second approach in which the cathode is removed during the first exposure and the telescope is focused well behind the test cell. As many as 125 fringes occurred in these interferograms. The fringes are too fine to reproduce clearly in this report.

Figure 45-6 is a result from a computer simulation of a boundary layer measurement. It is included here to illustrate the error reduction as results are iteratively improved by the computer code. This code was used to process the experimental data to produce the results presented in the remainder of this subsection.

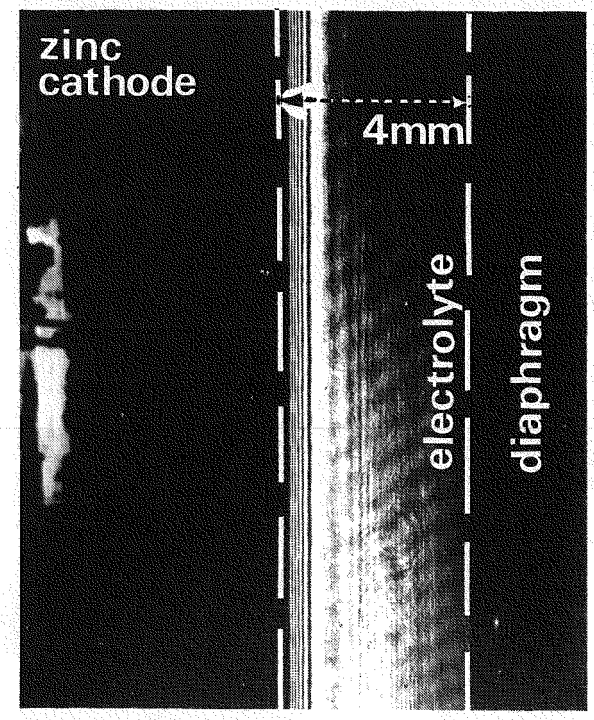

Figure 45-4. Cathodic boundary layer. This interferogram was recorded at a current density of 3 mA/cm^2. Refraction is negligible so the fringes represent lines of constant concentration.

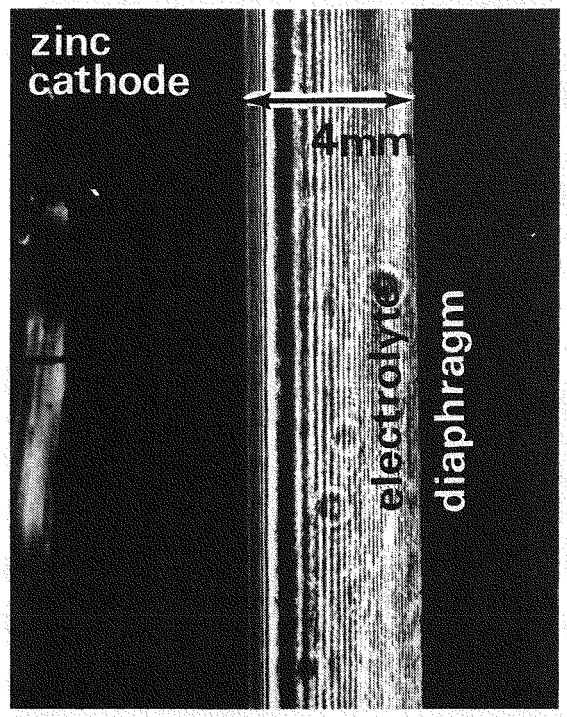

Figure 45-5. Cathodic boundary layer. This interferogram was recorded at a current density of 10 mA/cm^2. Refraction is significant, so computer processing is required to determine the concentration.

Figure 45-7 shows several of the concentration profiles determined by holographic interferometry. Some errors occur near the outer edge of the boundary layer because a boundary layer thickness must be assigned during the computer analysis. This slightly distorts the outer portion of the boundary layer; however, computer simulations indicated that this effect dampens out rapidly and does not affect the interior of the boundary layer.

Figure 45-8 is the primary quantitative result of this investigation. It is a plot of the concentration gradient at the cathode as a function of current density. Two different symbols are used on this figure to differentiate

data recorded in the two different formats described above.

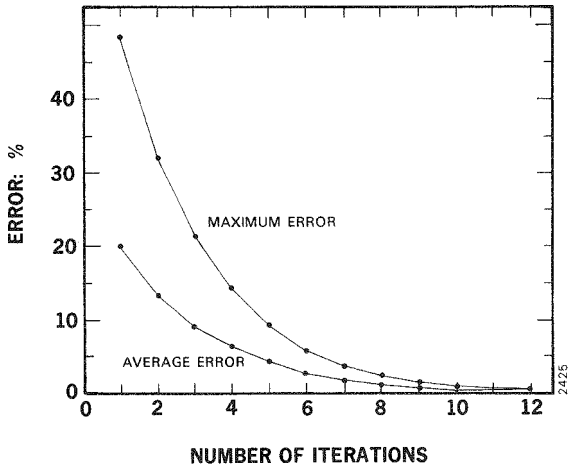

Figure 45-6. Computational error reduction. The maximum error and average error of concentration measurements across the boundary layer are continuously improved by an iterative computer code.

By necessity, much of the effort during this investigation was devoted to the development of this novel approach to measuring concentration profiles in the exceedingly thin and highly refracting boundary layers relevant to this project. Accurate measurements of concentration gradients which are stronger than any measured previously by interferometry were successfully made and some of the limitations of the method were overcome.

The gradients of concentration at the cathode were found to increase approximately linearly with current density up to 25 mA/cm^2. An apparent leveling of the gradient occurred as 30 mA/cm^2 was approached. The accuracy of the measurements below 20 mA/cm^2 is quite good; however, measurements above 20 mA/cm^2 were made only with extreme difficulty. This is because the accuracy of the available optical imaging and positioning equipment was less than satisfactory for these experiments. With appropriate equipment and a modified test cell, the method could be extended to somewhat higher current densities.

DISCUSSION

Boundary Layer Thickness

Holographic interferometry was used to experimentally determine the concentration profiles of $ZnCl_2$ in the electrolyte layer adjacent to the zinc cathode under natural convection in a vertical slot. See Figure 45-7. By linearly extending the concentration gradients at the surface of the electrode to the 1.5M $ZnCl_2$ (bulk) concentration, values for the Nernst diffusion layer of 0.15-0.20 mm are obtained for applied current densities in the range of 15-30 mA/cm^2. In Section 44, based on the tracer experiments, a Nernst diffusion-layer thickness of 0.28 mm was obtained for copper deposition. Considering the diversity of the techniques, the uncertainties in the tracer analysis and the assumptions involved, the agreement between the two values of diffusion layer thickness is fairly good.

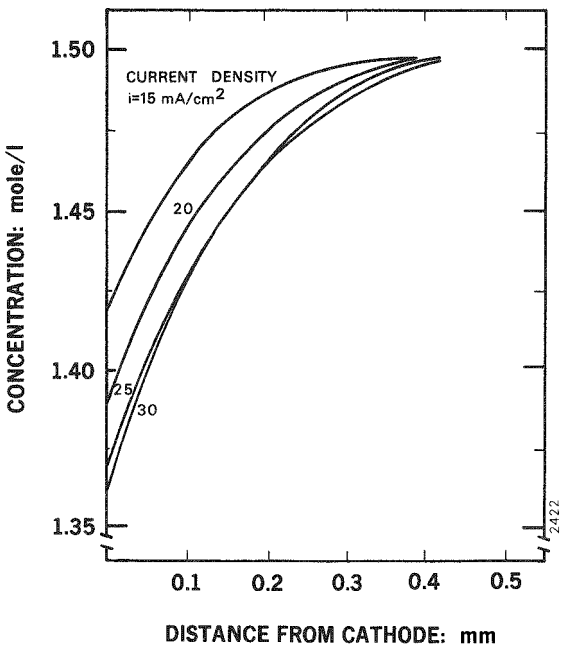

Figure 45-7. Typical measured concentration profiles. Computer analysis of holographic interferograms yields concentration profiles across the cathodic boundary layer.

Effective Diffusion Coefficient of Zn

In Figure 45-8, the concentration gradient at the zinc electrode is plotted as a function of applied current density. The effective diffusion coefficient can be calculated from this plot based on the equation:

$$i_a = nFD^* \left.\frac{dc}{dx}\right|_{x=o} \qquad (45\text{-}7)$$

where i_a is the applied current density, n is the number of electrons, F is the Faraday, D* is the effective diffusion coefficient of the zinc species and (dc/dx) at x=o is the concentration gradient at the zinc electrode. The effective diffusion coefficient of the zinc species would include some contribution of electrical migration and concentration dependence, if any.

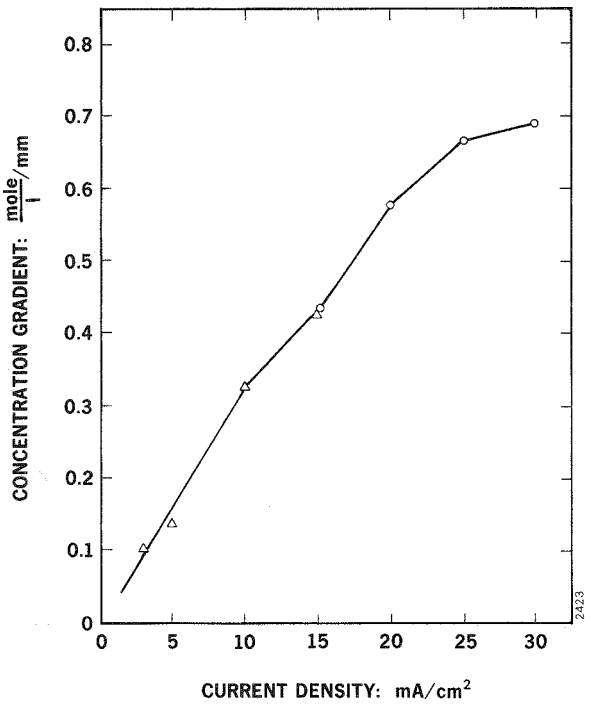

Figure 45-8. Concentration gradient at the cathode. The gradient at the surface of the cathode initially increases nearly linearly with current density but appears to have a reduction in the rate of increase above 25 mA/cm^2. Triangles denote measurements made with the interferometric object plane at the cathode (mild refraction), and circles denote measurements with the interferometric object plane behind the cathode (strong refraction).

Since the experimental data are reliable below 20 mA/cm^2 and the concentration gradient at the zinc electrode is linear with current density below this value, the slope of this region was used to calculate D*. The value of the effective diffusion coefficient of Zn species was calculated to be 1.75 x 10^{-5}cm^2/sec. This value is significantly higher than the measured diffusion coefficient values for Zn species in 1.5M $ZnCl_2$ of 1.135 x 10^{-5} cm^2/sec. As mentioned, the value from the present work is an effective diffusion coefficient which includes electrical migration. Based on the transference number (Section 41) for Zn in 1.5M $ZnCl_2$ of 0.07, the measured diffusion coefficient value will be modified to 1.22 x 10^{-5} cm^2/sec in the presence of migration. The effective diffusion coefficient of the present work is even higher, and this may be possibly due to the variation of the diffusion coefficient with electrolyte concentration. However, the concentration variation in the boundary layer is not significantly different from that in the bulk. Hence, a totally satisfactory explanation of the difference in the effective diffusion coefficients is not available at the present time.

Corrosion Current Due to Natural Convection

The effective diffusion coefficient and the electrolyte concentration difference were experimentally determined under natural convection conditions. These data have been used in calculating the contribution natural convection would make in the mass-transfer of dissolved chlorine to the zinc surface. As discussed in Section 44, the Sherwood number describes the mass transfer situation under natural convection and can be calculated with an

appropriate constant k and Grashof (Gr) and Schmidt (Sc) numbers based on the following equations:

$$Sh = k\ (Gr.Sc)^{1/4} \qquad (45\text{-}8)$$

$$\text{and } i_{cor} = \frac{nFD\,\Delta C}{h}\,Sh \qquad (45\text{-}9)$$

$$\text{where } Gr = \frac{g(\rho_b - \rho_w)\,h^3}{\rho_b \nu^2} \qquad (45\text{-}10)$$

$$\text{and } Sc = \frac{\nu}{D} \qquad (45\text{-}11)$$

where n is the number of electrons, F is the Faraday, D is the diffusion coefficient, ΔC the concentration difference between the bulk and the electrode surface, h is the electrode height, g, the acceleration due to gravity, ρ_b and ρ_w are the electrolyte densities in the bulk, and at the electrode, respectively, ν is the kinematic viscosity, and i_{cor} is the corrosion current density.

For the case where the concentration difference is 0.14M and using $D^* = 1.75 \times 10^{-5}$, cm^2/sec and available density and viscosity values for the average concentration, the Grashof number was calculated to be 0.091×10^9. The Schmidt number for the transport properties of dissolved chlorine (diffusion coefficient of 0.664×10^{-5} cm^2/sec in 1.5M $ZnCl_2$ was calculated to be 1720.

$$i_{cor} = \frac{nFD\Delta C}{h} \times k(Gr.Sc) \qquad (45\text{-}12)$$

Substituting k = 0.359 (Section 44), C for dissolved Cl_2 of 1 g/ℓ (14.1×10^{-6} mole/cc) since its surface concentration would be zero for the mass-transfer limited reaction, the normalized chlorine corrosion current density is calculated to be 0.4 (mA/cm^2) per (g/ℓ).

This value is a little lower than the one theoretically calculated in Section 42 of 0.7 (mA/cm^2) per (g/ℓ). Nevertheless, it is in the same range considering the theoretical calculation was made for a different set of conditions, e.g., mixed electrolyte of a higher concentration and a higher applied current density.

CONCLUSIONS

1. Concentration profiles of zinc-chloride under natural convection conditions were determined by holographic interferometry at a working zinc electrode. This method has been successfully extended to strong refraction conditions with the help of a reiterative computational code.

2. The concentration gradients at the zinc electrode are linear with current density up to 20 mA/cm^2. At current densities above this value, the concentration gradient appears to level off. This may be associated with the problem of resolving the high density of interference fringes.

3. From the concentration profiles, a boundary layer thickness of 0.16 mm was calculated. From the concentration gradient versus current density plot an effective diffusion coefficient of 1.75×10^{-5} cm^2/sec was determined.

4. Based on the experimental values for the $ZnCl_2$ concentration difference between the bulk, the zinc surface, and the effective diffusion coefficient, a normalized corrosion current density of 0.4 (mA/cm^2)/(g/ℓ) Cl_2 was estimated, which is in the same range as predicted by the theory.

Section 46

COULOMBIC EFFICIENCY: V. COMBINED CONVECTION AT AMBIENT PRESSURE

ABSTRACT

Under typical charging conditions for zinc-chloride cells, three fluid-convection sources -- forced, natural, and bubble-induced convections -- combine to control the mass transport of dissolved chlorine to the zinc electrode. This section presents experimentally determined chlorine-transport rates (coulombic efficiency losses) due to combined convection at ambient pressure. Data are given for the following conditions: (a) dissolved chlorine concentrations of 0.4-3.0 g/ℓ, (b) cell gas of 0.1-1.25 cm, (c) electrolyte flow rates of 1-7 cm^3/cm^2-min, (d) applied current densities of 20-60 mA/cm^2, and (e) temperatures of 20°C and 50°C. The results indicate a linear dependence of the chlorine corrosion rate on the dissolved chlorine concentration, as well as optimum flow rate and cell gap regions of 3-4 cm^3/cm^2-min and 0.3-0.4 cm, respectively. They also support an earlier conclusion that all three convective sources are important and that none of them is dominant.

INTRODUCTION

As discussed in Section 42, the coulombic inefficiency of the zinc electrode is due to the direct reaction of dissolved chlorine with electrodeposited zinc. Previous work by Kim and Jorne (1) has shown that the rate-determining step of this reaction is the mass transfer of dissolved chlorine to the zinc electrode. In a completely stagnant cell this transport would occur by molecular diffusion and the corresponding fractional current inefficiency of the zinc electrode would be less than 0.01 for practical cell gaps. In the actual cell, however, mass-transfer enhancement occurs via the combined influence of three convective mechanisms during electrodeposition (2-4):

- Forced Convection of electrolyte through the cell.
- Natural Convection of electrolyte adjacent to the zinc electrode created by depletion of ionic-zinc species.
- Bubble-induced Convection of electrolyte created by the anodic generation of chlorine gas.

These three mechanisms combine to establish a steady-state fluid-dynamic pattern in the inter-electrode gap which controls the rate of mass transfer of dissolved chlorine to the zinc electrode. Theoretical analyses of these mechanisms suggest that all three contribute significantly and that none of them dominates the mass transport of dissolved chlorine (2).

The present section reports on an experimental study carried out at ambient pressure to investigate the combined convection operating in the inter-electrode gap which controls the transport of dissolved chlorine to the zinc surface. Parameters such as cell gap, flow rate, current density, and chlorine concentration were evaluated.

EXPERIMENTAL

The coulombic efficiency of the zinc electrode was investigated in a zinc-chloride single cell over a practical range of operating conditions (5). The cell consisted of a zinc electrode and flow-through porous graphite chlorine

electrode. The chlorinated zinc chloride solution was fed through the porous graphite electrode and upward between the chlorine and zinc electrodes. Coulombic efficiencies were determined gravimetrically and corrosion current densities (i_{cor}) were calculated by assuming them to be constant during each experiment. An expanded view of the cell is shown in Figure 46-1. It consists of a chlorine electrode contact block made of dense graphite, porous-graphite electrode (PG-60, Union Carbide) which was activated electrochemically (6), plastic frame and mask for the chlorine electrode, a plastic spacer, and a dense graphite block (ATJ, Union Carbide) which serves as a zinc electrode. The electrochemical active area of the cell was 100 cm^2 (10 cm x 10 cm). The cell was constructed of Kynar and the electrical connections were made of titanium. The cell was clamped together and placed in a large glass jar which served as an electrolyte sump.

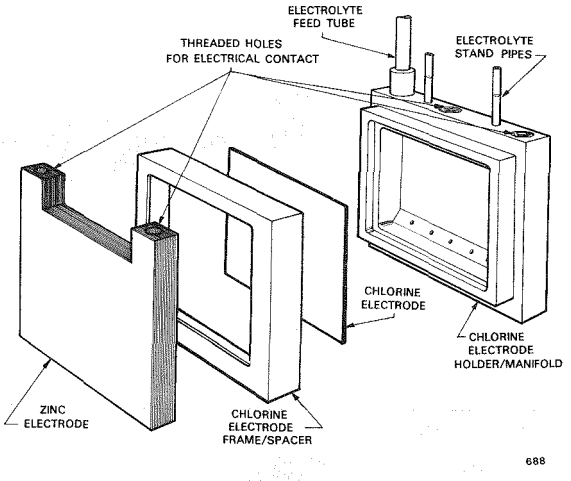

Figure 46-1. Expanded view of the zinc-chloride single cell. Cell was designed for easy disassembly and removal of electrodeposited zinc plate for gravimetric determination of charge coulombic efficiency.

The experimental apparatus is shown in Figure 46-2. The electrolyte was circulated from the sump into the cell by a pump (Micropump Corporation) and back to the sump by an overflow. Chlorine gas was bubbled through the sump, and the solution was dechlorinated by nitrogen sparging. The temperature was controlled by a constant temperature bath (Haake E52) to within ±1°C. Temperatures below 25°C were maintained by an ice bath. The electrolyte flow rate was measured by a Brook flowmeter (R-6-15-B tube size) which was calibrated at different temperatures and electrolyte compositions with an accuracy of ±5%.

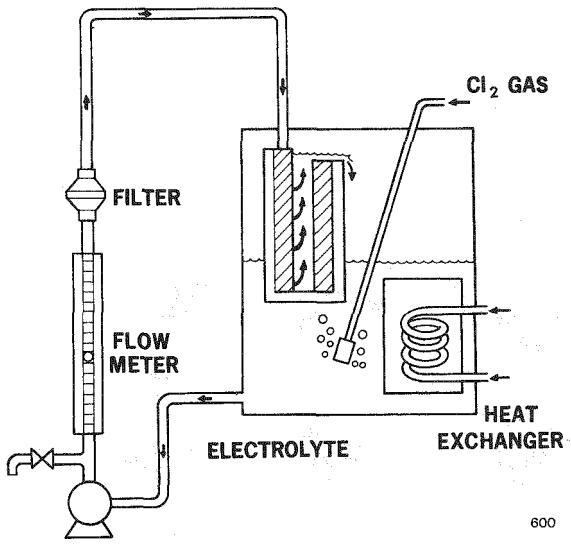

Figure 46-2. Schematic diagram of experimental apparatus. The dissolved chlorine concentration is controlled by sparging mixtures of chlorine and nitrogen.

The cell was charged by a constant current power supply (Udylite PC-10) and the electrical equipment (voltmeter, ammeter, and coulometer) was calibrated within 1% accuracy. Charging time varied between one and two hours (50-100 mAh/cm^2).

The coulombic efficiency during charge was calculated from the weight of the zinc deposit. The zinc deposit was peeled off the graphite substrate, washed thoroughly with distilled water and acetone, and was dried rapidly in an oven (80°C) in order to prevent oxide formation.

The electrolyte solution consisted of 1.5M $ZnCl_2$ and a proprietary leveling agent. This resulted in smooth depos-

its in all the experiments. The pH of the solution was adjusted to 0.0 by adding hydrochloric acid.

RESULTS AND DISCUSSION

The coulombic efficiency of the zinc electrode during charge was investigated over a range of operating conditions. The following parameters were investigated: concentration of dissolved chlorine, cell gap, flow rate, charge current density, and temperature (5).

Effect of Chlorine Concentration

The corrosion current density depends linearly on the dissolved chlorine concentration as shown in Figures 46-3 and 46-4. The corrosion currents are generally higher at 50°C (Figure 46-4) compared to those at 20°C (Figure 46-3) with all other conditions being similar. This is principally due to the higher diffusion coefficient of dissolved chlorine at the higher temperature. Kim and Jorne (1) have shown that the Stokes-Einstein product for dissolved chlorine in zinc-chloride solution ($D\mu/T$) is 5.85×10^{-10} g-cm/sec^2-°K, indicating a higher diffusion coefficient for the higher temperature.

The solubility of chlorine decreases at higher temperatures, and as a result the chlorine saturation at 50°C (Figure 46-4) is below 2 g/ℓ . The linear dependence of the corrosion current on the chlorine concentration verifies the findings of Kim and Jorne (1) that mass transfer of dissolved chlorine to the zinc surface is the rate-determining step in the corrosion process and the resulting coulombic inefficiency. At high chlorine concentrations, slightly below the limit of chlorine solubility, the corrosion currents increase sharply. Under these conditions, chlorine evolved in the cell leads to a significantly increased level of bubble-induced convection which, in turn, causes an increase in the corrosion current.

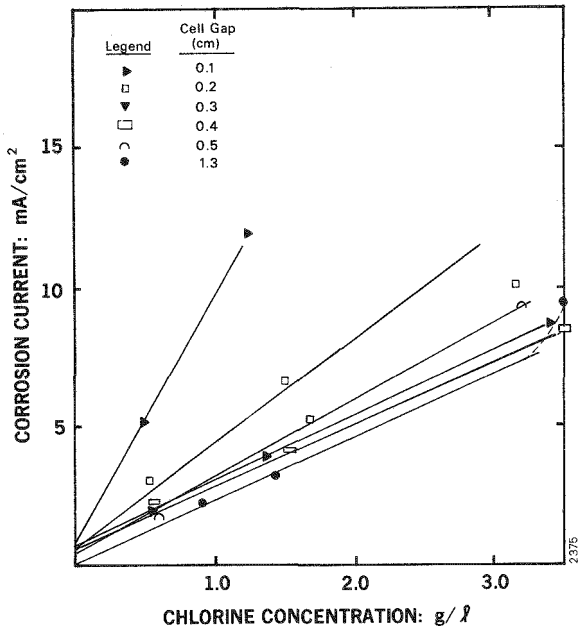

Figure 43-3. Effect of chlorine concentration on the corrosion current density at 20°C illustrating the first order dependence on chlorine concentration. The electrolyte flow rate here is 3 cm^3/cm^2-min.

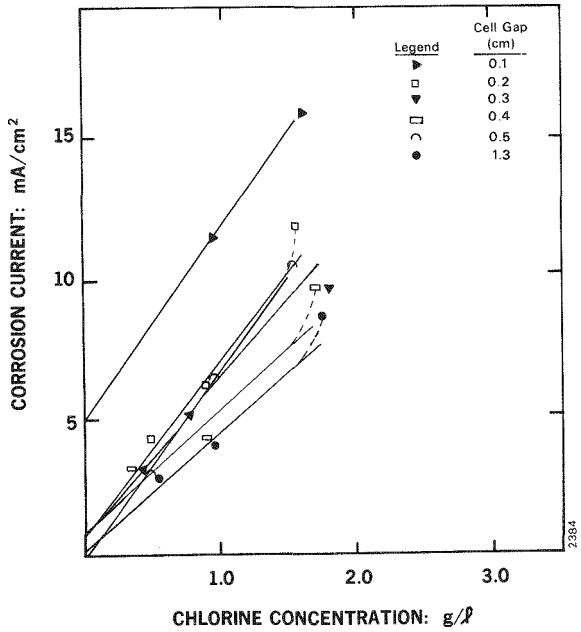

Figure 43-4. Effect of chlorine concentration on the corrosion current density at 50°C and 3 cm^3/cm^2-min flow rate. Again, the corrosion current density is directly proportional to the chlorine concentration.

Effect of Cell Gap

The relationship between the corrosion current density and the cell gap is given in Figure 46-5 for a variety of operating conditions. The corrosion current drops initially as the gap increases and reaches a minimum beyond which a maximum is observed. The corrosion current subsequently reaches an asymptotic value at the large cell gap.

The behavior is similar in all cases in Figure 46-5 and is quite reproducible. The initial decrease in corrosion current is due to the decrease in the forced convection of the electrolyte in the cell gap. As the cell gap increases further, the forced convection decreases, while a bubble-induced convection in the reverse direction takes over and causes an increase in the corrosion current. At even larger cell gaps, an asymptotic value of corrosion is approached which corresponds to the effects of natural convection at the zinc electrode in an infinite medium.

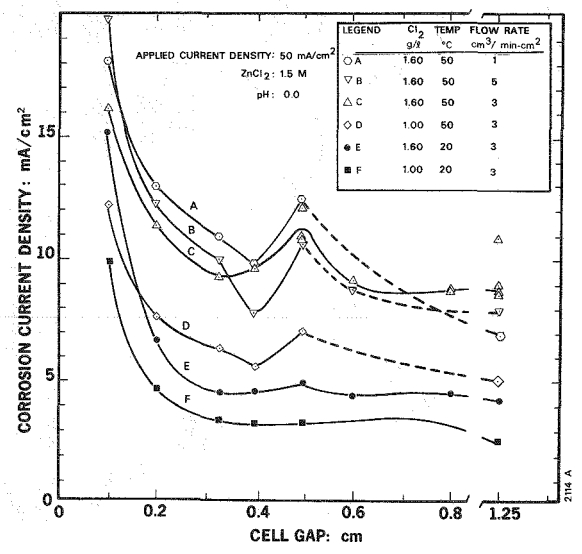

Figure 46-5. Effect of cell-gap on corrosion current density under different operating conditions. The data suggest intermediate minima and maxima in the corrosion current density.

The magnitude of the intermediate maximum is more pronounced at higher temperature, at higher flow rates, and at higher dissolved-chlorine concentration. The effects of the temperature, chlorine concentration and flow rate on the corrosion-current/cell gap behavior can also be seen in Figure 46-5. At higher temperatures the solubility of chlorine is lower and therefore most of the chlorine at the anode is evolved as gas bubbles, hence the effect of the bubble-induced convection is more pronounced (compare curves C and E and curves D and F). Similar behavior can be seen by comparing curves C and D and curves E and F. The maximum is more pronounced at higher chlorine concentration because the solution is closer to chlorine saturation and most of the chlorine evolves as gas bubbles causing larger bubble-induced convection.

Comparison of curves A, B, and C shows the effect of the flow rate on the corrosion current as a function of cell gap. As the flow rate increases from 1 to 5 cm^3/cm^2-min the positions of the minimum and the maximum are shifted to higher cell gaps. This behavior is due to the fact that the forced convection remains effective even at larger gaps. At higher flow rate, the forced convection dominates and the onset of reversed bubble-induced convection is shifted to a larger cell gap.

Effect of Flow Rate

Figures 46-6 and 46-7 show the dependence of the corrosion current density on the flow rate of the electrolyte at 50°C and 20°C, and chlorine concentrations of 1.60 and 4.25 g/ℓ, respectively. A minimum can be observed for most cell gaps. Again, this behavior can be explained by the opposing effects of forced convection and bubble-induced convection. At high flow rates, forced convection dominates and as the flow decreases, the mass transport-controlled corrosion current decreases. At a critical flow rate a reversed flow caused by the chlorine gas evolution at the anode starts to dominate and causes an increase in the corrosion current.

Notice in Figure 46-6 that the corrosion current generally decreases with the cell gap, except for a cell gap of 0.5 cm, the cell gap at which the corrosion current maximum was observed in Figure 46-5. At this cell gap the bubble-induced convection assumes its most predominant effect. Figure 46-7 shows similar behavior at 20°C and at higher chlorine concentrations.

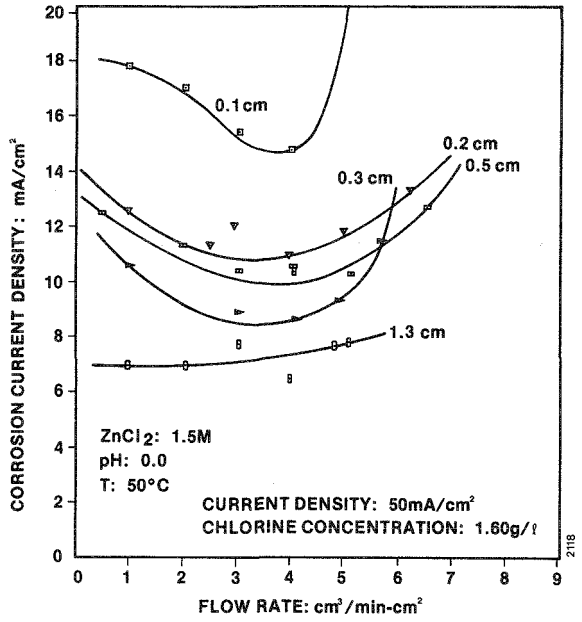

Figure 46-6. Effect of flow rate on the corrosion current density at 50°C. Minima in the corrosion current density occur in the range of 3-4 cm^3/cm^2-min.

Effect of Current Density

A weak linear dependence of the corrosion current density on the applied current density is shown in Figure 46-8. Hence, the coulombic efficiency during zinc deposition increases with the applied current density according to the relationship:

$$\varepsilon_c^c = 1 - \frac{i^c_{cor}}{i^c_a}$$

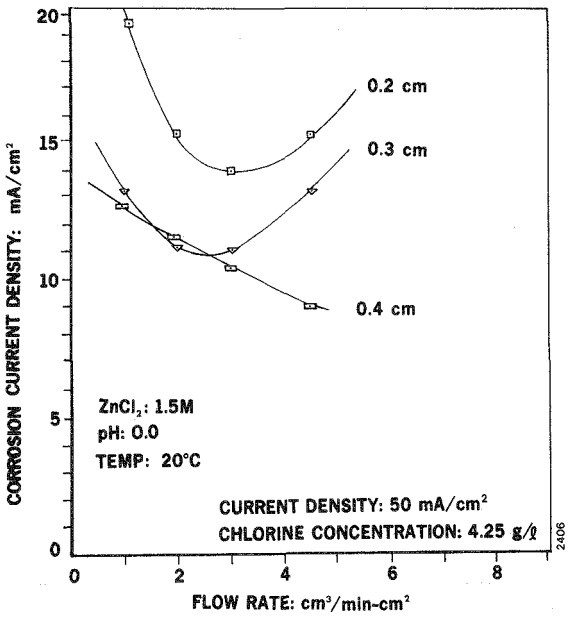

Figure 46-7. Effect of flow rate on the corrosion current density at 20°C. Minima in the corrosion current are again apparent in the range of 2-4 cm^3/cm^2-min.

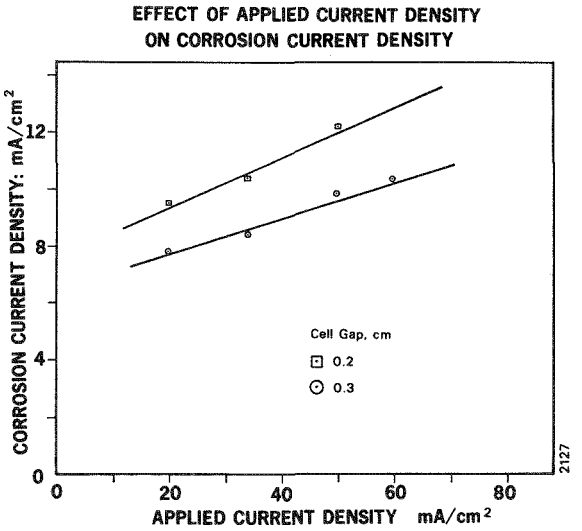

Figure 46-8. Effect of applied current density on the corrosion current density. The weak dependence indicates higher coulombic efficiencies are achievable at higher applied current densities.

Comparison of the Theoretical Model with Experimental Data

The effect of the cell gap on the coulombic efficiency of a zinc-chloride single cell is reported in Figure 46-5 under various experimental conditions. A comparison between the theoretical estimation of the corrosion current and typical experimental results is shown in Figure 46-9. The corrosion current density is plotted versus the cell gap for i = 50 mA/cm^2, V_o = 3 cm^3/cm^2-min, T = 50°C and a chlorine concentration of 1.6 g/ℓ in 1.5M $ZnCl_2$ solution at pH = 0.0. The cell gap was varied between 0.10 and 1.25 cm. The theoretical curve for the above conditions was calculated from equations given in Section 42 after substituting the relevant parameters and considering the contributions of the three convective mechanisms are additive.

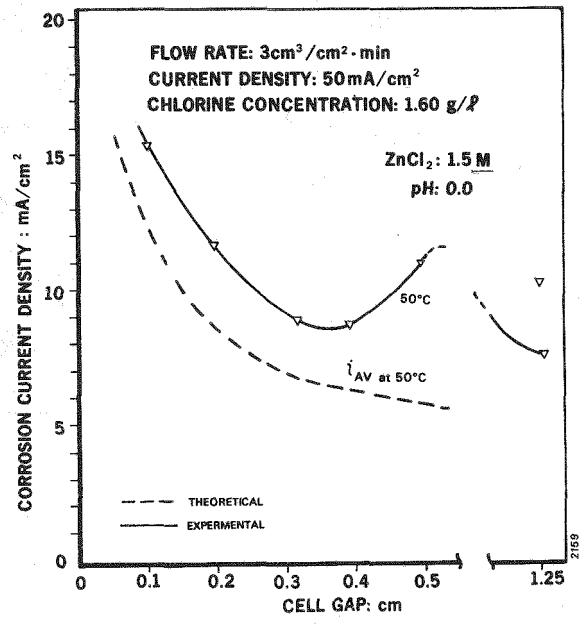

Figure 46-9. Comparison between the theoretical and experimental corrosion currents. Direct summation of the predicted contributions from forced, natural, and bubble-induced convections does not fully explain the experimental data.

The calculated corrosion current is plotted in Figure 46-9 along with the typical experimental results. The behavior is similar, although the theoretical calculations are significantly lower. The assumption that the various convective mechanisms are additive can be responsible for the deviation, as well as the fact that the zinc surface becomes progressively rougher. In addition, entrance effects are significant and the flow may not be fully developed as assumed in the forced convection model. The experimental results for the above conditions can be represented by the following experimental correlation:

$$i_{cor} = \alpha [Cl_2] \cdot d^{\beta} \qquad (46\text{-}1)$$

where the chlorine concentration is given in g/ℓ and the cell gap d in cm. The constants α and β are temperature-dependent and are given by:

Temp °C	α	β
20	1.0	-0.92
50	3.3	-0.49

This correlation holds for up to a cell gap of about 0.3 cm. Beyond this gap value, the behavior is more complicated due to the coupling between the opposing forced and natural convections.

CONCLUSIONS

The main source of coulombic efficiency loss in the zinc-chloride cells is the corrosion of zinc by dissolved chlorine. The experimental results of this work indicate that the coulombic efficiency loss is strongly affected by the fluid motion in the interelectrode gap. Hence, it depends on the cell gap, electrolyte flow rate, chlorine concentration, temperature, and to a small extent on the current density.

At small cell gaps and at high flow rates, forced convection is dominant.

At intermediate cell gaps (0.4 cm) coupling occurs between the three convections. At a cell gap of about 0.4-0.5 cm, the bubble-induced convection becomes significant and a flow reversal occurs which results in a sharp increase in coulombic inefficiency. At a large cell gap (>0.6 cm), the natural convection at the zinc surface dominates and the coulombic inefficiency is minimal. Under the practical operating conditions it appears that at a cell gap of 0.3-0.4 cm the charge coulombic efficiency is optimal.

REFERENCES

1. J. T. Kim and J. Jorne. "Mass Transfer of Dissolved Chlorine to a Rotating Zinc Hemisphere in $ZnCl_2$ Solution." J. Electrochem. Soc., Vol. 125, 1978, pp. 89-94.

2. G. L. Henriksen, S. Kodali, J. Jorne, and C. J. Warde. "Zinc-Electrode Current Efficiency in Zinc-Chlorine Hydrate Batteries: I. Theoretical Aspects." Extended Abstract No. 374, The Electrochemical Society Meeting, Boston, May 1979.

3. A. Kermani, J. Jorne, and S. Kodali. "Zinc-Electrode Current Efficiency in Zinc-Chlorine Hydrate Batteries: II. Experimental Study." Extended Abstract No. 378, The Electrochemical Society Meeting, Boston, May 1979.

4. S. Kodali, J. Jorne, and G. L. Henriksen. "Zinc-Electrode Current Efficiency in Zinc-Chlorine Hydrate Batteries: III. Natural Convection During Electro-deposition." Extended Abstract No. 375, The Electrochemical Society Meeting, Boston, May 1979.

5. A. Kermani. "Coulombic Efficiency Studies in Zinc-Chlorine Battery." MS thesis, Wayne State University, 1980.

6. A. F. Laethem and G. E. Sussman. "Activation of Porous-Graphite Chlorine Electrodes for Zinc-Chlorine Hydrate Batteries." In Extended Abstracts, The Electrochemical Society Meeting, pp. 193-5, May 1978.

Section 47

COULOMBIC EFFICIENCY: VI. COMBINED CONVECTION AT REDUCED PRESSURE

ABSTRACT

Operating a zinc-chloride cell under vacuum during charge reduces the solubility of chlorine in the electrolyte but increases the bubble-induced convection. In this section the opposing effects of these two phenomena are experimentally investigated at a current density of 50 mA/cm^2 for the following conditions: (a) dissolved chlorine concentrations of 0.4-3.0 g/ℓ, (b) cell gaps of 0.1-0.8 cm, (c) electrolyte flow rates of 1.5-5.0 cm^3/cm^2-min, (d) absolute pressures of 0.3-1.0 atm, and (e) temperatures of 20°C and 30°C. At a pressure of 0.66 atm an optimal gap is observed at 0.3 cm. For reduced pressures in the range of 0.6-0.7 atm, net improvements in charge coulombic efficiency are achieved, although the gains are somewhat suppressed by the increased level of bubble-induced convection.

INTRODUCTION

The previous section -- Section 46 -- reviewed the results of an experimental coulombic efficiency study performed at ambient pressure. In that study the concentration of dissolved chlorine was controlled by sparging mixtures of chlorine and nitrogen through the electrolyte. The results indicated that the corrosion current density during charge was directly proportional to the concentration of dissolved chlorine.

During the charge mode of the zinc-chloride battery, molecular chlorine is formed at the porous-graphite anode and the electrolyte is saturated with dissolved chlorine. Because dissolved chlorine reacts with zinc, resulting in coulombic efficiency losses (1), it is highly desirable to reduce the solubility of chlorine in the electrolyte. The solubility of chlorine can be reduced by (a) adding supporting electrolytes, (b) increasing the temperature, or (c) decreasing the partial pressure of gaseous chlorine.

The effect of the total pressure on the solubility of chlorine in 3M zinc chloride solution at various temperatures has been measured and is shown in Figure 47-1 (2). The solubility of chlorine at 30°C is shown in Figure 47-2 (2) where linear dependence is obtained between the chlorine solubility and the pressure in accordance with Henry's law.

$$P_{Cl_2} = k\, C_{Cl_2} \qquad (47\text{-}1)$$

and at 30°C

$$k = 0.39 \text{ liter atm/g}$$

The present work is an attempt to systematically investigate the effect of reduced pressure on the charge coulombic efficiency. As the pressure is reduced the chlorine solubility is lowered. The contribution of bubble-induced convection to the corrosion current may increase, however, due to the larger volume occupied by evolved chlorine gas. The following factors have been investigated in the present study:

1. The dependence of the corrosion current on the chlorine concentration at and below saturation.

2. The dependence of the corrosion current on the absolute pressure at and below chlorine saturation.

3. The dependence of the corrosion current on the interelectrode cell gap at low pressures and under various operating conditions.

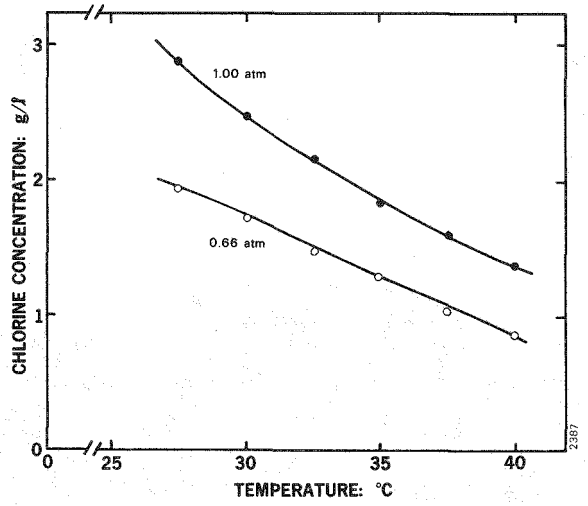

Figure 47-1. The dependence of chlorine solubility on the temperature and pressure in 3M zinc chloride solution.

EXPERIMENTAL

The coulombic efficiency of the zinc-electrode was investigated in a zinc-chloride single cell located in a low pressure chamber. The cell consisted of a zinc electrode and a flow-through porous-graphite chlorine-electrode. The chlorinated zinc-chloride solution (pH = 0.0) was fed through the porous-graphite electrode and upward between the chlorine and zinc electrodes. Coulombic efficiencies were determined by weighing the zinc plates and comparing them to the theoretical weights expected according to Faraday's law. An expanded view of the cell is shown in Figure 47-3. It consists of a chlorine electrode holder and manifold made of dense graphite, a porous-graphite electrode (Union Carbide PG-60) which was

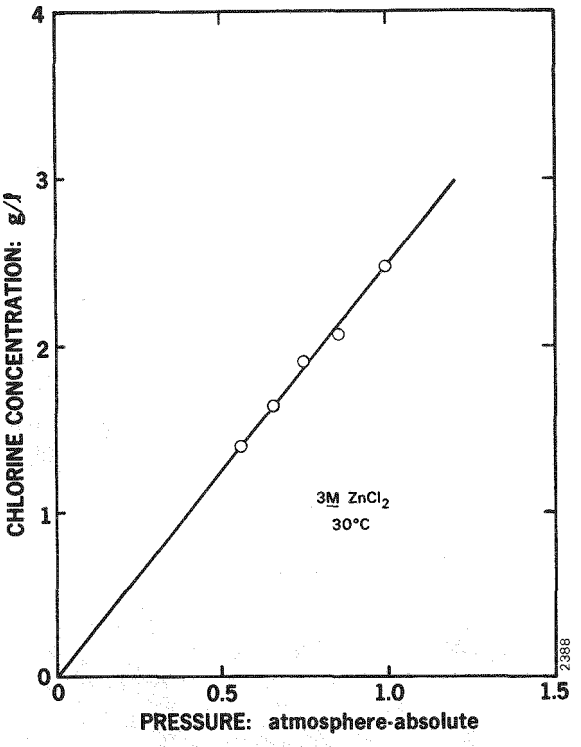

Figure 47-2. The effect of pressure on chlorine solubility in 3M zinc chloride and 30°C. Henry's law appears to be valid.

activated electrochemically (3), plastic frame and mask for the chlorine electrode, a plastic spacer, and a dense graphite block (Union Carbide ATJ) which served as the substrate for the zinc electrode. The electrochemical active area of the cell was 100 cm^2 (10 x 10 cm). The cell was constructed of Kynar and the electrical connections were made of titanium. The cell was clamped together and placed in a vacuum chamber which served also as the electrolyte sump. The experimental apparatus is shown in Figure 47-4. The electrolyte was circulated by a gear pump (Micropump Corp.) from the low pressure sump through a temperature control bath (Haake E52), a spectrophotometer (Turner 350), a flow meter (Brook R-6-15-B tube size), and flow shut-off and sampling valves.

The low pressure in the cell housing was maintained by a water aspirator. The gaseous chlorine was removed prior

to the aspirator by a sodium hydroxide scrubber. The pressure was regulated by a bleed valve and measured by a mercury manometer.

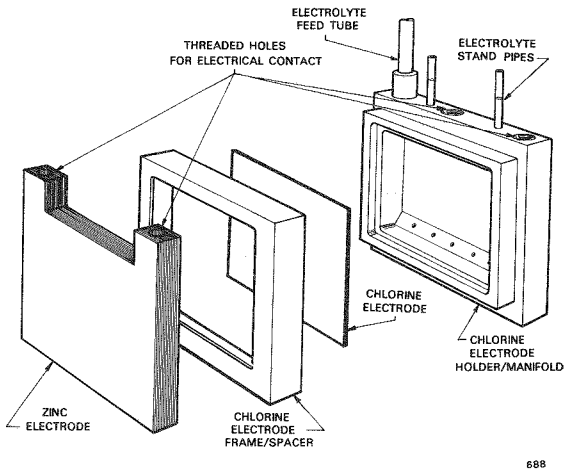

Figure 47-3. Expanded view of the experimental zinc-chloride single cell.

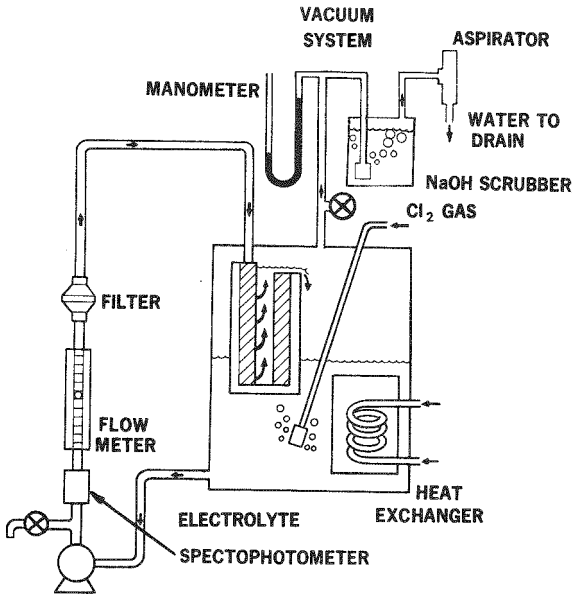

Figure 47-4. Flow diagram of experimental zinc-chloride single cell.

The dissolved chlorine concentration was monitored continuously in a 1/4-inch glass cell and a Turner 350 spectrophotometer set at 340 nm. The cell was calibrated by measuring the dissolved chlorine by titration with sodium thiosulfate and the calibration line is shown in Figure 47-5. The spectrophotometric analysis of dissolved chlorine allows a continuous reliable determination. The normal sampling involves some dechlorination of the sample and this introduces unknown errors. The spectrophotometric method is especially advantageous for operation under partial vacuum where electrolyte samples are difficult to obtain.

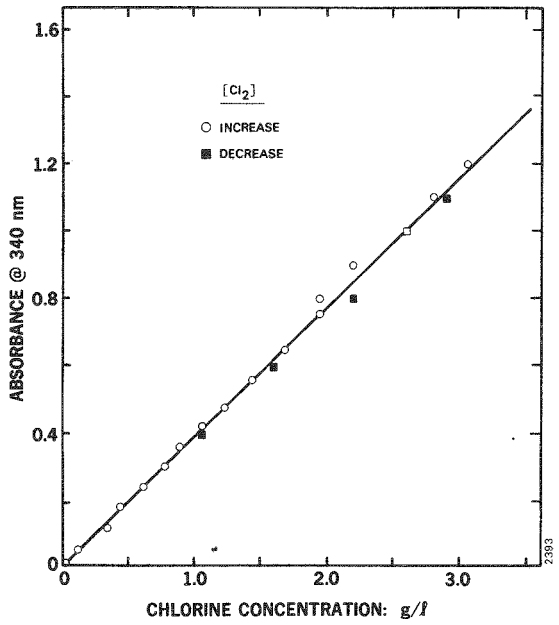

Figure 47-5. Calibration of the spectrophotometer. Absorbance at 340 nm vs. the chlorine concentration (obtained by titration). The data includes increased and decreased chlorine concentrations. 1.5M $ZnCl_2$ + leveling agent, pH=0.0, 20°C.

The cell was charged by a constant current power supply (Udylite PC-10) and the charging time was one hour at 50 mA/cm^2. The electrolyte solution consisted of 1.5M zinc chloride and a small amount of leveling agent. The pH of the solution was adjusted at pH = 0.0 by adding HCl. The coulombic efficiency during charge was calculated from the weight of the zinc plates. The zinc plates were peeled from the graphite substrate, washed thoroughly

with distilled water and acetone, and dried rapidly prior to weighing.

Before each experiment, the electrolyte was sparged initially with nitrogen, then with chlorine until the concentration of dissolved chlorine, as measured by the spectrophotometer, remained constant. The current was turned on only after the system stabilized to the desired pressure and the corresponding chlorine concentration.

RESULTS AND DISCUSSION

Effect of Pressure on Chlorine Solubility

Figure 47-6 shows the effect of pressure on chlorine solubility in 1.5M zinc chloride solution, pH = 0.0 and temperature of 20°C. Linear dependence can be observed, and the Henry's constant is calculated as k = 0.29 liter-atm/g at 20°C.

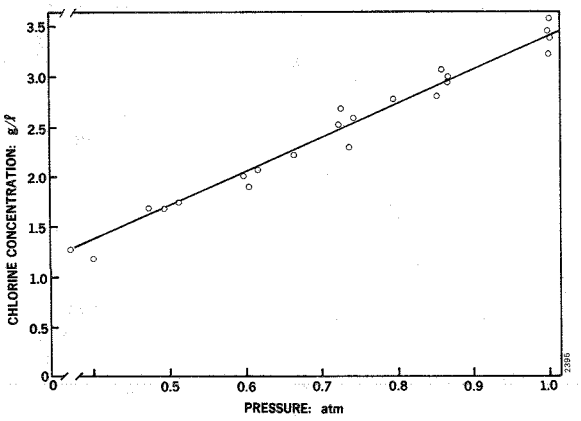

Figure 47-6. The effect of pressure on chlorine solubility in 1.5M zinc chlorine solution at 20°C.

Effect of Low Pressure at and Below the Chlorine Saturation.

In Figure 47-7 the corrosion current is plotted as a function of the dissolved chlorine concentration at cell gaps of 0.20, 0.28, and 0.38 cm. The experiments were conducted at absolute total pressure of 0.5 atm, and the various chlorine concentrations were maintained by sparging the electrolyte with mixtures of chlorine and nitrogen. The highest chlorine concentrations correspond to the saturation level. The corrosion current depends linearly on the dissolved chlorine concentration, although the common intercepts at i_{cor} = 1.0 mA/cm^2 indicate the presence of other corrosion losses, most probably hydrogen evolution. The corrosion current decreases with increasing the cell gap from 0.20 to 0.38 cm. Similar behavior was observed previously at ambient pressure, although a minimum was observed at higher gap and was attributed to coupling between the bubble-induced convection and the forced and natural convections. It is expected that bubble-induced convection is more significant at lower pressure because of the relatively larger volume of the evolved chlorine gas.

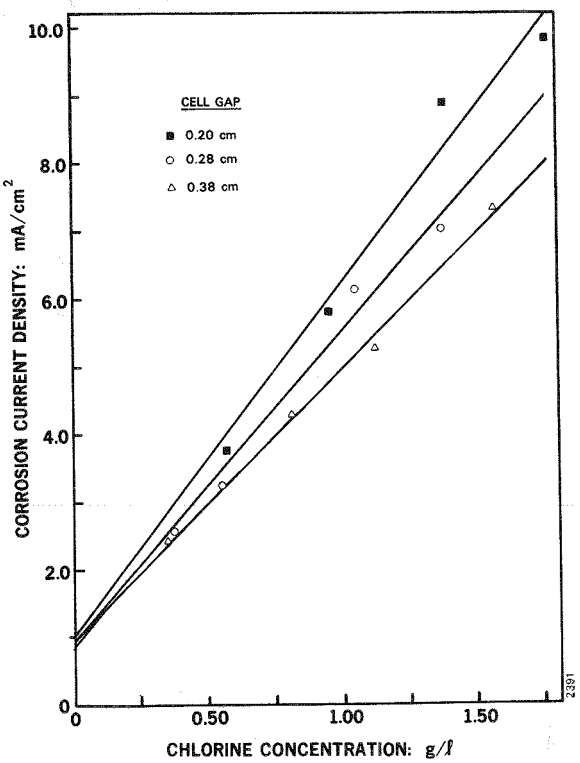

Figure 47-7. The corrosion current versus the dissolved chlorine concentration at and below chlorine saturation at the cell gaps of 0.2 cm, 0.28 cm, and 0.38 cm. P = 0.5 atm, T = 20°C, 1.5M $ZnCl_2$ (pH=0), and i = 50 mA/cm^2.

The effect of reduced pressure on the corrosion current is shown in Figures 47-8 and 47-9 for two different cell gaps, 0.20 and 0.38 cm, respectively. When the data at a pressure of 0.50 atm are compared to data at ambient pressure (1 atm), the apparent corrosion current is higher under low pressure for the same chlorine concentration.

In actual practice, when the pressure in the battery stack is altered, the dissolved chlorine concentration also changes, as shown in Figure 47-6. In 1.5M zinc chloride solution, the concentration of chlorine decreases from 3.4 g/ℓ to 1.7 g/ℓ as the total pressure is decreased from 1.0 atm to 0.5 atm. The corrosion current is found to be directly proportional to chlorine concentration with all the other conditions remaining constant as discussed in Section 42. Thus, as the chlorine concentration is lowered from 3.4 g/ℓ to 1.7 g/ℓ, the corrosion current should also decrease by a factor of 2. However, as shown in Figure 47-9, the observed corrosion current for the two chlorine concentrations 3.4 g/ℓ (1 atm), 1.7 g/ℓ (0.5 atm) are 11.3 mA/cm^2 and 7.4 mA/cm^2, respectively. Thus, at 0.5 atm pressure the corrosion current is larger than expected. At the lower pressure the volume of evolved gas in the chlorine saturated solution is larger and the bubble-induced convection under these conditions makes a larger contribution to the corrosion current. At chlorine concentrations below saturation, the evolved chlorine gas dissolves in the solution minimizing the bubble-induced convection and, hence, the corrosion current is smaller.

Effect of Low Pressure in Chlorine-Saturated Solutions.

The effect of low pressure on the corrosion current was investigated in chlorine-saturated solutions. The dissolved chlorine concentration was varied by controlling the pressure in the chamber. Therefore in all these experiments the solutions were saturated and most of the chlorine evolved in gaseous form.

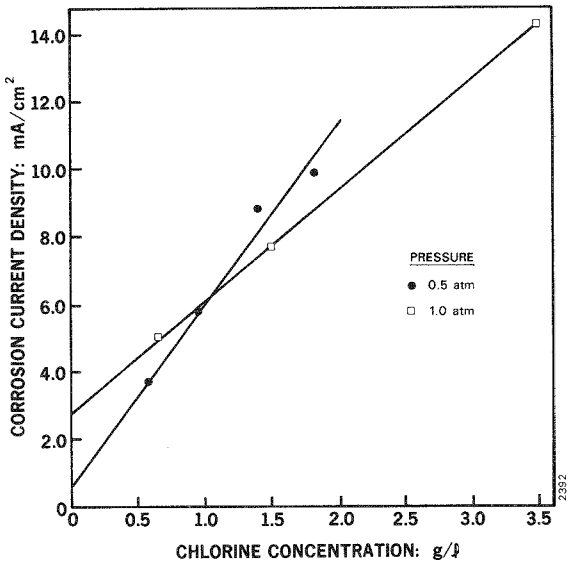

Figure 47-8. Comparison between the corrosion current at low pressure (0.5 atm) and ambient pressure (1.0 atm). 1.5M $ZnCl_2$ (pH=0), T = 20°C. Cell Gap: 0.2 cm; i = 50 mA/cm^2. Flow Rate: 3 cm^3/cm^2-min.

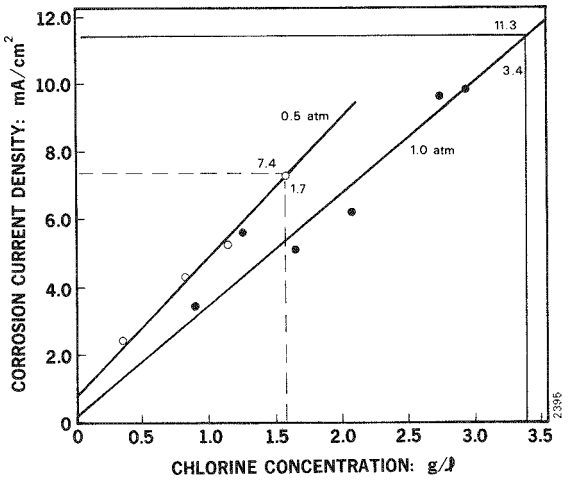

Figure 47-9. Comparison between the corrosion current at low pressure (0.5 atm) and ambient pressure (1.0 atm). 1.5M $ZnCl_2$ (pH=0), T = 20°C Cell Gap: 0.38 cm; i = 50 mA/cm^2. Flow Rate: 3 cm^3/cm^2-min.

Figure 47-10 shows the effect of pressure (or correspondingly saturated chlorine concentration) on the corrosion current for two cell gaps. Deviations from linear behavior can be seen as the pressure decreases. The deviations possibly can be explained by the stronger effect of bubble-induced convection at lower pressure where the volume of the evolved gaseous chlorine is larger.

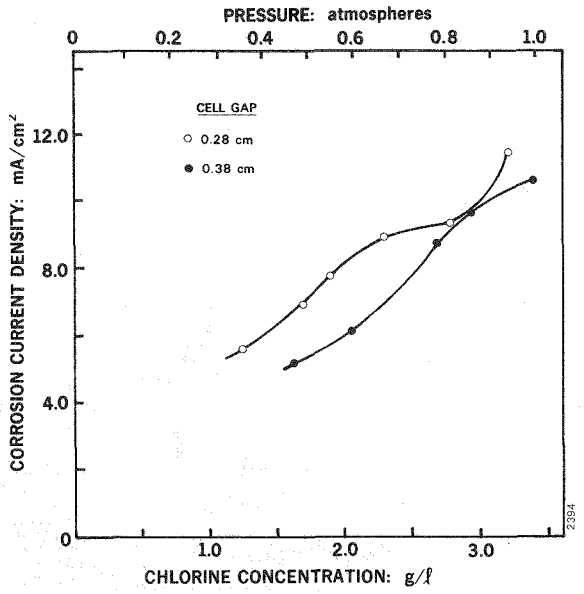

Figure 47-10. The corrosion current vs. chlorine solubility (or pressure) at saturation for cell gaps of 0.28 cm and 0.38m cm. Solution: 1.5M $ZnCl_2$ (9 pH=0); Chlorine Saturated: T = 20°C. Flow Rate: 3 cm^3/cm^2-min. Current Density: i = 50 mA/cm^2.

Figure 47-11 shows the effect of the pressure on the corrosion current for various electrolyte flow rates. These experiments were performed in order to investigate the effect of forced convection on the region where bubble-induced convection is dominant. As can be seen in Figure 47-11, deviations from linearity are observed at all three flow rates. The corrosion current increases as the flow rate increases from 1.5 to 5 cm^3/cm^2 min. The main observation is that the region of deviation from linear behavior shifts to the left, or to a lower pressure as the flow rate is increased. As the flow rate increases, the effect of bubble-induced convection is shifted to lower pressures where it is more pronounced. At the lowest pressure (0.34 atm) the effect of the varying flow rate is negligible because the bubble-induced convection is predominant.

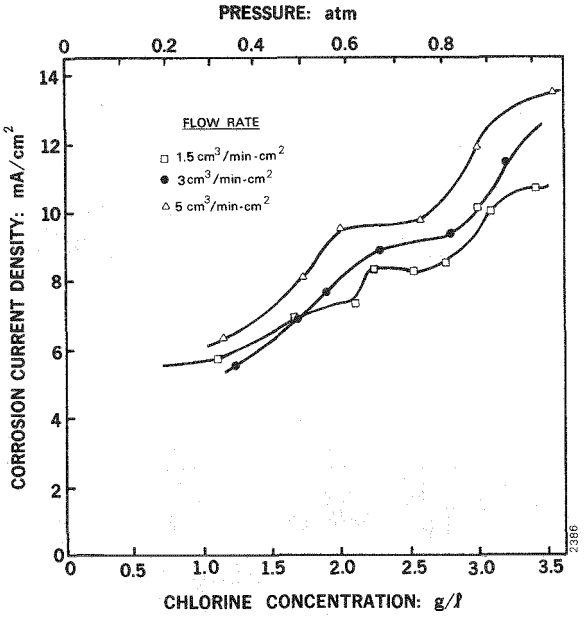

Figure 47-11. The corrosion current vs. chlorine solubility (or pressure) at saturation for flow rates of 1.5 cm^3/cm^2-min; 3.0 cm^3/cm^2-min; 5.0 cm^3/cm^2-min. Solution: 1.5M $ZnCl_2$ (pH=0); Chlorine Saturated: T = 20°C; Cell Gap: 0.26 cm; Current Density: i = 50 mA/cm^2.

Effect of Cell Gap on Charge Coulombic Efficiency

The effect of cell gap on the charge coulombic efficiency was studied under reduced pressure. Experiments were conducted under two different sets of conditions: (1) 0.66 atm absolute pressure and 30°C, and (2) 1.0 atm absolute (ambient) pressure and 50°C. In both cases the electrolyte was saturated with dissolved chlorine at 1.6 g/ℓ. One would predict a higher corrosion current density at the elevated temperature due to the larger diffusion coefficient for dissolved

chlorine and also a reduction in the diffusion boundary-layer thickness due to a reduction in the electrolyte viscosity.

Figure 47-12 compares the data from the two experiments. The data are surprisingly similar despite the different conditions. The reason is believed to be due to increased bubble-induced convection in the 30°C experiments conducted at 0.66 atm pressure.

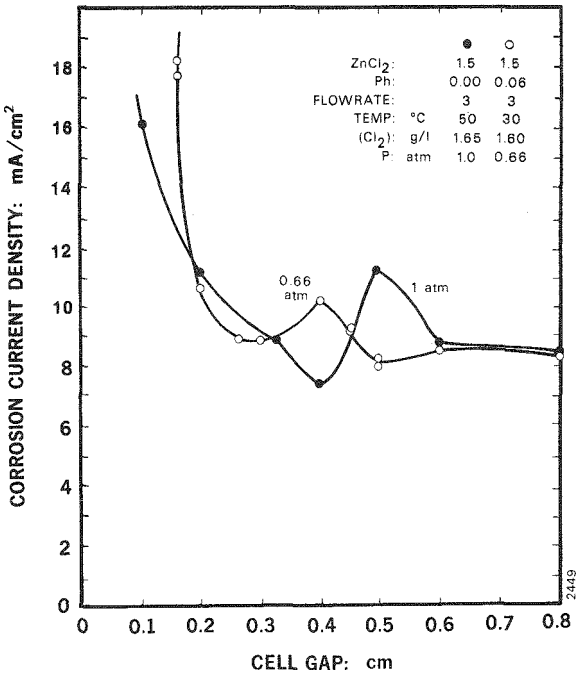

Figure 47-12. Effect of cell-gap on charge coulombic efficiency under reduced pressure and atmospheric pressure.

The effect of pressure is noticeable, however, at cell gaps between 0.3-0.5 cm where local maxima can be observed. The maximum corrosion current density occurs at lower cell gap under reduced pressure. This shift can be explained by the coupling between the bubble-induced convection and the forced convection. By decreasing the pressure, the bubble-induced convection is intensified and the resultant increase in corrosion current will occur at a smaller cell gap. The minimum is believed to be a result of a balance between the opposing forced and bubble-induced convections. Since, the bubble-induced convection is stronger at a lower pressure, the minimum occurs at smaller cell gap for which the forced convection is also stronger.

The results suggest that a maximum charge coulombic efficiency occurs at cell gap of 0.3 cm when the operating pressure is 0.66 atm.

Effect of Low Pressure on the Mass Transfer Coefficients of Dissolved Chlorine to the Zinc Electrode

In order to separate the pressure effect from the corresponding dissolved chlorine concentration, the mass transfer coefficients of chlorine were calculated by dividing the molar flux of chlorine to the zinc surface by the bulk concentration of chlorine.

$$k_{Cl_2} = \frac{i_{cor}}{nF \cdot C_{Cl_2}} \qquad (47\text{-}2)$$

If we express i_{cor} in mA/cm^2 and C_{Cl_2} in g/ℓ, the mass transfer coefficient in (cm/sec) is given by:

$$k_{Cl_2} = 3.67 \times 10^{-4} \frac{i_{cor}}{C_{Cl_2}} \qquad (47\text{-}3)$$

Mass transfer coefficients, k_{Cl_2}, are plotted vs. the pressure for two cell gaps in Figure 47-13, and for three different flow rates in Figure 47-14. Although the data are scattered, there appears to be a general trend toward high mass transfer coefficient at low pressure.

The mass transfer coefficient is higher at the smaller cell gap as can be seen from Figure 47-13, probably due to the higher forced convection. The mass transfer coefficient increases generally with the electrolyte flow rate as can be seen in Figure 47-14, again due to higher forced convection. Both figures indicate that the mass transfer

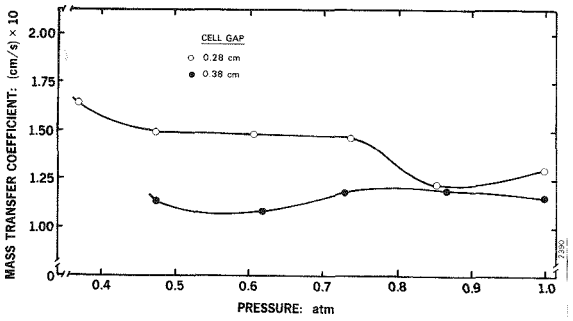

Figure 47-13. Mass transfer coefficients of dissolved chlorine at the zinc surface vs. the pressure for the cell gaps of 0.28 cm, 0.38 cm. Solution: 1.5M $ZnCl_2$ (pH=0) - Chlorine Saturated: T = 20°C; Current Density: i = 50 mA/cm^2; Flow Rate: 3 cm^3/cm^2-min.

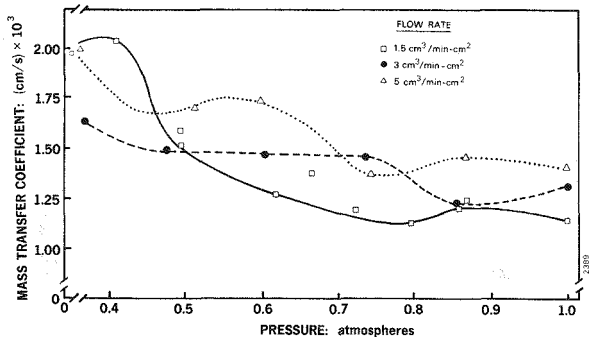

Figure 47-14. Mass transfer coefficients of dissolved chlorine at the zinc surface vs. the pressure for the flow rates of 1.5 cm^3/cm^2 min; 3.0 cm^3/cm^2 min; 5.0 cm^3/cm^2 min. Solution: 1.5M $ZnCl_2$ (pH=0); Chlorine Saturated: T = 20°C; Current Density: i = 50 mA/cm^2; Cell Gap: 0.26 cm.

coefficient tends to increase as the pressure drops below 0.4 atm, however lower pressure could not be reached due to the experimental limitations of the system.

CONCLUSIONS

The operation of the zinc-chloride battery under partial vacuum during charge results in opposing phenomena:

1. The solubility of dissolved chlorine decreases proportionally.

2. The effect of bubble-induced convection increases due to the larger volume of the evolved chlorine.

The effect of the first phenomenon is to increase the coulombic efficiency, while the effect of the second is to decrease the coulombic efficiency. The net result is improved charge coulombic efficiency at reduced pressure, but the magnitude of the improvement is reduced due to increased bubble-induced convection.

REFERENCES

1. G. L. Henriksen, S. Kodali, J. Jorne, and C. J. Warde. "Zinc-Electrode Current Efficiency in Zinc-Chlorine Hydrate Batteries: I. Theoretical Aspects." Abs. 374, 155th Meeting of the Electrochemical Society, Boston, May 1979.

2. Development of the Zinc-Chlorine Battery for Utility Applications. Palo Alto, Calif.: Electric Power Research Institute. April 1979. EM-1051.

3. A. F. Laethem and G. E. Sussman, "Activation of Porous-Graphite Chlorine Electrodes for Zinc-Chlorine Hydrate Batteries." In Extended Abstracts, The Electrochemical Society Meeting. Vol. 78-2, 1978, pp. 193-5.

4. A. Kermani, J. Jorne, and S. Kodali, "Zinc Electrode Current Efficiency in the Zinc-Chlorine Hydrate Battery: II Experimental Studies." Abs. 378, 155th Meeting of the Electrochemical Society, Boxton, May 1979.

Section 48

OPTIMAL CELL GAP FOR ENERGY EFFICIENCY

ABSTRACT

The electrochemical energy efficiency of zinc-chloride cells depends on the inter-electrode gap through the coulombic and voltaic efficiencies. In this section the dependence of the coulombic and voltaic efficiencies on cell gap is analyzed during charge. Their product, the electrochemical energy efficiency during charge, is maximized as a function of cell gap. Previously obtained experimental data are used for the coulombic efficiency, while a mathematical relationship is developed for the voltaic efficiency. For selected conditions of 50 mA/cm^2 current density, 1.5M $ZnCl_2$ electrolyte, and a dissolved chlorine concentration of 1 g/ℓ, the optimal cell gaps at 20°C and 50°C are 0.3 cm and 0.4 cm, respectively. The electrochemical energy efficiencies corresponding to these conditions are predicted to be 0.87 and 0.84, respectively.

INTRODUCTION

A fractional electrochemical energy efficiency target of 0.75 has been established in the development of the zinc-chloride battery for the electric-utility load-leveling application (1). Because no separators are used, the coulombic efficiency of the battery presents the main obstacle in obtaining electrochemical energy efficiencies in the range of 0.75. See Table 48-1.

As can be seen in Sections 42 through 47, an extensive effort has been pursued in order to identify and measure the sources of coulombic inefficiencies. The potential sources of coulombic inefficiencies are dendrites, hydrogen evolution, and the corrosion reaction between electrodeposited zinc and dissolved chlorine. It has been shown that the last source is the major cause of coulombic inefficiency, especially during charge when the solution is chlorine-saturated and three convective mechanisms combine to enhance the transport of chlorine to the zinc surface (2-4). Forced convection, natural convection, and bubble-induced convection are the three sources of convective transport in the inter-electrode gap.

While efforts to improve the coulombic efficiency must be continued, it is important to keep in mind that the electrochemical energy efficiency is the parameter to be maximized. The inter-electrode cell gap is a critical parameter in determining the electrochemical energy efficiency of the battery because it affects the voltaic efficiency directly through the ohmic resistance of the electrolyte and it affects the coulombic efficiency indirectly by changing the magnitude of the convective flows in the inter-electrode gap. This section presents an approach for optimizing the cell gap based on maximization of the electrochemical energy efficiency during charge. The optimization is performed only for the charge process. However, a similar approach can be applied for the discharge process and for the entire charge-discharge operation.

ELECTROCHEMICAL ENERGY EFFICIENCY DURING CHARGE

The electrochemical energy efficiency during charge, ε_e^c, is defined as the

Table 48-1

EFFICIENCY STATUS AND GOALS

	System (kWh)	System (volts)	Fractional Efficiencies ε_v	ε_c	ε_e
Status:	1.7	2	0.82	0.78	0.64
	20	20	0.79	0.75	0.60
	50	20	0.83	0.71	0.59
Goals:	Commercial Battery		0.88	0.85	0.75

ratio of the energy stored, in the form of electrodeposited zinc and evolved chlorine, to the dc energy input during charge. It is the product of the coulombic efficiency, ε_c^c, and the voltaic efficiency, ε_v^c, during charge:

$$\varepsilon_e^c = \varepsilon_c^c \cdot \varepsilon_v^c \qquad (48\text{-}1)$$

COULOMBIC EFFICIENCY DURING CHARGE

The coulombic efficiency during charge can be expressed as the ratio of the current density equivalent to the actual rate of zinc deposition and the applied current density:

$$\varepsilon_c^c = \frac{i_a^c - i_{cor}^c}{i_a^c} \qquad (48\text{-}2)$$

where i_a^c is the applied current density and i_{cor}^c is the corrosion current rent density due to the reaction of dissolved chlorine with zinc throughout the charge process. The corrosion current during charge has been measured by Kermani, Jorne, and Kodali (3) and discussed in Section 46.

Typical results of corrosion current versus cell gap at 20°C and 50°C are shown in Figures 48-1 and 48-2, respectively. The increase in corrosion current at intermediate cell gap, 0.4-0.5 cm, has been correlated to the coupling between the forced, natural, and bubble-induced convections (2-4). For the cell gaps of practical interest, which are below the range where maximum in corrosion current has been observed, namely below d = 0.3 cm, the corrosion current density can be expressed by:

$$i_{cor}^c = \alpha \cdot d^{\beta} \cdot [Cl_2] \qquad (48\text{-}3)$$

where α and β are constants which depend on the temperature, $[Cl_2]$ is the concentration of dissolved chlorine in g/ℓ, and d is the cell gap (cm).

Curve fitting of the data in Figures 48-1 and 48-2 gives the following numerical values for α and β :

Temp °C	α	β
20	1.0	-0.92
50	3.3	-0.49

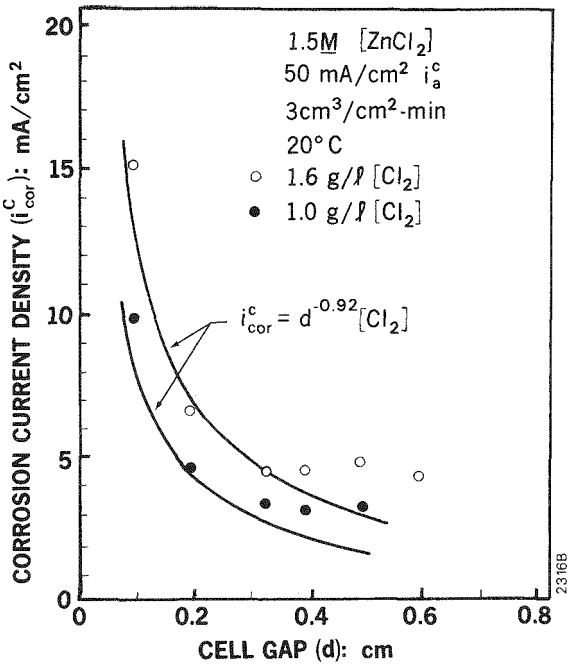

Figure 48-1. The corrosion current density vs. the cell gap at 20°C. The lines represent empirical equations up to d = 0.3 cm.

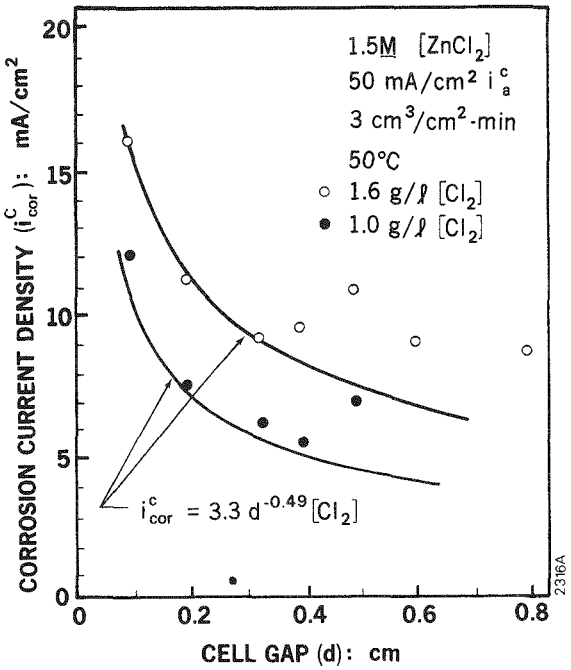

Figure 48-2. The corrosion current density vs. the cell gap at 50°C. The lines represent empirical equations up to d = 0.3 cm.

The linear dependence of the corrosion current on the chlorine concentration substantiates previous findings (7) that the process is mass transfer limited.

VOLTAIC EFFICIENCY DURING CHARGE

The voltaic efficiency during charge is the ratio between the equilibrium potential of the cell, and the potential during charge:

$$\varepsilon_v^c = \frac{E}{E + \eta + i_a^c A R_{eff}} \qquad (48\text{-}4)$$

where E is the equilibrium potential, η is the cell overpotential, i_a^c is the applied current density during charge, A is the electrode area, and R_{eff} is the effective resistance of the electrolyte-chlorine gas mixture in the inter-electrode gap.

The effective resistance of the cell without taking into consideration the void fraction due to gas is given simply by:

$$R_{eff} = \frac{\rho d}{A} \qquad (48\text{-}5)$$

where ρ is the electrolyte's resistivity (ohm·cm), d is the cell gap (cm), and A is the electrode's area (cm^2).

At small cell gap, typically below 0.1 cm, the effective resistance of electrolyte-gas mixture behaves nonlinearly with the cell gap due to the increasing buildup of gas bubbles in the inter-electrode space. Tobias (5) and Nagy (6) developed expressions for the effective resistance of electrolyte-gas mixtures as a function of the void fraction, the cell gap, and the rising velocity of the gas bubbles:

$$R_{eff} = \frac{2 R T \rho \; i_a^c}{W P n F S} \left[\frac{1}{f (1-f) (2-f)^2} \right] \qquad (48\text{-}6)$$

where R is the gas constant, T is the temperature (°K), is the resistivity of gas-free electrolyte (ohm·cm), W is the width of the electrode (cm), P is the pressure (atm), F is Faraday's constant (96,487 coul/equiv), n is the number of electrons transferred in unit reaction, S is the average rising velocity of the gas bubbles in the electrolyte (cm/s), and f is the average void fraction in the inter-electrode space (dimensionless). The behavior of the voltaic efficiency during charge is presented in Figures 48-3 and 48-4, as a function of the cell gap for typical charge conditions, at 20°C and 50°C, respectively. As can be seen clearly from these figures, the effect of void fraction is noticeable at very small cell gap, well below the practical gaps which are being considered for the zinc-chloride battery. A cell gap of at least 0.2 cm is required in order to reach a delivered capacity of 200 mAh/cm^2. Therefore, for the practical conditions the effective resistance of the cell can be described by Eq. 48-5 which neglects the void fraction. The voltaic efficiency can be described for practical conditions by:

$$\varepsilon_v^c = \frac{E}{E + \eta + i_a^c \rho d} \qquad (48\text{-}7)$$

In the following calculations, the overpotential was taken as $\eta = 0.050$ V following previous results.

OPTIMAL CELL GAP

The electrochemical energy efficiency during charge is the product of the charge coulombic and voltaic efficiency as given by Eq. 48-1. The experimental coulombic efficiency and the voltaic efficiency are given by Eq. 48-2, 48-3, and 48-7, which can be substituted in Eq. 48-1 to give:

$$\varepsilon_e^c = \left[1 - \frac{\alpha[Cl_2]\, d^{\beta}}{i_a^c}\right]\left[\frac{E}{E + \eta + i_a^c \rho d}\right] \qquad (48\text{-}8)$$

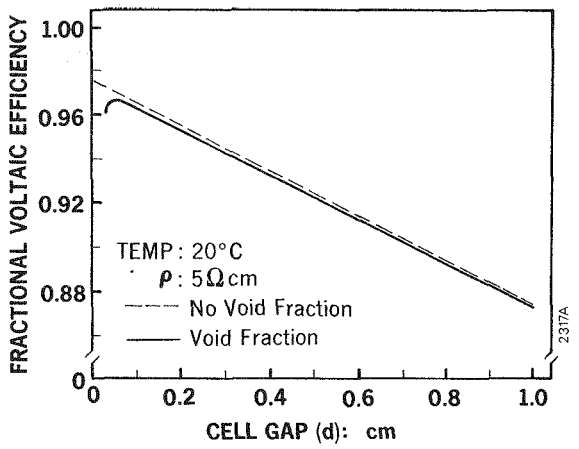

Figure 48-3. The voltaic efficiency during charge vs. the cell gap at 20°C.

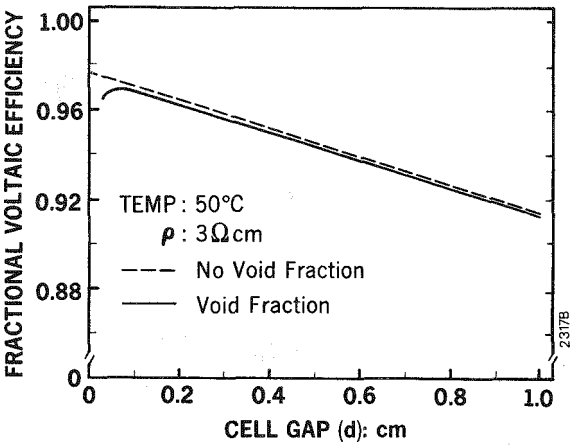

Figure 48-4. The voltaic efficiency during charge vs. the cell gap at 50°C.

The cell gap corresponding to the maximum energy efficiency during charge can be obtained by setting the partial derivative with respect to the cell gap, d, equal to zero:

$$\frac{\partial \varepsilon_e^c}{\partial d} = 0 \qquad (48\text{-}9)$$

Since the empirical equation for the corrosion current (Eq. 48-3) holds only for cell gaps below 0.3 cm, the optimi-

zation can be done generally by plotting the product of the coulombic and voltaic efficiencies and finding the cell gap which corresponds to the maximal energy efficiency.

The plots of the coulombic, voltaic, and energy efficiencies as a function of the cell gap are shown in Figures 48-5 and 48-6 for 20°C and 50°C, respectively. The resistivities of 1.5M $ZnCl_2$ solution are taken as 5 ohm·cm and 3 ohm.cm at 20°C and 50°C, respectively. The chlorine concentration is 1 g/ℓ in both cases. The optimal cell gap is 0.3 cm and 0.4 cm at 20°C and 50°C, respectively. In these calculations the effect of the gas void fraction on the voltaic efficiency is neglected since the effect is insignificant at the practical cell gaps. Using these assumptions the calculated optimal energy efficiencies during charge are 0.87 and 0.84 at 20°C and 50°C, respectively.

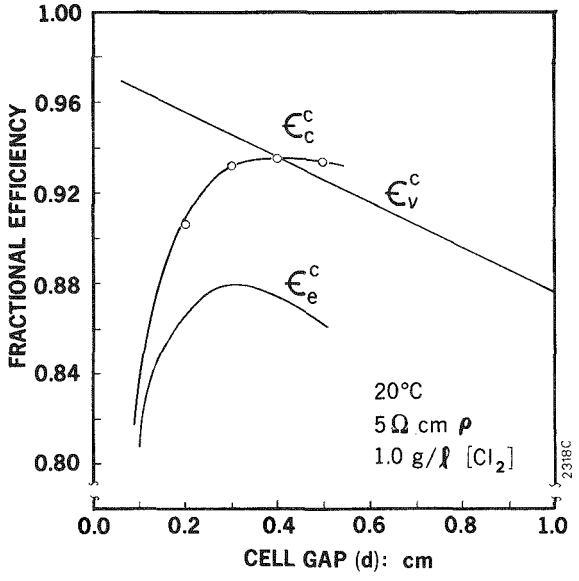

Figure 48-5. Optimization of the cell gap: the dependence of the coulombic, voltaic, and energy efficiency during charge on the cell gap at 20°C.

The optimal cell gap can be determined similarly for various chlorine concentrations. Generally, the optimal cell gap is larger at higher chlorine concentration because the relative magnitude of the coulombic efficiency is more important, hence, requiring a larger cell gap. However, this effect is relatively small.

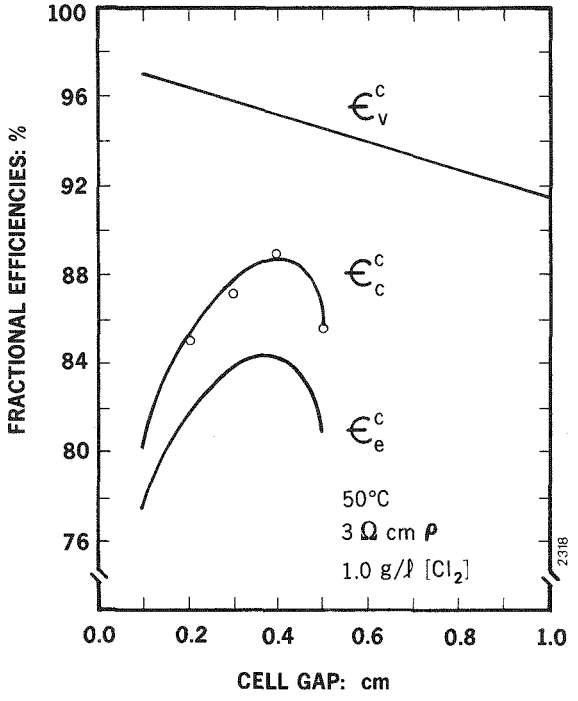

Figure 48-6. Optimization of the cell gap: the dependence of the coulombic, voltaic, and energy efficiency during charge on the cell gap at 50°C.

A general rule can be established: the optimal cell gap is generally slightly smaller than the cell gap at which a maximum in the coulombic efficiency occurs. The optimal cell gap therefore corresponds to a range where the forced convection is weak and the bubble-induced convection opposes the forced and natural convections and minimizes the convective diffusion of chlorine to the zinc electrode.

CONCLUSIONS

For typical charging conditions the optimal cell gap is in the range of 0.3 and 0.4 cm at 20°C and 50°C, respective-

ly. Using these cell gaps and assuming a dissolved chlorine concentration of 1 g/ℓ during charge, the predicted electrochemical energy efficiency lies in the range of 0.84-0.87. Although different conditions during charge will give different efficiencies, the optimal cell gap will not vary significantly. Higher chlorine concentration will generally result in a larger cell gap for maximum energy efficiency.

The optimal cell gap corresponds to a range where the forced convection is relatively weak and the bubble-induced convection opposes the forced and natural convections. Although the present optimization is for the charging process, a similar approach can be applied for the discharge process and for the entire cycle.

REFERENCES

1. Development of the Zinc-Chloride Battery for Utility Applications, RP226-3: Interim Report. Palo Alto, Calif: Electric Power Research Institute, April 1979. EM-1051.

2. Henriksen, G., S. Kodali, J. Jorne, and C. Warde. "Zinc Electrode Current Efficiency in Zinc-Chlorine Hydrate Batteries: I. Theoretical Aspects.", Extended Abstract No. 374, 155th Meeting of the Electrochemical Society, Boston, May 1979.

3. Kermani, A., J. Jorne, and S. Kodali. "Zinc Electrode Current Efficiency in Zinc-Chlorine Hydrate Batteries: II. Experimental Studies." Extended Abstract No. 378, 155th Meeting of the Electrochemical Society, Boston, May 1979.

4. Henriksen, G., S. Kodali, and J. Jorne. Coulombic Efficiency Modeling of Zinc-Chloride Cells: I. Theoretical Background. Madison Heights, MI.: Energy Development Associates, January 10, 1980, Report No. 53S.

5. C. W. Tobias. J. Electrochem. Soc., 106, 833 (1959).

6. Z. Nagy. J. App. Electrochem., 6, 171-181 (1976).

7. J. T. Kim and J. Jorne. "Mass Transfer of Dissolved Chlorine to a Rotating Zinc Hemisphere in $ZnCl_2$ Solution." J. Electrochem. Soc., 124, 1978, pp. 89-94.

Section 49

CELL GAPS AND ELECTROLYTE COMPOSITIONS FOR EFFICIENCY AND CAPACITY

ABSTRACT

Electrochemical energy efficiency and delivered capacity density are two factors which affect the cost of electricity delivered from zinc-chloride load-leveling batteries. This section presents an experimental evaluation of four cell gaps -- ranging from 0.25 cm to 0.40 cm -- and nine electrolyte compositions -- ranging from 2.5+0+0 to 2.5+4+1 and 2.5+3+2 ($ZnCl_2$ + KCl + NaCl molarities) -- on the electrochemical energy efficiency (ε_e) of zinc-chloride cells at 45 mA/cm^2 current density and 250 mAh/cm^2 charge capacity densities. Two cells with gaps of 0.25 and 0.30 cm delivered 195-212 mAh/cm^2 at ε_e's of 68.4-73.3% using three different electrolytes: 2.5+2+2, 2.5+4+1, and 2.5+3+2. In selected experiments at 50 mA/cm^2 with 2.5+3+2 electrolyte, delivered capacity densities >250 mAh/cm^2 were demonstrated at ε_e's of 73-74%.

INTRODUCTION

Energy-storage batteries for the electric-utility load-leveling application must be economically competitive with other alternatives, such as gas turbines, in terms of the levelized busbar cost of delivered electricity. Capital cost and operating efficiency are two factors which contribute to the cost of electricity delivered from a load-leveling battery. Capital cost of the battery is related to the quantity of energy which can be delivered per unit area of electrode. This translates to the quantity of zinc which can be deposited per unit area of electrode during charge (charge-capacity density or zinc loading) without the growth of dendrites which can cause shorts resulting in loss of coulombic efficiency. The extent to which the zinc is utilized during discharge is the delivered capacity density. Capacity density is usually expressed in mAh/cm^2. The net energy efficiency of the battery directly affects the operating cost of electricity, and it is the ratio of energy delivered during discharge to the energy used during the charging cycle. As this ratio increases, the cost of delivered electricity decreases.

For the successful commercialization of zinc-chloride batteries for the load-leveling application the delivered capacity and electrochemical energy efficiency (ε_e) targets are 200-250 mAh/cm^2 and 75%, respectively. At the present time the battery-stack technology being incorporated into the BEST-battery modules should deliver 165 mAh/cm^2 -- 33 mA/cm^2 for five hours -- at an energy efficiency of 65%. This technology incorporates an inter-electrode cell gap of 0.20 cm. The 250 mAh/cm^2 delivered-capacity density target suggests a current density of 50 mA/cm^2 for a five-hour discharge.

The objective of the present study is to establish the feasibility of achieving the electrochemical energy efficiency of $\sim$75% at a delivered capacity density of 250 mAh/cm^2 at the single-cell level. To this end in the initial evaluation, interelectrode cell gaps -- 0.25, 0.30, 0.35, and 0.40 cm -- and nine different electrolyte compositions were evaluated in terms of electrochemical performance at delivered-capacity densities of 200 mAh/cm^2. The electrolyte compositions were selected on the basis of their physical properties, e.g., chlorine solubility and conduc-

tivity (Sections 37-41). The electrode gaps similarly were suggested by the coulombic efficiency studies (Sections 42-47). Analysis of variance was used to establish the statistical significance of the selected cell gaps and electrolyte formulations on electrochemical performance. Additional experiments were carried out based on the optimized conditions to establish the energy efficiency and capacity density targets.

EXPERIMENTAL

Materials Used

The salts used in this study, sodium chloride and potassium chloride, were analytical reagent grade. The zinc chloride stock solution (∿5M) was prepared at EDA by the reaction of chlorine gas with 99.99+% pure zinc metal. The concentrated hydrochloric acid used to adjust the pH of the electrolytes was also analytical reagent grade. Chlorine gas was supplied by Matheson Gas Products.

Test Equipment

Four small two-volt cells consisting of one "profiled" porous-graphite chlorine electrode (PG-60) and two zinc electrodes (ATJ) with interelectrode spacing of 0.25 cm, 0.30 cm, 0.35 cm, and 0.40 cm were used. The test cell is illustrated in Figure 49-1.

The profiled porous-graphite electrode pairs were formed by gluing two machined electrodes together to form a cavity. The outer surfaces of the zinc electrodes were coated with Kynar™. Electrolyte was circulated through the cells using a small gear pump. Electrolyte temperature was controlled using a heat-exchanger placed in line between the cell and the pump. The four cells were manifolded to a chlorine scrubbing tower where chlorine coming from the cells was reacted with sodium hydroxide. Common manifolding of the four cells was used to produce the same vacuum on each cell during charge. The pH measurements were performed using a temperature controlled Corning Scientific pH meter, model 12. Specific gravity measurements were made using ERTCO hydrometers calibrated at 60°/60°F.

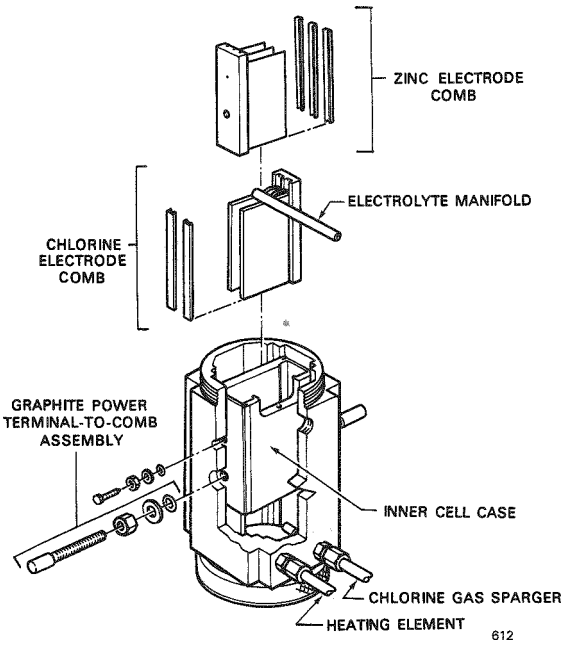

Figure 49-1. Test cell used for evaluation of cell geometry and electrolyte compositions.

Procedure

The electrolytes were prepared in molar concentrations. Salts were weighed-out on an Ohaus triple-beam balance (sensitivity ±0.1 g). Zinc chloride electrolyte of 2.5M concentration was prepared from the stock zinc-chloride (∿5M) solution. The specific gravity of the desired electrolyte composition was calculated from Eq. 49-1 (see Section 37). The desired electrolyte compositions were prepared by weighing and adding the appropriate quantities of KCl and NaCl to a known volume of assayed zinc chloride solution and then diluting with distilled water to obtain the proper specific gravity. The initial zinc chloride concentration was kept constant at 2.5M in all runs while the NaCl and KCl concentrations were changed. A low level of proprietary leveling agent was used in all of the electrolyte formulations.

$$\text{Specific gravity} = 1.027 + 0.091\ M_1 + 0.0353\ M_2 + 0.027\ M_3 \qquad (49\text{-}1)$$

where

$\underline{M}_1$ = Molarity of zinc chloride

$\underline{M}_2$ = Molarity of potassium chloride

$\underline{M}_3$ = Molarity of sodium chloride

Initially and between electrolyte changes the cells were rinsed three to four times with 250 ml of the electrolyte that was to be tested. After the rinsing, 350 ml of the same electrolyte was placed into each of the four cells. The 350 ml was calculated from Eq. 49-2 for 1.5 moles/ℓ zinc swing during a 5.5-hour charge at 45 mA/cm^2 assuming a charge coulombic efficiency of 90%.

$$\frac{(5.625\ \text{Amps})\ (5.55\ \text{h})}{(53.6\ \text{Ah/mol})\ (1.5\underline{M}/\ell)}\ (0.90) = 0.35\ell \qquad (49\text{-}2)$$

Prior to initiation of the charge cycle, electrolyte flow rates were adjusted to 2.2 ±0.2 cm^3/cm^2.min and the temperature was brought to 30°C. The temperature was maintained at 30° ±2°C during charge using a Variac controlled heat exchanger. Cells were sealed with glass plates and excess chlorine was sparged into the electrolyte sump to ensure saturation. Vacuum was obtained by the aid of the vacuum/scrubbing system illustrated in Figure 49-2. The exhaust gas from the scrubber was connected to a water aspirator to suction the air from the system initially and maintain a vacuum on the cells during charge. NaOH was pumped through the packed tower at a flow rate sufficient to react with the counter flow of chlorine coming from the cells to yield NaOCl. This vacuum/scrubber system provided a 37 ±1 cm Hg vacuum in the cells during charge.

The cells were charged at a constant current density of 45 mA/cm^2 for 5.55 hours to achieve a charge capacity density of 250 mAh/cm^2. Specific gravity and pH measurements were made before and after the charge cycles. Cells were discharged on the day following the charge. The discharges were conducted at atmospheric pressure and 40° ±2°C temperature at the same current density. The flow rate of the electrolyte was the same as charge and excess chlorine was fed into the cells to ensure saturation.

The amp-min counts and corresponding cell voltages were recorded every 15 minutes, during both charge and discharge. Sufficient data were obtained to estimate the mean charge and discharge voltages. The amp-min count corresponding to 1.6 volt at 5 mA/cm^2 during discharge was used to calculate the usable coulombic efficiency.

RESULTS

A total of nine electrolytes were evaluated in charge-discharge cycles and the pertinent test results are listed in Table 49-1. In all, a total of 36 round-trip cycles were obtained.

A limited number of experiments were carried out to maximize the capacity density while maintaining the high electrochemical energy efficiency. A higher current density was used in these experiments to shorten the charging time. These data are reported in Table 49-2.

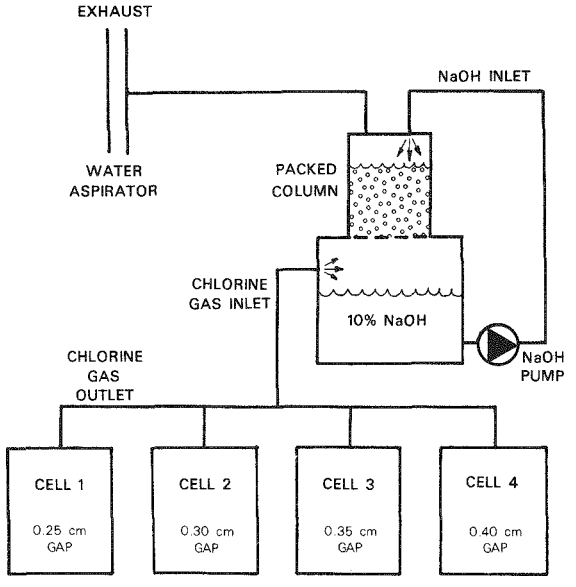

Figure 49-2. Vacuum/scrubbing system used to establish the partial vacuum (-37 ±1 cm Hg) on all four test cells during the charge portion of each cycle.

Table 49-1

ELECTROCHEMICAL ENERGY EFFICIENCY AND DELIVERED CAPACITY DENSITY AS A FUNCTION OF ELECTROLYTE COMPOSITION AND INTER-ELECTRODE SPACING (CURRENT DENSITY OF 45 mA/cm^2)

Run No.	Electrolyte Composition (M) $[ZnCl_2]+[KCl]+[NaCl]$	Cell Gaps (cm)	ε_e (%)	Delivered Capacity Density (mAh/cm^2)
1	2.5 + 0 + 0	0.25	64.4	186.75
		0.30	65.3	193.25
		0.35	61.5	189.50
		0.40	61.3	194.25
2	2.5 + 2 + 0	0.25	68.4	194.75
		0.30	69.6	203.00
		0.35	66.9	200.00
		0.40	67.9	202.75
3	2.5 + 1 + 1	0.25	64.7	185.00
		0.30	66.7	195.30
		0.35	62.7	190.50
		0.40	60.8	189.25
4	2.5 + 3 + 1	0.25	63.4	181.25
		0.30	64.5	186.50
		0.35	58.6	176.25
		0.40	58.0	175.35
5	2.5 + 4 + 1	0.25	72.2	205.50
		0.30	73.3	211.75
		0.35	70.1	209.50
		0.40	68.8	205.75
6	2.5 + 2 + 2	0.25	63.9	185.50
		0.30	69.9	205.00
		0.35	65.3	200.50
		0.40	63.0	193.50
7	2.5 + 3 + 2	0.25	69.8	201.85
		0.30	71.4	210.50
		0.35	64.6	200.50
		0.40	63.9	197.25
8	2.5 + 3 + 0	0.25	62.2	178.75
		0.30	69.0	199.00
		0.35	64.0	190.50
		0.40	65.1	192.75
9	2.5 + 2 + 1	0.25	61.5	178.21
		0.30	69.4	202.25
		0.35	60.9	185.00
		0.40	63.0	191.52

Table 49-2

PERFORMANCE DATA FOR CELLS WITH HIGH CAPACITY DENSITY
(CURRENT DENSITY 50 mA/cm^2)

Electrolyte $ZnCl_2$+KCl+NaCl (mole/ℓ)	Electrode Gap (cm)	Coulombic Efficiency (%)	Voltaic Efficiency (%)	Energy Efficiency (%)	Delivered Capacity Density (mAh/cm^2)
2.5 + 3 + 0	0.30	79.7	87.6	69.8	239
2.5 + 3 + 2	0.25	85.5	85.6	73.2	256
2.5 + 3 + 2	0.40	86.4	85.8	74.0	259

DISCUSSION

Energy Efficiencies

Figure 49-3 shows the calculated electrochemical energy efficiencies for the cells using different electrolytes. Runs 2, 5, and 7 (Table 49-1) produced the highest average energy efficiencies. The results are fairly consistent and an analysis of variance was performed on the data given in Table 49-1. The analysis of variance is summarized in Table 49-3.

The calculated F values exceed the critical F value in both cases showing that both cell gap and electrolyte composition affect the electrochemical energy efficiency. The Duncan multiple-

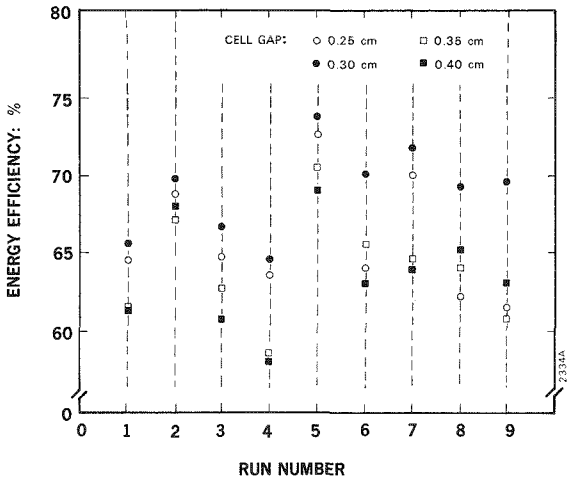

Figure 49-3. Energy efficiency vs. nine electrolyte compositions.

Table 49-3

ANALYSIS OF VARIANCE OF CELL EFFECTS AND ELECTROLYTE EFFECTS ON ROUND-TRIP ENERGY EFFICIENCIES

Source of Variation	Degree of Freedom	Sum of Squares	Mean Square	F calculated	$F_{0.01}$ Critical
Cell	3	156.8	52.3	19.5	4.72
Electrolyte	8	294.7	36.8	13.7	3.36
Error	24	64.3	2.7		

range test pairs the 0.40, 0.35, and the 0.25 cm gap cells and the 0.30 cm gap cell stands alone. The Duncan multiple-range test was also applied to the electrolytes and the results are summarized in Table 49-4. Note that the run numbers are listed in order of increasing energy efficiency.

The lines under the means indicate electrolytes which give results that are statistically indistinguishable from one another. Thus, the electrolyte, corresponding to runs 3, 9, and 8 produce similar energy efficiencies. The electrolyte composition with 2.5M $ZnCl_2$ + 4M KCl + 1M NaCl gives the highest energy efficiency with >200 mAh/cm^2 delivered capacity density. The 2.5M $ZnCl_2$ + 3M KCl + 2M NaCl electrolyte also gives satisfactory results.

Capacity Density

The electrolyte compositions 2.5M $ZnCl_2$ + 4M KCl + 1M NaCl and 2.5M $ZnCl_2$ + 3M KCl + 2M NaCl consistently yielded delivered capacity densities $\geq$200 mAh/cm^2, as shown in Table 49-1, while giving energy efficiencies of about 70%. In the second group of experiments, for which the data are reported in Table 49-2, capacity densities of >250 mAh/cm^2 were attained at energy efficiencies of 73-74% with the electrolyte composition of 2.5M $ZnCl_2$ + 3M KCl + 2M NaCl. These results establish the feasibility of achieving the electrochemical energy efficiency target of 75% while attaining the delivered capacity density target of 250 mAh/cm^2.

CONCLUSIONS

The results of this study show that both the cell gap and the electrolyte composition affect the energy efficiency of a zinc-chloride battery.

This study has also identified three electrolyte compositions, namely, 2.5+2+0, 2.5+4+1 and 2.5+3+2 molar concentrations of $ZnCl_2$+KCl+NaCl, respectively, that produce 70% electrochemical energy efficiency and >200 mAh/cm^2 capacity density. From energy efficiency considerations, the 0.30 cm gap appears to be most promising.

This work has established the feasibility of achieving 74% electrochemical energy efficiency while obtaining delivered capacity densities $\geq$250 mAh/cm^2. Optimization studies involving chlorine partial pressure during charge and discharge, current density, temperature and flow rates should be performed using the most promising electrolyte formulations and cell gaps.

Table 49-4

ELECTROLYTE COMPARISONS BASED ON THE DUNCAN MULTIPLE-RANGE TEST

Run #	4	1	3	9	8	6	7	2	5
Mean ε_e	61.1	63.1	63.6	63.1	65.1	65.5	67.4	68.2	71.1

Section 50

SHORT-CIRCUIT CHARACTERISTICS OF ZINC-CHLORIDE CELLS

ABSTRACT

The transient discharge characteristics of a zinc-chloride cell into a 17-milliohm load have been investigated to simulate an accidental short-circuit of a zinc-chloride battery in operation. The peak current, which lasts several tens of milliseconds, was limited solely by the internal resistance of the cell and the external load. The shape of the transient decay curve approximates that of a resistance-capacitance series circuit. The number of coulombs discharged during a transient depends on the amount of chlorine sorbed on the chlorine electrode. On open circuit, this amounts to about 3 coulombs per cm^2 of chlorine electrode. The results indicate that a 20-volt, 50-kWh battery can deliver an instantaneous current of about 35,000 amperes into a zero-resistance load.

INTRODUCTION

The zinc-chloride battery is somewhat unique in that only one electrochemically active material, zinc, is stored in the battery stack. Because the chlorine electrode does not store its own reactant, electrolyte circulation is essential for the discharge of the battery. The sustained discharge rate of the battery is limited by the rate at which chlorine is supplied to the electrode. A substantial amount of data on the steady-state operation under a variety of conditions are available. The transient response characteristics of the battery under conditions approaching an external short-circuit have not been evaluated.

In commercial applications, accidental short-circuiting of the battery terminals may occur. Such external shorts will cause extremely high currents to flow through the battery and its terminals. The high current will cause resistance heating in the terminals. If they become hot enough, the seal between the terminals and the battery case may be destroyed, causing physical damage to the battery. The amount of terminal heating depends on both the magnitude and duration of the current transient. The objective of the work presented in this section was to experimentally determine the transient current characteristics of a zinc-chloride cell under conditions approaching a no-load fault, i.e., short-circuit.

A 40-Wh zinc-chloride test cell was used in this study. All external and contact resistances were minimized to simulate a no-load fault under both conditions where the electrolyte circulation was continued and where it was terminated. The results were employed to develop an equivalent circuit for zinc-chloride cells. In addition, the test data allowed prediction of the instantaneous no-load short-circuit current for a 50-kWh battery module. A series of experiments, performed subsequently to determine the short-circuit current for the refurbished 45-kWh module, is described in Section 19.

EXPERIMENTAL

Test Equipment

The test cell contained one chlorine-electrode pack and two end-zinc electrodes. The chlorine electrodes were made of Union Carbide porous graphite

grade-60 (PG-60). The zinc electrodes were Union Carbide dense graphite, ATJ. All electrode-to-bus connections were press-fitted. The current collectors were made of metal-filled graphite and screwed into the buses. The external load circuit consisted of 34 inches of #8 stranded wire, a 2-milliohm shunt, and a mercury pool that acted as a switch. A schematic of the circuit is shown in Figure 50-1.

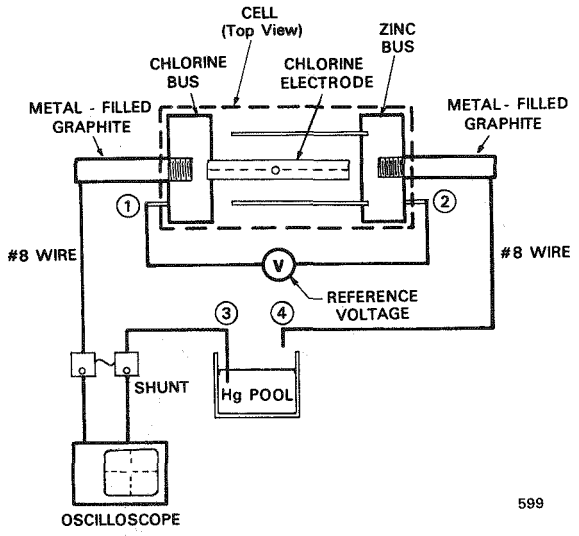

Figure 50-1. Schematic of the external load circuit.

Experimental Procedures

The resistance of the external circuit was determined by applying current at points 3 and 4 in Figure 50-1, and by measuring the voltage at points 1 and 2 and at points 3 and 4 while the battery was charging. The voltage (IR) drop in the external circuit was obtained by subtracting the reference voltage from the voltage obtained at points 3 and 4. The external-circuit resistance was determined by dividing the IR drop by the applied current. The external circuit resistance was measured at three different currents and a value of 17.8 ±0.2 milliohms was obtained.

The internal resistance of the cell was calculated from the available data. For example, with the cell gap of 2.5 mm and the geometric area of 125 cm^2 and the electrolyte conductivity of 0.2 mho/cm (2.5M $ZnCl_2$ + 2M KCl) the cell resistance was 10 milliohms.

To simulate battery module conditions, the battery contained a 2.5M $ZnCl_2$ + 2M KCl electrolyte. The cell was charged for four hours at 32 mA/cm^2 before the transient measurements were made. The measurement sequence was to operate the battery in a normal charge or discharge mode for several minutes and then remove the rectifier leads, placing the cell at open circuit. The cell was then connected to the load by placing the shorting contact (point 4, Figure 50-1) into the mercury pool. The appropriate transient response was recorded on a Hewlett-Packard HP-1741A oscilloscope using either an internal or external trigger.

RESULTS AND DISCUSSION

Short-Term Transient Response

The transient response of the cell to the load is shown in Figure 50-2. The peak current was about 72 amperes and did not diminish in the first 16 milliseconds. The rate of rise was very fast and appeared to be limited by the rate at which the electrical contact was made. The absence of current spikes or ramps suggests that the circuit is a predominantly resistive network.

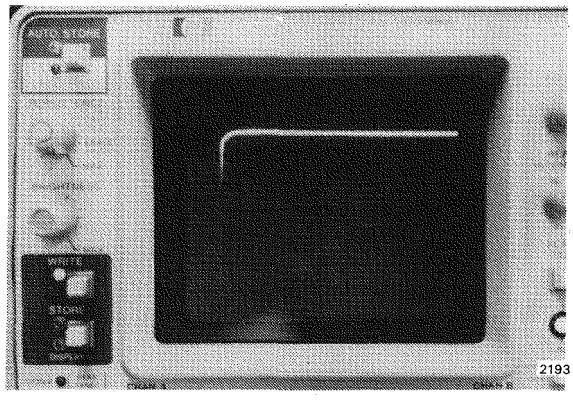

Figure 50-2. Oscilloscope representation of the transient response of the cell to the load. Time base: 2 msec/division. Current: 25 A/division.

The oscillographic traces of the cell current and voltage are shown in Figures 50-3 and 50-4, respectively. Both traces were taken with the electrolyte pump operating. A limiting current of about 37 amperes was sustained after 10 seconds. The corresponding voltage trace is shown in Figure 50-4. Again, it is noted that the peak output voltage was maintained for less than 0.2 seconds.

The internal and external resistances may be calculated from the instantaneous current and voltage shown in Figures 50-2, 50-3, and 50-4. The cell resistance, R, is equal to $(E^{O}-V)/I$. The external impedance is equal to V/I. From Figures 50-2 and 50-3, the instantaneous, or peak, current was measured to be 72 amperes at a battery voltage of 1.2 volts. From these values, the external load was calculated to be 1.2/72 amperes = 16.7 milliohms, and the cell resistance was calculated to be 0.9/72 = 12.5 milliohms. These values are in good agreement with the previously determined values of 18 milliohms (steady-state) and 10 milliohms (calculated for 2.5M $ZnCl_2$ + 2M KCl electrolyte), respectively.

In a second series of tests, the electrolyte in the cell was changed to increase the electrolyte conductivity. Also, a strip-chart recorder was connected across the reference terminals on the cell so that accurate voltage traces of the entire transient could be obtained. The peak-current transient for this electrolyte is shown in Figure 50-5. For the first 2 milliseconds, a peak current of 81-82 amperes is observed and, at the end of 18 milliseconds, the current dropped slightly to a value of about 78 amperes.

In Figure 50-6, a typical voltage trace for the entire transient is shown. For the time interval of 0.02 seconds to 0.2 seconds, the voltage has been approximated. From the voltage trace, the cell voltage during the peak is measured to be 1.40 volts. From this value, and the measured open circuit value of 2.13 volts, the cell resistance and load resistance were found to

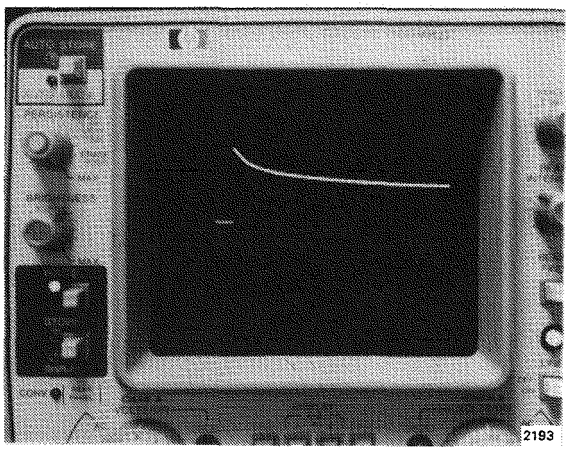

Figure 50-3. Oscillographic trace of the cell current, with the peak output voltage maintained for less than 0.2 seconds. Time base: 1 sec/division. Current: 25 A/division.

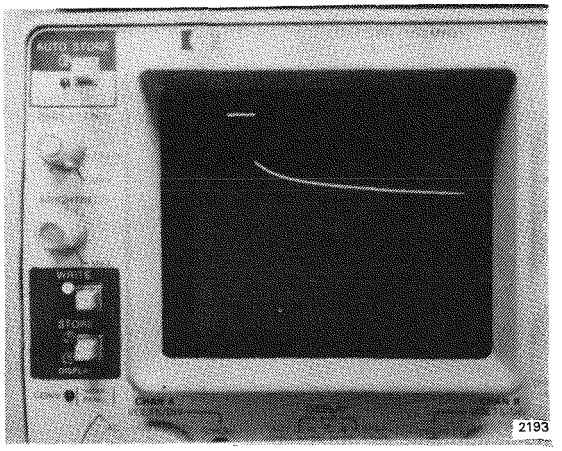

Figure 50-4. Oscilloscope reading of the voltage transient across the cell terminals. Time base: 2 sec/division. Voltage: 0.5 V/division.

be 9 milliohms and 17 milliohms, respectively. These values are again in agreement with those measured earlier.

Long-Term Transient Response

The transient characteristics were determined for two different conditions. For the first test, the electrolyte pump remained on for the duration of the experiment. Under these conditions, chlorine was continuously

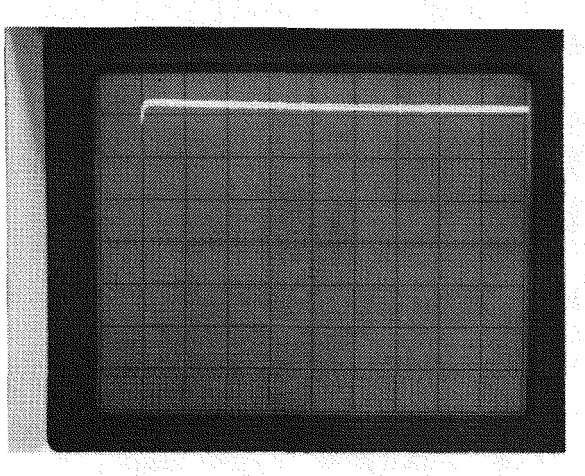

Figure 50-5. Oscillographic trace of the cell current transient when connected to a 17-milliohm load. Time base: 0.2 msec/division. Current: 25 A/division.

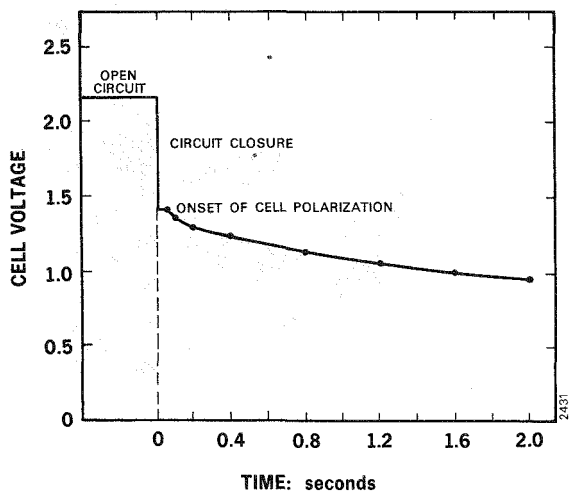

Figure 50-6. Cell voltage transient when test cell is connected to a 17-milliohm load.

supplied to the electrode. Non-zero limiting values for the current and voltage were approached. In the second group of experiments, the pump was turned off before the external load was connected across the cell. In this case, the voltage and current values rapidly approached zero. The polarization characteristics of the cell under the two conditions can be compared by constructing characteristic impedance curves for each condition. The impedance, or cell resistance at a point in time, is defined as the voltage drop across the cell divided by the current passing through the cell.

In Figure 50-7, the cell resistance thus calculated is plotted as a function of the number of coulombs discharged. Thus, the calculated cell resistance is independent of the external load and time. It is seen that both curves (pump on or pump off) are virtually identical for the first 175 coulombs of discharge. With the pump off, a total of 425 coulombs of charge passed through the cell in 16 seconds. Calculations indicate that the amount of chlorine available from the electrolyte is 25-50 milligrams, or 70-140 coulombs. This suggests that the principal source of chlorine for the transient is the chlorine sorbed on the electrode and it amounts to 280-350 coulombs.

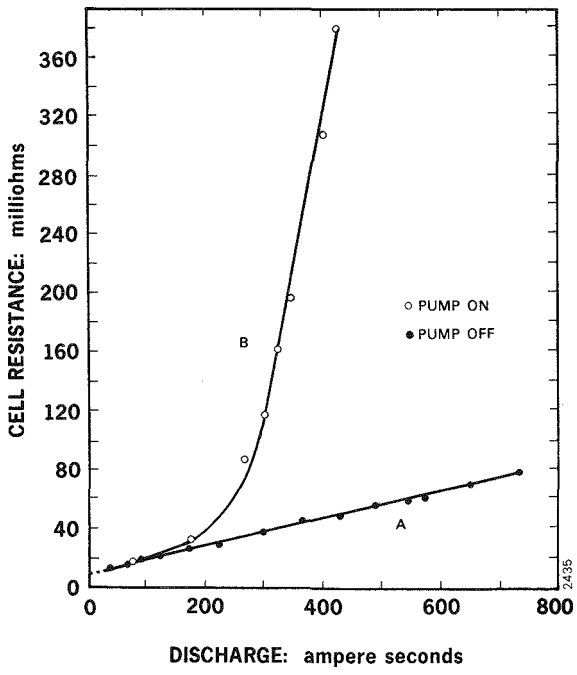

Figure 50-7. Cell resistance as a function of ampere-seconds of discharge into a 17-milliohm load.

Equivalent Circuit Analogy

With the pump off, the cell can be electrically characterized as a series circuit containing a resistor and a capacitor. The capacitor represents the stored charge on the chlorine electrode. The current decay during the discharge of such a circuit is given by:

$$I = I_o e^{-t/RC} \qquad (50\text{-}1)$$

where I = current at time, t

t = time, seconds

I_o = current at time, t = 0

R = total resistance of the circuit (internal + external)

C = capacitance, farads

From Eq. 50-1, a graph of ln I_o/I versus time should yield a straight line with a slope equal to t/RC. The transient data are plotted in a similar fashion to produce the curve in Figure 50-8. A straight line is obtained for the first eight seconds of the transient and a linear regression analysis of this linear portion yields a slope of 0.21.

For R = 0.026 ohms, the equivalent value of C is 183 farads. The 183 farads may be thought of as representing the available chlorine for charge transfer during a transient. Thus, it is very similar to a capacitor. For the test cell, Eq. 50-1 becomes:

$$I = I_o e^{-t/[(R_i+R_e)(183)]} \qquad (50\text{-}2)$$

where R_i = internal resistance of the battery

R_e = external load resistance

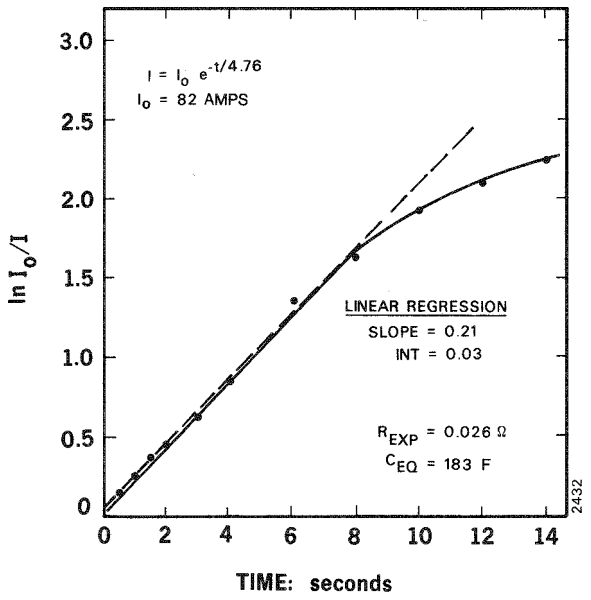

Figure 50-8. Resistance capacitance circuit analogy. $I = I_o e^{-t/4.76}$, I_o = 82 amps. Equation describes the transient for the RC network where R = 26 milliohms and C = 183 farads.

In Table 50-1, the stored energy and charge calculated by equivalent circuit analogy are compared to the experimental transient results. The agreement is very good and therefore, such an analogy would be useful in predicting the electrical characteristics of transients in zinc-chloride cells or batteries.

Table 50-1

COMPARISON OF RC CIRCUIT TRANSIENT RESULTS WITH EXPERIMENTAL TRANSIENTS

Parameter	RC Circuit	Experimental
Energy (watt-seconds)	403	420 (by integration)
Stored Charge (coulombs)	390	425 (by integration)
Time Constant (sec)	4.76	4.5

CONCLUSIONS

- The transient peak current from a zinc-chloride cell is given by $I_p = E^o/R$ where E^o is the open circuit voltage and R is the total resistance.

- The current decay during a short-circuit is given by $I = I_o e^{-t/RC}$. Where I is the cell current, I_o is the instantaneous current at time t = 0, R is the total of internal cell resistance and the load resistance, and C the capacitance due to the sorbed chlorine on the porous-graphite chlorine electrode.

- On open circuit, the chlorine electrode contains about 3 coulombs of sorbed chlorine per cm^2 of geometrical area.

- The discharge transient from the cell can be analyzed as an electrical transient from a series resistance-capacitance network. The calculated energy of 400-450 watt-seconds, and a charge of 390 coulombs from the RC circuit analysis are in good agreement with the experimental results.

- The internal resistance of a 50-kWh module is estimated to be 0.6 milliohms. With an open circuit voltage of 21.1 volts, a zero resistance external short could result in a transient current peak of 35,000 amperes.

- Because of the limited amount of chlorine avilable on the chlorine electrode, a sustained short-circuit should present no safety hazards if the electrolyte pump is turned off.

Section 51

ELECTRODE SIZE STUDY

ABSTRACT

Larger electrodes in zinc-chloride batteries provide the potential for lowering the capital cost by utilizing fewer parts. On theoretical grounds, use of larger electrodes is feasible. The present section describes an on-going effort to evaluate the performance characteristics of larger electrodes -- 14 cm x 19 cm -- as compared to the normal 6.6 cm x 10 cm electrodes. At the present state of development, a 6% lower energy efficiency is observed with the larger electrodes compared to that for the smaller electrodes. The voltaic and coulombic efficiencies are each lower by $\sim$ 4%. The zinc deposit thickness variation of 16-20% with the larger electrodes is in the same range as that for the smaller electrodes. Work continues on establishing the technical feasibility of larger electrodes.

INTRODUCTION

Zinc-chloride batteries in the electric-utility load-leveling application must be economically competitive with other options, such as gas turbines, in terms of the cost of delivered electricity. The capital cost of the battery is related to the quantity of energy which can be delivered per unit area of the electrode. This is dependent on the electrochemical energy efficiency and the capacity density or the zinc-loading. In the capital costs for a battery module the electrode comb assemblies assume a significant proportion, 47% in the present estimates. In the operating cost, again, the largest cost factor is the amortized capital cost. The energy efficiency (delivered energy/used energy) is also an important factor in determining the operating cost. For the commercial load-leveling application, the electrochemical energy efficiency target is $\geq$75% at a delivered capacity density of >200 mAh/cm^2.

A substantial amount of effort has been devoted at Energy Development Associates (EDA) to qualify alternative materials to lower the overall capital costs of the battery. There is a small on-going effort to increase the size of the electrodes thereby potentially lowering the capital costs, without offsetting the performance of the zinc-chloride battery. A capital cost reduction can be affected by using a smaller number of electrodes, frames, and the associated hardware parts. The present battery module consists of 6.6 cm by 10 cm electrodes. In this study, electrodes having four times the area and measuring 14 cm by 19 cm, are being evaluated. This section summarizes the present status of this on-going effort.

BACKGROUND

The main purpose of this study is to increase the electrode size without significantly affecting the electrochemical energy efficiency or the capacity density. Electrochemical energy efficiency is the product of the coulombic efficiency (ε_c) and the voltaic efficiency (ε_v). The capacity density is directly related to the zinc loading during charge.

The voltaic efficiency is dependent on the ohmic drops in the electrodes and

contacts, the IR drop in the electrolyte and the non-ohmic polarizations at the electrodes. Provided the chlorine electrodes are equally well activated, increasing the electrode size affects the voltaic efficiency only via the larger IR drops in the electrodes.

The coulombic efficiency loss in a zinc-chloride cell is the result of the mass-transfer-limited reaction of dissolved chlorine with electrodeposited zinc (cf Section 42). Mass transfer of chlorine is supported by three sources of fluid motion in the inter-electrode gap: (a) forced convection by the electrolyte flow in the inter-electrode gap; (b) natural convection generated by the concentration or density difference caused by the depletion of ionic zinc at the zinc electrode, and (c) bubble-induced convection of electrolyte by the buoyancy effects created by the evolution of gaseous chlorine at the chlorine electrode.

As discussed in Sections 42 and 43, corrosion-current density or the coulombic inefficiency due to forced convection is not dependent on the height of the electrode (Eq. 42-8). If the electrolyte flux ($ml/cm^2/min$) is held constant, the contribution of forced convection should not change with the width of the electrode. The contribution of natural convection to the corrosion-current density is proportional to $h^{-0.25}$ where h is the height of the electrode. The contribution of bubble-induced convection to corrosion-current density is estimated to be proportional to $h^{0.1}$ (1). Thus, increasing the height dimension should not affect the coulombic efficiency drastically. Increasing the electrode width should not affect the coulombic efficiency substantially except when the variation in zinc deposit thickness is large. A wide zinc deposit thickness distribution leads to higher local current densities which promote zinc dendrites. Zinc dendrites can cause short-circuits lowering the coulombic efficiency.

Capacity density or the zinc loading is a function of the current density distribution. Current-density distribution is a strong function of the width, as discussed below. A schematic of a single cell in Figure 51-1 (2) shows the zinc distribution during a full charge-discharge cycle. Immediately after initiation of charge, the current-density is uniform because of the similarity of the sheet resistance of the graphite electrodes. Soon after the initiation of charge, current-density distribution becomes asymmetrical and is determined by the resistance across the chlorine electrode width because the zinc electrode substrate is coated with the more-highly conductive zinc metal. At the end of charge, the zinc deposit is consequently thickest near the chlorine-electrode busbar. This increases the probability of edgewise dendrite formation due to the higher local current density. Thus, the current distribution along the electrode width can determine the capacity density of a zinc-chloride cell especially when using larger electrodes.

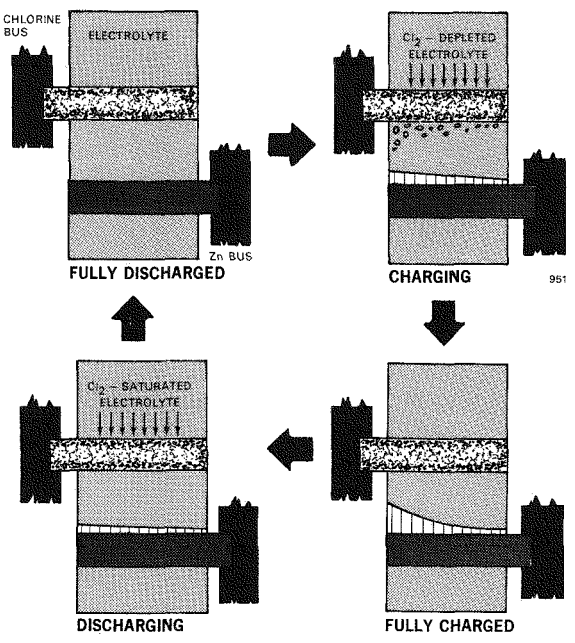

Figure 51-1. Sequence of schematics showing the distribution of zinc on the zinc-electrode substrate during a full-charge-discharge cycle.

Coughlin and Warde (3) have developed a model based on network analysis theory for the current-density distribution as a function of the various parameters, such as, electrode width, thickness, graphite conductivity, electrolyte resistivity, and the inter-electrode gap. According to this model, the current-density distribution can be calculated from the equation:

$$J_t = \frac{m\ I}{h} \frac{\cosh(mW-my)}{\sinh(mW)} \qquad (51\text{-}1)$$

J_t is the current density, I, is the total current, h is the cell height, W is the width of the electrode, y is the distance from the electrode-bus along the chlorine electrode, and m is given by:

$$m = \frac{\rho_g}{\delta_g \cdot \rho_t \cdot \delta_e} \qquad (51\text{-}2)$$

where ρ_g is the chlorine-electrode resistivity, ρ_t is the compound resistivity (which includes the non-ohmic and ohmic contributions), δ_g is the chlorine-electrode thickness, and δ_e is the inter-electrode gap.

Based on Eq. 51-1, the variation of current density as a function of chlorine electrode width is plotted in Figure 51-2. Only the width parameter was varied while maintaining other parameters constant. It can be seen that the current-density distribution becomes wider as the cell width is increased. In Figure 51-3, current-density variations for two thicknesses of chlorine electrodes are given. This figure shows that a more even current-density distribution, and hence, a more even zinc deposit thickness can be obtained by using a thicker chlorine electrode. On theoretical grounds, there are no reasons which preclude the use of larger electrodes for zinc-chloride cells.

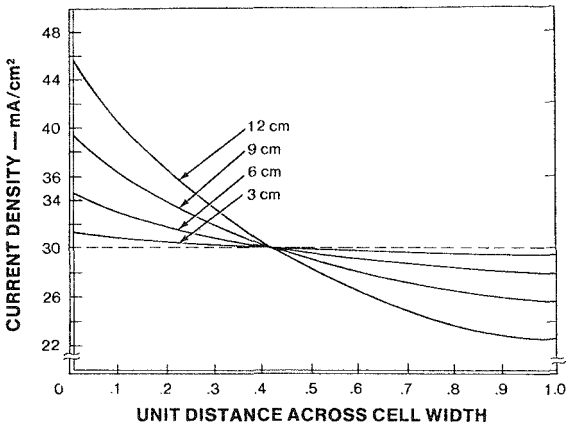

Figure 51-2. Current-density distribution as a function of cell width.

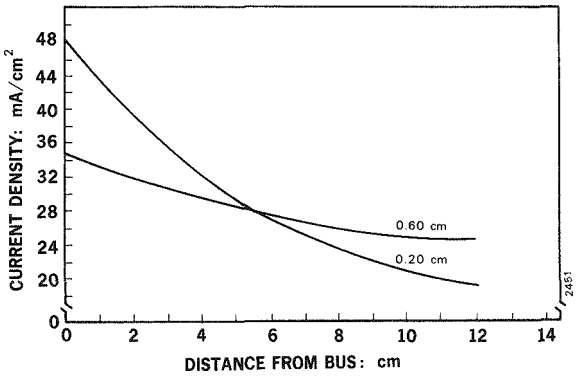

Figure 51-3. Variation of current density distribution as a function of cell width for two thicknesses of chlorine electrode.

EXPERIMENTAL

Materials Used

The potassium chloride and hydrochloric acid used in this study are of analytical reagent grade. The zinc chloride stock solution (∿5M) is prepared at EDA by the reaction of chlorine gas with 99.99+% pure zinc metal. Chlorine gas used in the study is supplied by Pennwalt Corporation. The graphite material is supplied by Union Carbide.

Test Equipment

The test cell consists of one porous graphite (PG-60) chlorine electrode and

one dense graphite (ATJ) zinc electrode as depicted in the expanded view in Figure 51-4. The active area of the electrode is 266 cm^2. The chlorine electrode assembly consists of a profiled dense graphite block in which a Kynar spacer is placed for adjusting the gap behind the porous-graphite electrode. The porous-graphite plate is held tightly against the edges of the dense graphite block by a PVC frame which in turn is bolted to the dense graphite block. The porous graphite electrode makes electrical contact only on one vertical edge of the dense-graphite block to simulate the contact a chlorine electrode makes with the bus in a comb assembly. An assembled chlorine electrode is shown in Figure 51-5. After the assembled chlorine electrode is tested for the ohmic voltage drop across the contact, it is placed in a PVC case along with a PVC spacer and the zinc electrode (see Figure 51-6). The electrodes and the spacer are pressed together by a titanium pressure plate in the PVC case. The electrolyte sump is below the cell and the electrolyte is circulated by a titanium micropump.

The test cell system is shown in Figure 51-6. The electrolyte temperature is controlled by an electric heater placed in the sump. The electrolyte is saturated with chlorine by sparging chlorine into the sump. To prevent entrained gas bubbles from entering the cell, a gas-liquid separator is provided.

The electrolyte consists of 2.5M $ZnCl_2$ + 2M KCl with a small amount of a leveling agent. Before the initiation of charge, the electrolyte flow rate is adjusted to 2 ml/cm^2min. The electrolyte temperature is adjusted to 30°C and the cell case is sealed with a glass plate. Vacuum is obtained by an aspirator and adjusted to 0.5 atm. Electrolyte pH, specific gravity and chlorine concentrations are measured before and after charge. The discharge cycles are conducted at ambient pressure and a temperature of 40°C.

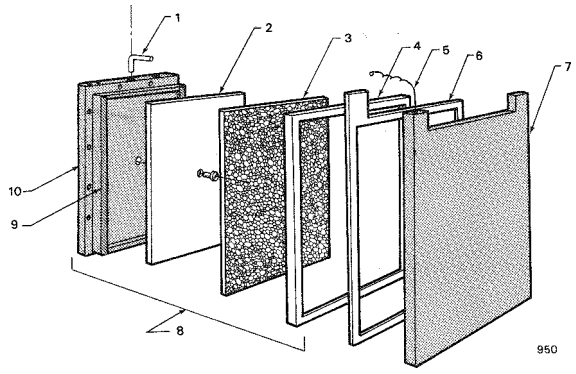

1 GAS VENT
2 KYNAR SPACER
3 CHLORINE ELECTRODE SUBSTRATE (POROUS GRAPHITE)
4 ELECTRODE SUPPORT FRAME
5 VOLTAGE PROBE
6 INTER-ELECTRODE SPACER
7 ZINC ELECTRODE SUBSTRATE (DENSE GRAPHITE)
8 CHLORINE ELECTRODE COMPONENTS
9 BUS-ELECTRODE JUNCTION
10 CHLORINE ELECTRODE BUS (DENSE GRAPHITE)

Figure 51-4. Expanded view of the internal components of the larger electrode test cell.

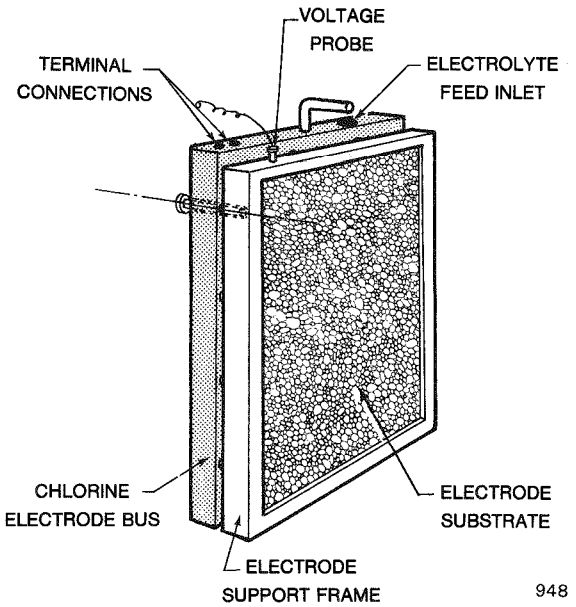

Figure 51-5. A view of the assembled chlorine electrode for the larger electrode (14 cm x 19 cm) test cell.

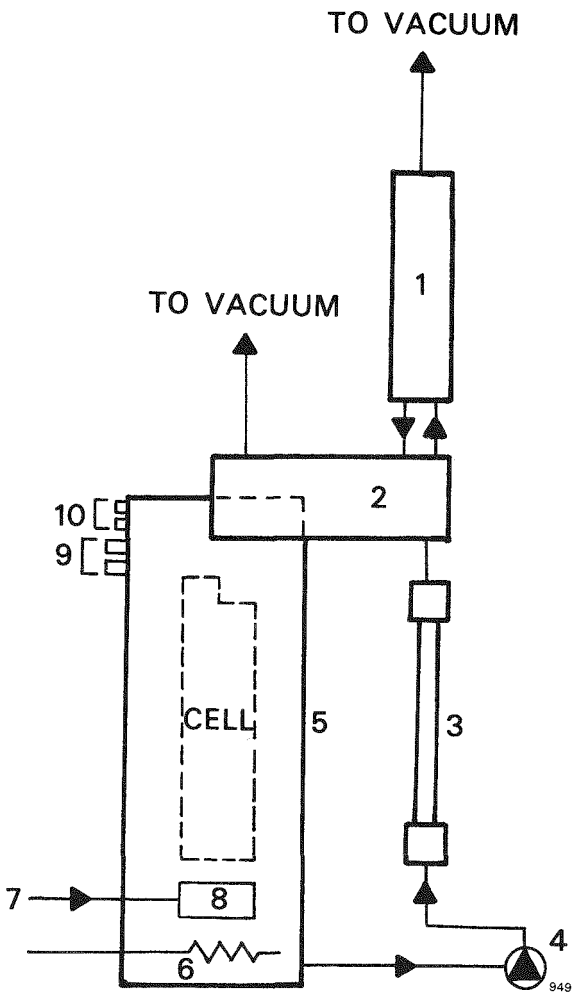

1 GAS SEPARATOR SYSTEM
2 ELECTROLYTE MANIFOLD
3 ELECTROLYTE FLOW METER
4 ELECTROLYTE PUMP
5 CELL CASING
6 ELECTROLYTE HEATER
7 CHLORINE INLET
8 CHLORINE SPARGER
9 WORKING TERMINALS
10 VOLTAGE PROBE TERMINALS

Figure 51-6. A schematic of the larger electrode test cell apparatus.

Full cycle efficiencies are calculated using amp-minute and watt-hour counters. Charge coulombic efficiencies are obtained by removing the zinc deposits from the graphite substrate following charge and weighing the metal. Zinc distribution profiles are made by weighing 1/4 inch diameter discs punched from the zinc plates.

RESULTS AND DISCUSSION

Energy Efficiency

Performance data obtained with the larger electrode cell at several current densities are presented in Table 51-1. Using a 0.40 cm thick porous-graphite chlorine electrode and an electrode gap of 0.30 cm, the electrochemical energy efficiencies are in the range of 60-63%. Smaller electrode cells with this gap and electrolyte typically achieve electrochemical energy efficiencies of 68-70% under similar conditions. At the present state of large-electrode cell development, there appears to be a penalty of about 6% in energy efficiency compared to the data for the smaller cells with similar electrode gap and current density. The voltaic efficiency with the larger cell appears to be about 4-5% lower than that for the smaller cell. This is partly due to the higher ohmic drop in the chlorine electrode of the larger cell. Lower voltaic efficiency may also be partly due to insufficient activation of the porous graphite. The data in Table 51-1 show that the voltaic efficiency drops from 85% to 81% as the current density is increased from 33 mA/cm^2 to 50 mA/cm^2. The coulombic efficiency for the larger cell is also a little lower than that for the small cell by about 4% under comparable conditions. The lowering of coulombic efficiency to the extent observed cannot be explained at this time. In one single experiment, a charge capacity density of 322 mAh/cm^2 was achieved with no short-circuiting due to zinc dendrites.

Zinc Plate Thickness Variation

Zinc plate thickness variation across the width and the height is shown in Table 51-2 for three current densities. These measurements were made at low capacity densities. The zinc thickness

at these capacity densities across the width varies by about 16-20%. At capacity densities of 230 mAh/cm^2 for the small cells, a thickness variation of 18% has been calcalated by theory and verified experimentally (2). Thus, a slightly larger thickness variation will be observed for full capacity density runs with the larger cells as predicted by the cell model (2). There is a small thickness variation along the height which appears to decrease with increasing current density. This is not understood at this time. The zinc plate thickness variation across the width of the cell is shown in Figure 51-7. The variation is almost linear.

Table 51-1

PERFORMANCE CHARACTERISTICS OF THE LARGER ELECTRODE CELL.

- Chlorine Electrode Thickness 0.40 cm;
Interelectrode Gap 0.30 cm -

Current Density mA/cm^2	No. of Cycles	Average Coulombic Efficiency %	Average Voltaic Efficiency %	Average Energy Efficiency %
33	7	71.4	84.9	60.6
40	5	74.5	83.6	62.3
50	3	77.2	81.1	62.6

Table 51-2

ZINC PLATE THICKNESS DISTRIBUTION FOR LARGER ELECTRODES

Current Density mA/cm^2	Capacity Density mAh/cm^2	Charge Coulombic Efficiency %	Deviation Across the Width %	Deviation Along the Height %
33	165	83.5	19.7	7.5
40	153	85.5	19.8	5.1
50	135	87.7	16.0	0.55

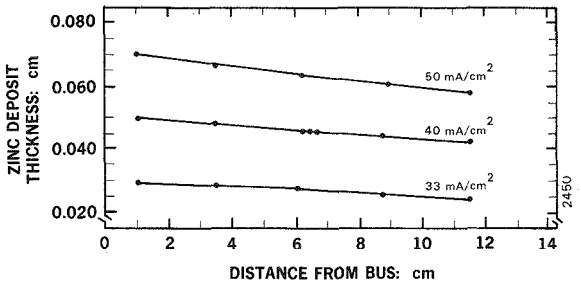

Figure 51-7. Zinc deposit thickness variation across the width of the larger electrode cell at 33 mA/cm^2 at a capacity density of ~150 mAh/cm^2.

STATUS

1. On theoretical basis, increasing the electrode size should not significantly affect the overall energy efficiency. A small decrease is, however expected in the voltaic efficiency due to the IR drop in the porous graphite electrode. Also, a small decrease in the coulombic efficiency is expected due to the increase in height.

2. A larger variation in zinc plate thickness is to be expected across the cell width with the larger electrodes. This may limit the capacity density of the larger electrode cells.

3. At the present stage of development, a decrease of about 6% in the energy efficiency has been observed with 14 cm x 19 cm electrodes compared to 6.6 cm x 10 cm electrodes, under the operating conditions of 0.30 cm cell gap at 50 mA/cm^2 current density. The voltaic efficiency and coulombic efficiency each decrease by about 4-5% with the larger electrodes compared to the smaller ones.

4. At 70% of the capacity density used for smaller cells, the zinc plate thickness for larger electrodes already varies by 16-20% across the cell width. In comparison, the zinc plate thickness varies by 18% across the width of the smaller cells.

5. Work continues on establishing the technical feasibility of using larger electrodes. A more conventional test cell will be designed and built to eliminate problems which may be specific to the present design.

REFERENCES

1. Kermani, A. M.S. Thesis, Department of Chemical Engineering, Wayne State University, February 1980.

2. Development of the Zinc-Chlorine Battery for Utility Applications. Palo Alto, Calif.: Electric Power Research Institute, April 1979. EM-1051. Part IV, Section 31.

3. W. J. Coughlin and C.J. Warde. "Current Distribution in Zinc-Chlorine Batteries." In Proceedings of the Symposium on Battery Design and Optimization, Volume 79-1, 1979.